CHARACTERISING NANOSCALE ORGANISATION OF REPAIR FOCI DURING REPAIR OF DOUBLE STRAND BREAKS USING EXPANSION MICROSCOPY

By

EMMA LOUISE FAULKNER

A thesis submitted to the University of Birmingham for the degree

DOCTOR OF PHILOSOPHY

School of Chemistry

College of Engineering and Physical Sciences

University of Birmingham

September 2020

UNIVERSITY OF
BIRMINGHAM

University of Birmingham Research Archive

e-theses repository

This unpublished thesis/dissertation is copyright of the author and/or third parties. The intellectual property rights of the author or third parties in respect of this work are as defined by The Copyright Designs and Patents Act 1988 or as modified by any successor legislation.

Any use made of information contained in this thesis/dissertation must be in accordance with that legislation and must be properly acknowledged. Further distribution or reproduction in any format is prohibited without the permission of the copyright holder.

Abstract

Double strand breaks are highly deleterious lesions, and their inefficient repair can lead to mutations and chromosomal translocations. These events cause severe phenotypes such as cancer, immunodeficiencies and neurodegenerative disease. Double strand breaks can be repaired by several mechanisms and the decision of repair pathway is crucial to faithful repair and preservation of genomic integrity.

Repair pathway choice is regulated by numerous factors including cell cycle phase, kinetics of repair and resection of DNA at the break site. Recent studies applying fluorescence microscopy have provided compelling evidence that repair factors are assembled at the break site in a highly spatially and temporally organised manner, and that the spatial dimension of repair is critical to faithful damage resolution. The aim of this thesis is to characterise the spatial organisation of double strand break repair factors to corroborate a spatial model of repair progression.

In this work, I applied novel fluorescence microscopy technique, Expansion Microscopy. This technique enables three-dimensional nanoscale imaging of specimens on a conventional microscope. This is achieved by a specialised chemical preparation in which cells are embedded into a polyelectrolyte gel which can subsequently be swollen by the addition of water. The net effect of this is a de-crowding of molecular information in the specimens and lateral and axial resolution of 70 nm and 200 nm, respectively. Super resolution images can be acquired rapidly, with minimal constraints on fluorophore choice, and without need for sophisticated hardware or software. Specimens are optically cleared during the preparation, which removes the effects of light scattering through the sample. Increased imaging depths and volumes are achievable as compared to other super resolution imaging modalities. In this work, I demonstrate an ability to visualise thousands of repair structures using expansion microscopy which are analysed by a spot

detection-based analysis and provide a novel quantitative insight into spatial organisation of repair foci during double strand break repair.

Acknowledgements

I would firstly like to thank my supervisors Rob Neely, Jo Morris, Steve Thomas and Iain Styles for their support and input throughout my PhD. Special thanks to Rob and Jo for their continual guidance and direction throughout my project. I would also like to thank EPSRC for funding this project.

Thanks to the members of the Neely group, especially Ashleigh, Mo, Krystian and Elodie. Thanks to the members of the Morris group, including Ruth, James, Manolo, George, Alexa and Helen. Special thanks to Ruth who was there at the beginning of my PhD and has been invaluable in my learning throughout and to Alexa and James for listening to my worries and their advice. Thanks to Jeremy Pike for advice in designing image analysis and providing scripts for analysis. Thanks to Evie Garlick for her advice in structured illumination microscopy (SIM), for help with correlative imaging experiments and for overall support during the final stages of my PhD.

Many thanks go to my friends for supporting me and helping me stay positive and motivated throughout my PhD.

Special thanks to my family for their love and support, especially to my mum and my sister for always being on the end of the phone to listen when I was having a stressful time.

Table of Contents

Abstract i
Acknowledgements iii
Table of Contents v
List of Tables xi
List of Figures xiii
Abbreviations xxi
1. Double Strand Break (DSB) repair and visualising the DNA damage response (DDR). 1
1.1 DNA damage response (DDR) 1
1.1.1 Biological significance of double strand breaks (DSBs) 2
1.1.2 Repair of DSBs 3
1.1.3 Repair pathway choice 5
1.1.4 Structure of chromatin and its role in DDR 11
1.2 Fluorescence microscopy 16
1.2.1 Removing effects of optical blurring 17
1.2.2 Improving optical sectioning capability 19
1.2.3 Breaching the diffraction limit: Super resolution microscopy 21
1.2.4 Choosing the correct microscopy technique 25
1.3 Expansion Microscopy (ExM) 27
1.3.1 Ensuring robust, isotropic expansion of specimens 29
1.3.2 Optimising labelling and anchoring in ExM 32
1.3.3 Improving resolving power of ExM 38
1.4 DNA damaging agents induce different types of damage 42
1.4.1 Fluorescence microscopy reveals a complex spatial dimension to repair pathway choice 44
1.4.2 Super resolution microscopy (SRM) reveals nanoscale organisation of repair foci. 45
1.4.3 Functional significance of repair foci sub-compartmentalisation 47
1.5 Summary 51
1.6 Aims 52
2. Methods and Materials 53
2.1 Molecular biology 53
2.1.1 Bacterial transformation 53
2.1.2 Plasmid DNA preparation 53
2.1.3 Quantification of nucleic acids 53

2.2 Protein methods 53
2.2.1 SDS polyacrylamide gel electrophoresis (SDS PAGE) 53
2.2.2 Western blot 54
2.3 Cell biology 55
2.3.1 Tissue culture 55
2.3.2 Plasmid transfection 56
2.3.3 siRNA transfection 56
2.3.4 Stable cell line creation 56
2.3.5 Irradiation protocol 58
2.3.6 Immunofluorescence staining 59
2.3.7 EdU staining 59
2.4 Standard expansion microscopy (ExM) protocol 59
2.4.1 EdU staining and immunostaining of cultured cells 60
2.4.2 Anchor synthesis 60
2.4.3 Anchoring of DNA and proteins for ExM 60
2.4.4 Gelation, digestion and expansion 60
2.4.5 X10 Expansion Microscopy (X10 ExM) gelation, digestion and expansion 61
2.4.6 Expanded specimen handling for imaging 62
2.4.7 Characterising nuclear expansion and Correlative imaging of nuclei. 63
2.4.8 Assessing use of H2A-dendra2/ -mCherry as markers of chromatin post-expansion 63
2.5 Microscopes 64
2.5.1 Nikon N-SIM 64
2.5.2 Widefield microscopy 64
2.5.3 ASI iSPIM microscopy 64
2.6 Image processing 64
2.7 Image analysis 66
2.7.1 Segmentation of nuclei in matlab 66
2.7.2 Segmentation of nuclei in ImageJ 67
2.7.3 Determining Pearson's correlation coefficient (PCC) values 69
2.7.4 Bead-based registration of SPIM image data 69
2.7.5 Spot-detection based analysis of repair structures 70
2.7.6 Generation of average foci structures and colocalisation analysis 74
2.7.7 Measuring 53BP1 occupancy in S phase nuclei 76
2.7.8 Quantifying Pearson's correlation coefficient 77

2.8 Summary of ExM experiments 77
2.9 siRNA sequences 78
2.10 Antibodies 78
2.11 Buffers 79
2.12 Antibiotics 80
2.12.1 Tissue culture antibiotics 80
2.12.2 Bacterial antibiotics 80
3. Investigating retention of nuclear architecture following ExM preparation. 81
3.1 Introduction 81
3.2 Nuclear DNA expands isotropically during ExM treatment 83
3.2.1 Characterising nuclear expansion in 2D 84
3.2.2 Visualising nuclear expansion in three dimensions (3D) using selective plane illumination microscopy (SPIM) 89
3.2.3 Sample handling and optimising image acquisition on SPIM 90
3.2.4 Measuring isotropy of nuclear expansion in 3D 95
3.2.5 Correlative imaging of nuclei 97
3.3 Fluorescently-tagged H2A is a marker of chromatin post-expansion 103
3.3.1 Generation of H2A-fluorescent protein (H2A-FP) cell lines 103
3.3.2 Quantification of retention of chromatin marker following ExM in 2D 105
3.3.3 Visualising chromatin in 3D 110
3.3.4 Quantification of retention of chromatin marker following ExM in 3D 114
3.4 Discussion and Conclusions 115
4. Visualising the nanoscale organisation of 53BP1 and BRCA1 repair foci in three-dimensions (3D) 121
4.1 Introduction 121
4.2 BRCA1 and 53BP1 foci distributions alter as a function of cell cycle 123
4.2.1 EdU and PCNA allow discrimination between early, mid and late S-phase cells 124
4.2.2 53BP1 and BRCA1 foci distributions are recapitulated following ExM 128
4.2.3 Nanoscale features of repair foci are visible following ExM 134
4.3 Analysing nanostructure of repair foci throughout S-phase 136
4.3.1 Design of image analysis to describe foci nanostructures in S-phase 140
4.3.2 Spot detection-based analysis of BRCA1 and 53BP1 in mid and late S-phase nuclei 143
4.4 Investigating functional significance of foci classes 146
4.4.1 Class 1 foci are associated with function of BRCA1 in replication 146

4.4.2 Class 4 foci are complex and heterogeneous 155
4.4.3 Mutual exclusivity of BRCA1 and 53BP1 in class 5 foci 158
4.4.4 BRCA1 is responsible for redistribution of 53BP1 in mid and late S-phase nuclei. 162
4.4.5 RIF1 is closely associated with 53BP1 structures 171
4.5 Characterising foci nanostructures as a function of recovery time 177
4.6 Discussion and Conclusions 187
5. Describing the impact of chromatin regulators on nanoscale organisation of repair proteins 197
5.1 Introduction 197
5.2 SMARCAD1 activity is required for positioning of 53BP1 199
5.3 USP48-depletion increases 53BP1 repositioning relative to BRCA1 213
5.3.1 RAD51 recruitment is increased following USP48-depletion 227
5.3.2 Multi-colour capability of ExM allows nanoscale visualisation of multiple repair factors in repair foci 239
5.3.3 Describing the spatial organisation of multiple repair factors is complex 242
5.3.4 Design of analysis to investigate the spatial organisation of RAD51, BRCA1 and 53BP1 in S-phase nuclei 243
5.4 Chromatin compaction state can be investigated following ExM 259
5.4.1 Effect of SMARCAD1-depletion on chromatin architecture 260
5.4.2 Effect of USP48-depletion on chromatin architecture 268
5.4.3 Increasing resolving power of ExM to visualise chromatin architecture 268
5.5 Discussion and Conclusions 272
6. Discussion and Future Perspectives 285
6.1 Introduction 285
6.2 Investigating retention of nuclear architecture following Expansion Microscopy (ExM) preparation 287
6.3 Nanoscale organisation of repair foci can be visualised following ExM preparation 288
6.4 The impact of chromatin remodelling on foci sub-compartmentalisation can be detected using ExM 291
6.5 Increasing ExM resolution to investigate chromatin architecture 293
6.6 Investigating RAD51 nucleofilament formation following USP48 depletion 293
6.7 Future Questions 295
6.7.1 Investigating how BRCA1 complex composition alters during HR 295
6.7.2 Investigating chromatin architecture at DSBs using ExM 297
6.7.3 Investigating RAD51 nucleofilament formation 299
6.8 Conclusions and Future perspectives 301

Appendix 303
A1 Correlative imaging of nuclei 303
A2 Discriminating between early, mid and late S-phase using PCNA and EdU 304
A3 Investigating 53BP1 structures following BRCA1-depletion 313
A4 53BP1 and RIF1 are closely associated 315
A5 Characterising 53BP1 and BRCA1 foci distributions as a function of recovery time 315
A6 Describing positioning of 53BP1 relative to BRCA1 following SMARCAD1-depletion 319
A7 Describing positioning of 53BP1 relative to BRCA1 following USP48-depletion 325
A8 Investigating RAD51 foci structures following USP48-depletion 329
A9 Characterising the nanoscale spatial organisation of 53BP1, BRCA1 and RAD51 after USP48 depletion 334
A10 Visualising repair foci in the context of chromatin 342
A11 Increasing resolution of ExM 343
7. References 345

List of Tables

Table 2.1. SDS polyacrylamide gel solutions. 54
Table 2.2. Components of the Flp-In T-REx expression system. 57
Table 2.3. Maximum and minimum size of nuclei pre- and post-expansion. 67
Table 2.4. Spot detection-based analysis performed for nanoscale analysis of repair factors. 74
Table 2.5. Summarising cell treatments prior to ExM preparation of specimens. 77
Table 2.6. siRNA sequences..... 78
Table 2.7. Antibodies including species raised in, concentration, conditions and protocols. 78

List of Figures

Figure 1.1.Fate of cells following DNA damage. 2
Figure 1.2. Resection determines DSB repair pathway choice.. 5
Figure 1.3. The 53BP1-RIF1-Shieldin repair axis promotes NHEJ. 8
Figure 1.4. Repair of DSBs through homologous recombination (HR). 11
Figure 1.5. Schematic of changes in chromatin compaction as a function of time. 14
Figure 1.6. Chromatin remodelling controls resection lengths during HR. 16
Figure 1.7. Principles of LSFM. 20
Figure 1.8. Principle of Structured illumination microscopy (SIM). 22
Figure 1.9. Resolution enhancement using structured illumination. =. 23
Figure 1.10. Principle of stimulated emission depletion (STED) microscopy. 24
Figure 1.11. Principle of single molecule localisation microscopy (SMLM). 25
Figure 1.12. General ExM protocol.. 29
Figure 1.13. Osmotic forces are key to expansion of polyelectrolyte gels. 30
Figure 1.14. Loss of fluorescent signal in ExM prepared samples.. 34
Figure 1.15. MAP and U-ExM approaches to ExM. 36
Figure 1.16. Synthesis of LabelX. 38
Figure 1.17. Iterative expansion microscopy (iExM) approach. 40
Figure 1.18. 53BP1-RIF1 structural module freezes chromatin proximal to DSBs to prevent hyper-resection. 49
Figure 2.1. Generation of Flp-In T-REx host cell line (adapted from ThermoFisher, 2012). 57
Figure 2.2. Generating inducible expression cell lines (adapted from ThermoFisher 2012). 58
Figure 2.3 Top down view of set up of ExM gels for image acquisition on inverted microscopes. . 62
Figure 2.4. Principle of non-linear iterative deconvolution algorithms. 66
Figure 2.5. Segmentation of nuclei to measure volume of nuclei pre- and post-expansion. 68
Figure 2.6.User defined parameters for spot detection-based analysis of two-colour Z series. 71
Figure 2.7. User defined parameters for spot detection-based analysis of three-colour Z series.. 72
Figure 2.8. User defined parameters for spot detection-based analysis of four-colour Z series. ... 73
Figure 2.9. Determining volume of 53BP1 structures in ImageJ. 76
Figure 3.1. Schematic of EdU detection.. 84
Figure 3.2. Visualising Nuclear Expansion. 85
Figure 3.3. Quantifying nuclear expansion factor. 87
Figure 3.4. Process of quantification of nuclear expansion factor in Matlab. 87

Figure 3.5. Example of Segmentation for quantification of nuclear area. 88
Figure 3.6. Nuclear Expansion Factor measurement. 88
Figure 3.7. ExM gels pre- and post-ExM. 89
Figure 3.8. Schematic of SPIM illumination pattern. 90
Figure 3.9. Top-down schematic of immobilisation of ExM gels for SPIM imaging. 91
Figure 3.10. Visualising nuclear architecture on SPIM. 93
Figure 3.11. Visualising nuclear architecture on SPIM. 94
Figure 3.12. Visualising nuclear architecture in 3D on SPIM. 95
Figure 3.13. Measuring volumes of nuclei pre- and post-expansion.. 96
Figure 3.14. Measuring nuclear volumes pre- and post-expansion. 96
Figure 3.15. Correlative imaging of EdU-stained nuclei. 100
Figure 3.16. Registration of pre- and post-expansion images of nuclei. 102
Figure 3.17. Generation of stable cell lines using Flp-In host cell line.. 104
Figure 3.18. U2OS cells expressing H2A-dendra2 or H2A-mCherry. 104
Figure 3.19. Visualisation of chromatin and DNA. 107
Figure 3.20. Calculation of Pearson's correlation coefficient. 109
Figure 3.21. Pearson's correlation coefficient values assessing retention of H2A distribution pre- and post-expansion. 109
Figure 3.22. Visualising nuclear architecture in 3D.. 110
Figure 3.23. Tetraspeck bead testing. 112
Figure 3.24. Tetraspeck beads as fiducial markers. 113
Figure 3.25. Post-expansion SPIM images of DNA and Chromatin. 114
Figure 3.26. Pearson's correlation coefficient values assessing retention of H2A distribution post-expansion. 115
Figure 4.1. Schematic of changes in distribution of replication foci during the cell cycle. 125
Figure 4.2. EdU and PCNA staining patterns allow discrimination of early, mid and late S-phase. 126
Figure 4.3. Confirming colocalisation between PCNA and EdU staining.. 127
Figure 4.4. Visualising 53BP1 and BRCA1 foci as a function of cell cycle. 129
Figure 4.5. Visualising BRCA1 and 53BP1 foci post-expansion. 130
Figure 4.6. Quantification of BRCA1 and 53BP1 foci as a function of cell cycle. 132
Figure 4.7. The importance of deconvolution. 135
Figure 4.8. Investigating 53BP1 and BRCA1 accumulations in early S-phase nuclei. 138

Figure 4.9. Investigating 53BP1 and BRCA1 accumulations in mid and late S-phase nuclei. 139
Figure 4.10. Schematic of analysis designed for mid and late S-phase nuclei. 141
Figure 4.11. Structure classification process. 142
Figure 4.12. Classifying foci appearances in cells with markers of mid and late S-phase. 144
Figure 4.13. Describing repair structures as a function of cell cycle. 145
Figure 4.14. Visualising BRCA1 foci in non-irradiated U2OS cells.. 147
Figure 4.15. Visualising BRCA1 foci in non-irradiated U2OS cells. 148
Figure 4.16. Quantification of BRCA1 and 53BP1 foci as a function of cell cycle in undamaged cells. 150
Figure 4.17. Assessing correlation between BRCA1 and EdU in irradiated and non-irradiated cells. 152
Figure 4.18. Classifying 53BP1 and BRCA1 accumulations according to EdU association in irradiated and non-irradiated cells.. 154
Figure 4.19. Sub-classifying class 4 structures. 156
Figure 4.20. Sub-classifying class 4 structures. 157
Figure 4.21. Visualising mutual exclusivity of BRCA1 and 53BP1 in class 5 repair structures.. 158
Figure 4.22. Visualising mutual exclusivity of BRCA1 and 53BP1 in class 5 repair structures. 160
Figure 4.23. Visualising mutual exclusivity of BRCA1 and 53BP1 in class 5 repair structures.. 161
Figure 4.24. Confirming BRCA1-depletion. 162
Figure 4.25. Immunostaining BRCA1-depleted cells. 163
Figure 4.26. Quantification of BRCA1 and 53BP1 foci as a function of cell cycle in BRCA1-depleted cells. 165
Figure 4.27. Immunostaining BRCA1-depleted cells.. 168
Figure 4.28. BRCA1 is responsible for redistribution of 53BP1 in repair foci. 170
Figure 4.29. Visualising 53BP1 and RIF1 foci pre-expansion. 172
Figure 4.30. Quantification of RIF1 and 53BP1 foci numbers as a function of cell cycle. 173
Figure 4.31. Visualising 53BP1 and RIF1 post-expansion. 174
Figure 4.32. Visualising RIF1 and 53BP1 foci nanostructure. 176
Figure 4.33. Design of time course experiment to visualise temporal progression of 53BP1 and BRCA1 co-enriched accumulations. 178
Figure 4.34. Quantification of foci throughout time course pre-expansion. 179
Figure 4.35. Visualising DSB repair progression. 180
Figure 4.36. Visualising DSB repair progression. 181

Figure 4.37. Visualising DSB repair progression: a nanoscale view. 182
Figure 4.38. Visualising DSB repair progression: a nanoscale view. 183
Figure 4.39. Assessing DSB repair progression. 184
Figure 4.40. Prevalence of class 4 subclasses as a function of recovery time. 186
Figure 5.1. SMARCAD1-depletion in U2OS-FlpIn cells. 199
Figure 5.2. Pre-expansion imaging of SMARCAD1-depleted cells..... 200
Figure 5.3. Quantifying 53BP1 and BRCA1 foci following SMARCAD1-depletion pre-expansion.. 202
Figure 5.4. Post-expansion imaging of SMARCAD1-depleted cells. 204
Figure 5.5. Classification of BRCA1 and 53BP1 structures in SMARCAD1-depleted cells.. 205
Figure 5.6. Classifying BRCA1 and 53BP1 structures in SMARCAD1-depleted cells..... 206
Figure 5.7. Investigating class 5 structure distributions in SMARCAD1-depleted cells. 207
Figure 5.8. Investigating class 5 structure distributions in SMARCAD1-depleted cells. 208
Figure 5.9. Generation of average radial profile. 209
Figure 5.10. Profiling class 5 structures in SMARCAD1 depleted cells. 209
Figure 5.11. Summary of correlation between 53BP1 and BRCA1 in SMARCAD1-depleted cells. 211
Figure 5.12. Sub-classifying class 5 structures based on positioning of 53BP1 relative to BRCA1. 212
Figure 5.13. USP48-depletion in U2OS Flp-In cells. 214
Figure 5.14. Pre-expansion imaging of USP48-depleted cells. 215
Figure 5.15. Quantifying foci numbers following USP48-depletion pre-expansion. 217
Figure 5.16. Post-expansion imaging of USP48-depleted cells.. 218
Figure 5.17. Classification of BRCA1 and 53BP1 accumulationsin USP48-depleted cells. 219
Figure 5.18. Classifying BRCA1 and 53BP1 accumulations in USP48-depleted cells..... 220
Figure 5.19. Investigating class 5 structure distributions in USP48-depleted cells..... 221
Figure 5.20. Investigating class 5 structure distributions on USP48-depleted cells. 222
Figure 5.21. Profiling class 5 foci in USP48 depleted cells. 223
Figure 5.22. Summary of correlation between 53BP1 and BRCA1 in USP48-depleted cells.. 224
Figure 5.23. Sub-classifying class 5 structures based on positioning of 53BP1 relative to BRCA1. 225
Figure 5.24. Summarising the effect of SMARCAD1- and USP48-depletion on class 5 structure organisation. 227
Figure 5.25. Pre-expansion imaging of USP48-depleted cells. 229
Figure 5.26. Quantifying foci numbers following USP48-depletion pre-expansion. 231
Figure 5.27. Quantifying intensity of RAD51 foci pre-expansion. 232
Figure 5.28. Post-expansion imaging of USP48-depleted cells.. 233

Figure 5.29. Visualising the structure of RAD51 and 53BP1 co-enriched foci in USP48-depleted cells. 234
Figure 5.30. Classification of RAD51 and 53BP1 accumulations in USP48-depleted cells. 235
Figure 5.31. Classifying RAD51 and 53BP1 distributions in USP48-depleted cells 236
Figure 5.32. Describing the relative spatial organisation of RAD51 and 53BP1 in class 4 structures. 237
Figure 5.33. Sub-classification of class 4 foci structures. 238
Figure 5.34. Visualising RAD51, BRCA1 and 53BP1 pre-expansion. 240
Figure 5.35. Visualising RAD51, BRCA1 and 53BP1 post-expansion. 241
Figure 5.36. Investigating heterogeneity of RAD51, BRCA1 and 53BP1 accumulations in USP48-depleted cells.. 243
Figure 5.37. Schematic representation of HR progression. 245
Figure 5.38. Classification of RAD51, BRCA1 and 53BP1 structures using spot detection-based analysis. 248
Figure 5.39. Describing the relative spatial organisation of RAD51, BRCA1 and 53BP1 in repair structures. 250
Figure 5.40. Classifying BRCA1, 53BP1 and RAD51 distributions on USP48-depleted cells. 251
Figure 5.41. Examples of BRCA1 (white), 53BP1 (red) and RAD51 (green) co-enriched structures from USP48-depleted and control cells. 254
Figure 5.42. Investigating RAD51 structures in USP48-depleted cells.. 256
Figure 5.43. Describing the placement of BRCA1 spots in class 9 structures in USP48-depleted cells compared to control cells. 258
Figure 5.44. Confirming SMARCAD1-depletion in U2OS cells expressing H2A-dendra2.. 260
Figure 5.45. Pre-expansion imaging of H2A-dendra2-expressing cells following SMARCAD1 depletion.. 261
Figure 5.46. Post-expansion imaging of H2A-dendra2-expressing cells following SMARCAD1 depletion.. 262
Figure 5.47. Visualising spectral overlap from H2A-dendra2 (488) channel to BRCA1 (561) channel. 263
Figure 5.48. Classifying BRCA1 and 53BP1 accumulations in SMARCAD1-depleted H2A-dendra2-expressing cells. 265
Figure 5.49. Classifying class 5 structure organisation in SMARCAD1-depleted cells. 267
Figure 5.50. X10 ExM optimisation. 270

Figure 5.51. Quantifying nuclear expansion factor. 271
Figure 5.52. SPIM acquisitions of DNA and H2A dendra2 following X10 ExM. 272
Figure 5.53. Effect of USP48 depletion on foci sub-compartmentalisation..... 278
Figure 5.54. Spatial organisation of repair factors indicating steps of HR. 281
Figure A1. Measuring nuclear areas and inter-nuclear distances in correlative images..... 306
Figure A2. Confirming EdU and PCNA distribution in U2OS cells 307
Figure A3. Confirming cell cycle phase using PCNA and EdU as markers. 309
Figure A4. Confirming cell cycle phase using PCNA and EdU as markers. 312
Figure A5. Confirming cell cycle phase using PCNA and EdU as markers. 313
Figure A6. Quantifying PCC between EdU and PCNA in S-phase cells..... 315
Figure A7. Visualising 53BP1 distribution in BRCA1-depleted compared to control cells. 317
Figure A8. Measuring correlation between 53BP1 and RIF1..... 318
Figure A9. Visualising DSB repair progression. 319
Figure A10. Visualising DSB repair progression..... 321
Figure A11. Visualising DSB repair progression..... 322
Figure A12. Visualising DSB repair progression..... 323
Figure A13. Sub-classifying class 5 foci structures in control cells for comparison to SMARCAD1-depleted cells..... 324
Figure A14. Sub-classifying class 5 foci structures in control cells for comparison to SMARCAD1-depleted cells. 325
Figure A15. Sub-classifying class 5 foci structures in SMARCAD1-depleted cells for comparison to control cells. 326
Figure A16. Sub-classifying class 5 foci structures in SMARCAD1-depleted cells for comparison to control cells. 327
Figure A17. Sub-classifying class 5 foci structures in control cells for comparison to USP48-depleted cells. 329
Figure A18. Sub-classifying class 5 foci structures in control cells for comparison to USP48-depleted cells. 330
Figure A19. Sub-classifying class 5 foci structures in USP48-depleted cells for comparison to control cells..... 331
Figure A20. Sub-classifying class 5 foci structures in USP48-depleted cells for comparison to control cells. 332
Figure A21. Investigating RAD51 enrichment in USP48-depleted cells..... 333

Figure A22. Investigating RAD51 enrichment in USP48-depleted cells. ……335
Figure A23.Investigating RAD51, BRCA1 and 53BP1 enrichment in USP48-depleted cells……338
Figure A24. Investigating RAD51, BRCA1 and 53BP1 enrichment in USP48-depleted cells……..340
Figure A25. Classifying BRCA1, 53BP1 and RAD51 foci distributions on USP48-depleted cells…..343
Figure A26. Poor intensity from H2A-dendra2 observed when investigating the effects of SMARCAD1- and USP48-depletion on chromatin proximal to sites of damage. ……..345
Figure A27. X10 ExM reveals nanoscale topology of chromatin and DNA. ……347

Abbreviations

53BP1	p53-Binding protein 1
AA	Acrylamide
AcX	Acryloyl-X (6-((acryloyl)amino)hexanoic acid, succinimidyl ester)
APS	Ammonium persulfate
ATM	Ataxia telangiectasia mutated
ATP	Adenosine triphosphate
ATR	ATM and Rad4 related
BARD1	BRCA1-associated RING domain protein 1
BLM	Bloom syndrome protein
BRCA1	Breast cancer associated gene 1
BRCA2	Breast cancer associated gene 2
BRCC36	BRCA1/BRCA2 containing complex 36
BRCT	BRCA1 C-terminus
BrdU	Bromodeoxyuridine
BSA	Bovine Serum Albumin
Cdk	Cyclin dependent kinase
ChAM	Chromatin associated motif
Cpt	Camptothecin
CST	CST telomere replication complex component 1 (CTC1)-subunit of CST complex (STN1)- telomere length regulation protein (TEN1)
CtIP	Ct-BP interacting protein
CUE	Coupling of ubiquitin conjugation to endoplasmic reticulum degradation
DDR	DNA damage response
DMAA	Dimethylacrylamide
DMEM	Dulbecco's modified eagle medium
DMSO	Dimethylsulfoxide
DNA	Deoxyribonucleic acid
Dna2	DNA replication helicase/nuclease 2

DNase	Deoxyribonuclease
DNA-PKcs	DNA-dependent protein kinase catalytic subunit
Dox	Doxycycline
DSB	Double strand break
dsDNA	Double stranded DNA
DSS1	Deleted in split hand/split foot malformation gene 1
DUB	Deubiquitinating enzyme
E3	Ubiquitin ligase enzyme
ECL	Enhanced chemiluminescence
E.Coli	*Escherichia Coli*
EDTA	Ethylene diamine tetra-acetic acid
EdU	5-ethynyl-2'-deoxyuridine
ExM	Expansion Microscopy
Exo1	Exonuclease 1
FA	Formaldehyde
FBS	Foetal Bovine Serum
FLIM	Fluorescence lifetime imaging microscopy
FRET	Forster resonance energy transfer
G1/G2	Growth phase 1/2
GA	Glutaraldehyde
GFP	Green fluorescent protein
H2A	Histone 2A
H2AX	Histone 2AX
HCl	Hydrochloric acid
HJ	Holliday junction
HR	Homologous recombination
HRP	Horseradish peroxidase
iExM	Iterative expansion microscopy
IF	Immunofluorescence
IR	Irradiation

LB	Luria Bertani
M	Mitosis
MA-NHS	Methacrylic acid N-hydroxysuccinimidyl ester
MAD2L2	Mitotic Arrest Deficient 2 Like 2
MAP	Magnified analysis of the proteome
MDC1	Mediator of DNA damage checkpoint protein 1
Merit40	Mediator of Rap80 interactions and targeting 40 kd
MMEJ	Microhomology-mediated end joining
MOPS	3-(N-Morpholino)propanesulfonic acid
MRN	Mre11/Rad50/Nbs1
NHEJ	Non-homologous end-joining
NTC	Non-targeting control
OB	Oligosaccharide-binding
PAGE	Polyacrylamide gel electrophoresis
PALB2	Partner and localizer of BRCA2
PALM	Photo-activated localisation microscopy
PAR	Poly-ADP ribose
PARP	Poly-ADP ribose-polymerase
PBS	Phosphate buffered saline
PCNA	Proliferating cell nuclear antigen
PFA	Paraformaldehyde
Pol	Polymerase
PP4C	Serine/ threonine protein phosphatase
ProExM	Protein retention expansion microscopy
PSF	Point spread function
PTM	Post-translational modification
PTIP	Pax interacting protein 1
Rad51	Radiation sensitivity gene 51
RAD52	DNA repair protein RAD52 homolog
Rap80	Receptor associated protein 80

RIF1	RAP1 Interacting factor 1
RING	Really interesting new gene
RNF	Ring finger protein
ROS	Reactive oxygen species
RNA	Ribose nucleic acid
RPA	Replication protein A
S-phase	Synthesis phase
SA	Sodium Acrylate
SCE	Sister chromatid exchange
SDS	Sodium Dodecyl Sulfate
SHLD	Shieldin complex subunit
SIM	Structured illumination microscopy
siRNA	Small interfering RNA
SMARCAD1	SWI/SNF-related matrix-associated actin-dependent regulator of chromatin subfamily A containing DEAD/H box 1
SMLM	Single molecule localisation microscopy
SPIM	Selective plane illumination microscopy
SRM	Super resolution microscopy
ssDNA	Single stranded DNA
SSA	Single strand annealing
SSB	Single strand break
STED	Stimulated emission depletion
STORM	Stochastic optical reconstruction microscopy
SUMO	Small ubiquitin-related modifier
TAD	Topologically associated domain
TAE	Tris, Acetic acid, EDTA buffer
TEMED	Tetramethylethylenediamine
TIRF	Total internal reflection
TOPBP1	DNA topoisomerase 2 binding-protein 1
U-ExM	Ultra Expansion microscopy

Ub	Ubiquitin
UGRF1	E3 ubiquitin protein ligase
USP48	Ub specific protease 48
UV	Ultraviolet
WB	Western blot
WT	Wild type

1. Double Strand Break (DSB) repair and visualising the DNA damage response (DDR).

1.1 DNA damage response (DDR)

Protection of genomic stability and integrity is critical to cellular and organismal function, yet genetic material is under continuous assault by various exogenous (e.g. UV light) and endogenous (e.g. intracellular production of reactive oxygen species, stalled replication forks) DNA damaging agents (Jackson and Bartek, 2009). Such damaging agents drive genomic instability and impair DNA integrity (Panier and Boulton, 2013). The presence of this threat has necessitated the evolution of a complex array of DNA repair mechanisms (Jackson and Bartek, 2009) broadly termed the DNA damage response (DDR).

The DDR is organised in a hierarchical fashion into a cascade involving three main steps: sensing of DNA damage, signalling of DNA damage and induction of the appropriate cellular response (Matt and Hoffman, 2016). Different damaging agents induce different types of lesions requiring distinct repair processes for their faithful resolution (detailed in Section 1.4) (Nagy and Soutoglou, 2009). The sensing of DNA damage is a task set for numerous specialised multimeric protein complexes capable of qualitative recognition of various types of damage (e.g. double strand breaks (DSBs), single strand breaks (SSBs), DNA adducts). All sensors will activate key Ser/Thr kinases of the PI3-like kinases responsible for initiation of the DNA damage signalling cascade. DDR drives cell fate decisions, resulting in transient cell cycle arrest and subsequent DNA repair, apoptosis, differentiation or cellular senescence (summarised in Figure 1.1).

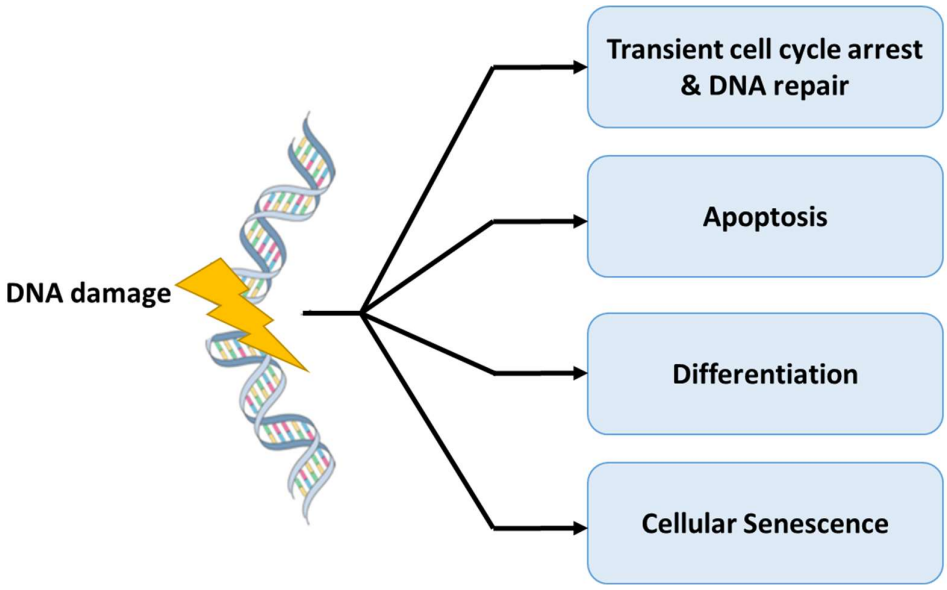

Figure 1.1. Fate of cells following DNA damage. Following the induction of DNA damage, this will be sensed by numerous proteins which subsequently initiate a kinase-driven signalling cascade which ultimately affects the fate of the cell. This can result in transient cell cycle arrest and repair of lesions, apoptosis, differentiation or cellular senescence (adapted from Matt and Hoffman, 2016).

An impaired DDR can result in severe phenotypes including premature aging, tissue dysfunction, immunodeficiency, neurodegenerative disorders and cancer; the presence of a well-balanced, tightly regulated response system is crucial to preserving genomic stability and preventing disease (Matt and Hoffman, 2016).

1.1.1 Biological significance of double strand breaks (DSBs)

Double Strand Breaks (DSBs) are highly toxic lesions induced by both endogenous and exogenous assaults to genetic material. DSBs are considered to be the most lethal type of DNA damage, as a single DSB is sufficient to perturb genomic integrity and trigger cell death (Bohgaki *et al*, 2010 & Misteli and Soutoglou, 2009). DSBs can be induced by exogenous agents (e.g. irradiation). DSBs also result during DNA metabolic processes e.g. transcription, replication (Clouaire and Legube, 2019). Additionally, DSBs can occur in a programmed manner and are important to other physiological processes (Bohgaki *et al*, 2010). DSBs are induced in a highly regulated manner during meiosis enabling homologous recombination (described in Section 1.1.2) events to promote pairing

interactions and connections between homologous chromosomes which is essential to proper segregation of chromosomes during the first meiotic division (Borde and de Massy, 2013). DSBs are also generated during VDJ recombination in lymphoid cells. B cell receptor (BCR) and T cell receptor (TCR) loci consist of variable (V), diversity (D) and joining (J) genes which are recombined. Mature B cells also undergo further genomic alterations in the form of class switch recombination (CSR) and somatic hyper-mutation (Prochazkova and Loizou, 2015). On the most part, the repair following VDJ recombination and CSR is completed by non-homologous end joining (NHEJ) (Section 1.1.2). As is the case with pathological DSB formation, it is crucial that programmed DSBs are correctly repaired since defective repair can result in mutations and chromosomal translocations (Misteli and Soutoglou, 2009).

The complexities of the DDR are continually being investigated, revealing defects in specific components of the genome stability network which are associated with disease (O'Driscoll, 2012). The nature and identity of a defect directly impacts the resultant phenotype. DSBs may be repaired by two key repair pathways: non-homologous end joining (NHEJ) and homologous recombination (HR). Defects in these pathways have been associated with immunodeficiencies and malignant transformation, respectively. The choice of repair pathway is dependent on a number of factors (discussed in Sections 1.1.2-1.1.4). There is now irrefutable evidence that mutations in DDR components or aberrant regulation of genomic surveillance drives numerous human diseases. Elucidation of the molecular mechanisms driving disease adds to the extensive network of the DDR. This knowledge can be used to optimise specific therapeutic strategies.

1.1.2 Repair of DSBs

DSBs may be repaired by several mechanisms: non-homologous end joining (NHEJ), microhomology-mediated end joining (MMEJ), homologous recombination (HR) or single-stand annealing (SSA) (summarised in Figure 1.2) (Densham and Morris, 2019). The decision of repair pathway is critical in determining faithful repair and preservation of genomic integrity (Escribano-

Diaz *et al*, 2013). NHEJ involves re-ligation of DNA ends at a break, and can involve processing of ends or activity of polymerases to fill in gaps prior to ligation. NHEJ is active throughout the cell cycle, but predominates in G1 and G2 phases (Mao *et al*, 2008). NHEJ is rapid and accounts for approximately 80% of all DSB repair events. NHEJ can be considered an error-prone repair pathway; where no processing occurs and two correct DNA ends are ligated, the repair is error-free, however, if processing has occurred or incorrect ends are ligated then mutations and translocations can result. MMEJ is an alternative EJ pathway which uses short sequences of homology revealed by DNA resection to align the ends prior to ligation (Symington and Gautier, 2011) and minimise resection at the break; this pathway is commonly used where NHEJ components are lacking (Densham and Morris, 2019). MMEJ can be highly mutagenic due to loss of the intervening sequence (Daley and Sung, 2014).

HR and SSA are homology-directed repair (HDR) pathways (Densham and Morris, 2019). Both pathways involve resection to generate a ssDNA 3' overhang which is subsequently coated by replication protein A (RPA). During HR, RPA will be exchanged for RAD51 which forms a nucleofilament on the ssDNA. The ssDNA-RAD51 nucleofilament invades the sister chromatid and searches for the homologous sequence. A single stand is displaced in the DNA and a synapse is formed with the homologous sequence on the other strand to form a DNA-loop (D-loop). The invading strand will act as a primer for polymerases which extend along the template. If two cross-over products (Holliday Junctions) are cleaved then the repair is error-free. HR is restricted to S/G2 phases of the cell cycle due to the requirement of a homologous sequence present in the sister chromatid. SSA differs to HR as resection extends to reveal homology directly on either side of the break and repair will occur by direct annealing; a process facilitated through RAD52. This is highly error prone as the intervening sequence information is lost.

NHEJ involves binding of Ku70/Ku80 to DNA ends and binding of DNA-dependent protein kinase catalytic subunit (DNAPkcs) which keeps broken DNA ends proximal and allows recruitment of end

processing enzymes. Ligase VI mediates direct ligation of DNA ends (Panier and Boulton, 2014). NHEJ is appropriate on minimally processed DNA ends; resection inhibits this pathway. Resection is initiated by CtIP/MRE11-RAD50-NBS1 (MRN) complexes which removes Ku from the DNA ends and allows short range resection. CtIP-MRN complex is subject to post-translational modifications, in particular phosphorylation mediated by CDK1, which limits resection to S/G2 phase of the cell cycle where the sister chromatid is present for homology directed repair (Densham and Morris, 2019). For longer range resection nucleases EXO1 and DNA2 are required, together with BLM helicase (Escribano-Diaz *et al*, 2013). Resected ends are rapidly coated with RPA and then replaced with RAD51 for HR, or RAD52 for SSA.

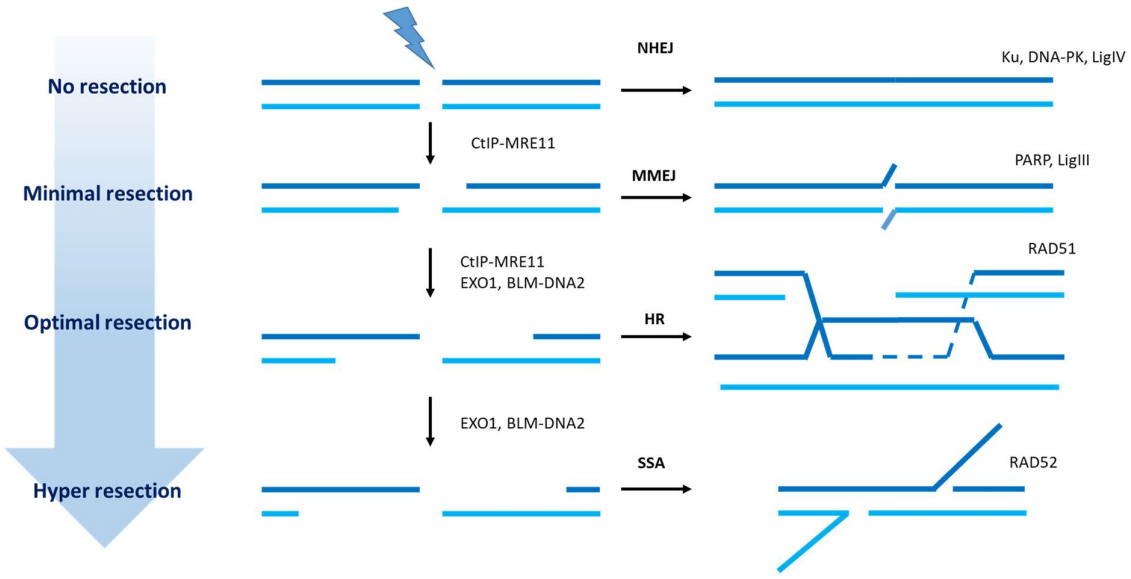

Figure 1.2. Resection determines DSB repair pathway choice. The role of resection in each repair pathway is shown schematically. NHEJ involves simple re-ligation with no resection. MMEJ involves minimal resection prior to re-ligation. HR requires optimal resection to generate 3' overhang for subsequent D-loop formation. SSA involves extended resection lengths resulting in direct annealing of homologous sequences and loss of the intervening sequence. Key proteins involved are shown in black (Adapted from Morris and Densham, 2019).

1.1.3 Repair pathway choice

NHEJ and HR are the major mechanisms of DSB repair. It is now apparent that regulation of DSB repair pathway choice is crucial to safeguarding of genomic integrity, and is controlled by multiple

factors. Repair pathways must be activated in the correct cellular context. Factors influencing repair pathway choice include cell cycle position, resection and chromatin environment, all of which are intimately connected.

Kinetics of repair plays a role in repair pathway progression. Increasing evidence suggests that repair is first attempted by NHEJ (Her and Bunting, 2018). If this is unsuccessful, then resection and homology-directed repair is initiated. Reporter assays in human cell lines revealed that NHEJ is rapid, completing within 30 minutes, compared to HR which occurs over several hours. Further NHEJ accounts for approximately 80% of DSB repair events. It seems that HR acts in specific contexts, where NHEJ is insufficient to restore genomic integrity.

DSB repair pathway choice is dependent on cell cycle phase. Tracking of repair pathway choice in live cells revealed that HR reaches peak activity in mid S-phase, whilst NHEJ dominates in G1 and G2 phases of the cell cycle (Her and Bunting, 2018). Use of fluorescent reporter assays to investigate NHEJ and HR preference as a function of cell cycle similarly revealed that NHEJ is active throughout the cell cycle but has highest activity in G2/M phase. HR is nearly absent in G1, most active in S phase and is low in G2/M (Mao *et al*, 2008). These changes between HR and NHEJ as a function of cell cycle are regulated by numerous factors and post-translational modifications.

Initiation of resection is a critical determinant in repair pathway choice (Symington and Gautier, 2011). NHEJ is inhibited by resection as then DNA ends become poor substrates for Ku binding, thus repair proceeds via HR. The role of cell cycle phase in repair pathway decision is intimately linked to this process; HR requires the presence of a homologous sequence which is found in the sister chromatid during S phase. It was identified that cyclin-dependent kinase (CDK)-mediated phosphorylation of CtIP stimulates resection (Her and Bunting, 2018), and phosphorylation of DNA2 allows its localisation to DSBs (Daley and Sung, 2014). These finding suggested that phosphorylation initiates resection during S-phase, but the regulation of DSB repair pathway progression is much more complex.

53BP1 and BRCA1 are crucial in determining repair pathway choice, promoting NHEJ and HR, respectively (Chapman, Taylor and Boulton, 2012). In mammalian cells, damage is sensed by MRN (MRE11-Rad50-NBS1) complex, which subsequently enables the recruitment and activation of kinase Ataxia telangiectasia mutated (ATM). ATM is recruited as inactive dimers which undergo autophoshorylation at serine 1981 to form active monomers (Matt and Hofmann, 2016). ATM is responsible for phosphorylation of histone variant H2AX, forming its isoform yH2AX, at nucleosomes surrounding the DSB. This is followed by the binding of MDC1 to the DSB-flanking chromatin, which acts as a platform for upstream and downstream effectors. MDC1 drives recruitment of additional copies of ATM and MRN which leads to the spreading of repair machinery along the chromosome. MDC1 also recruits ubiquitin ligases RNF8 and RNF168, which ultimately enable the recruitment of 53BP1 and BRCA1. The antagonism between 53BP1 and BRCA1 regulates repair pathway choice (Panier and Boulton, 2014). Understanding how 53BP1 and BRCA1 direct repair pathway choice has been an intense area of research.

53BP1 is a chromatin bound protein which primarily acts by preventing resection to promote repair via NHEJ (Noordermeer *et al*, 2018). The blockade posed to resection relies on the interaction of 53BP1 with its downstream effectors, PTIP and RIF1, the latter of which recruits REV7/MADL2L. It was unclear how these proteins actually inhibit resection. Two models were proposed: 1) these proteins act by strengthening the nucleosomal barrier to nucleases which perform resection, or 2) further proteins are recruited to ensure protection of DNA ends against resection.

The shieldin complex has been identified as a downstream effector of 53BP1. The shieldin complex is comprised of C20orf196 (SHLD1), FAM35A (SHLD2), CTC-534A2.2 (SHLD3) and REV7, and is recruited to DSBs in a 53BP1- and RIF1-dependent manner. SHLD2 interacts with ssDNA via three OB-fold domains (reminiscent of those present in ssDNA binding proteins POT1 and RPA); this activity is critical to the function of shieldin complex (Noordermeer *et al*, 2018, Dev *et al*, 2018, Ghezraoui *et al*, 2018 & Gupta *et al*, 2018). It has further been shown that Shieldin contacts another

complex comprised of CST telomere replication complex component 1 (CTC1)-subunit of CST complex (STN1)- telomere length regulation protein (TEN1), known as the CST complex. This complex acts as an accessory protein to pol-α. CST-pol-α is known to regulate integrity of telomeres where it performs C-strand fill in, and it appears to be performing a similar function at DNA ends during DSB repair. This suggests that the 53BP1-RIF1-Shieldin repair axis is not only preventing resection, but is also able to reverse the process (Mirman *et al*, 2018 & Densham and Morris, 2019). This complex is shown in Figure 1.3.

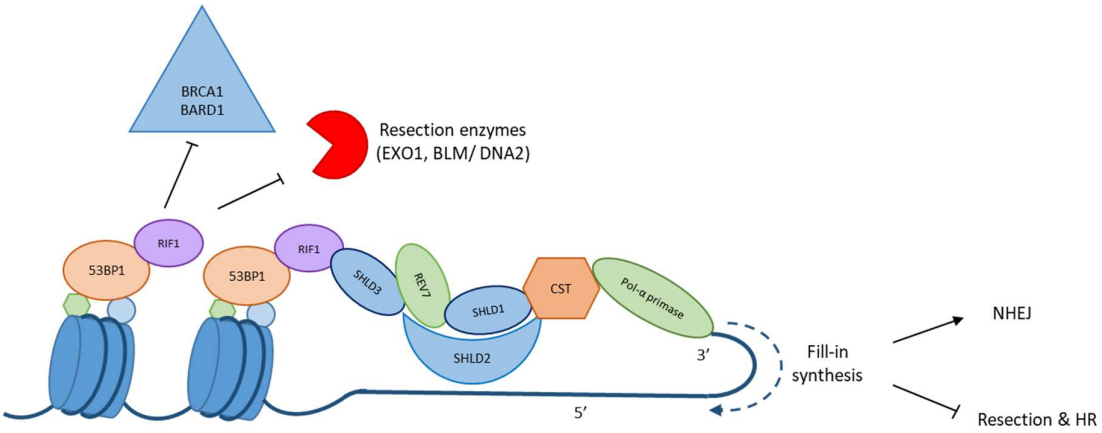

Figure 1.3. The 53BP1-RIF1-Shieldin repair axis promotes NHEJ. Following DSB induction, 53BP1 interacts with modified histones proximal to the break site via H4K20 dimethyation and H2A-H15-ubiquitin (shown as green hexagons and blue circles), allowing for recruitment of its downstream effectors RIF1 and the Shieldin complex. The shieldin complex is comprised of SHLD1, SHLD2, SHLD3 and REV7. SHLD2 binds ssDNA via its OB-fold domains. The shieldin complex allows for recruitment of CST complex and accessory protein, pol-α, which allows filling in of resected DNA thereby preventing long range resection and supressing repair by HR (Adapted from Densham and Morris, 2019).

The discovery of this complex has particular relevance in BRCA1-deficient malignancies which are commonly treated with PARP inhibitors. Removal of any of the components in the 53BP1 repair axis results in impaired NHEJ and resistance to PARP inhibition. It is hypothesised that HR is restored in BRCA1-deficient cells by the absence of the blockade to resection posed by these proteins. This observation also highlights that whilst BRCA1 is not required for resection, it is critical in promotion of resection and commitment to HR through removal of the 53BP1-mediated block.

The mechanism by which BRCA1 overcomes the blockade to resection is still not fully understood. One proposed mechanism that E3 ubiquitin ligase UHRF1 is phosphorylated by CDK2 during S-phase, allowing its recruitment to DSBs by BRCA1. UHRF1 causes RIF1 displacement through ubiquitination and partially overcomes the block to resection (Her and Bunting, 2018). Another proposal is that BRCA1 overcomes this blockade by mediating dephosphorylation of 53BP1 and release of RIF1 through activity of phosphatase, PP4C (Isono *et al*, 2017). More recently it was proposed that BRCA1-BARD1 heterodimer has an E3 ubiquitin ligase function which allows placement of a ubiquitin mark on H2A. This mark is read by chromatin remodeler, SMARCAD1. Both activities are required for repositioning of 53BP1 and commitment to HR (Densham *et al*, 2016). This observation points to a critical role of chromatin in the regulation of repair pathway choice (discussed in Section 1.1.4).

HR is a multi-step process which is initiated by BRCA1 overcoming the 53BP1-mediated block to resection and allowing access of nucleases (e.g. CtIP, EXO1) and helicases (e.g. BLM) which generate a 3' ssDNA overhang which is rapidly coated by RPA to protect the nascent DNA (Panier and Boulton, 2014 & Cejka, 2017). RPA is replaced by RAD51 to form a DNA-RAD51 nucleofilament which will then invade the homologous duplex to form a nascent DNA joint with the homologous sequence known as the D-loop. The homologous sequence is used as a template for DNA synthesis and then DNA intermediates are resolved marking the completion of repair. BRCA1 is thought to have a multi-faceted role during HR progression (Prakash *et al*, 2015). In addition to promoting access of nucleases and resection required for HR commitment, it has also been hypothesised that BRCA1 plays a role in loading of RAD51 and subsequent recombination events. The mechanisms underlying these processes was poorly understood, and the interplay between crucial repair factors (e.g. BRCA1, BRCA2, RAD51) had not been elucidated.

Further mechanistic insights were provided by in vitro work using purified BRCA1-BARD1 (Zhao *et al*, 2017). In these works, the authors showed that BRCA2 (together with its partner protein DSS1)

promoted exchange of RPA for RAD51; an activity not observed with BRCA1-BARD1. More strikingly, BRCA1-BARD1 was shown to promote RAD51-ssDNA nucleofilament engaging with and invading the homologous DNA template, suggesting that BRCA1-BARD1 plays a direct role in stimulating D-loop formation. RAD51 was shown to directly interact with BARD1 and if this interaction was ablated then impaired association of the BRCA1-BARD1 complex with RAD51 and defective stimulation of recombination were observed.

PALB2 (partner and localiser of breast cancer 2 (BRCA2)) has been identified as a pivotal tumour suppressor protein which functions in the Fanconi anemia (FA)/ HR pathways of DNA repair (Zhang *et* al, 2009 & Nepomuceno *et al*, 2017). BRCA1 was identified as a breast and ovarian cancer predisposing gene (Miki *et al*, 1994). As it became evident that BRCA1 did not explain all cases of hereditary cancer, a second predisposing gene, BRCA2 was identified (Wooster *et al*, 1995). BRCA1 and BRCA2 were thought to have resembling biological functions despite their lack of structural homology, and their functions appeared to converge on interaction with RAD51. PALB2 was identified as the bridging protein between BRCA1 and BRCA2 (Zhang *et al*, 2009).

PALB2 interacts with BRCA1 through a conserved coiled coil motif in its N terminus; this association is not increased upon damage induction suggesting a constitutive interaction between BRCA1 and PALB2 (Zhang *et al*, 2009). PALB2 can also interact with RAD51 through this N terminal region and enhances activity of RAD51 during HR (Nepomuceno *et al*, 2017). BRCA2 interacts with PALB2 through its C terminal WD40 domain. This domain can also interact with RAD51. PALB2 possesses two DNA binding regions which allow its interaction with D loops and ssDNA. Additionally, PALB2 has a chromatin-associated motif (ChAM) which interacts with H2B and H3. The chromatin binding activity of PALB2 is crucial to recombination during HR (Bleuyard *et al*, 2011).

These observations suggest that following loading of RPA onto ssDNA, BRCA1 recruits BRCA2 through the bridging protein, PALB2, to mediate exchange of RPA for RAD51. The BRCA1-PALB2-BRCA2 complex is important to RAD51 nucleofilament formation and strand invasion. PALB2 is a

pivotal regulator of HR progression (Nepomuceno *et al*, 2017). These mechanistic insights are summarised in Figure 1.4.

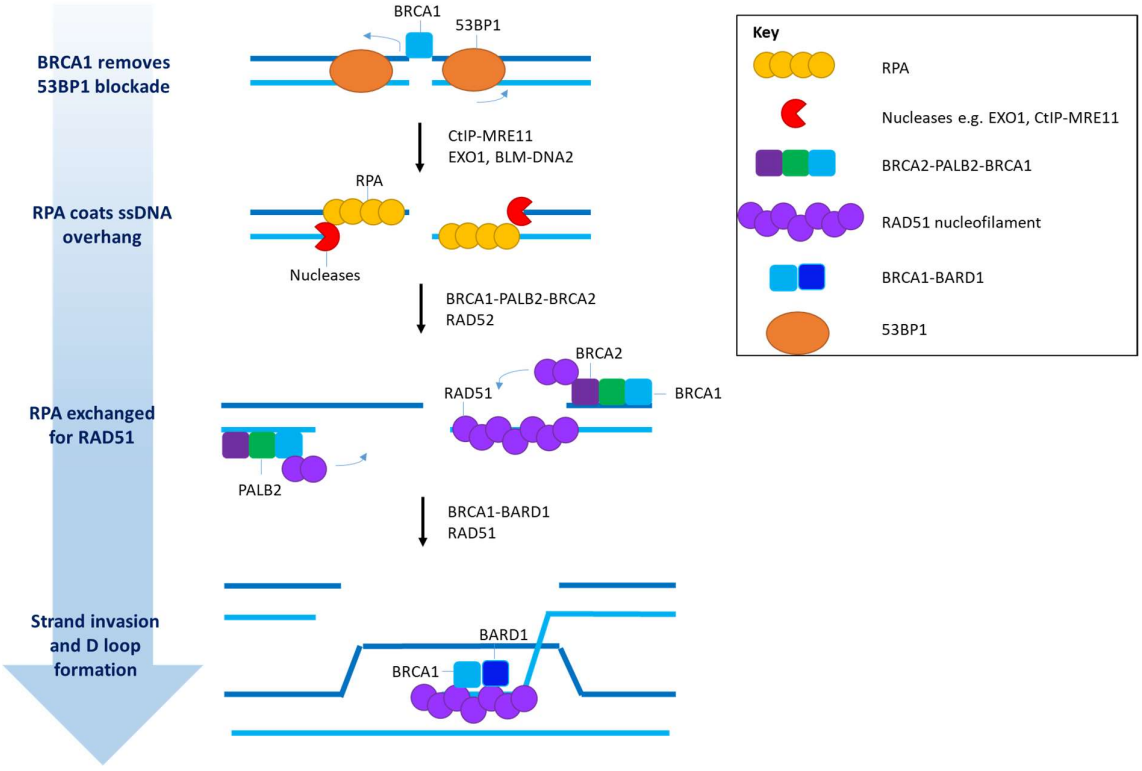

Figure 1.4. Repair of DSBs through homologous recombination (HR). HR is initiated by the removal of the 53BP1 blockade to resection by BRCA1. This allows access of nucleases (e.g. EXO1) and helicases (e.g. BLM) which generate a 3' ssDNA overhang. This overhang is rapidly coated by RPA. The exchange of RPA for RAD51 is mediated by the action of BRCA1, BRCA2 and PALB2 to form the RAD51 nucleofilament. This nucleofilament is responsible for invasion of the homologous duplex to form a D-loop. The homologous sequence is used as a template for repair, and resolution of the DNA intermediates occurs to complete the repair. (Adapted from Cejka, 2017).

1.1.4 Structure of chromatin and its role in DDR

Selection of repair pathway in the appropriate cellular context is regulated by numerous factors (discussed in Section 1.1.2 & Section 1.1.3). DSB repair, like all DNA metabolic processes, is occurring within the highly organised chromatin environment (Clouaire and Legube, 2019). Chromatin is the complex scaffold comprised of DNA wrapped around nucleosomes, enabling compaction of 6 million base pairs of DNA into the nucleus. Nucleosomes are made up of histones:

two H2A-H2B dimers flanking a $(H3\text{-}H4)_2$ tetramer (Soria *et al*, 2012). Interactions between histones are stabilised by linker histones, non-histone proteins and structural RNA components, driving the compaction of chromatin into fibres (Polo, 2014 & Polo and Almouzni, 2015). Chromatin structure is organised at many different levels. The primary level is the winding of DNA around nucleosomes forming a 'beads on a string' structure. This forms the basic structure of chromatin and is organised into a range of configurations which form the 3D organisation of chromosomes in the nuclear space (Clouaire and Legube, 2019).

The highly compacted organisation of chromatin is considered to be protective; in the context of DNA damage, chromatin acts as a barrier impeding access to sites of damage by repair factors (Polo, 2014). The presence of this barrier necessitates a transient disorganisation of chromatin for efficient repair. This process is described in the access/prime-repair-restore model, in which numerous regulatory factors are recruited and drive the remodelling of the chromatin environment for repair. Following repair, the chromatin structure is restored.

Variations in chromatin structure are derived from the presence of histone variants, and the concerted action of two classes of enzymes: ATP-dependent chromatin remodelers and histone modifiers (Smeenk and Attikum, 2013). The former are capable of inducing profound rearrangements in the nucleosomal fibre (Polo, 2014), and can slide nucleosomes, alter or exchange the histone composition of chromatin fibres (Gonfloni, 2013). The latter place post-translational modifications on histone tails (e.g. acetylation, ubiquitination, SUMOlyation), some of which affect histone packaging. Yet, the best studied histone modifiers are crucial to recruitment of repair factors to chromatin. Histone code is regulated by writers which place modifications, readers capable of binding histone marks and erasers which removes the marks (Smeenk and Attikum, 2013). These variations in chromatin structure can control many properties of the chromatin fibre such as mobility, topology and stiffness (Clouaire and Legube, 2019). It has been established that chromatin is extensively modified during, and actively participates in, repair of

DSBs. Numerous mechanisms of chromatin remodelling have been proposed including nucleosomes sliding, histone recycling and histone eviction, yet the precise mechanism by which this occurs has remained elusive.

Upon DSB induction, ATM is recruited to sites of damage and facilitates recruitment of repair proteins, including E3 ubiquitin ligase, RNF8. RNF8 ubiquitination results in recruitment of repair factors (e.g. 53BP1) and proteins responsible for chromatin de-compaction or nucleosome eviction. Factors mediating chromatin compaction (e.g. heterochromatin protein 1) are also recruited. It was unclear how these opposing chromatin dynamics coincide during DSB repair and how these functions affect global chromatin structure. Application of fluorescence lifetime imaging microscopy (FLIM)-Forster resonance energy transfer (FRET) techniques revealed that chromatin undergoes an initial compaction following damage induction (Lou *et al*, 2019). This compaction is thought to stabilise the DNA ends, and allow preparation of the chromatin landscape for repair. Chromatin then undergoes a rapid de-compaction, resulting in a ring of condensed chromatin forming further away from the break site. Interestingly, these highly dense regions are correlated with regions of chromatin decorated with 53BP1. The presence of this chromatin "wave" beyond 53BP1 has led to the hypothesis that chromatin remodelling is required for long range resection to occur and results in bunching of chromatin outside the resected region. Alternatively, the liquid-like properties of 53BP1 assemblies may mechanically displace chromatin as repair machinery spreads (Kilic *et al*, 2019 & Shin *et al*, 2018). These observations are summarised in Figure 1.5 and discussed further in Chapter 5.

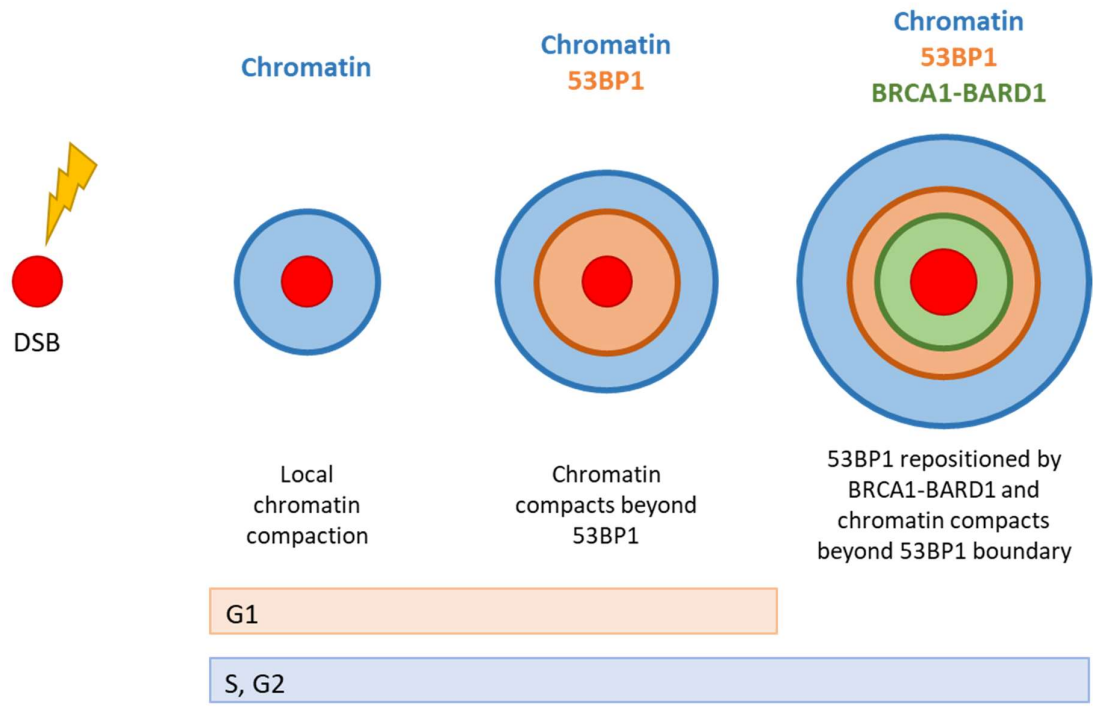

Figure 1.5. Schematic of changes in chromatin compaction as a function of time. Following induction of a DSB, local chromatin rapidly compacts to limit movement of DNA ends and to allow preparation of the chromatin landscape for repair. 53BP1 is recruited to chromatin and chromatin compacts beyond the 53BP1 boundary. When initiating HR, BRCA1-BARD1 activity repositions 53BP1 away from the break site. Chromatin compacts beyond the 53BP1 boundary (Adapted from Densham and Morris, 2019)

Extent of resection is a key determinant in repair pathway choice (Section 1.1.2). Accumulating evidence suggests that chromatin and chromatin-bound complexes play an active role in controlling resection during DSB repair (Densham and Morris, 2019). BRCA1 is responsible for initiating HR by removing the blockade to resection posed by 53BP1. BRCA1 forms an obligate heterodimer with BARD1, and this heterodimer possesses E3 ubiquitin ligase activity. Densham *et al* demonstrated that if BRCA1 defective cells were reconstituted with BRCA1-BARD1 lacking ligase activity, these cells were sensitive to camptothecin, etoposide, PARP inhibition and irradiation, indicating defective HR (Densham *et al*, 2016). Where BRCA1-BARD1 lacked ligase activity, resection lengths were reduced. This was alleviated by a loss of 53BP1. Interestingly, the authors observed that 53BP1 positioning away from sites of damage was also reduced in cells with defective BRCA1-

BARD1 E3 ligase function. These observations suggest that BRCA1-BARD1 E3 ubiquitin ligase activity mediates resection and affects positioning of 53BP1. The substrate of BRCA1-BARD1 was identified as H2A. The ubiquitin mark placed on H2A is read by ATP-dependent chromatin remodeler, SMARCAD1. SMARCAD1 has two N-terminal binding CUE domains. It was shown that both the ATPase activity and CUE domains were required for HR and positioning of 53BP1 away from the break site. This suggests that SMARCAD1-mediated remodelling is important in removing the 53BP1 blockade to resection.

Resection length is tightly regulated (Section 1.1.2). USP48 has been identified as a H2A-specific deubiquitinating enzyme (DUB) (Uckelmann *et al*, 2018). USP48 levels affected resection lengths; over-expression of USP48 resulted in decreased resection lengths, and USP48 deficiency resulted in increased resection lengths. USP48 was shown to function in the same pathway as BRCA1-BARD1 and SMARCAD1; deficiency in either the "writer" (BRCA1-BARD1) or the "reader" (SMARCAD1) resulted in shortened resection lengths. These observations indicated that USP48 loss had little impact where there is no mark to cleave, or there is a lack of the reader of this mark. The authors suggest therefore that USP48 fine-tunes resection lengths to prevent repair via mutagenic SSA therefore preserving genomic integrity. These mechanisms are summarised in Figure 1.6.

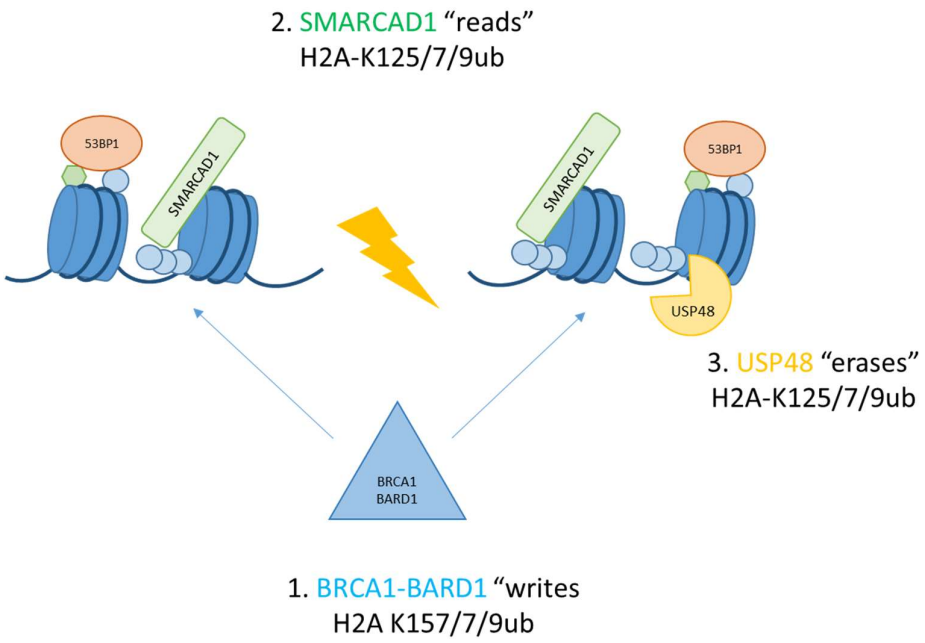

Figure 1.6. Chromatin remodelling controls resection lengths during HR. 1) BRCA1-BARD1 places a ubiquitin mark on H2A (blue circles). 2) This mark is subsequently read by chromatin remodeler SMARCAD1 which results in resection and changes in the positioning of 53BP1 (53BP1 is bound to nucleosomes by H2A K15-ub modification (blue circles) and H4K20-dimethylation (green hexagons)). The H2A-ub mark is removed by USP48 to constrain resection lengths, favouring HR over SSA (Adapted from Densham and Morris, 2019).

1.2 Fluorescence microscopy

Detailed genetic and biochemical analyses have allowed determination of the molecular framework responsible for DNA DSB repair pathways (Misteli and Soutoglou, 2009). The application of fluorescence microscopy has provided further insight into how these pathways are regulated (Section 1.4.1-1.4.3). Much of our knowledge of cellular and subcellular processes is derived from the ability to directly visualise them (Huang *et al*, 2009). Fluorescence microscopy is one of the most powerful tools in biology due to its specificity and sensitivity, but successful application of microscopy to biological questions is complex and must be done with care (Schermelleh *et al*, 2019).

Despite wide application, standard fluorescence microscopy is limited in its resolution to 250 nm in the lateral direction, and 450-700 nm in the axial direction (Galbriath and Galbriath, 2011). The diffraction of light as it passes through the optical system give rise to this limit which means that a single point of light will be visualised as a blurred dot with a diameter of 250 nm. The diffraction limit defines the minimum distance between two objects which can be resolved; any features closer together than this limit cannot be resolved. The width of the point spread function (PSF) for a diffraction-limited optical system is quantified by the Rayleigh (R) criterion:

$$R = 0.61\lambda/NA \text{ (Lateral)}$$

$$R=2\lambda/NA^2 \text{ (Axial)}$$

Where λ is the wavelength of light, and NA is the numerical aperture of the microscope, typically limited to 1.4 (Bates *et al*, 2008), (Huang *et al*, 2009) (Garini *et al*, 2005).

Fundamental components of biology, on the orders of tens to a few hundred nanometres, were rendered beyond the reach of conventional fluorescence microscopes due to the diffraction limit (Schermelleh *et al*, 2010). This challenge is further compounded by the fact that numerous factors can affect the resolution which can be achieved. Factors contributing to achieving maximum resolution include: presence of homogeneous refractive indices, high signal intensity and minimal background noise. In practice, optical aberrations and out-of-focus fluorescence reduce signal-to-noise ratio (SNR) and also decrease resolution.

1.2.1 Removing effects of optical blurring

Resolution and contrast in images may be improved removing the effects of optical blurring and noise. Optical blurring is a consequence of light diffracting in the optical path, and an inherent properly of optical systems which can be predicted theoretically and experimentally (Sibarita, 2005). The statistical distribution of noise can be predicted if the mechanics of the source are known (Wallace *et al*, 2001).

Optical blur can be removed by deconvolution which is a computational technique commonly applied to Z series acquired on a widefield microscope. Optical blurring is defined mathematically as a convolution of each point in an image with the PSF (Wallace *et al*, 2001). Convolution can be calculated and reversed by deconvolution. As noise is statistically predictable, this can be removed by application of filters in pre-processing of images prior to deconvolution.

Confocal microscopy eliminates optical blurring by preventing detection of out-of-focus fluorescence. This is achieved by the presence of a pinhole aperture between the sample and the detector, which only allows light originating from the focal plane to pass through to the detector and rejects out-of-focus fluorescence (Wallace *et al*, 2001). The image can be reconstructed by mapping the detected signal based on the position of the scanning spot. This process can require the pinhole to be closed below the size of the diffraction limited Airy disk (Heintzmann *et al*, 2003), and therefore limits the detected emission from the sample.

Both deconvolution and confocal microscopy yield images of comparable resolution. Despite the requirement of post-acquisition processing, widefield images are typically acquired more rapidly than in confocal systems.

3D imaging can be challenging as when imaging deeper into specimens, the contributions of light scattering are increased. Optical sectioning requires acquisition of slices through the Z-axis of the sample (perpendicular to the focal plane). 3D image data can be computationally reconstructed from these slices (Conchello and Lichtman, 2005). Optical sectioning capability is improved by extraction of the in-focus information within each slice. In widefield microscopy, this is achieved by deconvolution, whereas in confocal microscopy images are built up sequentially by scanning illumination on the specimen. A pinhole aperture is required in confocal systems to reject out-of-focus light (Huisken and Stainier, 2009 & Conchello and Lichtman, 2005).

1.2.2 Improving optical sectioning capability

The use of deconvolution and confocal microscopes enable optical sectioning by removing contributions of out-of-focus fluorescence. Light sheet fluorescence microscopy (LSFM) can, in principle, achieve optical sectioning with SNR at least one order of magnitude better than confocal microscopes (Swoger *et al*, 2014). In LSFM the excitation beam is focussed by a cylindrical lens resulting in a sheet of light of illumination which reaches minimal thickness at the centre of the field of view, meaning only the focal plane is illuminated. This removes out-of-focus fluorescence and also limits photo-damage to the focal plane only. The total number of fluorophore excitations required for 3D acquisitions is greatly reduced compared to confocal systems (Huisken *et al*, 2004).

There are many different LSFM approaches but the underlying principles are similar in the majority of systems. LSFM consists of two independent lenses for illumination and detection in an orthogonal arrangement (illustrated in Figure 1.7) (Swoger *et al*, 2014). This decoupling of the illumination and detection optical paths allows for novel illumination strategies which allow optimal photon collection efficiency.

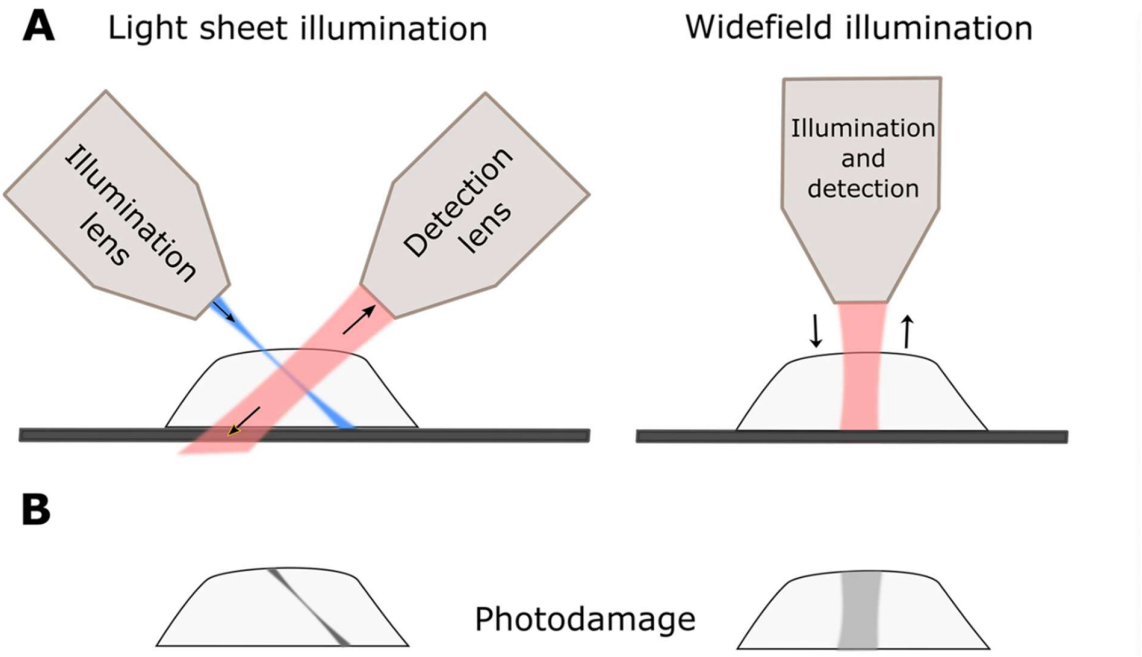

Figure 1.7. Principles of LSFM. A) Comparison of sample illumination and fluorescence detection in light sheet and widefield microscopy. In a light sheet microscope, the illumination is focussed into a single plane which reaches its minimal thickness at the focal plane of the specimen, and emission is detected by an objective arranged orthogonally to the illumination objective. In widefield, the same objective is used for sample illumination and emission detection. The entire sample is illuminated simultaneously. B) Photo-damage in specimens following light sheet and widefield microscopy. Photo-damage is limited to the focal plane only in light sheet microscopy, whereas in widefield microscopy photo-damage affects in- and out-of-focus planes.

Illumination of the focal plane means no out-of-focus fluorescence light is generated. The lateral resolution of the system is defined by the NA of the objective (commonly these are lower NA and longer working distance objectives than in confocal systems), and the axial resolution is dictated by the thickness of the light sheet focussed by the cylindrical optics in the system. Multiple slices can be acquired by scanning the light sheet through the specimen and these slices can be reconstructed to yield a three-dimensional image. Multi-view acquisitions may be reconstructed yielding high isotropic resolution (Swoger *et al*, 2014).

1.2.3 Breaching the diffraction limit: Super resolution microscopy

The diffraction limit was thought to be an insurmountable barrier in the resolution of optical systems since it breaking it involves breaching Abbes law (Betzig, 2015). The introduction of super resolution microscopy (SRM) techniques has provided scientists with a plethora of techniques able to challenge the diffraction limit, approaching resolutions previously only observed in electron microscopy (EM). SRM techniques retain advantages of conventional fluorescence microscopy in terms of sample preservation, ease of imaging and target specificity (Schermelleh *et al*, 2019). SRM can enable extraction of quantitative information regarding proteins localisation, spatial organisation and absolute levels of macromolecules. Moreover, this can be done in three-dimensions (3D) allowing reconstruction and modelling of complex biological processes. Super resolution techniques may be broadly defined as near field and far field, with the former including total internal reflection (TIRF) microscopy and the latter including structured illumination microscopy (SIM), stimulated emission depletion (STED) microscopy and stochastic optical reconstruction microscopy (STORM) (Schermelleh *et al*, 2010). Each technique possesses advantages and limitations, requiring careful consideration when applied to new biological questions (Betzig, 2015).

SIM is a commonly used technique which improves resolution approximately two-fold by illuminating the sample with a series of sinusoidal excitation patterns with high spatial frequency which encode previously inaccessible information into the observed image. This new information is extracted and reconstructed yielding images with a resolution at approximately half the diffraction limit (Schermelleh *et al,* 2010 & Gustafsson, 2000). SIM is based on the Moiré effect; if two fine patterns are superimposed, they combine to form Moiré fringes. One pattern is the unknown spatial pattern of fluorescent dyes in the sample and the other is the known structured pattern of illumination. Information extracted from the Moiré fringes allows reconstruction of the unknown pattern in the sample (Gustafsson *et al*, 2008). This reconstruction is enabled by algorithms which shift the Moiré information back onto the original frequency locations to

synthesise the image (Figure 1.8) (Schermelleh *et al*, 2010). 3D-SIM enables doubling of resolving power in both the lateral and axial dimensions. This is achieved by using a grating which can generate three mutually coherent light beams. These interfere with the specimen to form an illumination pattern in 3D (Gustafsson *et al*, 2008).

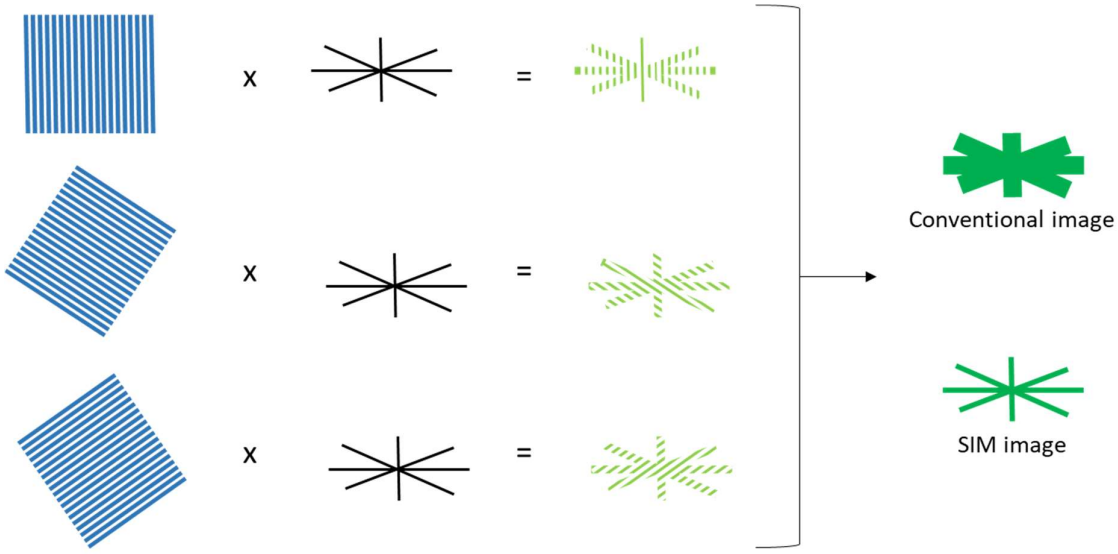

Figure 1.8. Principle of Structured illumination microscopy (SIM). SIM relies on non-uniform illumination of the sample which is enabled by an optical grating. A stripe-shaped sinusoidal interference pattern is generated, rotated and phase-shifted such that the convolution of the illumination pattern (blue lines) with the fluorescently labelled sample (shown in black) generates Moiré fringes. These fringes contain high frequency information which is mathematically reconstructed to give an image with resolution about double the diffraction limit (Adapted from Chozinski, 2018).

To better understand how structured illumination extends resolving capability, it is useful to consider the sample structure in reciprocal space, or its Fourier transform (Gustafsson *et al*, 2000). In a diffraction-limited system, a set of low resolution information is detected in the circular observable region of reciprocal space. By applying structured illumination, information from regions outside of this region are moved inside making it observable. The Fourier transform of the sinusoidal stripe pattern applied in SIM has three non-zero points; the origin and two others which are offset from the original in a direction defined by the orientation of the stripe pattern. Additional

information is contained in the image (moiré fringes) which correspond to information which has been offset by the same amounts in reciprocal space. The observable region now contains information originating from the offset regions and these regions represent information not observable in conventional microscopes. This is summarised in Figure 1.9.

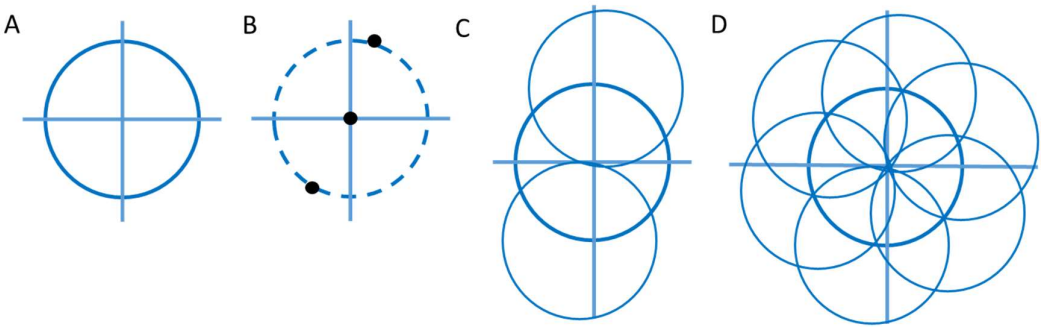

Figure 1.9. Resolution enhancement using structured illumination. A) In a conventional diffraction-limited microscope, information can be detected in the circular observable region in reciprocal space. B) The sinusoidal stripe illumination pattern has three Fourier components; in addition to the original there are two other components which are limited by the original circle which defines the observable region. Moiré fringes are produced by structured illumination and reflect the information that has changed position in reciprocal space. Information is encoded from these offset regions. D) Images are acquired with different orientation and phase of patterns which means it is possible to recover information from an area twice the size of the normal observable region (adapted from Gustafsson *et al*, 2000).

STED microscopy relies on the controlled de-excitation of fluorophores via stimulated emission. Stimulated emission is achieved by a depletion beam which has a doughnut shape with zero intensity at the centre. Fluorophores outside of the zero intensity region will be rapidly de-excited (Huang *et al*, 2009). Emission from fluorophores in the zero intensity region of the depletion beam is detected. In STED acquisitions both the excitation and depletion beams are scanned across the sample simultaneously to build up a super resolution image (Figure 1.10). The size of the zero intensity spot of the depletion beam dictates the resolution of STED, with resolution between 30-80 nm being reported. Theoretically, STED can reach the size of a molecule, the absolute limit of a microscope, but this is impractical since resolution is related to the intensity of the depletion beam

and can lead to photo-destruction of the sample and fluorophores where high powers are used (Vicidomini *et al*, 2018).

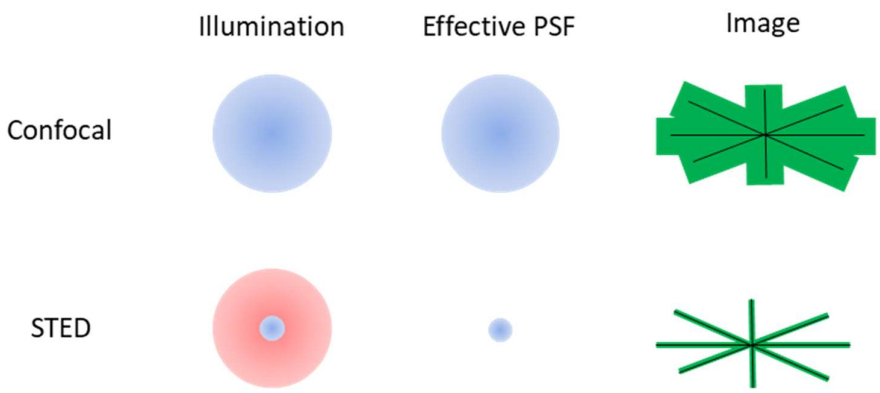

Figure 1.10. Principle of stimulated emission depletion (STED) microscopy. Unlike in confocal microscopy, where resolution is limited to 250 nm, STED allows for 30-80 nm resolution. In STED, two overlapping beams are applied, the excitation (blue) and the depletion beam (red). The depletion beam is at a longer wavelength and is tuned to de-excite fluorophores by simulated emission and is engineered to give a doughnut-shaped foci intensity distribution with zero intensity at the centre. All fluorophores will be depleted except those in the zero intensity region whose emission is detected (Adapted from Chozinski, 2018).

Single molecule localisation microscopy (SMLM) techniques are based on the ability to detect the fluorescence emitted by a single fluorophore and precisely determine its position. Examples of such techniques include stochastic optical reconstruction microscopy (STORM) (Schermelleh *et al,* 2019) and photoactivated localisation microscopy (PALM) (Hess *et al*, 2006). In both cases, small random subsets of optically resolvable fluorophores are activated, localised and inactivated. These events are collected over thousands of frames (Van De Linde *et al*, 2011). Providing enough photoactivation events are detected per fluorophore, their localisation is precisely determined and all collected points are subsequently reconstructed into a super resolution image (Figure 1.11) (Huang, 2010).

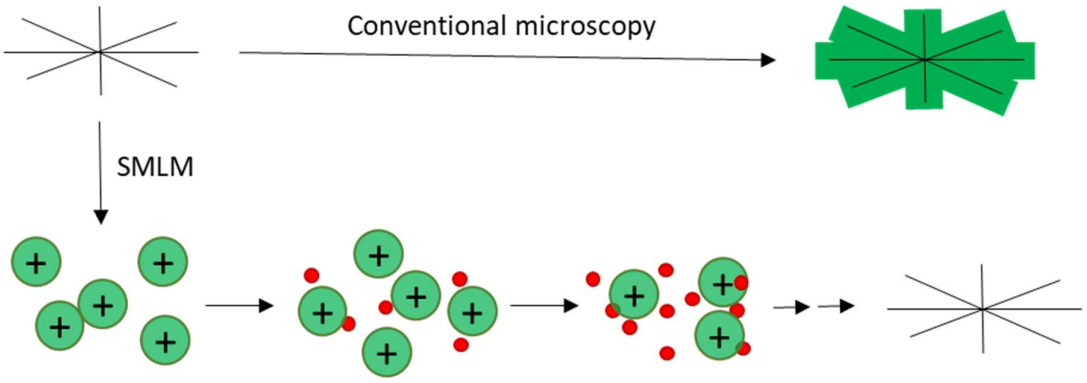

Figure 1.11. Principle of single molecule localisation microscopy (SMLM). SMLM techniques rely on a sparse subset of fluorophores being activated sequentially (green circles) and detected over thousands of frames. Gaussian fitting enables precise localisation (black crosses) of the detected points (red dots) which are then reconstructed (Adapted from Chozinski, 2018).

SMLM is advantaged in its ability to localise fluorophores with a lateral precision of ~20 nm and in its simplicity to implement using widefield microscopic set ups. One of the main disadvantages of these approaches is the challenge of 3D acquisitions; most experiments using SMLM require TIRF or highly inclined and laminated optical sheet (HILO) illumination to remove out-of-focus light which would otherwise affect precision of localisation (discussed in Section 1.2.4).

1.2.4 Choosing the correct microscopy technique

When applying microscopy, one must match the experimental requirements to the technical performance of the imaging set up. Resolution is often considered the most important parameter. More recently, increased consideration has been placed in other factors required for SRM. These factors include: live cell imaging compatibility (e.g. photodamage, energy intensity); multi-dimensionality (e.g. multi-colour capability, labelling density); and versatility (e.g. ease of access, artefact induction) (Schermelleh *et al*, 2010).

When applying microscopic techniques to DDR we require 3D, multicolour capability to capture the interplay between different repair factors in the complex topology of the genome. SIM is a commonly applied technique as it requires no complex sample preparation, and is suited to live

and volumetric imaging. Further, there are minimal constraints on fluorophores used meaning multicolour applications can be achieved with ease. The major caveat of SIM is the requirement of sophisticated computational procedures to enable image reconstruction. This renders the technique susceptible to reconstruction artefacts, requiring the trained eye to recognise and avoid them (Heintzmann and Huser, 2017 & Schermelleh, 2019). SIM has a resolution of 100-130 nm laterally, and 250-350 nm axially. Whilst this is substantially improved compared to diffraction-limited systems, it also renders this technique unable to clearly delineate relative boundaries between proteins in repair foci, particularly due to Z axis resolution being poorer than XY.

STED microscopy can achieve resolutions between 30-80 nm, yet its practical application can be challenging (Schermelleh *et al*, 2010). STED is hampered by stringent requirements of fluorescent dyes; dyes must have broad stokes shift and high quantum yield, and the excitation range of the dye should not coincide with the STED beam. High intensity laser power is required to achieve complete fluorescence quenching which causes significant challenges with photo-damage. STED is also costly and has complex set up requirements (Vicidomini *et al*, 2018). Multicolour applications of STED are challenging, although two colour applications have been demonstrated (Reindl *et al*, 2015).

When optimally applied, SMLM techniques achieved lateral resolution of 5-20 nm. One of the main drawback of SMLM techniques is challenges in 3D acquisitions. Use of a cylindrical lens in the optical path creates an astigmatism meaning the PSF is distorted according to its Z position. When imaging in 3D, because STORM is widefield, out-of-focus probes are excited which increases background and affects accuracy of localisation (Fischer *et al*, 2011). SMLM approaches commonly apply TIR illumination to remove the effects of out-of-focus fluorescence, constraining these techniques to two dimensions (Schermelleh *et al*, 2019). As with STED, dyes used require specific properties, limiting multicolour applications. The long acquisition times of SMLM induce significant photo-damage.

Imaging depth is a significant challenge in all cases, largely due to the effects of refractive index mismatch (between objective immersion and the specimen, and indeed within the specimen). To overcome some of the limitations of current SRM techniques, we selected Expansion Microscopy (ExM) for visualisation of repair proteins during DSB repair.

1.3 Expansion Microscopy (ExM)

Expansion microscopy (ExM) is a novel fluorescence microscopy technique which allows three-dimensional (3D) nanoscale visualisation of preserved biological specimens on conventional, diffraction-limited microscopes. This is enabled by embedding the specimen in a polyelectrolyte gel which is synthesised evenly and densely throughout the specimen. The polyelectrolyte gel is subsequently swollen by the addition of water, resulting in a physical isotropic expansion up to 100-fold volume (Chen *et al*, 2015). The net effect of this is a de-crowding of features within the specimen, allowing access to nanoscale information on a diffraction-limited microscope (Chozinski *et al*, 2016). The use of this innovative sample treatment eliminates the need for sophisticated software and expensive hardware as exists with other super resolution microscopy approaches (Section 1.2.3 & 1.2.4) (Gao *et al*, 2017). ExM samples are optically cleared during the preparation, which eliminates the effect of light scattering through the sample. As a result, ExM allows for rapid image acquisition with imaging depths and volumes orders of magnitude higher than those possible using other super resolution techniques. ExM is optimal for scalable super resolution imaging in cells and thicker specimens e.g. tissue sections.

Several variants of ExM methodology have been developed since its first demonstration by Boyden and co-workers in 2015 to develop application of the technique. There has been a focus on improving the methodology by i) developing labelling strategies compatible with ExM, ii) enabling multi-colour labelling of different biomolecules simultaneously and iii) improving resolving power. ExM methodologies broadly involve the same steps (summarised in Figure 1.12) (Tillberg *et al*, 2016 & Chozinski *et al*, 2016). Specimens are labelled (e.g. immunofluorescence, fluorescent proteins).

Labels are chemically equipped with anchors which allow their incorporation into the polyelectrolyte gel which is formed evenly and densely throughout the specimen. The polymer-embedded specimens are homogenised to remove any features which would hinder isotropic expansion. Homogenisation can be achieved enzymatically (e.g. proteinase K) or chemically through heating or denaturation. Finally, the gel is immersed in an excess of water which diffuses through the polymer and drives swelling of the gel through osmotic forces. The result is a 4-4.5x expansion of specimens in all three dimensions. Labelled structures can be visualised with an effective resolution of ~70 nm laterally, and ~200 nm axially (Gao *et al*, 2017).

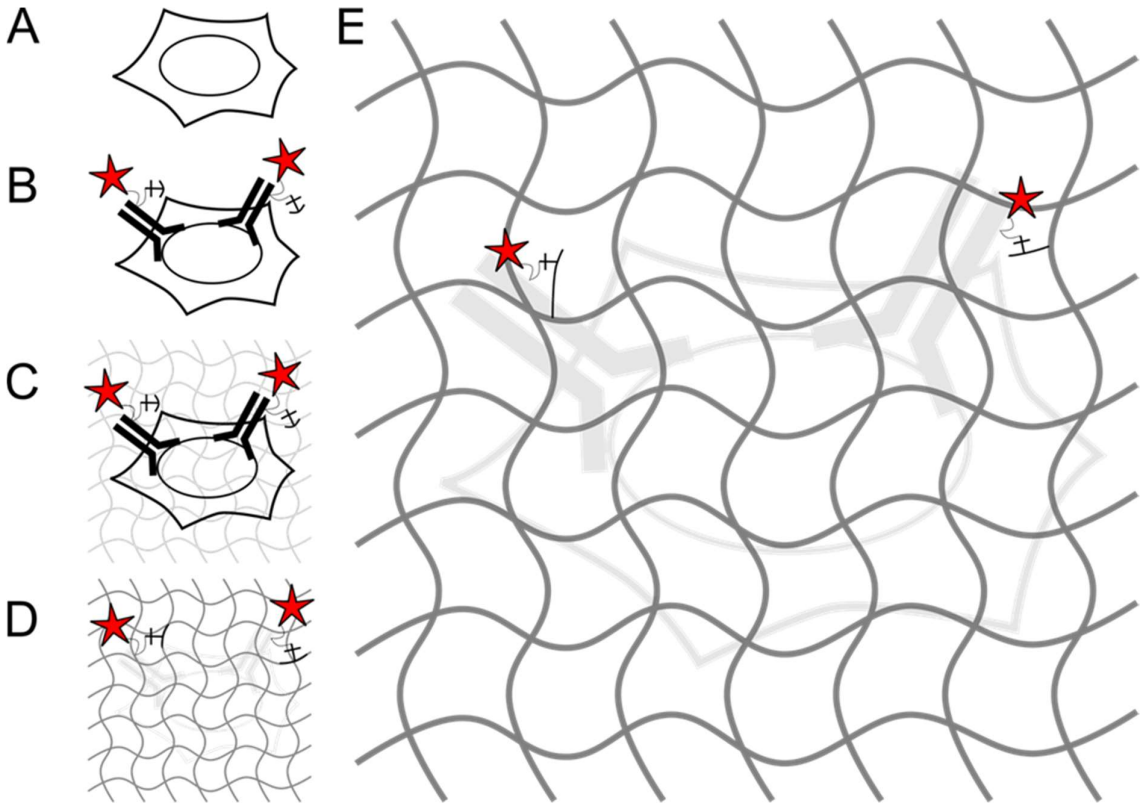

Figure 1.12. General ExM protocol. A) Cells are fixed and permeabilised. B) Cells are immunolabelled using conventional fluorescent antibodies, and are chemically equipped with anchors to allow their incorporation into the polyelectrolyte gel. C) The labelled cells are then infused with monomers, sodium acrylate and acrylamide, and cross-linker N,N'-methylenebisacrylamide. Free radical polymerisation is induced by addition of initiator ammonium persulfate (APS) and accelerator tetramethylethylenediamine (TEMED). D) Samples are homogenised (e.g. using proteinase K). E) Samples are immersed in an excess of water resulting in 4-4.5-fold expansion of specimens in each dimension. The resultant gel contains anchored labels which are imaged post-expansion (Faulkner, Neely and Thomas, 2020).

1.3.1 Ensuring robust, isotropic expansion of specimens

A key consideration when applying ExM is ensuring that expansion is isotropic on the macro- and nanoscale (Pesce *et al*, 2019). Isotropy of expansion is a measure of the uniformity of expansion at the nanoscale, where anisotropy in the expansion leads to distortion in the expanded image. Isotropy of expansion is controlled by two key parameters: formation of a homogenous, dense polymer network throughout the specimen, and efficient homogenisation of features which impede isotropic expansion (Wassie *et al*, 2019). The composition of the gel is critical to robust and

reproducible expansion of specimens. Boyden and co-workers formulated a gel composition to ensure optimal expansion of specimens and mechanical stability of gels for ease of imaging (Chen *et al*, 2015). ExM gels are swellable polyelectrolyte gels which expand rapidly in the presence of solvent (Tanaka *et al*, 1980) whilst preserving nanoscale organisation of specimens. The principles underlying expansion of polyelectrolyte gels is summarised in Figure 1.13 (Cho *et al*, 2018).

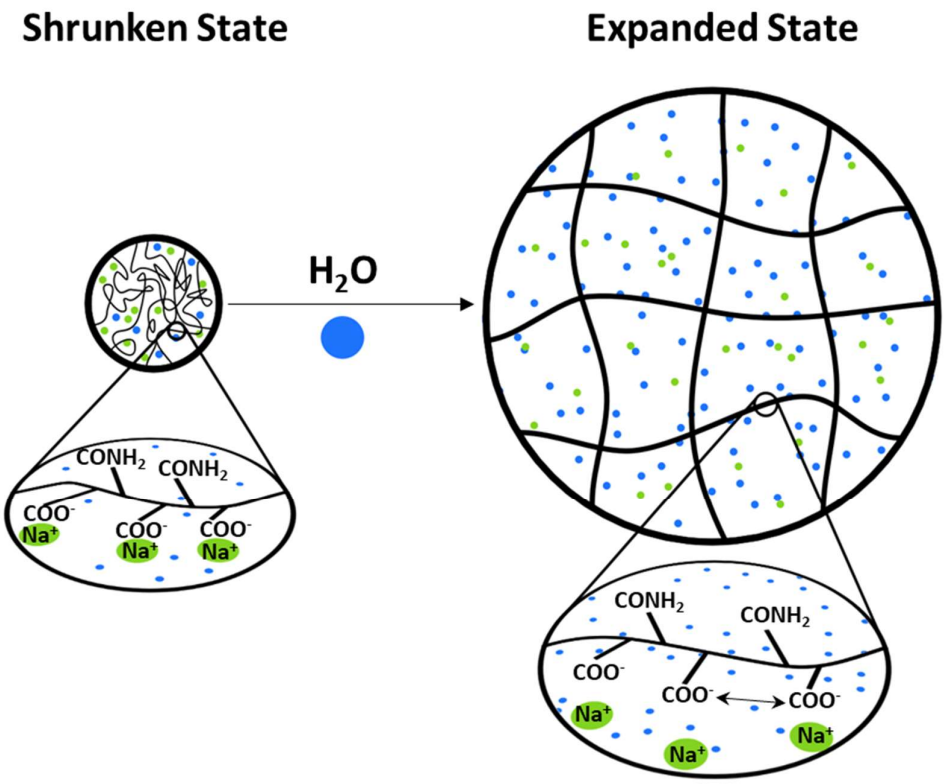

Figure 1.13. Osmotic forces are key to expansion of polyelectrolyte gels. Polymers with ionically charged monomer subunits can be swollen or contracted in a controlled manner by addition of water or salt, respectively. Gels are held in their shrunken state by sodium ions which mask the negatively charged polymer backbone. Upon addition of water, the sodium ions are removed and electrostatic repulsion between the negative charges of the polymer backbone results in stretching (Adapted from Chozinski, 2018).

A key feature of these gels is the meshwork is estimated to be 1-2 nm in its shrunken state; well below the size of biomolecules, meaning they can be pulled apart from each other whilst retaining

their relative spatial organisation down to a precision of 5-10 nm (Wassie *et al*, 2019). The cross-linked topology of the gel is thought to be critical to retaining nanoscale information with minimal distortions in ExM prepared samples (Gao *et* al, 2017 & Tillberg and Chen 2019).

For each variant of ExM, distortions induced during the expansion process have been carefully quantified (Chen *et al*, 2015, Chozinski *et al*, 2016, Tillberg *et al*, 2016, Chen *et al*, 2016, Chang *et al*, 2017, Pernal *et al,* 2020). This has commonly been achieved by use of a correlative imaging approach in which images of highly conserved, well-defined features (e.g. microtubules) are acquired pre-expansion on a super resolution system (e.g. SIM). ExM preparation is completed and then the same features in the same cells are imaged on a diffraction-limited system (e.g. confocal). The features in each image are compared and distortions are quantified by non-rigid affine registration of the images (Wassie *et al*, 2019). Using this approach, 1 – 4% errors in length measurements on the scale of tens to hundreds of microns have been determined.

Determining isotropy of expansion is crucial to account for induction of distortions and heterogeneities induced by the ExM preparation (Pesce *et al*, 2019). Determining expansion factor of structures of interest to allow accurate quantitative measured of structures is hampered by the presence of 'differential expansion' within specimens (Pernal *et al*, 2020). Expansion factor has previously been correlated to the expansion factor of the gel, yet this approach is insufficient to account for differences in expansion factor across all measurement scales. Differential expansion is a derived from varying ionic conditions in samples, resulting in differential expansion factors across these samples. Zhao *et al* report differential expansion of different tissues which were prepared for pathology, with expansion factors between four- and five-fold, and an average expansion factor of 4.7-fold (Zhao *et al*, 2017). Further, the authors observed different portions of a human kidney had different physical size expansion, suggesting anisotropic expansion was occurring. Pernal *et al* observed differential expansion of specimens between tissues, organelles

and within organelles themselves. The presence of anisotropic expansion renders absolute measurements within specimens challenging.

Pesce *et al* demonstrated that nuclear pore complex, Nup153, could be used as an intrinsic measure to verify isotropy of expansion and accurately measure expansion factor, with a precision of 5-10 nm (Pesce *et al*, 2019). This was determined by measurements of large numbers of this highly conserved, macromolecular complex with STED following ExM preparation. Minimal distortions were observed, but the authors note this does not exclude effects on other complexes within specimens, so users should carefully characterise isotropy and expansion factor within their structures of interest. Martinez *et al* observed anisotropic expansion of regions of the hydrogels containing or devoid of cells, which they conclude is due to changes in ionic properties across the gels (Martinez *et al*, 2020). They further demonstrate that expansion across cells is isotropic, and accurate determination of expansion factors can be achieved by use of molecular standards such as microtubules.

These observations highlight a need for users to carefully consider sources of anisotropy in their experimental set ups. Where possible measures of isotropy and quantification of expansion factor should be determined within structures of interest, and these measures should be corroborated by comparison to other techniques. We carefully validate isotropy of expansion in the nuclear sub-compartment and measure expansion factor in Chapter 3.

1.3.2 Optimising labelling and anchoring in ExM

Successful application of ExM requires a labelling strategy which results in labels retaining their relative spatial organisation through the digestion and expansion steps (Chen *et al*, 2015). Chen *et al* originally achieved this by use of a custom-made trifunctional probe which was comprised of a DNA oligomer conjugated to an antibody. The oligomer was modified with an anchoring moiety for incorporation of the probes into the polyelectrolyte gel, and a fluorophore for detection. Several

trifunctional probes bearing different fluorophores and oligomers were synthesised and their use was validated in both cells and tissue sections.

The requirement for expensive, custom-made probes limited the wider application of ExM. This limitation was overcome by use of commercially available cross-linking monomers as the anchoring moiety (e.g. glutaraldehyde) (Chozinski *et al*, 2016). The authors hypothesised that it would be possible to retain labels through the digestion and expansion steps required by ExM if sufficient linkages could be formed between the antibodies and the polyelectrolyte gel. They demonstrated good retention of fluorescent signal in cells and tissues following use of commercially available cross-linkers glutaraldehyde and methacrylic acid N-hydroxysuccinimidyl ester (MA-NHS). The retention of labels using commercially available anchoring moieties was similarly demonstrated in the development of protein retention ExM (ProExM) using 6-((acryloyl)amino)hexanoic acid (AcX) (Tillberg *et al*, 2016). Both approaches were shown to be compatible with use of genetically encoded fluorescent proteins. GFP and GFP-like proteins have high stability to proteases so can survive the enzymatic digestion step. A range of fluorescent proteins were tested and most retained >50% of their fluorescence intensity post-digestion.

A key limitation of ExM is reduced contrast in images due to a number of factors; 100-fold volumetric dilution of fluorescence signal due to expansion (Wassie *et al*, 2019), loss of fluorescently labelled antibody fragments due to digestions (Wen *et al*, 2020 & Shi *et al*, 2019), and destruction of fluorophores during gelation (Min *et al*, 2020). These limitations are summarised in Figure 1.14. Several approaches have been developed to mitigate these effects. As a result, there are now a multitude of specially designed labelling protocols and the chosen approach depends on experimental parameters and the identity of the target molecules (Wen *et al*, 2020).

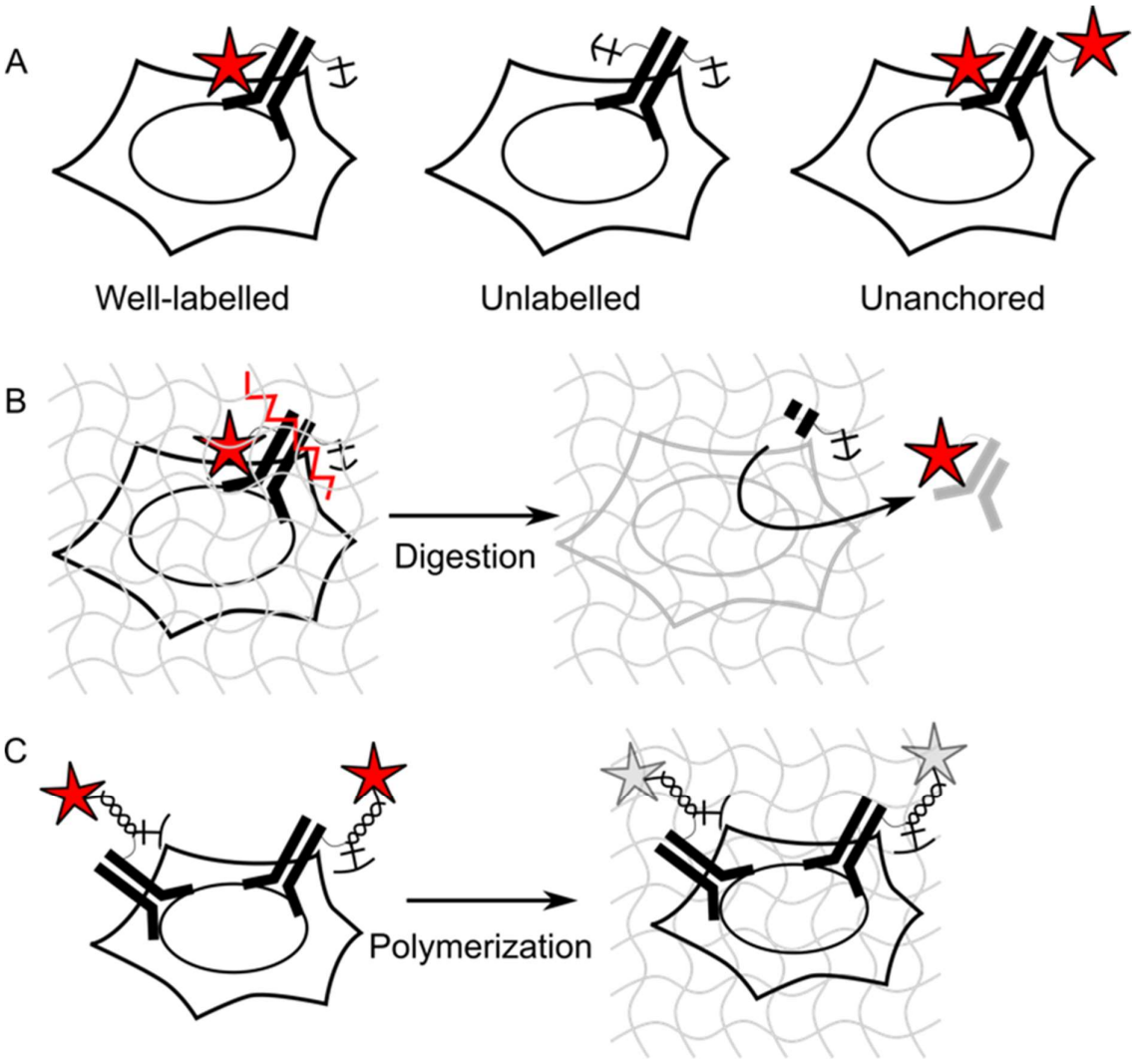

Figure 1.14. Loss of fluorescent signal in ExM prepared samples. A) Heterogeneity in antibody labelling results in only a fraction of labels being retained for post-expansion imaging. B) Fragmentation of fluorescent antibodies during digestion of specimens may result in loss of fluorescent fragments which have not been anchored to the polyelectrolyte gel during the expansion step. C) Free radicals formed during polymerisation of the polyelectrolyte gel results in damage to fluorophores rendering them non-fluorescent (Faulkner, Neely and Thomas, 2020).

An approach to overcome the effects of volumetric dilution of fluorescence and destruction of fluorophores due to free radical production during gel polymerisation is post-expansion labelling of specimens. This was attempted in the development of ProExM where the non-specific proteinase digestion was replaced with milder homogenisation conditions (e.g. LysC) to retain epitopes for post-expansion labelling. Although this approach did support post-expansion antibody

labelling, labelling efficacy was dependent on antibody identity, and the incomplete homogenisation of specimens resulted in anisotropic expansion of specimens. Post-expansion labelling has since been successfully achieved in the development of magnified analysis of the proteome (MAP) (Ku *et al*, 2016) and Ultra-ExM (U-ExM) (Gambarotto *et al*, 2019). Both MAP and U-ExM rely on principles underlying tissue clearing methods combined with ExM to retain endogenous proteins and allow for nanoscale imaging of samples (Figure 1.15). These approaches improve contrast in post-expansion images and increased labelling density due to accessibility created by the expansion process, but labelling efficiency is dependent on antibody identity.

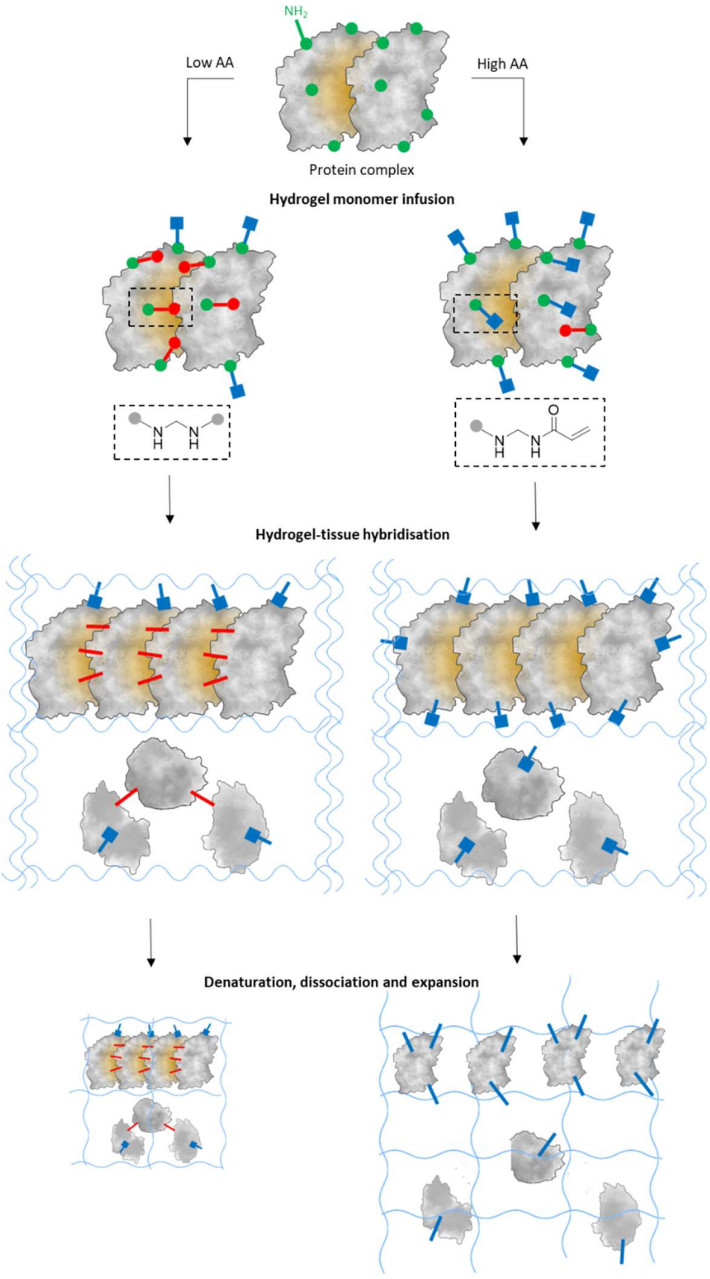

Figure 1.15. MAP and U-ExM approaches to ExM. In addition to standard fixation using 4% PFA, a formaldehyde-acrylamide solution is used. When acrylamide (AA) concentration is low the formaldehyde interacts with proteins to form methylol groups which react with amide groups within and between proteins to form methylene bridges. These structures prevent dissociation of complexes during expansion which limits expansion factor. When acrylamide (AA) concentration is high, acrylamide masks the methylol groups and prevents formation of methylene bridges, thus limiting inter- and intra-protein crosslinking whilst simultaneously maximally anchoring proteins to the polyelectrolyte gel. As a result, proteins readily disassociate during expansion. Homogenisation of samples is achieved by use of denaturing buffer and heating in these approaches (Adapted from Ku *et al*, 2016).

Whilst a portion of antibody fragments are bound to the hydrogel through use of simple, commercially available crosslinking reagents, the non-specific proteolytic digestion step results in fragmentation and loss of up to 50% of fluorescently labelled antibody fragments during the expansion step. This issue has been addressed by direct grafting strategies (Wen *et al*, 2020) and label retention ExM (Shi *et al*, 2019). These approaches rely on use of trifunctional probes comprised of a targeting moiety, a reporter functionality and a polymerisation group. By conjugating the fluorophore directly to the anchoring moiety, loss of fluorescently labelled fragments during digestion and expansion steps is mitigated. Additionally, the process is simplified as the labelling and anchoring steps can be performed simultaneously.

Shi *et al* developed trifunctional probes which were compatible with use of enzymatic tags (e.g. SNAP-tag, CLIP-tag) in addition to conventional immunofluorescence, extending the labelling approaches compatible with ExM. Direct grafting strategies developed by Wen *et al* focussed on the development of small molecule targeting trifunctional labels in addition to immunostaining trifunctional labels. A range of phalloidin conjugates modified with a range of fluorophores were developed and validated for labelling actin in cells. Applying phalloidin in ExM protocols had previously been limited by difficulties in functionalising phalloidin with an anchoring moiety and a fluorophore. Small molecule trifunctional probes targeting membrane lipids (e.g. trivalent fluorescent lipids carrying 1,2-Distearoyl-sn-glycero-3-phosphoethanolamine (DSPE)) were also developed. Following permeabilisation, digestion and expansion steps required by ExM, much of the lipid content is solubilised and washed out meaning that labelling of lipids had previously been incompatible with ExM. By substituting the lipid structure with a permanently anchored label prior to expansion, the structural information is retained for post-expansion imaging. The authors hypothesised this approach could be used to investigate asymmetry between the inner and outer leaflet of membranes.

The polymerisation reaction is thought to lead to chemical damage of particular fluorophores, rendering them non-fluorescent (Chen *et al*, 2015 & Chozinski *et al*, 2016). The extent of damage depends on fluorophore identity, with some (e.g. Alexa Fluor 647) being completely destroyed following gelation, whilst others (e.g. Alexa Fluor 488) retain >50% of their brightness. This observation means that fluorophore choice is crucial in all ExM approaches. The best-performing fluorophores for ExM were identified as AF488, Tamra, Atto565 and Atto647N (Chen *et al*, 2015). This list has since been further extended to include AF405, AF546, AF568 and GFP (Chozinski *et al*, 2018). Min *et al* methodically characterised a range of Alexa Fluor (AF) and cyanine-based dyes to achieve four colour imaging with maximum signal-to-noise ratio following standard ExM preparation (Min *et al*, 2020). The authors quantified fluorescence intensity following gelation and concluded CF405S, CF488, CF568 and CF660R were optimal for 4 colour imaging.

Many of the labelling approaches focus on imaging of proteins post-expansion. It has also been demonstrated that ExM is compatible with labelling of nucleic acids in the development of expansion fluorescence in situ hybridisation (ExFISH) (Chen *et al*, 2016). A small molecule linker termed LabelX (Figure 1.16) was applied to retain the localisation of RNA transcripts for post-expansion imaging. These transcripts were detected using FISH probes. It was shown that LabelX also allowed to the expansion of the nucleus.

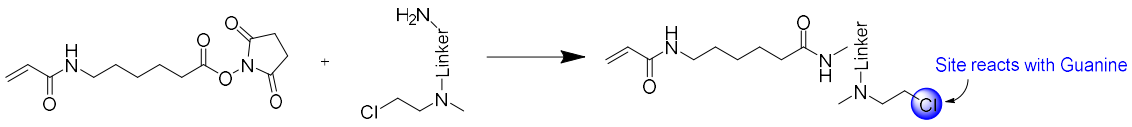

Figure 1.16. Synthesis of LabelX. Synthesis of LabelX, achieved by reaction of AcX monomer with label-IT reagent. The formed LabelX can bind Guanine.

1.3.3 Improving resolving power of ExM

ExM protocols typically result in 4.5x expansion factor in all three dimensions, resulting in an effective resolution of 70 nm laterally and 200 nm laterally (4.5-fold smaller than the diffraction limit). It was hypothesised that increased expansion factor would increase the resolving power of

ExM, which lead to the development of two approaches: iterative ExM (iExM) (Chang *et al*, 2017) and X10 ExM (Truckenbrodt *et al*, 2018). iExM enables 25 nm resolution on diffraction-limited microscopes. This was achieved by performing a preliminary expansion of specimens, followed by formation of a second polymer mesh in the spaces created by the first expansion. The molecular information contained in the first gel is then chemically transferred to the second gel, and the first gel is dissolved. Finally the second gel is expanded resulting in a 4.5 x 4.5, or 20x physical expansion of molecular information contained in the second hydrogel. The chemical transfer of molecular information is enabled by use of antibodies bearing oligonucleotides. iExM approach is shown in Figure 1.17.

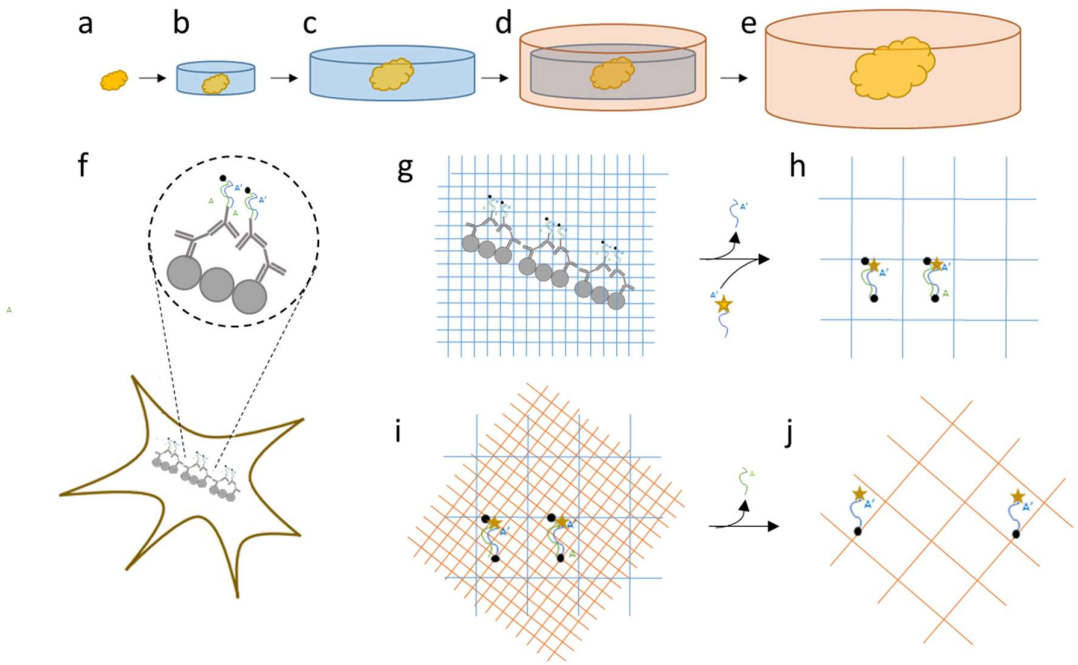

Figure 1.17. Iterative expansion microscopy (iExM) approach. a) The specimen is labelled and labels are chemically equipped with anchors. b) The sample is embedded into a polyelectrolyte gel network containing a cleavable cross-linker c) and then homogenised and expanded. d) A second gel meshwork is formed in the spaces created by the first expansion. e) The first gel is dissolved and the second gel containing the anchored labels is expanded. f) Biomolecules of interest are labelled with a primary antibody followed by a secondary antibody which is conjugated to DNA (blue A') and a complementary strand (green A) which has an anchor shown as a black dot. g) These labels are anchored to the first gel via the cleavable anchoring moiety on the green A strand. h) Following the first round of expansion a new A' DNA strand modified by a fluorophore and an anchoring moiety is added and will hybridise to the anchored green A strand. i) The second gel is formed and the blue A' strand bearing the fluorophore is incorporated via its anchoring moiety. j) the second gel containing the fluorescently labelled blue A' strands is expanded following the digestion of the first gel (Adapted from Chang *et al*, 2017).

iExM is compatible with fast, large-scale imaging of specimens using light sheeting microscopy, due to the optical clearing which is inherent to the ExM protocol. The presence of the second gel meshwork endows iExM processed samples with enough mechanical stability to support sectioning of the gels. A key consideration when applying iExM is the volumetric dilution of fluorescence is increased, resulting in lower densities of labels for post-expansion imaging than in standard ExM

approaches. This can be mitigated by use of amplification chemistries (e.g. hybridisation chain reaction (HCR)) which can be performed in the space created by the expansion.

X10 ExM offers a simple approach to achieve 25-30 nm resolution on diffraction-limited systems. This approach is compatible with the use of commercially available cross-linking molecules (e.g. AcX). Increased expansion factor is achieved by modifying the gel composition to incorporate N,N-dimethylacrylamide (DMAA) and sodium acrylate. DMAA is a self-crosslinking monomer meaning the gel can form without additional multifunctional monomers. These gels have excellent mechanical stability and are super-absorbent, able to absorb 3000x their weight in water. These gels also have a more uniform distribution of crosslinks in their networks than the standard ExM gels reducing local stress and distortions induced by the expansion.

Another approach to increase resolving power of ExM is combining it with other super resolution techniques including structured illumination microscopy (SIM) (Halpern *et al*, 2017), stimulated emission depletion (STED) microscopy (Gao *et al*, 2018) and stochastic optical reconstruction microscopy (STORM) (Xu *et al*, 2019). These combinations result in an effective resolution of ∼30 nm, ∼10 nm and ∼10-20 nm, respectively. Care must be taken to minimise trade-offs in the imaging experiment when combining ExM with other super resolution approaches (Gao *et al*, 2018). The imaging depth is increased 4-fold in expanded samples, necessitating use of water-based immersion objectives to reduce spherical aberrations. To overcome the volumetric dilution of fluorescence inherent to ExM approaches acquisition parameters may need to be altered. For each combined approach, specific changes to sample preparation or acquisition conditions may be required. For example, in the case of SIM, ExM gels need to be completely immobilised to prevent movement of the sample during image acquisition which would induce reconstruction artefacts in the final image. When applying STED to expanded samples, an intensive labelling approach to achieve sufficient labelling density is required.

1.4 DNA damaging agents induce different types of damage

Our genomic material is under continuous assault from numerous exogenous and endogenous agents which induce a number of different lesions which will be resolved through distinct repair processes depending on the nature of the resulting damage (Nagy and Soutoglou, 2009). It is therefore important to consider the type of method used to induce damage when applying fluorescence microscopy as this will affect the accumulation of repair factors in the nucleus and the type of information which can be acquired.

Commonly applied agents to induce DNA damage include: γ-irradiation, chemical agents (e.g. radiomimetic agents, topoisomerase I (TopoI) and topoisomerase II (TopoII) inhibitors, cross-linking agents), UV irradiation, α-particles and heavy ions, lasers and site-specific nucleases. Each of these produces different types of DNA lesions through different mechanisms; the type of damaging agent will be selected based on the repair pathway under study.

In this work, we applied γ-irradiation, which is commonly used in cell cycle profiling, survival and check point activation assays (Nagy and Soutoglou, 2009). The spatial distribution of lesions induced by irradiation are dictated by discrete energy deposition through the nucleus during the passage of the ionising track (Lomax, Folkes and O'Neill, 2013). Irradiation typically induces around 850 pyrimidine lesions, 450 purine lesions, 1000 single strand breaks (SSBs) and 20-40 DSBS/ cell/ Gy.

DSBs are considered the most toxic damage type; both simple and complex breaks can be formed, with the latter commonly having an increased frequency of oxidised base modifications and abasic (AP) sites adjacent to the DSB ends which can impede their repair. It is also important to note that more relaxed regions of DNA have an increased propensity for damage. Non-DSB clustered damage sites are comprised of two or more lesions within 1-2 turns of the DNA helix and can be bi-stranded or in tandem. As irradiation increases the yield and complexity of clustered damage increases. Non-DSB clusters are commonly repaired by base excision repair (BER), however, the efficiency of repair

is compromised in clustered lesions when compared with isolated lesions. This is affected by a number of factors including the inter-lesion separation, the number of lesions and their orientation. This reduction in repair efficiency is further compounded by the hierarchical nature of repair; SSBs are repaired ahead of excision of bases, and excision of one base impedes the excision of further base lesions. These factors extend the lifetime of clustered damage and increase their mutagenic potential through increased likelihood of these clusters encountering a replication fork. Collision of the replication fork with damage clusters can result in fork collapse and produce DSBs which are chemically distinct from prompt DSBs.

The kinetics of damage induction and repair should also be considered. Where a frank or prompt DSB is formed either through direct energy absorption, or by production of reactive oxygen species, these breaks are evident almost immediately after IR (Nickoloff *et al,* 2017). These breaks will be repaired via NHEJ or HR as described in Section 1.1.2. Alternatively, secondary DSBs occur several hours after irradiation as a result of replication forks colliding with unrepaired SSBs or single strand lesions thereby causing replication stress. It is important to note that for each frank DSB formed, approximately 30-fold more single strand breaks are produced.

Stalled replication forks can be stabilised by factors e.g. ATR, BLM, BRCA2, but if not restarted in a timely manner they can be cleaved by structure specific nucleases and collapse to form DSBs. Stalled or collapsed replication forks can be restarted by HR, but there is also a risk of HR factors mediating formation of branched recombination intermediates (e.g. “chicken feet”). Some structures are toxic recombination intermediates which can drive genomic instability. NHEJ-mediated repair of collapsed replication forks can occur but comes with a risk of large scale genomic rearrangements.

Ionising radiation can result in the formation of different lesions, some of which exist as clusters of lesions, and the heterogeneous damage landscape induced by irradiation must be considered when

characterising accumulations of repair proteins using super-resolution microscopy as we do in this work.

1.4.1 Fluorescence microscopy reveals a complex spatial dimension to repair pathway choice

Maintenance of genomic stability is facilitated by highly organised redistribution of repair proteins to contain the damaged DNA. These rearrangements can be visualised as nuclear aggregates known as “foci”. Foci comprise thousands of copies of proteins. The functional significance of these accumulations of repair proteins was not understood. Bekker-Jensen *et al* sought to address whether repair foci possess internal structure. Furthermore, they aimed to investigate if these assemblies were dependent on cell cycle progression (Bekker-Jensen *et al*, 2006).

Following damage induction by UV micro-irradiation, the redistribution of key DSB repair proteins was investigated using confocal microscopy. DNA damage proteins were broadly classified as binding to the chromatin proximal to the break site (e.g. 53BP1), binding to single stranded DNA following resection at DSBs during initiation of HR (e.g. Rad51) or as being at the interface between these (e.g. BRCA1). This work prompted the concept of a spatial map of DSB repair proteins. Their hypothesis was that the temporal and spatial redistribution of repair factors may be predictive of involvement or exclusion from the increasingly complex DSB repair network. They confirmed that chromatin-bound proteins could assemble throughout the cell cycle, whilst ssDNA-binding proteins were restricted to assembling during S-G2 phase of the cell cycle. This is consistent with the suggestion by Jazaveri *et al* that resection is cell cycle-dependent and restricted to S-G2 phase (Jazayeri *et al*, 2006). The ssDNA associated components, termed “micro-foci” were located at the centre of the irradiation tracks, encapsulated in the chromatin-bound protein compartment.

Whilst it could be concluded that repair proteins exist in structural/ functional subcompartments, it was not possible to complete a detailed analysis of colocalisation or exclusion of proteins within

repair foci as confocal microscopy is diffraction-limited and does not have the requisite resolution (Reindl *et al*, 2015).

1.4.2 Super resolution microscopy (SRM) reveals nanoscale organisation of repair foci

Significant advances made in super resolution microscopy (SRM) have overcome the diffraction limit via innovative technical and computational solutions (Ryabichko et al, 2017). SRM techniques (e.g. stimulated emission depletion (STED), and structured illumination microscopy (SIM)) have provided further insight into DSB repair mechanisms. SRM has revealed there is a spatial element to the switch from NHEJ to HR; rearrangements of the proteins within repair foci have a role in determining repair pathway choice.

3D-SIM investigating the spatial organisation of key repair proteins, 53BP1 and BRCA1 revealed that these proteins exist in adjacent but distinct focal compartments (Chapman *et al*, 2012). Analysis of foci enriched with both proteins showed that BRCA1 and 53BP1 are inversely correlated and occupy largely non-overlapping volumes. It was determined that the focal enrichment of these proteins is cell cycle-dependent. During G1, 53BP1 is enriched as dense, globular structures with little or no BRCA1 association. During S phase, BRCA1 is enriched and drives the exclusion of 53BP1 to the periphery of repair foci. This exclusion of 53BP1 requires BRCA1, and it was hypothesised that BRCA1 represents a temporal switch in DSB repair; by repositioning 53BP1, NHEJ is inhibited and HR initiated. CtIP and RPA similarly occupy the central region of foci and are encapsulated by 53BP1 (Chapman *et al*, 2012 & Kakarougkas *et al,* 2013). This lead to the hypothesis that the central region of repair foci represents the ssDNA region generated during resection and commitment to HR (Reindl *et al*, 2015). This is consistent with the observation that ssDNA binding components form “micro-foci” during S phase only (Bekker-Jensen *et al*, 2006).

Localisation of 53BP1 and recombination marker, RAD51, in repair foci has been investigated using STED (Reindl *et al*, 2015). RAD51 was observed as a homogeneous sphere encapsulated by 53BP1 accumulations, consistent with the appearance of other ssDNA binding components. 53BP1 was

visualised as a continuous structure with several intensity maxima. RAD51 was shown to occupy the intensity minima of 53BP1. It was hypothesised that the RAD51 spheres represented the kilobase (kb)-size resection lengths, covering a much smaller region than the megabase (mb) spanning chromatin-bound proteins.

The temporal distribution of 53BP1, BRCA1 and RAD51 was investigated following damage induction using STED microscopy (Schwarz *et al*, 2017). It was shown that 53BP1 foci form almost instantly, and persist until 6 hours, at which point 53BP1 foci numbers begin to decline. BRCA1 and RAD51 foci form only marginally slower than 53BP1 foci, and maximum foci numbers occur at 6-8 hours following damage. Interestingly, BRCA1 foci persist even after RAD51 foci numbers begin to decline. It was speculated that the persistence of BRCA1 foci following decline of RAD51 may be due to changes in BRCA1 complex composition (explored in Section 4.4.2 & 4.5).

Rothenberg and co-workers applied STORM to investigate the spatiotemporal dynamics of key repair proteins BRCA1, BRCA2 and RAD51 during HR repair at collapsed replication forks (Whelan *et al*, 2018). In this work, they revealed a complex, interwoven progression of repair events. RAD51-ssDNA nucleofilament formation is mediated by RAD52, or BRCA2 in the absence of RAD52. Further, they identified that upstream activity of BRCA1 was required for the downstream activity of BRCA2. Overall, the authors conclude the action of RAD51 during repair of collapsed replication forks is mediated by the collective action of BRCA1, BRCA2 and RAD52 in a spatially and temporally regulated manner. The application of SMLM technique, STORM, allowed investigation of individual repair foci at various time points following damage induction. The authors revealed interactions and dependencies between repair foci with unprecedented detail.

HR progression was previously described as a linear progression involving key steps: 1) ssDNA overhang generation; 2) RPA coating; 3) exchange of RPA for RAD51 dependent on BRCA2; 4) strand invasion and homology search. Strikingly, the authors here conclude that these steps coexist, with particular focus on the formation of the RAD51 nucleofilament. Their analyses revealed that RAD51

nucleofilament formation begins in the absence of BRCA2 accumulation and is facilitated by RAD52, with BRCA2 arriving later and operating subsections of the nucleofilament during the homology search and resolution of damage.

1.4.3 Functional significance of repair foci sub-compartmentalisation

It is established that chromatin proximal to sites of damage plays a major role in repair pathway choice (Section 1.1.4). The mechanism by which chromatin participates in repair is unclear. Advances in super resolution imaging modalities have allowed biologists to visualise repair proteins in the heterogeneous nuclear environment with unprecedented resolution (Section 1.4.1). Collectively, these studies have revealed that a repair focus is not a continuous structure in which proteins co-localise, but is comprised structural and functional subcompartments in which repair proteins exist. The functional relevance of foci sub-compartmentalisation is unclear.

Ochs *et al* applied super resolution techniques SIM and STED to visualise details of chromatin-bound 53BP1 and its downstream effector, RIF1 (Ghodke and Soutoglou, 2019 & Ochs *et al*, 2019). The authors provide evidence that 53BP1 and RIF1 form a structural module which freezes chromatin around DSBs to stabilise its architecture, and prevent unwanted DNA resection. This process is initiated by recruitment of 53BP1 to chromatin proximal to the break. 53BP1 is subsequently phosphorylated at its N terminus which allows binding of its downstream effector RIF1. 53BP1 and RIF1 recruit the Shieldin-CST complex which blocks extensive resection and directs repair via NHEJ. This DNA shield is thought to be oriented such that 53BP1 and RIF1 mark the chromatin ends whilst the shieldin-CST complex binds the DNA (Ochs *et al*, 2019 & Ghodke and Soutoglou, 2019). Loss of any of the 53BP1-RIF1-Shieldin-CST pathway results in uncontrolled resection and favouring of HR.

Ochs *et al* observed that 53BP1 is comprised of distinct nano-domains (53BP1-NDs) which are assembled in a circular fashion around single DSBs. These assemblies were termed 53BP1 micro-domains (53BP1-MDs). Similar assemblies have been observed for γH2AX (Natale *et al*, 2017).

These studies suggest that repair foci are not continuous structures, but are comprised of highly organised assemblies of nanostructures.

Recruitment of RIF1 and shieldin coincided with the circular 3D arrangement of 53BP1 suggesting RIF1-shieldin plays a role in shaping of these domains. Interestingly, depletion of shieldin components had no impact on the structure, but RIF1 depletion resulted in disrupted and elongated 53BP1 structures, indicating that RIF1 plays a role in stabilising 53BP1-MDs.

53BP1-MDs were shown to be associated with multiple topologically associated domains (TADs), and each 53BP1-ND represents a singular TAD within this structural module. TADs are kilo- to mega-base sized modules in chromatin which are characterised by strong interactions between components in the same genomic loci, and weakened interactions between components in distinct loci to demarcate regions in the nucleus. RIF1 localised to the boundaries of 53BP1-NDs in an alternating pattern suggesting that RIF1 may stabilise the 53BP1-MDs by acting as a spacer between 53BP1-NDs. Unlike RIF1 depletion, loss of shieldin components did not impact on the arrangement of the 53BP1-MDs suggesting that shieldin occupies the non-chromatin regions of this structure. These findings are summarised in Figure 1.18.

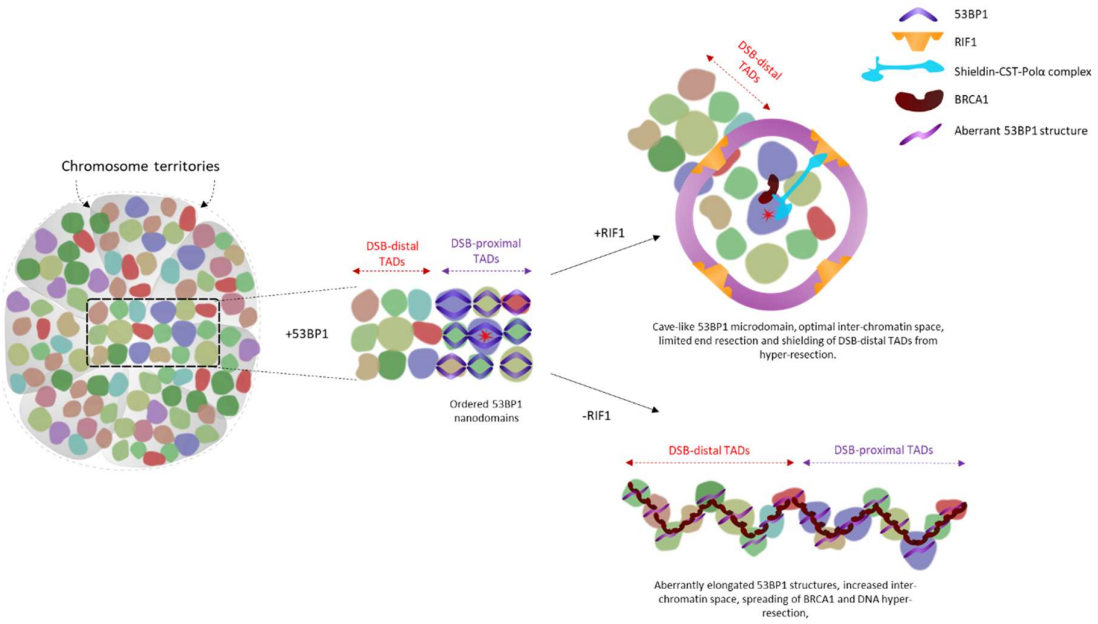

Figure 1.18. 53BP1-RIF1 structural module freezes chromatin proximal to DSBs to prevent hyper-resection. Chromatin is organised into distinct territories comprised of TADs. Following induction of DSBs, 53BP1 organises itself onto TADs distal to the site of damage and forms 53BP1-NDs. These 53BP1-NDs are assembled into a cave-like-53BP1-MD structure proximal to the break. The shieldin-CST-Polα complex is recruited and is thought to occupy the inside of this cave-like structure and prevents end resection. In the absence of RIF1, the 53BP1-NDs cannot mature to form the 53BP1-MD resulting in aberrant elongation of 53BP1 which allows spreading of BRCA1 and end resection to occur (Adapted from Ghodke and Soutoglou, 2019).

Cohesin is a regulator of TAD boundaries. Depletion of cohesin pheno-copied RIF1 depletion, resulting in disrupted 53BP1-MDs. This indicates RIF1 and cohesin may act cooperatively to allow stabilisation and maturation of 53BP1-MDs. Strikingly, it appears this functional module may relate to general genomic organisation as it was also observed in undamaged regions of chromatin. A possible function of the module may be to separate damaged and undamaged regions of chromatin removing the risk of chromosomal translocation, or it may form a cave in which repair factors can accumulate.

Interrogating the spatiotemporal organisation of repair proteins during DSB repair progression was previously hampered by the diffraction limit; an obstacle which has been addressed by the application of SRM techniques to visualisation and analysis of DSB repair. These studies collectively

have enhanced the understanding of underlying mechanisms DNA damage resolution, and provide explanation to the clinical relevance of mutations in proteins with pivotal regulatory roles in this process.

The clinical relevance of understanding the spatiotemporal organisation of repair proteins has been highlighted by work from Rotenberg and co-workers. In this work, they applied stochastic optical reconstruction microscopy (STORM) to investigate the localisation of key repair proteins during resolution of DSBs (Whelan *et al*, 2018). They showed that RAD51 nucleofilament formation initially occurs independently of BRCA2, a surprising observation since previous work suggested the primary role of BRCA2 was mediating RAD51 nucleofilament formation (Zhao *et al*, 2017). Interestingly, Whelan *et al* observed an accumulation of RAD52 ahead of BRCA2 during RAD51 nucleofilament formation. From this, they suggested that RAD52 may play a role in mediating early RAD51 association with DNA and BRCA2 may function later in HR. BRCA2 associated with subsections of the RAD51 nucleofilament, suggesting it may play a role in co-ordinating later events in HR.

BRCA2 depletion had no impact on initial RAD51 recruitment. RAD52 depletion similarly had no effect on the initial accumulation of RAD51, but BRCA2 association was increased in RAD52-depleted cells compared to controls. BRCA2 is able to substitute for RAD52, but RAD52 is insufficient to substitute for BRCA2 as indicated by an absence of RAD51 in later HR following BRCA2 depletion. The redundancy between RAD52 and BRCA2 functions explains synthetic lethality of combined RAD52 and BRCA2 deficiencies. A similar synthetic lethality has been observed in cells with combined deficiency of RAD52 and BRCA1. The authors here demonstrate that BRCA1 deficiency results in defective localisation of BRCA2 to sites of damage and RAD51 association decreased more quickly than in controls. This was consistent with their observations following BRCA2 depletion. In cells deficient of both RAD52 and BRCA1, synthetic lethality was observed. By

determining the mechanism of synthetic lethality between BRCA1/2 and RAD52, this may direct development of therapeutic targets for cancer treatment.

Despite their capabilities in providing insight into the spatiotemporal dimension of the DDR, super resolution imaging modalities suffer from inherent limitations (discussed in Section 1.2.4). In this work, we challenge some of these limitations by using Expansion Microscopy (ExM) (described in Section 1.3).

1.5 Summary

Application of fluorescence microscopy and super resolution techniques has substantially improved our knowledge of underlying mechanisms of DNA damage resolution, and provides further insight into clinical relevance of mutations in proteins with crucial regulatory roles in the repair process (Section 1.4.1-1.4.2). These studies have revealed that spatiotemporal organisation of repair proteins at DSBs plays a critical role in repair pathway choice, repair progression and resolution of damage.

Despite these advances, super resolution imaging modalities such as SIM, STED and SMLM (Section 1.2.3) suffer from inherent limitations including insufficient resolution, difficulty in achieving multi-colour imaging and requirements for sophisticated computational reconstruction of images (discussed in Section 1.2.4). By applying ExM, this project aims to overcome some of the limitations posed by other imaging modalities.

ExM relies on an innovative sample preparation which allows nanoscale three-dimensional imaging of preserved specimens on conventional diffraction-limited systems. Samples are optically cleared during ExM preparation, which removes the effect of light scattering through the sample. As a result, ExM allows for fast image acquisition with imaging depths and volumes accessible orders of magnitude higher than achievable with other super resolution techniques (Wassie *et al*, 2019). Additionally, there are minimal constraints on fluorophore choice meaning that multicolour setups can be achieved with ease.

This project aims to use ExM to quantitatively describe the nanoscale organisation of multiple repair factors within repair foci to corroborate a spatial map of repair factors during DSB repair progression. We hypothesise that the resolving power of ExM will allow clear delineation of the relative boundaries between multiple repair factors within repair foci subcompartments. Rapid image acquisition with minimal software and hardware requirements will allow visualisation of a large number of repair structures to capture the heterogeneous process of DSB repair.

1.6 Aims

1. Determine that isotropic, robust expansion of the nuclear sub-compartment is achievable with retention of nanoscale topology of the nuclear architecture.

2. Explore the spatial organisation of pivotal DSB repair proteins, 53BP1 and BRCA1, in repair structures following damage induction by irradiation in S-phase cells using ExM.

3. Investigate the role of SMARCAD1 and USP48 in the nanoscale organisation of repair foci.

4. Enable visualisation of chromatin architecture during DSB repair progression.

2. Methods and Materials

2.1 Molecular biology

2.1.1 Bacterial transformation

1-50 ng of pcDNA5/FRT/TO plasmid DNA was transferred to pre-chilled eppendorfs with 10 µl of Escherichia Coli DH5α (Bioline). The bacteria were incubated on ice for 20 minutes prior to heat shocking at 42 °C for 30 seconds. Bacteria were transferred back onto ice for 2 minutes prior to addition of 250 µl of Luria Bertani (LB) being added. Cells were incubated at 37 °C for 1 hour with shaking. Transformed bacteria were added directly to LB containing Ampicillin (50 µg/ml) according to antibiotic resistance of transformed plasmids, and allowed to grow overnight.

2.1.2 Plasmid DNA preparation

300 ml starter cultures were grown overnight at 37 °C at 200 rpm for Maxipreps. Bacterial cultures were spun down in a centrifuge at 3000 rpm for 30 minutes to pellet bacteria. The supernatant was discarded and DNA extraction was performed using Genejet from ThermoFisher Maxiprep kits following the manufacturer's protocol.

2.1.3 Quantification of nucleic acids

DNA was quantified using a Labtech Spectrophotometer using ND-1000 software. Blank measurements were made using the resuspension solution of the nucleic acid, H_2O. 1 µl of sample was loaded onto the pedestal and the concentration of nucleic acid measured.

2.2 Protein methods

2.2.1 SDS polyacrylamide gel electrophoresis (SDS PAGE)

Polyacrylamide gels were made using Biorad gel casting equipment. The percentage of acrylamide was dependent on the protein being studied (see Table 2.1).

Table 2.1. SDS polyacrylamide gel solutions.

Constituent (ml)	Resolving gel			Stacking gel
	6%	**10%**	**12%**	**5%**
H2O	**7.9**	**5.9**	**5.1**	2.7
30% polyacrylamide mix	3.0	5.0	6.0	0.67
1.5M Tris pH 8.8	3.8	3.8	3.75	-
1.0M Tris pH 6.8	-	-	-	0.5
10% SDS	0.15	0.15	0.15	0.04
10% APS	0.15	0.15	0.15	0.04
TEMED	0.012	0.006	0.006	0.004
Final Volume (ml)	15	15	15	4

The resolving gel was poured between the glass plates and covered in water-saturated isobutanol and allowed to set. The water-saturated isobutanol was removed before the stacking gel was poured on top. Plastic combs were inserted to form wells. The comb was removed once the stacking gel was set.

Gels were loaded into a Biorad tank and filled with 1x SDS running buffer. 5 µl of ThermoFisher PageRuler Prestained protein ladder was loaded into one of the wells. Protein samples were loaded in 4x SDS loading buffer and sonicated before loading onto the gel which was run at 120 volts. Gels were then western blotted (Section 2.2.2).

2.2.2 Western blot

Protein gels were transferred onto PVDF immobillon membranes which had been activated in methanol and then stored in water. Transfers were set up in Biorad Trans-blot cassettes, sponges and 3 mm filter paper which had been soaked in transfer buffer. The transfer was built with sponge and two pieces of filter paper either side of the membrane and the gel. The cassette was then

placed in the transfer tank and submerged in 1 x Transfer buffer. Transfer was run at 100 volts for 2 hours.

Once the transfer was complete, the membrane was blocked in 5% marvel milk in PBS with 0.1% Tween (PBST) for at least 30 minutes prior to being transferred into primary antibodies in 5% marvel milk in PBST overnight at 4 ^{o}C on a roller. Blots were washed 3x for 10 minutes in PBST and then transferred into secondary HRP antibodies in 5% marvel milk in PBST for at least 1 hour with rocking. The blots were washed again 3x for 10 minutes in PBST. Once washed the membranes were probed with ECL (ThermoFisher Scientific). Excess ECL was removed and membranes were placed inside a plastic wallet inside a cassette. Fuji film X-ray film was placed in the cassette for varying lengths of time and the film developed inside a Xograph Compact X4 developer.

2.3 Cell biology

2.3.1 Tissue culture

U2OS Flp-In parental cell line kindly gifted by G. Stewart (University of Birmingham) were used. U2OS cells were selected for this project as they are flat epithelial-like cells, and therefore suitable in imaging applications. Mycoplasma testing was performed through Hoechst DNA staining. Cells were not authenticated at the source.

U2OS cells were grown in Dulbeccos Modified Eagle media (DMEM) (Sigma) supplemented with 10% fetal bovine serum (FBS) and 1% Penicillin/ streptomycin. Monolayers of cells were cultured in Corning T75 flasks and kept at 37 ^{o}C and 5% CO_2. When cells reached 80% confluency, they were passaged by removing all media and washing cells with 1 x PBS. 1.5 ml of typsin/ EDTA was added and cells were left at 37 ^{o}C until cells detached. Cells were split 1:10 into new flasks.

Stocks of cells were stored at -80 ^{o}C or in liquid nitrogen at a concentration of $1x10^6$ cells/ ml. In order to freeze cells, a confluent flask of cells was trypisinised and cells were counted using a haemocytometer. Cells were then pelleted and re-suspended in the relevant amount of freezing

medium (70% DMEM, 20% FBS, 10% DMSO) Cells were cooled at -1 ^{o}C/ min in the -80 ^{o}C freezer prior to transfer to liquid nitrogen.

2.3.2 Plasmid transfection

DNA plasmids were transfected into cells using transfection reagent FuGENE 6 (Promega) at a ratio of 4 µl: 1 ng FuGENE: DNA following the manufacturer's guidelines.

2.3.3 siRNA transfection

siRNA transfections were carried out using the transfection reagent Dharmafect1 (Dharmacon) following the manufacturer's instructions.

2.3.4 Stable cell line creation

Stable cell lines were generated using a doxycycline-inducible U2OS Flp-In parental cell line kindly gifted by G. Stewart (University of Birmingham). Flp-In T-REx doxycycline inducible U2OS cell lines were grown in 10% tetracycline-free fetal calf serum (Clontech) supplemented with 1% penicillin/ streptomycin. The Flp-In T-Rex system enables generation of stable cell lines which have tetracycline-inducible expression of your gene of interest derived from a specific genomic location (ThermoFisher, 2012). This system allows for rapid, efficient generation of cell lines. To generate these cell lines, three major steps are required:

1. A plasmid containing a Flp recombination target (FRT) site and a plasmid expressing the Tet repressor are independently integrated into the genome.
2. An expression vector containing your gene of interest under the control of a tetracycline-inducible promoter is integrated into the genome through Flp recombinase mediated recombination at the FRT site.
3. Gene expression is induced by addition of tetracycline (Doxycycline may also be used).

The plasmids used in this process are summarised in Table 2.2 and the process of generating Flp-In T-Rex host cell lines and generating inducible expression cell lines are summarised in Figures 2.1-2.2.

Table 2.2. Components of the Flp-In T-REx expression system.

Component	Function
pFRT/ *lac*Zeo vector	Generation of the Flp-In host cell line with FRT site.
pcDNA6/TR plasmid	Expression of Tet repressor under control of the human CMV promoter
pcDNA5/ FRT/ TO plasmid	Expression plasmid containing a FRT site linked to Hygromycin resistance gene to allow Flp recombinase mediated integration and selection of stable cell line expressing gene of interest which is under the control of CMV/$TetO_2$ promoter.
pOG44 plasmid	Expression of Flp recombinase under the control of human CMV promoter.

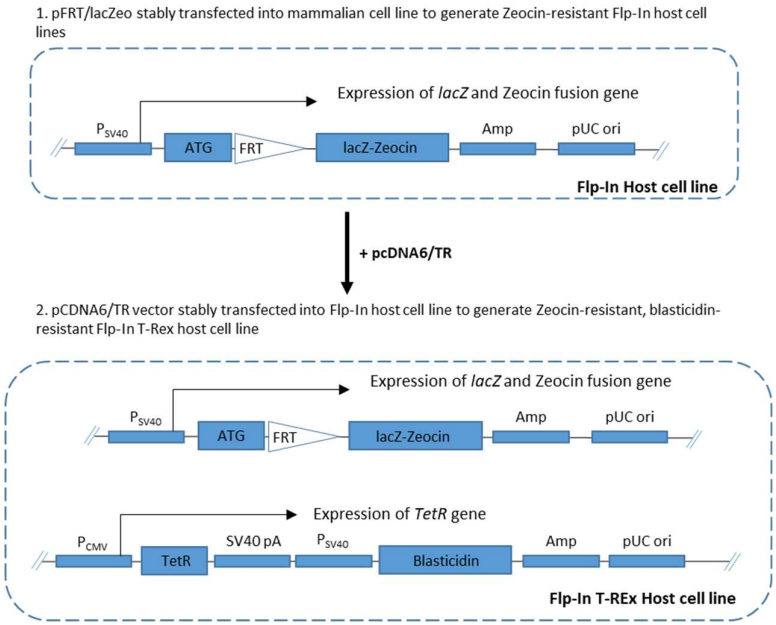

Figure 2.1. Generation of Flp-In T-REx host cell line (adapted from ThermoFisher, 2012).

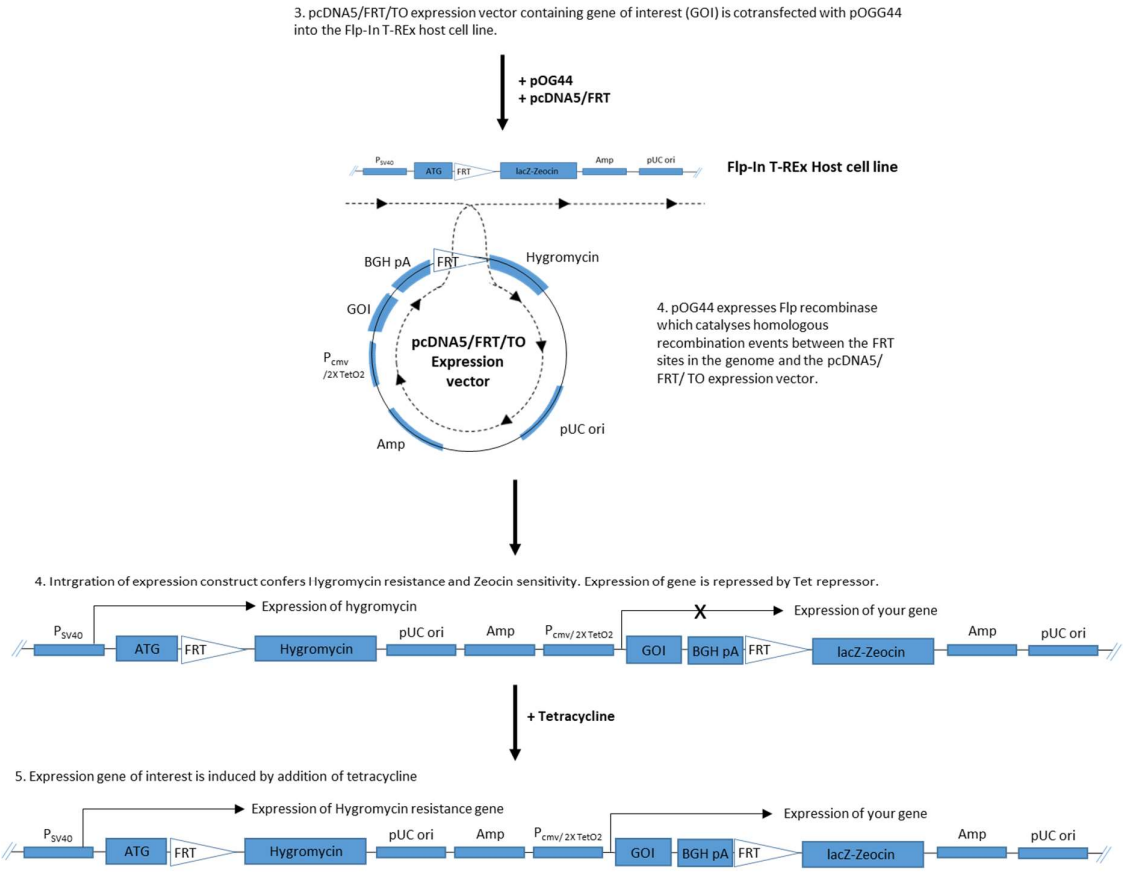

Figure 2.2. Generating inducible expression cell lines (adapted from ThermoFisher 2012).

U2OS Flp-In T-REx host cells were plated in 10 cm dishes and transfected with pcDNA5/FRT/TO-H2A constructs along with pOG44 recombinase at a ratio of 3:1. Cells were left for 48 hours and then treated with hygromycin to select cells which had been successfully transfected. Control transfections were carried out without Pog44 recombinase (Invitrogen). Colonies were selected and expanded.

2.3.5 Irradiation protocol

Prior to irradiation cells were treated with EdU (Section 2.3.7). Cells were exposed to irradiation with a Gamma-cell 1000 Elite irradiator (cesium-137 source). Cells were allowed to recover for 1 hour (unless otherwise stated) in DMEM supplemented with 10% FBS and 1% Penicillin/ streptomycin. Following recovery, cells were washed with 1 x PBS, pre-extracted with CSK and fixed in 4% PFA (Section 2.3.6).

2.3.6 Immunofluorescence staining

Immunostaining of Flp-In U2OS cells was performed as follows. Cells were seeded at a density of cells $3x10^4$ cells/ ml in 24-well plate containing 13 mm #1.5 coverglass and incubated overnight. Cells were treated as required. Cells were optionally pre-extracted with CSK buffer prior to fixation. Specimens were fixed for 10 minutes in 4% paraformaldehyde (unless otherwise stated) in PBS followed by brief washing in PBS. Cells were permeabilised with 0.5% Triton X-100 for 15-20 minutes. Cells were then blocked with 10% FBS in PBST for 10-15 minutes prior to performing the click reaction for labelling of EdU. Cells were washed three times with PBS. Where stated, specimens were then incubated with primary antibodies in the blocking buffer at stated concentrations for either 1 hour at room temperature or overnight at 4 ^oC (Table 2.7). After three washes with PBS cells were incubated with secondary antibodies in blocking buffer for 1 hour at room temperature. After three further washes with PBS, cells for pre-expansion imaging were mounted onto slides using Immunomount mounting media. Post-expansion specimens were treated with standard expansion microscopy (ExM) protocol (Section 2.4).

2.3.7 EdU staining

U2OS cells were plated on 13 mm coverslips in a 24-well plate at a density of $3x10^4$ cells/ mL and treated as required. EdU (ThermoFisher Scientific) stock concentration was 10 mM in DMSO and stored at -20 ^oC. Cells were incubated with 10 μM final concentration of EdU. Staining was carried out following Click-iT® EdU Imaging Kits. Where stated, cells were additionally stained with antibodies.

2.4 Standard expansion microscopy (ExM) protocol

This ExM protocol was used for preparation of all specimens unless stated otherwise. ExM protocol was adapted from the ExFISH approach (Chen *et al*, 2016) and ProExM approach (Tillberg *et al*, 2016).

2.4.1 EdU staining and immunostaining of cultured cells

U2OS Flp-In cells were seeded and treated as required (summarised in Section 2.8). EdU staining was performed as in Section 2.3.7. Immunostaining was performed as in Section 2.3.6.

2.4.2 Anchor synthesis

Acryloyl-X (6-((acryloyl)amino)hexanoic acid, succinimidyl ester) (AcX) (ThermoFisher Scientific) was re-suspended in anhydrous DMSO with a final concentration of 10 mg/mL. This was then aliquoted and stored in a frozen desiccated environment for up to 2 months. Label-IT amine (Mirus Bio) (100 µg) was re-suspended in reconstitution solution (100 µl) with a final concentration of 1 mg/ml. 10 µl of AcX was added to label-IT amine and reacted overnight with shaking at room temperature to produce LabelX. Subsequently this was aliquoted and stored in a frozen desiccated environment for up to 2 months.

2.4.3 Anchoring of DNA and proteins for ExM

For expansion specimens, cells were treated with nucleic acid anchor, LabelX, and protein anchor, Acryloyl-X. Cells were washed with 20 mM MOPS pH7.7 (Sigma Aldrich), and incubated with LabelX (at a final concentration of 0.006 mg/ml) in MOPS at 37 ^{o}C overnight followed by two washes with 1xPBS. Following two washes with 1xPBS, cells were incubated with AcX (0.1 mg/ml) in PBS for >6 hours at room temperature. Specimens were washed with 1xPBS prior to gelation.

2.4.4 Gelation, digestion and expansion

All components of the gelation solution were purchased from Sigma Aldrich. Monomer solution (1xPBS, 2M NaCl, 8.625% (w/w) sodium acrylate, 2.5% (w/w) acrylamide, 0.15% (w/w) N,N'-methylenebisacrylamide) was mixed, frozen in aliquots of 940 µl and thawed prior to use. Concentrated stocks of ammonium persulfate (APS) and tetramethylethylenediamine (TEMED) at 10% (w/w) in water were diluted into the monomer solution to concentrations of 0.2% (w/w) on ice prior to gelation, with the initiator (APS) added last. The gelation solution (80 µl) was placed on a parafilm-covered slide in a humidified chamber. Coverslips were inverted onto the droplet with

cells face down. Gelation was allowed to proceed at 37 ^{o}C for two hours. Gels were removed from the slide and immersed in digestion buffer (1xTAE, 0.5% Triton X-100, 0.8 M guanidine HCl) containing 8 units/ml Proteinase K (New England Biolabs Inc.) which was added freshly to the digestion buffer. Gels were digested either at room temperature overnight or 37 ^{o}C for 4 hours. The gels (sometimes still attached to the coverglass) were removed from the digestion buffer and placed in 50 ml of water to expand. Water was exchanged every 30 minutes until expansion was complete (typically 3-4 exchanges).

2.4.5 X10 Expansion Microscopy (X10 ExM) gelation, digestion and expansion

X10 ExM approach used by Truckenbrodt *et al* was used. Cells were treated as in Section 2.4.1. Anchoring of specimens was carried out as in Section 2.4.2. Gelation solution was prepared by dissolving 33% (w/w) of N,N-dimethylacrylamide (DMAA) (Sigma Aldrich) and sodium acrylate (SA) monomers at a molar ratio of 4:1. The solution was bubbled for 40 minutes at room temperature using argon to remove any molecular oxygen from the solution as oxygen slows the polymerisation reaction. To 940 µl of monomer solution, 50 µl of 10% APS and 4 µl of TEMED were added on ice to prevent premature polymerisation. The gelation solution was placed on a parafilm covered slide in a humidified chamber and coverslips were inverted onto the droplet with the cells face down. Gelation was allowed to proceed for 6-24 hours at room temperature to ensure the gels were fully polymerised. Gels were placed in the digestion buffer (1xTAE, 0.5% Triton X-100, 0.8 M guanidine HCl) containing 8 units/ mL Proteinase K (New England Biolabs Inc) and digestion was allowed to proceed overnight at 50 ^{o}C. Gels were then transferred to an excess of water (10x the final gel volume) for expansion. Water was replaced every 20-30 minutes (typically requiring 5-6 exchanges).

2.4.6 Expanded specimen handling for imaging

For widefield imaging, expanded gels were cut to fit in Mattek dishes with a glass coverslips of 35 mm diameter. Excess water was removed and gels were embedded in 2% LMP agarose to limit gel movement during image acquisition (illustrated in Figure 2.3).

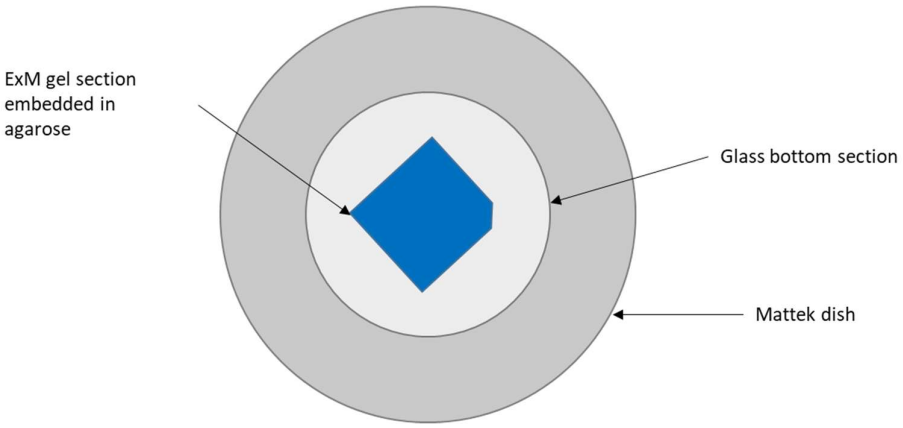

Figure 2.3 Top down view of set up of ExM gels for image acquisition on inverted microscopes. For imaging on inverted microscopes (e.g. widefield). Expanded gel sections were cut to fit in 14 mm diameter glass bottom section of 35 mm mattek dishes. 2% agarose was pipetted around the ExM gel to immobilise the gel. Water was added to the top of the ExM gel to ensure it does not dehydrate during imaging.

For SPIM imaging, gels were cut to fit the SPIM holder and placed cell-side up in the SPIM holder. 2% agarose was pipetted into the holder until the bottom of the holder was covered, taking care not to get agarose in the interface between the top of the ExM gel and the objective lens. Deionised water was then added to the SPIM holder containing the gel to fully immerse the gel for imaging (details in Section 3.2.3).

In both widefield and SPIM imaging set ups, gels were left for at least an hour prior to imaging to aid stability of the specimens during image acquisition.

For correlative imaging, pre-expansion specimens were treated as described in Section 2.4.7 and then ExM protocol was performed. Following digestion samples were not expanded. Samples were instead cut into a distinct shape for ease in orientating sample and finding the same cells pre- and

post-expansion. The unexpanded gel sections were placed in Mattek dishes and pre-expansion images were acquired on a structured illumination microscope (SIM). Following pre-expansion imaging, these gel sections were expanded in deionised water and post-expansion imaging was performed on a widefield microscope.

2.4.7 Characterising nuclear expansion and correlative imaging of nuclei

U2OS cells were seeded at $5x10^4$ cells per well in a 24-well plate and incubated with EdU overnight. Cells were fixed with 4% paraformaldehyde and washed with 1xPBS. Cells were permeabilised with 0.5% Triton X-100 in PBS, and then treated with Alexa Fluor 488 azide dye in click-it reaction buffer. Specimens were washed three times with 1xPBS and once with 20 mM MOPS, pH 7.7. Cells were then incubated with LabelX (0.006 mg/mL) in MOPS. Gelation and digestion were completed. For correlative imaging experiments, gels were cut into a distinctive shape and then images of nuclei acquired pre-expansion on a structured illumination microscope. Expansion was completed on the cut gel and images acquired post-expansion on a widefield microscope. For widefield experiments to quantify nuclear expansion factor, pre-expansion images were acquired following labelling with Alexa Fluor 488 azide dye, then ExM protocol was carried out and post-expansion images were acquired.

2.4.8 Assessing use of H2A-dendra2/ -mCherry as markers of chromatin post-expansion

U2OS cells were seeded at $3x10^4$ cells/ ml and treated with doxycycline at a final concentration of 1 µg/ml to induce expression of H2A-dendra2/-mCherry and allowed to grow overnight. Cells were treated with EdU (Section 2.3.7) and incubated overnight. The identity of the Alexa Fluor azide dye used for the click-IT reaction was Alexa Fluor 488 for H2A-mCherry-expressing cells and Alexa Fluor 647 for H2A-dendra2-expressing cells. As Alexa Fluor 647 does not survive the polymerisation reaction required by ExM, the click-IT reaction mixture was applied post-gelation in H2A-dendra2-expressing cells.

2.5 Microscopes

2.5.1 Nikon N-SIM

Nikon N-SIM-S system (Ti-2 stand, Hamamatsu Flash 4 scientific CMOS dual cameras with Cairn splitter system, Perfect Focus, Nikon laser bed). For both set ups, Nikon 100x 1.49 NA TIRF oil objectives were used.

2.5.2 Widefield microscopy

Widefield imaging was performed on an ASI RAMM microscope, equipped with a Nikon 100x objective. Illumination was from a 100 mW OBIS CW lasers via a quad-band dichroic mirror (405/488/561/640) and images were collected using an Evolve Delta EM-CCD camera via a quad band emission filter (Semrock, 432/515/595/730 nm). Micromanager was used to control the system and scan the sample.

2.5.3 ASI iSPIM microscopy

SPIM imaging was performed on an ASI RAMM microscope with SPIM-MOUNT, equipped with Nikon 40x objectives attached to piezo object movers to scan the sample. Illumination was from a 100 mW OBIS CW lasers. A Hamamatsu Flash 4 scientific CMOS camera was used for imaging. Micromanager was used to control the system and scan the sample.

2.6 Image processing

Images acquired on the Nikon N-SIM-S system were reconstructed using stack reconstruction in the NIS elements software. Where stated, post-expansion image data was deconvolved using Huygens professional version 19.04 (Scientific Volume imaging, the Netherlands, http://svi.nl).

Deconvolution is a mathematical operation which enables restoration of images which have been degraded by convolution. Deconvolution mainly removes effects of optical blurring, but is also able to remove effects of statistical noise during pre-processing of image data (Wallace *et al*, 2001)

(Section 1.4.1). For deconvolution we used commercially available software: Huygens (Scientific Volume Imaging).

Huygens requires a point spread function (PSF). A PSF can be determined theoretically based on the microscope parameters, or experimentally by 3D visualisation of spherical beads on the microscope. We used a theoretically determined PSF. Upon provision of PSF, Huygens can then apply different mathematical algorithms to effectively solve convolution problem and subsequently do the deconvolution. For this, we used Classic Maximum Likelihood Estimation (CMLE). This is a common type of restoration method, and is valid for most image types. It iteratively optimises the likelihood the objects estimated in the image are correctly localised based on the image and the PSF. Likelihood in this procedure is determined by a quality criterion which assumes that the poisson statistics govern the noise in the image. The quality criterion is derived from a concept of Maximum Likelihood: the I-divergence, meaning it is possible to escape local minima which would otherwise lead to the incorrect solution. This procedure is suited to low-signal images (like those in ExM). It is also optimal in restoring images of point- or plane-like objects.

The basic concept of non-linear iterative restoration methods (Figure 2.4) involves the generation of an estimate of an object (synthetic image) which is compared to the measured image. The result of this is used to improve the original, until the point that the “difference” between the synthetic and measured image reach a minimum at which point the procedure stops. Such a process is advantaged in being quick and versatile, although it is computationally intensive.

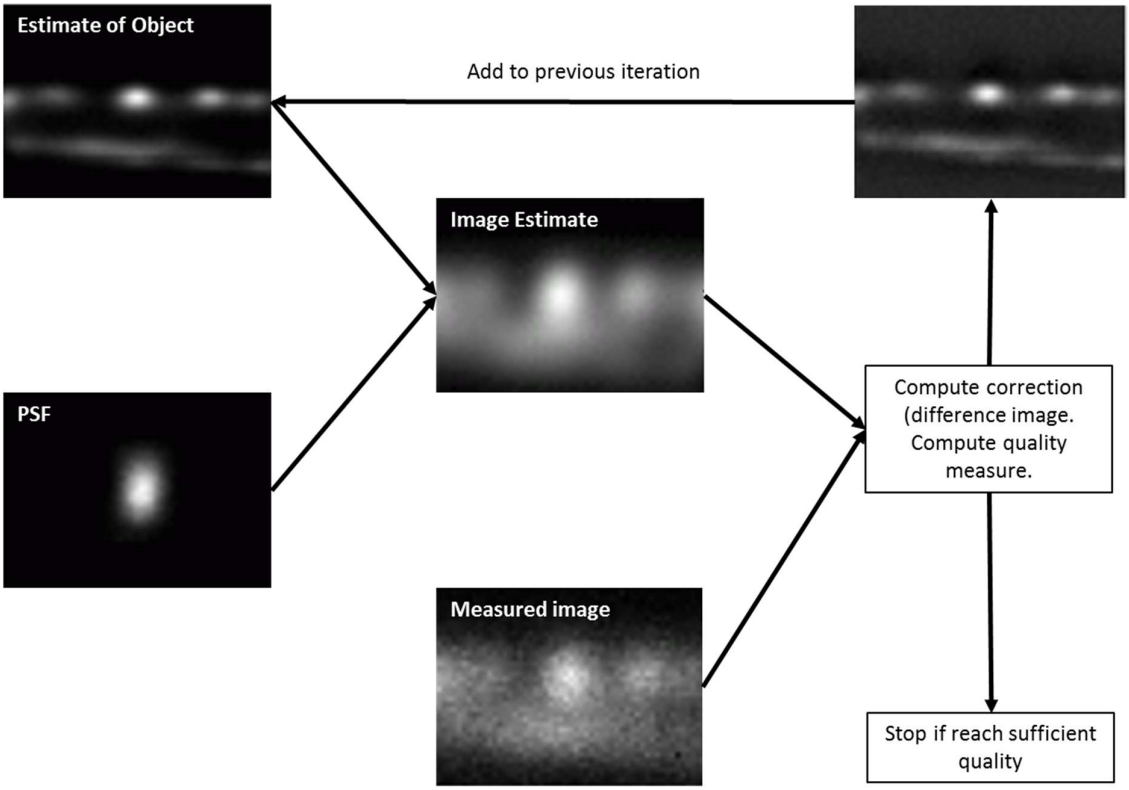

Figure 2.4. Principle of non-linear iterative deconvolution algorithms. This example illustrates the van Cittert algorithm which minimises the difference image output by subtracting the estimated image from the recorded image. First, a smart initial estimate of the object is made. This is convolved with the PSF. The result is compared with the original image and the difference is assigned a quality measure which allows improvement of the estimate. This process repeats until sufficient quality is reached (Scientific Volume imaging, Huygens).

Parameters for deconvolution were tested on example data sets for each experiment to determine optimal values, and these deconvolution templates were used for subsequent image processing and experimental repeats.

2.7 Image analysis

2.7.1 Segmentation of nuclei in matlab

Quantification of nuclear areas pre- and post-expansion was performed using a script written in Matlab (illustrated in Section 3.2.1). Briefly, pre- and post-expansion images were processed by performing a rolling ball background subtraction and .tif files were saved into corresponding

directories. A test set of images from each data set were used to determine a manual threshold for segmentation based on histograms generated for the test images. Nuclei were segmented resulting in a mask of pixels where fluorescence is above the manually determined threshold. Boundaries were traced onto the binary image and then these boundaries were super-imposed onto the original image to determine the efficacy of segmentation. Centroids for each nucleus were determined and labelled. The areas of the labelled objects were calculated in pixels and microns^2. Optimal parameters were determined and then used to determine nuclear areas pre- and post-expansion using for loops.

To ensure the measured areas corresponded to whole nuclei, a maximum and minimum size was defined based on nuclei conforming to a circle (summarised in Table 2.3).

Table 2.3. Maximum and minimum size of nuclei pre- and post-expansion.

Radius pre-expansion (µm)	Area pre-expansion (pixels)	Area pre-expansion (µm^2)	Area post-expansion (pixels) (100x)	Area post-expansion (pixels) (20x)	Area post-expansion (µm^2)
5	3066	78.5	49062.5	1962.5	1256
10	12273	314.2	196375	7855	5027.2

2.7.2 Segmentation of nuclei in ImageJ

For determination of nuclear volumes pre- and post-expansion, cells were treated as in Section 2.4.7. Pre-expansion Z series were acquired on a widefield microscope and deconvolved as in Section 2.6. Post-expansion Z series were acquired on an ASI iSPIM microscope. Images were segmented using auto-threshold in ImageJ and used to generate a mask. Otsu threshold was most efficient at segmenting nuclei from background pixels. The generated mask was eroded and dilated, and any gaps were filled in. The volumes of the final mask was measured for each image. For each image, an object map was generated and compared to the original images to determine the efficacy of the segmentation. This process is illustrated in Figure 2.5.

Figure 2.5. Segmentation of nuclei to measure volume of nuclei pre- and post-expansion. Key steps to segment and measure nuclear volumes pre- and post-expansion in ImageJ are shown. 1) Each file is opened and 2) Otsu threshold is applied using auto-threshold and the resultant mask is eroded and dilated then any holes are filled in. 3) The segmented areas are measured using 3D object counter and 4) an object map is generated for comparison to the original file to ensure segmentation has occurred efficiently.

2.7.3 Determining Pearson's correlation coefficient (PCC) values

Pearson's correlation coefficient was quantified between DNA (EdU) and chromatin (H2A-dendra2/-mCherry) in cells treated as in Section 2.4.8. To do this, nuclei were segmented using Ilastik software. PCC values were determined using a workflow in KNIME generated by Dr Jeremy Pike.

Ilastik is an interactive segmentation toolkit (Berg *et al*, 2019). We used the pixel classification on a test dataset for pre- and post-expansion image data to assign labels to pixels which were background or signal (i.e. nuclei). This pixel classification allowed easy segmentation of nuclei to give accurate PCC values.

The KNIME workflow developed is represented in Section 3.3.2 (Dietz and Berthold, 2016). Briefly, the pre- and post-expansion images were loaded and then channels were split. The segmentation was then performed using the pixel classification defined in Ilastik. For post-expansion images, the images were resized (4-fold smaller according to the expansion factor of the gel) to allow direct comparisons of "diffraction-limited" images. PCC values were calculated for all images and written into an .xls file. Additionally, histograms of intensity values for each channel in both pre- and post-expansion images can be generated using this workflow.

For Z series, PCC values were determined using the JACoP plugin in ImageJ. Nuclei were segmented using auto-threshold and then PCC values were measured.

2.7.4 Bead-based registration of SPIM image data

For bead-based registration of SPIM image data, we required fiducial markers as described in Section 3.3.3. Briefly, fiducial markers are spatially fixed landmarks in specimens which can be used to register images accurately (Balinovic *et al*, 2019). In this case we used tetraspeck beads (ThermoFisher) which were 100 nm in diameter. These beads can be visualised in all four channels with good separation between their excitation and emission spectra.

Tetraspeck beads were sonicated prior to addition to ExM gels to remove any aggregations of beads as these possess different photo-physical characteristics to singular beads which would otherwise prevent these being good fiducial markers. Teflon wells (Sigma Aldrich) were placed on coverslips with cells facing upwards. 10 µl of the bead solution (with a bead density of ~1.8×10^{11} particles/ml) was added to the coverslips and then the remainder of the well was filled with 90 µl of gelation solution. Gelation, digestion and expansion were performed as in Standard ExM protocol (Section 2.4.4). Post-expansion images were acquired on an iSPIM (described in Section 2.5.3). Bead-based registration was performed using the multiview reconstruction plugin in ImageJ (Preibisch *et al*, 2010). This plugin allows users to register SPIM datasets using fluorescent beads. In this case, we used the expansion gel as the rigid mounting medium to embed the fiducial markers in, so visualised the sample and the beads simultaneously. I used the translation and rotation invariant local genomic descriptor; this identifies each bead as part of a constellation with its neighbouring beads. These constellations are matched in through translation and rotation in three dimensions.

2.7.5 Spot-detection based analysis of repair structures

Spot detection-based analysis of foci structures was performed using a .groovy script written by Dr Jeremy Pike. The script applied an open source Fiji plugin called TrackMate (Tinevez *et al*, 2017). Trackmate allows automated, semi-automated and manual tracking of single particles in image data. It is advantaged in being simple and intuitive, and can be easily adapted for batch processing as has been done for this work. Users are able to develop detection, particle linking, visualisation and analysis algorithms using TrackMate. Here, we applied TrackMate to localise spot structures within repair foci and visually analyse their spatial organisation. Spot detection-based analysis was carried out as described in Sections 4.3.1 & 5.3.4. Briefly, deconvolved Z series were organised into directories according to cell cycle phase classified by EdU incorporation. The file extension for the Z series was selected and spot detection parameters were defined based on a test set of images in each experiment (parameters are shown in Figures 2.6-2.8). Spot detection was automated and performed according to user defined parameters and structures of interest were shown to the user

as zoomed in sections of the whole image. The user then manually defines the class of structure based on the relative spatial organisation of features in the structure. Each feature and associated classification data (e.g. file number, location, class) is saved in the directory. For each Z series, a .csv file is generated, summarising features and classification information.

In this work, three scripts were used to analyse Z series depending on the number of features being analysed. These scripts allowed for analysis of two-, three- and four-colour image data sets, and differed in the user defined parameters which are highlighted in Figure 2.6-2.8. The experiments using each of these scripts are summarised in Table 2.4.

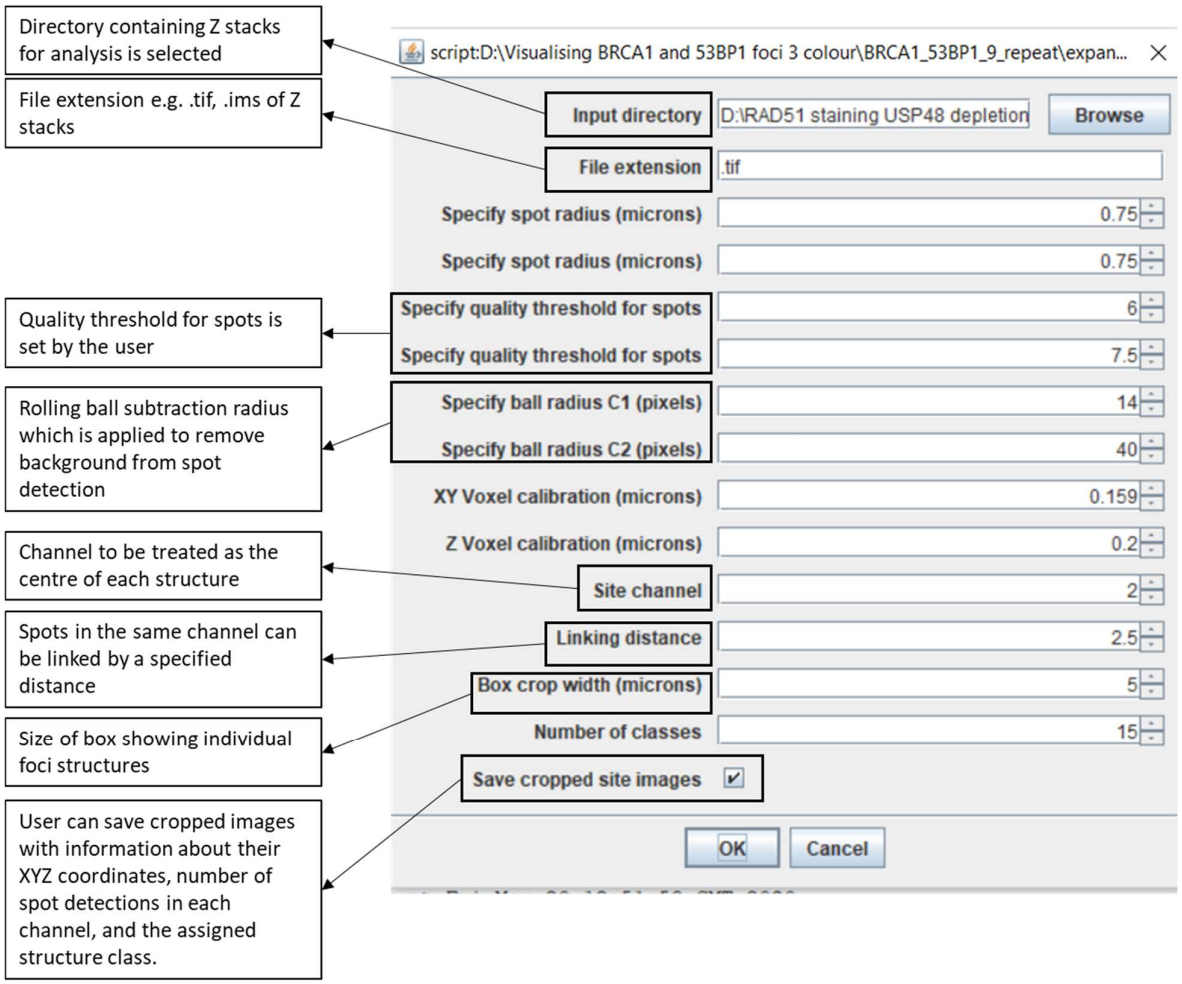

Figure 2.6. User defined parameters for spot detection-based analysis of two-colour Z series. All user defined parameters are defined.

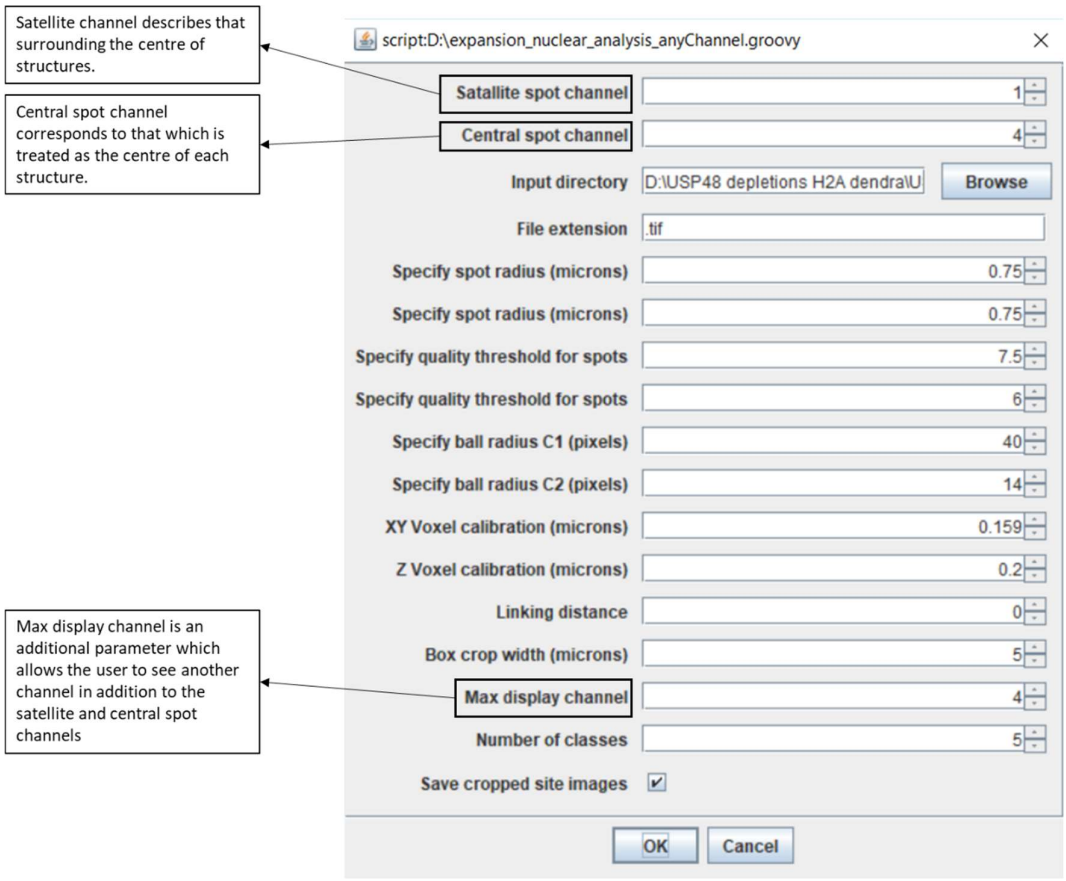

Figure 2.7. User defined parameters for spot detection-based analysis of three-colour Z series. Parameters which differ from those in Figure 2.6 are defined.

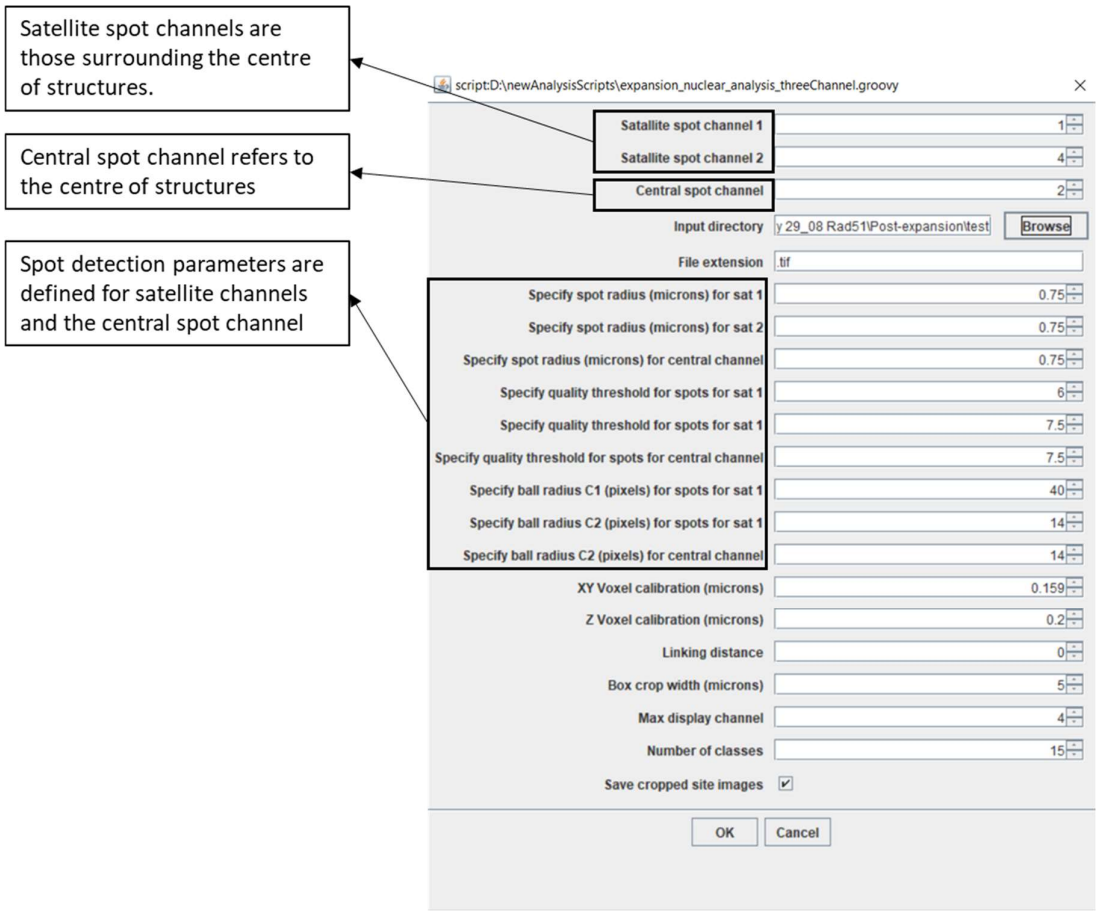

Figure 2.8. User defined parameters for spot detection-based analysis of four-colour Z series. Parameters which differ from those in Figure 2.6 & 2.7 are defined.

Table 2.4. Spot detection-based analysis performed for nanoscale analysis of repair factors.

Spot detection-based analysis script	Experimental	Central spot	Satellite spot(s)
Two-colour Z series	Nanoscale analysis of BRCA1 and 53BP1 foci (Section 4.3.2)	BRCA1	53BP1
	Analysis of BRCA1/ 53BP1 foci structures as a function of recovery time (Section 4.5)	BRCA1	53BP1
	Visualising effects of SMARCAD1 and USP48-depletion on foci subcompartmentalisation (Section 5.2, 5.3 & 5.3.1)	BRCA1 / RAD51	53BP1
Three-colour Z series	Nanoscale analysis of BRCA1/ 53BP1 foci on irradiated vs. non-irradiated cells (Section 4.4.1)	BRCA1	53BP1 (EdU as 3rd channel, no spot detection.
Four-colour Z series	Investigating relative spatial organisation of BRCA1, 53BP1 and RAD51 (Section 5.3.4)	RAD51	53BP1 & BRCA1
	Investigating the effect of SMARCAD1-depletion on chromatin organisation (Section 5.4)	BRCA1	53BP1 & H2A-dendra2

2.7.6 Generation of average foci structures and colocalisation analysis

To generate average structures of class 5 structures (described in Sections 4.4.3, 5.2, 5.3 and 5.4), examples of structures were selected where BRCA1 and 53BP1 were oriented parallel to the focal plane. The example structures were organised into directories, and then an average structure was generated using a Matlab script written by Dr Jeremy Pike. The script generates the average structures as three-dimensional .tif files which were used to generate the maximum projections

and orthogonal views. Additionally, the script generated a radial profile for each channel in the average structure (as described in Section 5.2). Briefly, multiple radii were drawn from the central spot on the central slice of average profiles. The average intensity maximum of the central spot and the satellite spots were measured from the average of the multiple radii.

In addition to generating average structures and radial profiles, the Matlab script also enables the user to quantify Pearson's correlation coefficient (PCC) and Mander's correlation coefficient (MCC) (Dunn *et al*, 2011). To do this, the average structure generated was segmented using an Otsu threshold to remove any fluorescence intensity derived from the background as this can artificially inflate correlation values (described in Section 3.3.2). PCC measures pixel-by-pixel covariance between two channels. Its values range from 1 (perfect linear correction) to -1 (perfect inverse correlation). PCC subtracts the mean intensity of the image from each pixel value to is unaffected by signal fluctuations. PCC is quantified as shown in Equation 1.

Equation 1. Pearson's Correlation coefficient (PCC). Where R_i and G_i are the intensity values of the red and green channels, respectively. R and G refer to the mean intensities across the entire image of the red and green channels, respectively.

$$\mathrm{PCC} = \frac{\sum_i \left(R_i - \overline{R}\right) \times \left(G_i - \overline{G}\right)}{\sqrt{\sum_i \left(R_i - \overline{R}\right)^2 \times \sum_i \left(G_i - \overline{G}\right)^2}}$$

Mander's correlation coefficient measures the co-occurrence of signal between two channels regardless of signal level because in this case the mean intensity of the image is not subtracted from each pixel. MCC values range from 0 (anti-correlated) and 1 (correlated). MCC quantification gives two values: M1 & M2 which correspond to the fractional overlap of channel 1 to channel 2 and vice versa. MCC values are quantified as shown in Equation 2.

Equation 2. Mander's correlation coefficient (MCC).

$$M_1 = \frac{\sum_i R_{i,\text{colocal}}}{\sum_i R_i}$$ where $R_{i,\text{colocal}} = R_i$ if $G_i > 0$ and $R_{i,\text{colocal}} = 0$ if $G_i = 0$

$$M_2 = \frac{\sum_i G_{i,\text{colocal}}}{\sum_i G_i}$$ where $G_{i,\text{colocal}} = G_i$ if $R_i > 0$ and $G_{i,\text{colocal}} = 0$ if $R_i = 0$

2.7.7 Measuring 53BP1 occupancy in S phase nuclei

Volumes of 53BP1 were determined similarly to the volume of nuclei (Section 2.7.2). Images were segmented using auto-threshold in ImageJ to generate a mask. Otsu threshold efficiently segmented 53BP1 from background pixels. The volumes of the final mask were measured for each image. For each image an object map was generated and compared to the original image to ensure accurate segmentation had occurred (Figure 2.9). Additionally, 53BP1 structures were measured manually to determine a maximum and minimum volume. Features smaller than 3 μm^3 were excluded from the final measurements, and features larger than 50 μm^3 were also excluded. It is likely the larger volume measurements are derived from segmentation combining >1 feature.

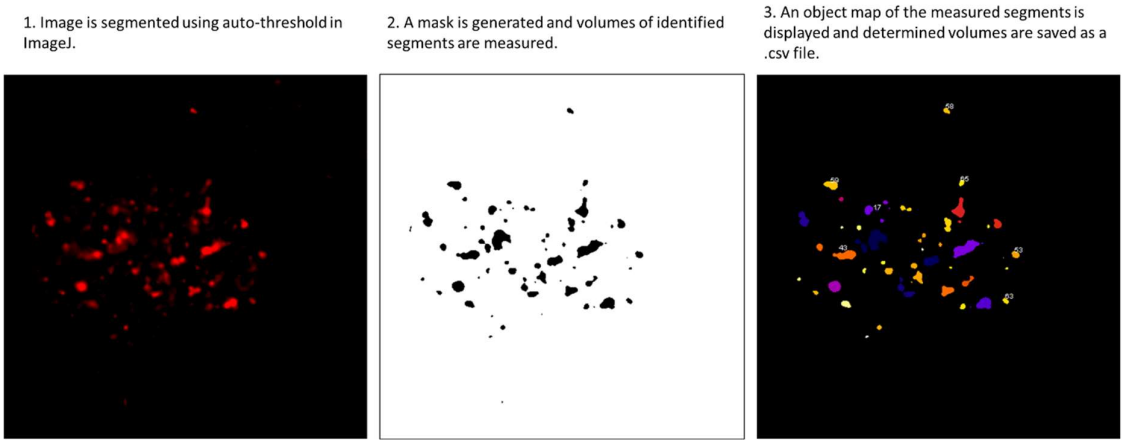

Figure 2.9. Determining volume of 53BP1 structures in ImageJ. Z series acquired post-expansion were opened. For each file channels were split and segmentation is performed on the 53BP1 channel. 1) 53BP1 structures were segmented from the background pixels using auto-threshold and an Otsu Threshold was applied. 2) A mask was generated and the volumes of the identified segments were measured. 3) Measurements were saved as a .csv file (not shown) and an object map of the segments identified by the threshold is generated to confirm the segmentation is accurate.

2.7.8 Quantifying Pearson's correlation coefficient

To quantify PCC values between PCNA and EdU (Section 4.2.1) and 53BP1 and RIF1 accumulations (Section 4.4.5), examples of early, mid and late S-phase classified nuclei were selected from pre- and post-expansion images. Features were segmented using auto-threshold in ImageJ and a mask of each was generated. PCC values were determined using the JACoP plugin in ImageJ.

2.8 Summary of ExM experiments

Cells were treated as in Table 2.5 prior to preparation using standard ExM protocol (Section 2.4).

Table 2.5. Summarising cell treatments prior to ExM preparation of specimens.

<table>
<tr><th>Experiment</th><th>siRNA</th><th>Doxycycline treatment</th><th>EdU treatment</th><th>Irradiation</th><th>Recovery time (s)</th><th>Primary antibodies</th></tr>
<tr><td>Investigating 53BP1 and BRCA1 foci structures (Section 4.2 & 4.3)</td><td rowspan="3">None</td><td rowspan="5">No treatment with doxycycline</td><td rowspan="4">Cells treated with EdU immediately before irradiation and EdU left on for irradiation and recovery time</td><td>Irradiation (2Gy)</td><td rowspan="4">1 hour</td><td rowspan="3">BRCA1
53BP1</td></tr>
<tr><td>Investigating 53BP1 and BRCA1 foci structures in absence of damage (Section 4.4.1)</td><td>No irradiation</td></tr>
<tr><td>Confirming mutual exclusivity between 53BP1 and BRCA1 is BRCA1-dependent (Section 4.4.4)</td><td>siBRCA1</td><td rowspan="4">Irradiation (2Gy)</td></tr>
<tr><td>Investigating spatial organisation of RIF1 and 53BP1 (Section 4.4.5)</td><td>None</td><td>53BP1
RIF1</td></tr>
<tr><td>Characterising 53BP1 and BRCA1 structures as a function of recovery time (Section 4.5)</td><td>None</td><td>Cells pulsed with EdU for 10 minutes.</td><td>10 minutes, 30 minutes, 1 hour, 2 hours</td><td>BRCA1
53BP1</td></tr>
<tr><td>Investigating impact of SMARCAD1 and USP48 depletion on foci sub-compartmentalisation (Section 5.2 & 5.3)</td><td rowspan="2">siSMARCAD1
siUSP48</td><td rowspan="2">Cells treated with EdU immediately before irradiation and EdU left on for irradiation and recovery time</td><td rowspan="2">1 hour</td><td>BRCA1
53BP1
RAD51</td></tr>
<tr><td>Investigating impact of SMARCAD1 and USP48 depletion on chromatin architecture (Section 5.4)</td><td>Treatment with doxycycline 48 hours prior to fixation</td><td>BRCA1
53BP1</td></tr>
</table>

2.9 siRNA sequences

Table 2.6. siRNA sequences.

siRNA Name	5'-3' Sequence
NTC (Renilla Luciferase)	Sense: CUUACGCUGAGUACUUCGA[dT][dT] Antisense: [Phos]UCGAAGUACUCAGCGUAA G[dT][dT]
BRCA1 3'UTR 1	Sense: GCUCCUCUCACUCUUCAGU[dTdT] Antisense: [Phos]ACUGAAGAGUGAGAGGAGC[dT][dT]
BRCA1 3'UTR 2	Sense: AAGCUCCUCUCACUCUUCAGU[dT][dT] Antisense: [Phos]ACUGAAGAGUGAGAGGAGCUU[dT][dT]
SMARCAD1 #1	Sense: GAC GAU UGA AGA AUC CAU GCU [dTdT] Antisense: [Phos] AGC AUG GAU UCU UCA AUC GUC [dTdT]
SMARCAD1 #2	Sense: AUG UAG UUA UAA GGC UUA UGA [dTdT] Antisense: [Phos] UCA UAA GCC UUA UAA CUA CAU [dTdT]
USP48 Exon 5	Sense: GCGUAAGCAAAGUGUGGAUAA[dT][dT] Antisense: [Phos]UUAUCCACACUUUGCUUACGC[dT][dT]
USP48 Exon 11	Sense: GAAUCCAGAUGUGCGCAAUAU[dT][dT] Antisense: [Phos]AUAUUGCGCACAUCUGGAUUC[dT][dT]

2.10 Antibodies

Table 2.7. Antibodies including species raised in, concentration, conditions and protocols.

Antibody	**Animal**	**Procedure**	**Concentration**	**Time**	**Supplier & Cat. number**
53BP1	Goat	IF	1:5000	1 hour	R&D systems Af1877
β-actin	Rabbit	WB	1:5000	Overnight	Abcam Ab8227
BRCA1 (D9)	Mouse	IF	1:500	Overnight	Santa Cruz Sc6954
BRCA1 (MS110)	Mouse	WB	1:500	Overnight	Calbiochem OP94
HA	Mouse	WB	1:1000	Overnight	Sigma H336
Lamin B1	Rabbit	WB	1:3000	Overnight	Abcam Ab16048

PCNA	Mouse	IF	1:2000	1 hour	Abcam ab29
RAD51	Rabbit	IF	1:1000	Overnight	Santa Cruz SC8349
RIF1	Rabbit	IF	1:800	Overnight	Bethyl A300-569A
SMARCAD1	Rabbit	WB	1:1000	Overnight	Bethyl a301-593a-m
USP48	Rabbit	WB	1:1000	Overnight	Abcam Ab72226
Vincullin	Rabbit	WB	1:5000	Overnight	Abcam Ab129002
Donkey α Mouse AlexaFluor 488	Donkey	IF	1:5000	1 hour	Life technologies A21202
Donkey α Goat CF 633	Donkey	IF	1:5000	1 hour	Biotium 20127
Donkey α Mouse AlexaFluor 568	Donkey	IF	1:5000	1 hour	Life technologies A10037
Donkey α Rabbit AlexaFluor 488	Donkey	IF	1:5000	1 hour	Life technologies A32790
Donkey α goat AlexaFluor 568	Donkey	IF	1:5000	1 hour	Life technologies A-11057
Rabbit α Mouse HRP	Rabbit	WB	1:10,000	1 hour	Dako P0161
Swine α Rabbit HRP	Swine	WB	1: 10,000	1 hour	Dako P0217

2.11 Buffers

PBS

1 Tablet (Sigma) in 200 ml H_2O

LB Broth

10g LB Broth powder (Sigma) in 500 ml H_2O

4x SDS Loading Buffer

0.25M Tris pH 6.8, 8% SDS, 40% Glycerol, 6 M Urea, 10% β-Mercaptoethanol

1x SDS Running Buffer

10% 10x Tris/Glycine/SDS in 90% H_2O

1x Transfer Buffer

10% 10x Tris/Glycine, 10% Methanol, 80% H_2O

Protein Lysis Buffer

50 mM Sodium Phosphate pH 7, 300 mM Sodium Chloride, 5% Glycerol, 10 mM β-Mercaptoethanol

2.12 Antibiotics

2.12.1 Tissue culture antibiotics

100x Penicillin/ Streptomycin (Invitrogen) was kept in 5 ml aliquots at -20 ^oC and used at a working concentration of 1x. Stock concentration 10,000 U.

Doxycycline (Invitrogen) was kept in 1 ml aliquots at 20 ^oC and used at a working concentration of 1µg/ml. Stock concentration 1 mg/ml.

Hygromycin was used at a working concentration of 400 µg/ml.

2.12.2 Bacterial antibiotics

Ampicillin was stored in 1 ml aliquots at -20 ^oC. Stock concentration of 50 mg/ml in H_2O and working concentration of 50 µg/ml

3. Investigating retention of nuclear architecture following ExM preparation.

3.1 Introduction

Expansion Microscopy (ExM) is a relatively new super resolution technique and has undergone evolution with considerable pace, enabling innovative solutions to a variety of biological problems. As with any technique, ExM also contains pitfalls and limitations requiring careful consideration of parameters for optimal implementation to new biological questions. One of the main concerns when applying ExM is the isotropy of the expansion, from the macro- to nanoscale, and accurate determination of the expansion factor (Pesce *et al*, 2019). Isotropic expansion measures uniformity of expansion factor on the nanoscale, and anisotropic expansion may lead to distortions in the final image.

Expansion factor is largely determined by the monomer and cross-linker percentages in the gelation solution (Chen *et al*, 2015). Isotropy of ExM relies on homogeneous, uniform formation of the polyelectrolyte gel meshwork through the specimen, and complete homogenisation of the sample (Section 1.6.4). The gel network is synthesised evenly and densely throughout the sample, with an estimated spacing of 1-2 nm (Wassie *et al*, 2019). This is well below the size of biomolecules allowing them to be spread apart whilst retaining their relative spatial organisation. Mechanical homogenisation of the sample is often achieved by a non-specific proteinase (e.g. Proteinase K). Use of more specific enzymatic digestion (e.g. LysC) has been attempted to retain epitopes for post-expansion labelling, but these resulted in anisotropic expansion highlighting the need for complete homogenisation for reliable expansion (Tillberg *et al*, 2016). The gel uniformity is also critical to a controlled expansion process upon the addition of water; expansion relies on electrostatic repulsion between negative charges in the polymer backbone (Cho *et al*, 2018).

Macroscale expansion factor has been determined by measuring the gel pre- and post-expansion, however, this may not reflect expansion factor on smaller length scales as there is a potential for distortions and heterogeneity induced by the gelation, digestion and expansion steps (Pesce *et al*, 2019). ExM has been validated for use in a range of cell and tissue types (Alon *et al*, 2018) by determining isotropy of expansion and quantifying induced distortions. These parameters have commonly been measured through a correlative imaging approach which compares images of highly stereotyped features (e.g. microtubules) (Chen *et al*, 2015, Chozinski *et al*, 2016, Tillberg *et al*, 2016, Chen *et al*, 2016, Chang *et al*, 2017). Pre-expansion images are acquired on a super resolution microscope (e.g. SIM), the expansion protocol is performed and then images of the same features are acquired post-expansion on a diffraction-limited system (e.g. confocal). The pre- and post-expansion images are compared through image registration and distortions are quantified (Section 1.3.1). Whilst efficient at detecting gross deformations in samples, these measures are insufficient to account for changes in your structure of interest (Chozinski, 2018). How the physical features of specific cellular sub-compartments may affect the isotropy of the expansion is unclear. The nucleus is comprised of DNA which is densely packed in the form of chromatin. The nuclear sub-compartment has highly complex and variable topology. The effect of the expansion on this topology has not been clearly determined (Alon *et al*, 2018).

It was critical to characterise the isotropy of expansion in the nucleus on the micro- and nanoscale. It has been suggested that if the expansion of DNA is not isotropic, this could have an adverse effect on expansion of DNA-bound complexes such as those involved in transcription and repair (Geertsema & Ewers, 2016). Additionally, there is a distinct lack of consensus on how the expansion process affects the nucleus, or on how to treat the nucleus during sample preparation.

The aim of this chapter is to validate the isotropy of nuclear expansion in 2D and 3D. In this chapter, we verify that the nuclear sub-compartment may be expanded reproducibly in 2D and 3D. We confirm that nanoscale structural information is retained within the nucleus using a correlative

imaging approach. Further, we investigate the use of a marker of chromatin post-expansion to serve as an additional tool to verify retention of the nuclear architecture. This marker of chromatin is also applied to allow investigation of the role of chromatin remodelling during DSB repair (Chapter 5).

3.2 Nuclear DNA expands isotropically during ExM treatment

It has been demonstrated that nucleic acids can be covalently modified for incorporation into the gel by use of a molecule termed "LabelX". This anchor was originally developed for visualising localisation of RNA transcripts, but was also shown to allow expansion of the nucleus (Chen *et al*, 2016). We aimed to determine if applying LabelX would allow uniform and isotropic expansion of the nuclear sub-compartment.

For visualisation of the nuclear DNA, we applied 5-ethynyl-2'-deoxyuridine (EdU) which is a thymidine analogue used to detect DNA synthesis in proliferating cells (Salic and Mitchison, 2008). This is incorporated into actively replicating regions of DNA and is commonly used to determine cell cycle position. The alkyne functionality introduced into the DNA by EdU can subsequently be detected by reaction with fluorescent azide dye in a Copper (I)-catalysed azide alkyne cycloaddition (Figure 3.1). This approach is advantaged in the relatively small size of the fluorescent azides which enables efficient diffusion through samples.

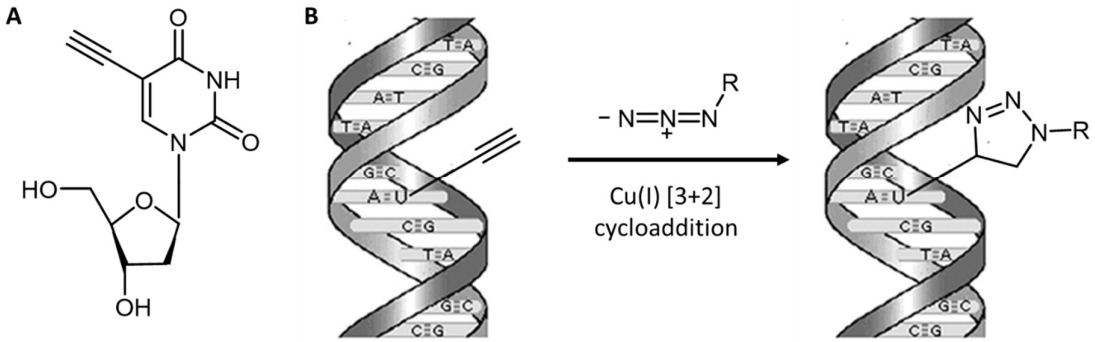

Figure 3.1. Schematic of EdU detection. A) The chemical structure of EdU, a thymidine analogue which carries an alkyne group in the place of a methyl group. B) The incorporation of EdU into actively replicating DNA results in an alkyne functionality present in the DNA. This can react with an azide (where R is a fluorophore) in a Copper-catalysed azide-alkyne cycloaddition allowing for its detection (Adapted from Salic and Mitchison, 2008).

3.2.1 Characterising nuclear expansion in 2D

Initially, we aimed to determine if the nuclear sub-compartment could be expanded on the microscale in 2D. To achieve this, U2OS cells were seeded and treated with EdU overnight so that it would be incorporated throughout the nucleus. Cells were fixed and treated with an Alexa Fluor 488 azide dye for detection of EdU. Images were acquired pre- and post-expansion on a widefield microscope (Section 2.4.7). Qualitatively, nuclear areas were substantially increased (Figure 3.2).

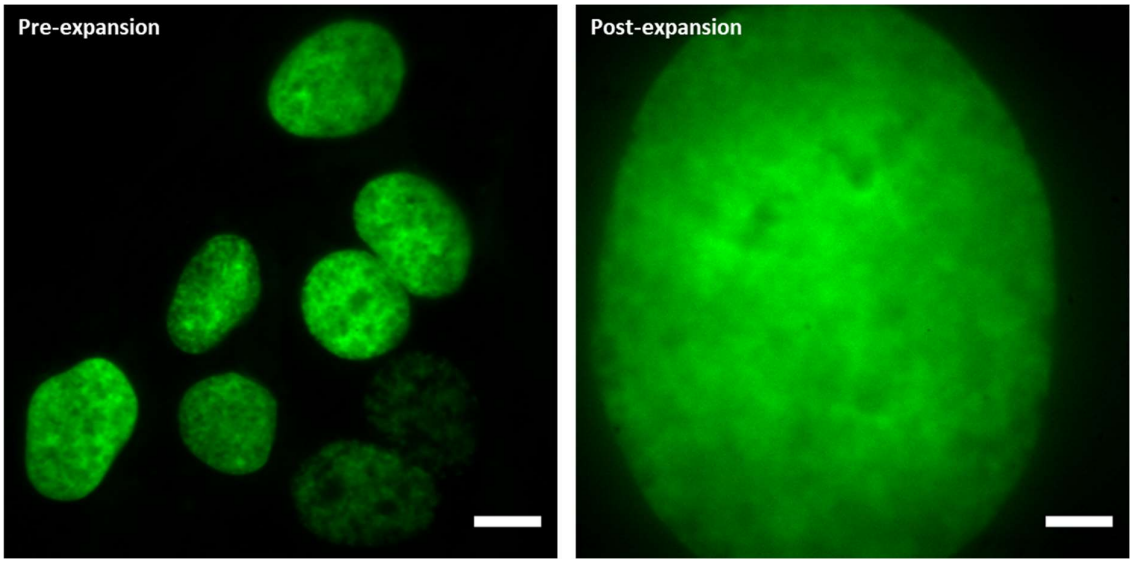

Figure 3.2. **Visualising Nuclear Expansion.** U2OS cells were seeded and incubated with EdU overnight prior to fixation. Cells were treated with Alexa Fluor 488 azide dye for detection of EdU. Images were acquired pre- and post-expansion on a widefield microscope. Images were acquired on different cells pre- and post-expansion. Standard ExM protocol was used (Section 2.4). For post-expansion samples, gels were mounted in a mattek dish prior to imaging. Scale bars 10 µm. 10 µm scale bar is equivalent to 2.5 µm scale pre-expansion. This was estimated from the macroscale expansion of the gel.

To quantify the expansion of nuclei in 2D, cells were seeded at two different densities and treated overnight with EdU prior to fixation and staining with an azide dye. Images of nuclei were acquired pre- and post-expansion and their areas were measured (Figure 3.3). Images were not acquired correlatively given the technical challenges of correlative imaging (Pesce *et al*, 2019). Nuclear size is known to alter depending on cell cycle progression (Umen, 2005 & Huber and Gerace, 2007). With these factors in mind, images of ~100 nuclei were obtained for each pre- and post-expansion sample.

Post-ExM images were obtained using a 20x objective to maximise acquisition speed, as nuclei visualised on a 100x objective fill the field of view. To semi-automate measurements of nuclear areas, I developed a workflow in Matlab (Figure 3.4 & 3.5) (Section 2.7.1). Nuclei were segmented from the background pixels using a manually determined threshold. The generated mask of the

segmented areas was then smoothed, eroded and dilated. This was done because nuclei are not perfectly round and the incorporation of the fluorescence azide used in the click chemistry does not result in uniform fluorescence *i.e.* fluorescence varies through the nucleus due to various factors e.g. chromatin compaction, presence of nucleoli, image acquisition artefacts. To ensure the segmentation was working effectively, the boundaries detected during the segmentation were superimposed onto the original images. Once satisfied that nuclei are being accurately segmented, areas were determined for pre- and post-expansion images.

To ensure the measured areas correspond to single nuclei, a maximum and minimum size threshold was set. Some nuclei may be very close, so the segmentation determined these are one object when in fact it is two, these were removed from the final measurements. Equally, features that are too small were also removed. These boundaries were set on the assumption that nuclei conform to a circle, and area boundaries set according to measured radii of the nuclei in the images (Table 2.2). Nuclear areas increased by ~16x, which equates to ~4x expansion in 1 dimension (Figure 3.6). Range of values determined pre- and post-expansion have a comparable distribution which suggests nuclear size variation is represented in both datasets.

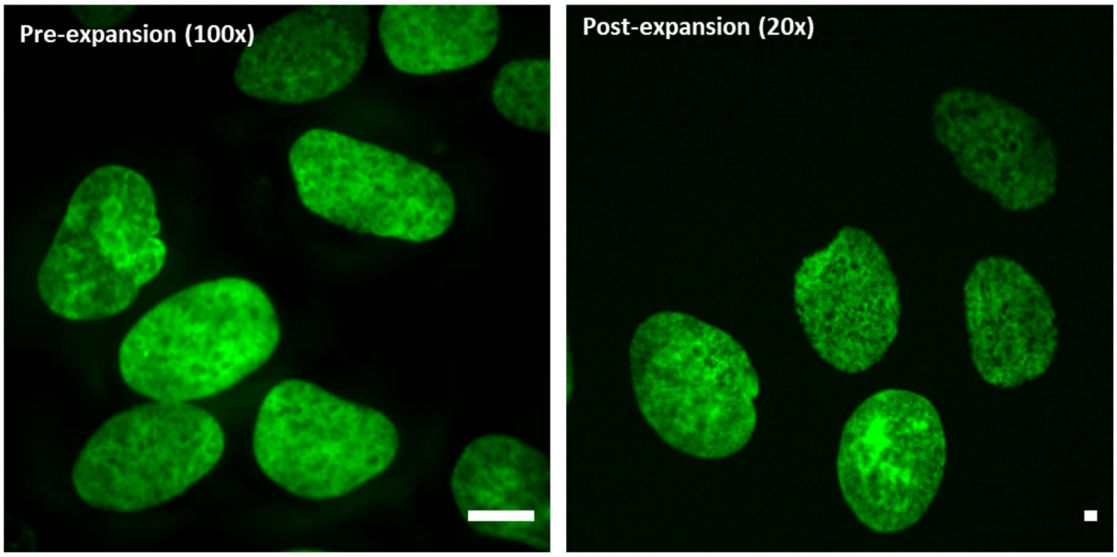

Figure 3.3. Quantifying nuclear expansion factor. U2OS cells were seeded at two different densities (representative images of 50,000 cells/ ml seeding density shown). Cells were incubated with EdU overnight and subsequently fixed. Pre-expansion samples were treated with Alexa Fluor 488 azide dye. Pre-expansion images were acquired on a 100x objective on a widefield microscope. Scale bar 10 µm. Expansion samples were treated with standard ExM protocol (Section 2.4) and then images acquired on a 20x objective on a widefield microscope. Scale bars 10 µm (equivalent to 2.5 µm pre-expansion).

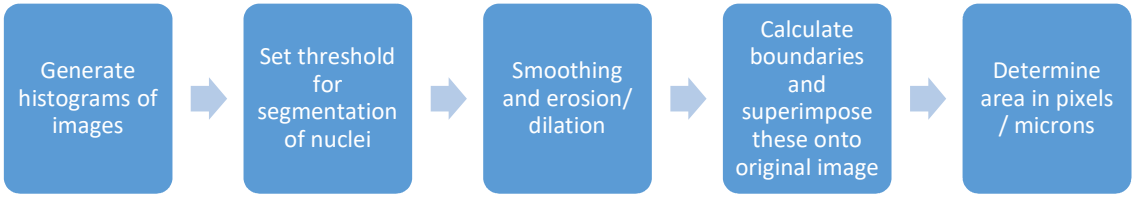

Figure 3.4. Process of quantification of nuclear expansion factor in Matlab. To determine a threshold for the segmentation of the nuclei from the background, histograms were generated from images and a threshold was manually set based on a collection of images pre- and post-ExM. Smoothing and erosion then dilation was performed on the generated mask. Determined boundaries per images were calculated and superimposed on the original image. The areas were determined in pixels and microns^2.

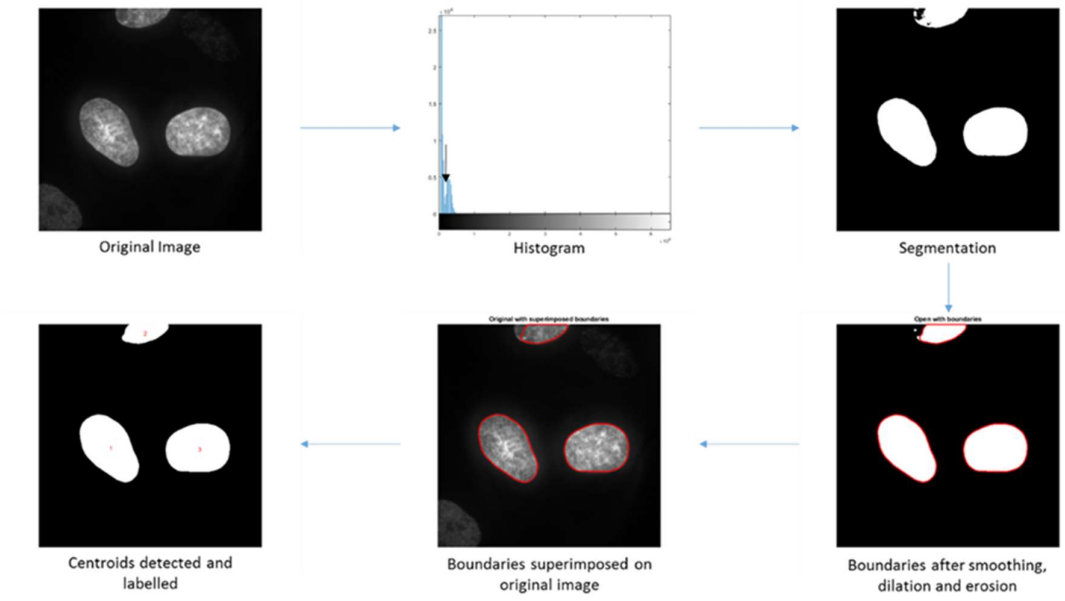

Figure 3.5. Example of Segmentation for quantification of nuclear area. An example of the segmentation process involved to measure nuclear area is shown. Each .tif file in a defined directory is loaded in. The user sets a manually determined threshold (shown by the black arrow) based on a histogram. This results in a mask of pixels where the fluorescence intensity is above the manually determined threshold. Boundaries are traced in this binary image (shown in red) after smoothing, erosion and dilation. The determined boundaries are then superimposed on the original image to check efficacy of the segmentation process. Then areas of the objects are calculated in pixels and converted into μm^2. This process was done for each experimental set by use of for loops (described in Section 2.7.1).

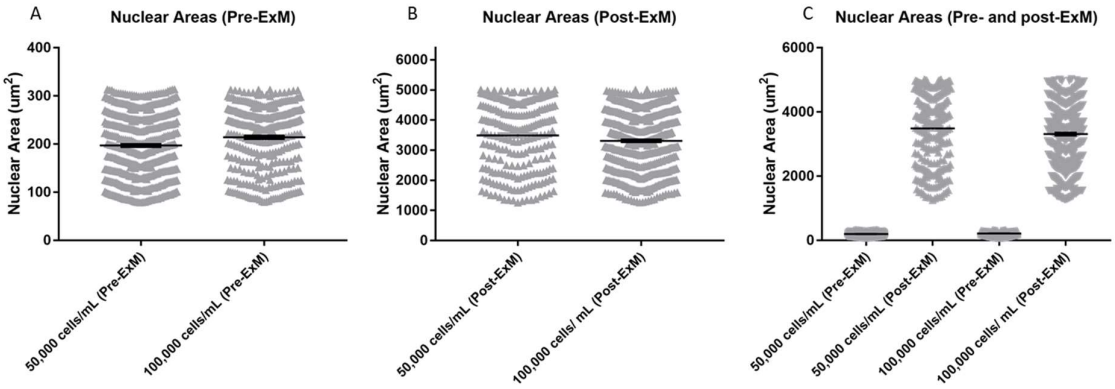

Figure 3.6. Nuclear Expansion Factor measurement. Nuclear area was quantified pre- and post-expansion for each sample using the segmentation analysis (Figure 3.5). A) Pre-ExM and B) Post-ExM. C) Nuclear areas pre- and post-ExM are summarised. N=3, >100 nuclei per sample.

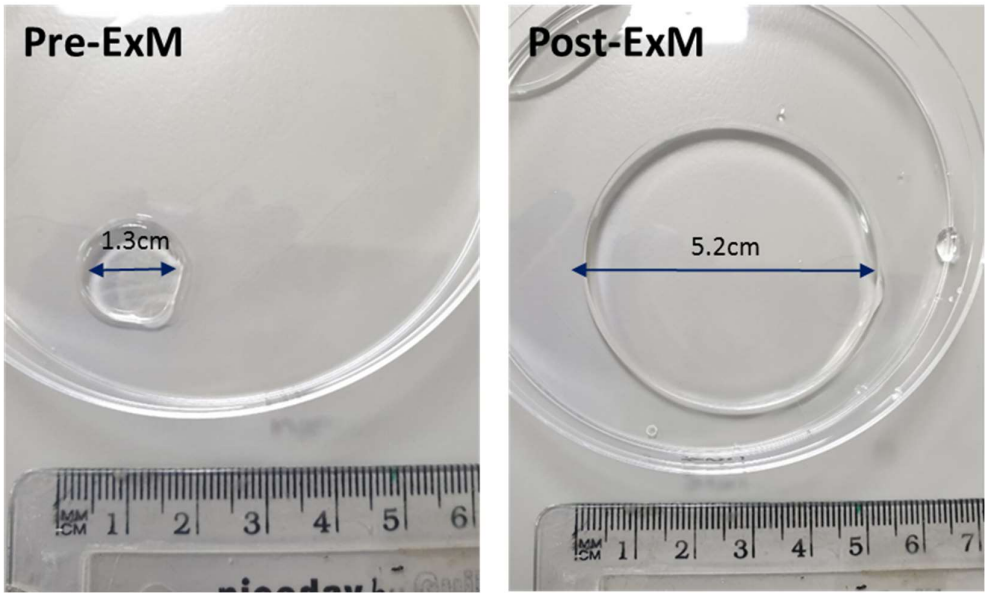

Figure 3.7. ExM gels pre- and post-ExM. Diameters of ExM gels were measured pre- and post-ExM.

Expansion Factor (EF) can be estimated by measuring the size of the gel on the macroscale. Diameters of gels were measured pre- and post-expansion. When gels reached their maximum size, the diameter was increased ~4x consistently (Figure 3.7). This expansion factor correlates with the microscale expansion factor of the nuclear areas, suggesting the physical features of the nucleus is not constraining the overall expansion of the nucleus.

3.2.2 Visualising nuclear expansion in three dimensions (3D) using selective plane illumination microscopy (SPIM)

We aimed to determine if expansion of the nucleus is isotropic in 3D. To do this, Z series were acquired pre-expansion and post-expansion. Pre-expansion images were acquired on a widefield microscope and deconvolved. For post-expansion images, we used selective plane illumination microscopy (SPIM) (Section 1.2.2). SPIM is advantaged in its ability to achieve optical sectioning with minimal photo-damage to specimens (Huisken and Stainier, 2009). Additionally, the ExM gels are optically transparent (Gao *et al*, 2017) due to the amount of water absorbed by the polymer. This feature means that the gels are optically matched to the water used as the immersion medium

on the SPIM. This minimises the presence of optical aberrations, allowing clear visualisation of the nuclear volume. ExM can be considered an optical clearing technique due to this property.

We used an ASI iSPIM system for imaging of ExM samples (Figure 3.8). iSPIM is a single-sided system meaning the light sheet is created through one objective and detected through the other. The light sheet can be moved through the sample using a scanner which is synchronised with the piezo stage to synchronously move the imaging objective. This set up is advantaged in faster acquisition speed than its diSPIM counterpart. It is also more economical and simpler to implement. However, its axial resolution is lower than the lateral resolution, similarly to diffraction-limited systems.

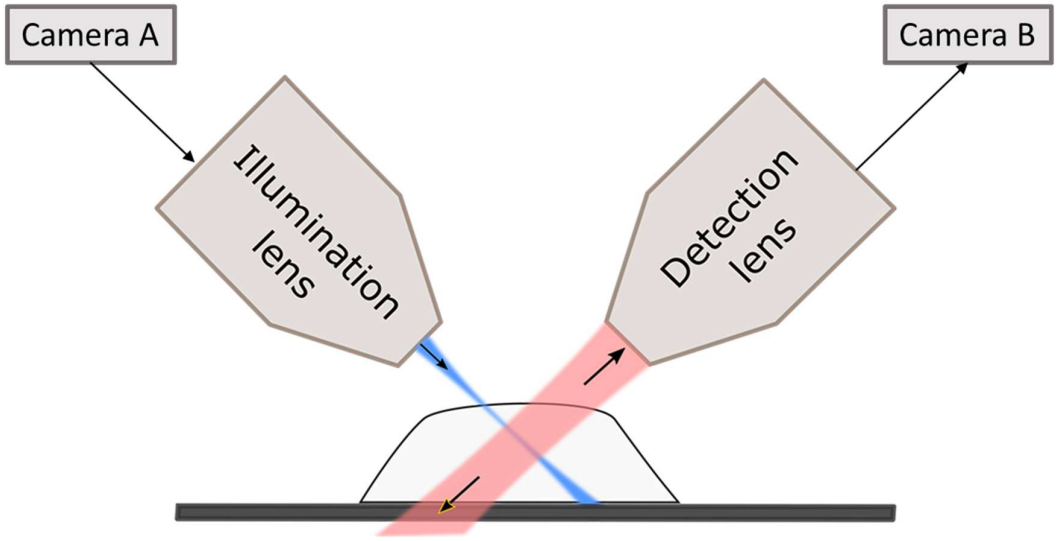

Figure 3.8. Schematic of SPIM illumination pattern. The two immersion objectives shown (A/B) are placed at a right angle above the sample which is mounted in a dish. Each objective is 45^{o} from vertical. In the iSPIM set up the sheet is created through objective A and passes through objective B and is detected by camera B. By moving the imaging objective synchronously with the piezo stage, stacks are acquired. In the diSPIM set up, a sheet may also be formed in objective B and subsequently detected by camera (Applied Scientific Instrumentation).

3.2.3 Sample handling and optimising image acquisition on SPIM

The first challenge in enabling 3D acquisitions using SPIM was successfully immobilising the samples. The immersion medium of the iSPIM microscope is water, meaning the gels float if not adequately mounted. There are methods to reduce or prevent the movement of gels during image

acquisitions (Gao *et al*, 2017). The use of poly-lysine coated surfaces limits sample movement and is advantageous in forming a transparent interface between the objective lens and the sample so it will not induce optical aberrations. This was effectively applied in this work for 2D acquisitions on widefield but was not suitable for the SPIM set up. Gao *et al* also suggest that samples may be fixed down with superglue. When this was attempted, we found this to be suboptimal as the immobilisation on the super glue is temporary, and superglue becomes immobilised in the water immersion medium overtime and can enter the interface between the objectives and the sample; it was concluded this is impractical for long acquisitions.

We found the most effective way to immobilise the ExM gels was embedding them in a low melting point agarose gel (Figure 3.9). This method successfully immobilises the samples and allows for long acquisitions with minimal sample movement. Whilst ideal, care is necessary as the agarose can enter the interface between the SPIM objectives and the sample, again causing optical aberrations. Application of agarose as a mount is useful as ExM gels can be removed from this following acquisitions by shrinking the ExM gels in phosphate-buffered saline solution. ExM gels could then be stored in their shrunken state, facilitating multiple rounds of imaging on samples.

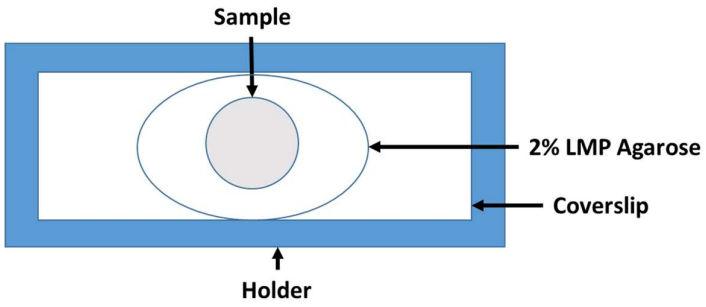

Figure 3.9. Top-down schematic of immobilisation of ExM gels for SPIM imaging. A section of ExM sample gel is place in the SPIM holder with a coverslip in it. The gel is orientated such that the cell side of the gel is nearest to the objectives. 2% agarose is added around the ExM gel taking care to preserve the interface between the ExM gel surface and the objectives. The agarose is allowed to set and becomes opaque when set. The holder is then filled with water prior to imaging.

To visualise DNA in 3D on the SPIM, cells were treated overnight with EdU prior to fixation and staining using Alexa Fluor 488 azide dye. The standard ExM protocol was performed and gels were mounted in agarose to immobilise them before addition of the water to immerse the sample prior to image acquisition. The architecture of DNA could be clearly visualised (Figure 3.10 - 3.12). The absence of optical aberrations meant minimal or no processing was required to reveal complex topology of the nucleus.

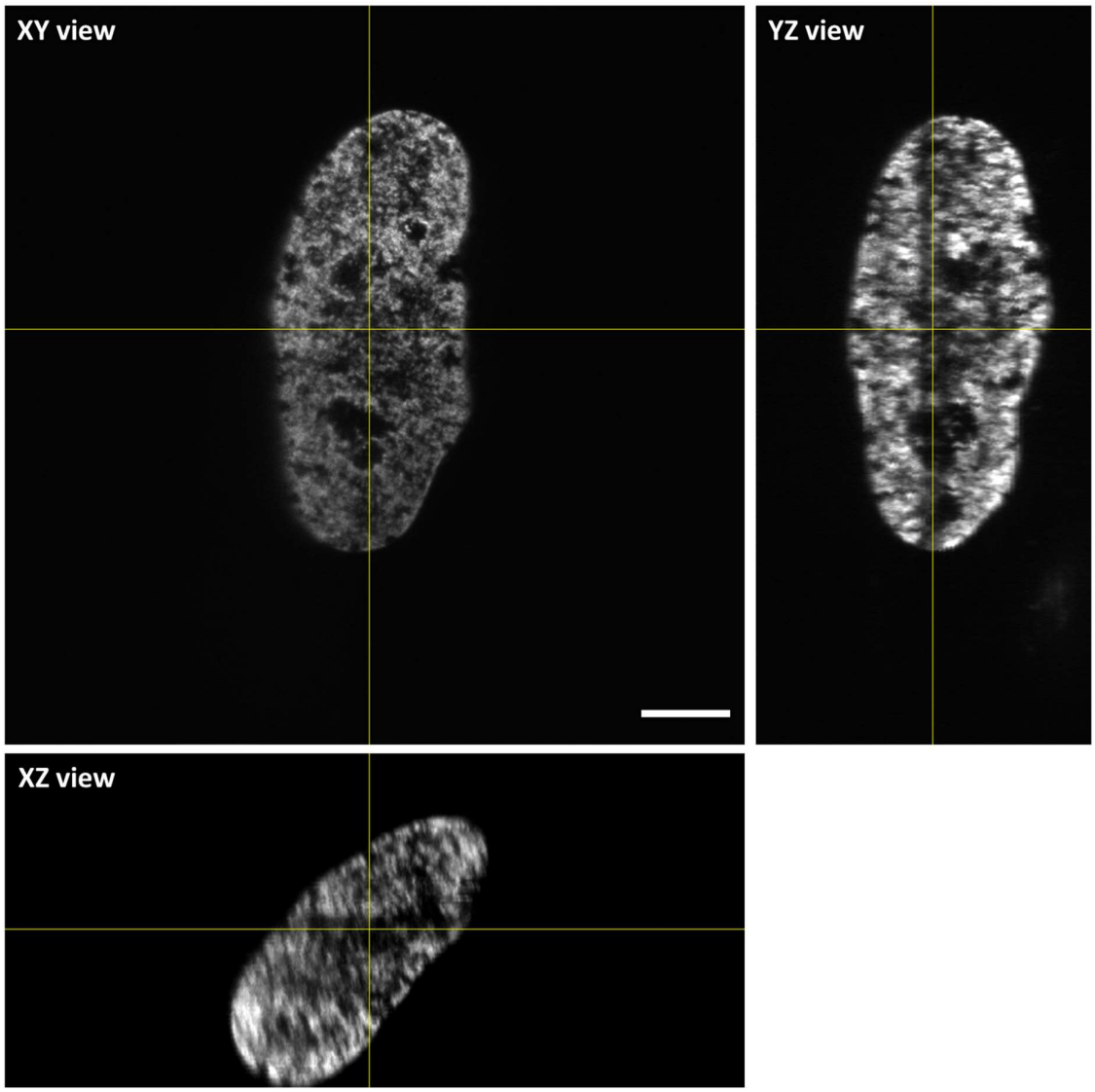

Figure 3.10. Visualising nuclear architecture on SPIM. U2OS cells were treated with EdU overnight and fixed. Cells were stained with Alexa Fluor 488 azide dye and ExM protocol was performed. Sections of ExM gels were embedded in agarose in the SPIM holder and immersed in water. Images were acquired using piezo scanning. Orthogonal views through the central slice of a nucleus is shown. Scale bar 20 µm.

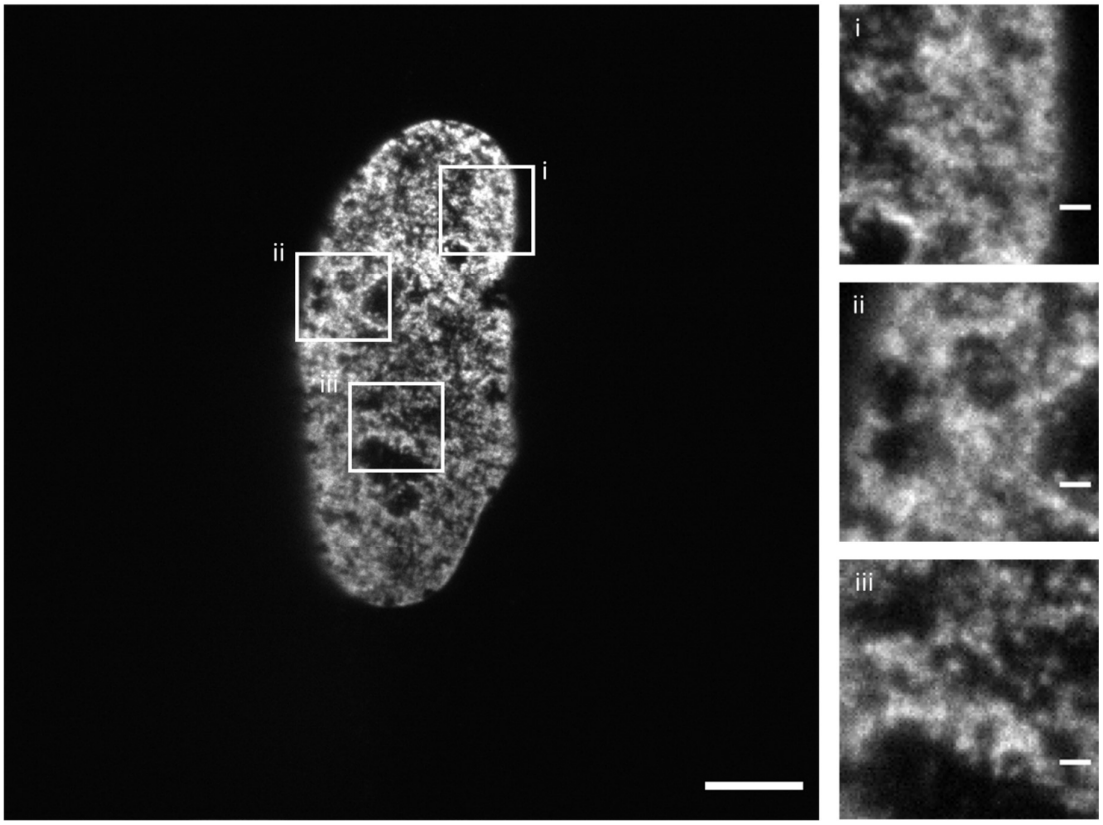

Figure 3.11. Visualising nuclear architecture on SPIM. Selected features were chosen from the image data in Figure 3.10 to illustrate the nanoscale detail visible in SPIM images acquired post-expansion. Scale bars 20 µm and 2 µm.

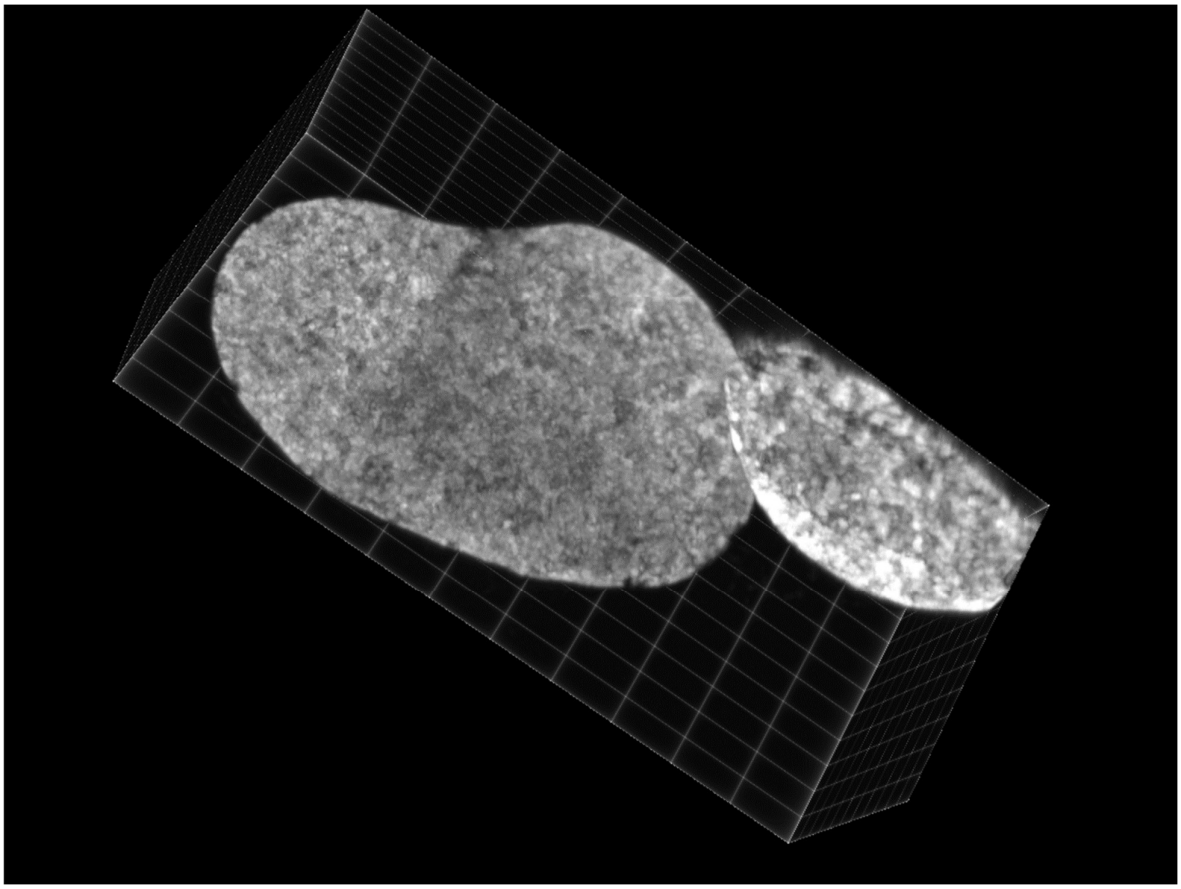

Figure 3.12. Visualising nuclear architecture in 3D on SPIM. 3D SPIM acquisition was reconstructed and visualised in Clear Volume on Fiji.

3.2.4 Measuring isotropy of nuclear expansion in 3D

To determine if the expansion of the nucleus is isotropic images in 3D, Z stacks were acquired pre-expansion and SPIM data was acquired post-expansion. The nuclear volumes were determined in each dataset through segmentation of nuclei and measurement of volume in μm^3 (described in Section 2.7.2). This was performed in ImageJ. The approach to segmentation and measurement of volumes is shown in Figure 3.13. The volumes of pre- and post-expansion nuclei are summarised in Figure 3.14.

Figure 3.13. Measuring volumes of nuclei pre- and post-expansion. Each Z series from a directory was opened. Auto-threshold using an Otsu method was applied to segment nuclei from background pixels. A mask was generated, eroded and dilated, and finally holes were filled in. The volumes of these regions were measured using 3D object counter. Results were saved for each Z series. Volume measurements were saved as a .csv file. Additionally, an object map was saved for comparison to the original image to confirm efficacy of segmentation and accuracy of volume measurements (described in Section 2.7.2).

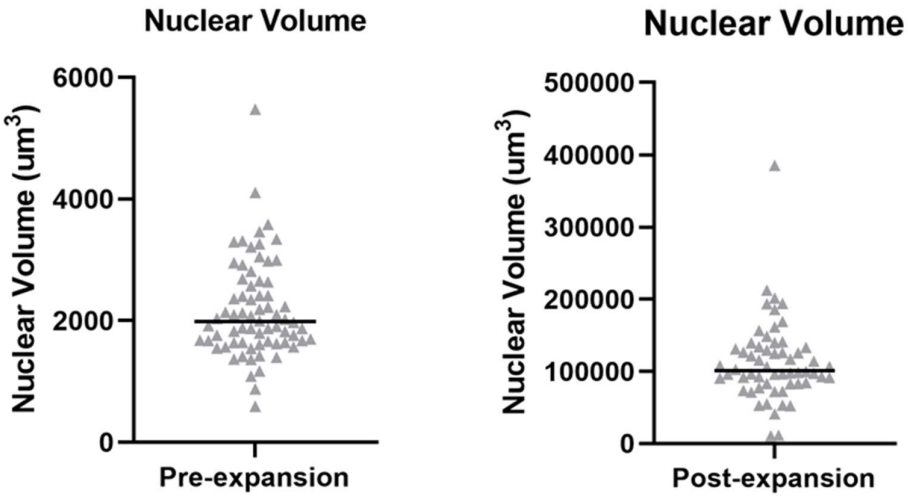

Figure 3.14. Measuring nuclear volumes pre- and post-expansion. Z series of nuclei were acquired pre-expansion on a widefield microscope and deconvolved. Z series of nuclei were acquired post-expansion using a SPIM. Nuclear volumes were measured by performing segmentation as described in Section 2.7.2. N=1; >50 nuclei per sample.

The volume measurements of nuclei pre- and post-expansion revealed an average increase of 52-fold in volume which is equivalent to 3.7x expansion in one dimension. The expansion factor determined by measuring nuclear areas is 4x therefore we expected a volumetric increase of 64x. The reason for this discrepancy may be due to the segmentation performed being insufficient in some of the post-expansion image data; some regions of nuclei had a lower fluorescence intensity

and were not segmented effectively, therefore these voxels would have been lost from the final volume determined in these images.

3.2.5 Correlative imaging of nuclei

The area and volume measurements of nuclei pre- and post-expansion suggest that the nuclear sub-compartment can be expanded isotropically. However, the effect of expansion on the nanoscale features of the genome architecture is unknown (Alon *et al*, 2018). It has been suggested that the nucleus is subject to differential expansion depending on the compaction state of the nucleus (Pernal *et al*, 2020). The authors concluded that heterochromatin regions expand up to 25% less than euchromatin regions, based on DAPI intensity measurements performed pre- and post-expansion. To determine if there are nanoscale distortions present in our approach to ExM, we performed correlative imaging. Images of nuclei were acquired on a SIM pre-expansion, standard ExM protocol performed and then post-expansion images of the same nuclei acquired on a widefield microscope.

The Z stacks acquired post-expansion were affected by optical blurring and noise which reduced the overall resolution and signal-to-noise ratio (Wallace *et al*, 2001) (described in Section 1.2.1). These effects were removed using deconvolution, a mathematical operation which enables restoration of images by removing optical blur, and correcting effects of statistical noise through pre-processing of image data. For deconvolution, we used a commercially available software: Huygens (detailed in Section 2.6) (Scientific volume imaging).

Briefly, upon provision of a theoretical PSF, Huygens can be used to apply different mathematical algorithms to solve the convolution and subsequently do the deconvolution. In this case, a classic maximum likelihood estimation was applied. This is a common method of restoration suitable for most image types. It works by iteratively optimising the likelihood that objects estimated in the image are correctly localised based on the PSF and source image information. This process is suited to low signal images (like those acquired following ExM preparation).

An optimal deconvolution template was generated and revealed the nanoscale information in widefield Z stacks. Pre-expansion SIM images and post-expansion widefield images were aligned using rotation and translation, and features within these were compared (Figure 3.15).

A. SIM pre-expansion

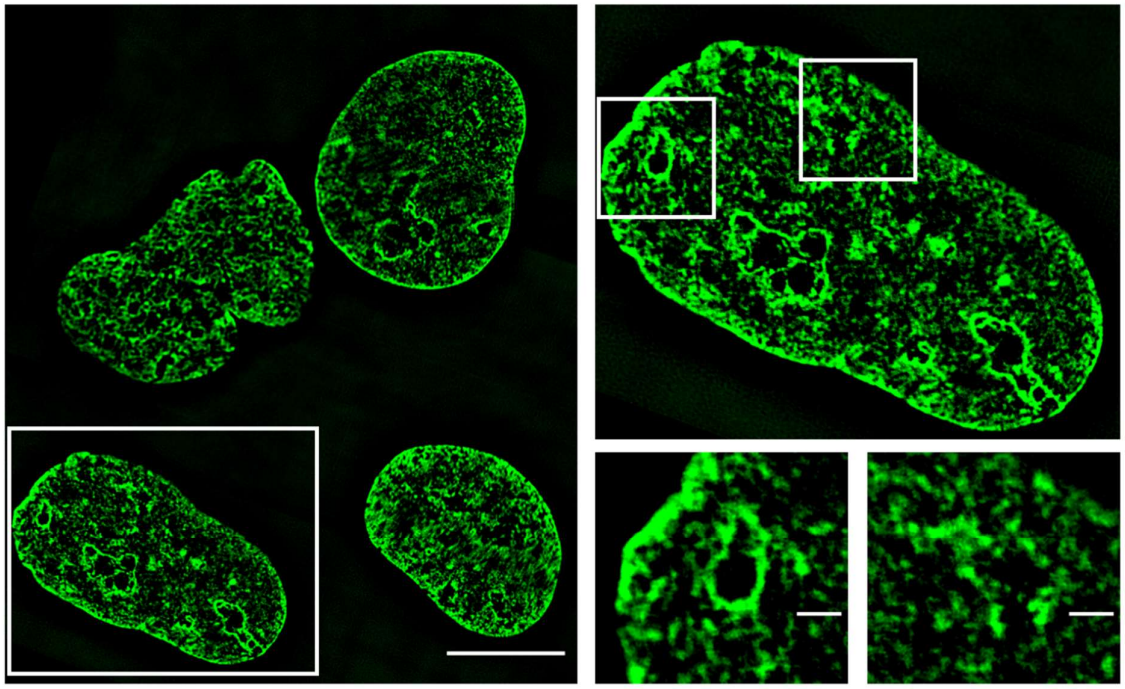

B. Widefield post-expansion

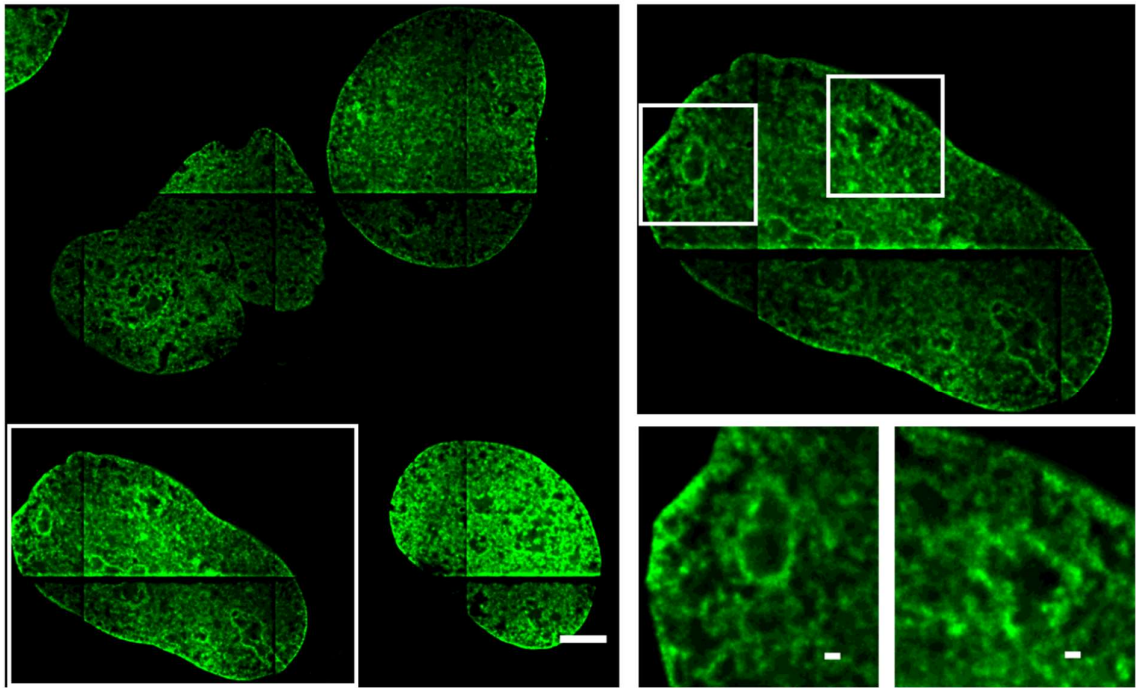

Figure 3.15. Correlative imaging of EdU-stained nuclei. Features in nuclei were compared between pre-expansion images acquired using structured illumination microscopy (SIM) and post-expansion images acquired on a widefield microscope. A) U2OS cells were seeded and incubated with EdU overnight. Cells were then fixed and click it reaction was performed for detection of EdU. Cells were treated with LabelX overnight and gelation and digestion were performed. At this stage, the SIM images were acquired on contracted gels. B) Expansion was performed on gels used for SIM acquisitions and post-expansion images were acquired on widefield and images were deconvolved using Huygens software. Representative slices are shown for the SIM and widefield acquisitions. Scale bars 20 μm. Example nucleus was selected from these acquisitions and example sections compared visually. Scale bars 2 μm.

The use of a correlative imaging approach allows visualisation of the same nuclei and features within these nuclei. Qualitatively, the morphology of the nucleus is retained following the expansion suggesting that the nuclear compartment expands isotropically (Figure 3.15). Additionally, the nanostructures visible in the post-expansion images are comparable to those in the SIM, though more fine details are detected in the post-expansion image data. This may be due to the increased resolution of ExM at 60-70 nm laterally, compared to SIM at 120-130 nm laterally. Some of this nanoscale information may also be lost in the process of SIM reconstruction.

To directly compare features present in pre-expansion SIM data to post-expansion widefield data, equivalent slices were selected from each data set and compared side-by-side (Figure 3.16). In addition, nuclear areas and inter-nuclear distances were measured (Appendix Figure A1). Nuclei were observed to expand ~3x and inter-nuclear distances increased by ~2.7x in one dimension. The reduced nuclear expansion factor is derived from the fact that ExM gels were partially expanded (~1.4x) by the digestion step prior to acquisition of the SIM images.

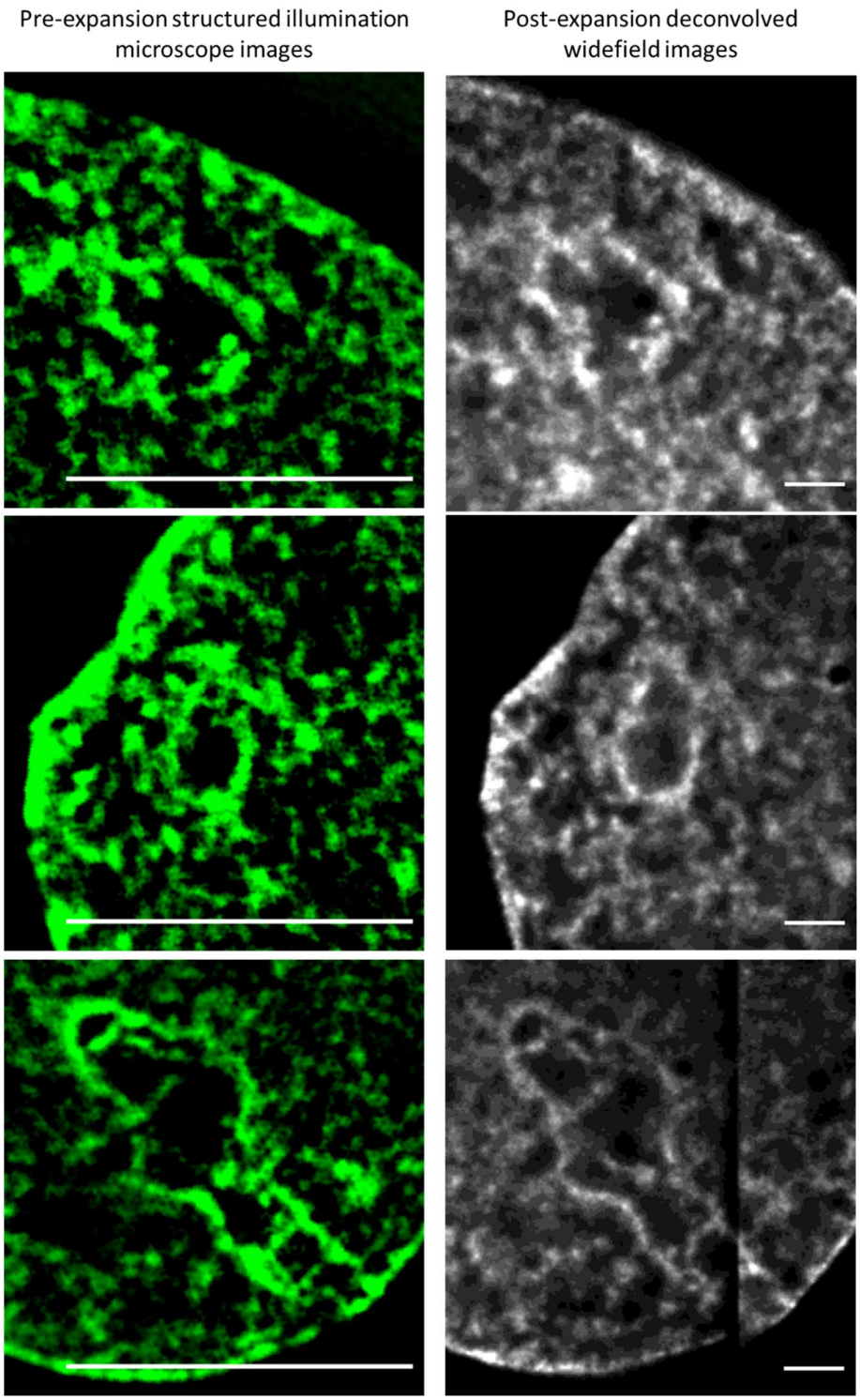

Figure 3.16. Registration of pre- and post-expansion images of nuclei. Features were extracted from Z series shown in Figure 3.15. Features were compared side-by-side to confirm retention of nuclear topology following standard ExM preparation. Scale bars 10 µm.

3.3 Fluorescently-tagged H2A is a marker of chromatin post-expansion

Chromatin forms the landscape for DNA metabolic processes (e.g. repair, replication). Given the intimate link between the DDR and chromatin (Misteli and Soutoglou, 2009), it is critical we accurately represent chromatin in ExM procedure. We hypothesised that the digestion step using proteinase K required in standard ExM preparation may result in proteolysis of histones forming chromatin. In order to represent chromatin we generated cell lines expressing fluorescently tagged H2A. Use of fluorescent proteins during ExM was demonstrated during the development of protein retention ExM (ProExM) (Tillberg *et* al, 2016). GFP and GFP-like proteins were shown to have good stability towards proteases, and most retained their fluorescent signal for post-expansion imaging.

3.3.1 Generation of H2A-fluorescent protein (H2A-FP) cell lines

For the generation of cell lines expressing H2A-fluorescent proteins, we used U2OS Flp-In T-REx cell lines. Flp-In cell lines have an integrated Flp Recombination Target (FRT) site in their genome, which directs integration of genes into a specific location. An expression vector containing our gene of interest is the integrated into the FRT site through Flp recombinase-mediated DNA recombination (illustrated in Figure 3.17) (Section 2.3.4).

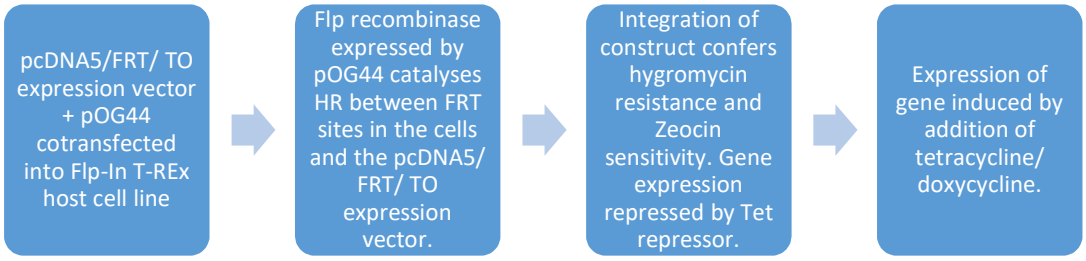

Figure 3.17. Generation of stable cell lines using Flp-In host cell line. This diagram summarises the key steps involved in the generation of stable cell lines expressing a gene of interest: H2A-dendra2 and H2A-mCherry (detailed description provided in Section 2.3.4).Briefly, cells are co-transfected with pcDNA5/ FRT/ TO expression vector containing your gene of interest, and pOGG44 which expresses Flp recombinase required for HR events between FRT sites in the genome and in the pcDNA5/ FRT/TO vector. After 48 hours, cells are selected by treatment with Hygromycin. Expression of gene of interest is induced by addition of doxycycline.

Cell lines expressing H2A fluorescently tagged with either Dendra2 or mCherry were generated (referred to as H2A-FP(s)). A DNA construct was designed for each of these proteins incorporating a HA tag and either dendra2 or mCherry. The expression of H2A-FPs was confirmed by western blot following induction with doxycycline (Figure 3.18). There was an additional band present suggesting post-translational modification via ubiquitin was occurring.

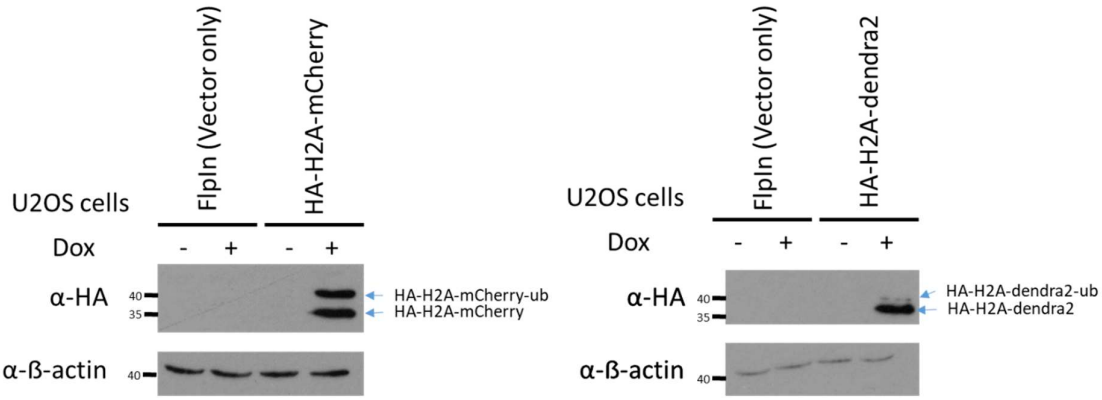

Figure 3.18. U2OS cells expressing H2A-dendra2 or H2A-mCherry. Western blot of cell lysates from U2OS FlpIn cell lines +/- Doxycycline to induce expression of H2A-dendra2/ -mCherry probed for HA and controls as indicated showing that U2OS FlpIn cells express H2A-Dendra2/ mCherry.

3.3.2 Quantification of retention of chromatin marker following ExM in 2D

We aimed to demonstrate that H2A-FPs are retained as markers of chromatin during ExM. DNA is wrapped around nucleosomes to form chromatin (Section 1.1.4), so we predicted that if we imaged markers of DNA and chromatin we would observe high colocalisation between these features pre- and post-expansion. U2OS cells were treated with doxycycline to induce expression of H2A-FPs and then treated with EdU overnight to allow incorporation throughout the nucleus. Images were acquired pre- and post-expansion. Colocalisation was firstly assessed visually on merged images of DNA and chromatin. We observed colocalisation between the DNA and chromatin markers pre- and post-expansion (Figure 3.19). This indicates that the relationship between DNA and H2A-FPs is retained through the ExM protocol.

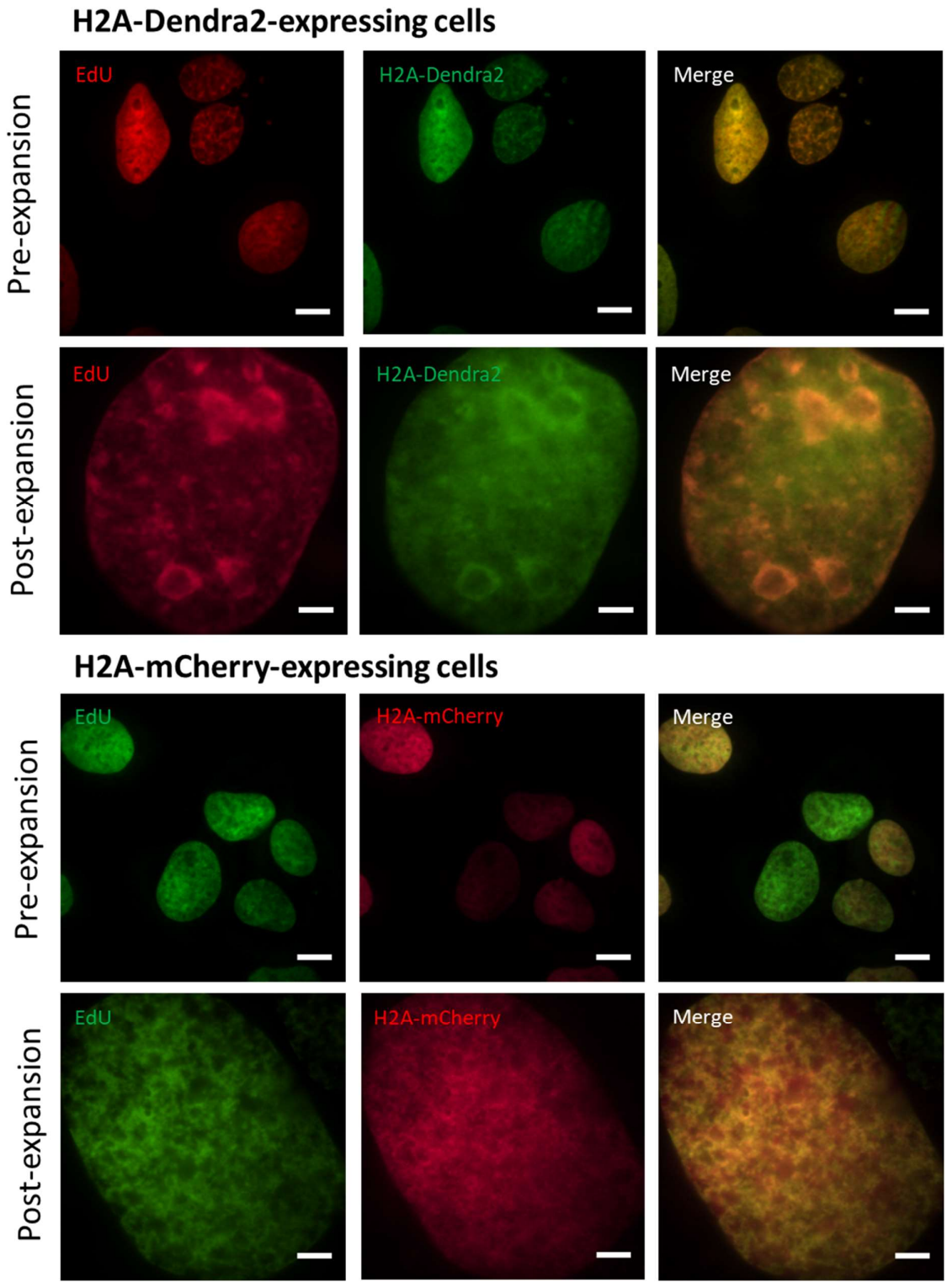
H2A-Dendra2-expressing cells
Pre-expansion
EdU
H2A-Dendra2
Merge
Post-expansion
EdU
H2A-Dendra2
Merge
H2A-mCherry-expressing cells
Pre-expansion
EdU
H2A-mCherry
Merge
Post-expansion
EdU
H2A-mCherry
Merge

Figure 3.19. Visualisation of chromatin and DNA. U2OS Flp-In cell lines were induced with doxycycline to express H2A-mCherry or H2A-dendra2 for 48 hours, and stained with EdU overnight and fixed. Click it reaction was performed for the detection of EdU (described in Section 2.4.8). Images were acquired pre- and post-expansion for each cell line on a widefield microscope. Representative 2D images are shown. Scale bars 10 μm.

To quantify the retention of colocalisation between chromatin and DNA, U2OS cells were induced to express either H2A-mCherry or H2A-Dendra2 and stained with EdU overnight prior to fixation. Images of >100 nuclei were taken pre- and post-expansion for each cell line. To measure colocalisation, we calculated Pearson's correlation coefficient (PCC) between EdU (DNA) and H2A-FP (chromatin) pre- and post-ExM. PCC is advantaged in its simplicity; it measures pixel-by-pixel covariance in the signal of two images. It subtracts the mean intensity from each image, removing the effects of signal levels and background. PCC values range from 1, where two fluorescent intensities are completely linearly correlated with each other, to -1, where two fluorescent intensities are completely inversely correlated with one another. Localisation of molecules of interest is a crucial consideration in application of PCC. It is ideal that the two exist in the same compartment of the cell such that a linear relationship describes their position. We predicted that the localisation of DNA and chromatin could be described linearly (Dunn *et al*, 2011).

PCC can be applied to whole images, but it is ideal to measure this value for individual cells or regions of interest. This is because PCC values can be artificially reduced due to effects of heterogeneous expression or uptake of target molecules, meaning that the degree of correlation is under-represented. Further, it is possible for signal emanating from background pixels to artificially inflate PCC values as these pixels may contain signals which are significantly below the average (Dunn *et al*, 2011). To avoid these effects, we segmented the nuclear areas from the background pixels by using Ilatsik software to classify pixels on a training data set. This allowed clear separation of signal regions from background. A workflow in KNIME was developed to complete the calculations (Figure 3.20) (described in Section 2.7.3).

Figure 3.20. Calculation of Pearson's correlation coefficient. The process to determine PCC values is shown. Pre- and post-expansion images are loaded in and split into their respective channels. Nuclear areas are segmented based on pixel classification defined in Ilastik software meaning that PCC values were determined for the nuclei, not the background pixels. Post-expansion images were scaled down such that they are relative to the pre-expansion data. PCC was calculated via a matlab script. Subsequently the PCC values per image were written into a CSV and plotted.

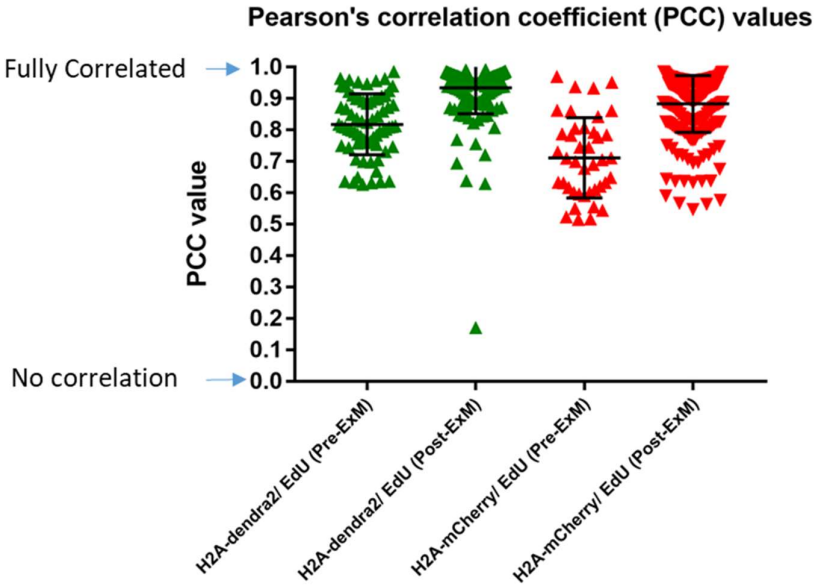

Figure 3.21. Pearson's correlation coefficient values assessing retention of H2A distribution pre- and post-expansion. U2OS Flp-In cell lines expressing H2A-mCherry or H2A-dendra2 were induced with doxycycline, stained with EdU overnight and fixed. Click it reaction was performed for detection of EdU. Images of 100+ nuclei were taken pre- and post-expansion per condition (n=3, >100 nuclei per sample). PCC values were determined using the approach outlined in Figure 3.20.

PCC values indicate good linear correlation between H2A-FPs and EdU in cells expressing H2A-mCherry and H2A-Dendra2 pre- and post-expansion (Figure 3.21). PCC values determined for post-expansion images are higher than for pre-expansion data. Overall, this suggests that our chosen

markers of chromatin (H2A-FPs) represent the native chromatin following ExM procedure, as it still correlates with nuclear DNA which is unaffected during ExM procedure (Section 3.2.5).

3.3.3 Visualising chromatin in 3D

Chromatin has a complex, heterogeneous 3D structure. To investigate if the relationship between DNA and chromatin is retained in 3D we visualised these features using two approaches: widefield Z stacks and deconvolution (Figure 3.22), and SPIM (Figure 3.24 & 3.25). In both the deconvolved widefield images and SPIM images, the complex topology of the DNA and chromatin is visible in nuclei following ExM preparation. In the deconvolved Z stacks we visualised colocalisation between the DNA and chromatin as in the 2D image data.

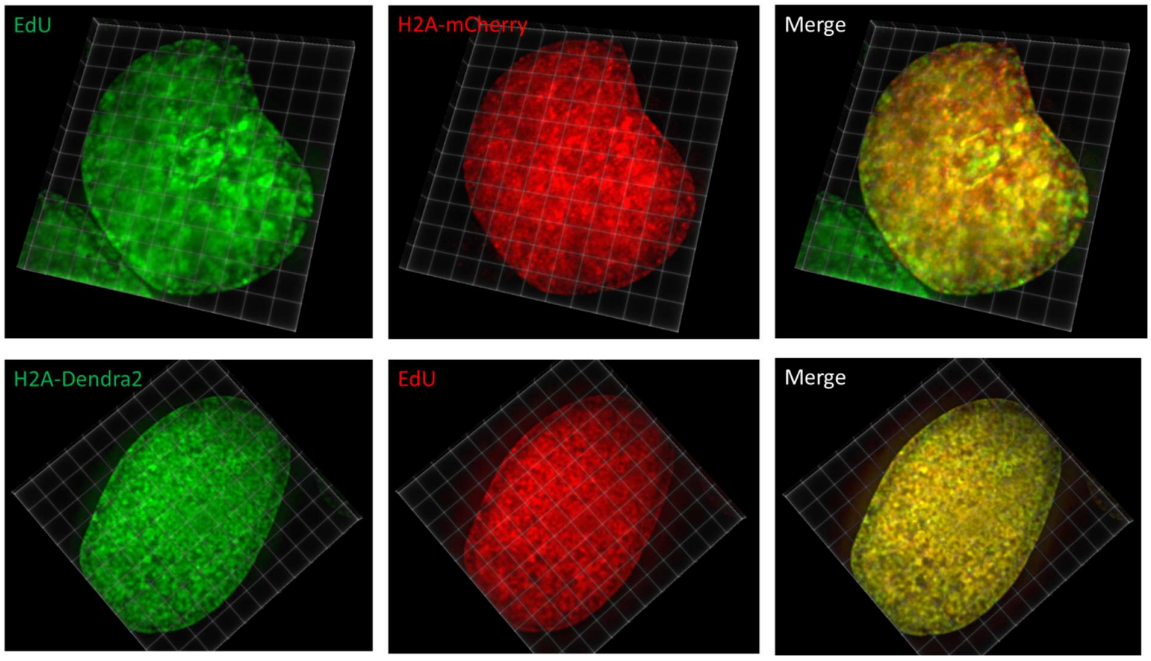

Figure 3.22. Visualising nuclear architecture in 3D. U2OS Flp-In cell lines were induced with doxycycline to express H2A-mCherry or H2A-dendra2 for 48 hours, and stained with EdU overnight and fixed. Click it reaction was performed for EdU detection and images were acquired post-expansion for each cell line on a widefield microscope. Images were deconvolved. Representative 3D acquisitions reconstructed and visualised in Clear Volume are shown.

In the multicolour SPIM acquisitions, the channels were not correctly aligned. This misalignment can be corrected by registration of the two channels. This is challenging as registration requires

presence of enough similar features to allow faithful registration. Although similar, chromatin and DNA cannot be assumed to have the same features occupying the same regions precisely.

To rectify this, we opted to use fiducial markers. These markers are spatially fixed landmarks in a sample, or the embedding medium which allow for drift correction (Balinovic *et al*, 2019) and registration of images (Preibisch *et al*, 2010). Examples include gold nanoparticles and fluorescent beads. For registration, we used Tetraspeck beads, which are impregnated with four fluorescent dyes with well separated excitation and emission peaks, meaning they are clearly visualised in the 405, 488, 561 and 640 channels. Tetraspeck beads are commonly used in calibration of microscopes and in drift correction, but can also serve as a reference for overlaying different spectral channels (Balinovic *et al*, 2019).

When applying Tetraspeck beads as fiducial markers in ExM, there are some key considerations: 1) beads must be immobilised in the sample; 2) beads should be monodispersed not aggregated; 3) 4-10 markers are required for optimum registration (Balinovic *et al*, 2019). We hypothesised that the small size of the meshwork in the ExM gel would be sufficient to encapsulate and immobilise the Tetraspeck beads. Beads were sonicated prior to addition to gels to ensure no aggregates were present as these have different photo-physical properties to singular beads which makes them difficult to use in registration. Beads were added to the monomer solution prior to gelation to ensure they would be dispersed in the ExM gel. We carried out imaging of gels containing Tetraspeck beads only to determine optimal bead concentration (Figure 3.23).

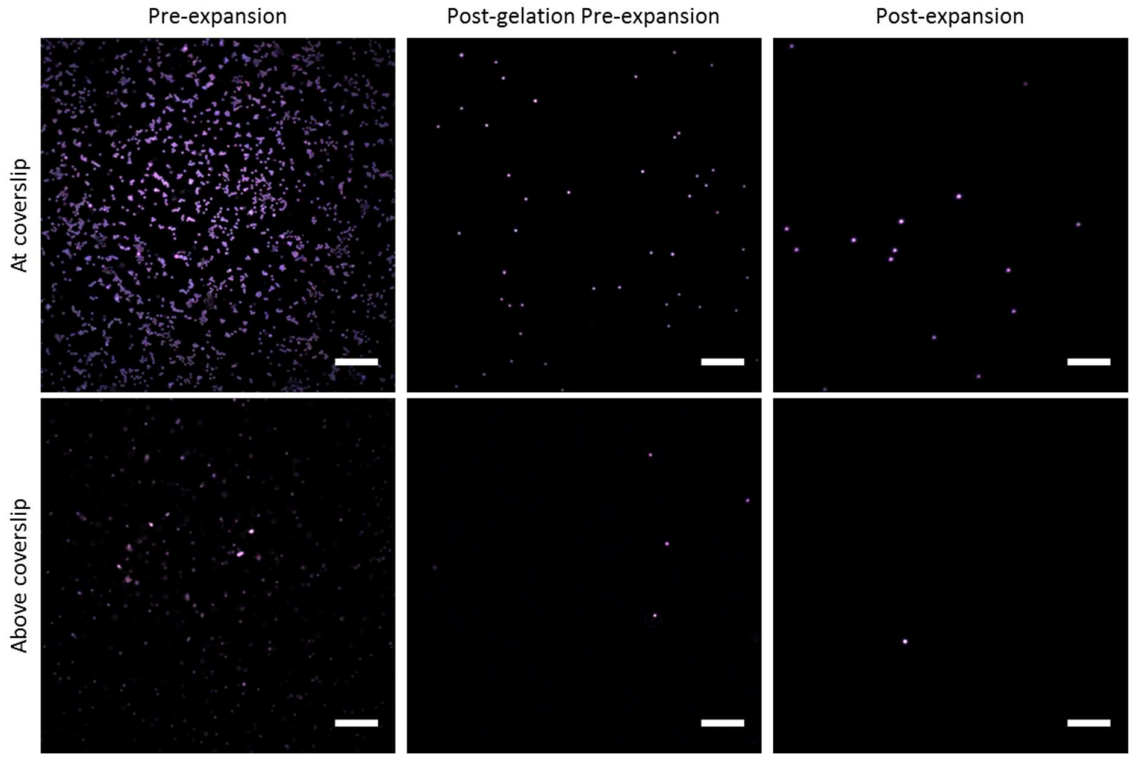

Figure 3.23. Tetraspeck bead testing. Tetraspeck beads were visualised at 3 stages: Pre-expansion, post-gelation pre-expansion and post-expansion. For pre-expansion images, 10 µl of the bead solution was dropped onto a coverslip and allowed to dry then mounted for visualisation. For post-gelation, pre-expansion imaging, 10 µl of the bead solution was dropped into the chamber well and ExM gelation solution was added and allowed to polymerise for 2 hours at 37 degrees as normal. These samples were expanded following imaging and are then the post-expansion sample set. Scale bars 10 µm.

Pre-expansion samples showed beads were very concentrated closer to the coverslip with a reduction in their density above the coverslip. A similar distribution was observed post-gelation pre-expansion, although less densely than the previous as beads have been diluted 10-fold by the addition of the monomer solution. Post-expansion beads had a good distribution at the focal plane where samples should be, with a less dense distribution deeper in the gel. For this to be useful in registration, we require a high enough concentration of beads at the focal plane in the ExM gel, ideally a few beads per three dimensional acquisition. This was achieved here, so we next applied this in ExM gels with cells embedded.

Tetraspeck beads as fiducial markers for bead-based registration of SPIM stacks was initially tested with 500 nm beads. However, it was found that the fluorescence signal from these beads was very bright compared to the fluorescence signal derived from the sample (Figure 3.21) meaning stacks of the beads and the structures of interest could not be obtained during the same acquisition since the beads would saturate, or conversely the signal from the sample would not be visible. The low signal levels from the sample was most significant in trying to visualise H2A-mCherry and H2A-dendra2. For this reason, we opted to attempt using beads of a smaller size in the hopes that these would exhibit a fluorescence profile compatible with the signal in the samples and could therefore be measured during the same acquisition (Figure 3.24).

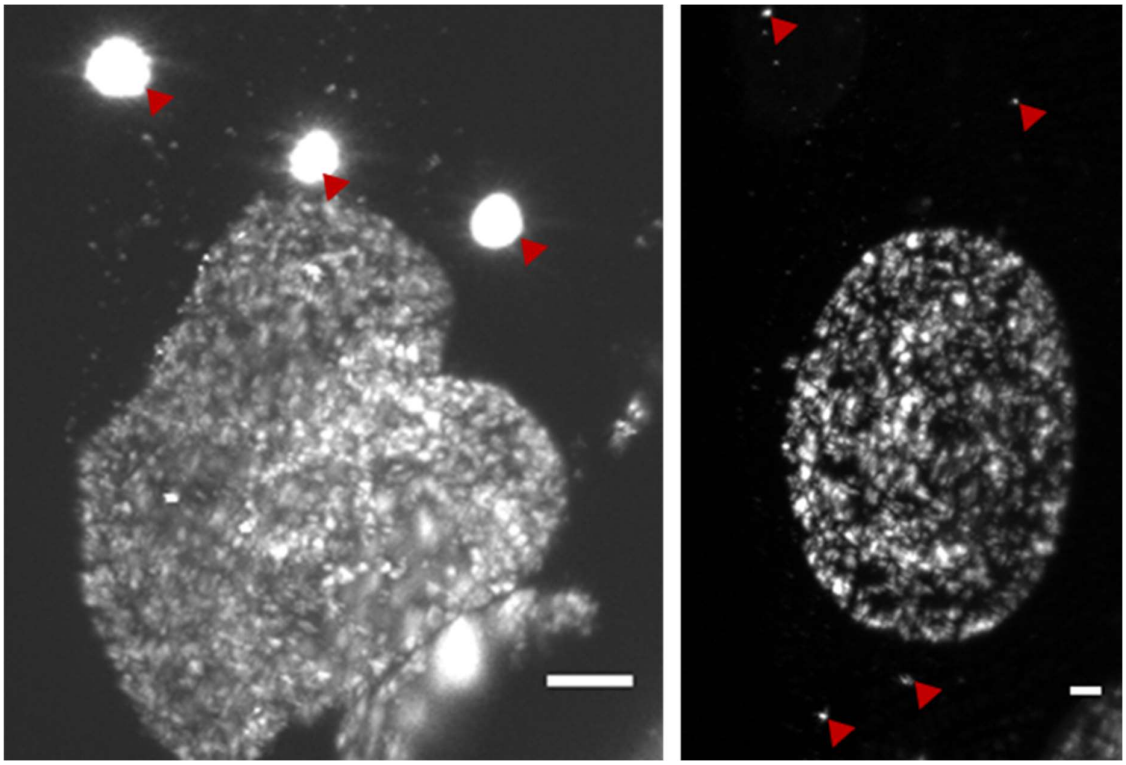

Figure 3.24. Tetraspeck beads as fiducial markers. U2OS cells were seeded and grown overnight. Cells were treated with EdU for 1 hour, followed by pre-extraction and fixation. Click it reaction was performed for EdU detection. Initial attempts utilise 500 nm beads (left) and later 100 nm beads (right) indicated by the red arrows. Scale bars 10 µm.

The smaller tetraspeck beads had compatible fluorescence profile for registration of SPIM acquisitions. Registration of SPIM acquisitions was performed using multi-view reconstruction

(described in Section 2.7.4) (Figure 3.25). Briefly, I used a translation and rotation invariant local geometric descriptor. This works by identifying the each bead in the sample as constellations relative to neighbouring beads. Z series are matched by rotation and translation to accurately match these constellations in three dimensions.

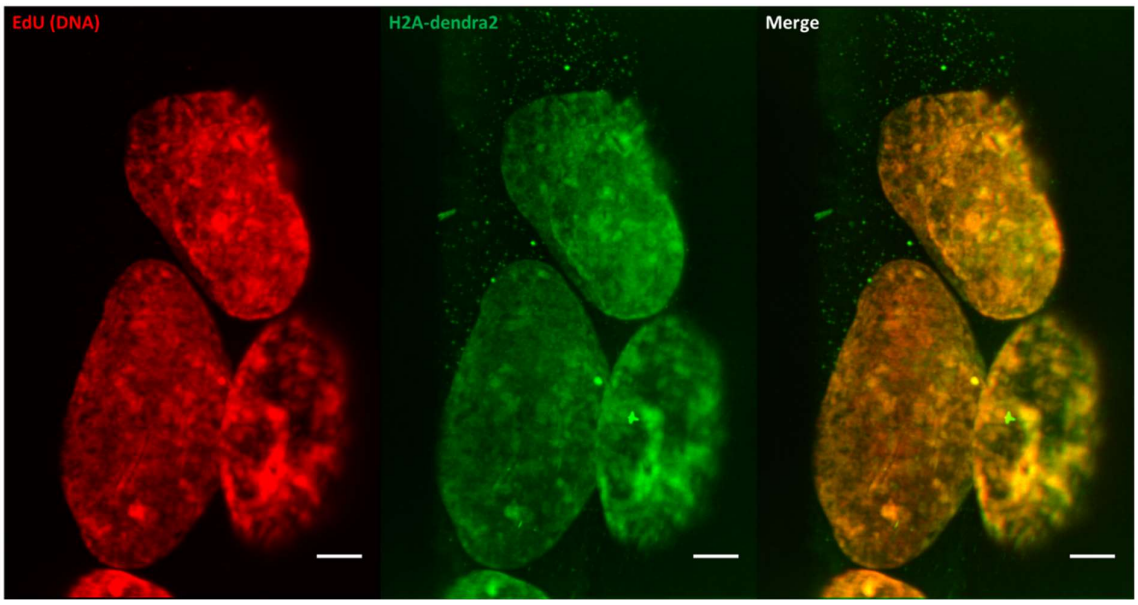

Figure 3.25. Post-expansion SPIM images of DNA and Chromatin. Cells were treated as in Figure 3.22. Z series were acquired on a SPIM post-expansion. Multi-view reconstruction plugin in ImageJ was used to register the channels in the image. An example stack which has been registered is shown as maximum projections. Scale bars 50 µm.

3.3.4 Quantification of retention of chromatin marker following ExM in 3D

To quantify retention of the marker of chromatin in 3D, we quantified PCC values for 3D datasets acquired by widefield and deconvolution, and by SPIM (described in Section 2.7.3). Notably the PCC value determined for H2A-dendra2-expressing cells is higher than in those expressing H2A-mCherry. This may be explained by differences in expression of H2A-FPs; during acquisition the expression of H2A-mCherry was observed to be more variable than in H2A-dendra2, with some cells exhibiting low expression of H2A-mCherry.

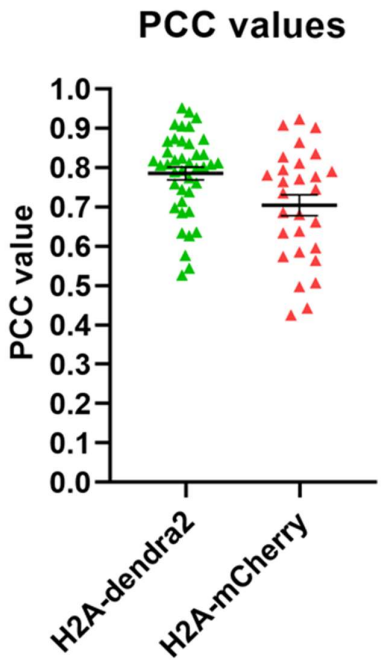

Figure 3.26. Pearson's correlation coefficient values assessing retention of H2A distribution post-expansion. U2OS Flp-In cell lines expressing H2A-mCherry or H2A-dendra2 were induced with doxycycline, stained with EdU overnight and fixed followed by staining with either AF488 or AF647 azide dye for DNA. Images of >35 nuclei were taken post-expansion on a widefield microscope or SPIM (n=2). PCC values shown are for widefield and SPIM images as acquired in Figure 3.22 and 3.25.

We have determined that H2A-FPs act as a reliable marker of chromatin during ExM. H2A-FPs are positively correlated with DNA pre- and post-expansion, in 2D and 3D. This suggests the overall nuclear architecture is retained. Additionally, this marker of chromatin can be used as a tool to interrogate chromatin architecture and dynamics during DSB repair (Chapter 5).

3.4 Discussion and Conclusions

Applications of ExM methodology have emphasised the importance of determining the isotropy of the expansion process and quantifying structural distortions induced during sample preparation. There is now a focus on validating ExM in different subcellular regions at a scale of tens of nanometres (Alon *et al*, 2018). The hypothesis is that the physical features of a compartment may impede concentration of the monomers required for the polymerisation, or these physical features

may themselves have an effect on expansion factor and isotropy. The nucleus is of particular interest due to its highly complex, compacted structure. The nucleus is not degraded during a standard ExM preparation as we apply here, meaning it is possible the nucleus may induce irregularity in the polymer matrix resulting in distortions in post-expansion images. This could therefore affect the isotropic expansion of DNA-bound complexes (Geertsema and Ewers, 2016). This prompts us to consider if the nucleus is affecting expansion, and what the effect of the expansion on the nucleus might be.

Thus far, there is a lack of consensus on how the expansion process affects the nucleus, or how to treat the nucleus during sample preparation. Expansion of the nucleus was first demonstrated in the development of ExFISH methodology in which Boyden and co-workers developed an anchoring strategy to characterise the nanoscale organisation of RNA transcripts (Chen *et al*, 2016). In this work they additionally showed that the nucleus can be expanded in the presence of the nucleic acid anchor, LabelX. There have since been other applications of ExM which investigate features of the nucleus (e.g. nuclear lamina, nuclear cytoskeleton, histones) (Tillberg *et al*, 2016, Chozinski *et al*, 2016 & Freifeld *et al*, 2017). Despite the wide application of ExM to the nucleus, there is a lack of validation of the isotropy of the expansion of the nucleus, particularly on the nanoscale. Interestingly, many of these applications do not employ the nucleic acid anchor, and it has been shown that although the nucleus can expand in the absence of anchoring, its expansion is anisotropic. Through this work, we methodically validate expansion of the nucleus in the presence of a DNA anchor.

The correlative imaging approaches classically applied to validate application of ExM do present some practical challenges. The user must identify the same feature in the same focal plane pre- and post-expansion; a challenge further complicated by the fact that ExM gels are expanded four-fold in the Z axis. 3D image acquisition is therefore required which is time consuming and induces photo-bleaching limiting photons which are present for detection post-expansion (Pesce *et al*,

2019). Due to these challenges, we initially opted to characterise the expansion of the nucleus by imaging a statistically significant number of nuclei within each dataset. This is to account for variability within and between samples derived from range of nuclear sizes and fluorescence intensity fluctuations, for example.

The isotropic expansion of the nucleus was determined by measuring areas and volumes of nuclei pre- and post-expansion. Nuclear areas increased 16x on average, and nuclear volumes increased 52x on average post-expansion, which is consistent with 3.7-4x expansion factor in 1D. The range of measurements in pre- and post-expansion samples have a similar size distribution suggesting we are accounting for variability in nuclear sizes. The macroscale expansion factor was determined by measuring the diameter of gels following expansion and was reproducibly 4x increased. This is consistent with the measures of area and volume which suggests that the physical features of the nucleus are not impeding its expansion.

Latterly, we performed a correlative imaging experiment in which nuclei were imaged post-gelation on a SIM microscope, expansion was completed and post-expansion images were acquired on a widefield microscope. Nuclei have the same morphology following expansion, suggesting no distortions are present on the microscale. The nanoscale features of nuclei were compared pre- and post-expansion revealing a similar distribution of features between the two data sets. This suggests that the nanoscale structure of the nuclei is not subject to warping during the expansion process.

Chromatin architecture and dynamics are known to play a critical role in DNA damage response (Section 1.1.4), therefore we sought to represent chromatin structure following expansion. We speculated the strong proteolytic digestion step in ExM may result in loss of histones, so we opted to generate cell lines expressing fluorescently-tagged H2A, which resists proteolysis, to represent chromatin (Tillberg *et al*, 2016). We visualised colocalisation between H2A and DNA pre- and post-expansion. PCC values were determined pre- and post-expansion on 2D and 3D datasets to quantify

correlation between DNA and H2A. PCC values indicate a strong correlation between these features, suggesting that their relationship is retained through the ExM preparation. Increased PCC values are observed for the post-expansion data sets. This is likely derived from the design of analysis; post-expansion images were scaled down in accordance with the expansion factor of the gel such that direct comparisons of "diffraction-limited" images could be made.

It has been proposed that the nuclear sub-compartment is subject to differential expansion and heterochromatin can expand up to 25% less than euchromatin (Pernal *et al*, 2020). This was determined by staining nuclei with DAPI and measuring the ratio of the area of intensely fluorescent regions of nuclei to the area of the whole nucleus. The ratio of intensely labelled regions of the nucleus was shown to be 25% less in the expanded samples compared to the pre-expansion nuclei. These observations led Pernal *et al* to suggest that areas of the nucleus with different composition expand differentially and overall nucleus expansion is anisotropic. A caveat of this work is these measurements were not performed correlatively, so may be derived from changes in cell cycle phase for example. Further, DAPI is not covalently bound to the DNA so it is possible that some of the fluorescence intensity loss is derived from a loss of DAPI and not anisotropically expanded areas of the nucleus. In this chapter, these limitations were addressed by use of EdU which is directly incorporated into DNA as it replicates, which mitigates the effects of fluorescence loss. Additionally, by performing correlative imaging we visualised a retention of DNA topology and nanostructure which suggests the expansion of the nucleus is isotropic. Pesce *et al* used nuclear pore complex (NPC), Nup153 as an intrinsic measure of the expansion process, since NPCs have well characterised and conserved molecular structure. They determined macro-, micro- and nanoscale isotropy of ExM, facilitated by combination of ExM with STED allowing resolution of 5-10 nm. They concluded that the NPC structure is well retained throughout the ExM protocol, and any distortions were due to heterogeneous labelling of features. Further, it was suggested that ExM is a suitable protocol for the investigation of nuclear proteins and large distortions are not expected, but validation should be carried out on features such as DNA and chromatin (Pesce *et al*,

2019). Interestingly, the authors did report lower intra-nuclear expansion factor of NPCs, which has since been speculated to be due to residual integrity of the genomic DNA (Tillberg and Chen, 2019). We do not observe any alterations in intra-nuclear expansion factor based on measurement of nuclear areas in the pre-expansion SIM images and the post-expansion widefield images; the average expansion of nuclei was observed to be 3x. As the gels were partially expanded during pre-expansion image acquisition this measurement is consistent with a 4x expansion of the nuclei. Interestingly, the inter-nuclear expansion measurements are smaller than the intra-nuclear expansion measurements; a phenomenon which may be explained by observations of Martinez *et al*; in their work they show that areas of the hydrogel containing cells expand more than areas containing no cellular components (Martinez *et al*, 2020).

In this chapter, I have demonstrated isotropic expansion of DNA and a marker of chromatin with minimal distortion of micro- and nanoscale structure following four-fold expansion of specimens in the presence of the nucleic acid anchor, LabelX. Our hypothesis is that the dense polymer network formed throughout the cells may be able to intercalate through the nucleus, meaning the nuclear compartment would be embedded in and expand with the gel. The strong proteolytic treatment applied to homogenise the sample may be sufficient to digest the histones which the DNA is compacted around, meaning the DNA may be able to unwind as the gel expands. This may explain why the nucleus can expand in the gel, but naturally raises questions about nanoscale alterations to the nuclear architecture. Through correlative imaging of nuclei, I demonstrate that the distortions induced in the nuclear architecture by expansion are minimal. By applying LabelX in our protocol, we may control the expansion of the nucleus such that it is robust and isotropic.

4. Visualising the nanoscale organisation of 53BP1 and BRCA1 repair foci in three-dimensions (3D)

4.1 Introduction

DSBs are highly toxic types of DNA damage as their inaccurate repair can result in mutations and chromosomal translocations (Misteli and Soutoglou, 2009). These events have been associated with human diseases including cancer and immunodeficiencies (Matt and Hoffman, 2016). DSBs can be repaired by several mechanisms. The choice of repair pathway is critical to maximally preserving genomic integrity, and is tightly regulated to ensure the correct mechanism of repair occurs in the appropriate cellular context (Densham and Morris, 2019). Repair pathway choice is controlled by numerous factors including: 1) kinetics of repair; 2) cell cycle position; 3) extent of resection; 4) chromatin environment (Sections 1.1.2-1.1.4). Recent application of fluorescence microscopy to investigate the structure of repair foci has led to the hypothesis that spatial organisation of repair factors is also a determinant and possible indicator of repair pathway choice and progression (Section 1.4.1-1.4.2).

Upon induction of DSBs, repair factors are redistributed in a highly ordered fashion. These rearrangements are visualised as nuclear aggregates known as "foci". When visualised on conventional diffraction-limited microscopes, these accumulations appear as relatively homogeneous spherical structures. Confocal microscopy revealed that repair proteins accumulate in a cell cycle-dependent manner; chromatin-bound components (e.g. 53BP1) accumulate at sites of damage throughout the cell cycle, whilst ssDNA-bound components (e.g. BRCA1, RAD51) are restricted to S-phase (Bekker-Jensen *et al*, 2006). Further, it was shown that repair foci possess an internal structure, with ssDNA-bound components occupying the core of decorated chromatin. Due to the diffraction limit, it was not possible to perform detailed colocalisation or exclusion analysis on the observed structures (Reindl *et al*, 2015).

This limitation has been addressed by application of super resolution techniques SIM and STED microscopy (detailed descriptions in Sections 1.4.1). These studies revealed that the spatial organisation of repair proteins in foci determines repair pathway progression (Chapman *et al*, 2012 and Reindl *et al*, 2015). Chapman *et al* revealed that BRCA1 drives exclusion of 53BP1 to periphery of repair foci during HR initiation; this represents the temporal switch of repair pathway choice. 53BP1 was shown to be retained at sites of damage when ssDNA has been coated by RAD51 (Reindl *et al*, 2015). RAD51 was shown to be encapsulated by 53BP1 oligomers in a similar way to BRCA1. It has also been shown that accumulations of proteins and their relative spatial organisation alters as a function of recovery time (Schwarz *et al,* 2019). These findings have prompted the concept of a spatial map of repair proteins; temporal and spatial redistribution of repair factors may be predictive of involvement or exclusion from functions during DSB repair.

SIM and STED microscopy are commonly applied techniques when investigating DDR. SIM is an attractive technique due to its simplicity to implement; no complex sample preparation is required, volumetric and live imaging are possible, and minimal constraints on fluorophore choice means multi-colour applications can be achieved (Heintzmann and Huser, 2017 & Schermelleh, 2019). STED microscopy is advantaged in resolving capability, with reported resolutions of 30-80 nm laterally (Vicidomini *et al*, 2018). Despite their capabilities, both of these approaches have caveats. SIM requires sophisticated computational image reconstruction, which can induce artefacts in the image. STED has stringent dye requirements meaning multi-colour applications are challenging, and photo-bleaching is a challenge due to the high intensity power required by the STED beam. A key limitation we address herein, is the compromise between resolution and throughput; the current view of DSB repair derived from fluorescence microscopy studies is based on measurements of hundreds of structures at a lower resolution (e.g. SIM) (Chapman *et al*, 2012), or of tens of structures at a higher resolution (e.g. STED) (Reindl *et al*, 2017 & Schwarz *et al*, 2019).

ExM offers advantages which we sought to exploit to provide improved insight into DSB repair: 1) images can be acquired rapidly on a conventional diffraction-limited system with a four-fold increase in lateral and axial resolution (equivalent to 70 nm lateral and 200 nm axial resolution); 2) ExM prepared samples are optically clear so greater imaging volumes and depths are easily accessible (Wassie *et al*, 2019). We hypothesised that this resolving power would allow clear delineation of boundaries between repair proteins at sites of damage, and that an ability to rapidly image samples in 3D with nanoscale resolution would allow characterisation of hundreds of features. This approach has the potential to corroborate a spatial map of repair factors during DSB repair.

The focus of this chapter is characterising the spatial organisation of 53BP1 and BRCA1 in S-phase nuclei. These are known pivotal regulators in repair pathway choice, promoting NHEJ and HR, respectively (Chapman, Taylor and Boulton, 2012). Their spatial organisation has been characterised via other super resolution techniques, which makes these suitable candidates for validation of ExM protocol in visualising the nanoscale organisation of repair foci. In this chapter, we confirm that known distributions of 53BP1 and BRCA1 foci numbers can be reproduced pre- and post-expansion. The increased resolution of ExM reveals novel nanoscale information in repair foci, and that spatial organisation of accumulations is heterogeneous. The heterogeneity of repair structures is quantitatively described by use of spot detection-based analysis. The functional significance of structures is explored. Changes in structure prevalence as a function of recovery time are also investigated.

4.2 BRCA1 and 53BP1 foci distributions alter as a function of cell cycle

Chapman *et al* showed that 53BP1 and BRCA1 foci distributions alter as a function of cell cycle (Chapman *et al*, 2012). During G1, 53BP1 associates with chromatin proximal to the break and appears as dense, globular structures with very little BRCA1 occupancy. During S-phase, there is an increased occupancy of BRCA1 which drives repositioning of 53BP1 to the periphery of repair foci.

This spatial reorganisation represents the temporal switch in repair pathway choice. We aimed to recapitulate this known distribution of BRCA1 and 53BP1 foci as a function of cell cycle. To achieve this, we firstly investigated if we could discriminate between early, mid and late S-phase cells (Section 4.2.1).

4.2.1 EdU and PCNA allow discrimination between early, mid and late S-phase cells

Cell cycle position was confirmed by pulse-labelling cells with EdU and using another marker of S-phase: Proliferating cell nuclear antigen (PCNA). EdU is a thymidine analogue which is incorporated into actively replicating DNA. Distinct EdU incorporation patterns are visualised and allow discrimination of early, mid and late S-phase (Chapman *el* al, 2012, Salic and Michison, 2008 & Dimitrova and Berezney, 2002). PCNA is an auxiliary protein of DNA polymerase δ, and is associated with DNA synthesis and repair. PCNA staining results in three distinct patterns: small nuclei with diffuse distribution of fine dots, large nuclei with many distinct dots and large nuclei with few fine dots. These distinct patterns enable dissection of early, mid and late S-phase (Beppu and Ishida, 1994). This distinction has been further characterised (Leonhardt *et al*, 2000). DNA replication factories were characterised in living cells by use of GFP-PCNA. Replication foci change in pattern in a coordinated, but asynchronous manner throughout S-phase. The distribution and size of replication foci during S-phase were described. During early S-phase, many small foci are formed throughout the nucleus with the exception of the nucleoli. Mid S-phase foci are characteristically clustered around the nucleoli and the nuclear periphery. Late S-phase replication foci were seen to decrease in number, but their size was larger. The schematic of this pattern is illustrated (Figure 4.1).

To allow accurate discrimination between early, mid and late S-phase these known patterns of EdU incorporation and PCNA staining were reproduced. To do this, U2OS cells were seeded and grown overnight. Cells were treated with EdU for 5 minutes or 1 hour prior to fixation and immunostaining for PCNA (Appendix Figure A2, Figure 4.2).

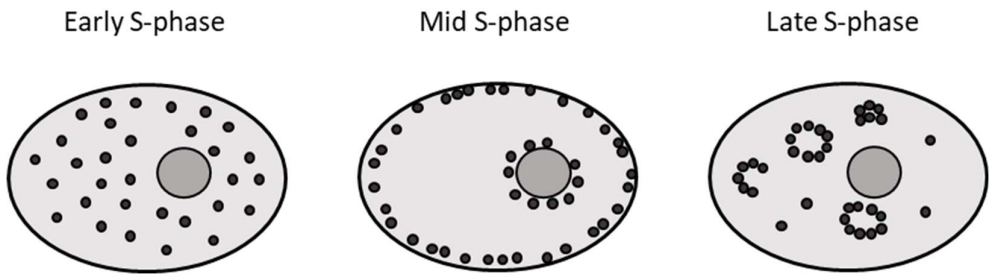

Figure 4.1. Schematic of changes in distribution of replication foci during the cell cycle. Typical patterns of replication factories of early, mid and late S-phase are shown. This was determined by monitoring cells stably transfected with GFP-PCNA over 3 days. This distribution was determined by monitoring a cell in early S-phase, and watching the progression from fine foci (Early S-phase) to perinucleolar foci (Mid S-phase) and finally characteristic late S-phase pattern with few but larger foci (Adapted from Leonhardt *et al*, 2000).

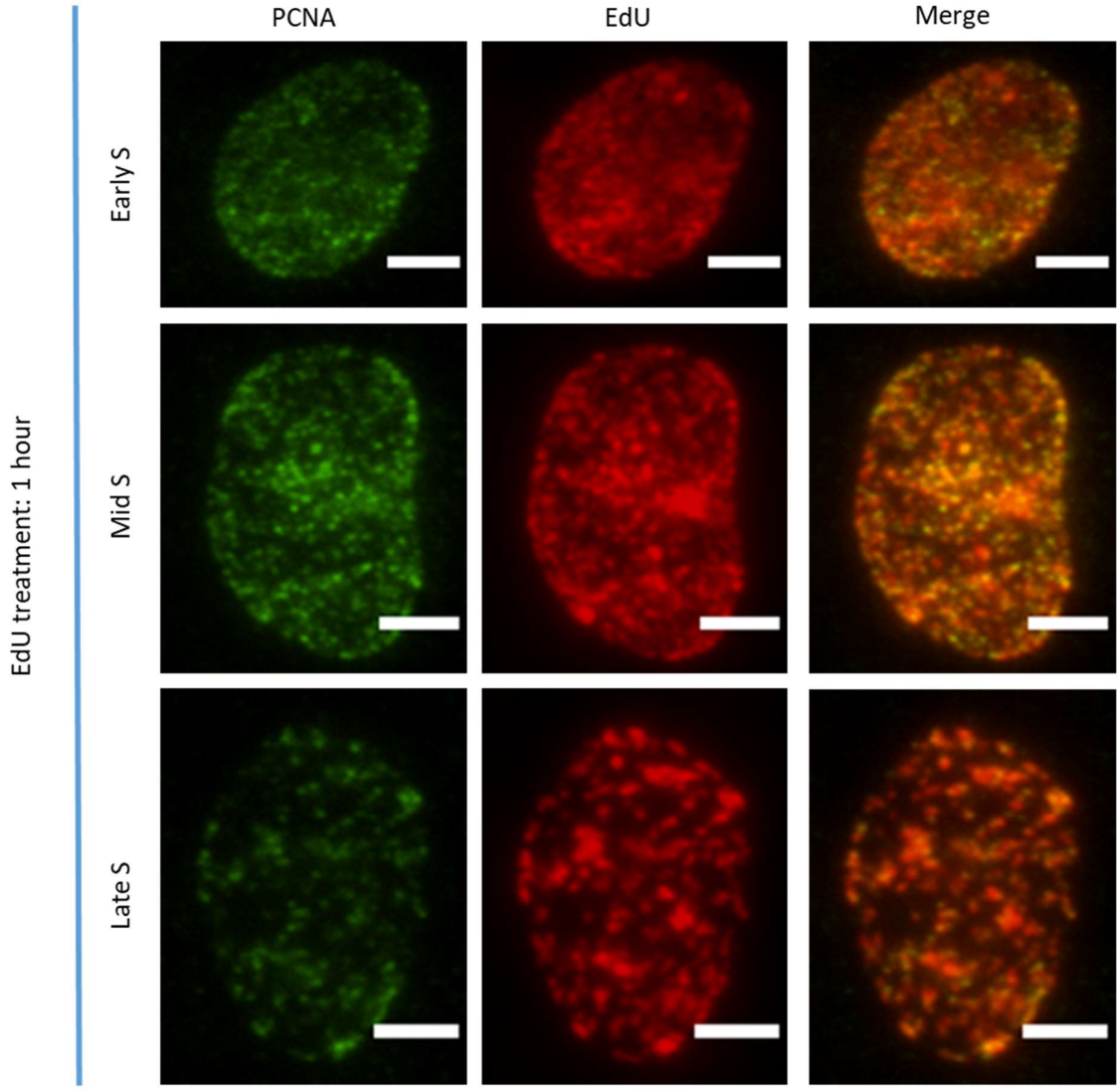

Figure 4.2. **EdU and PCNA staining patterns allow discrimination of early, mid and late S-phase.** U2OS cells were treated with EdU for 1 hour prior to washing with CSK buffer, permeabilisation with Triton-X and fixation with methanol. Click-it reaction was performed for detection of EdU. Cells were immunostained for PCNA and images were acquired on a widefield microscope. Scale 5 μm.

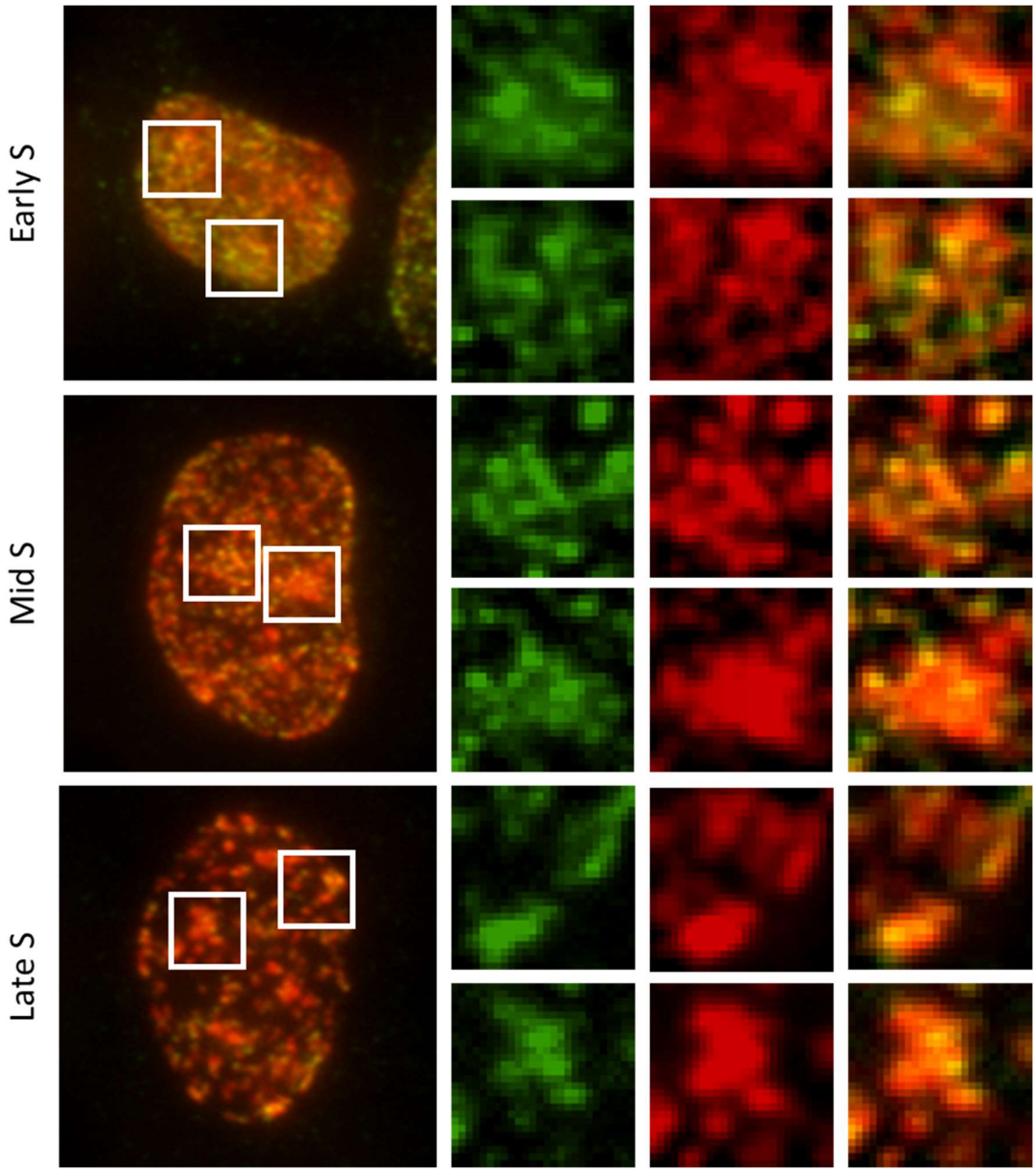

Figure 4.3. Confirming colocalisation between PCNA and EdU staining. Examples of nuclei from cells treated as in Figure 4.2 were selected based on incorporation of EdU and staining pattern of PCNA. In each selected example, zoomed in sections are highlighted.

In cells stained with EdU and immunostained for PCNA, characteristic patterns of nuclei in early, mid and late S-phase could be clearly identified (Figure 4.2, Appendix Figures A3-A5). A high degree of colocalisation was observed between PCNA staining and EdU incorporation (Figure 4.3, Appendix Figure A6), which is to be expected as EdU is incorporated into actively replicating DNA and PCNA

is a component of replication machinery. This data shows that cell cycle phase can be discriminated by observing known patterns of EdU incorporation and PCNA staining. We opted to use the 1 hour treatment of EdU in subsequent experiments as the increased incorporation of EdU made discrimination between early, mid and late S-phase more accurate.

4.2.2 53BP1 and BRCA1 foci distributions are recapitulated following ExM

Distributions of BRCA1 and 53BP1 foci were then investigated as a function of cell cycle using EdU as a marker of cell cycle. Cells were treated with EdU prior to damage induction by irradiation. Cells were allowed 1 hour to recover prior to fixation and staining. Click-it reaction was performed for EdU detection, and cells were immunostained for 53BP1 and BRCA1. Images were acquired on a widefield microscope and nuclei were grouped according to their cell cycle phase indicated by patterns of EdU incorporation (Figure 4.4) and numbers of foci were quantified (Figure 4.6).

Distributions of BRCA1 and 53BP1 foci were also investigated post-expansion for comparison with pre-expansion images, to determine their retention following ExM preparation. U2OS cells were treated as for pre-expansion samples (Figure 4.4). ExM protocol was completed and post-expansion Z stacks were acquired. Z series were organised according to cell cycle phase determined by EdU incorporation as with pre-expansion images (Figure 4.5). Foci numbers were quantified post-expansion (Figure 4.6). In expanded samples, colocalisation is no longer observed between 53BP1 and BRCA1. For direct comparison of quantification of colocalisation between 53BP1 and BRCA1 in pre-expansion specimens, in post-expansion Z series colocalisation was redefined as BRCA1 and 53BP1 structures within 1 µm of each other in any direction (x, y or z axis). These are described as proximal.

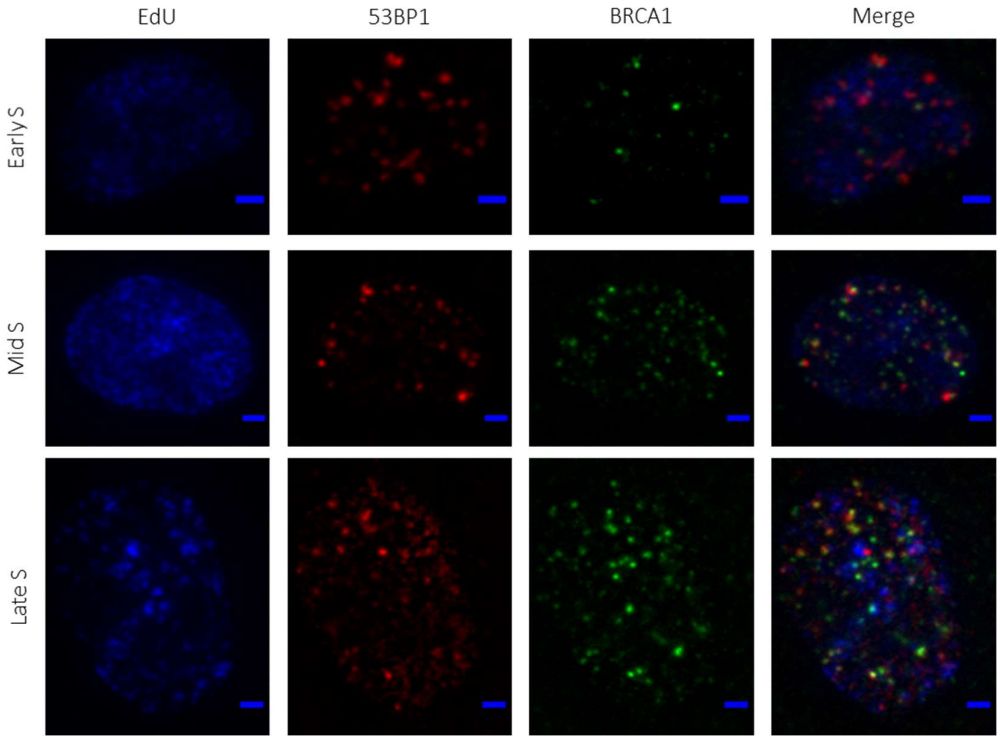

Figure 4.4. Visualising 53BP1 and BRCA1 foci as a function of cell cycle. Cells were treated with EdU prior to irradiation (2 Gy) and allowed 1 hour to recover prior to pre-extraction and fixation. Click-it reaction was performed for EdU detection and cells were immunostained for BRCA1 and 53BP1. Images were acquired on a widefield microscope. Scale bar 2.5 µm.

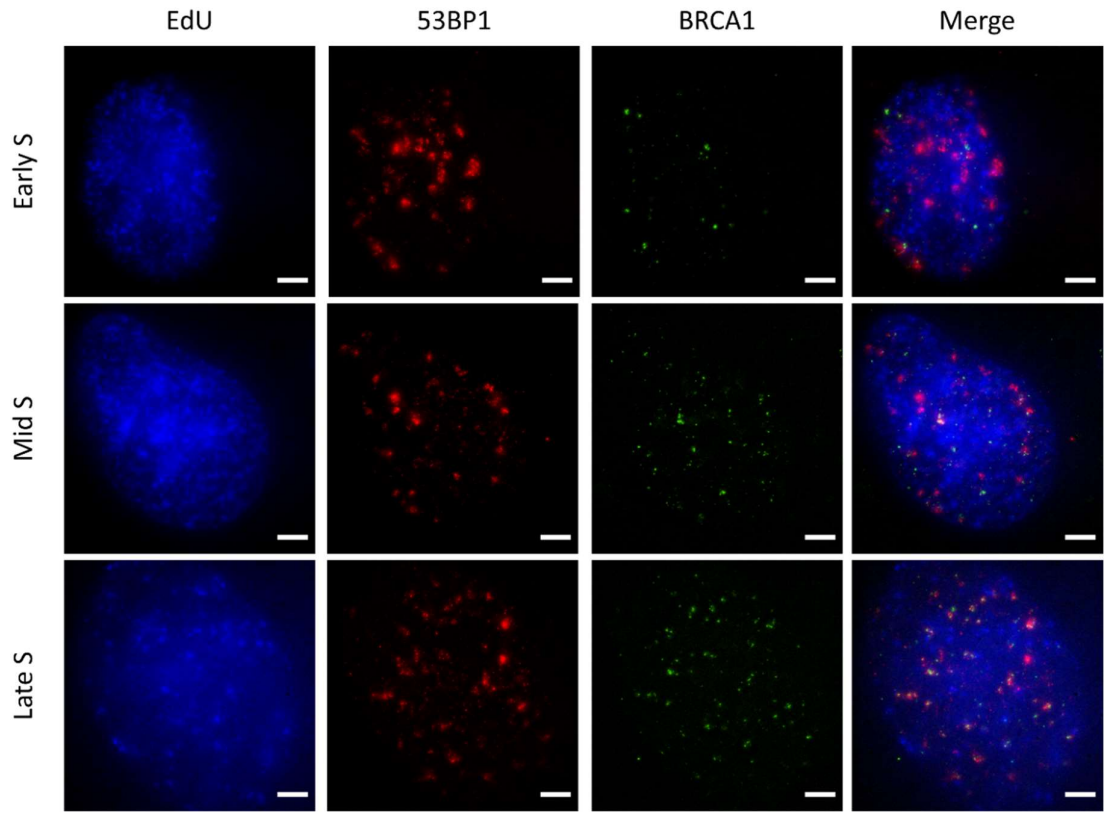

Figure 4.5. Visualising BRCA1 and 53BP1 foci post-expansion. U2OS cells were treated with EdU prior to irradiation (2 Gy) and allowed to recover for 1 hour. Cells were pre-extracted and fixed, then click-it reaction was performed for EdU detection. Cells were immunostained for BRCA1 and 53BP1. ExM protocol was performed and Z stacks acquired post-expansion on a widefield microscope. Z projections of maximum intensity are shown for nuclei classified as early, mid and late S-phase. Scale bars 10 µm.

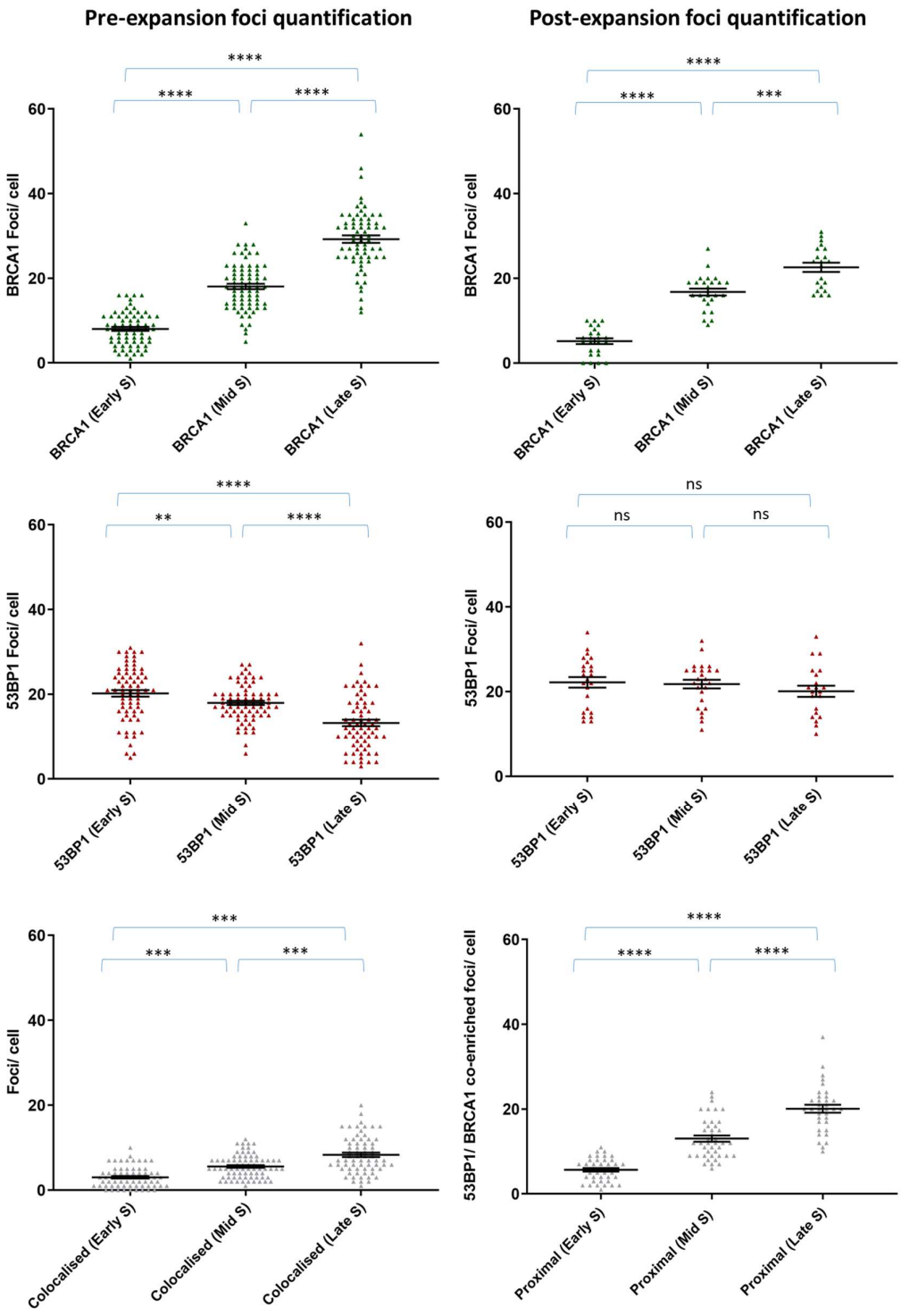
Pre-expansion foci quantification
Post-expansion foci quantification
BRCA1 Foci/ cell
53BP1 Foci/ cell
Foci/ cell
53BP1/ BRCA1 co-enriched foci/ cell
BRCA1 (Early S)
BRCA1 (Mid S)
BRCA1 (Late S)
53BP1 (Early S)
53BP1 (Mid S)
53BP1 (Late S)
Colocalised (Early S)
Colocalised (Mid S)
Colocalised (Late S)
Proximal (Early S)
Proximal (Mid S)
Proximal (Late S)
****
***
**
ns
0
20
40
60

Figure 4.6. Quantification of BRCA1 and 53BP1 foci as a function of cell cycle. Foci quantification was performed on nuclei as treated in Figure 4.4 and 4.5. Cell cycle position was determined by EdU staining and foci numbers were counted. In post-expansion Z stacks, foci numbers were counted in 3D. In pre-expansion images, colocalisation was determined by visualising overlapping pixels in foci containing both proteins. Colocalisation was not observed in expanded nuclei. Proximal structures are defined as those where 53BP1 and BRCA1 are present within 1 μm of each other in any dimension. N=3, >60 nuclei per cell cycle position pre-expansion, >30 nuclei per cell cycle position post-expansion. Throughout Figure, ***P < 0.005; *P < 0.05 NS, not significant by two-sided Student's t test.

In pre-expansion images, nuclei were categorised as early, mid and late S-phase according to EdU incorporation and foci numbers were quantified. BRCA1 foci numbers increased from early to late S-phase whilst 53BP1 foci numbers conversely decreased (Figure 4.4 & 4.6). BRCA1 and 53BP1 colocalisation increased from early to late S-phase. Similarly, post-expansion Z stacks of nuclei were organised into early, mid and late S-phase according to patterns of EdU incorporation and foci numbers were quantified (Figure 4.5). We observed a revealed a similar distribution to that of pre-expansion image data (Figure 4.6). We speculated that the decrease in 53BP1 foci from early S-phase to late S-phase in the pre-expansion images may be derived from redistribution of 53BP1 accumulations, at least in part driven by BRCA1-exclusion of 53BP1 to the periphery; since this event has been shown to reduce the volume occupied by 53BP1 it may be that some accumulations are too small to be visually defined as foci. The increase in BRCA1 may be derived from increased use of HR in mid-late S-phase cells; it is also possible that BRCA1 accumulations represent other types of damage due to the heterogeneous damage induced by irradiation (discussed in Section 1.4).

Notably, there is a decrease in numbers of 53BP1 foci in late S-phase classified nuclei pre-expansion which is not observed in the post-expansion images. Additionally, BRCA1 foci numbers are lower in post-expansion samples than in pre-expansion specimens. This may be explained by the increased axial depth of nuclei; it is possible that not all foci are accounted for in the 3D images post-expansion. Another consideration is that direct comparison between pre- and post-expansion images is challenging owed to the increased resolution in the expanded nuclei. In these experiments, I found that distributions of 53BP1 and BRCA1 in S-phase nuclei post-expansion were comparable to distributions observed pre-expansion. This suggests foci distributions are retained post-expansion.

4.2.3 Nanoscale features of repair foci are visible following ExM

Upon in depth investigation of structures in the 3D acquisitions, nanoscale structures were visible within foci. However, the 3D acquisitions were affected by optical blurring and noise which served to reduce the resolution and signal-to-noise ratio of the images. In order to remove these effects deconvolution was applied to the Z series acquired (Wallace *et al*, 2001) (described in Section 2.6). Deconvolution was performed using Huygens software. Deconvolution parameters were optimised on a test set of images, and deconvolution results were compared to raw image data to ensure preservation of nanoscale information (Figure 4.7). These deconvolution parameters were applied in all repeats.

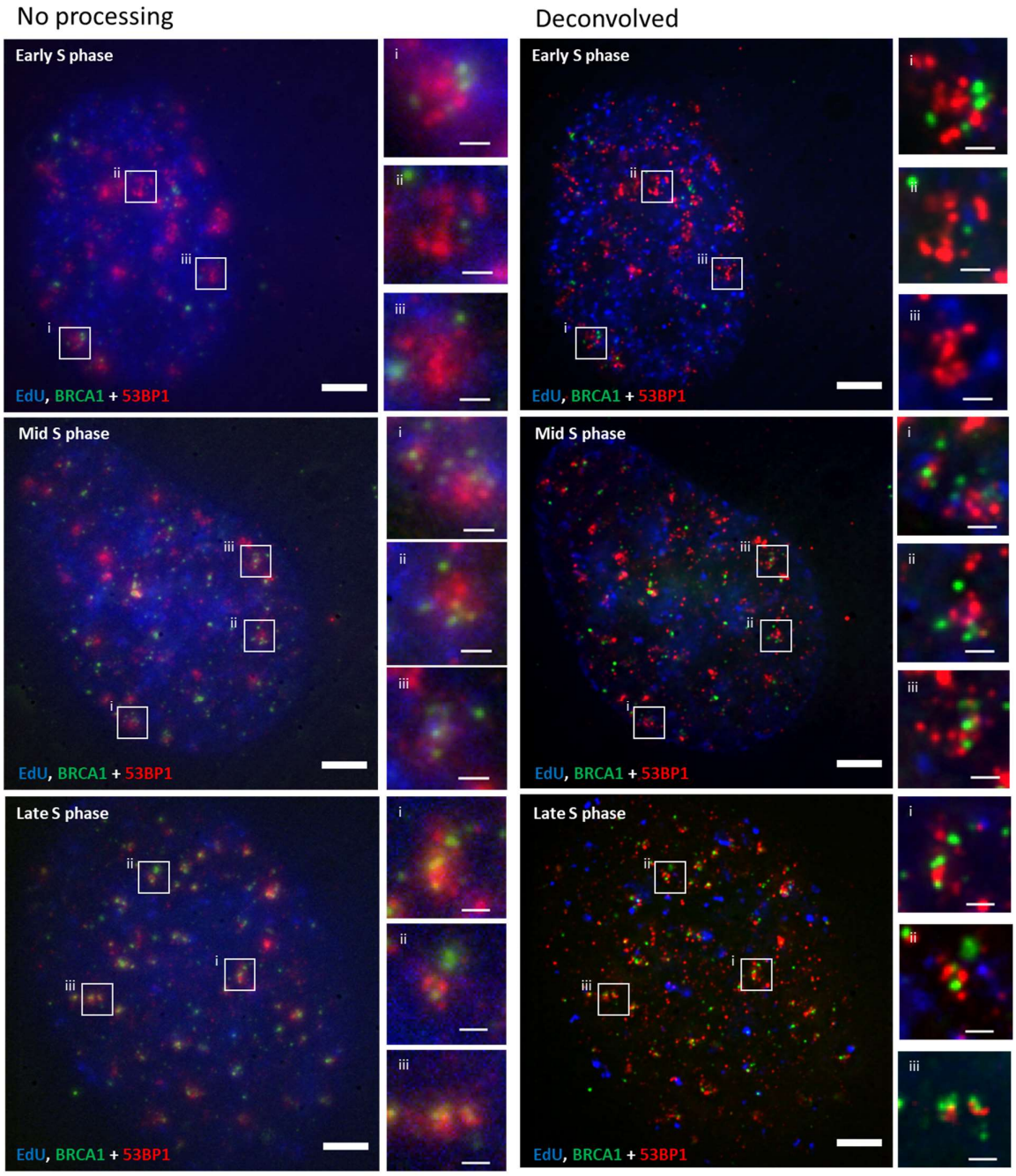

Figure 4.7. The importance of deconvolution. Examples of nuclei classified as early, mid and late S-phase treated as in Figure 4.5 were selected. Z stacks are shown as maximum projection prior to deconvolution with foci of interest highlighted (left) and following deconvolution (right). Scales bars 10 µm and 2 µm.

The deconvolution successfully removed the effects of blurring and noise to reveal a somewhat unexpected feature. 53BP1 has been described as having a continuous structure with several

maxima and minima (Chapman *et al*, 2012 & Reindl *et al*, 2015). However, the data acquired from expanded samples following deconvolution reveals a spot-like appearance of the 53BP1 (Figure 4. 7). These observations suggest that the increased resolution offered by ExM and removal of blurring by deconvolution reveals novel structure within repair foci. We further noted that not all foci were colocalised with EdU in the example images shown. This may be due to the fact that EdU is incorporated into actively replicating regions of DNA, and damage may occur in regions where active replication did not occur over the 1 hour recovery time. The association of foci with EdU is assessed in Section 4.4.1 (Figure 4.18).

4.3 Analysing nanostructure of repair foci throughout S-phase

Novel nanoscale structural information was revealed in the deconvolved post-expansion images of cells with markers of early, mid and late S-phase. In cells with markers of early S-phase, 53BP1 appeared as dense accumulations comprised of multiple 53BP1 spots, with little or no association with BRCA1. Further, 53BP1 structures were heterogeneous in their size and the number of 53BP1 spots in each region of interest (Figure 4.8). The absence of BRCA1-association suggests HR initiation is not prevalent during this phase. It is possible that the 53BP1 accumulations observed in early S-phase classified nuclei could be associated with frank DSBs which occurred during G1 and may be repaired rapidly by NHEJ (Lomax, Folkes & O'Neill, 2013 & Nickoloff *et al*, 2017).

By contrast, in cells with markers of mid and late S-phase, the majority of foci are enriched with both BRCA1 and 53BP1 (Figure 4.9). 53BP1 and BRCA1 exist in different compartments of repair foci, with BRCA1 existing centrally to 53BP1. This is consistent with the previously described exclusion of 53BP1 by BRCA1 (Chapman *et al,* 2012). However, we also noted there is heterogeneity in foci patterns observed in mid and late S-phase which have yet to be investigated. In addition to foci with a profile comparable to exclusion previously reported, we also visualised simpler foci occupying a smaller region, and more complex foci structures incorporating multiple 53BP1 and BRCA1 spots occupying larger regions (Section 4.3.1 and 4.3.2). The heterogeneity in BRCA1 and

53BP1 accumulations may be derived from heterogeneous damage induced by irradiation (Lomax, Folkes & O'Neill, 2013 & Nickoloff *et al*, 2017) (described in Section 1.4). It may be that the accumulations observed in mid-late S-phase nuclei represent different pools of lesions (e.g. clustered damage sites, collapsed replication forks) compared to those in early S-phase.

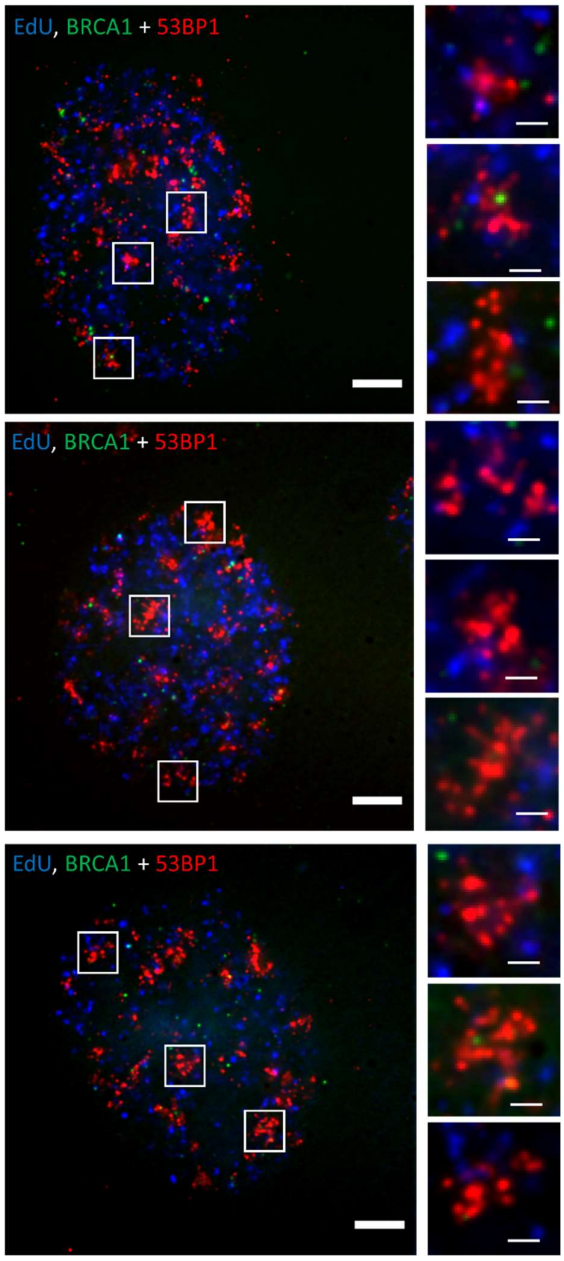

Figure 4.8. Investigating 53BP1 and BRCA1 accumulations in early S-phase nuclei. U2OS cells were treated with EdU prior to irradiation (2 Gy). Cells were allowed 1 hour to recover, pre-extracted and fixed prior to staining for EdU and immunostaining for BRCA1 and 53BP1. ExM protocol was performed and post-expansion Z stacks were acquired and deconvolved. Nuclei were organised according to markers indicative cell cycle phase and nanostructure of accumulations visually investigated. Examples of nuclei identified as early S-phase are shown. Scale bars 10 µm and 2 µm.

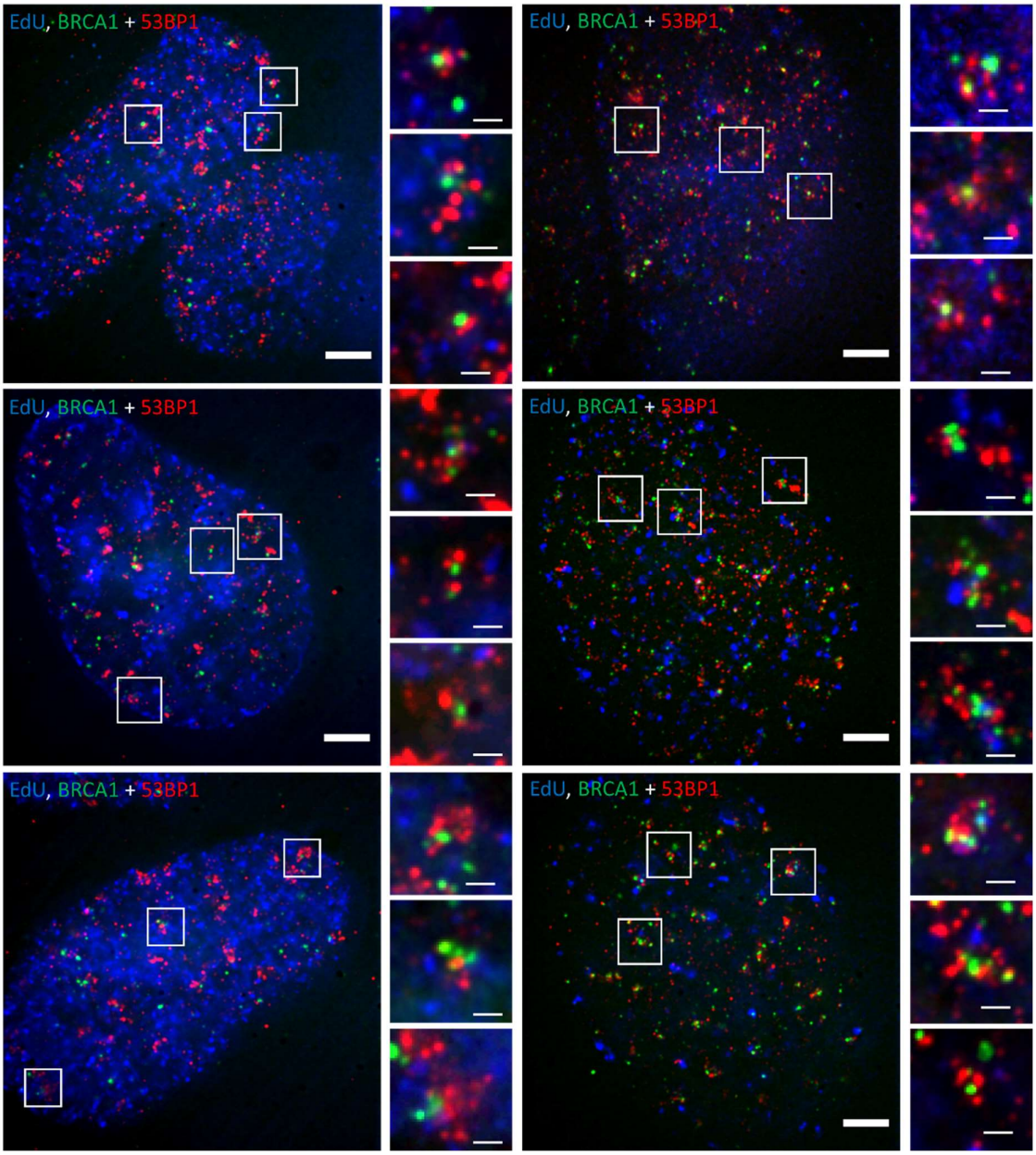

Figure 4.9. Investigating 53BP1 and BRCA1 accumulations in mid and late S-phase nuclei. U2OS cells were treated with EdU prior to irradiation (2 Gy). Cells were allowed 1 hour to recover, pre-extracted and fixed prior to staining for EdU and immunostaining for BRCA1 and 53BP1. ExM protocol was performed and post-expansion Z stacks were acquired and deconvolved. Nuclei were organised according to markers of cell cycle phase and nanostructure of accumulations visually investigated. Examples of nuclei identified as mid (left) and late S (right) phase are shown. Scale bars 10 µm and 2 µm.

4.3.1 Design of image analysis to describe foci nanostructures in S-phase

The aim of this work was to investigate the spatial organisation of repair factors in S-phase cells, with particular focus on the spatial organisation of repair factors during HR. HR has been shown to reach its peak activity in mid S-phase (Her and Bunting, 2018). In cells with markers of mid and late S-phase we observed an increase in BRCA1 foci numbers, and its association with 53BP1 as compared to early S-phase cells. This led us to focus our analysis on cells where HR activity is likely to be at its peak: mid and late S-phase. A workflow was developed to describe the structural heterogeneity of repair structures during mid and late S-phase. 53BP1 and BRCA1 are visualised as collections of spots, therefore spot detection-based analysis was used to semi-automate the characterisation the relative spatial relationship between 53BP1 and BRCA1.

As BRCA1 is reported to exclude 53BP1 to the periphery of repair foci during HR initiation (Chapman *et al*, 2012) BRCA1 spots were arbitrarily assigned as the centre of repair foci meaning that each BRCA1 spot indicates a site of interest. By assigning BRCA1 as the site channel, structures containing only 53BP1 were omitted from the analysis. The design of analysis is illustrated schematically (Figure 4.10).

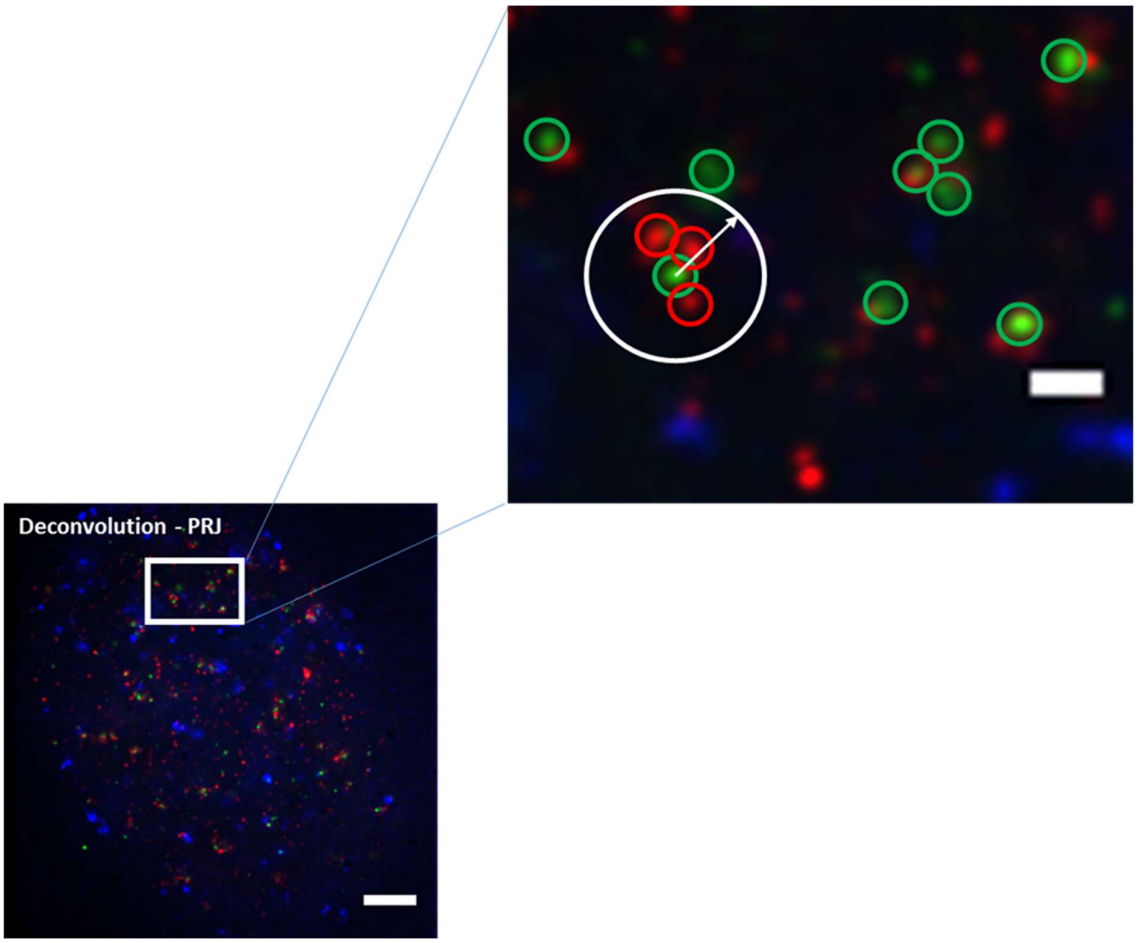

Figure 4.10. Schematic of analysis designed for mid and late S-phase nuclei. For each 3D series, spot detection was performed in the BRCA1 (green) and 53BP1 (red) channel. The number and coordinate position of spots was determined. Each central BRCA1 spot and any 53BP1 (or additional BRCA1) spots within a set radius were scored according to their relative spatial arrangement. The user manually classifies structures based on clearly described parameters. Scale bars 10 µm and 2 µm.

A script was written by Dr Jeremy Pike to allow such classification of structures (Figure 4.11) (detailed in Section 2.7.5). Acquired Z series were organised according to their cell cycle markers and placed in separate directories for analysis. The classification process involves the user manually determining parameters. The directory is the file location and file extension defines the type of file (e.g. tif). The spot radius in both channels is defined, and a quality threshold is set, ensuring only spots corresponding to foci are selected and not background fluorescence. The voxel dimensions are defined. Further, it is possible to choose the site channel, which defines the channel to be

treated as the central point of structures. For this, BRCA1 or channel 2, is the site channel. It is also possible to add a linking distance to the analysis e.g. 0.1 means if spots within the site channel are within 0.1 µm of one another, these will be grouped as one structure. This was not applied during analysis of 53BP1 and BRCA1 accumulations. The number of possible classifications is defined by the user. All scored structures can be saved as cropped images, and their position in the whole image is also stored.

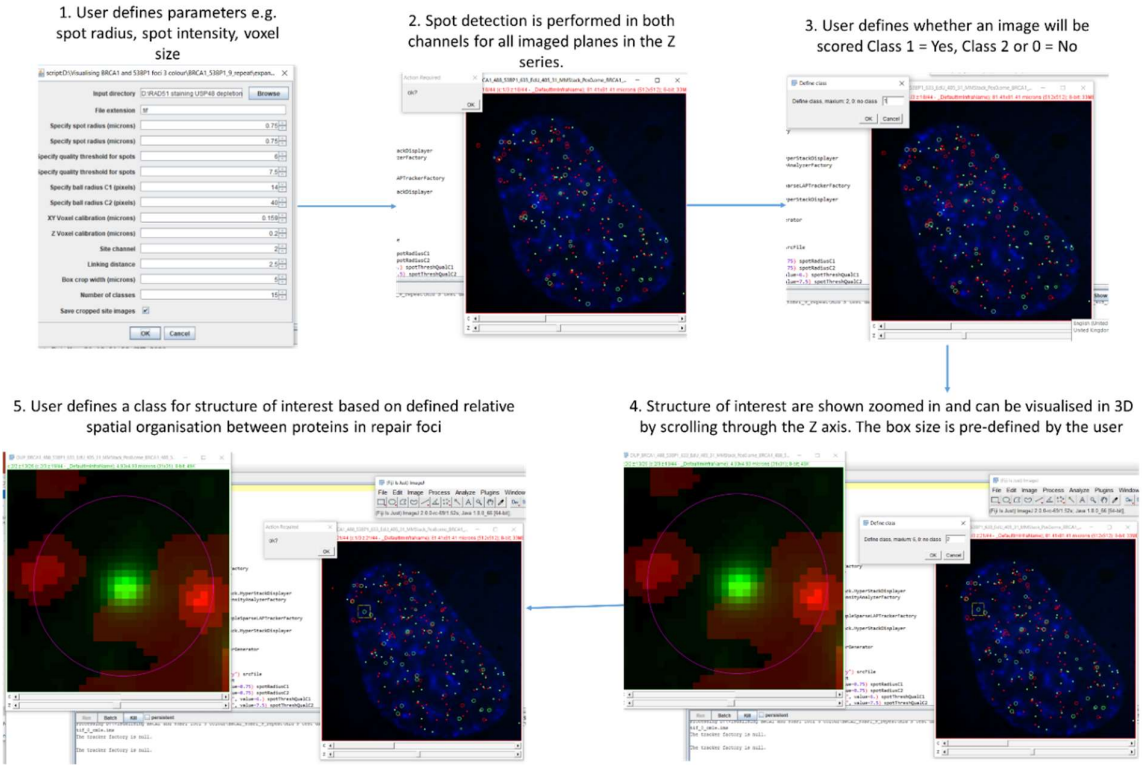

Figure 4.11. Structure classification process. Classification was semi-automated. 1) User defines parameters e.g. file locations, spot radius, pixel parameters. 2) Spot detection was completed on channel 1 and channel 2, corresponding to 53BP1 and BRCA1 respectively here. 3) The user determined if the image quality is sufficient for analysis. 4) Structures are shown zoomed in and in the context of the whole image (shown by yellow box on the main image). 5) Structures were classified based on their appearance qualitatively. For each detected spot parameters e.g. intensity, position were recorded and stored in a spreadsheet.

Following the input of user-defined parameters, the first Z series in the directory is shown (Figure 4.11, step 2). Spot detection is performed in both channels and then the script pauses for the user.

The user will be prompted to classify the Z series as being used for scoring or being skipped and the next Z series will be shown (Figure 4.11, step 3). The user may opt to skip a Z series if there is visible movement of the sample in the acquisition, or if background fluorescence is being detected by the spot detection, for example. The first structure of interest will be shown as a zoomed in section and the script will pause for the user (Figure 4.11, step 4). The user can scroll through the Z axis at this stage so classification is three-dimensional. The user will assign a class to the structure based on the spatial organisation between the visualised proteins (Figure 4.11, step 5). This analysis was designed to maximally detect heterogeneity in foci structures observed in mid and late S-phase cells.

4.3.2 Spot detection-based analysis of BRCA1 and 53BP1 in mid and late S-phase nuclei

In order to gain a view of the distributions of 53BP1 and BRCA1 in accumulations co-enriched with both proteins, spot detection-based analysis (illustrated in Figure 4.10 and Figure 4.11) was performed on Z stacks of nuclei with markers of mid and late S-phase (Figure 4.9). Five classes of structure were identified to describe the heterogeneity in relative spatial organisation of BRCA1 and 53BP1 in structures (Figure 4.12).

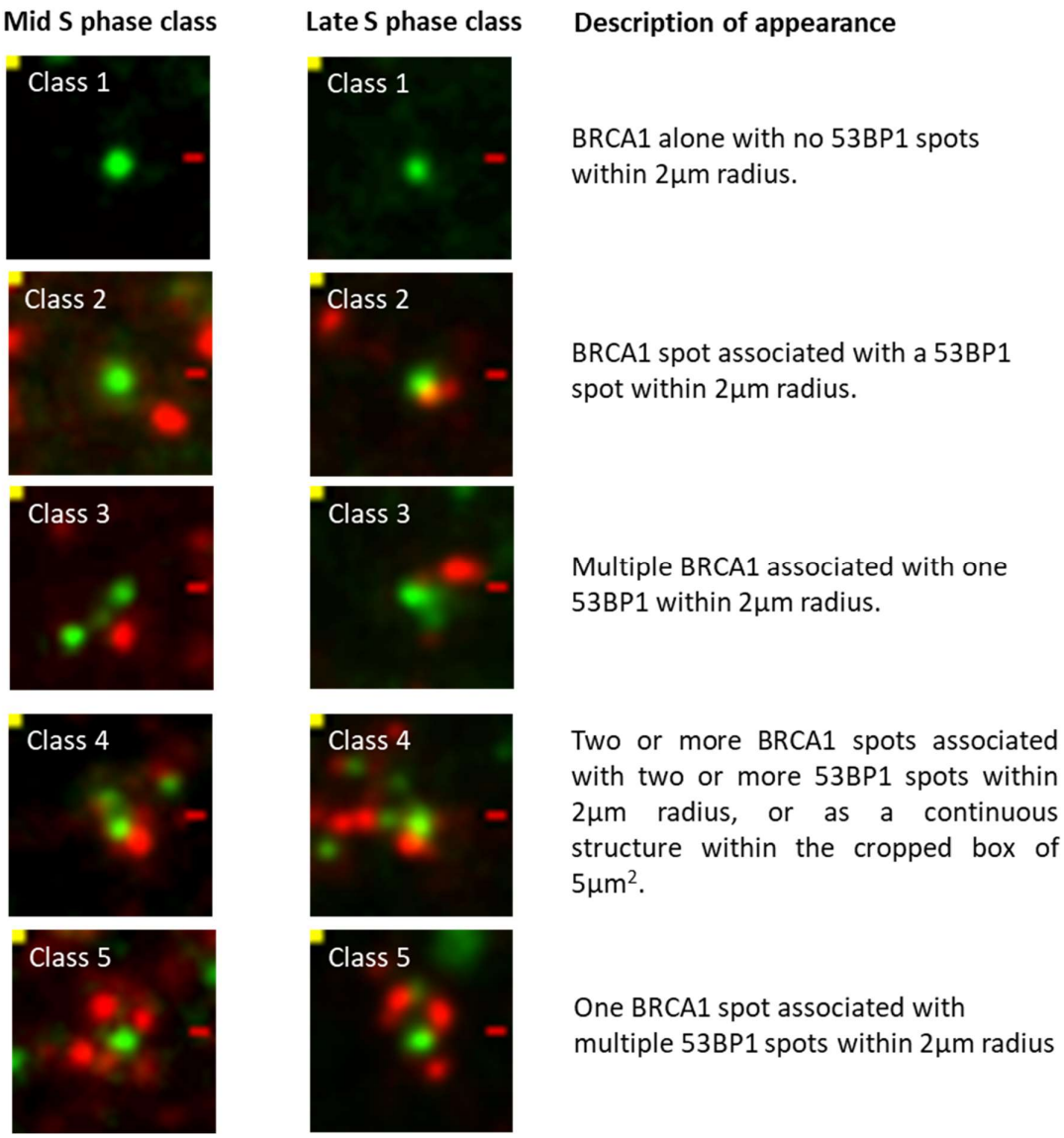

Figure 4.12. Classifying foci appearances in cells with markers of mid and late S-phase. Foci structures were classified as shown. Class 1 is defined as a BRCA1 spot with no associated 53BP1 spots within a 2 µm radius. Class 2 is defined as a BRCA1 spot associated with a 53BP1 spot within a 2 µm radius. Class 3 is defined as multiple BRCA1 spots associated with one 53BP1 spot within a 2 µm radius. Class 4 is defined as multiple BRCA1 spots associated with multiple 53BP1 spots within a 2 µm radius. Class 5 describes foci with one BRCA1 spot encapsulated by multiple 53BP1 spots within a 2 µm radius. Scale bar 0.5 µm. EdU was omitted from the representative images of foci.

Following identification of classes in mid and late S-phase nuclei, further repeats were performed in U2OS cells treated as in Figure 4.9. Structures were classified according to the classes identified

(Figure 4.12). This classification data is summarised as fractions of total detected structures in nuclei, and as absolute numbers of structures counted (Figure 4.13).

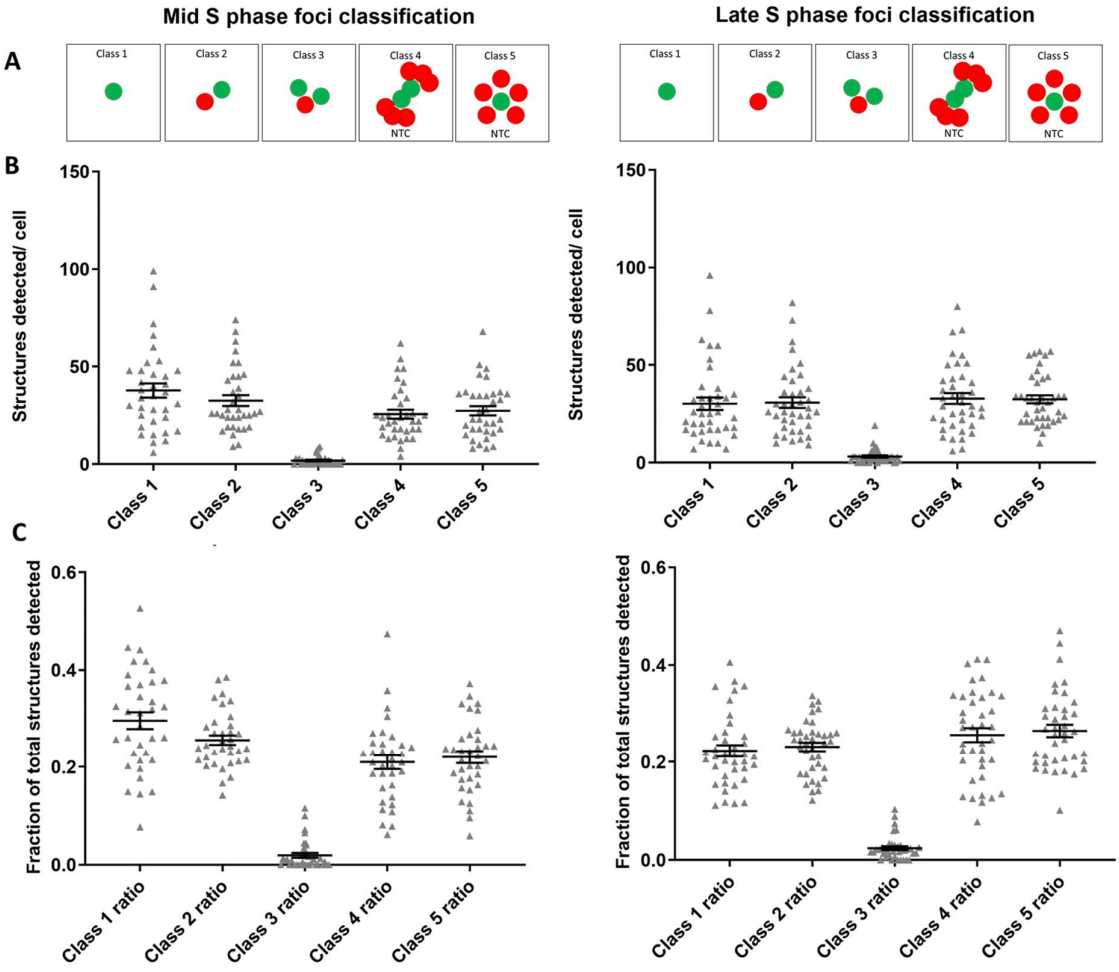

Figure 4.13. Describing repair structures as a function of cell cycle. U2OS cells were treated with EdU prior to irradiation (2 Gy) and allowed 1 hour to recover prior to CSK pre-extraction and fixation. Cells were immunostained for 53BP1 and BRCA1. ExM protocol was performed and post-ExM Z stacks were acquired. Spot detection-based analysis was applied and structures were scored for nuclei in mid and late S-phase according to the identified classes shown schematically (Panel A). Scoring is shown as a total numbers of structures detected (Panel B) and fractions of the total numbers of structures detected (Panel B). N=3, >10 nuclei per phase, per independent experiment. Error = s.e.m.

Scoring of structures in mid and late S-phase assigned nuclei showed that classes 1, 2, 4 and 5 are evenly distributed across both phases. There was no significant change in the number of class

structures detected in cells with mid and late S-phase classification. Given the low abundance of class 3 structures, it is possible these structures represent random associations of 53BP1 and BRCA1 which are in close spatial proximity and may not represent a structure associated with damage resolution. By applying ExM to visualisation of repair foci, we were able to rapidly acquired images of hundreds of features in 3D for subsequent analysis. In the analysis, five classes of repair foci were identified, some of which have not been previously described.

4.4 Investigating functional significance of foci classes

Thus far, structures visualised in mid and late S-phase nuclei have been classified into five groups (Figure 4.12) and the numbers of each structure type quantified per nucleus (Figure 4.13). Four of the five assigned classes are relatively evenly distributed in terms of absolute numbers of structures. The functional significance of each class was investigated.

4.4.1 Class 1 foci are associated with function of BRCA1 in replication

BRCA1 is known to function in response to replication stress (Feng and Jasin, 2017). To determine if class 1 structures are related to replication stress, cells were pulsed with EdU for 1 hour with no damage induction prior to fixation. Cells were then immunostained for BRCA1 and 53BP1. Pre-expansion images were acquired (Figure 4.14) and foci numbers were quantified as a function of cell cycle (Figure 4.16). ExM was performed and Z series were acquired and deconvolved (Figure 4.15). Foci numbers were quantified as a function of cell cycle post-expansion (Figure 4.16)

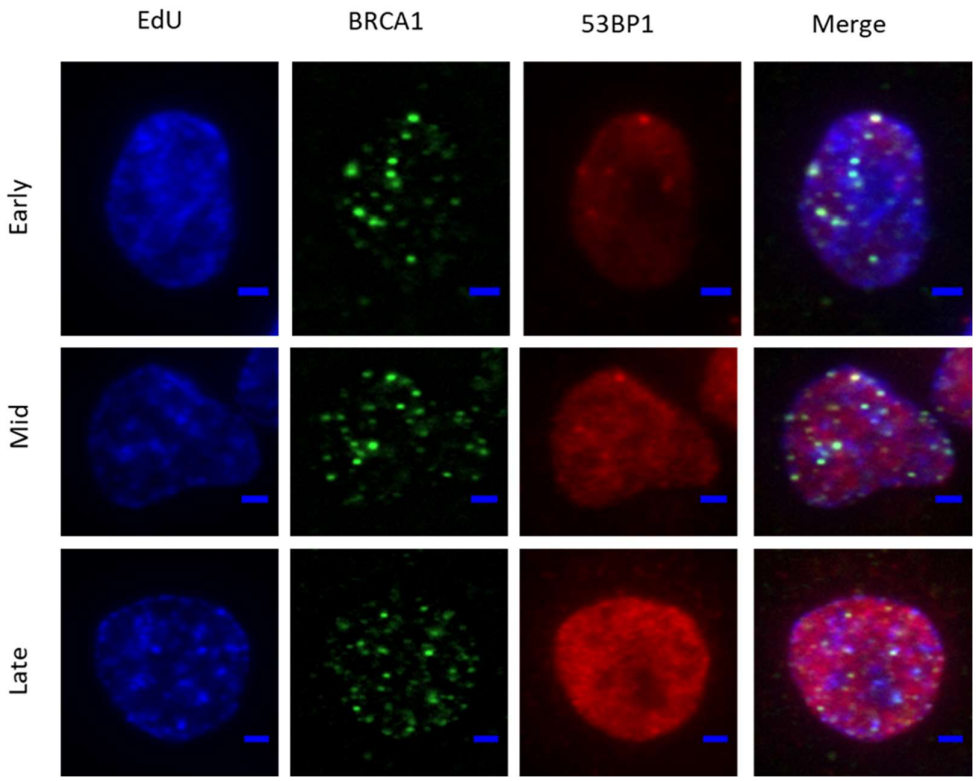

Figure 4.14. Visualising BRCA1 foci in non-irradiated U2OS cells. Cells were treated with EdU for 1 hour prior to CSK pre-extraction and fixation with 4% PFA. Click-it reaction was performed for detection of EdU and cells were immunostained for 53BP1 and BRCA1. Pre-expansion images were obtained on a widefield microscope. Representative images of nuclei with early, mid and late S-phase EdU patterns are shown. Scale bars 2.5 µm.

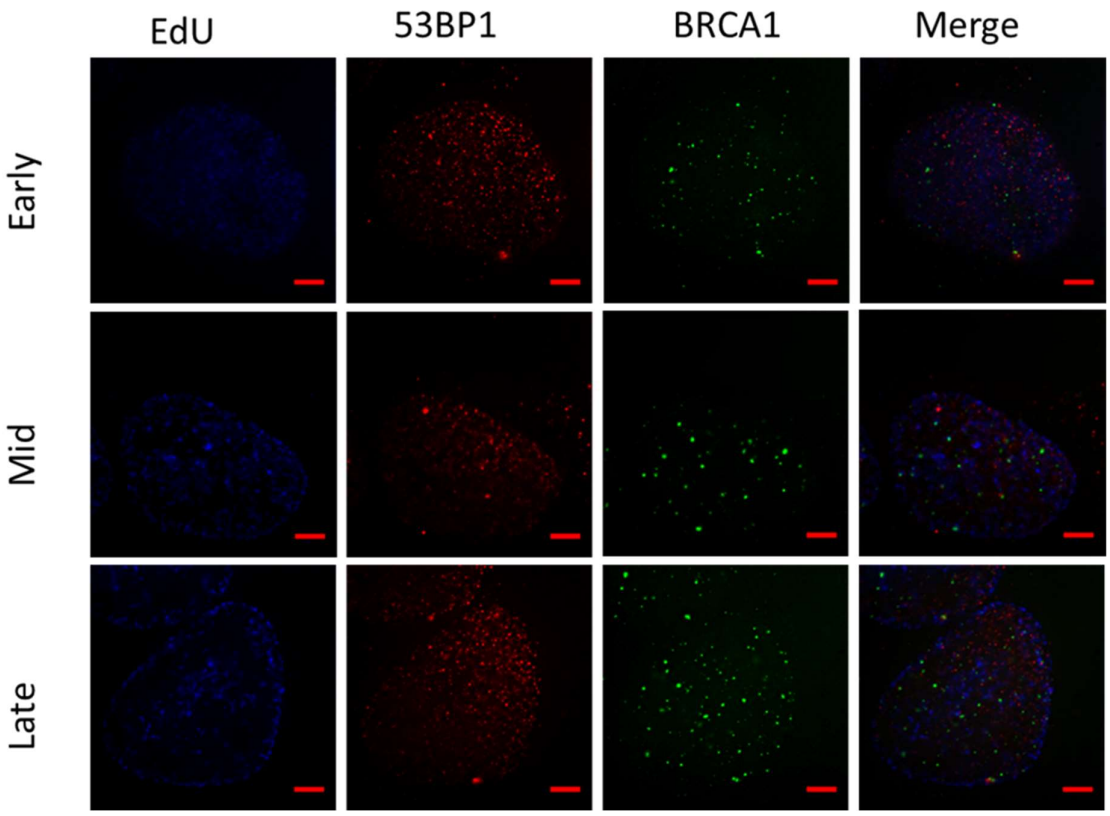

Figure 4.15. Visualising BRCA1 foci in non-irradiated U2OS cells. Cells were treated with EdU for 1 hour prior to CSK pre-extraction and fixation with 4% PFA. Click it reaction was performed for detection of EdU and cells were immunostained for 53BP1 and BRCA1. Standard ExM protocol was performed (Section 2.4). Post-expansion Z stacks were obtained on a widefield microscope. Representative images of nuclei with early, mid and late S-phase EdU patterns are shown. Scale bars 10 µm.

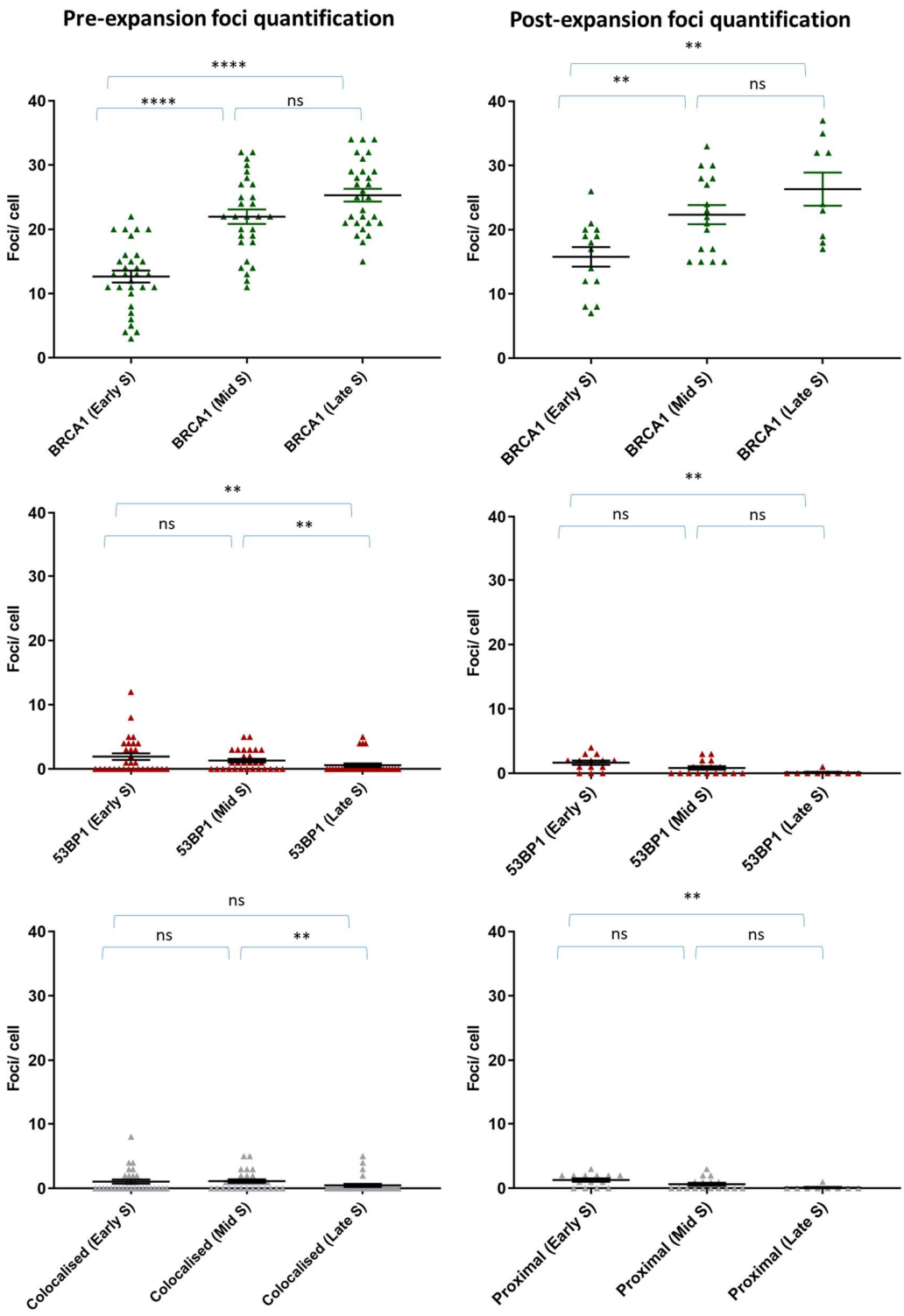
Pre-expansion foci quantification
Post-expansion foci quantification
Foci/ cell
****
ns
**
BRCA1 (Early S)
BRCA1 (Mid S)
BRCA1 (Late S)
53BP1 (Early S)
53BP1 (Mid S)
53BP1 (Late S)
Colocalised (Early S)
Colocalised (Mid S)
Colocalised (Late S)
Proximal (Early S)
Proximal (Mid S)
Proximal (Late S)

Figure 4.16. Quantification of BRCA1 and 53BP1 foci as a function of cell cycle in undamaged cells. Foci quantification was performed on nuclei as treated in Figure 4.14 and 4.15. Cell cycle position was determined by EdU staining patterns and foci numbers were counted. In post-expansion Z stacks, foci numbers were counted in 3D. Colocalisation was determined by visualising overlapping pixels in foci containing both proteins. Colocalisation was not observed in expanded nuclei. Proximal structures are defined as those where 53BP1 and BRCA1 are present within 1µm of each other in any dimension. N=1, >30 nuclei per cell cycle position pre-expansion, >10 nuclei per cell cycle position post-expansion.

In cells immunostained for BRCA1 and 53BP1 with no damage induction, BRCA1 foci were visualised throughout S-phase with numbers of foci increasing from early to late S-phase. The prevalence of 53BP1 foci is low or absent in most nuclei in S-phase. This pattern is also retained in post-expansion images.

Since class 1 structures (defined as BRCA1 with no associated 53BP1 within a 2 µm radius) were present in the absence of damage, we hypothesised these structures may be related to replication stress. This led us to look at the association of BRCA1 alone foci with EdU; we predicted a high degree of association between BRCA1 alone foci and EdU if these are related to replication. The relationship between BRCA1 and EdU was investigated using spot detection-based analysis in irradiated and non-irradiated cells for direct comparison. BRCA1 structures were defined as being EdU positive and EdU negative (Figure 4.17A).

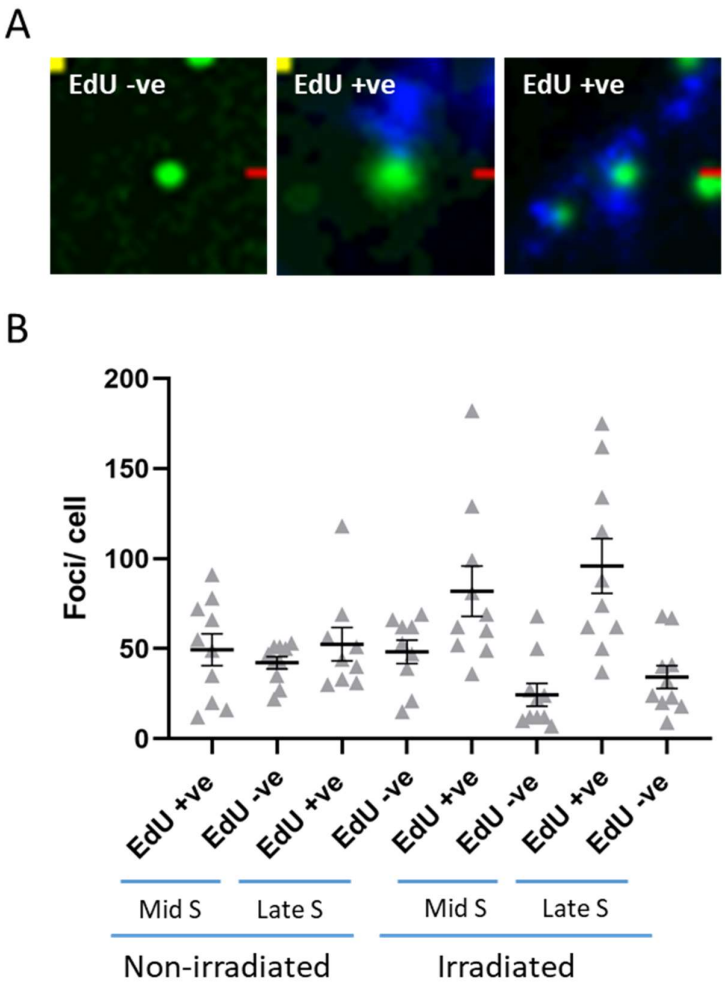

Figure 4.17. Assessing correlation between BRCA1 and EdU in irradiated and non-irradiated cells. A) Representative examples of EdU positive and EdU negative structures are shown. These classifications were used to compare EdU association of BRCA1 and EdU in irradiated and non-irradiated cells. Scale bars 0.5 µm. B) The overall numbers of BRCA1 spotswhich were positive and negative for EdU were determined for mid and late S-phase nuclei in non-irradiated and irradiated cells. Error = s.e.m.

EdU positive structures were lower in non-irradiated cells than their irradiated counterparts, whilst EdU negative structures were observed to be increased in non-irradiated cells compared to irradiated cells (Figure 4.17B). Given the higher numbers of EdU negative BRCA1 accumulations in non-irradiated cells, these data suggest the BRCA1 accumulations may not relate to endogenous replication stress. To understand the cause of this distribution, I performed further spot detection-

based analysis on the irradiated and non-irradiated data sets, taking into account association of BRCA1 with both 53BP1 and EdU (Figure 4.18). To do this, structures were defined as being class 1-5 (previously defined in Figure 4.12) and their EdU positive or negative status was accounted for additionally.

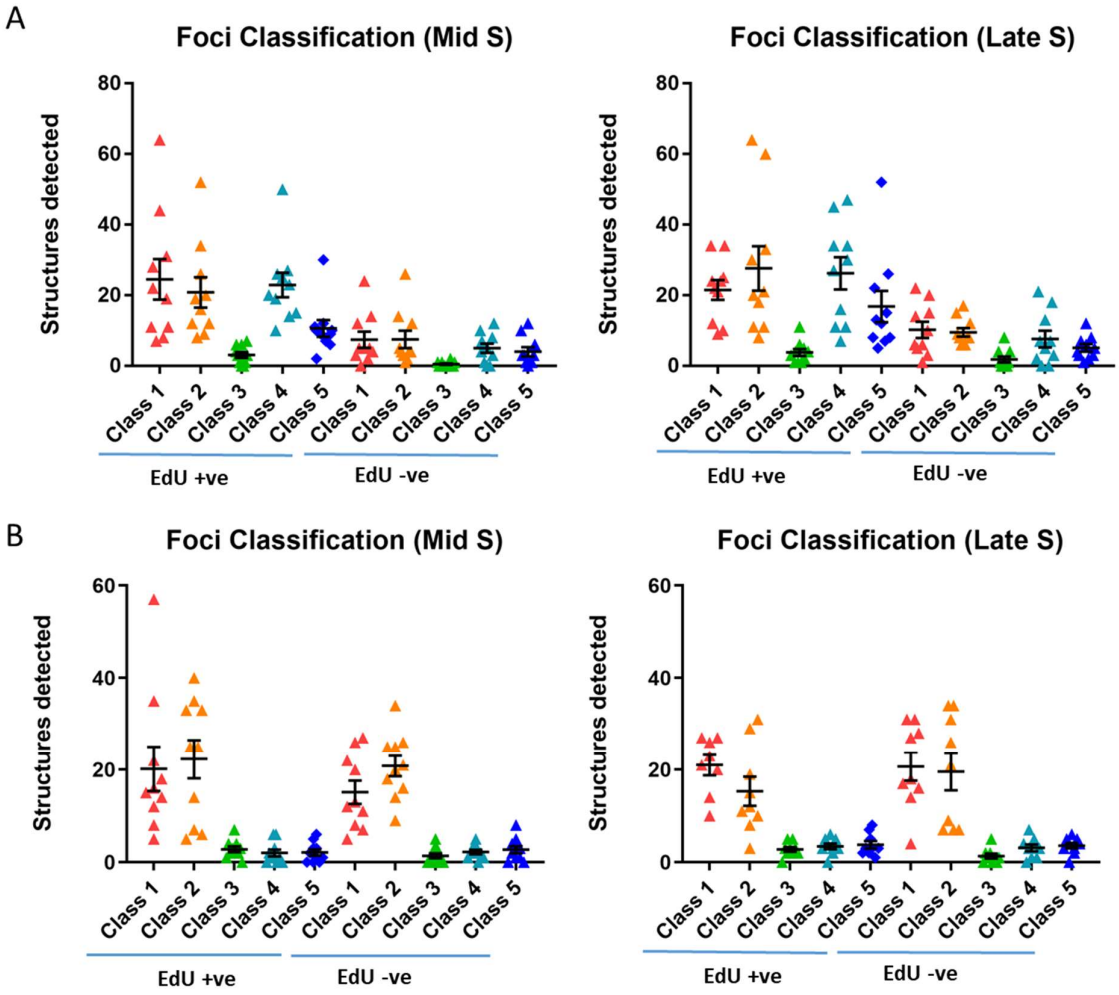

Figure 4.18. Classifying 53BP1 and BRCA1 accumulations according to EdU association in irradiated and non-irradiated cells. A) U2OS cells were treated with EdU prior to damage induction with irradiation (2 Gy) and allowed 1 hour to recover. Cells were pre-extracted and fixed, then stained for EdU and immunostained for BRCA1 and 53BP1. ExM protocol was performed and Z stacks were acquired on a widefield microscope and deconvolved. Structures were scored using spot detection-based analysis. B) U2OS cells were treated with EdU for 1 hour with no damage induction prior to pre-extraction and fixation. Cells were stained for EdU and immunostained for BRCA1 and 53BP1. ExM protocol was performed and Z stacks were acquired on a widefield microscope and deconvolved. Structures were scored using spot detection-based analysis.

In the irradiated cells (Figure 4.18A), EdU positive accumulations are higher than EdU negative accumulations in mid and late S-phase classified nuclei. By contrast, in the non-irradiated cells (Figure 4.18B), classes 1 and 2 have comparable distributions for EdU positive and negative. Classes

3-5 are low (<10) for both EdU positive and EdU negative foci in non-irradiated cells. The prevalence of EdU positive accumulations of BRCA1 and 53BP1 in irradiated cells may be explained by replication stress resulting from irradiation; the presence of clustered damage means repair is slower and increases the chance of replication fork stalling and collapse. The EdU positive class 1 and class 2 structures observed in non-irradiated cells may be indicative of endogenous replication stress. The presence of class 2 foci structures in non-irradiated cells was somewhat unexpected as 53BP1 was not observed to form foci in these cells; however, smaller accumulations of 53BP1 are seen throughout the nuclei in S-phase. These accumulations may resemble the pool of 53BP1 constitutively associated with chromatin (Panier and Boulton, 2014). These observations are based on one experimental repeat; further repeats are required to corroborate and explain these observations.

4.4.2 Class 4 foci are complex and heterogeneous

I have defined class 4 structures as those where multiple BRCA1 and 53BP1 spots are present. In this class, we observed heterogeneity in the placement of BRCA1 spots relative to 53BP1, which was described by four main subclasses (Figure 4.19). These types of structures were observed by Reindl *et al* but their functional relevance is unclear. One possibility is that these structures indicate multiple DSBs or clusters of single stranded lesions in close proximity (Reindl *et al*, 2015, Lomax, Folkes & O'Neill, 2013 & Nickoloff *et al*, 2017). Further, these could be repair factories, similar to those observed in yeast cells. Such complex organisation of BRCA1 relative to 53BP1 may also be reflective of BRCA1 complexes performing different functions during HR progression (Schwarz *et al*, 2019).

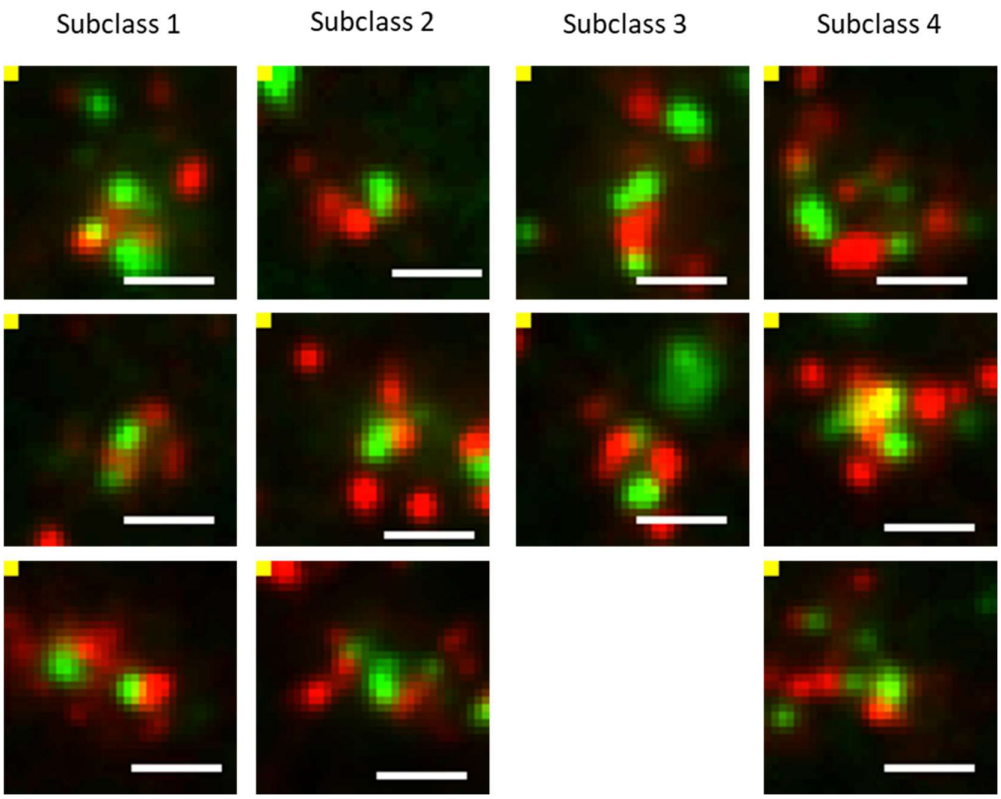

Figure 4.19. Sub-classifying class 4 structures. Class 4 structures were visually assessed and further sub-classified into four groups according to their spatial organisation relative to 53BP1. Examples were selected from late S-phase classified nuclei following irradiation (2 Gy) and 1 hour recovery. Subclass 1 describes structures in which BRCA1 is closely associated with 53BP1 external to the centre of foci. Subclass 2 describes structures where BRCA1 spots are centrally located inside 53BP1. Subclass 3 describes a combination of subclass 1 and 2 where some BRCA1 spots are centrally located and others are associated externally. Subclass 4 describes more complex accumulations where there are >3 BRCA1 spots associated with 53BP1. Scale bar 2 µm.

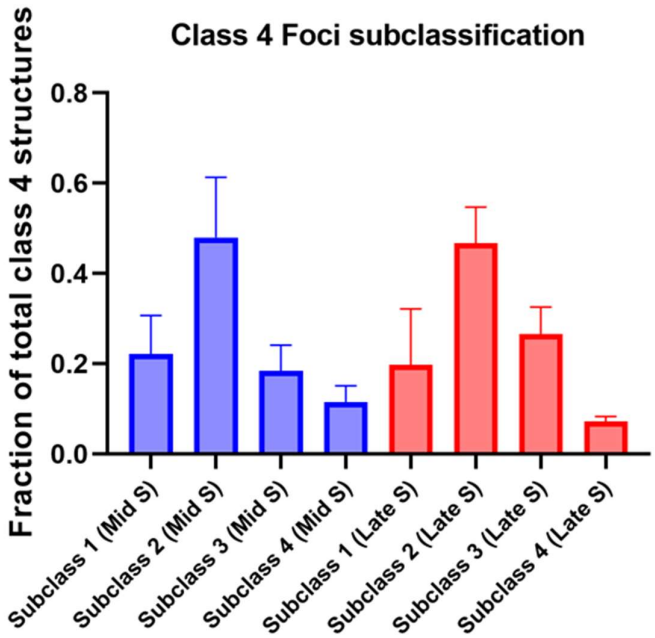

Figure 4.20. Sub-classifying class 4 structures. Class 4 structures from nuclei treated as in Figure 4.13 were sub-classified according to those identified in Figure 4.19. Sub-classes are shown as a fraction of the total number of structures in each repeat. N=3, mid S phase = 848 structures, late S phase = 1227 structures, error= s.e.m.

Each subclass of class 4 structures were defined: I observed that in subclass 1 BRCA1 is closely associated with or outside of 53BP1 accumulations. In subclass 2, BRCA1 is more centralised relative to 53BP1 spots. Subclass 3 is a combination of subclasses 1 and 2. These structures may indicate a shift in BRCA1 composition during repair progression. I have defined subclass 4 as containing >3 BRCA1 spots. The increased occupancy of BRCA1 may indicate more complex, clustered damage, or closely associated DSBs (Reindl *et al,* 2017, Lomax, Folkes & O'Neill, 2013 & Nickoloff *et al*, 2017). The number of structures for each sub-class were quantified and revealed no differences in distribution in mid and late S-phase cells. Notably, subclass 2 were most prevalent in mid and late S-phase cells. These are defined as multiple BRCA1 spots encapsulated by multiple 53BP1 spots. These types of structures are further investigated in Section 4.5.

4.4.3 Mutual exclusivity of BRCA1 and 53BP1 in class 5 foci

I have defined class 5 structures as one BRCA1 spot encapsulated by multiple 53BP1 spots. This type of structure has previously been reported with 53BP1 being visualised as a continuous oligomeric structure, with several maxima and minima, surrounding the central BRCA1. By contrast, following ExM, 53BP1 was visualised as a series of discontinuous spots with a spherical arrangement around BRCA1 (Figure 4.21). 53BP1 maxima appear to be discrete spots and 53BP1 minima are in fact gap between these spots. Strikingly, there is a void visible between the central BRCA1 spot and 53BP1 spots which has not been previously resolved.

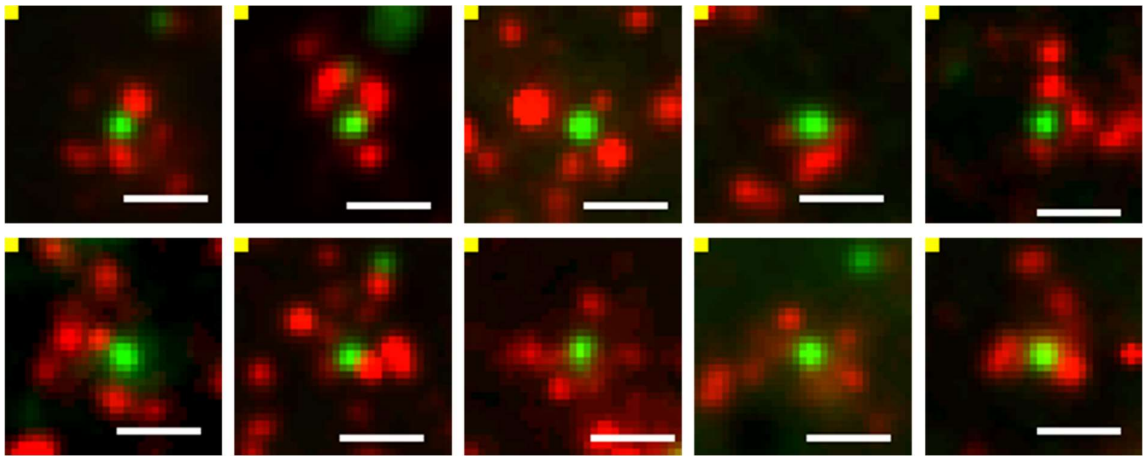

Figure 4.21. Visualising mutual exclusivity of BRCA1 and 53BP1 in class 5 repair structures. Representative examples of class 5 structures from late S-phase nuclei treated as in Figure 4.9 are shown. Briefly, U2OS cells were treated with EdU prior to irradiation (2 Gy) and allowed 1 hour to recover prior to pre-extraction and fixation. Cells were then stained for EdU and immunostained for BRCA1 and 53BP1. EdU staining is omitted from selected examples here. Scale bars 2 µm.

To visualise the average distribution of BRCA1 and 53BP1 in class 5 structures, examples structures were selected where BRCA1 and 53BP1 were oriented parallel with the focal plane. These examples were combined to form an average class 5 structure and line profiles were generated for these average structures (Figure 4.22). These profiles were further evaluated in 3D (Figure 4.23).

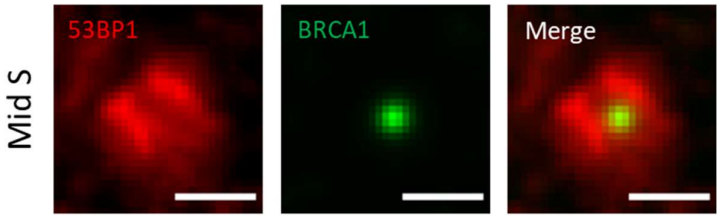
Mid S
53BP1
BRCA1
Merge

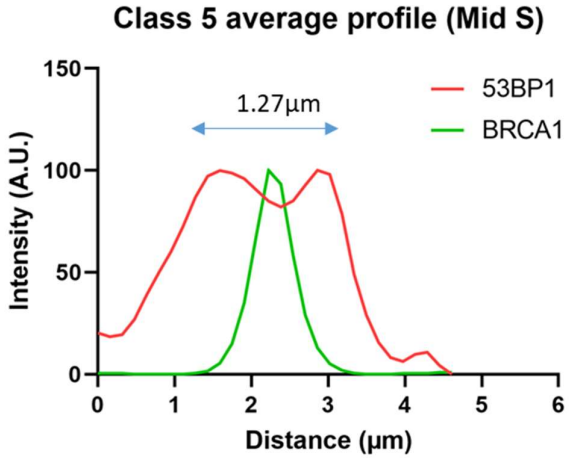
Class 5 average profile (Mid S)
1.27µm
53BP1
BRCA1
Intensity (A.U.)
150
100
50
0
0
1
2
3
4
5
6
Distance (µm)

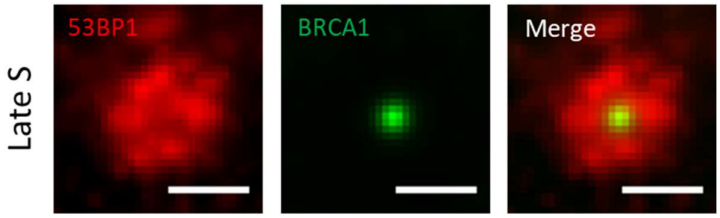
Late S
53BP1
BRCA1
Merge

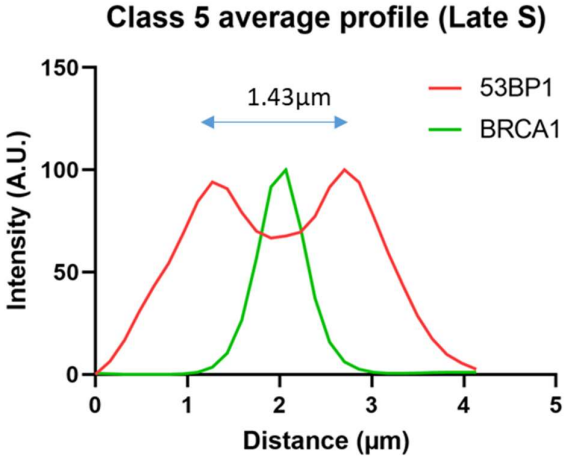
Class 5 average profile (Late S)
1.43µm
53BP1
BRCA1
Intensity (A.U.)
150
100
50
0
0
1
2
3
4
5
Distance (µm)

Figure 4.22. Visualising mutual exclusivity of BRCA1 and 53BP1 in class 5 repair structures. Examples of class 5 structures were selected where 53BP1 and BRCA1 spots were oriented parallel to the focal plane. Intensity of BRCA1 and 53BP1 across examples was averaged to give the profiles shown as maximum intensity projections. Line profiles were generated through the central slice of each average focus and are shown below the maximum projections. N=3, mid S-phase 130 structures (from 3 repeats), and late S-phase 125 structures (from 3 repeats) are averaged. Scale bar 2 μm.

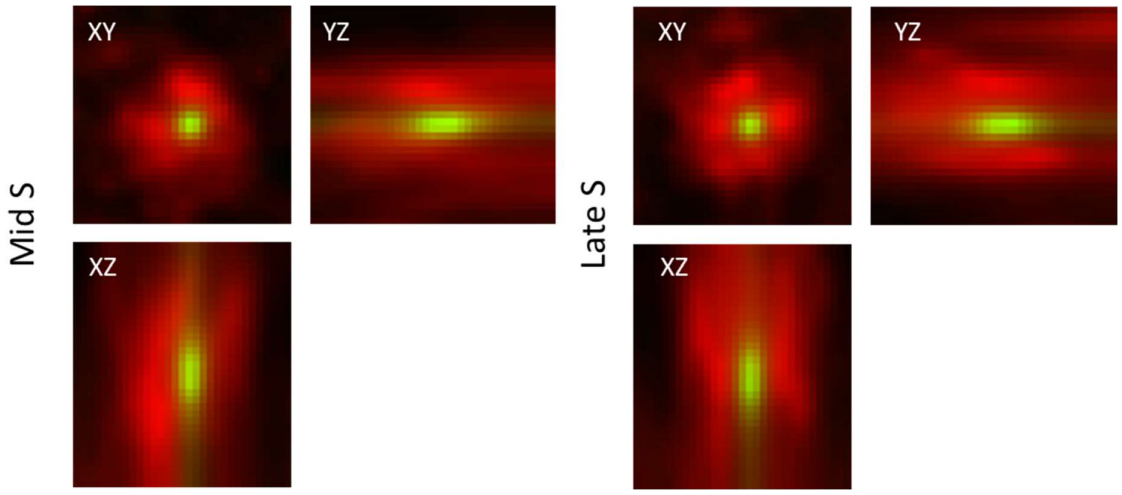

Figure 4.23. Visualising mutual exclusivity of BRCA1 and 53BP1 in class 5 repair structures. To complement the maximum intensity projections shown in Figure 4.22, orthogonal views of class 5 average profiles are shown.

Average profiles of class 5 structures based on BRCA1 as a central spherical spot were generated. In these average structures, BRCA1 was spanning approximately 800 nm, equivalent to 200 nm pre-expansion. 53BP1 was visualised as a continuous structure encapsulating BRCA1 spanning between 2.5-3 µm diameter, equivalent to 625-750 nm pre-expansion (Figure 4.22). The peak-to-peak distance of 53BP1 was measured as 1.27 µm and 1.43 µm (equivalent to 0.32 µm and 0.36 µm pre-expansion) in mid and late S-phase average class 5 structures, respectively. These measurements suggest a separation as small as 80 nm between 53BP1 and BRCA1. In the orthogonal views of the averaged class 5 structures, it was observed that BRCA1 and 53BP1 occupy distinct sub-focal regions with no visible overlap (Figure 4.23). The void between BRCA1 and 53BP1 is not as readily appreciated in the average structure profiles when compared to examples of individual structures (shown in Figure 4.21). This may be due to differences in relative placement of 53BP1 spots in individual examples.

We further noted that the average peak-to-peak distance in late S-phase average class 5 structures is larger than that in mid S-phase average class 5 structures. These differences in peak-to-peak distance may be real phenomena. However, given that we are creating these average structures

based on hundreds of individual structures, these measurements represent the spatial organisation of the selected population of structures.

4.4.4 BRCA1 is responsible for redistribution of 53BP1 in mid and late S-phase nuclei

To confirm if the spatial organisation of BRCA1 and 53BP1 observed in class 5 structures is dependent on BRCA1, we depleted BRCA1 using siRNA and compared to control cells. This was confirmed by western blot (Figure 4.24) and by immunostaining BRCA1-depleted and control cells for 53BP1 and BRCA1 (Figure 4.25). Foci numbers were quantified for cells with markers of early, mid and late S-phase in BRCA1-depleted and control cells (Figure 4.26). ExM protocol was performed and Z stacks of BRCA1-depleted and control cells were acquired and deconvolved (Figure 4.27).

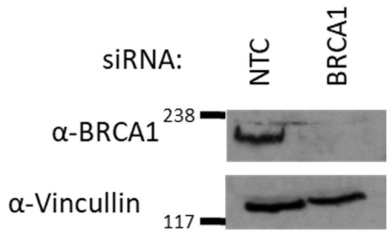

Figure 4.24. Confirming BRCA1-depletion. U2OS cells were treated with siBRCA1 or NTC siRNA for 72 hours prior to lysis. Western blotting was performed to confirm depletion of BRCA1 probing with the antibodies shown.

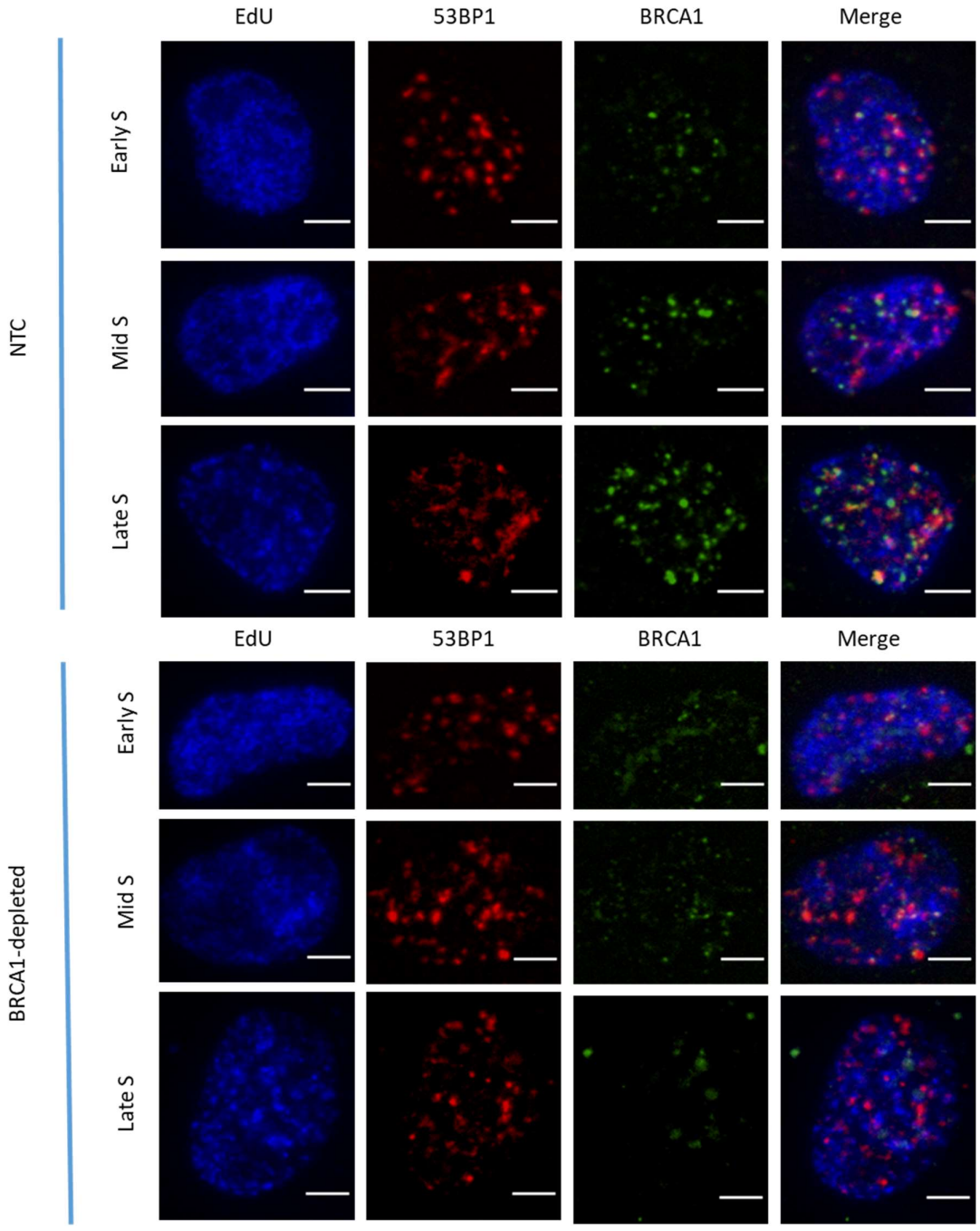

Figure 4.25. Immunostaining BRCA1-depleted cells. U2OS cells were seeded and grown overnight. Cells were treated with siBRCA1 or NTC siRNA for 72 hours. They were treated with EdU prior to damage induction by irradiation (2 Gy). Cells were allowed 1 hour to recover, pre-extracted and fixed. Cells were stained for EdU and immunostained for 53BP1 and BRCA1. Images were acquired on a widefield microscope. Scale bars 5 µm.

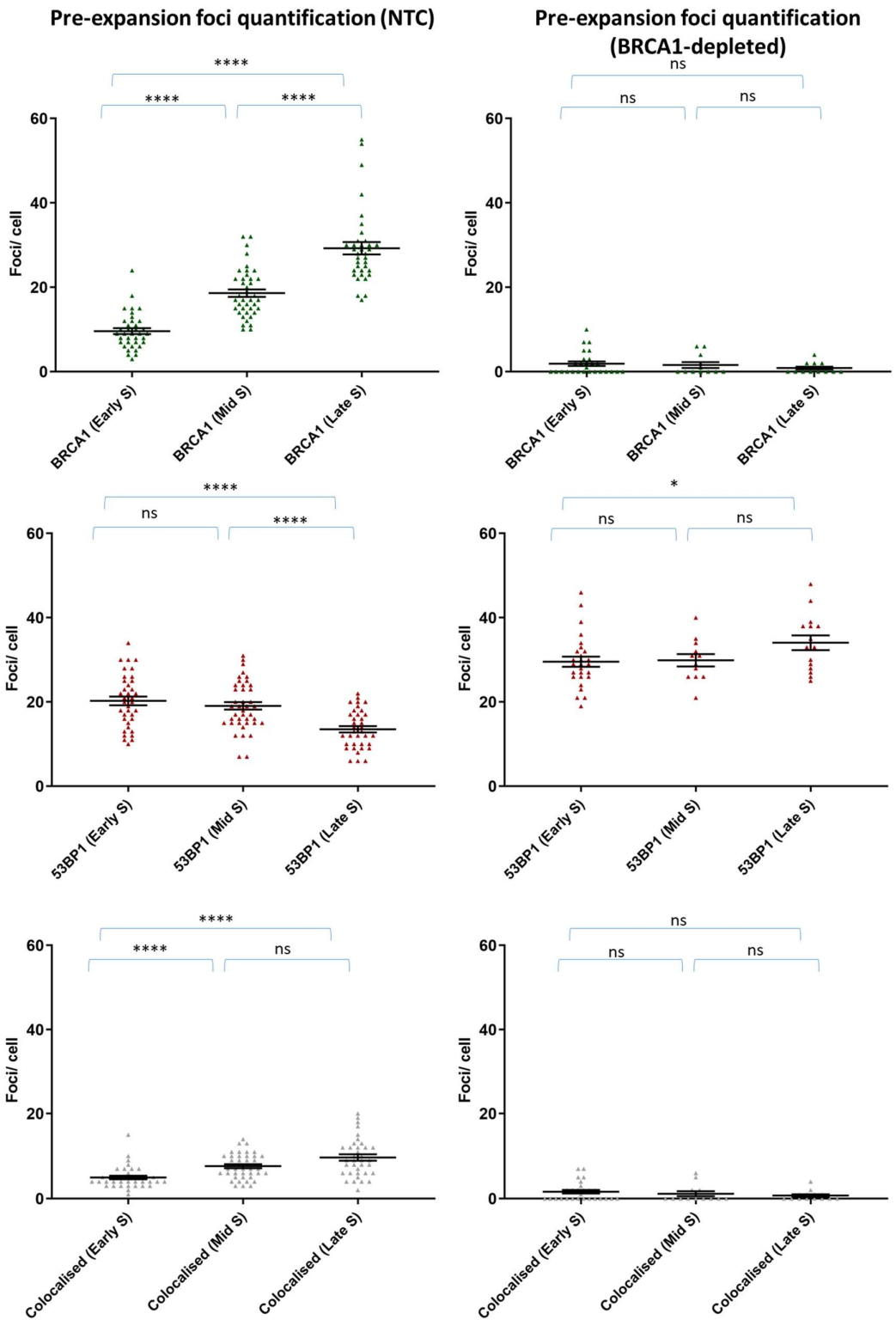
Pre-expansion foci quantification (NTC)
Pre-expansion foci quantification (BRCA1-depleted)
Foci/ cell
BRCA1 (Early S)
BRCA1 (Mid S)
BRCA1 (Late S)
53BP1 (Early S)
53BP1 (Mid S)
53BP1 (Late S)
Colocalised (Early S)
Colocalised (Mid S)
Colocalised (Late S)
****
ns
*

Figure 4.26. **Quantification of BRCA1 and 53BP1 foci as a function of cell cycle in BRCA1-depleted cells.** Foci quantification was performed on nuclei treated as in Figure 4.24 & 4.25. Cell cycle position was determined by EdU staining and foci numbers were counted. N=2, >50 nuclei per cell cycle position in both BRCA1-depleted and control cells. Throughout Figure, **** P<0.001; ***P < 0.005; *P < 0.05 NS, not significant by two-sided Student's t test.

Pre-expansion imaging and quantification of foci was completed in cells with markers of early, mid and late S-phase indicated by EdU staining (Figure 4.26). In the control cells, BRCA1 numbers were observed to increase from early to late S-phase, and 53BP1 was observed to decrease consistent with previous experiments (Section 4.2.2). Following BRCA1-depletion, little or no BRCA1 foci were present in S-phase marked nuclei. 53BP1 foci numbers increased between early and late S phase in BRCA1-depleted cells. We further noted an increase in 53BP1 foci numbers in BRCA1 depleted cells compared to controls in early, mid and late S-phase nuclei (P values <0.0001). This may in part be explained by loss of HR initiation in the absence of BRCA1, resulting in an increased number of 53BP1 accumulations associated with NHEJ. Incomplete resection may also affect suitability of substrates resulting in poor NHEJ (Densham *et al*, 2016).

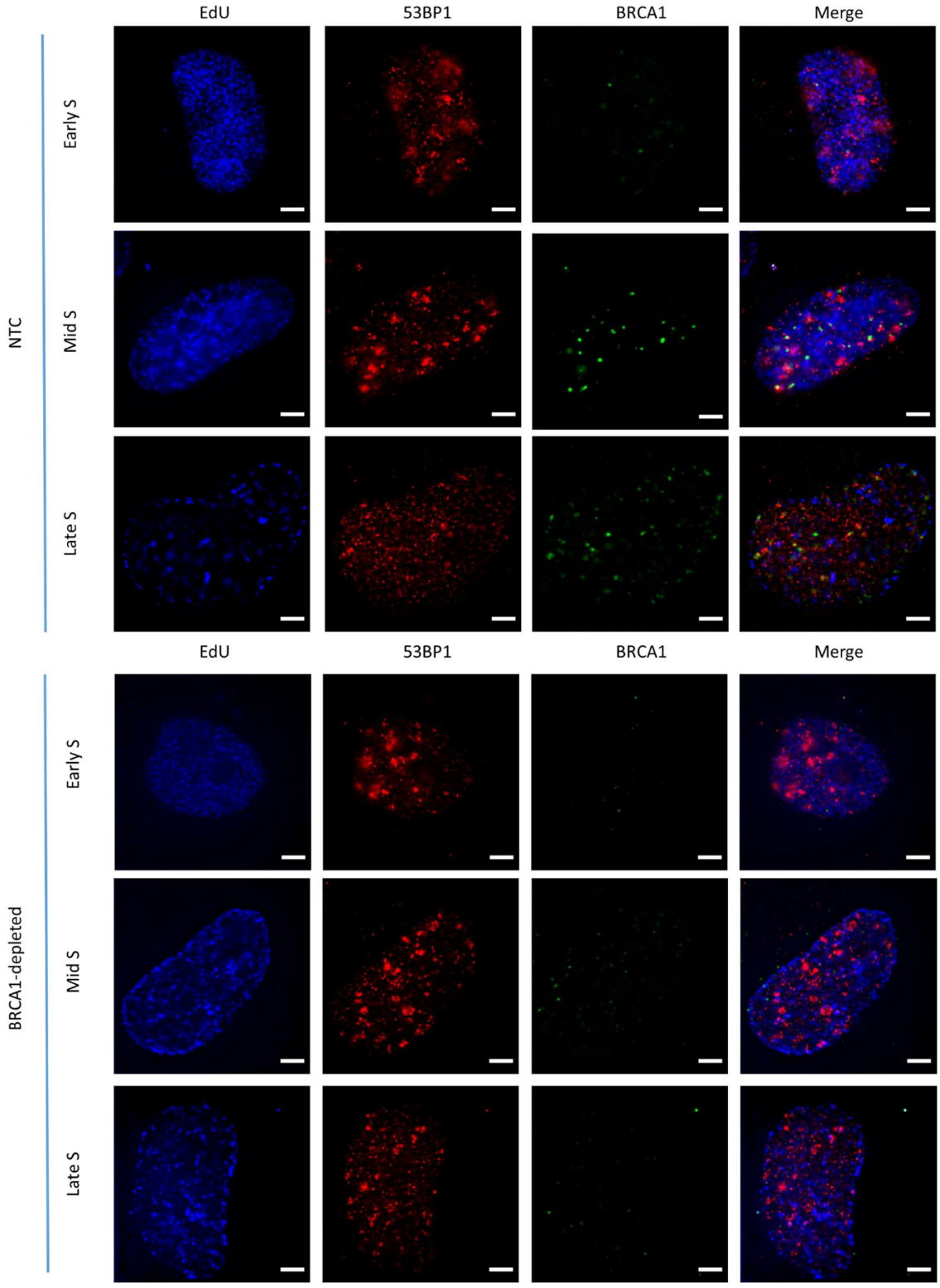
EdU
53BP1
BRCA1
Merge
NTC
Early S
Mid S
Late S
EdU
53BP1
BRCA1
Merge
BRCA1-depleted
Early S
Mid S
Late S

Figure 4.27. Immunostaining BRCA1-depleted cells. U2OS cells were seeded and grown overnight. Cells were treated with siBRCA1 or control siRNA for 72 hours. They were treated with EdU prior to damage induction by irradiation (2 Gy). Cells were allowed 1 hour to recover, pre-extracted and fixed. Cells were stained for EdU and immunostained for 53BP1 and BRCA1. ExM preparation was completed and post-expansion Z stacks were acquired on a widefield microscope. Scale bars 10 μm.

Post-expansion Z stacks were organised into early, mid and late S-phase and accumulations were firstly assessed visually (Figure 4.27). In the control cells, BRCA1 foci numbers were again observed to increase from early to late S-phase. 53BP1 accumulations were observed as dense continuous structures in early and mid S-phase marked cells, whilst in late S-phase cells 53BP1 appeared as diffuse collections of spots, and occupied a reduced volume overall. In the BRCA1 depleted cells, 53BP1 was visualised as dense oligomeric structures throughout early, mid and late S-phase. Chapman *et al* previously observed that the volume occupied by 53BP1 is reduced as BRCA1 drives its exclusion to the periphery of repair foci; we observe that 53BP1 is retained as dense structures with no visual redistribution following BRCA1 depletion suggesting that BRCA1 is indeed responsible for class 5 structure appearance (Appendix Figure A7).

We next sought to quantify changes in 53BP1 distribution as a function of cell cycle in BRCA1-depleted cells as compared to controls. As BRCA1 is absent in the depleted cells, the spot detection based analysis used previously was not possible; we instead opted to compare the volume occupied by 53BP1 in nuclei classified as early, mid and late S-phase in BRCA1-depleted and control cells.

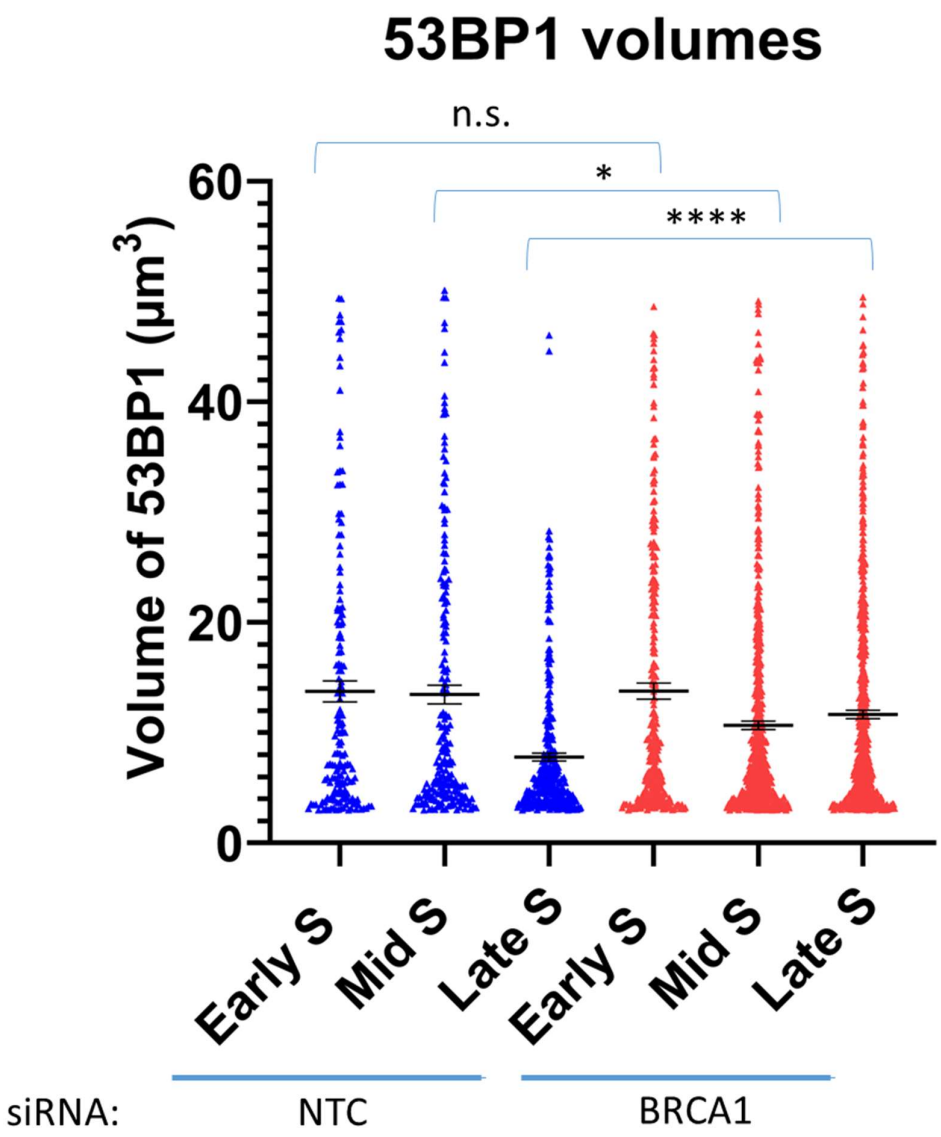

Figure 4.28. BRCA1 is responsible for redistribution of 53BP1 in repair foci. Volumes of 53BP1 structures were measured in BRCA1-depleted cells compared to controls in nuclei treated as in Figure 4.27. Volumes were measured by performing segmentation in ImageJ (described in Section 2.7.7). Measurements were taken from >6 nuclei per cell cycle phase. N=1; error = s.e.m. Throughout figure, ***P < 0.005; *P < 0.05 NS, not significant by two-sided Student's t test.

The volume of 53BP1 was observed to decrease significantly late S-phase in the control cells as compared to BRCA1-depleted cells. This is consistent with observations made by Chapman *et al;* in the control cells, 53BP1 occupied a smaller volume in S-phase cells compared to cells in G1, whereas

in the BRCA1 depleted cells there was no significant change in 53BP1 volume between G1 and S-phase cells. This indicates that BRCA1 is required for redistribution of 53BP1 in S-phase cells.

4.4.5 RIF1 is closely associated with 53BP1 structures

53BP1, together with its downstream effectors RIF1, PTIP and Shieldin-CST-polα complex, restrains resection and promotes repair by NHEJ (Mirman *et al*, 2018). It has also been shown that loss of 53BP1 results in an increase in repair via mutagenic SSA; 53BP1 appears to play a role in fostering the homology of HR (Ochs *et al*, 2016). These observations together suggest that 53BP1 controls resection to ensure it occurs in the correct cellular context; where NHEJ is required, 53BP1 recruits the Shieldin-CST-polα complex to protect against nuclease-mediated resection, and where HR is required 53BP1 restrains resection lengths to prevent SSA. Additionally, super resolution microscopy has revealed that 53BP1 is retained break sites during HR progression (Reindl *et al*, 2015, Chapman *et al*, 2012 & Kakarougkas *et al,* 2013). It has therefore been hypothesised that 53BP1 plays a structural role during HR; it may stabilise chromatin proximal to the break, or may form channels for transit of repair factors to sites of damage. This information, together with the spacing between 53BP1 spots in class 5 structures, prompted us to investigate factors which may be interacting with, or stabilising 53BP1 on chromatin during HR. RIF1 was chosen for this as it is known to interact with and stabilise 53BP1 at chromatin during NHEJ repair (Ochs *et al*, 2019).

To investigate the organisation of 53BP1 and RIF1 during S-phase, U2OS cells were treated with EdU prior to damage induction by irradiation and allowed 1 hour to recover. Cells were subsequently fixed, stained for EdU to determine cell cycle position and immunostained for RIF1 and 53BP1. Images were acquired pre-expansion (Figure 4.28) and foci numbers were quantified as a function of cell cycle (Figure 4.29). ExM protocol was performed and Z stacks acquired post-expansion (Figure 4.30 and 4.31).

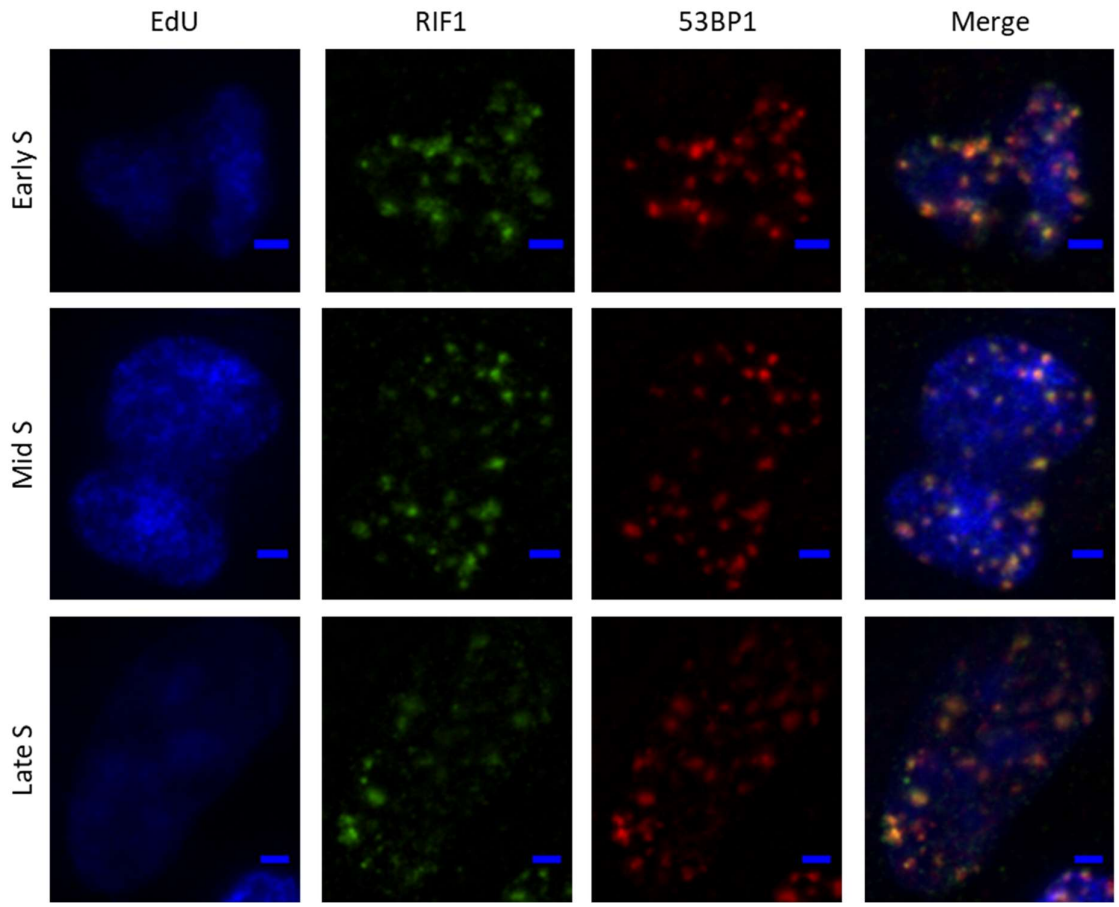

Figure 4.29. **Visualising 53BP1 and RIF1 foci pre-expansion.** U2OS cells were treated with EdU prior to irradiation (2 Gy) and allowed 1 hour to recover. Cells were pre-extracted and fixed. Click it reaction was performed for EdU detection, and cells were immunostained for 53BP1 and RIF1. Representative images are shown. Scale bar 2.5 µm.

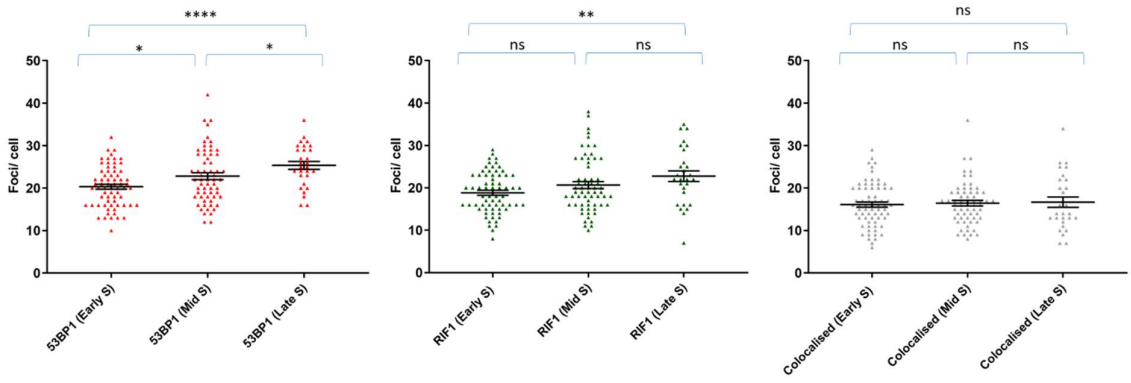

Figure 4.30. Quantification of RIF1 and 53BP1 foci numbers as a function of cell cycle. Pre-expansion images of nuclei stained for 53BP1 and RIF1 were organised according to markers of cell cycle phase. Foci numbers were quantified as shown. N=2, >30 nuclei per phase. Throughout Figure, **** P<0.001; **P <0.01; *P < 0.05 NS, not significant by two-sided Student's t test.

The pre-expansion images of 53BP1 and RIF1 immunostained cells revealed a high degree of colocalisation between the two proteins, as anticipated since both proteins are required for protection of DNA ends against resection and RIF1 contacts 53BP1 at its N-terminus through phosphorylation of 53BP1 (Chapman *et al*, 2013).

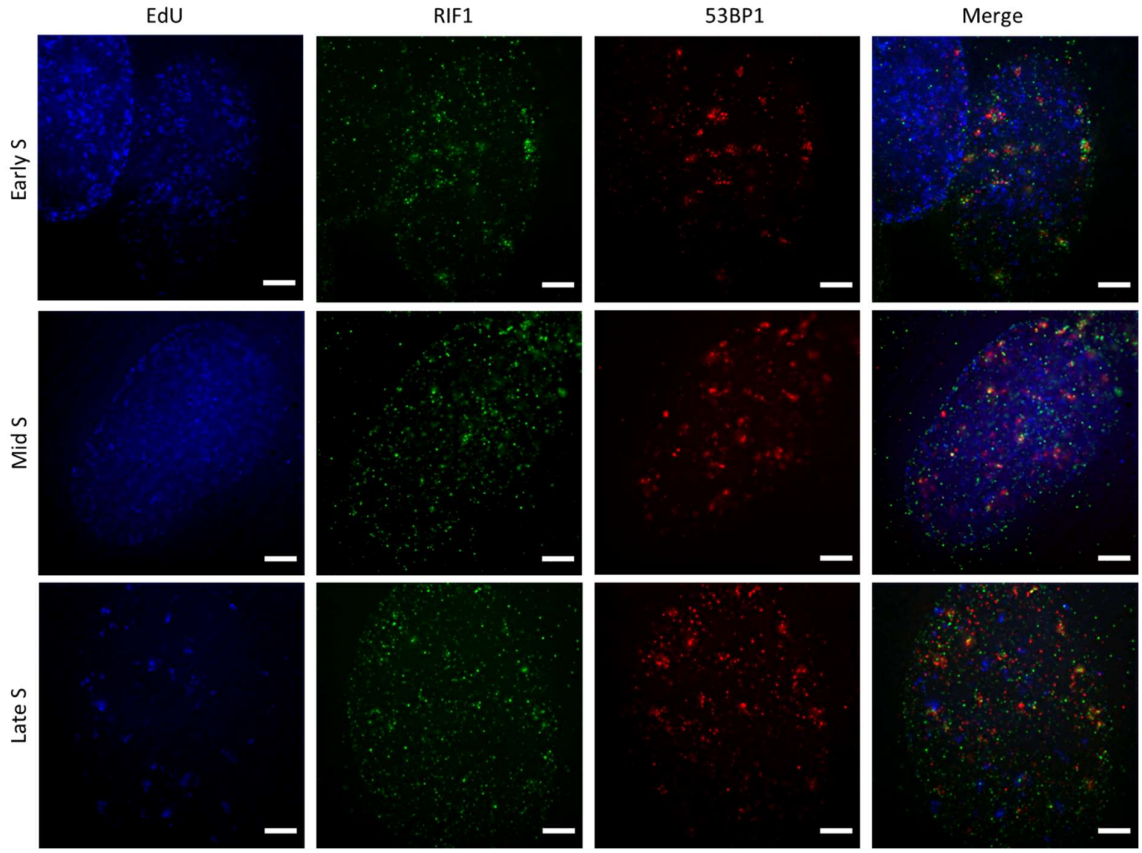

Figure 4.31. Visualising 53BP1 and RIF1 post-expansion. U2OS cells were seeded and grown overnight. Cells were treated with EdU prior to irradiation (2 Gy) and given 1 hour to recover prior to pre-extraction and fixation. Cells were stained for EdU and immunostained for 53BP1 and RIF1. ExM protocol was completed and post-expansion Z stacks were acquired and deconvolved. Scale bars 10 µm.

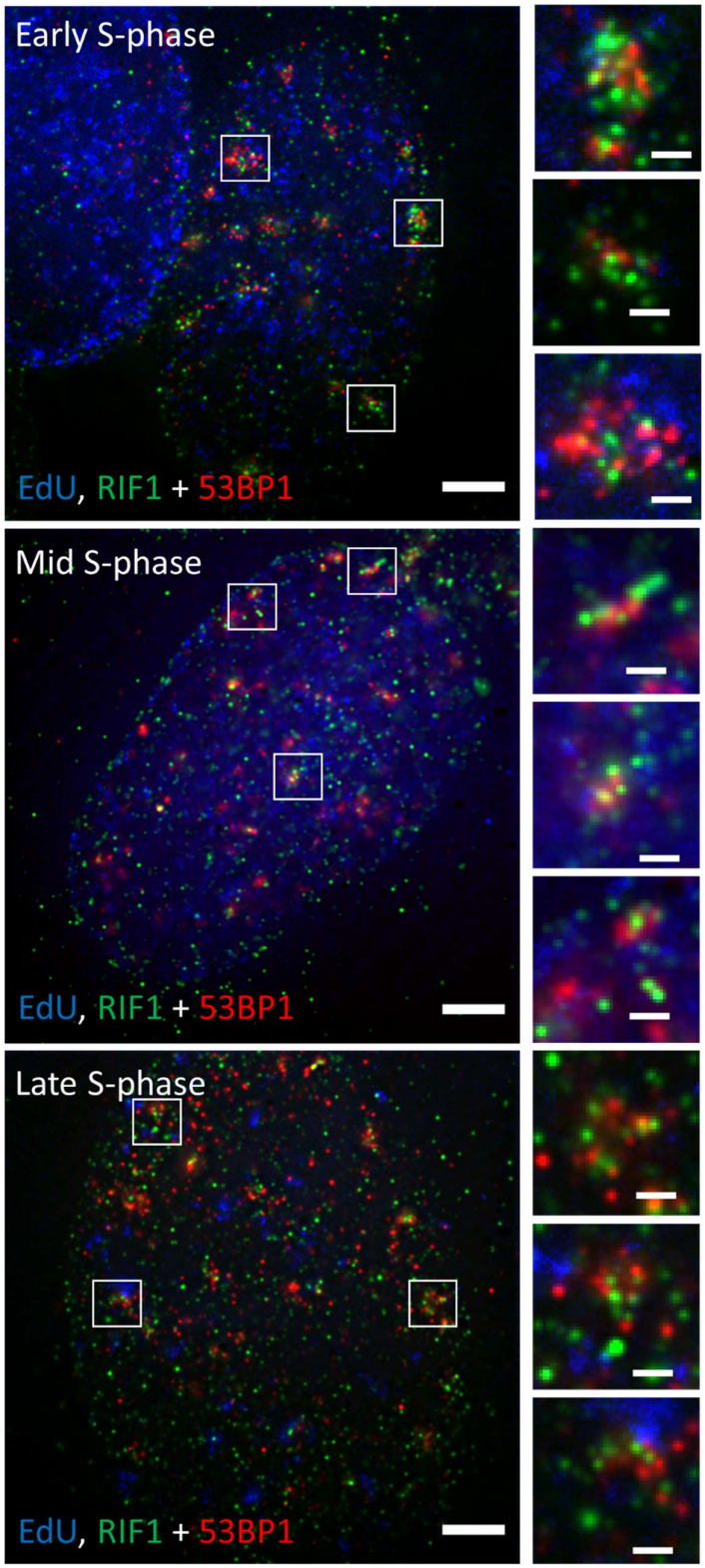
Early S-phase
EdU, RIF1 + 53BP1
Mid S-phase
EdU, RIF1 + 53BP1
Late S-phase
EdU, RIF1 + 53BP1

Figure 4.32. Visualising RIF1 and 53BP1 foci nanostructure. Nuclei were organised according to markers of cell cycle phase and nanostructure of 53BP1 and RIF1 accumulations visually investigated. Examples of early, mid and late S-phase classified nuclei are shown. Scale bar 10 µm and 2 µm.

Post-expansion imaging of nuclei stained for 53BP1 and RIF1 revealed that these proteins, whilst being intimately associated at sites of damage, appear to be largely anti-correlated. We measured PCC between RIF1 and 53BP1 in pre- and post-expansion images of early, mid and late S-phase classified nuclei (Figure A8). PCC values decreased from early to late S-phase in pre- and post-expansion images. Notably, PCC values were lower in post-expansion images, indicating 53BP1 and RIF1 are uncorrelated. Interestingly, there are some examples of RIF1 and 53BP1 have an alternating appearance, suggesting that RIF1 may act as a spacer for 53BP1 to ensure correct structural organisation at DSBs. This is consistent with observations made by Ochs *et al* (Ochs *et al*, 2019) (described in Section 1.4.2).

4.5 Characterising foci nanostructures as a function of recovery time

Repair of DSBs depends on the characteristics of each individual break and repair pathway choice is determined for each break separately (Schipler & Iliakis, 2013). Heterogeneity in the type of damage induced by irradiation may be a source of structural variability observed in BRCA1 and 53BP1 co-enriched accumulations (as described in Section 1.4). Another possible source of heterogeneity is BRCA1 complex formation and function (Schwarz *et al*, 2019). Firstly, BRCA1 binds to ubiquitinated histones via RAP80-Abraxas inhibiting resection (Hu *et al*, 2011). Loss of RAP80 and a shift in BRCA1 complex composition results in end resection and localisation of BRCA1 to a sub-compartment of repair foci proximal to the break ends from which 53BP1 has been removed. BRCA1 is later required for recruitment of PALB2 and BRCA2 which exchanges RPA with RAD51 (Zhang *et al*, 2009 & Nepomuceno *et al*, 2017). More recently it has been suggested that BRCA1 may also have a role in strand invasion (Cejka, 2017 & Zhao *at al*, 2017).

As BRCA1 forms multiple, functionally distinct complexes, this may be responsible for the heterogeneity in placement of BRCA1 spots relative to 53BP1 we observe here. There may also be a temporal progression in the organisation of BRCA1 relative to 53BP1 during DSB resolution. Under this hypothesis, a time course was performed and structures were characterised as a function of

recovery time and cell cycle phase. U2OS cells were seeded and pulsed with EdU prior to damage induction by irradiation. Cells were allowed differing amounts of time to recover prior to fixation and staining for 53BP1 and BRCA1 (illustrated in Figure 4.33).

Figure 4.33. Design of time course experiment to visualise temporal progression of 53BP1 and BRCA1 co-enriched accumulations. U2OS cells were seeded and grown overnight. Prior to damage induction cells were incubated with EdU for 10 minutes, washed with PBS and fresh media was added. Cells were irradiated (2 Gy) and allowed to recover for 10 minutes, 30 minutes, 1 hour or 2 hours. Cells were fixed and stained for EdU, 53BP1 and BRCA1. Pre-expansion images were acquired. For post-expansion imaging, ExM protocol was performed and post-expansion Z stacks were acquired for subsequent scoring.

Pre-expansion images were acquired at each time point to determine efficacy of staining and to quantify the distribution of foci as a function of cell cycle at each recover point (Appendix Figures A9-A11). Foci numbers were quantified pre-expansion for each time point according to cell cycle phase (Figure 4.34). Foci formation is rapid with 53BP1 and BRCA1 foci clearly observed at 10 minutes following damage. At each time point, BRCA1 foci numbers increased from early to late S-phase and 53BP1 foci numbers conversely decreased. Total BRCA1 foci numbers peak between 30 minutes and 1 hour and decrease at 2 hours. Foci observed at the 2 hour time point are visually smaller. Colocalisation was observed to decrease from 30 minutes to 2 hours. This may be indicative that some sites of damage have been successfully repaired.

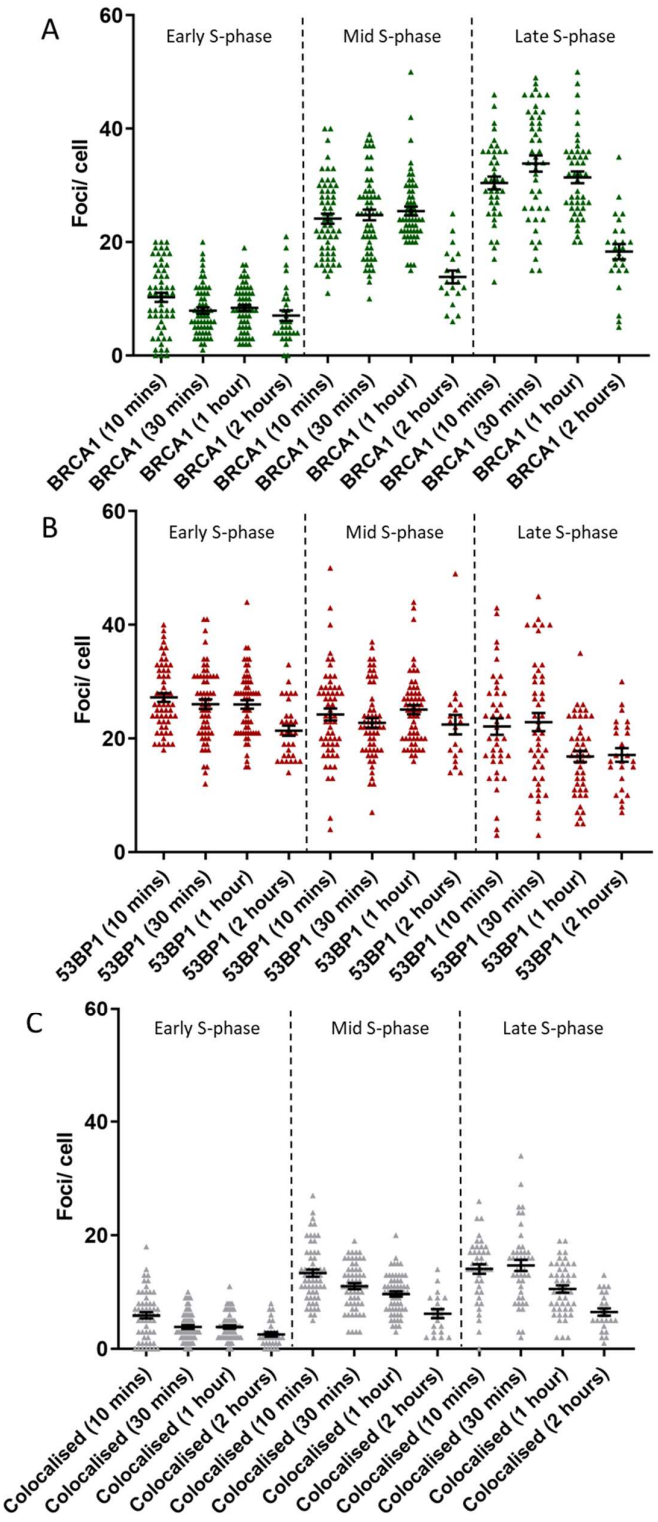

Figure 4.34. Quantification of foci throughout time course pre-expansion. Numbers of A) BRCA1, B) 53BP1 and C) colocalised repair foci were quantified for nuclei classified as early, mid and late S phase at each time point. Colocalised foci are defined as those where pixel overlap is observed between 53BP1 and BRCA1. Error = s.e.m.

ExM protocol was completed and post-expansion Z stacks were acquired and deconvolved. Nuclei classified as early, mid and late S-phase are shown for each time point (Appendix Figure A12, Figure 4.35 & 4.36). BRCA1 and 53BP1 structures at each time point were visually investigated in mid and late S-phase classified nuclei (Figure 4.37 & 4.38) and were classified as class 1-5 as previously defined in Section 4.3.2 and prevalence of classes 2, 4 and 5 were plotted (Figure 4.39).

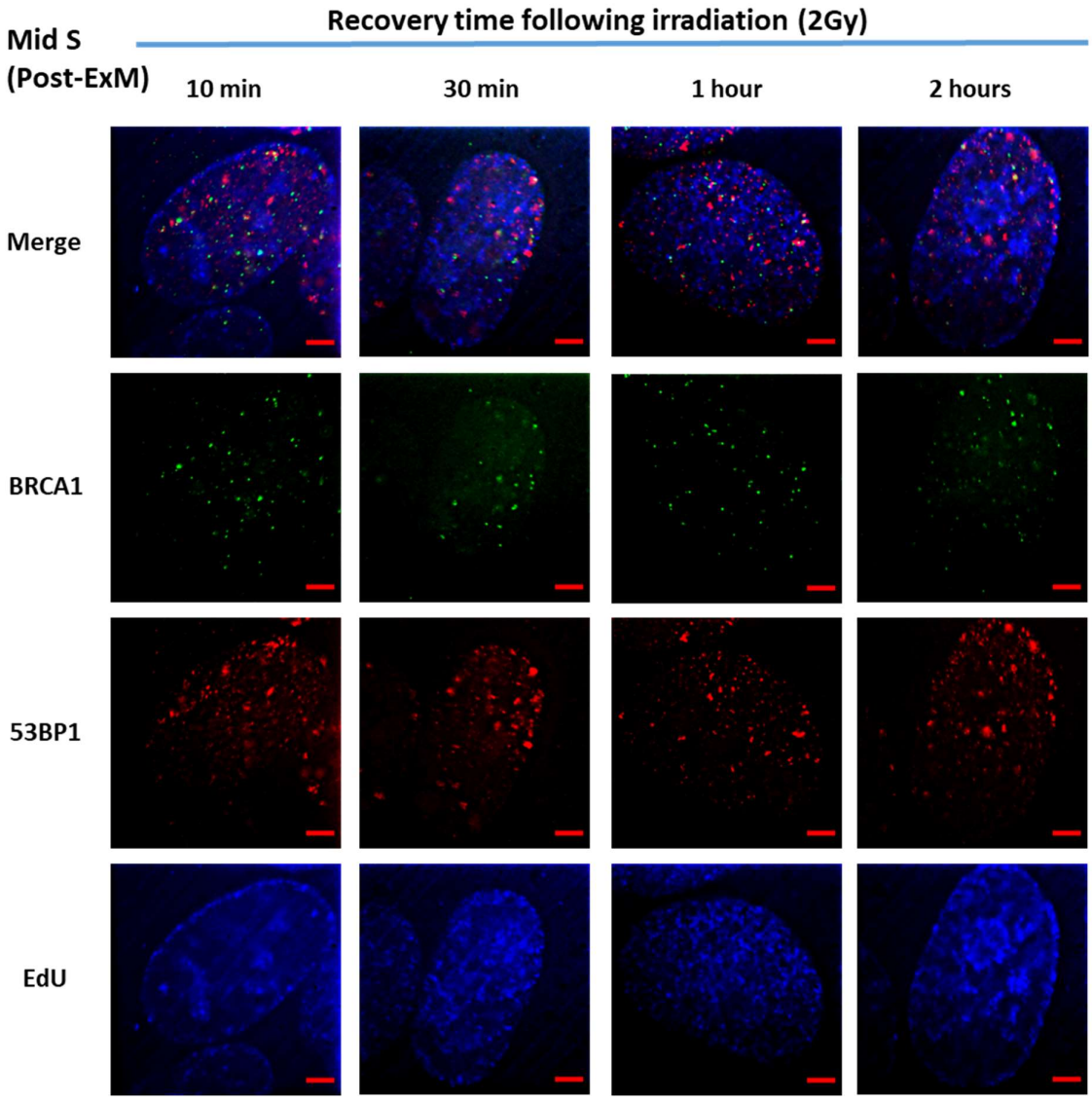

Figure 4.35. Visualising DSB repair progression. U2OS cells were pulsed with EdU for 10 minutes and washed prior to irradiation (2 Gy). Cells were allowed to recover for the times shown prior to CSK pre-extraction and fixation. Cells were stained for EdU and immunostained for BRCA1 and 53BP1. Standard ExM protocol (Section 2.4) was performed and post-ExM Z stacks were acquired on a wide field microscope. Scale bars 10 µm.

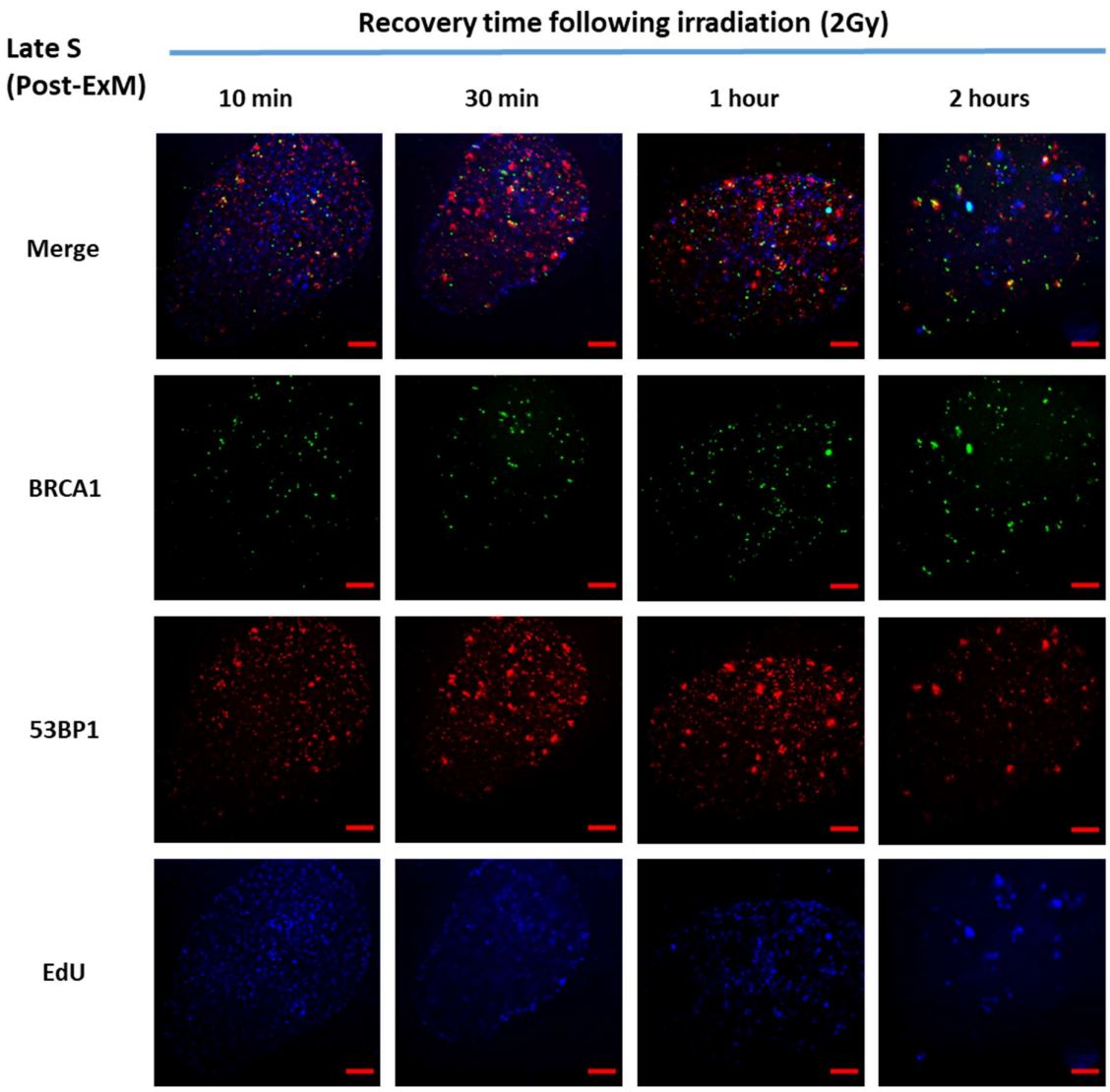

Figure 4.36. Visualising DSB repair progression. U2OS cells were pulsed with EdU for 10 minutes and washed prior to irradiation (2 Gy). Cells were allowed to recover for the times shown prior to CSK pre-extraction and fixation. Cells were stained for EdU and immunostained for BRCA1 and 53BP1. Standard ExM protocol (Section 2.4) was performed and post-ExM Z stacks were acquired on a wide field microscope. Scale bars 10 µm.

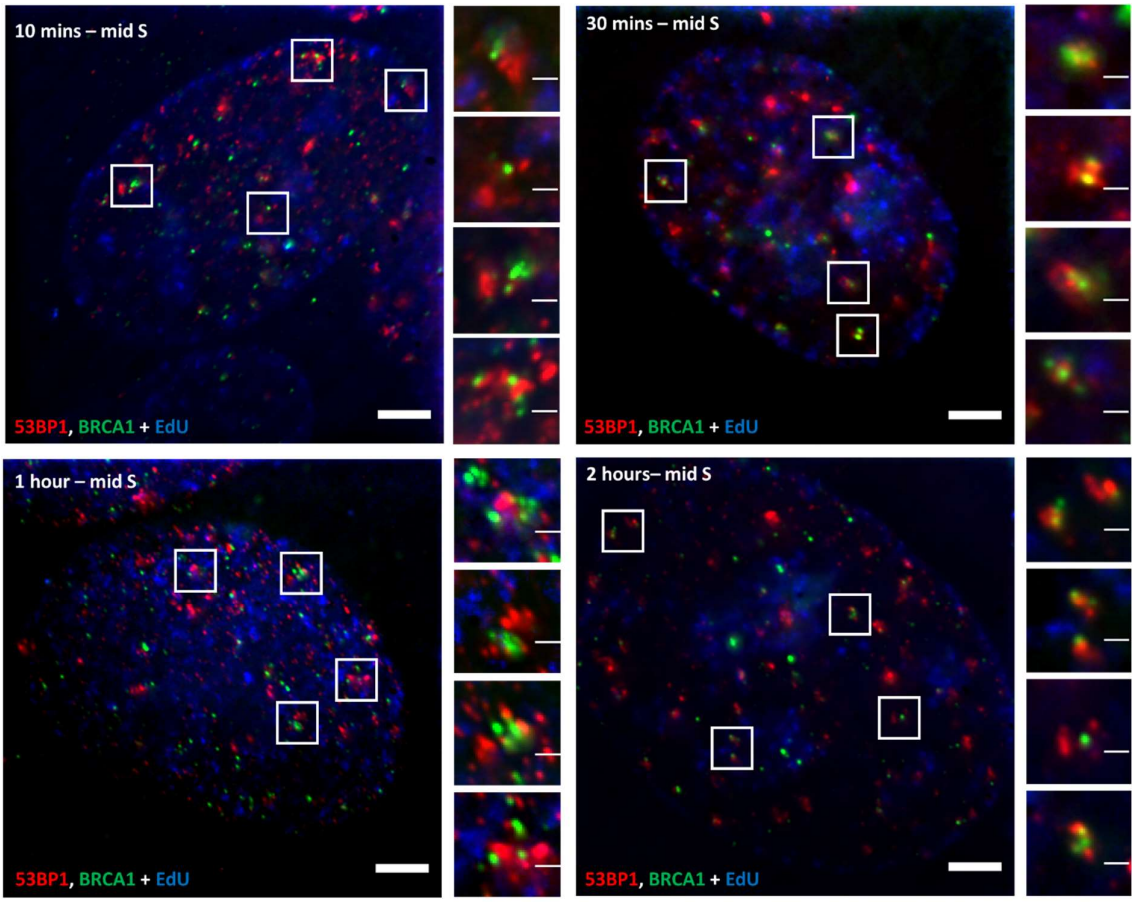

Figure 4.37. Visualising DSB repair progression: a nanoscale view. U2OS cells were pulsed with EdU for 10 minutes and washed prior to irradiation (2 Gy). Cells were allowed to recover for the times shown prior to CSK pre-extraction and fixation. Cells were stained for EdU and immunostained for BRCA1 and 53BP1. ExM protocol was performed and post-ExM Z stacks were acquired on a wide field microscope. Nuclei classified as mid S-phase were selected and structures visually investigated. Scale bars 10 µm and 2 µm.

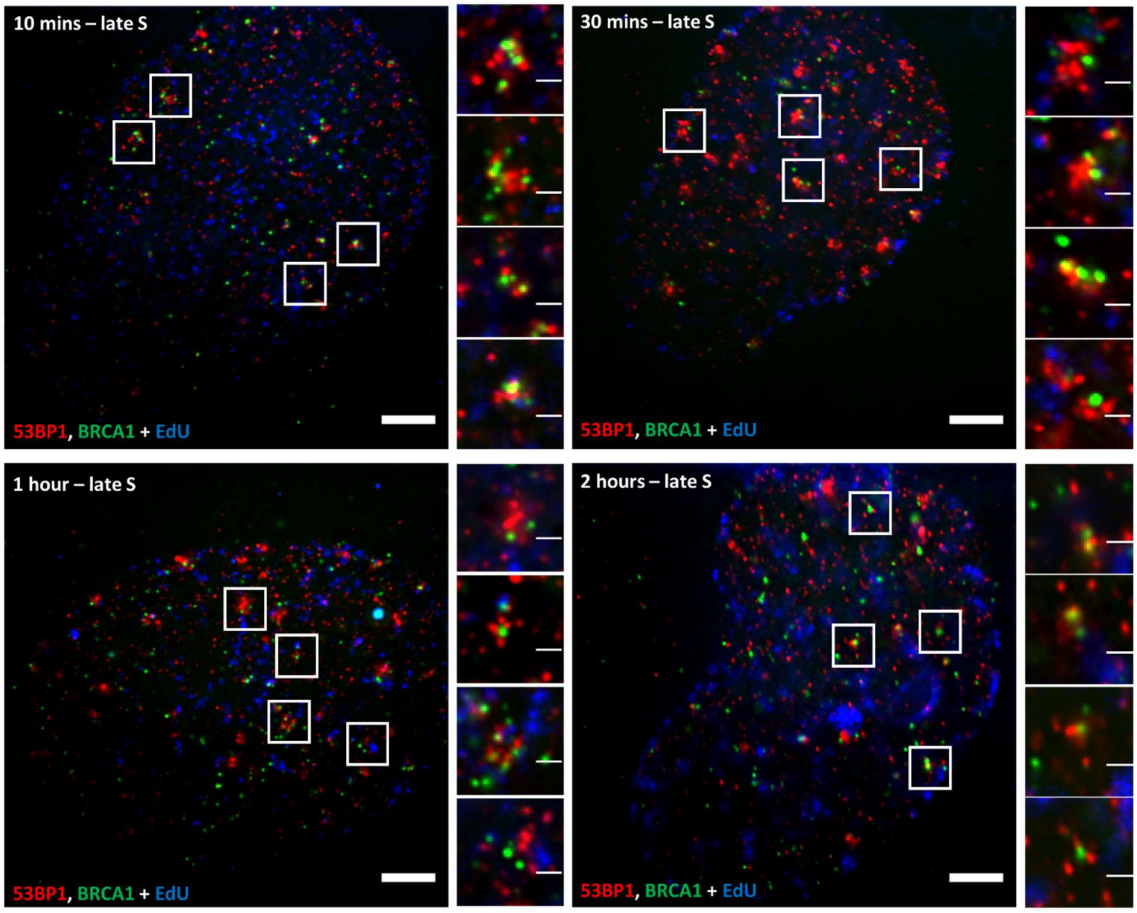

Figure 4.38. Visualising DSB repair progression: a nanoscale view. U2OS cells were pulsed with EdU for 10 minutes and washed prior to irradiation (2 Gy). Cells were allowed to recover for the times shown prior to CSK pre-extraction and fixation. Cells were stained for EdU and immunostained for BRCA1 and 53BP1. ExM protocol was performed and post-ExM Z stacks were acquired on a wide field microscope. Nuclei classified as late S-phase were selected and structures visually investigated. Scale bars 10 µm and 2 µm.

Example images from the time course were selected and visually assessed (Figure 4.37 & 4.38). Structures were scored and quantified (Figure 4.39). At 10 minutes, simple structures comparable to class 2, and complex accumulations comparable to class 4 were visualised. Class 4 prevalence is retained at 30 minutes and 1 hour time points. At 2 hours, a reduction in class 4 was observed, with structures adopting features similar to class 2 and class 5 structures. This was confirmed by spot detection-based classification of structures. The number of class 2, 4 and 5 structures detected at each time point were compared. Class 2 and 5 have a comparable trend; numbers of these

structures drop at 30 minutes, increase at 1 hour and then decrease again at 2 hours. Class 4 structures peak at 30 minutes and progressively decrease at 1 and 2 hours. Interestingly, this distribution was observed in both mid and late S-phase nuclei; this suggests the shift in structures is related to recovery time following damage induction.

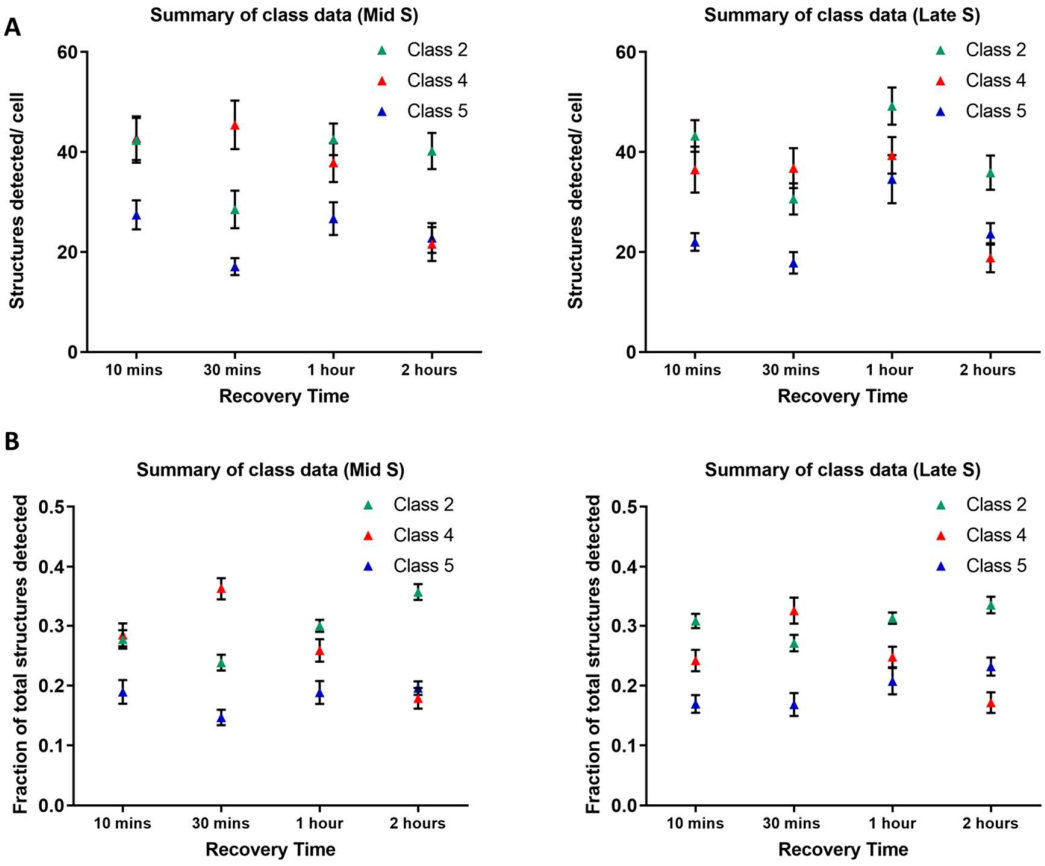

Figure 4.39. Assessing DSB repair progression. Spot detection based analysis was performed on Z stack data acquired across time points. Structure classification for each time point is represented the total number of structures detected (Panel A) and as a fraction of total number of structures identified (Panel B) in mid and late S-phase classified nuclei. N=2, >20 nuclei per time point.

Previously, we observed the placement of BRCA1 spots relative to 53BP1 was heterogeneous in class 4 accumulations (defined as multiple BRCA1 spots associated with multiple 53BP1 spots). We speculate that this heterogeneity may be derived from differences in damage types induced by irradiation, or may be due to BRCA1 forming different functional complexes during DSB repair. I

hypothesised that there may be a change in the distribution of class 4 subclasses as a function of recovery times if the changes in BRCA1 localisation is derived from the formation of different BRCA1 complexes, therefore these structures were characterised as a function of recovery time (Figure 4.39). Subclass 1 is defined as BRCA1 closely associated with or outside of 53BP1 accumulations. Subclass 2 is defined as multiple BRCA1 spots encapsulated by 53BP1. Subclass 3 is a combination of subclass 1 and 2. Subclass 4 contain >3 BRCA1 spots.

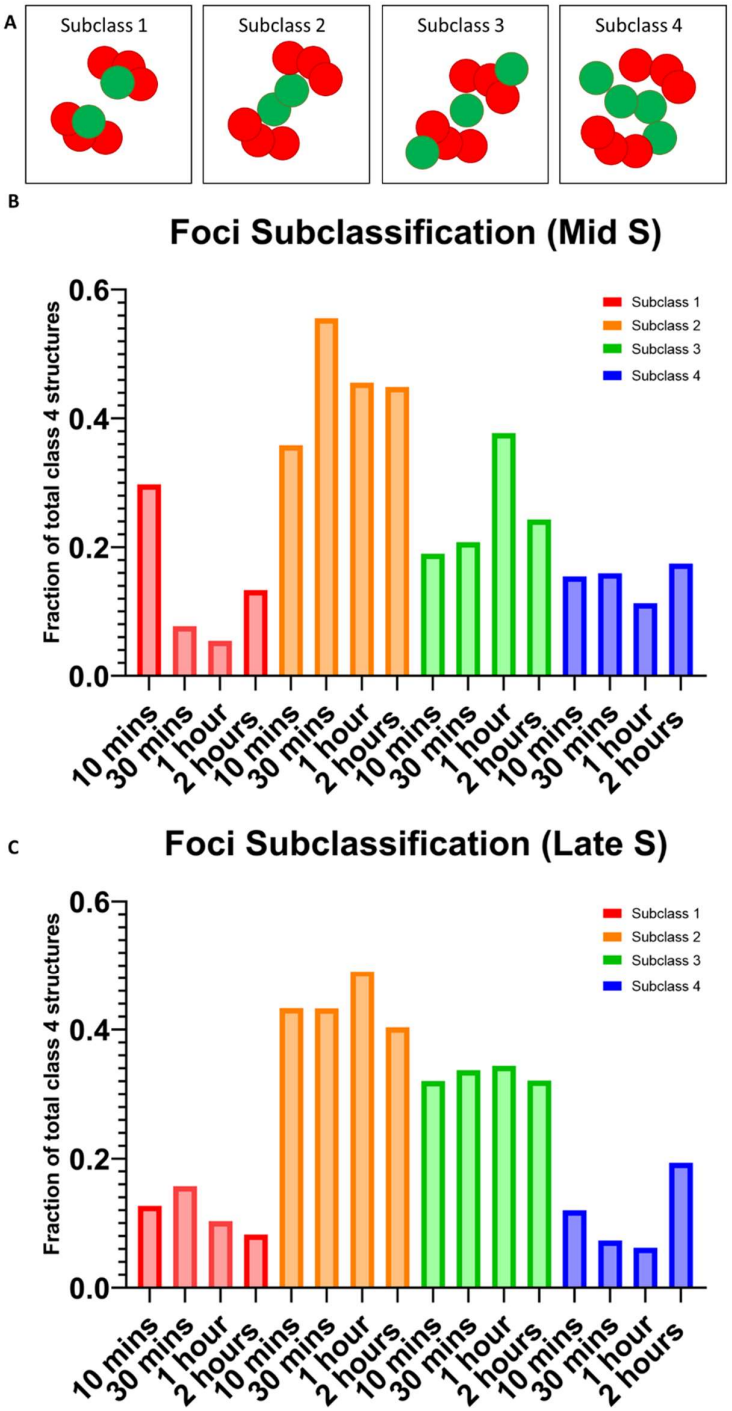

Figure 4.40. Prevalence of class 4 subclasses as a function of recovery time. Class 4 structures from the experiment shown in Figure 4.39 were classified as subclasses 1-4 (Panel A) and their prevalence at each time was plotted as a fraction of the total class 4 structures for mid and late S-phase classified cells (Panel B&C). N=2, a total of 4944 class 4 structures were classified.

In both mid and late S-phase classified cells subclass 2 was the prevalent structure type at each time point. Subclass 2 increased from 10 minutes to 2 hour recovery times. Subclass 3 structures peaked at 1 hour recovery time in mid S-phase classified cells whilst in late S-phase classified cells the prevalence of subclass 3 was comparable at all recovery times. There was no change in the prevalence of subclass 4 structures for each recovery time in both mid and late S-phase cells. Subclass 1 decreased from 10 minutes to 2 hour recovery time in late S-phase cells, whereas in mid S-phase cells subclass 1 increased from 1 hour to 2 hour recovery time. These results indicate there may be some shift in the prevalence of class 4 structures as a function of recovery time, and this may be due to BRCA1 having a multi-faceted role in HR. To corroborate this, cells would additionally be immunostained for proteins within the BRCA1 complexes (described in Section 6.7.1).

4.6 Discussion and Conclusions

Following induction of DSBs, repair proteins undergo highly organised redistribution to form microscopically visible aggregates termed “foci”. It is thought these foci comprise thousands of copies of numerous repair factors (Bekker-Jensen *et al*, 2006). The functional significance of such large accumulations of proteins, spanning mega base pair (Mbp) segments of the genome, is not understood (Schwarz *et al*, 2019). This observation is further confounded by the fact that some factors critical to repair progression only transiently interact at sites of damage. Investigating the structure of repair foci and its functional significance has been an intense area of research.

Confocal microscopy revealed that repair proteins are recruited to sites of damage in a temporally-controlled manner; chromatin-bound repair factors are recruited throughout the cell cycle and ssDNA-bound components are restricted to being recruited during S-phase (Bekker-Jensen *et al*, 2006). It was further observed that ssDNA-bound factors occupy the centre of 53BP1-decorated chromatin. However, it was not possible to complete detailed correlation or exclusion analysis on these structures as confocal microscopes do not have the requisite resolution to observe sub-compartments in repair foci (Reindl *et al*, 2015).

This limitation has been addressed by application of super resolution techniques to circumvent the diffraction limit. Examples include SIM (Chapman *et al*, 2012) and STED microscopy (Reindl *et al*, 2015 & Schwarz *et al*, 2019). The improved resolution offered by these techniques revealed that ssDNA-associated proteins (e.g. BRCA1, CtIP, RPA, RAD51) occupy the internal regions of the decorated chromatin at sites of damage, as structures which have been termed "micro-foci". These proteins are visualised as homogeneous spheres with one intensity maxima (Reindl *et al*, 2015). Chromatin-bound components (e.g. yH2AX, 53BP1) have been described as dense oligomeric structures which possess an internal structure which is thought to be indicative of higher order chromatin folding proximal to the break. These studies have revealed that the structural organisation of repair factors is critical in determining correct repair pathway progression.

Increasing evidence suggests that processing and repair of DSBs depends on characteristics of each individual break, and each repair pathway decision is made independently. It is becoming clear that an understanding of both mechanisms and structures underlying repair pathway choice is necessary to understand the complex network which is the DDR (Schwarz *et al*, 2019). Different types of damaging agents produce different DNA lesions which affects the detection of and accumulation of repair factors at damage sites (Nagy and Soutoglou, 2009).

In this work, we investigated the distribution of 53BP1 and BRCA1 accumulations following irradiation and ExM preparation. Irradiation produces several different DNA lesions including DSBs, purine and pyrimidine lesions and SSBs. Irradiation may also induce clustered damage, where multiple lesions are formed within 1-2 helical turns of the DNA (described in Section 1.4) (Lomax, Folkes & O'Neill, 2013 & Nickoloff *et al*, 2017). Describing BRCA1 and 53BP1 accumulations following irradiation is further complicated by the fact that cell cycle phases have distinct sensitivity and temporal responses to DNA damage (Hui *et al*, 2017). In this work, the authors observed distinct checkpoint dynamics following DSB induction by neocarzinostatin (a radiomimetic drug) in G1, S and G2 phase. The G1 checkpoint induces a complete halt following DSB induction, whilst in

S-phase, the checkpoint dynamics appear to be less sensitive and slows cell cycle progression rather than completely halting it. In G2, the most stringent cell cycle progression halt is observed. The suggestion therefore is that the cell cycle phase in which damage occurs and the response to the damage is distinct between phases. The authors suggest that when damage is detected during S-phase, there is a block late-replicating origins which reduces the chance of stalled replication forks which could collapse. These factors are carefully considered when describing BRCA1 and 53BP1 accumulations throughout this chapter.

To characterise BRCA1 and 53BP1 accumulations throughout S-phase, we firstly confirmed we could accurately discriminate between early, mid and late S-phase nuclei using EdU which forms well characterised patterns of incorporation throughout S-phase. We then investigated 53BP1 and BRCA1 accumulations following irradiation in ExM prepared cells.

In early S-phase nuclei, 53BP1 was visualised as dense accumulations comprised of multiple 53BP1 spots, with little or no BRCA1 association. These structures were heterogeneous in their size and the number of 53BP1 spots observed in each accumulation. The larger structures are consistent with bodies observed in G1 (Zimmerman and de Lange, 2014), whilst the smaller accumulations are more consistent with 53BP1 foci involved in NHEJ. 53BP1 bodies have been shown to form around DNA lesions generated during mitosis when replication is incomplete. 53BP1 bodies are largely processed during replication and are mostly processed at early S-phase, so are not visualised in mid and late S-phase (Fernandez-vidal *et al*, 2017). It is possible the 53BP1 foci formed in early S-phase represent frank DSBs which could be repaired via NHEJ, as suggested by the low enrichment of BRCA1 in these structures. As NHEJ occurs rapidly, these lesions may be resolved in mid-late S-phase cells which, in part, explains the heterogeneity in 53BP1 accumulations through S-phase

In mid-late S-phase classified nuclei, we observed the majority of structures were co-enriched with 53BP1 and BRCA1. In a proportion of these structures, BRCA1 was observed at the core and 53BP1 at the periphery. Further 53BP1 occupied a smaller area than in early S-phase nuclei. These are

consistent with observations of Chapman *et al* that BRCA1 promotes HR initiation by removing 53PB1 to the periphery of repair foci (Chapman *et al*, 2012). This exclusion of 53BP1 by BRCA1 results in a reduction in the overall volume of 53BP1 accumulations in S-phase compared to G1 phase. Interestingly, there was substantial heterogeneity in the structures which has not been previously characterised. This may be due to the different lesions induced by irradiation (Lomax, Folkes & O'Neill, 2013 & Nickoloff *et al*, 2017). In addition to frank DSBs, irradiation also induces single strand breaks and single strand lesions which can exist as clustered sites of damage. The complex nature of these lesions means the efficiency of their repair is reduced, increasing the likelihood of a replication fork colliding with these lesions, causing replication stress and fork collapse to form DSBs which are chemically distinct to those induced directly by irradiation. The cell cycle phase at the time of damage is an important consideration; it may be that accumulations in early S-phase classified nuclei represent frank DSBs which are repaired by NHEJ, whilst the BRCA1 and 53BP1 co-enriched accumulations visualised in mid-late S-phase classified nuclei represent distinct pools of lesions, such as complex DSBs, clustered damage sites and collapsed replication forks which would be repaired via HR, together with base excision repair.

The heterogeneity of 53BP1 and BRCA1 accumulations in mid and late S-phase nuclei were described using a spot detection-based analysis in which we identified five structure classes. Four of the five defined classes were observed to be evenly distributed across mid and late S-phase, and there were no significant changes in the numbers of structures observed in mid and late S-phase classified nuclei. The significance of structure classes were investigated.

We speculated that class 1 structures (defined as BRCA1 alone with no associated 53BP1 within a defined 2 µm radius) may be derived from BRCA1 responses during replication. BRCA1 accumulations were observed in S-phase nuclei in non-irradiated cells, with their numbers increasing from early to late S-phase. We anticipated that if these accumulations relate to replication stress that we would observe a high degree of correlation between EdU and BRCA1

accumulations. Interestingly, we observed that EdU positive BRCA1 accumulations were higher in irradiated cells than in non-irradiated cells. This may indicate an increase in replication associated lesions following irradiation. We additionally investigated 53BP1 and BRCA1 association with EdU in irradiated and non-irradiated cells and found that EdU positive structures were prevalent for all classes in irradiated cells, whereas in non-irradiated cells class 1 and class 2 structures (defined as 53BP1 spot associated with a BRCA1 spot within a 2 µm radius) were comparable in both EdU positive and EdU negative structures. From this we suggest that a proportion of these structures account for endogenous replication stress, but further interrogation is required.

In class 4 structures (defined as multiple BRCA1 and 53BP1 spots with a 2 µm radius), we noted heterogeneous organisation of 53BP1 and BRCA1 spots which we defined into four further sub-classes. It may be these accumulations represent clustered damage sites, or possibly replication forks which have collapsed to form DSBs distinct from prompt DSBs. These changes in relative spatial organisation may also be due to BRCA1 forming functionally distinct complexes during different stages of HR. We observed that subclass 2 (defined as multiple BRCA1 spots encapsulated by multiple 53BP1 spots) was prevalent in mid and late S-phase nuclei after 1 hour recovery time; these results may indicate BRCA1 is associated with the ssDNA region in the majority of class 4 structures at this time. We hypothesised that if the identified class 4 sub-classes are a result of BRCA1 complex composition shift that we might observe a shift in their overall prevalence throughout recovery following damage, therefore we performed a time course.

The prevalence of the five defined structure classes was assessed over 2 hour recovery. Class 2 (defined as one BRCA1 spot associated with one 53BP1 spot) and 5 (defined as one BRCA1 spot encapsulated by multiple 53BP1 spots) structures had a comparable trend; numbers of these structures drop at 30 minutes, increase at 1 hour and then decrease again at 2 hours. Class 4 structures were observed to peak at 30 minutes and progressively decrease at 1 and 2 hours. This

distribution was observed in both mid and late S-phase nuclei, suggesting that the shift in structure prevalence may be dependent on recovery time following damage induction.

We speculated that since class 4 structures are the most prevalent at 10 minutes after damage induction it may be the majority of repair structures adopt this organisation initially. There are comparable numbers of class 4 and class 5 structures at 1 hour, with the majority of class 4 structures being subclass 2 (defined as multiple BRCA1 spots encapsulated by 53BP1). These structures may be associated with resection initiation. A caveat of this experiment, and of ExM methodology, is that these observations were made based on cells fixed at different recovery times, therefore we are not able to describe the progression of repair structure organisation. This would need to be corroborated using live cell studies to follow a single DSB as repair progresses.

We previously suggest that the heterogeneous spatial organisation of 53BP1 and BRCA1 in class 4 repair structures may be indicative of complex damage, or of shifts in BRCA1 complex composition. Since the overall prevalence of these structures is reduced at 2 hours, we suggest that these structures may indeed be reflective of changes to BRCA1 complex composition as opposed to the presence of complex clustered damage inducing replication stress and fork collapse. Changes in the prevalence of class 4 sub-classes was observed at each time point.

BRCA1 binds ubiquitinated histones via RAP80-Abraxas complex and resection is inhibited (Hu *et al*, 2011). This stage may be represented by subclass 1 structures, in which BRCA1 is closely associated with or outside of 53BP1 accumulations. This is consistent with observations of Ochs *et al* (described in Section 1.1.4); the authors described a structural module comprised of 53BP1 and RIF1 which is capable of stabilising chromatin architecture proximal to the break. The localisation of BRCA1 relative to this structure was shown to be inside and outside of the 53BP1/ RIF1 structural module. Abraxas was shown to similarly localise outside of this module. Following loss of RAP80 and a shift in BRCA1 complex composition, resection is initiated and BRCA1 localises proximal to the DNA ends (Hu *et al*, 2011). This event may be correlated with subclass 2 where BRCA1 exists

centrally to the 53BP1 accumulations. It is possible that BRCA1 in this location may be associated with CtIP for resection (Her *et al*, 2016). BRCA1 is also responsible for recruitment of BRCA2 and PALB2 to allow exchange of RPA for RAD51. This localisation pattern may be represented by Subclass 3, where BRCA1 spots exist inside and outside of 53BP1 (Zhang *et al*, 2009 & Nepomuceno *et al*, 2017). These relationships are speculation and further experiments are required to corroborate the changes in BRCA1 complex composition (described in Section 6.7.1). Subclass 2 was the prevalent accumulation within class 4 structures in both mid and late S-phase classified nuclei; these results may indicate BRCA1 is associated with the ssDNA region in the majority of class 4 structures at 1 hour recovery.

The data we present here prompts further questions regarding shifts in BRCA1 complex composition and how this impacts repair progression. It is thought that BRCA1-A complex (Abraxas/ MERIT40/ BRCC36) functions to prevent or limit resection, opening the option it may prevent resection or it may prevent over-resection following action of BRCA1-C complex (Savage & Harkin, 2014). The changes in localisation of BRCA1 at different recovery times supports the idea that different complexes may form at different times and perform different functions, yet the interplay between complexes is as yet unclear (discussed in Section 6.7.1).

Class 5 structures (defined as one BRCA1 spot encapsulated by multiple 53BP1 spots) were reminiscent of the exclusion foci described by Chapman *et al.* In this work, the central BRCA1 was visualised as a spot with a single maximum and 53BP1 appeared as discontinuous spots in a spherical arrangement with a clear separation between 53BP1 and BRCA1 spots. This is in contrast to the previously described structure of 53BP1 forming a continuous oligomeric structure with multiple maxima and minima (Reindl *et al*, 2015). These observations suggest that the previously observed minima of 53BP1 are actual spaces which we are able to resolve using ExM.

The average profiles of class 5 structures showed BRCA1 as a sphere spanning approximately 800 nm diameter, equivalent to 200 nm pre-expansion. 53BP1 was observed to encapsulate the BRCA1

spot, spanning between 2.5-3 µm diameter, equivalent to 625-750 nm pre-expansion. This type of structural organisation of chromatin- and ssDNA-bound components has similarly been reported between 53BP1 and CtIP, RPA and RAD51. It has been suggested that the central 200 nm spots may be representative of regions of resected DNA inside decorated chromatin (Reindl *et al,* 2017). In our work, 53BP1 and BRCA1 were shown to occupy distinct and non-overlapping regions with a void observed between the two proteins. The improved resolution offered by ExM preparation has overcome the insufficient axial resolution of other techniques applied to look at organisation of repair proteins associated with chromatin and ssDNA compartments of DSB repair foci (Chapman *et al*, 2012 & Reindl *et al,* 2015).

In the average class 5 structures, we noted the peak-to-peak distance was larger in late S-phase structures than in mid S-phase structures. This may indicate changes in 53BP1 and BRCA1 accumulations occur in a cell cycle-dependent manner. However, it must be borne in mind that these average structures are generated based on hundreds of individual structures and therefore should be taken as indicative of the behaviour of the selected population of structures. To determine if there are changes in the separation distance between BRCA1 and 53BP1 throughout S-phase, we would ideally perform quantitative investigation of separation between accumulations of both proteins in individual class 5 structures.

There is evidence that 53BP1 and its downstream effectors can inhibit resection and drive repair via NHEJ (Mirman *et al*, 2019). 53BP1 loss is also associated with increased repair via mutagenic SSA; the absence of 53BP1 allows for unrestrained resection and therefore it appears 53BP1 also has a role in ensuring fidelity of HR repair (Ochs *et al*, 2016). 53BP1 is also retained at sites of damage following HR initiation (Reindl *et al*, 2015). It appears that 53BP1 plays a crucial structural role during DSB repair, potentially by stabilising chromatin proximal to sites of damage. These observations, in addition to our observation that 53BP1 adopts a discontinuous structure

encapsulating BRCA1 in class 5 foci structures, lead us to investigate if there is another protein present in the spaces between 53BP1.

Investigation of 53BP1 and RIF1 accumulations in S-phase nuclei following damage induction by irradiation revealed the presence of both proteins as collections of spheres within the same accumulation which were uncorrelated. This result is consistent with observations of Ochs *et al* in which 53BP1 and RIF1 were shown to form a structural module postulated to freeze the chromatin architecture proximal to the break, acting as a shield to protect against unwanted resection (Ochs *et al*, 2019). The authors also suggest that these accumulations, in which RIF1 occupies the intervening space between 53BP1 nano-domains, may allow for concentration of repair factors e.g. Shieldin complex. BRCA1 was observed both within the core and outer regions of the 53BP1 and RIF1 structural module. This together with our observations that BRCA1 has variable localisation within repair structures suggests investigation of relative spatial organisation of 53BP1, BRCA1 and RIF1 as a function of cell cycle phase warrants further investigation.

This chapter has highlighted the structural heterogeneity in BRCA1 and 53BP1 accumulations in S-phase nuclei following irradiation. This structural heterogeneity is complex and may be derived from heterogeneous lesions induced by irradiation, and may be affected by the cell cycle phase in which damage occurs. To further dissect the significance of these accumulations, it would be ideal to use a DNA damaging agent (e.g. endonucleases) which specifically induce DSBs (Nagy and Soutoglou, 2009). Nonetheless, the ability to rapidly image hundreds of structures in 3D with nanoscale resolution has the potential to allow us to dissect the functional significance of repair protein accumulations (discussed in Section 6.7.1).

5. Describing the impact of chromatin regulators on nanoscale organisation of repair proteins

5.1 Introduction

DSBs can be repaired by several mechanisms (Huertas, 2010). The choice of repair mechanism is critical to maximally preserve genomic integrity, meaning that repair pathway choice is highly regulated such that the correct mechanism is selected in the correct cellular context. One of the key determinants in repair pathway progression is the extent of resection at the break site. When initiating NHEJ, 53BP1 binds chromatin proximal to the break, and enables recruitment of RIF1 and downstream effector Shieldin-CST-polα complex (Noordermeer *et al,* 2018 & Mirman *et al*, 2018). These authors showed that the 53BP1 repair axis is responsible for shielding DNA ends against resection by forming a physical block to nucleases, and by enabling fill-in of any resected DNA through the activity of polα. BRCA1 is responsible for driving repair through HR; to allow this, BRCA1 removes the blockade posed by 53BP1 (Her and Bunting, 2018 & Isono *et al*, 2017). How BRCA1 removes this blockade is still not clearly understood. It has been suggested that this is mediated by destabilising the interaction of 53BP1 on the chromatin proximal to the break site.

It is becoming increasingly evident that chromatin architecture and dynamics also play a critical role in this process. The compaction of DNA into chromatin is known to affect repair in an active way. Numerous factors recruited into repair foci are capable of inducing effects on chromatin architecture which have structural and functional effects on damage resolution. During HR initiation, BRCA1-BARD1 E3 ubiquitin ligase activity results in the placement of ubiquitin on H2A (Densham *et al*, 2016). This mark is read by chromatin remodeler, SMARCAD1. Both BRCA1-BARD1 and SMARCAD1 are required to allow remodelling of the nucleosomes, positioning of 53BP1 and resection required to HR commitment. Resected DNA length is also tightly regulated. Chromatin remodelling, 53BP1 repositioning and resection length are restricted by the action of deubiquinating enzyme, USP48 (Uckelmann *et al*, 2018). USP48 is responsible for the removal of

the ubiquitin mark on H2A and therefore limits resection length. It is thought that this action of repressing resection preserves genomic integrity by preventing mutagenic SSA (Section 1.1.2).

The presence of tight regulation at the chromatin level points to chromatin having a pivotal role in repair pathway choice. How chromatin remodelling occurs is poorly understood. Numerous mechanisms of chromatin remodelling have been proposed including nucleosomes sliding, histone recycling and histone eviction (Polo, 2014). Conceptually, the sliding of nucleosomes may be inhibited by upstream nucleosomes, so one might be inclined to think that eviction of histones is a more likely model. However, the idea that nucleosomal eviction may be the primary mechanism of chromatin remodelling is confounded by recent findings which indicate that chromatin undergoes initial compaction around a break site, followed by a subsequent de-compaction of chromatin (Lou *et al*, 2019). The hypothesis here is that the nucleosomes compact to limit the movement of the DNA ends and to allow preparation of the chromatin landscape for modifications required for repair. The de-compaction of local chromatin, described as a "chromatin wave", indicates that chromatin is remodelling to allow resection to occur, resulting chromatin being compacted further away from the break site. Interestingly, there has also been suggestion that the chromatin is being mechanically displaced as the repair machinery spreads at the break site (Shin *et al*, 2018). An understanding of the 3D architecture of chromatin surrounding DSBs would provide an insight into what the structures represent, the reasons for their large scale and the mechanism of remodelling.

Towards this end, we firstly explore the effects of SMARCAD1 and USP48 depletions on organisation of repair proteins within repair foci. The absence of SMARCAD1, similarly to BRCA1, results in a defect in HR initiation which can be relieved by 53BP1 loss (Densham *et al*, 2016). Conversely, loss of USP48 results in hyper-resection and repair through SSA is preferred (Uckelmann *et al*, 2018). We theorised that the increased resolution offered by ExM may allow visualisation of subtle changes in foci compartmentalisation, which would indicate extent of remodelling, and corroborate the biochemical observations on these depletion backgrounds. We

then investigate the spatial relationship between repair proteins and chromatin proximal to the break following depletion of SMARCAD1 and USP48. We hypothesised that by inducing changes in chromatin remodelling, we would visualise changes in chromatin compaction through ExM, and this would extend the spatial mapping of repair sites to include the local chromatin architecture.

5.2 SMARCAD1 activity is required for positioning of 53BP1

SMARCAD1 is crucial to 53BP1 localisation relative to BRCA1 and commitment to HR (Densham *et al*, 2016). Where SMARCAD1 is depleted or lacks the domains required for recognition of the ubiquitin mark on histones, there is a marked reduction in the repositioning of 53BP1 to the periphery of BRCA1-associated foci and in resection. We aimed to determine if SMARCAD1 depletion would influence nanoscale organisation of 53BP1 and BRCA1 accumulations following irradiation.

U2OS cells were depleted of SMARCAD1 using siRNA compared to control siRNA. Depletion was confirmed by western blot (Figure 5.1). U2OS cells were treated with EdU to determine cell cycle phase. Cells were fixed and immunostained for 53BP1 and BRCA1. Images of nuclei in S-phase were acquired to determine efficacy of staining and distributions of foci as a function of cell cycle were quantified (Figure 5.2 & 5.3).

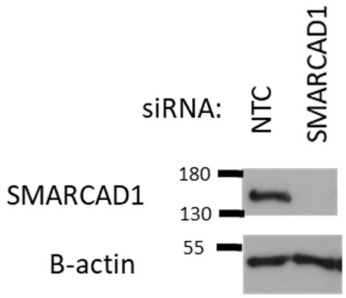

Figure 5.1. SMARCAD1-depletion in U2OS-FlpIn cells. U2OS cells were treated with either siSMARCAD1 or NTC siRNA for 72 hours. Cells were allowed to recover for 1 hour prior to lysis. SMARCAD1 depletion by siRNA was confirmed by western blot probing with the antibodies shown.

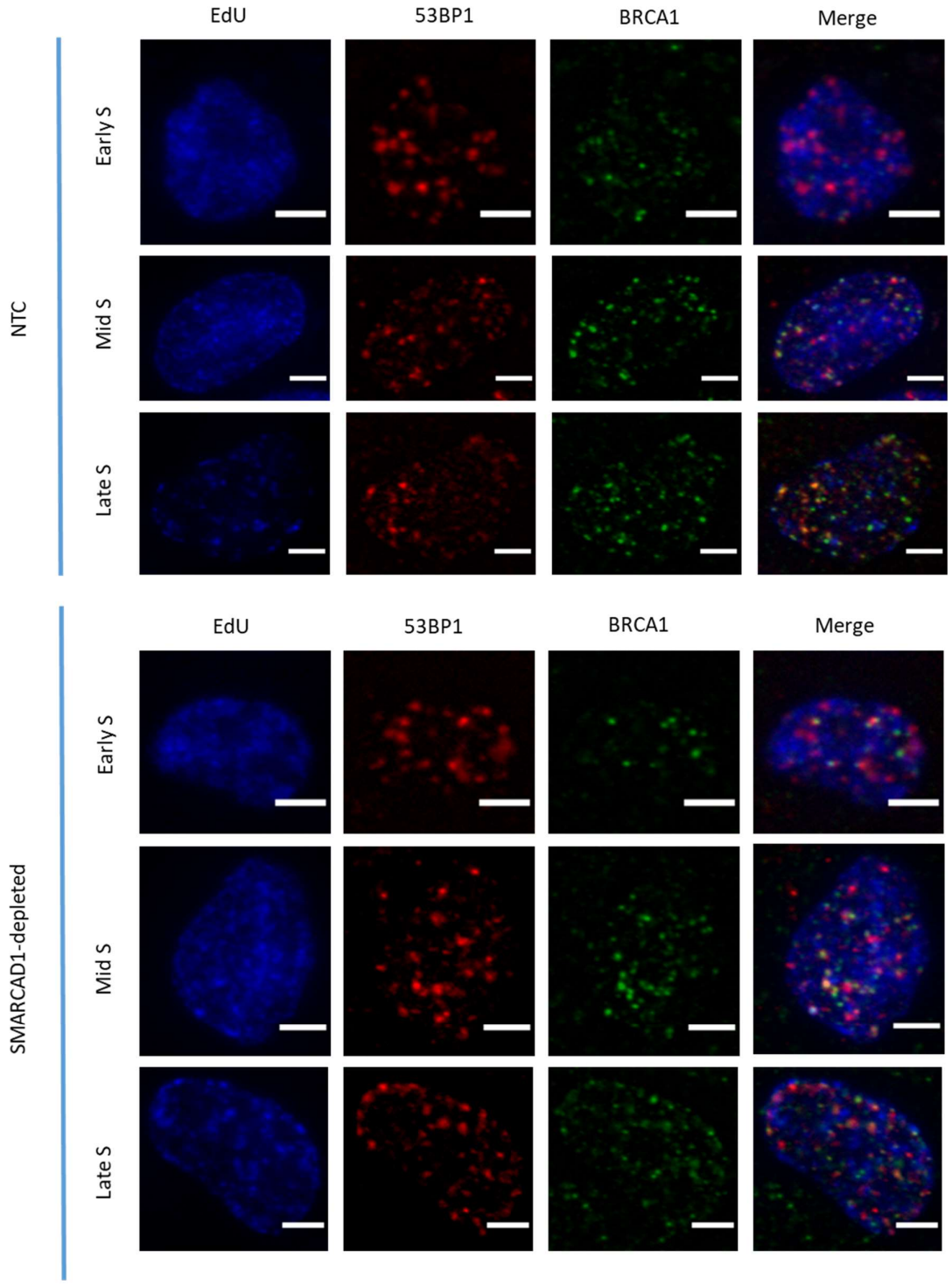

Figure 5.2. Pre-expansion imaging of SMARCAD1-depleted cells. U2OS cells were treated with either siRNA against SMARCAD1 or NTC siRNA for 72 hours. Cells were then treated with EdU and irradiated (2 Gy). Cells were allowed to recover for 1 hour prior to CSK pre-extraction and fixation with 4% PFA. Click-it reaction was completed to visualise the EdU and cells were immunostained for 53BP1 and BRCA1. Scale bar 5 µm.

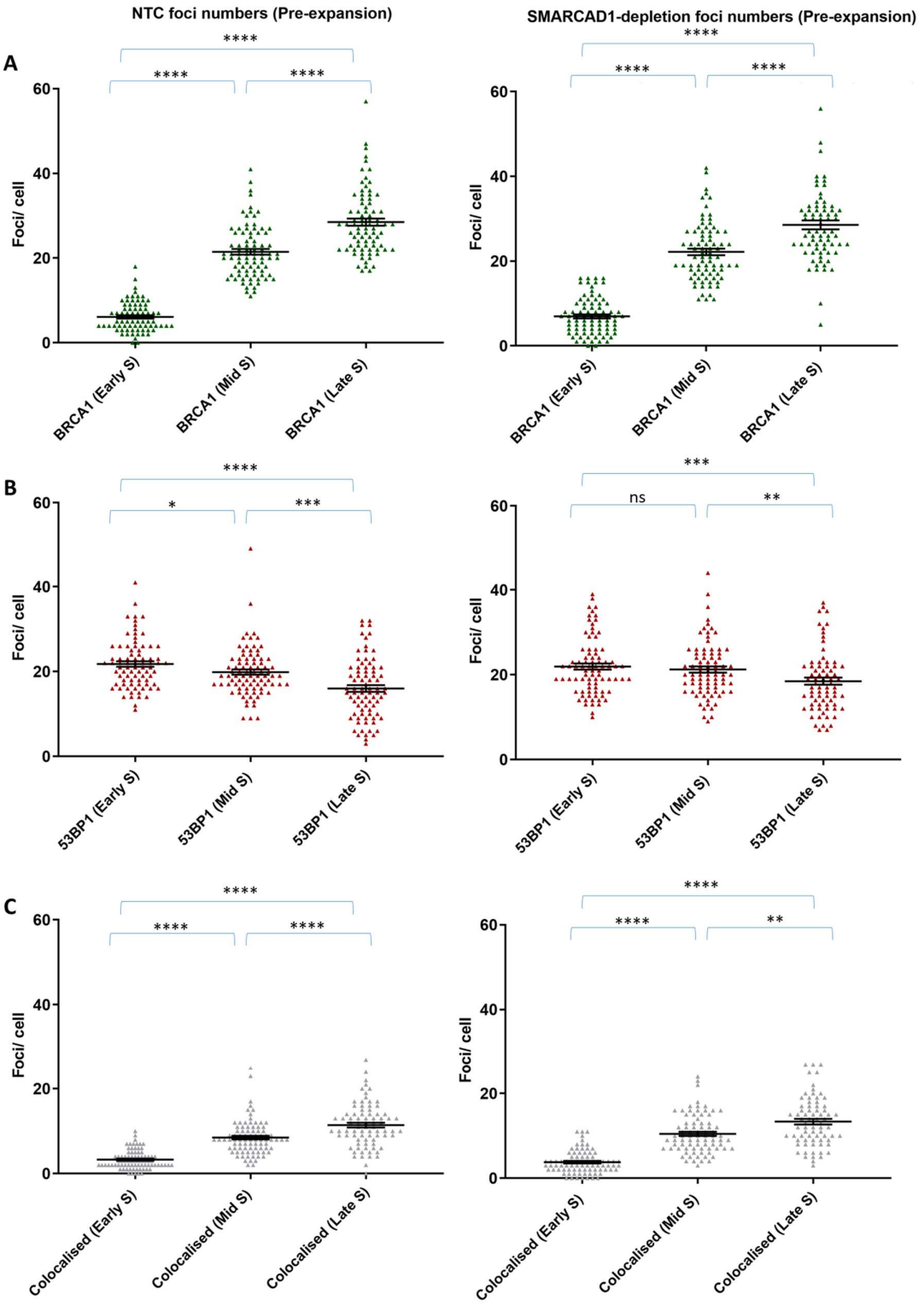
NTC foci numbers (Pre-expansion)
SMARCAD1-depletion foci numbers (Pre-expansion)
A
B
C
Foci/ cell
BRCA1 (Early S)
BRCA1 (Mid S)
BRCA1 (Late S)
53BP1 (Early S)
53BP1 (Mid S)
53BP1 (Late S)
Colocalised (Early S)
Colocalised (Mid S)
Colocalised (Late S)
****
***
**
*
ns

Figure 5.3. Quantifying 53BP1 and BRCA1 foci following SMARCAD1-depletion pre-expansion. Foci quantification was carried out on nuclei treated as in Figure 5.2. Nuclei were classified as early, mid or late S-phase based on EdU staining pattern. Numbers of A) BRCA1, B) 53BP1 and C) colocalised foci were determined for NTC and SMARCAD1-depleted cells. Colocalised foci were defined as those where overlapping pixels were seen between the BRCA1 and 53BP1 channels. **** P<0.001; ***P < 0.005; **P <0.01;*P < 0.05 NS, not significant by two-sided Student's t test. Error = s.e.m.

For quantification of foci, nuclei were classified as early, mid and late S-phase according to EdU incorporation (Figure 5.2). Quantification of foci numbers pre-expansion revealed a comparable distribution of BRCA1, 53BP1 and colocalised foci in SMARCAD1-depleted cells and control cells in which BRCA1 foci numbers were increased from early to late S-phase, whilst 53BP1 foci numbers were observed to decrease from early to late S-phase. The degree of colocalisation between 53BP1 and BRCA1 increased from early to late S-phase (Figure 5.3). These results suggest depletion of SMARCAD1 does not impact overall BRCA1 and 53BP1 foci numbers as a function of cell cycle phase.

Standard ExM protocol was completed on cells depleted of SMARCAD1 compared to control cells following damage induction by irradiation. Cells were immunostained for 53BP1 and BRCA1. Z stacks were acquired post-expansion and deconvolved. Z stacks were organised according to cell cycle position and structures were visually assessed (Figure 5.4) and then scored into one of five classes as in Section 4.3.2 (Figure 5.6).

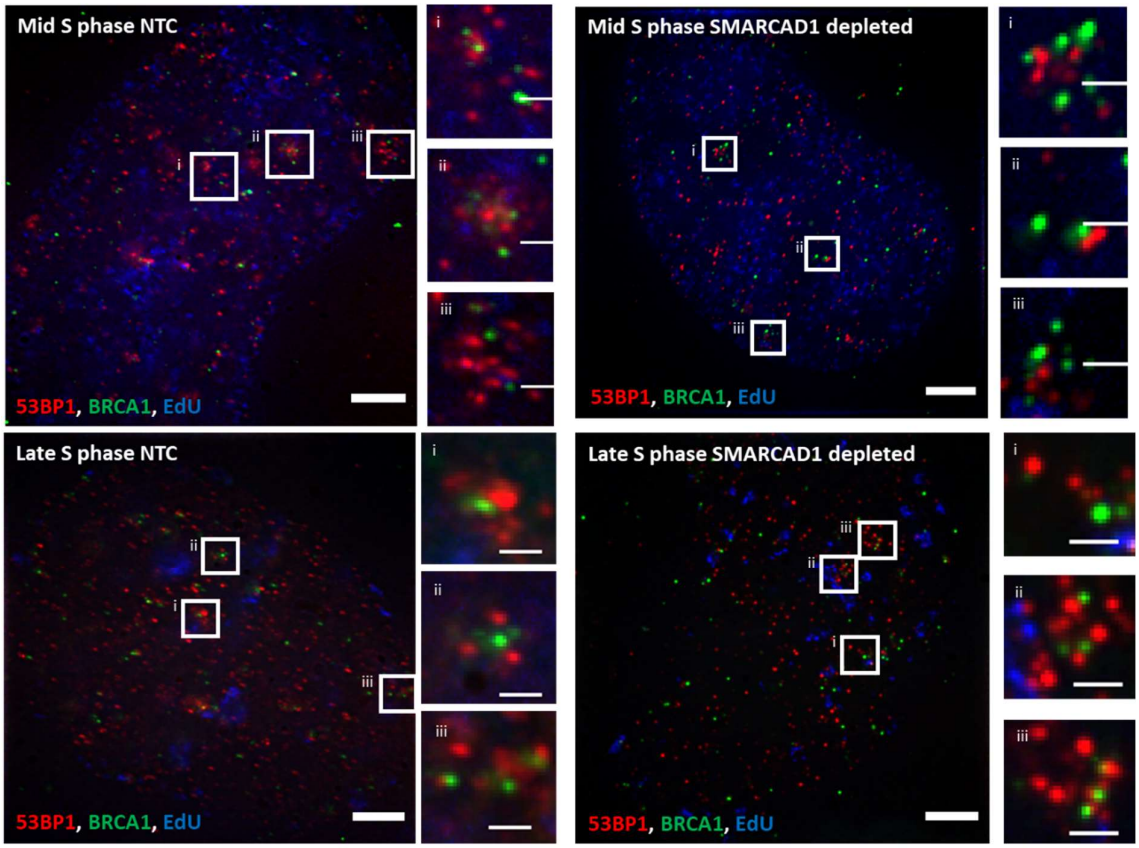

Figure 5.4. Post-expansion imaging of SMARCAD1-depleted cells. Cells were treated as in pre-expansion and standard ExM protocol was performed (Section 2.4). Post-expansion Z stacks were acquired on a widefield microscope and subsequently deconvolved. Representative examples of nuclei for mid and late S-phase cells selected from control and SMARCAD1-depleted cells are shown as maximum intensity Z projections. Scale bars 10 µm and 2 µm on zoomed in sections.

53BP1 and BRCA1 accumulations were classified using classes identified in Section 4.3.2 using spot detection-based analysis as described in Section 4.3.2 and 2.7.5. In a previous report, SMARCAD1-depletion resulted in disruption of 53BP1 repositioning by BRCA1 (Densham *et al*, 2016). With this in mind, the descriptions of classes 4 and 5 were altered to include no or a reduced separation between 53BP1 and BRCA1. I previously defined class 4 structures as multiple BRCA1 spots associated with multiple 53BP1 spots, and class 5 structures as one BRCA1 spot encapsulated by multiple 53BP1 spots (Section 4.3.2). Examples of these classes in control and SMARCAD1-depleted cells are shown in Figure 5.5.

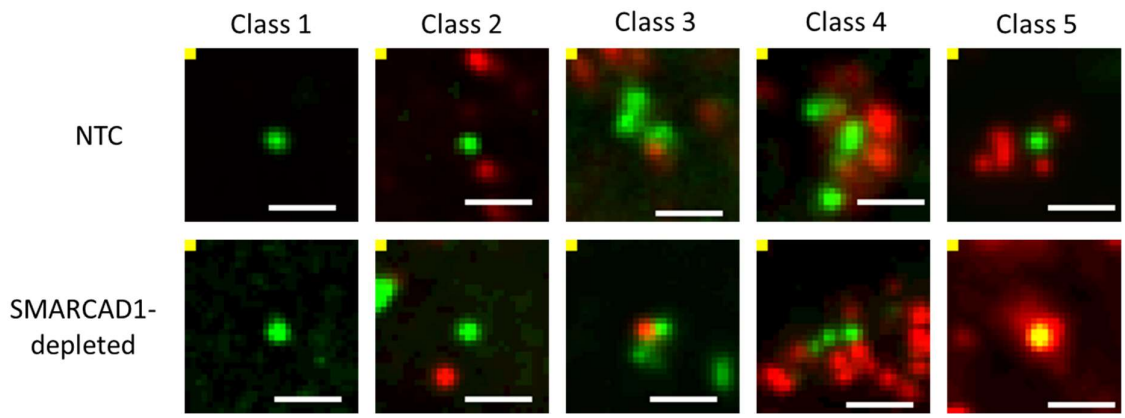

Figure 5.5. Classification of BRCA1 and 53BP1 structures in SMARCAD1-depleted cells. Representative examples of classes 1-5 are shown for NTC and SMARCAD1-depleted cells. Class 1 is defined as BRCA1 alone with no 53BP1 within a 2 µm radius. Class 2 is defined as BRCA1 associated with a 53BP1 spot within a 2 µm radius. Class 3 is multiple BRCA1 spots associated with one 53BP1 spot in a 2 µm radius. Class 4 is defined as multiple BRCA1 spots associated with the same 53BP1 oligomer within a 2 µm radius. Class 5 is one BRCA1 spot encapsulated by multiple 53BP1 spots within a 2 µm radius. Scale bars 2 µm.

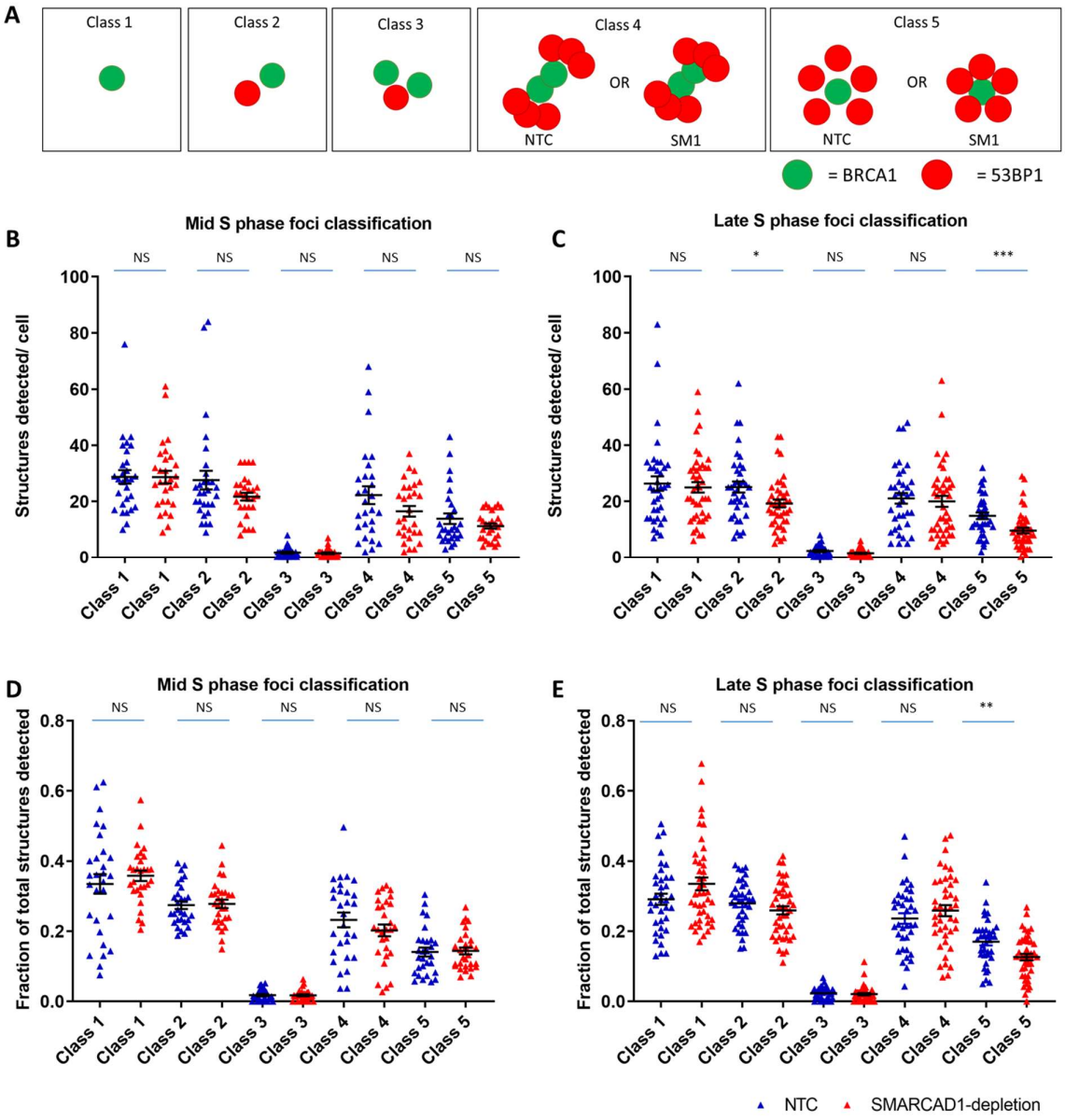

Figure 5.6. Classifying BRCA1 and 53BP1 structures in SMARCAD1-depleted cells. Spot detection-based analysis was performed on Z stack data acquired in control and SMARCAD1-depleted cells. Structures were scored for nuclei in mid and late S-phase according to the identified classes shown schematically (Panel A). Structure classification is shown as total numbers of each structure detected (Panel B&C) and as a fraction of structures detected per nucleus (Panel D&E). Control data is shown in blue and SMARCAD1-depleted data is shown in red. N=3, >20 nuclei per sample. Throughout Figure, **** P<0.001; ***P < 0.005; **P <0.01;*P < 0.05 NS, not significant by two-sided Student's t test. Error = s.e.m.

The example images of SMARCAD1-depleted cells show a visual reduction in the overall amount of 53BP1 compared to control cells (Figure 5.4). Structure classification (Figure 5.6) revealed no

difference in distribution of classes in mid S-phase cells. In late S-phase cells, structure classification showed a decrease in class 5 structures (defined as one BRCA1 spot encapsulated by multiple 53BP1 spots) in the SMARCAD1-depleted cells compared to control cells. Following this observation, the overall distribution of 53BP1 relative to BRCA1 in class 5 structures was investigated in control and SMARCAD1-depleted cells. Examples of class 5 structures were selected where 53BP1 and BRCA1 spots were oriented parallel to the focal plane. Average class 5 structures were generated using a Matlab script written by Dr Jeremy Pike (detailed in Section 2.7.6) (Figure 5.7). These profiles were further evaluated in 3D (Figure 5.8).

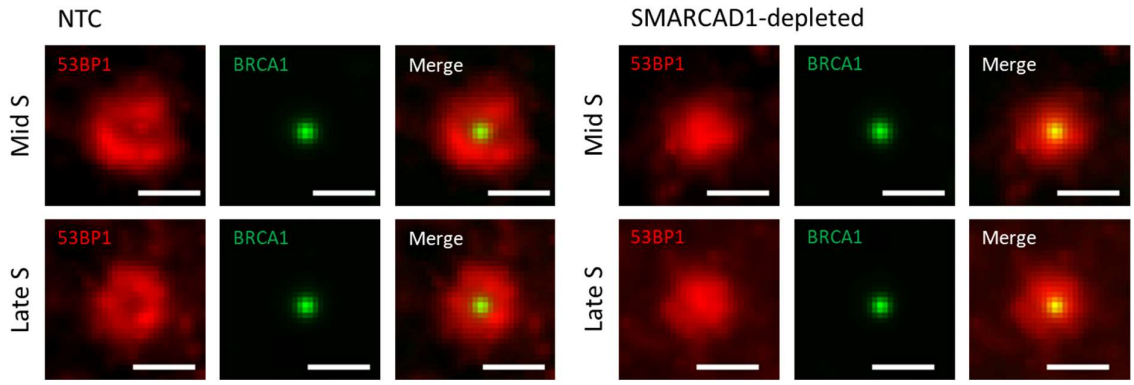

Figure 5.7. Investigating class 5 structure distributions in SMARCAD1-depleted cells. Class 5 structures where 53BP1 and BRCA1 were parallel to the focal plane were selected. Intensity of BRCA1 and 53BP1 across examples was averaged to give the final profiles shown as maximum intensity projections. Example structures were selected from three independent experiments. NTC mid S =143 structures, NTC late S = 184 structures, SMARCAD1-depleted mid S = 164 structures and SMARCAD1-depleted late S = 221 structures. Scale bar 2 µm.

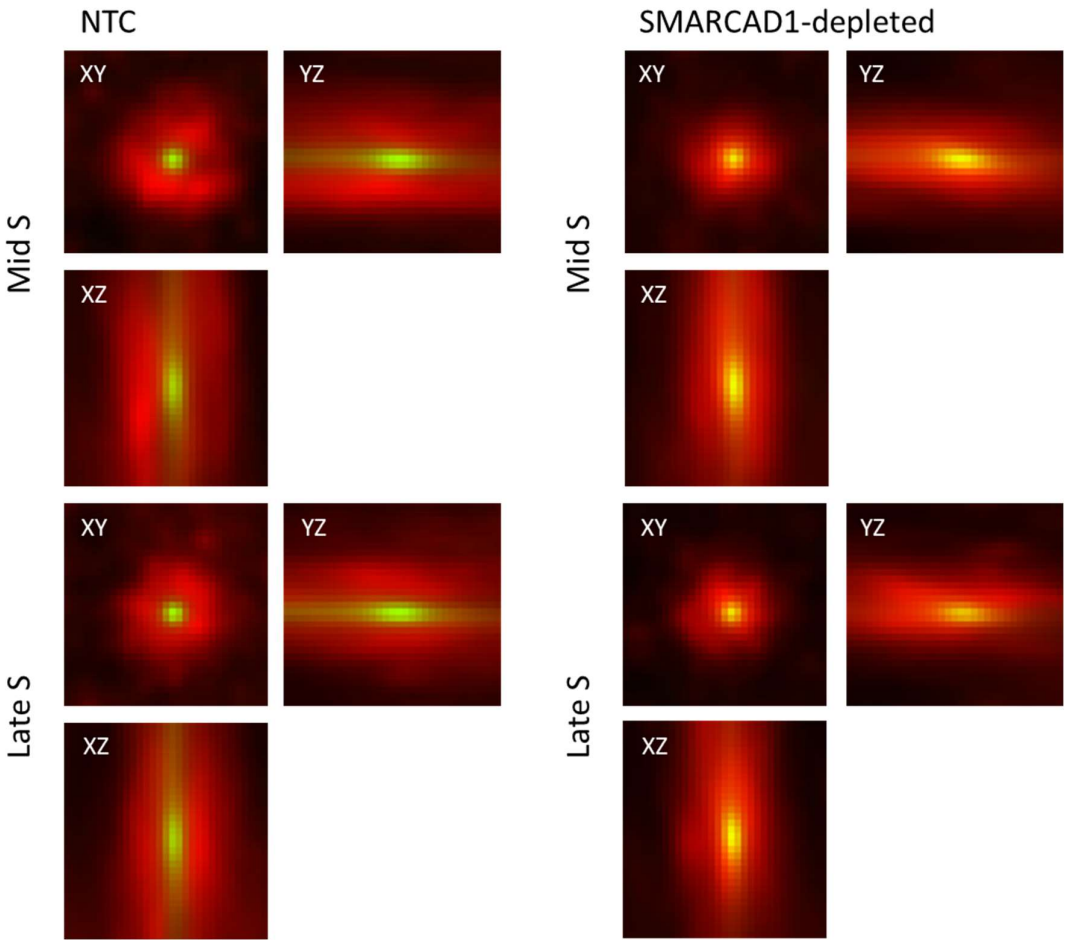

Figure 5.8. Investigating class 5 structure distributions in SMARCAD1-depleted cells. To complement the maximum intensity projections shown in Figure 5.7, orthogonal views of class 5 structure profiles are shown for mid and late S-phase cells treated with either control or SMARCAD1 siRNA. Example structures were selected from three independent experiments. NTC mid S =143 structures, NTC late S = 184 structures, SMARCAD1-depleted mid S = 164 structures and SMARCAD1-depleted late S = 221 structures.

To summarise the distributions of 53BP1 and BRCA1 on average, an average radial profile was generated using a Matlab script written by Dr Jeremy Pike (Figure 5.10) (detailed method in Section 2.7.6). This was determined from multiple radii drawn from the centre of the BRCA1 spot (illustrated in Figure 5.9).

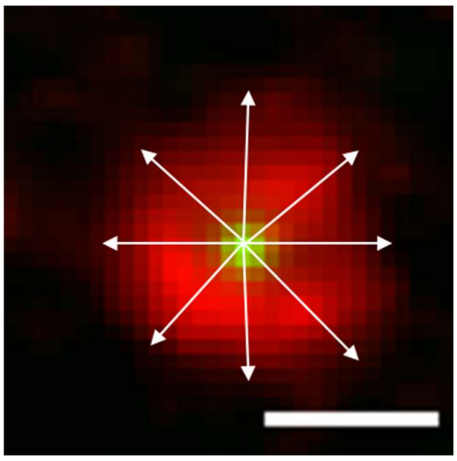

Figure 5.9. Generation of average radial profile. Multiple radial measurements are performed (each indicated by a white arrow) on the central slice of the averaged profiles. The radii are averaged together to give an overall distribution of the relationship between 53BP1 and BRCA1 intensities in average foci profiles. Scale bar 2 µm.

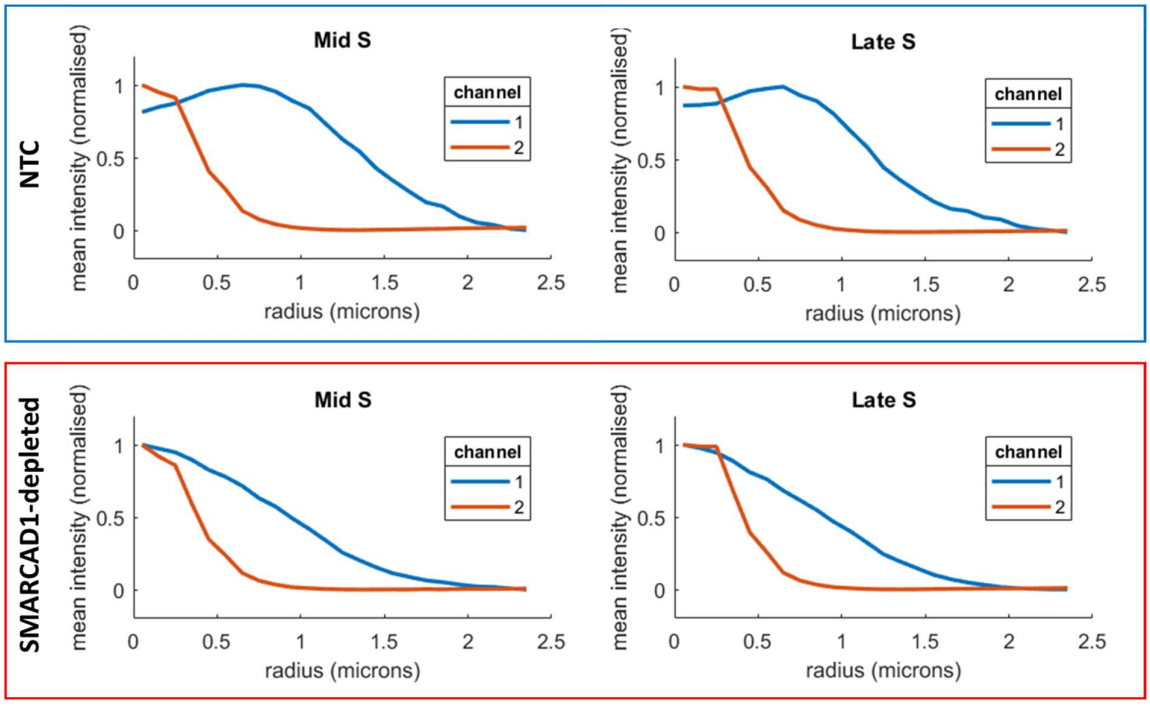

Figure 5.10. Profiling class 5 structures in SMARCAD1 depleted cells. Radial profiles for NTC and SMARCAD1-depleted cells are shown. These profiles were generated by drawing multiple radii from the centre of the BRCA1 spot in average class 5 structures as illustrated in Figure 5.9. Channel 1 represents 53BP1 (blue) and channel 2 represents BRCA1 (red). Plots are based on N=3, NTC mid S =143 structures, NTC late S = 184 structures, SMARCAD1-depleted mid S = 164 structures and SMARCAD1-depleted late S = 221 structures.

Investigation of class 5 structures in SMARCAD1-depleted cells compared to control cells revealed changes in the relative spatial organisation of 53BP1 and BRCA1 accumulations (Figure 5.7 & 5.8). In the control cells, BRCA1 is encapsulated by 53BP1 with a void between the two proteins. In SMARCAD1-depleted cells, 53BP1 occupies a smaller volume and the void between 53BP1 and BRCA1 is absent. These observations are recapitulated in the mean intensity profiles of 53BP1 and BRCA1 (Figure 5.10). In the control cells, 53BP1 maximum intensity is at ~0.75 microns (~0.188 microns pre-expansion) from the BRCA1 centre, while in SMARCAD1-depleted cells, 53BP1 and BRCA1 have comparable maximum intensities.

To quantify changes in protein distributions, we calculated Pearson's and Mander's correlation coefficients (Figure 5.11) (Dunn *et al*, 2011). Pearson's correlation coefficient (PCC) (detailed in Sections 2.7.6 & 3.3.2) measures pixel-by-pixel covariance between two channels. Its values range from 1 to -1, indicating perfect linear correlation and inverse correlation between the two channels, respectively. PCC subtracts the mean intensity of the image from each pixel value so is unaffected by signal levels and signal offset.

Mander's correlation coefficient (MCC) is another commonly applied measure of colocalisation which is sensitive to co-occurrence of signal regardless of signal level (detailed in Section 2.7.6). This is because the mean intensity of the image is not subtracted from each pixel, in contrast to PCC. MCC values range from 0 (anti-correlated) to 1 (correlated). The result of MCC quantification is two values: M1 and M2. These values correspond to the fractional overlap of channel 1 to channel 2, and vice versa.

Upon SMARCAD1 depletion, there was an increase in PCC values for both mid and late S-phase structures compared to controls, indicating an increased correlation between 53BP1 and BRCA1 in averaged class 5 structure profiles. Similarly, there was an increase in M2 values following SMARCAD1 depletion which indicates more BRCA1 pixels also contain intensity from the 53BP1 channel than in the control profiles.

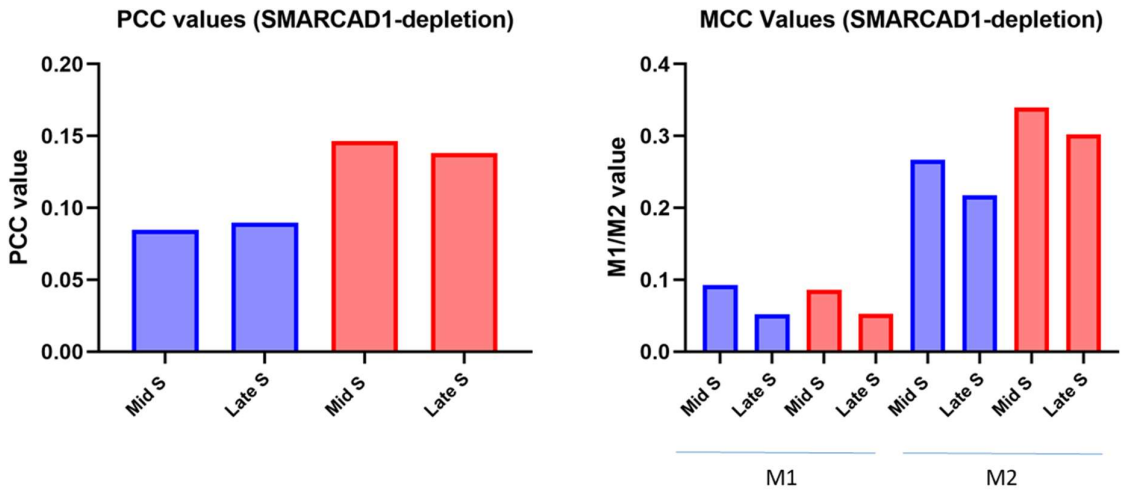

Figure 5.11. Summary of correlation between 53BP1 and BRCA1 in SMARCAD1-depleted cells. PCC and MMC values were calculated from the average profiles of class 5 structures in SMARCAD1-depleted cells compared to controls. Control values are shown in blue and SMARCAD1-depleted values are shown in red.

Further interrogation of class 5 structures revealed further heterogeneity in 53BP1 positioning relative to the core BRCA1 spot, which we described as a reduced separation distance (defined as a separation distance of <0.5 µm) or a control separation distance (defined as a separation of ~1.8-2 µm). All class 5 structures in SMARCAD1-depleted and control cells were classified under these definitions to determine their overall prevalence (Figure 5.12) Average structure and intensity profiles for BRCA1 and 53BP1 in each condition were generated (Appendix Figure 13-16).

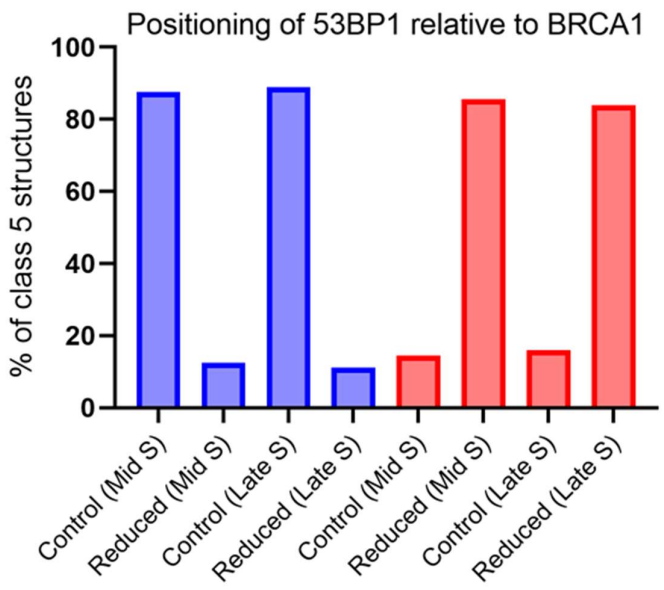

Figure 5.12. Sub-classifying class 5 structures based on positioning of 53BP1 relative to BRCA1. The total class 5 structures from nuclei scored in Figure 5.6 were classified as having a control or reduced separation distance between 53BP1 and the core BRCA1 spot in cells depleted of SMARCAD1 (red) compared to control cells (blue). N=3; total structures NTC mid S = 360 structures, NTC late S = 469 structures, SMARCAD1-depleted mid S = 298 structures and SMARCAD1-depleted late S = 311 structures.

In SMARCAD1-depleted cells, we observed that >80% of class 5 structures from mid and late S-phase classified nuclei had a reduced distance. By contrast, in control cells >80% of class 5 structures had a control separation distance (Figure 5.12). This is consistent with the idea that depletion of SMARCAD1 results in reduced positioning of 53BP1 relative to BRCA1. These data collectively suggest that depletion of SMARCAD1 disrupts the positioning of 53BP1 to the periphery of repair foci during mid and late S-phase of the cell cycle, further corroborating the idea that a lack of chromatin remodelling proximal to the repair site affects spatial organisation of 53BP1 and BRCA1 accumulations.

In chapter 4 we confirmed that a clear boundary can be visualised between 53BP1 and BRCA1 in class 5 structures (Section 4.4.3). Here, we reproduced this distribution in control cells, but also showcase the advantages of applying ExM; we demonstrate a capability to detect subtle changes

in placement of 53BP1 relative to BRCA1 in SMARCAD1-depleted cells. By applying spot detection-based analysis for classification of structures and generation of intensity profiles based on hundreds of features, we are able to quantitatively describe the impact of SMARCAD1-depletion on a significant number of repair structures.

5.3 USP48-depletion increases 53BP1 repositioning relative to BRCA1

Ubiquitin specific protease-48 (USP48) has been identified as a H2A specific deubiquitinating enzyme (DUB). USP48 antagonises the BRCA1 E3 ubiquitin ligase function (Uckelmann *et al*, 2018). In BRCA1-proficient cells USP48 depletion results in 53BP1 being positioned further from the break site, and extended resection lengths. USP48 is thought to promote genomic stability by antagonising BRCA1-BARD1 E3 ubiquitin ligase activity and preventing hyper-resection. As 53BP1 was observed to be positioned further away relative to BRCA1 in USP48-depleted cells, the impact of USP48-depletion on foci sub-compartmentalisation was investigated.

U2OS cells were depleted of USP48 using siRNA compared to control siRNA (Figure 5.13). Images were acquired pre-expansion (Figure 5.14) to determine efficacy of staining and distributions of foci as a function of cell cycle. Numbers of BRCA1, 53BP1 and colocalised foci were determined in nuclei classified as early, mid and late S-phase (Figure 5.15). Z stacks were acquired post-expansion and deconvolved. Z stacks were organised according to cell cycle position and foci were visually assessed (Figure 5.16) and then scored into one of five classes as in Sections 4.3.2 (Figure 5.18).

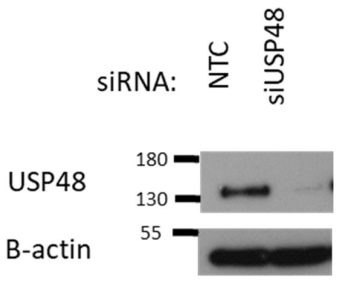

Figure 5.13. USP48-depletion in U2OS Flp-In cells. U2OS cells were treated with either siUSP48 or NTC siRNA for 72 hours. Cells were allowed 1 hour to recover prior to lysis. USP48 depletion by siRNA was confirmed by western blot probing with the antibodies shown.

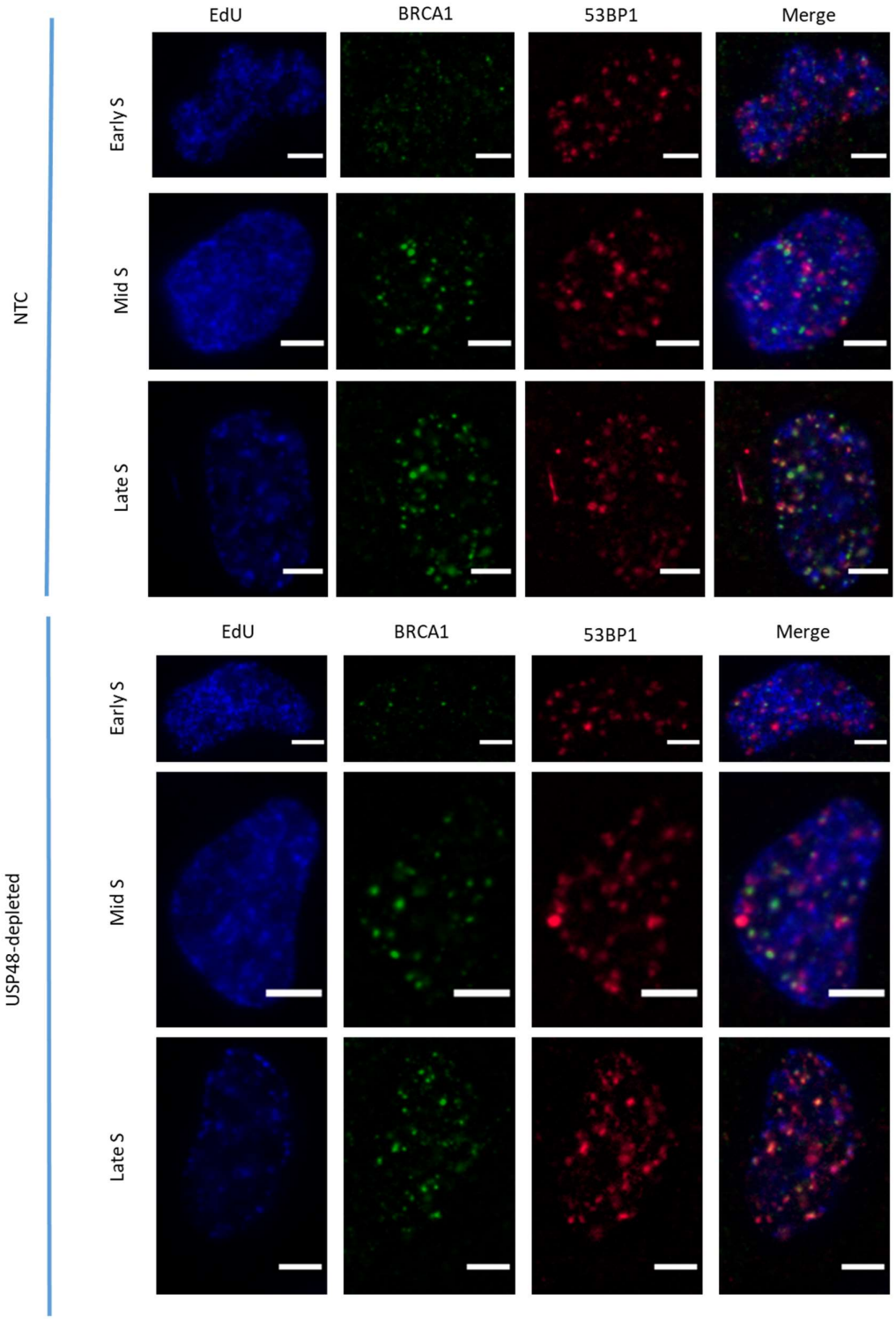

Figure 5.14. Pre-expansion imaging of USP48-depleted cells. U2OS cells were treated with either NTC or USP48 siRNA for 72 hours. Cells were then treated with EdU and irradiated (2 Gy). Cells were allowed to recover for 1 hour prior to CSK pre-extraction and fixation with 4% PFA. Click-it reaction was completed to visualise the EdU and cells were immunostained for 53BP1 and BRCA1. Scale bar 5 µm.

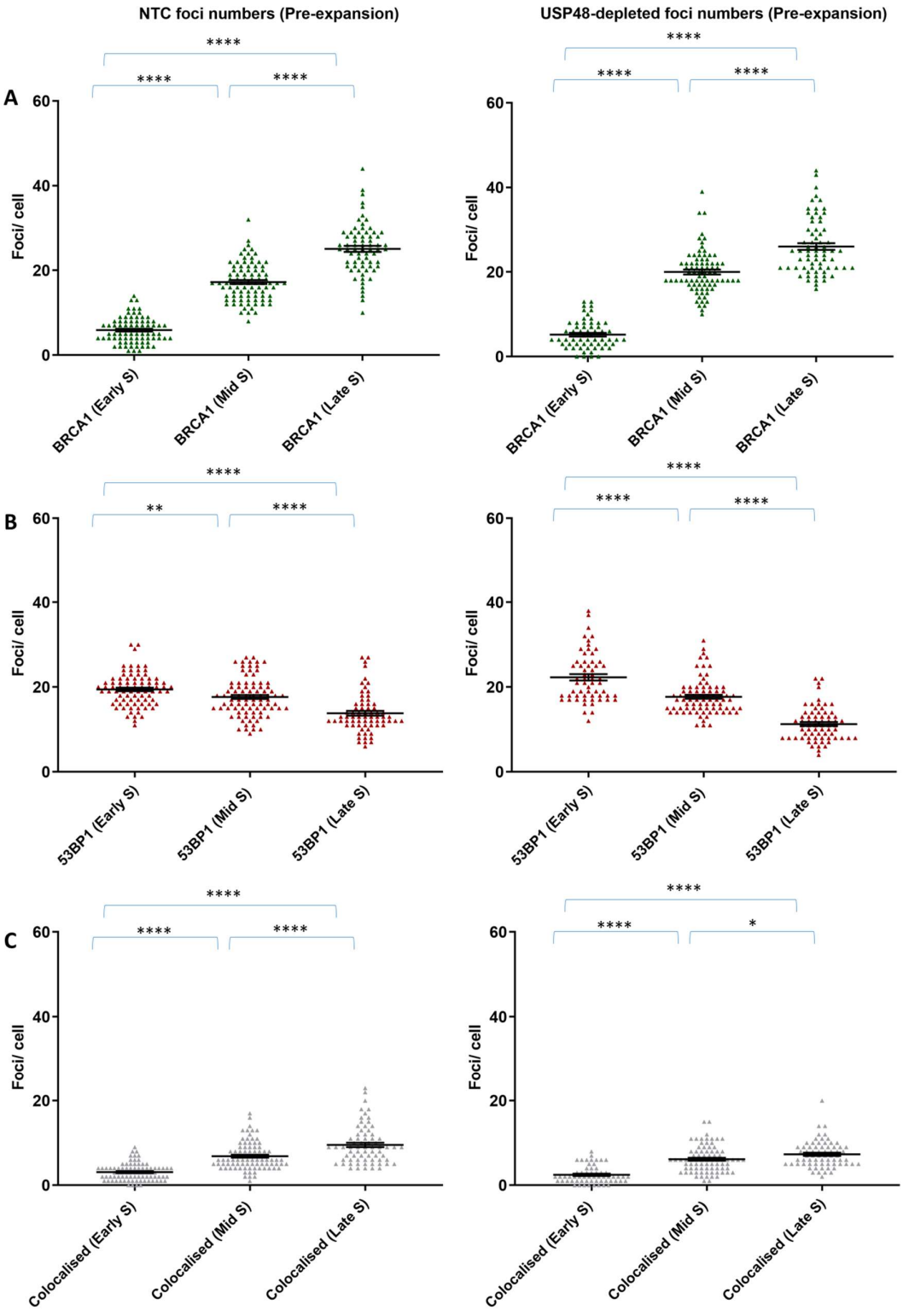
NTC foci numbers (Pre-expansion)
USP48-depleted foci numbers (Pre-expansion)
A
B
C
Foci/ cell
0
20
40
60
****
**
*
BRCA1 (Early S)
BRCA1 (Mid S)
BRCA1 (Late S)
53BP1 (Early S)
53BP1 (Mid S)
53BP1 (Late S)
Colocalised (Early S)
Colocalised (Mid S)
Colocalised (Late S)

Figure 5.15. Quantifying foci numbers following USP48-depletion pre-expansion. Foci quantification was carried out on nuclei treated as in Figure 5.15. Nuclei were classified as early, mid or late S-phase based on EdU staining pattern. Numbers of A) BRCA1, B) 53BP1 and C) colocalised foci were determined for NTC and USP48-depleted cells. Colocalised foci were defined as those where overlapping pixels were seen between the BRCA1 and 53BP1 channels. **** P<0.001; ***P < 0.005; **P <0.01;*P < 0.05 NS, not significant by two-sided Student's t test. Error = s.e.m.

BRCA1, 53BP1 and colocalised foci were quantified in nuclei classified as early, mid and late S-phase in USP48-depleted cells compared to control cells (Figure 5.15). Comparable numbers of foci were present in USP48-depleted and control cells. BRCA1 foci numbers were increased from early to late S-phase, whilst 53BP1 foci numbers decreased from early to late S-phase. The degree of colocalisation between 53BP1 and BRCA1 increased from early to late S-phase. These results suggest depletion of USP48 does not impact overall BRCA1 and 53BP1 foci numbers as a function of cell cycle phase.

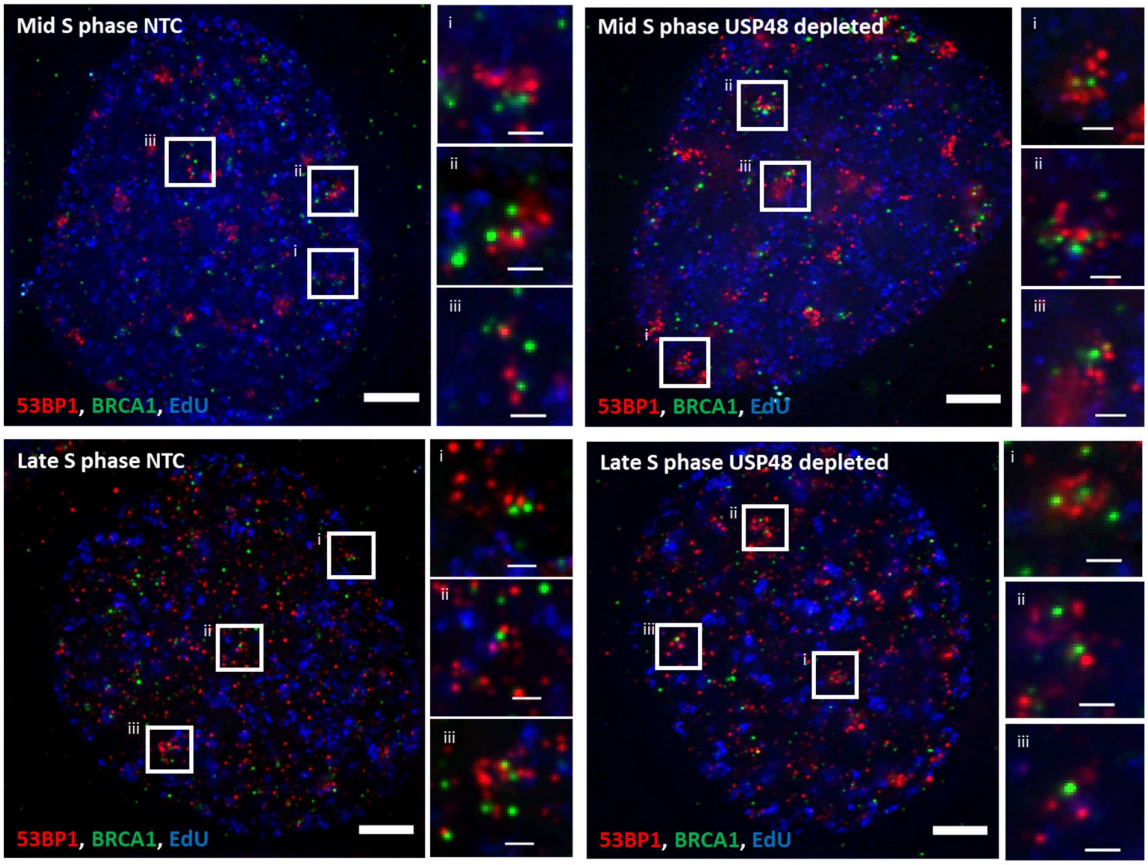

Figure 5.16. Post-expansion imaging of USP48-depleted cells. Cells were treated as in pre-expansion and standard ExM protocol was performed (Section 2.4). Post-expansion Z stacks were acquired on a widefield microscope and deconvolved. Representative examples of nuclei for mid and late S-phase cells selected from control and USP48 depleted cells are shown as maximum intensity Z projections. Scale bars 10 µm and 2 µm on zoomed in sections.

In post-expansion images of USP48-depleted cells we observed an increased amount of 53BP1 in the nucleus compared to control cells, and some structures had an increased spacing between 53BP1 and BRCA1. Additionally, in USP48-depleted cells in late S-phase, some 53BP1 foci appear to adopt an oligomeric arrangement, typically seen in mid S-phase in control cells (Figure 5.16). For consistency structures were scored under the same classes as identified in Section 4.3.2. Previous work showed that USP48-depletion results in further positioning of 53BP1 relative to BRCA1 due to uncontrolled chromatin remodelling by action of SMARCAD1. Uckelmann *et al* observed that following USP48 depletion 53BP1 accumulations have a larger spread (1.1 µm compared to 0.8 µm controls), and the hole at foci core is larger (peak-to-peak distance of 0.5 µm compared to 0.3 µm in controls). With these observations in mind, the analysis radius to describe the relationship between BRCA1 and 53BP1 in class 4 and class 5 structures was increased from 2 µm to 2.8 µm (estimated based on change in peak-to-peak distance of 0.2µm pre-expansion x 4-fold expansion factor). Examples of structures are shown (Figure 5.17).

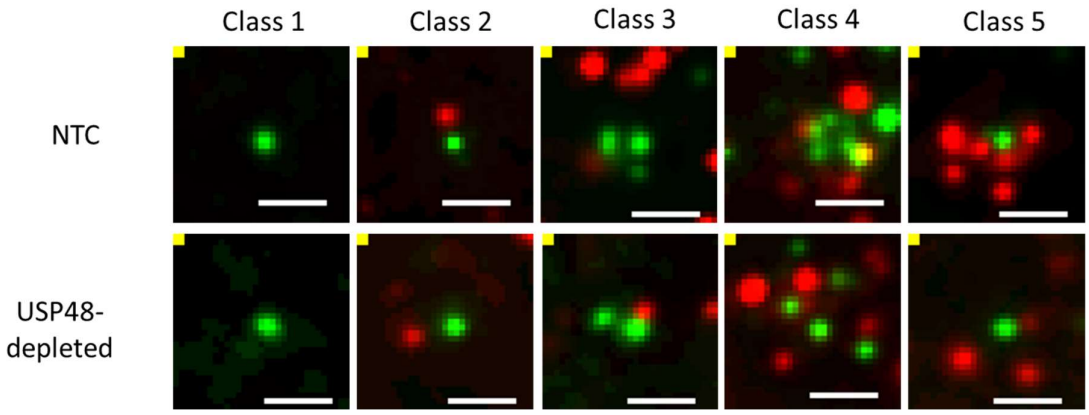

Figure 5.17. **Classification of BRCA1 and 53BP1 accumulations in USP48-depleted cells.** Representative examples of classes 1-5 are shown for NTC and USP48-depleted cells. Class 1 is defined as BRCA1 alone with no 53BP1 within a 2 µm radius. Class 2 is defined as BRCA1 associated with a 53BP1 spot within a 2 µm radius. Class 3 is multiple BRCA1 spots associated with one 53BP1 spot in a 2 µm radius. Class 4 is defined as multiple BRCA1 spots associated with the same 53BP1 oligomer. Class 5 is one BRCA1 spot associated with multiple 53BP1. In the USP48-depleted cells, the radius for class 4 and 5 foci has been increased to 2.8 µm.

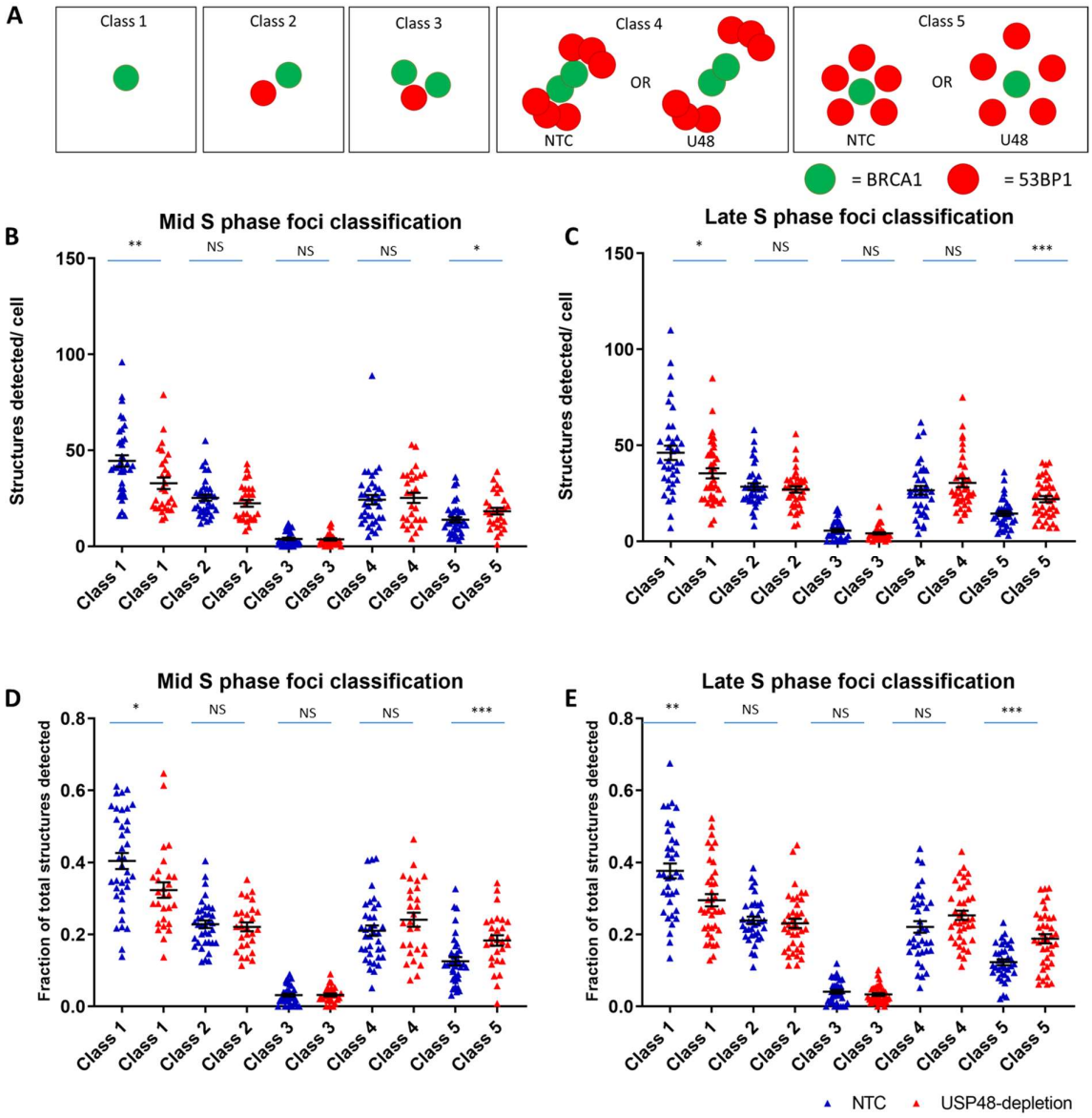

Figure 5.18. Classifying BRCA1 and 53BP1 accumulations in USP48-depleted cells. Spot detection based analysis was performed on Z stack data acquired in control and USP48 depleted cells. Structures were classified for nuclei in mid and late S-phase according to the identified classes shown schematically (Panel A). Structure classification is shown as total numbers of each structure detected per nucleus (Panel B&C) and as a fraction of structures detected per nucleus (Panel D&E). Control data is shown in blue and USP48-depleted data is shown in red. N=3, >20 nuclei per sample. Throughout Figure, **** P<0.001; ***P < 0.005; **P <0.01;*P < 0.05 NS, not significant by two-sided Student's t test. Error = s.e.m.

Following USP48 depletion, 53BP1 and BRCA1 accumulations were classified using spot detection-based analysis as described in Sections 4.3.2 and 2.7.5 (Figure 5.18). There was an increase in class

5 structures in both mid and late S-phase cells. We opted to do a detailed analysis of this structure class in control cells compared to USP48-depleted cells. Examples of class 5 structures were selected where both proteins were oriented parallel to the focal plane. Average profiles of class 5 structures were generated using a Matlab script written by Dr Jeremy Pike (detailed in Section 2.7.6) (Figure 5.19). These profiles were further evaluated in 3D (Figure 5.20).

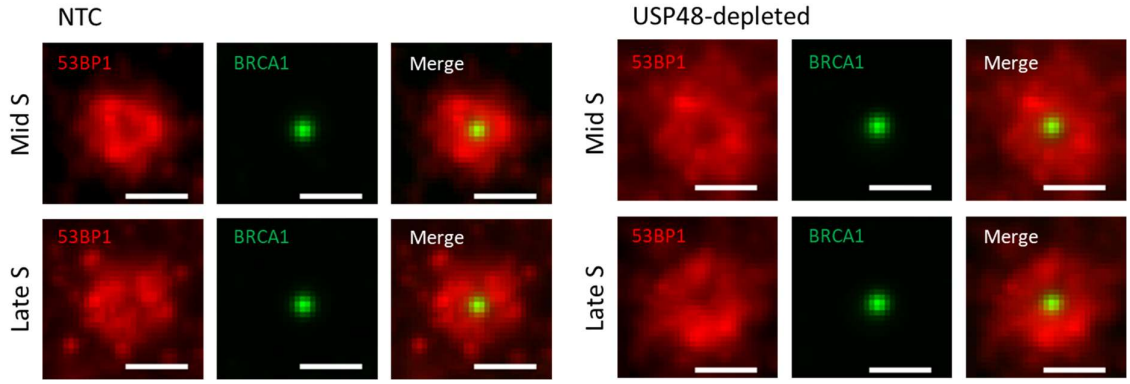

Figure 5.19. Investigating class 5 structure distributions in USP48-depleted cells. Class 5 structures where 53BP1 and BRCA1 were parallel to the focal plane were selected from experiment summarised in Figure 5.18. Intensity of BRCA1 and 53BP1 across examples was averaged to give the profiles shown as maximum intensity projections. Example structures were selected from three independent experiments. NTC mid S = 72 structures, NTC late S = 77 structures, USP48-depleted mid S = 93 structures and USP48-depleted late S = 135 structures. Scale bar 2 µm.

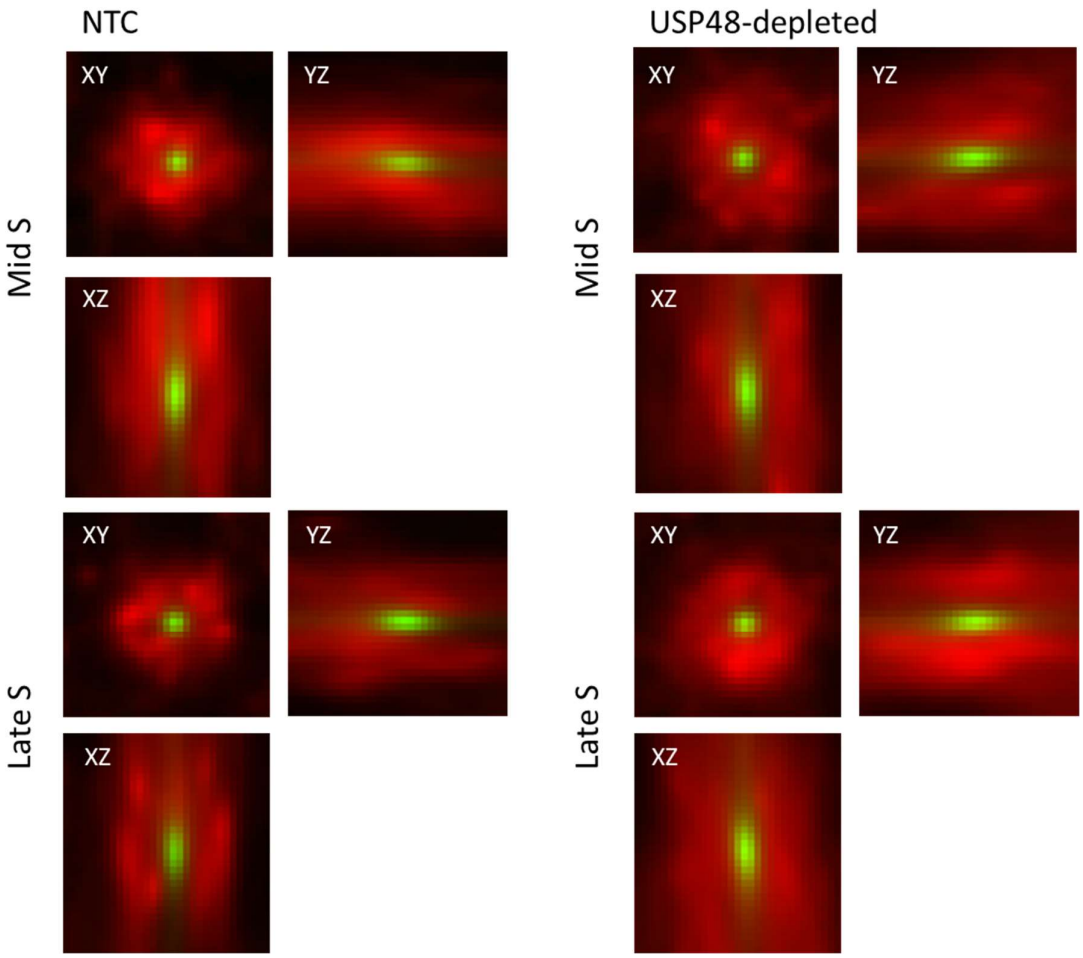

Figure 5.20. Investigating class 5 structure distributions on USP48-depleted cells. To complement the maximum intensity projections shown in Figure 5.19, orthogonal views of class 5 structure profiles are shown for mid and late S-phase cells treated with either NTC or USP48 siRNA. NTC mid S = 72 structures, NTC late S = 77 structures, USP48-depleted mid S = 93 structures and USP48-depleted late S = 135 structures.

To summarise the distributions of 53BP1 and BRCA1 in USP48 depleted and control cells, average radial profile of class 5 structures were generated using a Matlab script written by Dr Jeremy Pike (Figure 5.21) (detailed method in Section 2.7.6).

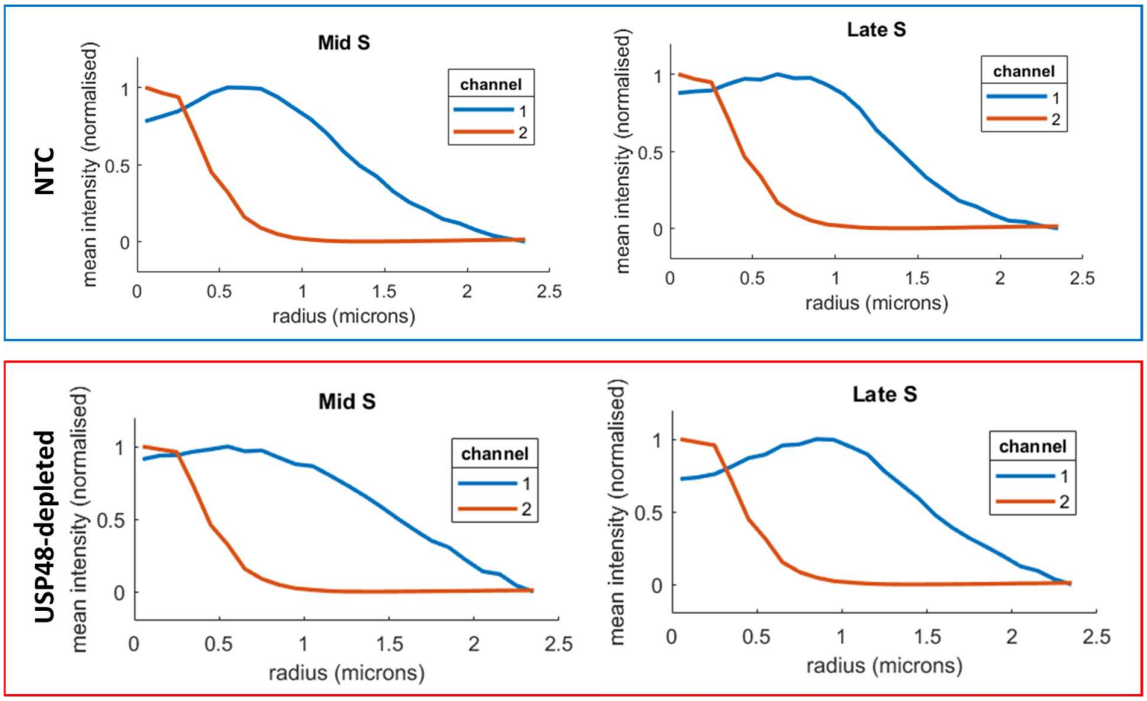

Figure 5.21. **Profiling class 5 foci in USP48 depleted cells.** Radial profiles for NTC and USP48-depleted cells are shown. These profiles were generated by drawing multiple radii from the centre of the BRCA1 spot in average class 5 structures as illustrated in Figure 5.9. . Channel 1 represents 53BP1 (blue) and channel 2 represents BRCA1 (red). Profiles based on N=1, NTC mid S = 72 structures, NTC late S = 77 structures, USP48-depleted mid S = 93 structures and USP48-depleted late S = 135 structures. Scale bar 2µm.

Investigation of class 5 structures in USP48-depleted cells compared to control cells revealed differences in organisation (Figure 5.19 & 5.20). In the USP48-depleted cells, we visualised an increase in the size of the void between 53BP1 and BRCA1. This is consistent with work from Uckelmann *et al*, which reported the depletion of USP48 results in further repositioning of 53BP1 from the break site. The mean intensity profiles confirm this change in organisation, with the 53BP1 maxima further from the BRCA1 centre in USP48-depleted cells as compared to control cells (Figure 5.21). Notably, the intensity profile for 53BP1 has a less appreciable peak in these examples, which could be due to heterogeneity in the location of 53BP1 relative to BRCA1 throughout chosen examples (described in Figure 5.23).

To quantify changes in 53BP1 accumulations, we measured Pearson's and Mander's correlation coefficients (Figure 5.22) (detailed in Section 2.7.6 & 5.2). PCC values decreased following USP48 depletion in mid and late S-phase nuclei as compared to control cells, suggesting the overlap between 53BP1 and BRCA1 is further reduced. M1 values were not significantly different. M2 values for mid S-phase nuclei were lower in USP48-depleted cells as compared to controls, whilst the opposite was observed in late S-phase nuclei. Overall, these data suggest the correlation of 53BP1 with BRCA1 is reduced following USP48-depletion.

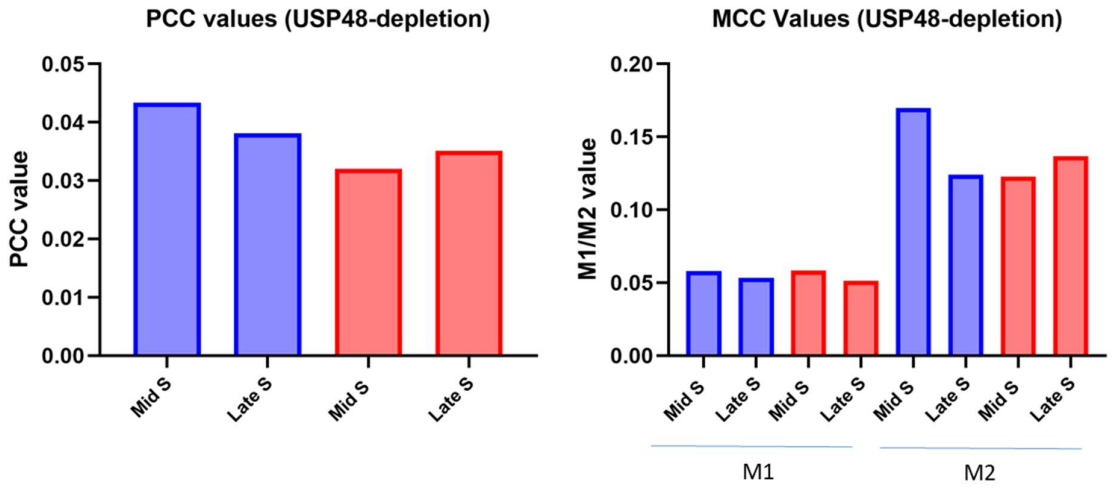

Figure 5.22. **Summary of correlation between 53BP1 and BRCA1 in USP48-depleted cells.** PCC and MMC values were calculated from the average profiles of class 5 structures in USP48-depleted cells compared to controls. Control values are shown in blue and USP48-depletion values are shown in red.

We observed heterogeneous spacing between 53BP1 and the core BRCA1 spot in USP48-depleted cells which we described as increased separation distance (defined as a separation distance of ~2-2.8 µm) or a control separation distance of ~1.8-2 µm). All class 5 structure in USP48 depleted and control cells were classified using these definitions to determine their overall prevalence (Figure 5.23). Average structure and intensity profiles were generated for each condition (Appendix Figures A17-A20).

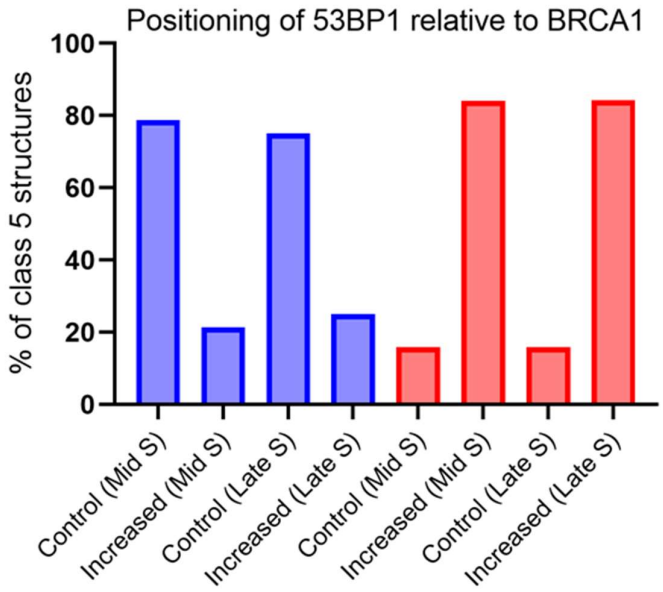

Figure 5.23. Sub-classifying class 5 structures based on positioning of 53BP1 relative to BRCA1. All class 5 structures from nuclei scored in Figure 5.18 were classified as having a control or increased separation distance between 53BP1 and BRCA1 in cells depleted of USP48 (red) compared to control cells (blue). N=3; total structures NTC mid S = 414 structures, NTC late S = 384 structures, USP48-depleted mid S = 404 structures and USP48-depleted late S = 609 structures.

In USP48-depleted cells, >80% of class 5 structures had an increased separation distance, whilst in the control cells >70% of class 5 structures had a control separation distance. These data are consistent with USP48-depletion causing in an increased repositioning of 53BP1 relative to BRCA1 due to unchecked chromatin remodelling driven by BRCA1-BARD1 E3 ubiquitin ligase and SMARCAD1. As in the case of SMARCAD1-depletion, applying ExM to investigate the impact of USP48-depletion on placement of 53BP1 relative to BRCA1 has allowed us to better define boundaries between subcompartments of repair foci. Further, by applying a spot detection-based analysis and intensity profiling of structures, we can quantitatively describe how depletion of USP48 impacts 53BP1 positioning on a significant number of structures. The resolution of ExM together with the nanoscale analysis of repair structures revealed subtle heterogeneity in foci sub-compartmentalisation which have not been previously seen.

To summarise the effects of depleting SMARCAD1 (Section 5.2) and USP48 (Section 5.3), average class 5 structures for SMARCAD1-depleted, USP48-depleted and control (NTC) cells are shown (Figure 5.24). To generate these structures, class 5 foci in which BRCA1 and 53BP1 were oriented parallel with the focal plane were selected and combined to form an average structure. Line profiles were generated for each average class 5 structure.

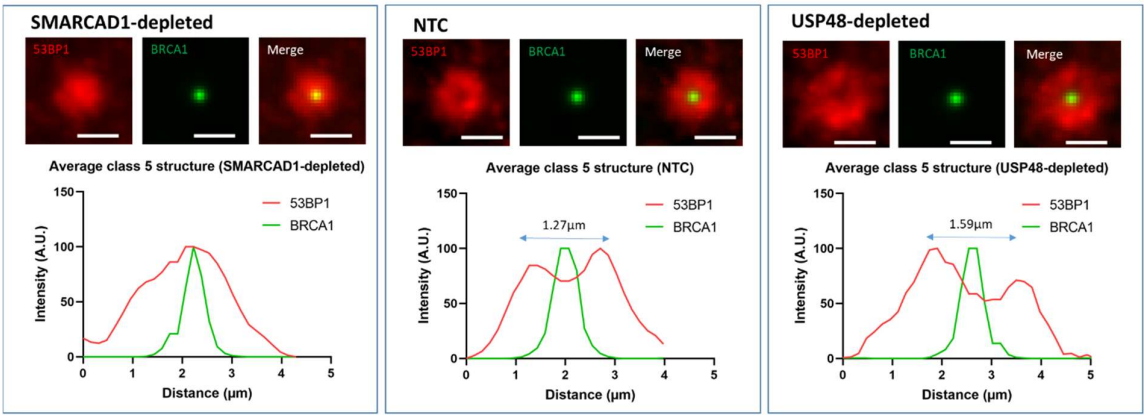

Figure 5.24. Summarising the effect of SMARCAD1- and USP48-depletion on class 5 structure organisation. Class 5 structures in late S-phase classified nuclei where BRCA1 and 53BP1 were oriented parallel to the focal plane were selected for SMARCAD1-depleted, USP48-depleted and control (NTC) cells. These structures were combined to generate an average intensity profile of class 5 structures on each background. Line profiles were generated for each condition. Each average profile is based on structures from three repeats. NTC = 184 structures, SMARCAD1-depleted = 221 structures and USP48-depleted = 135 structures. Scale bar 2 µm.

In the control class 5 structure, BRCA1 is visualised as a central spot with single intensity maxima and is encapsulated by 53BP1. A void between BRCA1 and 53BP1 was observed in the control structure and is recapitulated in the intensity profile where 53BP1 peak-to-peak distance was 1.27 µm (equivalent to 0.317 µm pre-expansion). In contrast, the void between 53BP1 and BRCA1 is absent in cells depleted of SMARCAD1 as indicated by the intensity profile where 53BP1 and BRCA1 have comparable intensity maxima. In USP48-depleted class 5 structure, the observable void between 53BP1 and BRCA1 is larger, with a 53BP1 peak-to-peak distance of 1.59 µm (equivalent to 0.397 µm pre-expansion). These changes in foci sub-compartmentalisation are likely related to the chromatin architecture surrounding the break site (explored in Section 5.4).

5.3.1 RAD51 recruitment is increased following USP48-depletion

Depletion of USP48 results in increased positioning of 53BP1 relative to BRCA1, and increased DNA resection. These events are dependent on the activity of BRCA1-BARD1 and SMARCAD1. In USP48-depleted cells there is an increased use of HR and SSA, promoted by RAD51 and RAD52,

respectively. These observations suggest that USP48 plays a role in fine-tuning resection lengths to prevent mutagenic SSA (Uckelmann *et al*, 2018 & Densham and Morris, 2019). Uckelmann *et al* observed increased numbers of RAD51 foci with increased intensity following USP48 depletion, together with increased DNA track lengths measured by BrdU. We hypothesised that the increased recruitment of RAD51 and increased resection lengths in USP48-depleted cells could be visualised using ExM.

To investigate this, cells were treated as in Section 5.3. Cells were immunostained for 53BP1 and RAD51. We opted to investigate RAD51 and 53BP1 alone initially, under the hypothesis we would visualise an increased amount of RAD51, or continuous RAD51 structures encapsulated by 53BP1 with an increased peak-to-peak distance in USP48 depleted cells compared to controls. This was due to the observation that 53BP1 has an increased spread and peak-to-peak distance surrounding BRCA1 (as shown in Figure 5.24), and we theorise that the increased void represents increased ssDNA-containing compartment of foci which is subsequently coated by RAD51. Images were acquired pre-expansion (Figure 5.25) and foci numbers were quantified as a function of cell cycle (Figure 5.26). ExM preparation was completed and post-expansion Z stacks were acquired and deconvolved (Figure 5.28). Classification of structures was carried out similarly to BRCA1 and 53BP1 using spot detection-based analysis (Figure 5.29 & 5.30).

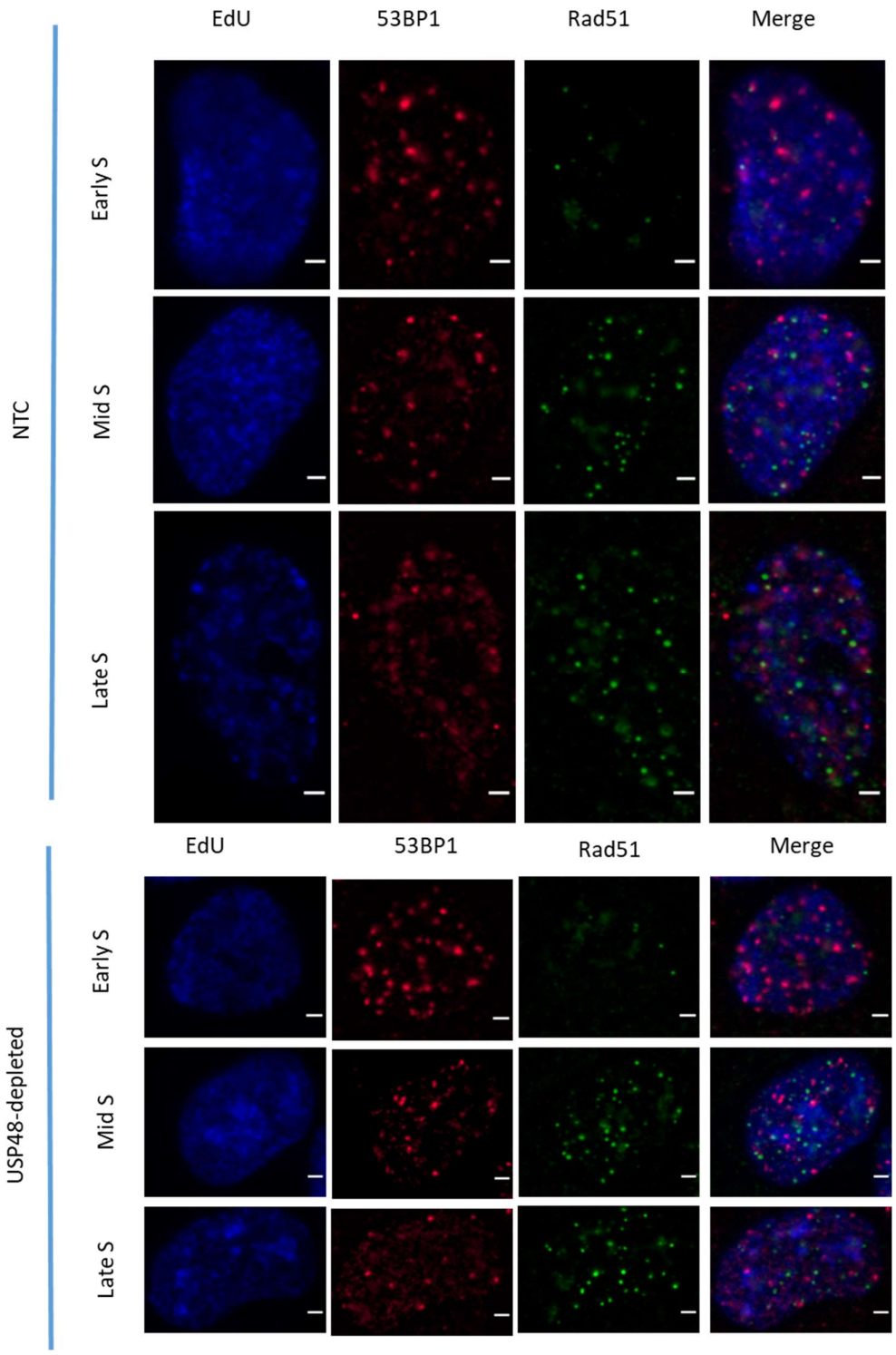

Figure 5.25. **Pre-expansion imaging of USP48-depleted cells**. U2OS cells were treated with either NTC or USP48 siRNA for 72 hours. Cells were then treated with EdU and irradiated (2 Gy). Cells were allowed to recover for 1 hour prior to CSK pre-extraction and fixation with 4% PFA. Click-it reaction was completed to visualise the EdU and cells were immunostained for 53BP1 and RAD51. Scale bar 2.5 µm.

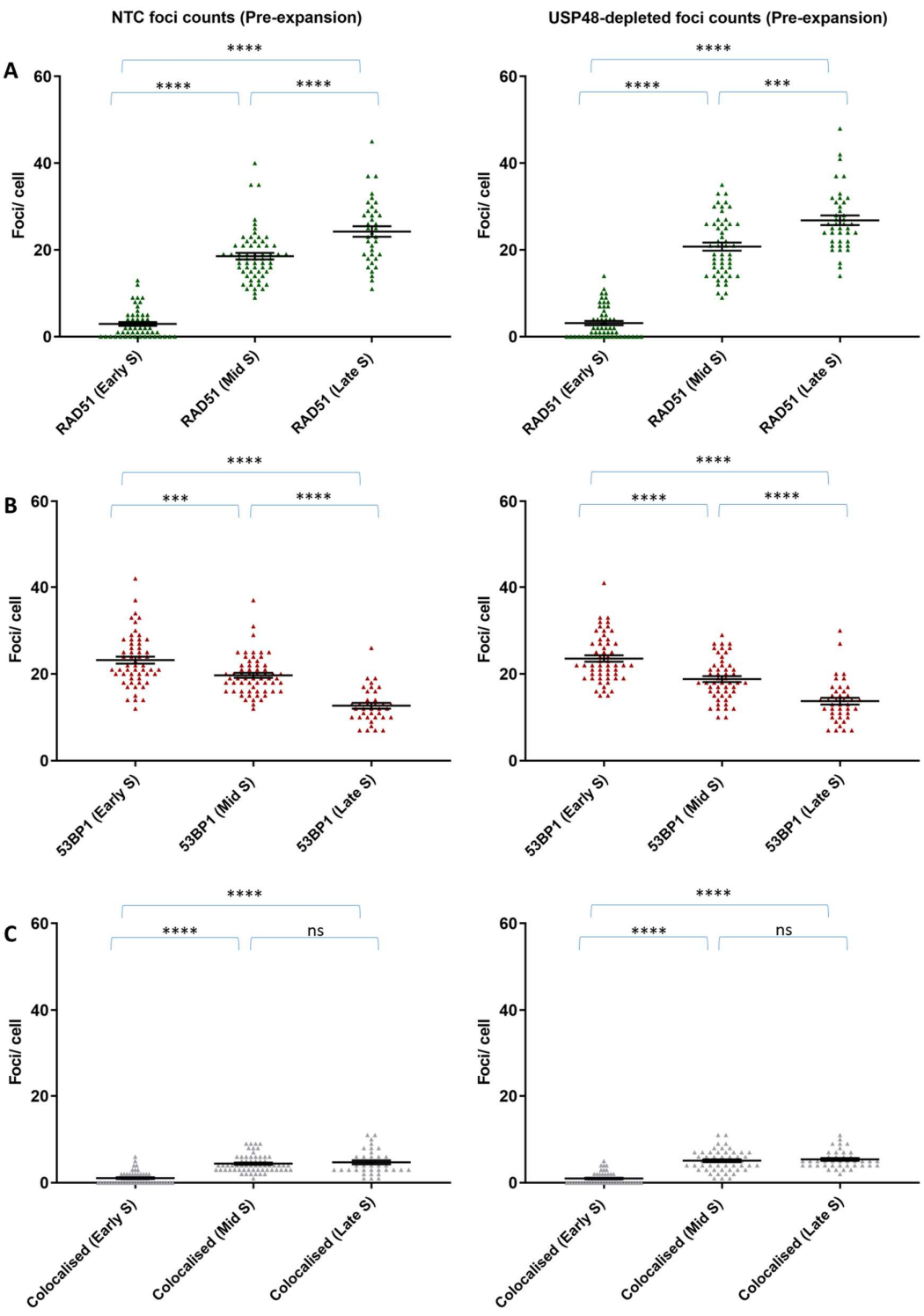
NTC foci counts (Pre-expansion)
USP48-depleted foci counts (Pre-expansion)
A
B
C
Foci/ cell
RAD51 (Early S)
RAD51 (Mid S)
RAD51 (Late S)
53BP1 (Early S)
53BP1 (Mid S)
53BP1 (Late S)
Colocalised (Early S)
Colocalised (Mid S)
Colocalised (Late S)
****
***
ns

Figure 5.26. Quantifying foci numbers following USP48-depletion pre-expansion. Foci quantification was carried out on nuclei treated as in Figure 5.25. Nuclei were classified as early, mid or late S-phase based on EdU staining pattern. Numbers of A) RAD51, B) 53BP1 and C) colocalised foci were determined in USP48-depleted and control (NTC) cells. Colocalised foci were defined as those where overlapping pixels were seen between the RAD51 and 53BP1 channels. Throughout Figure, **** P<0.001; ***P < 0.005; **P <0.01;*P < 0.05 NS, not significant by two-sided Student's t test. Error = s.e.m.

Nuclei were classified as early, mid and late S-phase according to EdU incorporation patterns and numbers of RAD51, 53BP1 and colocalised foci were quantified (Figure 5.26). RAD51 and colocalised foci numbers increased from early to late S-phase and 53BP1 foci numbers conversely decreased in both USP48-depleted cells and control cells. The average numbers of foci were comparable between USP48-depleted cells and control cells. These results suggest depletion of USP48 does not impact overall RAD51 and 53BP1 foci numbers as a function of cell cycle phase.

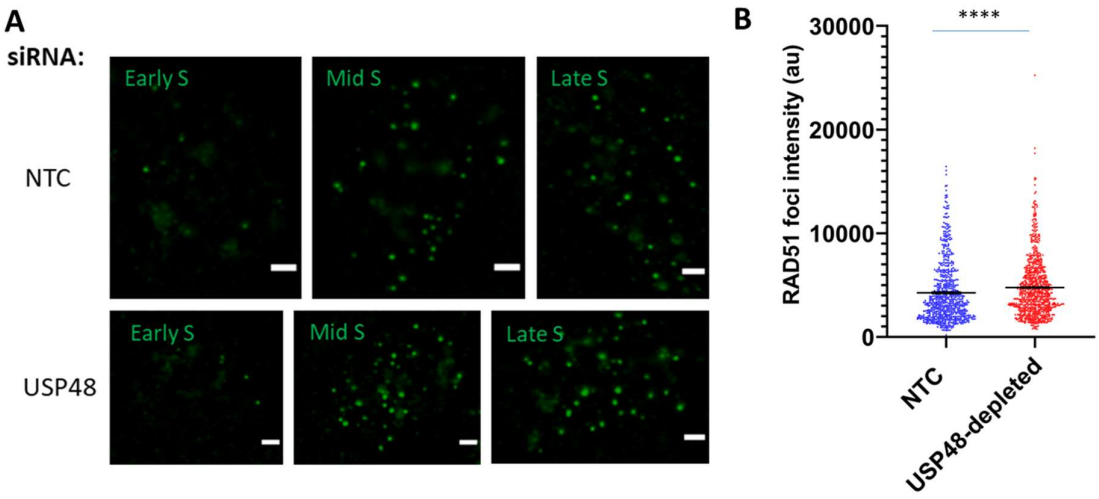

Figure 5.27. Quantifying intensity of RAD51 foci pre-expansion. U2OS cells were treated as in Figure 5.25. A) Example images of cells classified as early, mid and late S-phase were selected from USP48-depleted and control cells to illustrate changes in intensity of RAD51 foci following USP48-depletion. B) Intensity values were quantified in S-phase cells. N=2, 95 nuclei, n=709 foci NTC, n=930 foci USP48. Errors = s.e.m. **** $p<0.001$, students T-test.

In pre-expansion images, we observed an increased intensity of RAD51 in USP48-depleted cells compared to control cells (Figure 5.27A). The intensity of RAD51 foci was quantified in USP48-depleted and control cells (Figure 5.27B) and a significant increase in this intensity was observed in USP48-depleted cells. This suggests increased recruitment of RAD51 to repair foci and is consistent with increased resection lengths resulting from USP48-depletion.

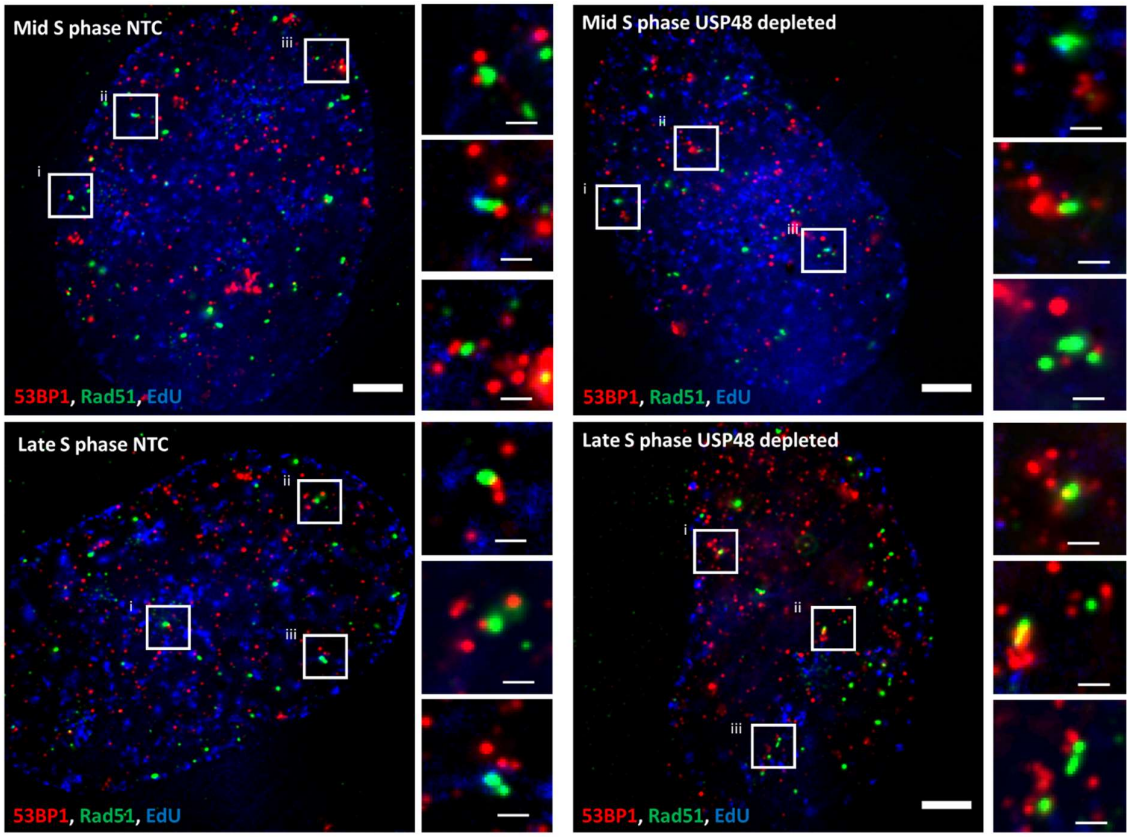

Figure 5.28. Post-expansion imaging of USP48-depleted cells. U2OS cells were treated with either control or USP48 siRNA for 72 hours. Cells were then treated with EdU and irradiated (2 Gy). Cells were allowed to recover for 1 hour prior to CSK pre-extraction and fixation with 4% PFA. Click-it reaction was completed to visualise the EdU and cells were immunostained for 53BP1 and RAD51. ExM protocol was completed and post-ExM images acquired. Scale bar 10 µm, 1 µm.

Post-expansion Z stacks of nuclei depleted of USP48 compared to control cells had similar distributions of RAD51 and 53BP1 foci in both mid and late S-phase cells (Figure 5.28). Post-expansion images of USP48-depleted cells classified as late S-phase have larger 53BP1 structures than in the control cells. The enrichment of RAD51 foci in cells identified as mid and late S-phase suggests that HR is occurring in these nuclei. RAD51 structures consistent with a nucleofilament were observed in both the control and USP48-depleted cells. Notably these nucleofilament-like structures appeared larger in the USP48-depleted cells than the control cells, consistent with increased resection resulting from USP48 depletion (Uckelmann *et al*, 2018). The prevalence of

these structures was qualitatively assessed across a range of example mid and late S-phase nuclei from USP48-depleted and control cells (Figure 5.29, Appendix Figure A21 & A22). In the majority of selected structures in the control images, RAD51 was present as a single spot-like structure. By contrast, in the USP48-depleted structures there was a shift to complex structures incorporating more than 1 RAD51 spot, or in some cases an elongated continuous structure which may be nucleofilaments.

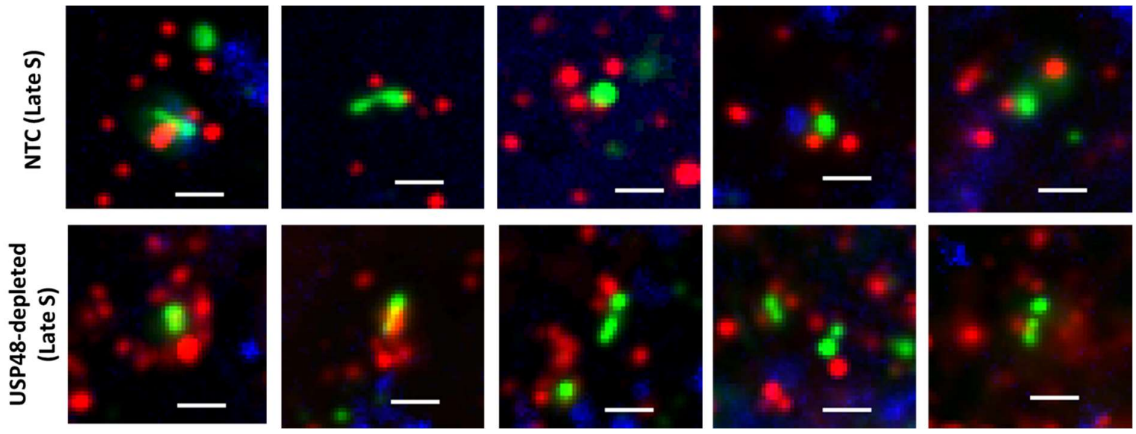

Figure 5.29. Visualising the structure of RAD51 and 53BP1 co-enriched accumulations in USP48-depleted cells. Examples of structures were selected from nuclei classified as late S-phase for control (NTC) cells and USP48-depleted cells. RAD51 is shown in green and 53BP1 is shown in red. Scale bar 2 µm.

Classification of 53BP1 and RAD51 accumulations was completed in a similar manner to the 53BP1 and BRCA1 datasets by applying the spot detection-based analysis (Section 2.7.5). A test set of images was analysed to determine if the classifications used for BRCA1 are comparable when looking at the appearance of RAD51. For classes 1-5, the structure classification for RAD51 was similar to BRCA1, however, the presence of RAD51 accumulations alone was noted and classified as class 6 (Figure 5.30).

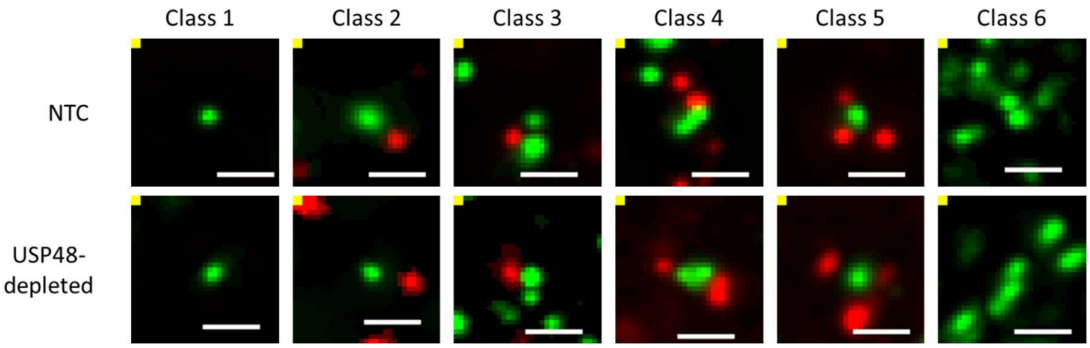

Figure 5.30. **Classification of RAD51 and 53BP1 accumulations in USP48-depleted cells.** Representative examples of classes 1-6 are shown for control and USP48-depleted cells. RAD51 is shown in green and 53BP1 in red. Class 1 is defined as RAD51 alone with no 53BP1 within a 2 µm radius. Class 2 is defined as RAD51 associated with a 53BP1 spot within a 2 µm radius. Class 3 is multiple RAD51 spots associated with one 53BP1 spot in a 2 µm radius. Class 4 is defined as multiple RAD51 spots associated with the same 53BP1 oligomer. Class 5 is one RAD51 spot associated with multiple 53BP1. Class 6 is defined as >3 RAD51 spots within a 2 µm radius. In the USP48-depleted cells, the radius for class 4 and 5 structures was increased to 2.8 µm.

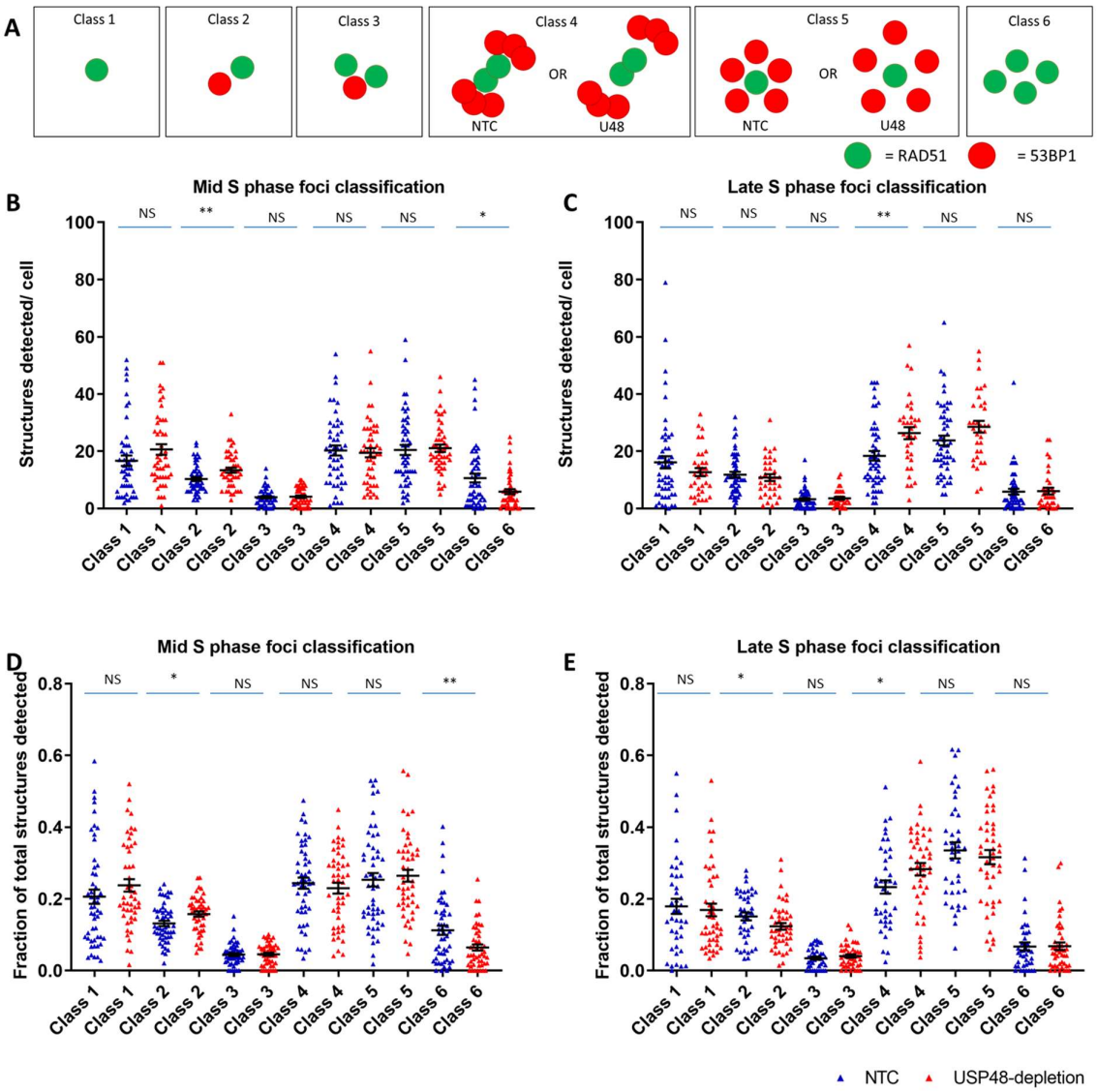

Figure 5.31. Classifying RAD51 and 53BP1 distributions in USP48-depleted cells. Spot detection based analysis was performed on Z stack data acquired in control and USP48 depleted cells. Structures were classified for nuclei in mid and late S-phase according to the identified classes shown schematically (Panel A). RAD51 was treated as the centre in these datasets. Classification is shown as total numbers of each structure detected per nucleus (Panel B&C) and as fractions of structures detected per nucleus (Panel D&E). Control data is shown in blue and USP48-depletion data is shown in red. Scoring is shown as numbers of structures detected for each time point (top panel) and as a ratio of total number of structures identified for each time point (bottom panel). N=3, >20 nuclei per sample. Throughout Figure, **** P<0.001; ***P < 0.005; **P <0.01;*P < 0.05 NS, not significant by two-sided Student's t test. Error = s.e.m.

53BP1 and RAD51 structures were classified using spot detection-based analysis (Figure 5.31). Classification of 53BP1 and RAD51 accumulations revealed an increase in class 4 structures (defined as multiple RAD51 spots associated with multiple 53BP1 spots) in USP48-depleted cells during late S-phase. Class 4 structures were further investigated to determine if subclasses could be identified as in the case of 53BP1 and BRCA1 class 4 foci (Section 4.4.2). Class 4 structures were sub-classified into three groups illustrated in Figure 5.32, with a particular interest in the prevalence of nucleofilament-like structures in USP48-depleted cells as compared to controls.

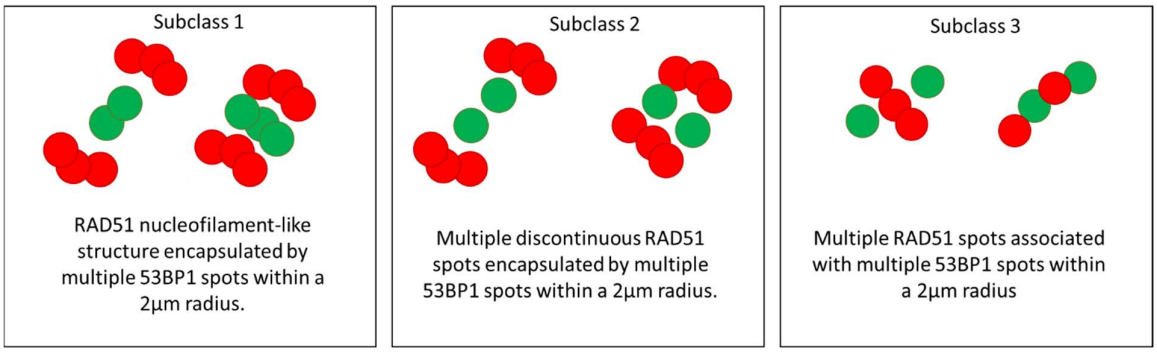

Figure 5.32. Describing the relative spatial organisation of RAD51 and 53BP1 in class 4 structures. A schematic representation of the identified class 4 sub-classes in USP48-depleted and control cells and their definitions are shown. Subclass 1 describes structures where RAD51 appears as a nucleofilament-like structure encapsulated by 53BP1. Subclass 2 described structures where multiple discontinuous RAD51 spots are encapsulated by 53BP1. Subclass 3 describes structures where multiple RAD51 spots are associated with multiple 53BP1 spots.

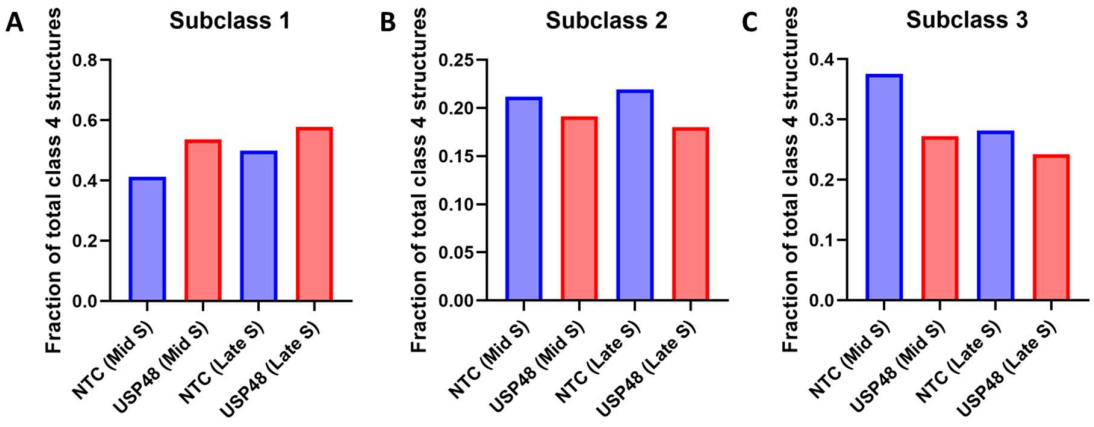

Figure 5.33. Sub-classification of class 4 foci structures. Class 4 structures were sub-classified as A) subclass 1, B) subclass 2 and C) subclass 3 as shown schematically in Figure 5.32. All class 4 structures from USP48-depleted and control cells were scored. Numbers quantified here are based on 3 experimental repeats. NTC mid S = 642 structures, NTC late S = 401 structures, USP48-depleted mid S = 518 structures, USP48-depleted late S = 756 structures.

Class 4 structures (defined as multiple RAD51 spots associated with multiple 53BP1 spots) were sub-classified according to classes shown schematically in Figure 5.32. Subclass 1 structures were the prevalent structure in both USP48-depleted and control cells, accounting for >40% of class 4 structures. Following USP48-depletion, there was an increase in the proportion of class 4 structures with a nucleofilament-like structure (subclass 1) as compared to controls. The proportion of subclasses 2 and 3 were reduced following USP48-depletion compared to controls.

Following USP48-depletion, there is an increased prevalence of class 4 structures consistent with RAD51 nucleofilaments as compared to controls. This observation, together with the previous observation that the void between BRCA1 and 53BP1 is increased following USP48 depletion, suggests that 53BP1 is positioned further away from the core of repair foci and is consistent with longer range resection. The increase in resection length following USP48 depletion may result in an increased prevalence of RAD51 nucleofilament structures.

5.3.2 Multi-colour capability of ExM allows nanoscale visualisation of multiple repair factors in repair foci

Thus far we have determined that BRCA1 and RAD51 both occupy the centre of structures encapsulated by 53BP1. It has been suggested that 53BP1 occupies the chromatin compartment, RAD51 occupies the ssDNA compartment and BRCA1 can interact with either sub-compartment (Bekker-Jensen *et al*, 2006). We investigated whether the spatial relationship of BRCA1, 53BP1 and RAD51 could be visualised simultaneously post-expansion. We chose to complete this investigation on USP48-depleted cells in addition to control cells, under the hypothesis that the extended resection lengths observed in the work of Ukelmann *et al* and confirmed by the work in this chapter resulting from USP48 depletion may allow us to better delineate the separation between these compartments.

U2OS cells were USP48-depleted using siRNA compared to control siRNA. Cells were treated with EdU prior to damage induction and fixed after 1 hour recovery time. Cells were immunostained for 53BP1, BRCA1 and RAD51. Images were acquired pre-expansion (Figure 5.34) to determine efficacy of staining and distributions of foci as a function of cell cycle. Z stacks were acquired post-expansion and deconvolved. Z stacks were organised according to cell cycle position (Figure 5.35) and structures were visually assessed (Figure 5.36).

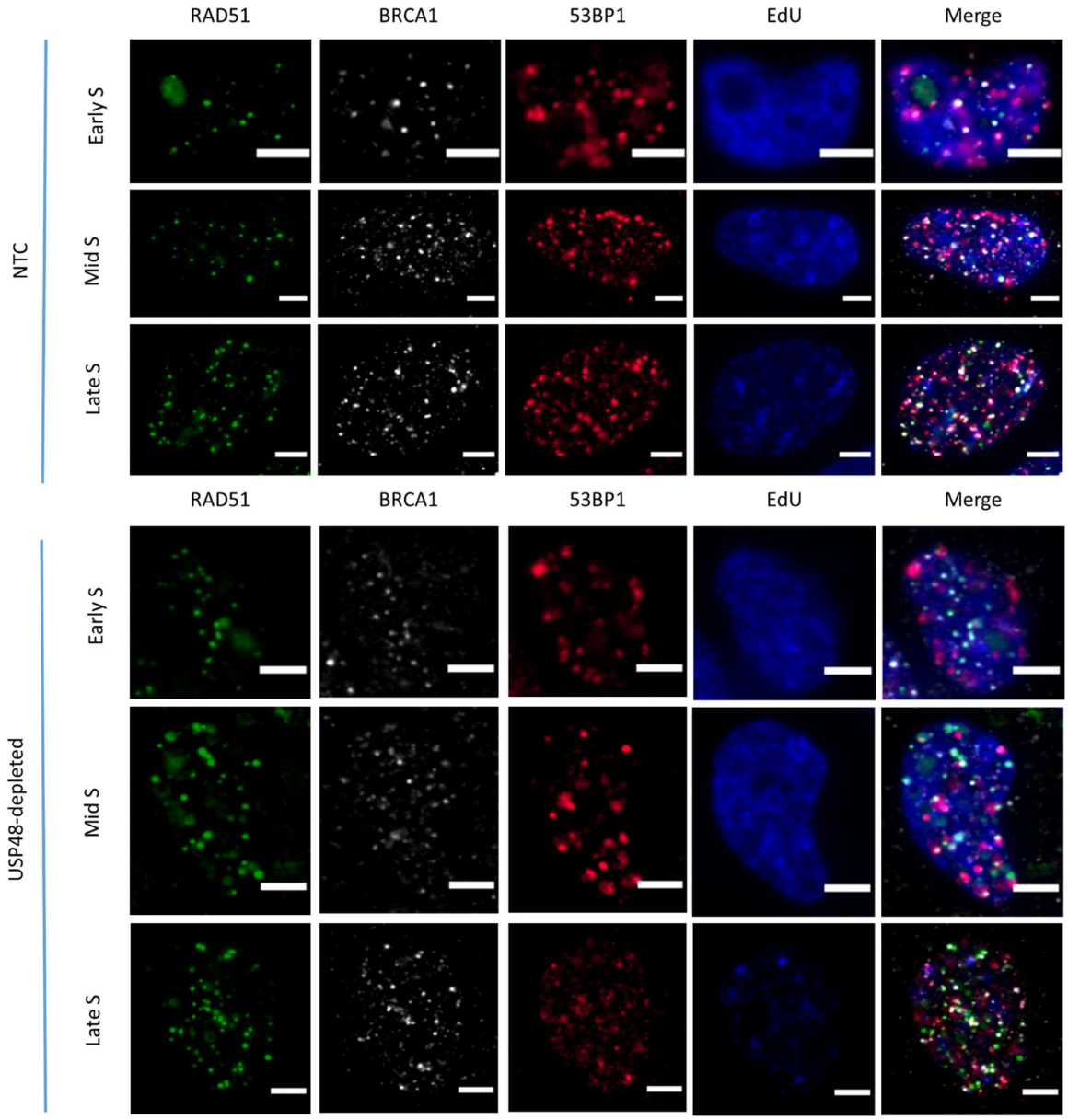

Figure 5.34. Visualising RAD51, BRCA1 and 53BP1 pre-expansion. U2OS cells were treated with NTC or USP48 siRNA for 72 hours. Cells were treated with EdU prior to irradiation (2 Gy) and allowed 1 hour to recover. Click-it reaction was performed to visualise EdU. Cells were immunostained for 53BP1, RAD51 and BRCA1. Scale bars 5 µm.

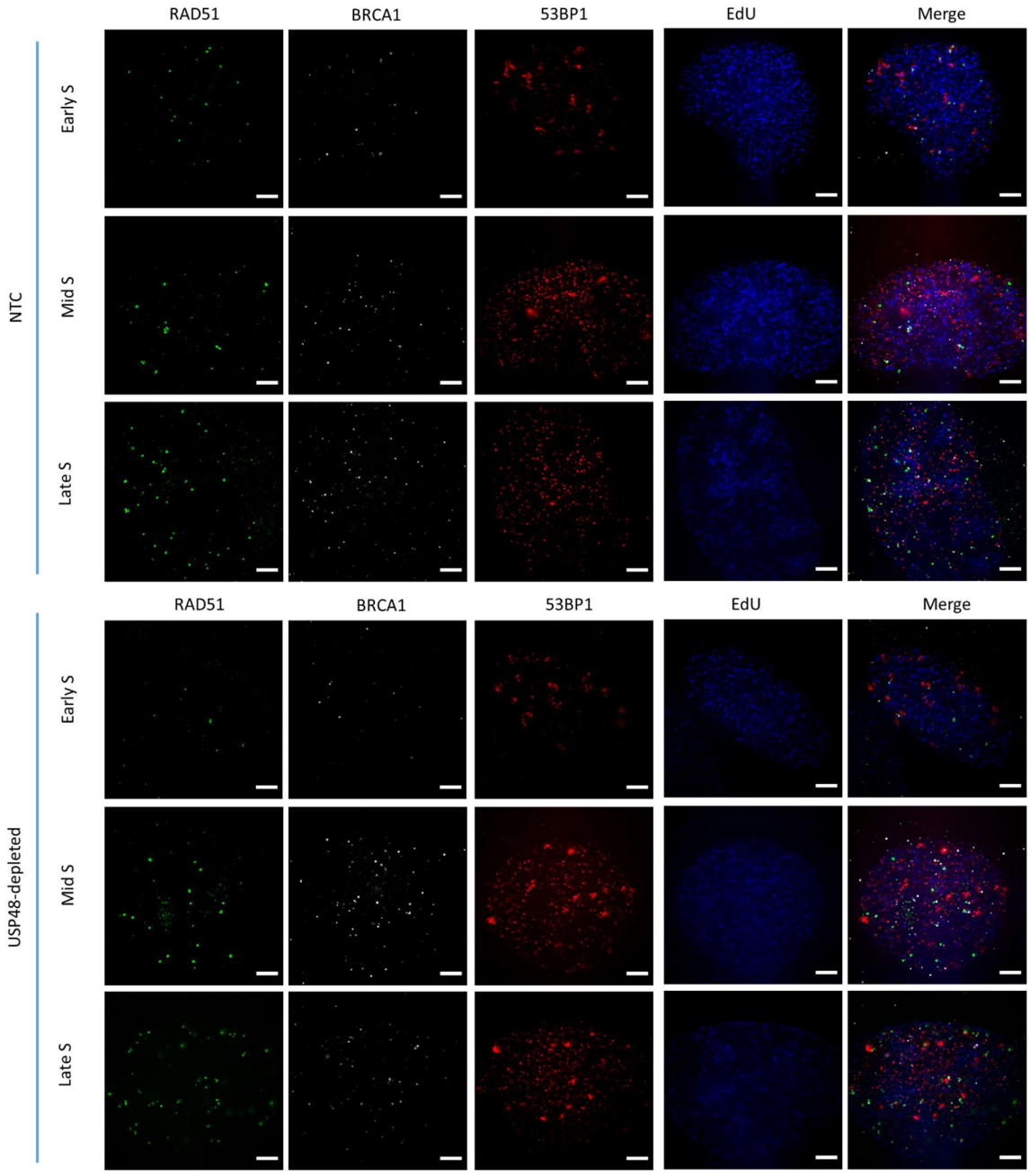

Figure 5.35. **Visualising RAD51, BRCA1 and 53BP1 post-expansion.** U2OS cells were treated with control or USP48 siRNA for 72 hours. Cells were treated with EdU prior to irradiation (2 Gy) and allowed 1 hour to recover. Click it reaction was performed for detection of EdU. Cells were immunostained for 53BP1, RAD51 and BRCA1. Standard ExM protocol was performed and Z stacks acquired post-expansion on a widefield microscope. Scale bars 10 µm.

In both pre- and post-expansion image data, BRCA1 and RAD51 foci numbers were increased in cells with markers of mid and late S-phase, whilst 53BP1 foci numbers decreased, consistent with

our previous observations (Figure 5.34 & 5.35) (Sections 5.3 & 5.3.1). Through this experiment, we have demonstrated a capability to visualise multiple repair proteins simultaneously with nanoscale resolution post-expansion.

5.3.3 Describing the spatial organisation of multiple repair factors is complex

The nanoscale organisation of structures co-enriched with BRCA1, RAD51 and 53BP1 was visually assessed (Figure 5.36, Appendix Figures A23-A24); substantial heterogeneity in the relative spatial organisation of these accumulations was observed. Thus far, this work has identified that BRCA1 and 53BP1 are anti-correlated, and in class 5 structures BRCA1 is visualised at the core and 53BP1 at the periphery (Section 4.4.3). This distribution is consistent with the observed exclusion of 53BP1 by BRCA1 during HR initiation (Chapman *et al*, 2012). In the case of RAD51 and 53BP1, similar anti-correlation was observed. In class 4 structures co-enriched with 53BP1 and RAD51, a similar exclusion profile was observed, consistent with RAD51 occupying the ssDNA compartment and 53BP1 being retained at sites of damage during HR. Since BRCA1 is known function in promoting resection, RAD51 loading and potentially strand invasion, we hypothesise that a proportion of the BRCA1 accumulations would occupy the ssDNA compartment together with RAD51 (Cejka *et al*, 2017, Zhang *et al*, 2009, Zhao *et al*, 2017). This idea is consistent with observations using confocal and super resolution microscopy (Chapman *et al,* 2012, Bekker-Jensen *et al,* 2006, *Schwarz et al*, 2019).

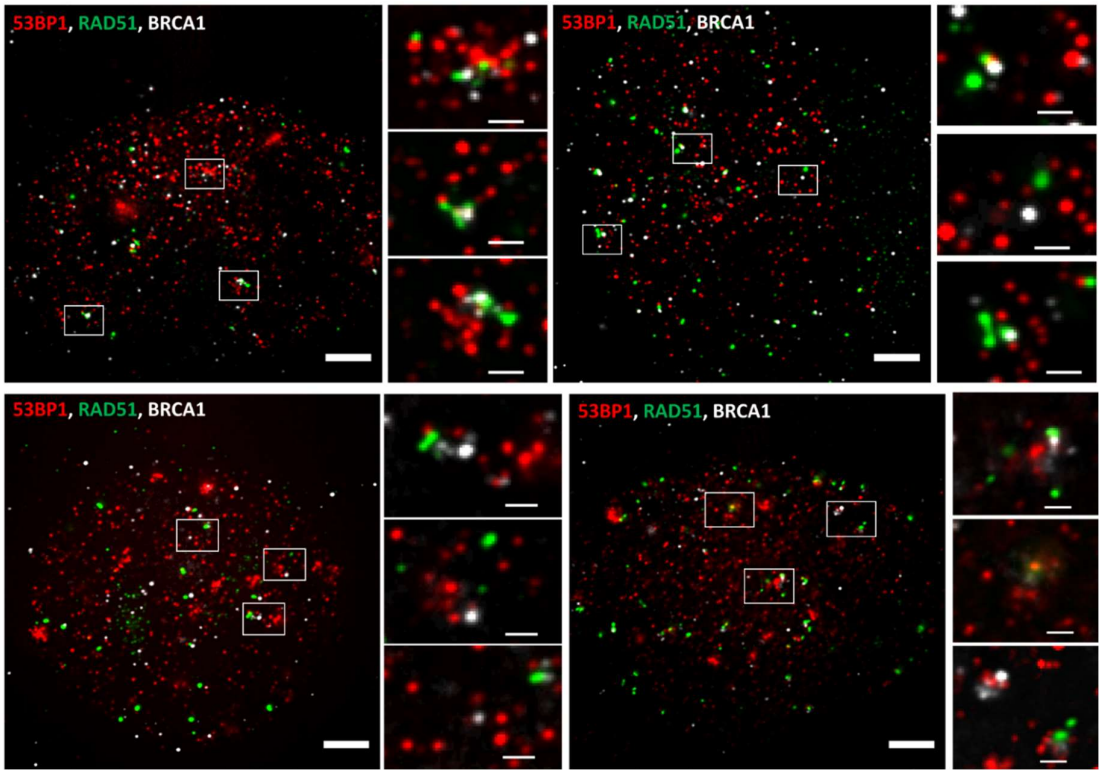

Figure 5.36. Investigating heterogeneity of RAD51, BRCA1 and 53BP1 accumulations in USP48-depleted cells. U2OS cells were treated with NTC or USP48 siRNA for 72 hours. Cells were treated with EdU prior to irradiation (2 Gy) and allowed 1 hour to recover. Click-it reaction was performed for detection of EdU (not shown here). Cells were immunostained for 53BP1, RAD51 and BRCA1. Standard ExM protocol was completed (Section 2.4) and Z stacks acquired post-expansion on a widefield microscope. Scale bars 10 µm and 2 µm.

We aimed to develop an analytical approach to describe the organisation of BRCA1, RAD51 and 53BP1 in nuclei classified as mid and late S-phase. The role of these repair factors is complex therefore we carefully approached the design of analysis based on known mechanistic information (detailed in Section 5.3.4).

5.3.4 Design of analysis to investigate the spatial organisation of RAD51, BRCA1 and 53BP1 in S-phase nuclei

The aim of this work was to investigate the spatial organisation of key repair proteins in S-phase nuclei with particular focus on mid and late S-phase cells where HR is expected reach its peak activity (Her and Bunting, 2018). In order to describe the spatial organisation of BRCA1, 53BP1 and

RAD51 in mid and late S-phase nuclei, we firstly considered what is understood mechanistically about HR progression to direct how we dissect the relationships between these proteins.

HR is a multi-step process (summarised in Figure 5.37) which begins with BRCA1 removing the blockade posed by 53BP1 to resection, and allowing access of nucleases (e.g. EXO1, DNA2) and helicases (e.g. BLM) to generate a 3' ssDNA overhang which is subsequently coated with RPA to stabilise the nascent DNA (Escribano-Diaz *et al*, 2013 & Cejka, 2017). RPA is subsequently replaced by RAD51 which forms the presynaptic filament (Zhao *et al*, 2017). Exchange of RPA for RAD51 is promoted by BRCA2, together with its binding partner DSS1. BRCA2 is recruited to sites of damage by BRCA1 through bridging protein, PALB2 (Zhang *et al*, 2009). The RAD51 filament searches for, engages with and invades the homologous duplex to form the displacement loop, or the D-loop. Following this, DNA synthesis and resolution of DNA intermediates occurs to complete HR.

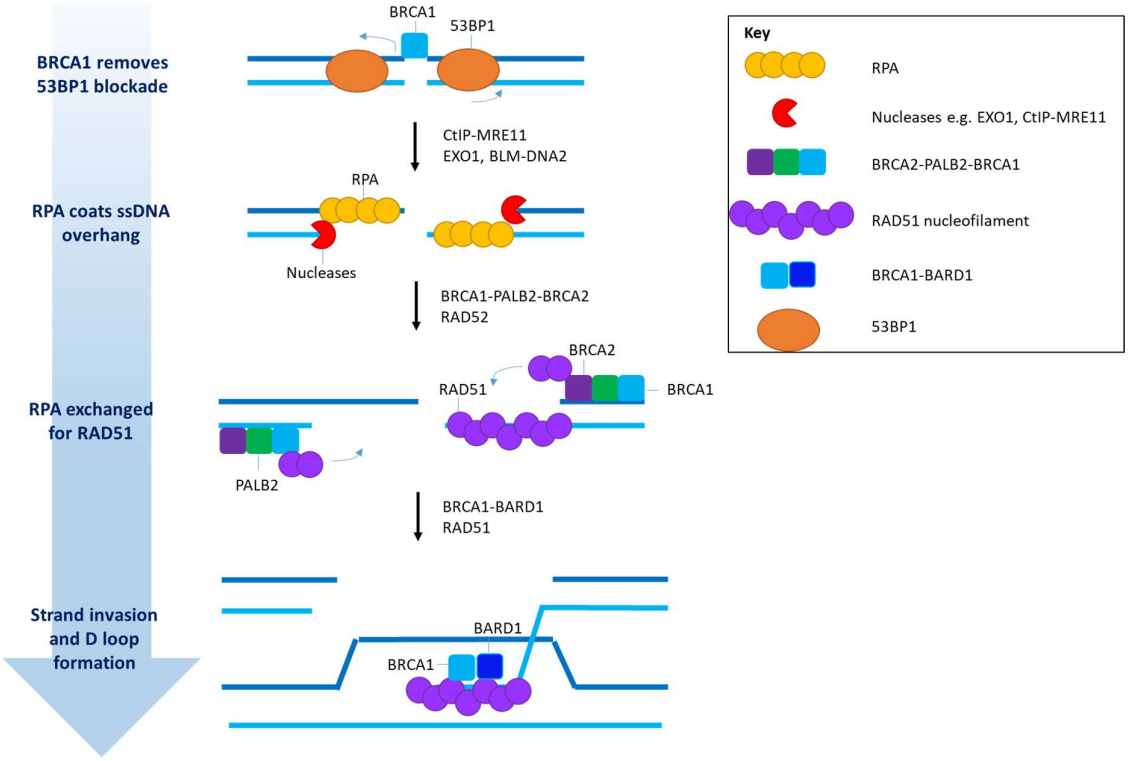

Figure 5.37. Schematic representation of HR progression. Following DSB induction, BRCA1 removes blockade posed by 53BP1 to resection and allows nucleases (e.g. EXO1, CtIP-MRE11) and helicases (e.g. BLM) to form a ssDNA overhang which is rapidly coated with RPA to stabilise the nascent DNA. RPA is replaced with RAD51 through the action of RAD52 (not shown) and BRCA2 (in conjunction with BRCA1 and PALB2). RAD51-DNA nucleofilament engages with and invades the homologous duplex to form a displacement loop (D-loop), a process which is promoted by BRCA1-BARD1 complex (Adapted from Cejka, 2017).

The role of BRCA1 during HR progression appears to be multi-faceted (described in Section 1.1.3) (Prakash *et al*, 2015). It has been shown that BRCA1-BARD1 overcomes the 53BP1 blockade to resection and initiates resection required for HR commitment (Densham *et al*, 2016). It has further been shown that BRCA1 recruits BRCA2 via the bridging protein PALB2 to facilitate exchange of RPA for RAD51 to form the RAD51-ssDNA nucleofilament (Nepomuceno *et al*, 2017). Interestingly, PALB2 contains two DNA binding regions which can bind D-loops and ssDNA regions during HR initiation. Additionally, PALB2 possesses a chromatin-association motif (ChAM) and is tightly associated with H2B and H3. The interaction of the BRCA1-PALB2-BRCA2 with chromatin is crucial to recombination (Bleuyard *et al*, 2012). Zhao *et al* demonstrated that BRCA1-BARD1 is required

for strand invasion and D-loop formation (Zhao *et al*, 2017). Further, strand invasion and D-loop formation is robust in the presence of both BRCA2 and BRCA1-BARD1.

Based on these mechanistic insights we speculated that there may be visible changes in spatial distribution of BRCA1, 53BP1 and RAD51 relative to each other which may correlate with different steps in HR process. To describe the spatial organisation of these proteins in USP48-depleted cells compared to control cells, I used spot detection-based analysis in which RAD51 was arbitrarily defined as the centre of each structure, and then the relative spatial organisation of 53BP1 and BRCA1 to the central RAD51 was described (illustrated in Figure 5.38) (Section 2.7.5). The spot detection-based analysis here differs to that used in classification of BRCA1/ 53BP1 and RAD51/ 53BP1 structures because the user is now shown four channels as opposed to two (i.e. BRCA1, RAD51, 53BP1 and EdU).

1. User defines parameters e.g. channels, spot radius

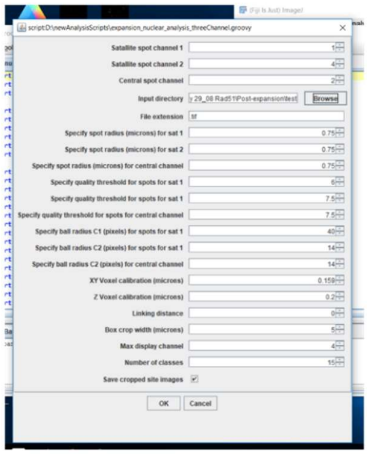

2. Structure of interest is shown to user. Radius highlighted by purple circle.

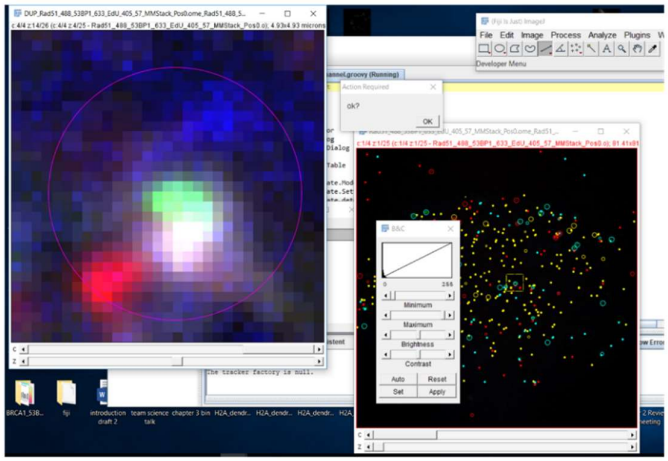

3. User classifies structure of interest according to spatial organisation of repair factors.

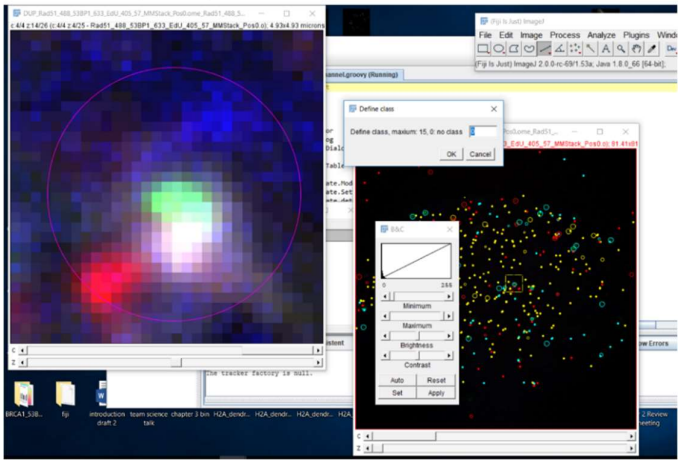

Figure 5.38. Classification of RAD51, BRCA1 and 53BP1 structures using spot detection-based analysis. An example of spot detection-based analysis is shown. 1) The user defines parameters for the analysis e.g. channels, file directory, spot radius, quality threshold (detailed in Section 2.7.5). 2) The user is shown an example structure of interest in a 5x5 µm box, with a purple circle indicating a 2 µm radius from the central spot. The region of interest is also highlighted in the whole image with a yellow box. 3) User defines the structure according to spatial organisation of repair factors.

Using this approach, I identified 10 classes of structures (illustrated in Figure 5.39). Class 1 describes structures where only RAD51 was observed within a 2 µm radius. Classes 2-5 describes structures where 53BP1 and RAD51 were co-enriched within a 2 µm radius. Class 6 describes clusters of RAD51 within 2 µm radius. Classes 7-9 described structures where RAD51, BRCA1 and 53BP1 were all present within a 2 µm radius. Class 10 described structures co-enriched with BRCA1 and RAD51 within a 2 µm radius. In the case of USP48 depleted cells, this radius was extended to 2.8 µm as described in Section 5.3. Structures in USP48-depleted and control cells were classified based on these parameters (Figure 5.40).

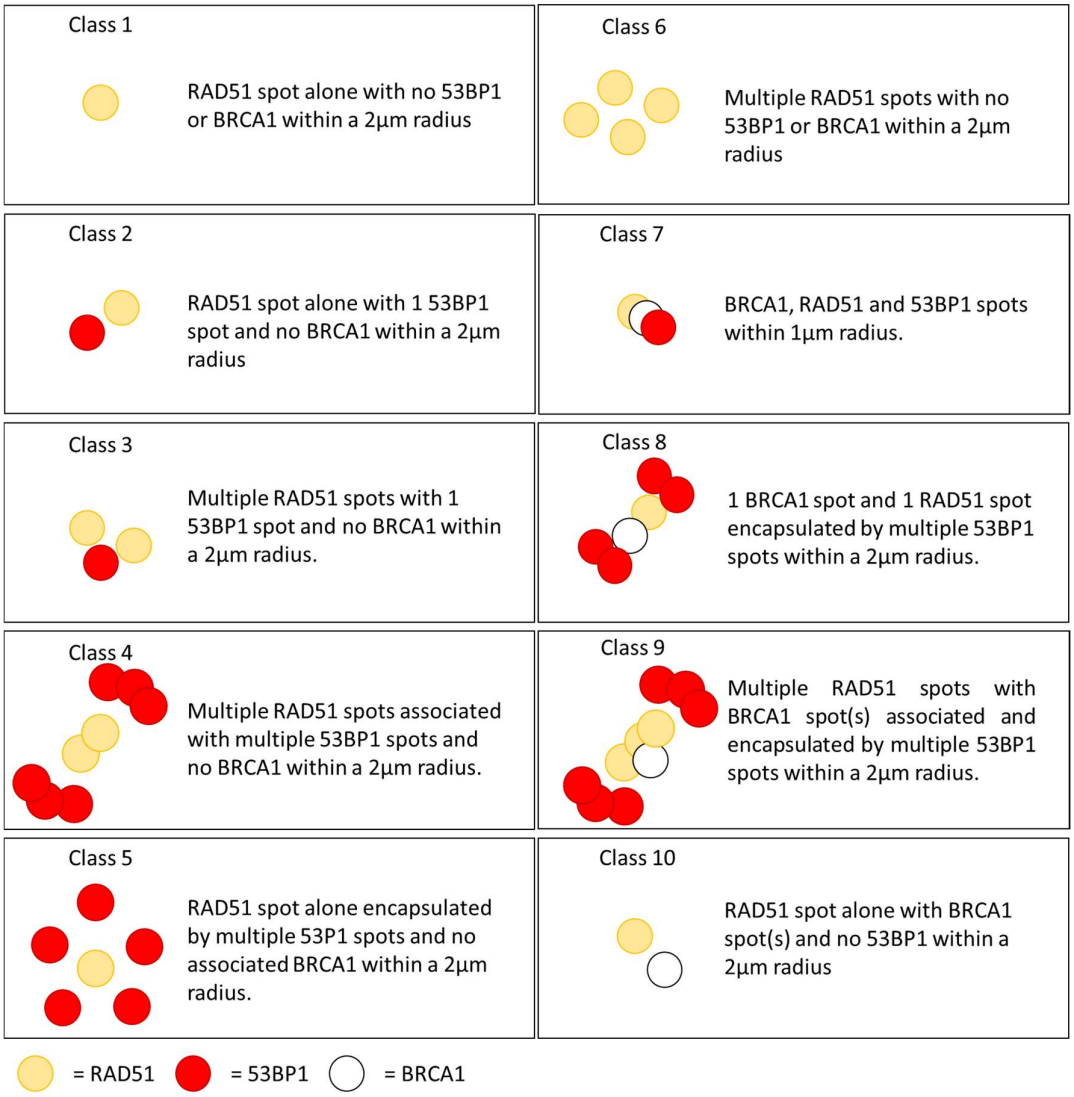

Figure 5.39. Describing the relative spatial organisation of RAD51, BRCA1 and 53BP1 in repair structures. A schematic representation of the identified structures in USP48-depleted and control cells and their definitions are shown. Class 1 describes structures where only RAD51 was observed within a 2 µm radius. Classes 2-5 describes structures where 53BP1 and RAD51 were co-enriched within a 2 µm radius. Class 6 describes clusters of RAD51 within 2 µm radius. Classes 7-9 describes structures where RAD51, BRCA1 and 53BP1 were all present within a 2 µm radius. Class 10 describes structures co-enriched with BRCA1 and RAD51 within a 2 µm radius.

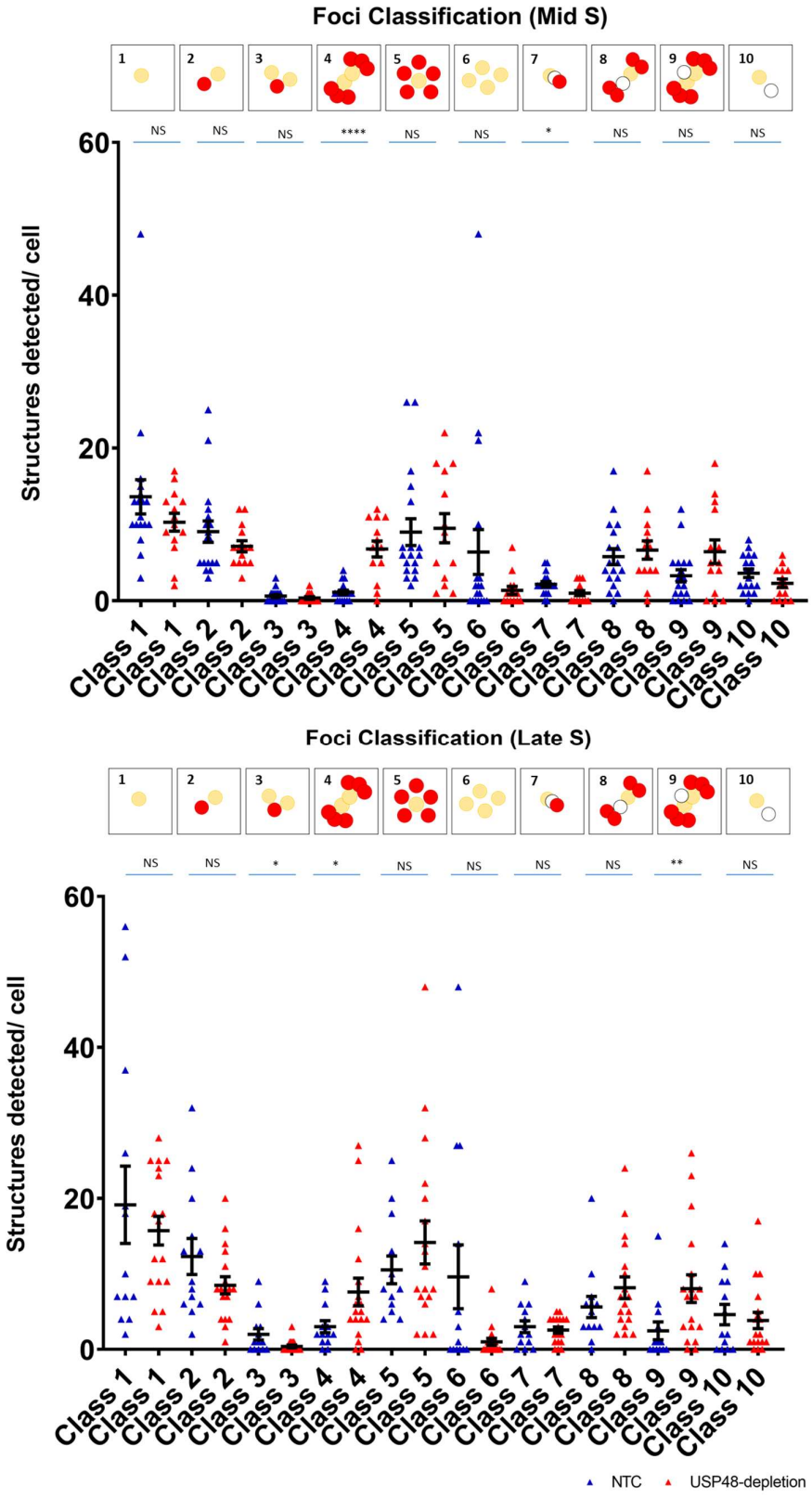
Foci Classification (Mid S)
1
2
3
4
5
6
7
8
9
10
NS
NS
NS
****
NS
NS
*
NS
NS
NS
Structures detected/ cell
60
40
20
0
Class 1
Class 1
Class 2
Class 2
Class 3
Class 3
Class 4
Class 4
Class 5
Class 5
Class 6
Class 6
Class 7
Class 7
Class 8
Class 8
Class 9
Class 9
Class 10
Class 10
Foci Classification (Late S)
1
2
3
4
5
6
7
8
9
10
NS
NS
*
*
NS
NS
NS
NS
**
NS
Structures detected/ cell
60
40
20
0
Class 1
Class 1
Class 2
Class 2
Class 3
Class 3
Class 4
Class 4
Class 5
Class 5
Class 6
Class 6
Class 7
Class 7
Class 8
Class 8
Class 9
Class 9
Class 10
Class 10
NTC
USP48-depletion

Figure 5.40. Classifying BRCA1, 53BP1 and RAD51 distributions on USP48-depleted cells. Spot detection-based analysis was performed on Z stack data acquired in control and USP48 depleted cells. Structures were scored for nuclei in mid and late S-phase according to the identified classes in Figure 5.39. RAD51 was treated as the centre in these datasets. Classifications are shown as numbers of structures detected per nucleus for mid and late S-phase classified nuclei. N=2, >14 nuclei per phase. Throughout Figure, **** P<0.001; ***P < 0.005; **P <0.01;*P < 0.05 NS, not significant by two-sided Student's t test. Error = s.e.m.

In mid S-phase classified nuclei, USP48 depletion was associated with an increase in class 4 structures (defined as >1 RAD51 spot associated with multiple 53BP1 spots) and a decrease in class 7 structures (defined as structures where RAD51, 53BP1 and BRCA1 spots are very closely associated). No differences were observed in the other structures classes. We did note an increase in class 8 (defined as structures containing 1 BRCA1 spot and 1 RAD51 spot encapsulated by multiple 53BP1 spots) and class 9 structures (defined as multiple RAD51 spots with BRCA1 spot(s) associated and encapsulated by multiple 53BP1 spots) in USP48-depleted cells compared to controls (P values = 0.5277 & 0.1284, respectively). In late S-phase classified nuclei, we observed an increase in class 4 and 9 structures in USP48-depleted cells compared to controls. No changes were observed in other structure classes. Notably, there was an increase in class 5 and class 8 structures in USP48-depleted cells compared to controls (P values = 0.5724 & 0.2199, respectively). A similar distribution of structures was observed when these data were normalised and plotted as fraction of structures per nucleus (Appendix Figure A25).

We next performed a detailed investigation of structures enriched with BRCA1, RAD51 and 53BP1 to determine if there were key differences between USP48-depleted and control cells. Towards this aim, examples of class 7-9 structures were selected for mid and late S-phase classified nuclei for USP48-depleted and control cells for comparison (Figure 5.41).

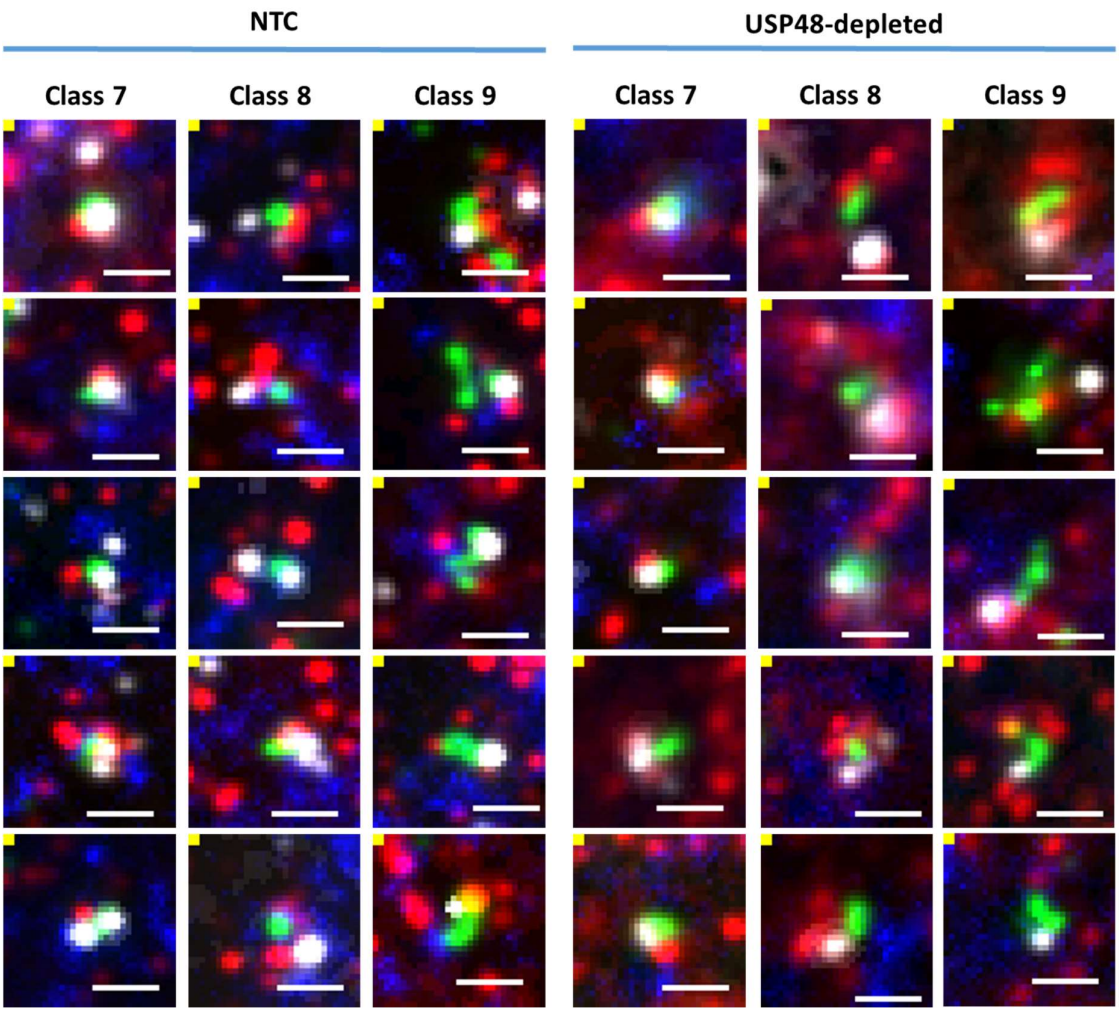

Figure 5.41. Examples of BRCA1 (white), 53BP1 (red) and RAD51 (green) co-enriched structures from USP48-depleted and control cells. Examples of class 7-9 structures were selected from USP48-depleted and control cells treated as in Figure 5.34 & 5.35. These examples were based on the structures classified in Figure 5.40. Scale bars 2 µm.

Class 7 structures (defined as BRCA1, RAD51 and 53BP1 spots which are closely associated) and class 8 structures (defined as 1 RAD51 spot, and 1 BRCA1 spot encapsulated by multiple 53BP1 spots) had comparable structural organisation in USP48-depleted and control cells. Notably, class 9 example structures were largely comprised of a RAD51 nucleofilament-like structure with BRCA1 associated and 53BP1 encapsulating the filament or associated with it. In the control cells, there were examples of structures where RAD51 does not adopt a continuous structure.

The increase in class 4 and 9 structures in cells depleted of USP48 compared to controls prompted us to further investigate these structures. Class 4 and class 9 structures were investigated to determine the proportion of these structures which are consistent with a nucleofilament structure. I defined a nucleofilament as a continuous, elongated RAD51 structure of >1.5 µm. All class 4 and 9 structures in mid and late S-phase classified nuclei were investigated for control and USP48-depleted cells (Figure 5.42).

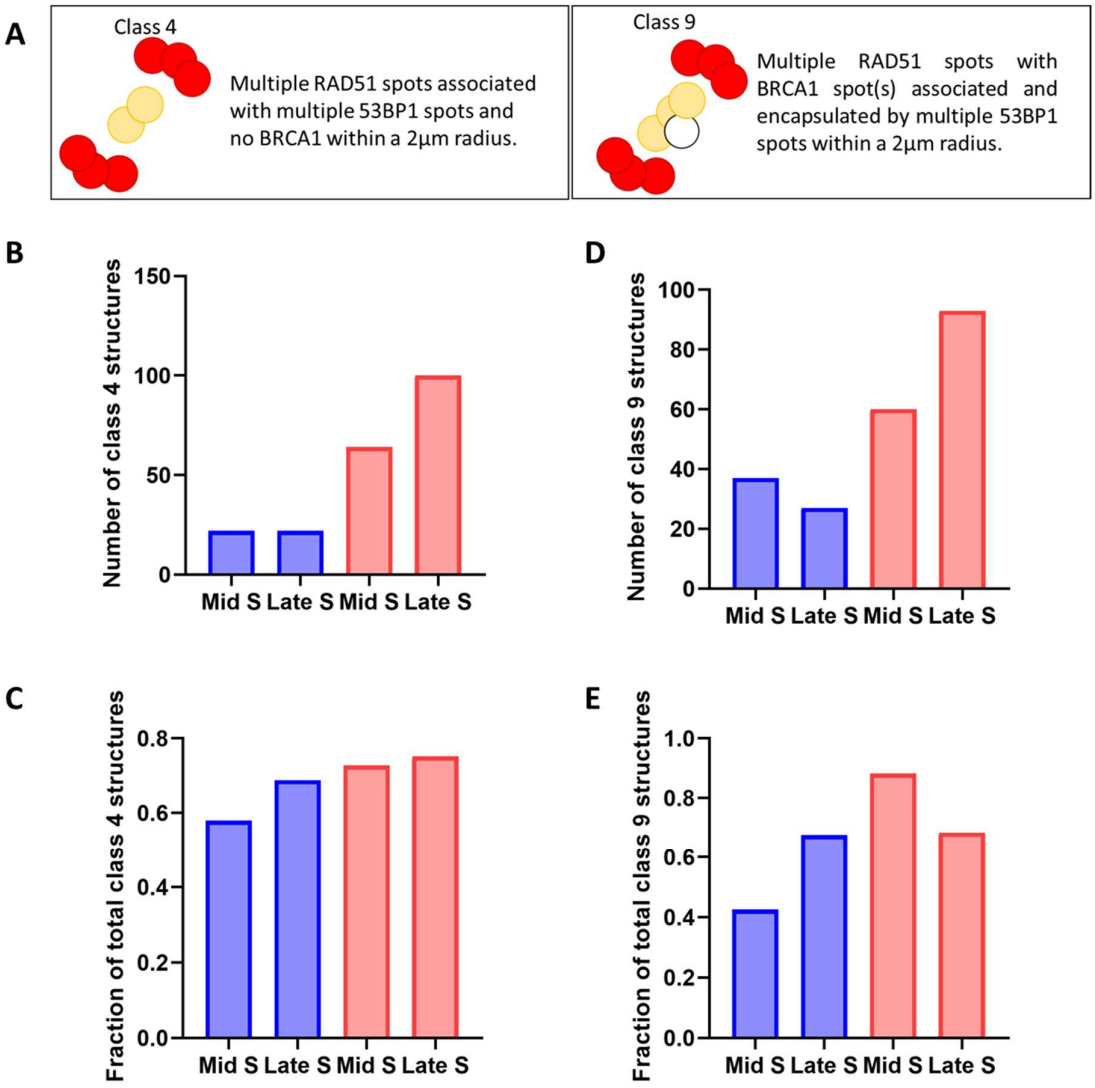

Figure 5.42. **Investigating RAD51 structures in USP48-depleted cells.** A) Class 4 structures (defined as multiple RAD51 spots associated with multiple 53BP1 spots) and class 9 structures (defined as multiple RAD51 spots with BRCA1 spot(s) associated and encapsulated by multiple 53BP1 spots) were investigated for USP48- depleted and control (NTC) cells. B) Total numbers of class 4 structures defined as nucleofilament-like structures were quantified. C) The fraction of nucleofilament-like structures of the total number of identified class 4 structures was quantified. D) Total numbers of class 9 structures defined as nucleofilament-like structures were quantified. E) The fraction of nucleofilament-like structures of the total number of identified class 9 structures was quantified. Structures were selected from two independent experiments.

The total number of class 4 and class 9 structures were higher in USP48-depleted cells compared to control cells (Figure 5.42B & 5.42D). >50% of identified class 4 structures in control and USP48-depleted cells are consistent with description of nucleofilaments (Figure 5.42C). There is an increase in proportion of nucleofilament structures in USP48-depleted cells compared to controls. Similarly, >40% of identified class 9 structures in control and USP48-depleted cells are consistent with the description of nucleofilaments, and there is an increased proportion of these structures in USP48-depleted cells compared to controls (Figure 5.42E). Intriguingly, we observed heterogeneity in the placement and number of BRCA1 spots in class 9 structures (Figure 5.43). We also noted that there were more class 4 structures than class 9 structures, i.e. more continuous RAD51 accumulations in which BRCA1 is not present.

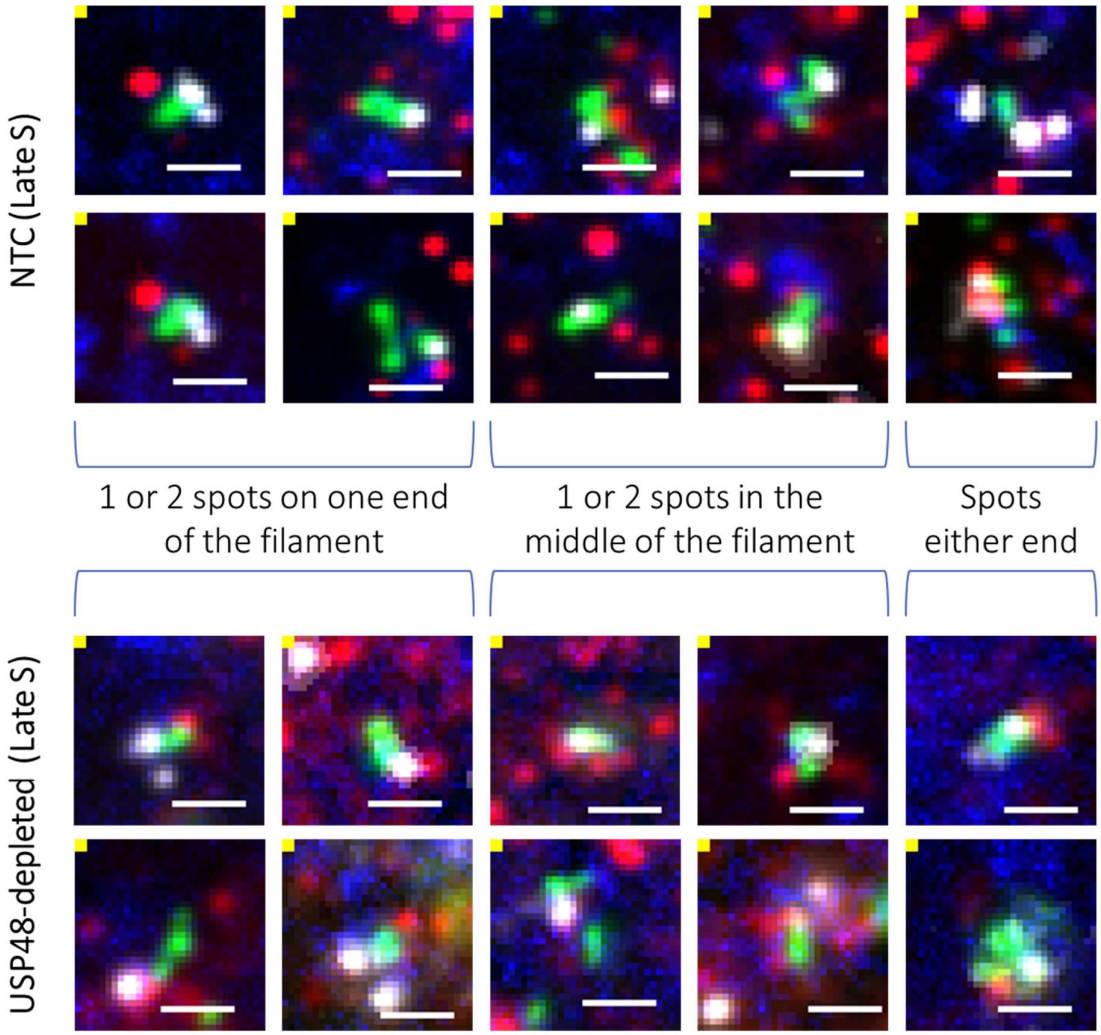

Figure 5.43. Describing the placement of BRCA1 spots in class 9 structures in USP48-depleted cells compared to control cells. Examples of class 9 structures were selected for late S-phase classified cells in USP48-depleted and control cells. Number and placement of BRCA1 spots in these structures was described. Scale bars 2 µm.

By applying ExM, we provide novel insight into the nanoscale organisation of BRCA1, 53BP1 and RAD51. Accumulations enriched with all three proteins were described using three distinct classes: class 7 (defined as 53BP1, BRCA1 and RAD51 spots within a 1 µm radius), class 8 (defined as 1 BRCA1 spot and 1 RAD51 spot encapsulated by multiple 53BP1 spots) and class 9 (defined as multiple RAD51 spots with BRCA1 spot(s) associated and encapsulated by multiple 53BP1 spots). These classes may be suggestive of different stages of RAD51 nucleofilament formation.

5.4 Chromatin compaction state can be investigated following ExM

DSB repair is occurring in the context of chromatin. Chromatin compaction is considered to protect our genomic material, yet in the context of damage it presents a physical barrier to the access of repair factors. This barrier is removed by a transient disorganisation of chromatin to allow for efficient repair (Polo, 2014). The structural rearrangement of chromatin is broadly described by the access/prime-repair-restore model and is mediated by the action of chromatin remodelers and histone modifiers (Section 1.1.4). Thus far, we have visualised nanoscale changes in BRCA1 and 53BP1 accumulations following depletion of SMARCAD1 and USP48, both of which influence chromatin proximal to DSBs (Densham *et al*, 2016 & Uckelmann *et al*, 2018). Briefly, these studies demonstrated that BRCA1-BARD1 possesses E3 ubiquitin ligase activity which is required for HR. H2A is the substrate for BRCA1-BARD1, and the ubiquitin mark placed on H2A is "read" by chromatin remodeler SMARCAD1. Both BRCA1-BARD1 and SMARCAD1 activity are required for positioning of 53BP1 away from the break site and for resection to occur. Resection length is fine-tuned by a H2A-specific DUB, USP48. USP48 "erases" the ubiquitin mark from H2A to constrain resection and thus prevents repair through mutagenic SSA. In this context, BRCA1-BARD1 acts as histone modifier, "writing" a ubiquitin mark on chromatin which is "read" by chromatin remodeler SMARCAD1, and subsequently "erased" by USP48.

How chromatin actually remodels has remained elusive, although new evidence suggests a model where chromatin initially compacts at the break, and then de-compacts in a chromatin wave which forms a condensed chromatin ring further from the break site (described in Section 1.1.4) (Lou *et al*, 2019). This condensed chromatin ring was correlated with regions of 53BP1-decorated chromatin. Further, this wave may be due to mechanical displacement of chromatin as repair machinery spreads (Shin *et al*, 2018). We therefore hypothesised that ExM may reveal changes in chromatin compaction following SMARCAD1 and USP48 depletions which could be directly related to the foci structures we have identified. To investigate this hypothesis, stable cell lines expressing H2A-dendra2 (Section 3.3.1) (Section 2.3.4) were used.

5.4.1 Effect of SMARCAD1-depletion on chromatin architecture

To investigate the effect of SMARCAD1-depletion on chromatin architecture in proximity to DSBs, H2A-dendra2-expressing cells were induced to express H2A-dendra2 with doxycycline and treated with siSMARCAD1 or NTC siRNA. Cells were damaged by irradiation, and allowed 1 hour to recover prior to fixation (or lysis for western blotting). Depletion was confirmed by western blotting (Figure 5.44). Cells were immunostained for 53BP1 and BRCA1. Pre-expansion images were acquired to confirm efficacy of staining and overall distributions of BRCA1 and 53BP1 foci prior to ExM preparation (Figure 5.45). ExM preparation was completed and post-expansion Z stacks were acquired (Figure 5.46).

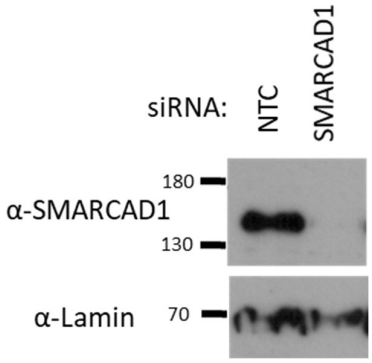

Figure 5.44. Confirming SMARCAD1-depletion in U2OS cells expressing H2A-dendra2. U2OS cells were induced to express H2A-dendra2 using doxycycline. Cells were treated with siSMARCAD1 or NTC siRNA for 72 hours. Cells were lysed and western blotting was performed with antibodies shown were used to confirm depletion.

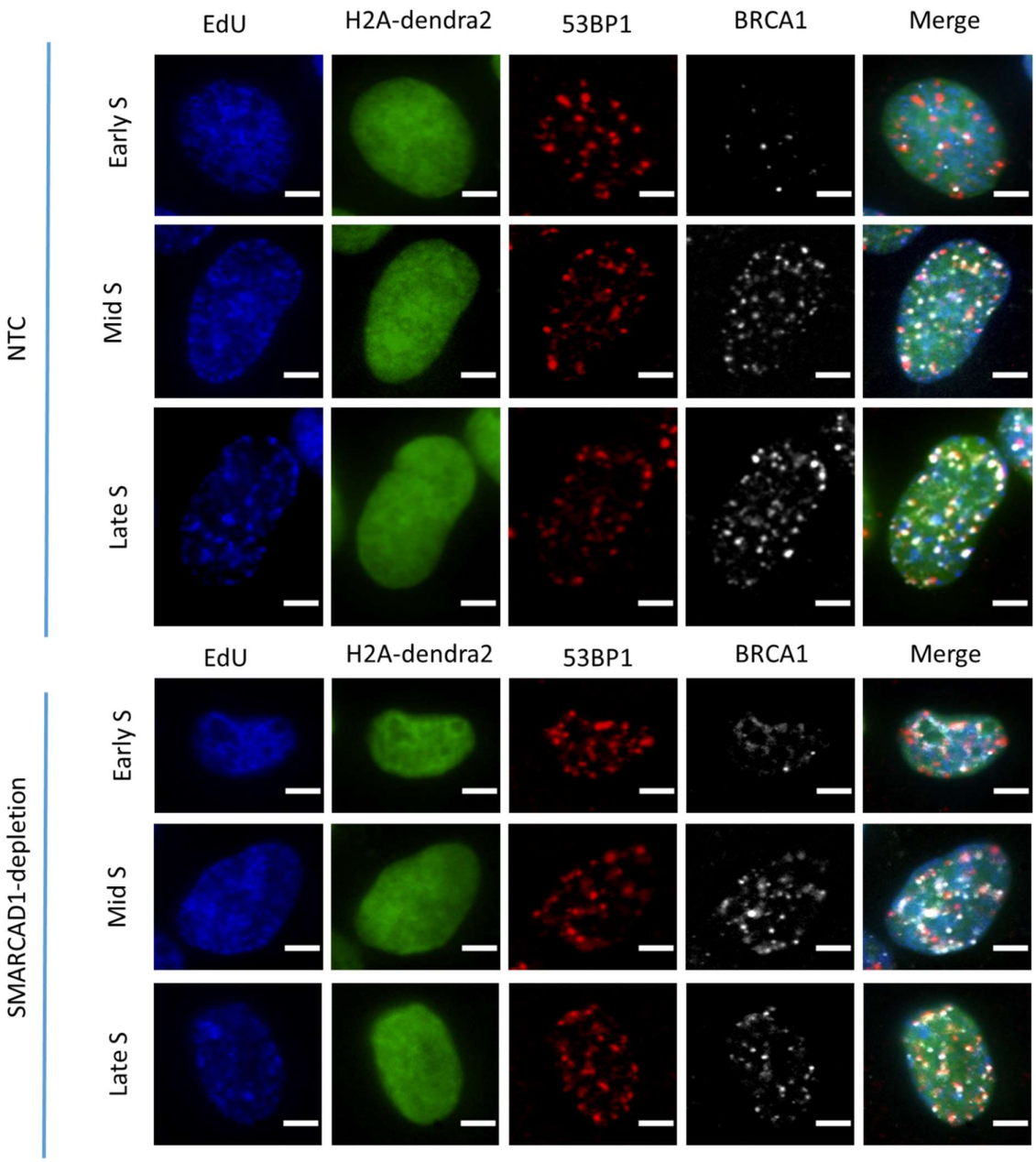

Figure 5.45. Pre-expansion imaging of H2A-dendra2-expressing cells following SMARCAD1 depletion. U2OS cells were induced to express H2A-dendra2 using doxycycline. Cells were treated with siSMARCAD1 or NTC siRNA for 72 hours. Cells were damaged with irradiation (2 Gy) and allowed 1 hour to recover prior to pre-extraction and fixation. Cells were immunostained with BRCA1 and 53BP1. Images were acquired on a widefield microscope. Scale bars 5 µm.

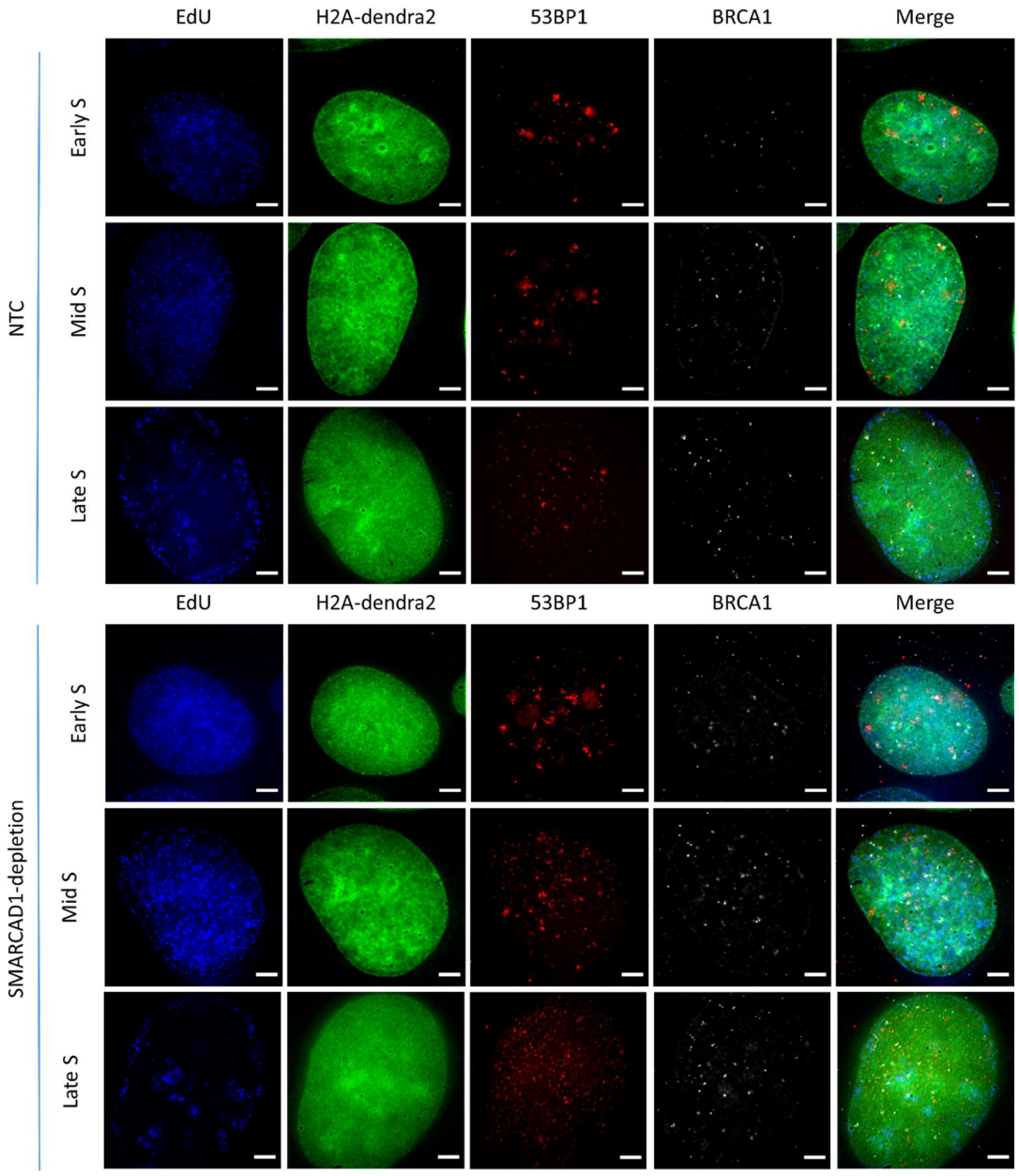

Figure 5.46. Post-expansion imaging of H2A-dendra2-expressing cells following SMARCAD1 depletion. U2OS cells were induced to express H2A-dendra2 using doxycycline. Cells were treated with siSMARCAD1 or NTC siRNA for 72 hours. Cells were damaged with irradiation (2 Gy) and allowed 1 hour to recover prior to pre-extraction and fixation. Cells were immunostained with BRCA1 and 53BP1. Standard ExM preparation was performed (Section 2.4) and Z stacks were acquired on a widefield microscope. Images were deconvolved and representative examples of nuclei classified as early, mid and late S-phase were selected for SMARCAD1-depleted cells and control cells. Scale bars 10 µm.

In both pre-expansion and post-expansion data, we observed BRCA1 foci numbers were increased in mid and late S-phase classified nuclei, and 53BP1 foci numbers were conversely decreased (Figure 5.45 & 5.46). Following acquisition of post-expansion Z stacks in SMARCAD1-depleted and control cells, nuclei were classified as early, mid and late S-phase according to EdU incorporation. We next applied spot detection-based analysis to classify BRCA1 and 53BP1 accumulations in the context of chromatin. In these experiments, H2A-dendra2 represents the chromatin architecture. The classes identified for this are shown schematically in Figure 5.48A. Based on the spot classification data, we aimed to describe average placement of chromatin relative to BRCA1 and 53BP1 for each foci class to provide insight into chromatin architecture in the presence and absence of SMARCAD1-mediated chromatin remodelling.

Nuclei classified as mid and late S-phase in control and SMARCAD1-depleted cells were selected for spot detection-based analysis. We observed that in some of the acquired Z stacks the fluorescence intensity of H2A-dendra2 was comparable to background and therefore these images were not suitable for the desired analysis (Appendix Figure A26). When spot detection-based scoring was attempted, I observed significant amount of spectral overlap for the dendra2 emission and that from the Alexa568 fluorophore conjugated to the BRCA1 antibody (Figure 5.47).

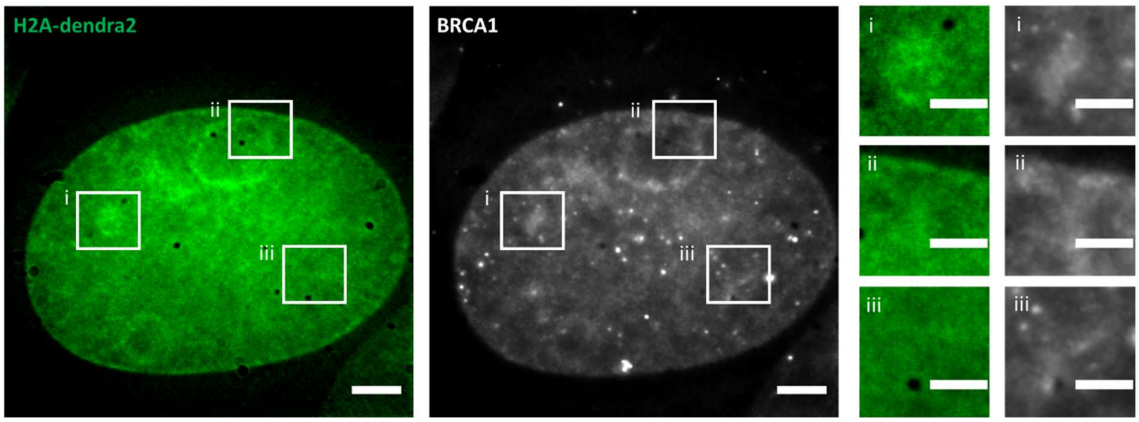

Figure 5.47. Visualising spectral overlap from H2A-dendra2 (488) channel to BRCA1 (561) channel. An example of Z series visualising H2A-dendra2 and BRCA1 to illustrate the presence of spectral overlap in the emission for dendra2 and Alexa Fluor 568 conjugated to the BRCA1 antibody. Scale bars 10 µm and 2 µm

This is due to the ability of the dendra2 chromophore to photo-convert between green- and red-emitting species (Gurskaya *et al*, 2006). In its non-activated state, dendra2 possesses excitation-emission maxima at 486 and 505 nm. Activation or photo-conversion is induced by high intensity irradiation at 460-500 nm resulting in excitation-emission maxima of 553 and 573 nm. To avoid undesired photo-conversion users should keep intensities of 460-500 nm wavelengths low. In this case, the intensities were kept low, but some photo-conversion may have resulted from the high exposure required for good signal-to-noise ratio of H2A-dendra2 in the post-expansion images. When spot detection-based analysis was initially attempted, many features were detected which were likely derived from significant emission from the red-emitting H2A-dendra2 fusion. Given these observations, images where spectral overlap was visualised were removed from any spot detection analysis.

Classification of structures was performed on nuclei classified as mid and late S-phase which had good fluorescence intensity in the H2A-dendra2 channel and little or no spectral overlap from H2A-dendra2 red-emission in the BRCA1 channel. Structures were classified as shown in Figure 5.48A.

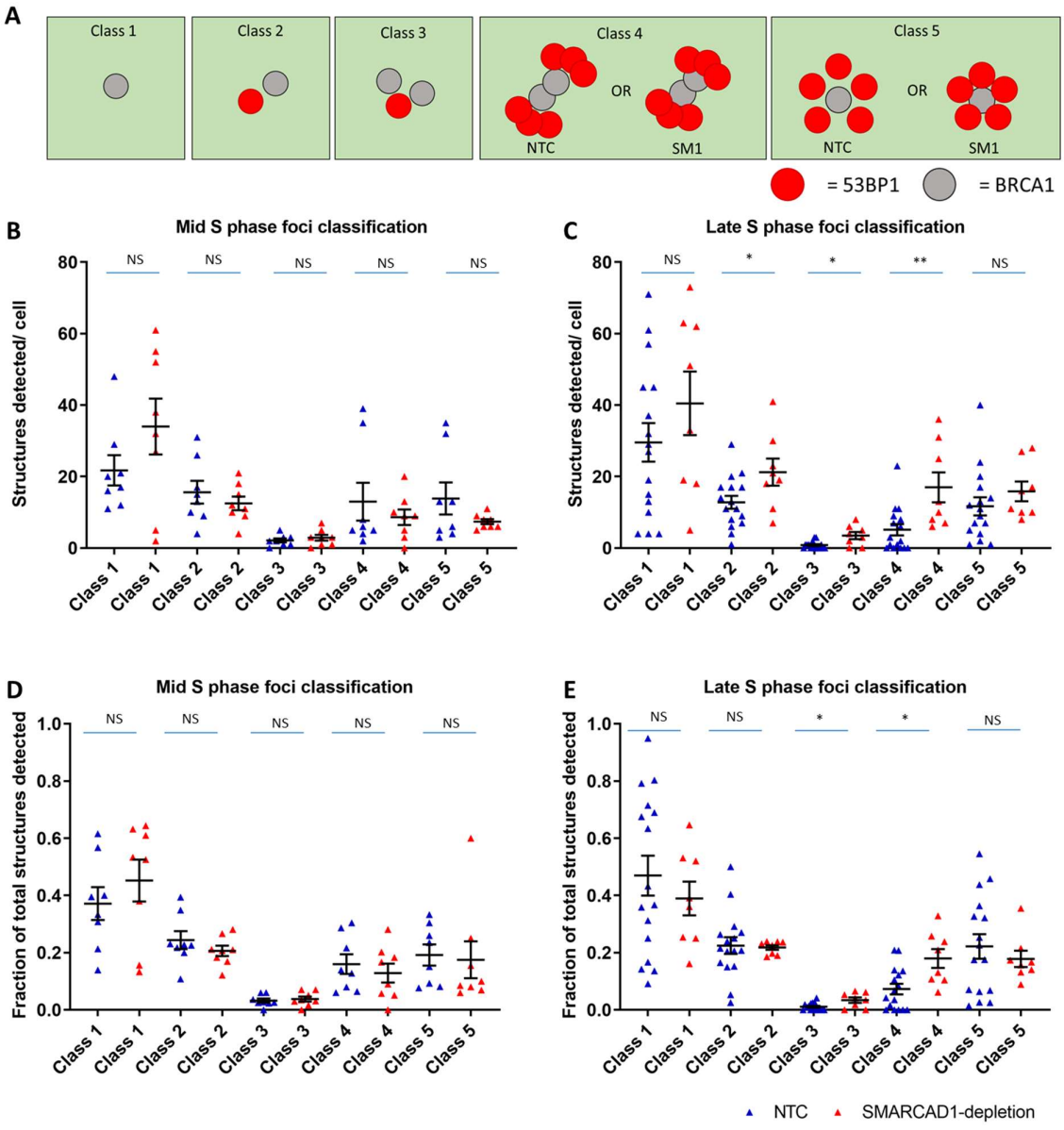

Figure 5.48. Classifying BRCA1 and 53BP1 accumulations in SMARCAD1-depleted H2A-dendra2-expressing cells. Spot detection-based analysis was performed on Z stack data acquired in control and SMARCAD1-depleted cells. Structures were scored for nuclei in mid and late S-phase according to the identified classes shown schematically (Panel A). Scoring is shown as the total number of structures identified per nucleus (Panel B&C) and as a fraction of structures detected per nucleus (Panel D&E). Control data is shown in blue and SMARCAD1-depleted data is shown in red. N=2, NTC mid S = 8 nuclei, NTC late S = 14 nuclei, SMARCAD1-depleted mid S = 8 nuclei, SMARCAD1-depleted late S = 8 nuclei. Throughout Figure, **P <0.01;*P < 0.05 NS, not significant by two-sided Student's t test. Error = s.e.m.

Structure classification (Figure 5.48) showed no differences in distribution of classes in mid S-phase cells. In late S-phase cells an increase in classes 2-4 was observed. This was inconsistent with the data acquired where SMARCAD1-depletion was performed on empty U2OS Flp-In cells (Section 5.2, Figure 5.6), where a decrease in class 5 structures was observed in SMARCAD1-depleted cells compared to control cells. This may be due to the low numbers of nuclei used for the analysis in the case of H2A-dendra2-expressing cells.

We opted to investigate the localisation of 53BP1, BRCA1 and H2A-dendra2 relative to each other in class 5 structures, since significant changes to structure organisation were observed in these structures following SMARCAD1-depletion previously (Section 5.2). We hypothesised that if chromatin remodelling is occurring through the sliding model we might visualise changes in the position of intensity maxima of H2A-dendra2 relative to BRCA1 +/ 53BP1. To investigate this, average profiles of H2A-dendra2, BRCA1 and 53BP1 were generated using a Matlab script written by Dr Jeremy Pike and line profiles were generated for these average profiles (described in Section 2.7.6) (Figure 5.49). These profiles were generated from examples of class 5 structures in which BRCA1 and 53BP1 were oriented parallel to the focal plane.

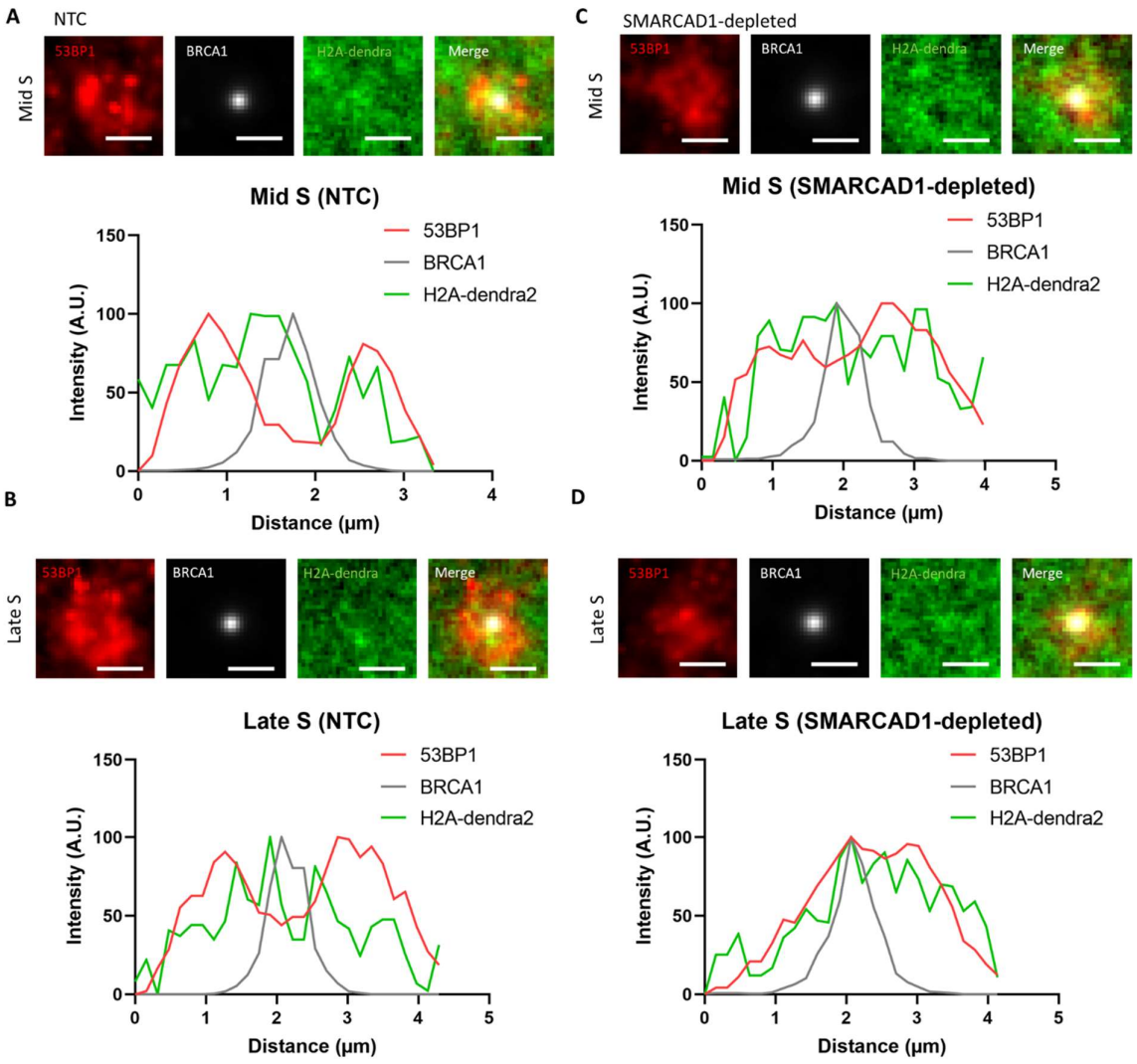

Figure 5.49. Classifying class 5 structure organisation in SMARCAD1-depleted cells. Class 5 structures were selected from experiment summarised in Figure 5.48. Intensity of BRCA1, H2A-dendra2 and 53BP1 across examples was averaged to give the profiles shown as maximum intensity projections. Line profiles of these average profiles were generated as indicated by the white lines and are shown below each maximum projection. Average profiles are based on structures selected from two independent experiments. NTC mid S = 63 structures, NTC late S = 97 structures, SMARCAD1-depleted mid S = 42 structures and SMARCAD1-depleted late S = 94 structures. Scale bar 2 µm.

In control cells, BRCA1 was encapsulated by 53BP1 and a void was present between the two proteins. A loss of the void between 53BP1 and BRCA1 was observed in SMARCAD1-depleted cells, consistent with our previous observations (Section 5.2). Intriguingly, the maxima for H2A-dendra2 was coincided with that of BRCA1 and 53BP1 in the SMARCAD1-depleted cells. By contrast, H2A-

dendra2 maxima in the control cells were located outside of BRCA1 and inside 53BP1 maxima. Notably, H2A intensity coincided with that of 53BP1 in the control cells. This profile was not observed in mid S-phase cells. This suggests that in the absence of SMARCAD1, remodelling of chromatin proximal to the ssDNA compartment of the break is prevented resulting in the maxima of H2A-dendra2 coinciding with BRCA1.

5.4.2 Effect of USP48-depletion on chromatin architecture

We aimed to investigate the effect of USP48 depletion on chromatin architecture proximal to DSBs similarly to SMARCAD1 depletion using H2A-dendra2-expressing cells which were immunostained for 53BP1 and BRCA1 following damage induction by irradiation. As with the SMARCAD1 depletion experiment (Section 5.4.1), we noted emission from photo-converted H2A-dendra2 in the BRCA1 channel in some of the Z series acquired. There were removed prior to performing the spot detection-based analysis. However, upon classification of structures and generation of average structure profiles for class 5 structures, we noted that there was an intensity maxima in the H2A-dendra2 channel which was correlated with the central BRCA1 spot in both the control and USP48 depleted cells. We speculated this may be derived from spectral emission overlap between H2A-dendra2 and Alexa Fluor 568 conjugated to the BRCA1 antibody. Due to this artefact, this experiment did not provide insight into chromatin architecture following USP48 depletion.

5.4.3 Increasing resolving power of ExM to visualise chromatin architecture

Chromatin architecture is organised at multiple scales, ranging from 1400 nm mitotic chromosomes to 10 nm “beads on a string” structure (Kostiuk *et al*, 2019). The inherently small size of nucleosomes (10 nm) and the spacing between these (2-50 nm) renders these features “invisible” using most super resolution techniques (Lou *et al*, 2019). Recent developments in super resolution microscopy now allows visualisation of chromatin structures (Kostiuk *et al*, 2019). The resolution of ExM is 60-70 nm laterally, meaning we are likely visualising chromatin loops and potentially some changes in nucleosomal packing, but the resolution of a standard ExM preparation is insufficient to

detect changes on a nucleosomal level. There have been significant advances in ExM methodology to increase its resolving power (described in Section 1.3.3).

One approach to improve resolution is to increase expansion factor. This has been demonstrated by Boyden and co-workers in the form of iterative ExM (iExM) and allows resolutions of 25nm on diffraction-limited microscopes (Chang *et al*, 2017). This is achieved by performing a preliminary expansion step, and then forming a second polymer mesh in the spaces created by the first expansion. The molecular information in the first gel is transferred to the second using custom-made antibody probes conjugated with oligomers (Section 1.3.3). This approach is hindered by being technically laborious and requiring custom-made antibody-based probes which are expensive to synthesise and are not compatible with the approach we have used in this work. Another approach is X10 ExM, which offers a cheap and simple solution to achieve comparable resolutions of 25-30 nm (Truckenbrodt *et al*, 2019). X10 ExM is also compatible with the commercially available crosslinking reagents (e.g. AcX, labelX) which we have applied in this work. This approach is based on changes to the composition of the polyelectrolyte gel which specimens are embedded in. Here, gels are comprised on dimethylacrylamide (DMAA) and sodium acrylate. DMAA is a self-crosslinking monomer, meaning there is no requirement for additional multifunctional monomers, and the network of crosslinks in the resultant gel is more uniform than in standard ExM preparations, reducing contributions of local stress and distortions in post-expansion images. These gels are super-absorbent, capable of absorbing 3000x their weight in water.

In this work, we attempted X10 ExM to determine if this approach could be used to visualise changes in nucleosomal compaction. To do this, cells were seeded and induced to express H2A-dendra2 using doxycycline. Cells were allowed to grow overnight and then treated with EdU and incubated overnight. Cells were fixed and prepared using X10 ExM approach (Section 2.4.5). Images

were acquired pre- and post-expansion (Figure 5.50). Nuclear areas were measured pre- and post-expansion to estimate the expansion factor (Figure 5.51).

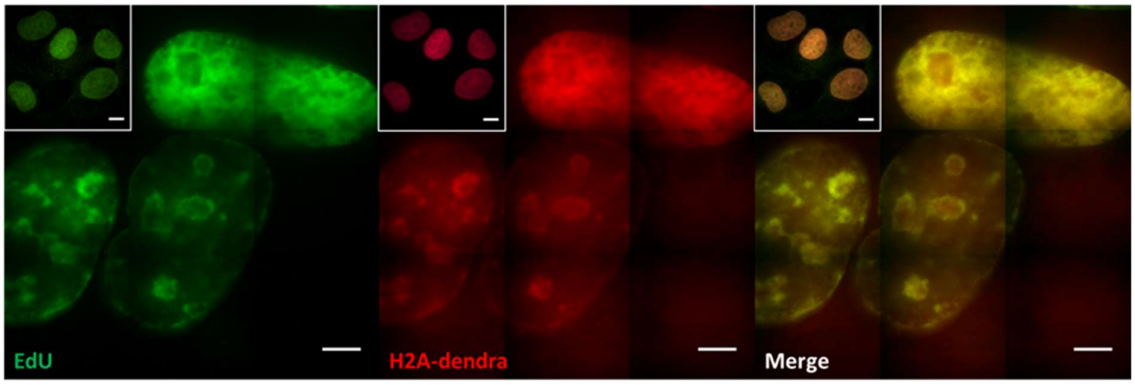

Figure 5.50. X10 ExM optimisation. U2OS Flp-In cell lines were induced with doxycycline to express H2A-dendra2 for 48 hours, and stained with EdU overnight and fixed. Click-it reaction was performed for EdU detection. X10 ExM protocol was performed as in Section 2.4.5. Pre- and post-expansion images were acquired on a widefield microscope. The pre-expansion images (inset) are shown on a relative scale to the post-expansion images. Scale bars 10 µm (pre-expansion) and 50 µm (post-expansion).

Following X10 ExM treatment, nuclei were qualitatively much larger than in pre-expansion images, and as compared to nuclei expanded with standard ExM protocol. To quantify nuclear expansion factor, nuclear areas were measured pre- and post-expansion (Figure 5.51). Nuclei were 6.3x expanded in one dimension, which was inconsistent with the macroscale expansion of the gel (7x expanded). This suggests the nuclear architecture may be constraining the expansion of the nucleus.

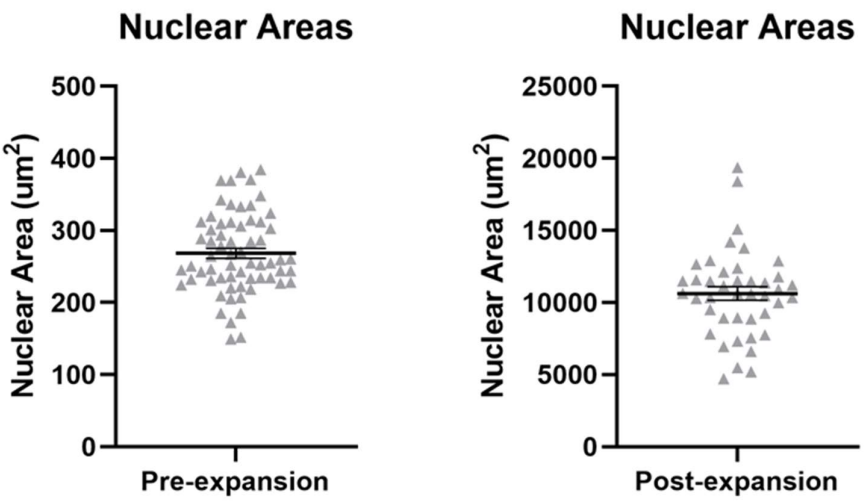

Figure 5.51. Quantifying nuclear expansion factor. Nuclear areas were measured pre- and post-expansion. N=1 >50 nuclei pre- and post-expansion.

Z series were acquired using SPIM to visualise the nanoscale topology of the nuclei (Figure 5.52, Appendix Figure A27). Intriguingly, both DNA and chromatin architecture resembled each other, indicating that the relative spatial relationship between these features is retained after expansion. Notably, there was no evidence of warping or distortion in any of the acquired images. It may be that although the nuclear expansion is constrained, the slower expansion together with the residual genomic integrity is sufficient to prevent gross structural deformation.

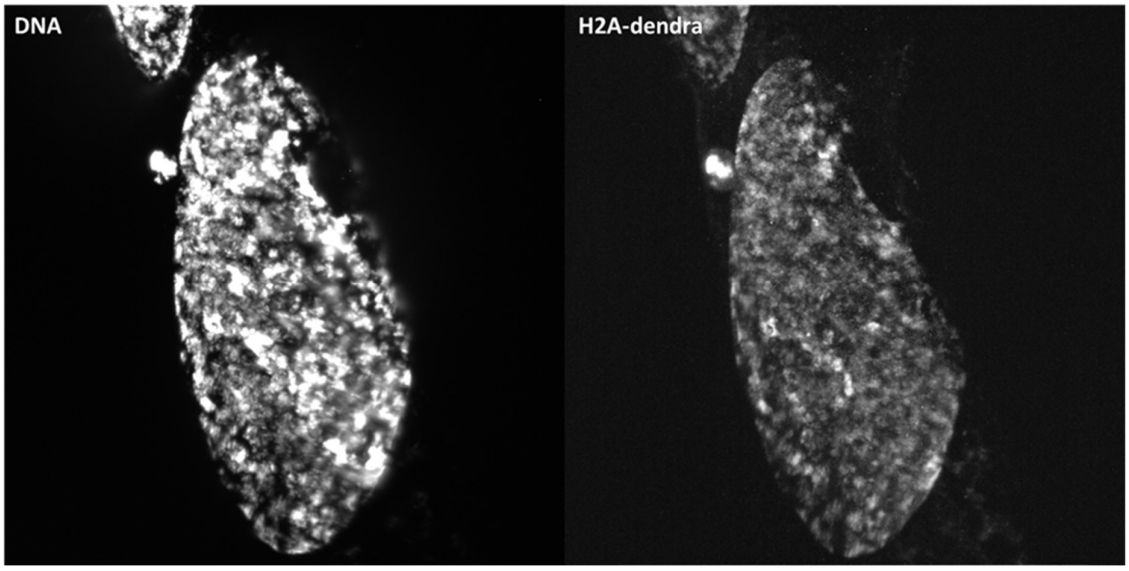

Figure 5.52. SPIM acquisitions of DNA and H2A dendra2 following X10 ExM. Z series of cells treated as in Figure 5.50 were acquired using SPIM. Maximum projections of DNA and H2A-dendra2 are shown.

This protocol requires further optimisation to achieve the reported 10-fold expansion factor, and nuclease treatment may be required to overcome the presence of residual genomic architecture which appears to be hindering the expansion of the nucleus as compared to the gel itself. Nonetheless, this data suggests that 10-fold expansion may be possible and could provide insight into nucleosomal packing proximal to sites of damage.

5.5 Discussion and Conclusions

In order to maximally preserve genomic integrity, DSBs must be repaired by the correct pathway in the correct cellular context. The choice of repair pathway is regulated by a number of factors (discussed in Section 1.1.2-1.1.4). Resection is a key determinant in repair pathway choice. For commitment to HR, BRCA1 mediates the removal of the blockade to resection posed by the 53BP1 repair axis. How BRCA1 removes this blockade is not clearly understood.

Recent evidence points to chromatin dynamics playing a pivotal role in resection required for HR. A potential mechanism for BRCA1-mediated removal of the 53BP1 block to resection is that BRCA1-BARD1 E3 ubiquitin ligase function results in the placement of a ubiquitin mark on H2A (Densham

et al, 2016). This modification is read by chromatin remodeler SMARCAD1 and allows for positioning of 53BP1 away from the break site, and for resection. Resection length is tightly regulated. USP48 has been identified as a H2A-specific DUB which removes the ubiquitin to prevent excessive chromatin remodelling and therefore extended resection lengths (Uckelmann *et al*, 2018). It remains unclear what the mechanism of chromatin remodelling is in this context.

The aim of this chapter was to determine how chromatin remodelling affects spatial organisation of repair structures and how any changes in spatial organisation correlate with chromatin at sites of damage. To investigate this, we initially looked at the organisation of 53BP1 relative to BRCA1 following SMARCAD1 or USP48 depletion as compared to controls. We then explored whether spatial organisation of RAD51 relative to 53BP1 and BRCA1 is indicative of resection initiation/ extent following USP48 depletion. Finally, we explored whether changes in chromatin compaction proximal to the break site could be visualised using ExM on these depletion backgrounds.

Densham *et al* demonstrated that BRCA1-BARD1 possesses E3 ubiquitin ligase function, and where this function is impaired, decreased resection and reduced positioning of 53BP1 relative to BRCA1 results. The authors identified H2A as the substrate of BRCA1-BARD1 E3 ubiquitin ligase function, and that the ubiquitin mark on chromatin is "read" by chromatin remodeler, SMARCAD1. Loss of SMARCAD1 similarly resulted in reduced resection lengths and positioning of 53BP1 away from sites of damage. This suggests that SMARCAD1-mediated remodelling is important to removal of 53BP1 blockade to resection.

We theorised that SMARCAD1-depleted would have a similar effect to BRCA1-depletion in positioning of 53BP1, but BRCA1 is still present for structure classification on this background. Classification data in SMARCAD1-depleted cells compared to control cells revealed a reduction in class 5 structures (defined as one BRCA1 spot encapsulated by multiple 53BP1 spots). These structures are reminiscent of the structures described by Chapman *et al* (Chapman *et al*, 2012). Average profiles of these structures were generated and there was a striking change in 53BP1

accumulations relative to BRCA1; in the control structures, BRCA1 was visualised as a single spherical structure encapsulated by 53BP1, with a visible void present between the proteins. By contrast, in SMARCAD1-depleted cells, 53BP1 occupied a smaller volume and the void between BRCA1 and 53BP1 was absent. These observations were recapitulated in radial profiles generated from average class 5 foci structures; in control cells, 53BP1 maximum intensity was ∼0.75 microns (∼0.188 microns pre-expansion) from the BRCA1 centre, while in SMARCAD1-depleted cells, 53BP1 and BRCA1 had comparable maximum intensities.

Intriguingly, the distribution of 53BP1 following SMARCAD1 depletion differs to that observed following BRCA1 depletion (Section 4.4.4). Following BRCA1 depletion, 53BP1 was observed as dense accumulations throughout early, mid and late S-phase in contrast to controls where we observed a reduction in 53BP1 accumulations in late S-phase cells. This change in 53BP1 distribution was quantified by measuring volumes of 53BP1 foci in BRCA1-depleted cells and control cells. Following SMARCAD1-depletion, 53BP1 occupies a smaller volume during mid and late S-phase as compared to controls. To summarise, following BRCA1 depletion 53BP1 is retained as dense accumulations at sites of damage throughout S-phase but following SMARCAD1 depletion there is a reduction in 53BP1 accumulations in mid and late S-phase cells. This indicates that on the SMARCAD1-depletion background, BRCA1 may retain an ability to redistribute the 53BP1 accumulations proximal to the break site, and an ability to occupy the “exclusion” space at the centre of repair structure, but in the absence of chromatin remodelling, BRCA1 is unable to remove the blockade to resection. This redistribution of 53BP1 following SMARCAD1 depletion may be due to destabilisation of 53BP1 on chromatin proximal to the break (Her and Bunting, 2018 & Isono *et al*, 2017).

PCC and MCC values were calculated for the average structure profiles. A small increase in PCC and M2 values was observed in SMARCAD1-depleted cells compared to controls. This may be due to BRCA1 only occupying a small region of interest and therefore only a small increment is observed

in correlation. However, this may also indicate that changes in class 5 structure organisation is due to 53BP1 positioning being reduced as opposed to an inability of BRCA1 to access the core region. Collectively, these data indicate that whilst SMARCAD1 is not required for recruitment of BRCA1 to sites of damage, its loss disrupts the positioning of 53BP1 away from the central BRCA1 at sites of damage. This is consistent with observations of Densham *et al*; the 53BP1 blockade to resection is retained and prevents longer range resection required for efficient HR.

Further investigation of class 5 structures in SMARCAD1-depleted compared to control cells revealed further heterogeneity in the placement of 53BP1 spots relative to the central BRCA1 spot, which we described as a reduced separation distance (defined as a separation distance of <0.5 µm) or a control separation distance (defined as a separation of ~1.8-2 µm). All class 5 structures in SMARCAD1-depleted and control cells were classified under these definitions to determine their overall prevalence, revealing that >80% of class 5 structures from mid and late S-phase classified nuclei had a reduced distance following SMARCAD1 depletion, whilst in control cells >80% of class 5 structures had a control separation distance. This data highlights the advantages of applying ExM to the study of repair protein accumulations. ExM allows for rapid, nanoscale visualisation meaning that hundreds of repair structures can be visualised and analysed. By applying spot detection-based analysis to classify structures and generation of intensity profiles we are able to quantitatively describe the impact of SMARCAD1-depletion on positioning of 53BP1 relative to BRCA1.

Resection length is tightly regulated to prevent hyper-resection and repair via mutagenic SSA. Uckelmann *et al* identified USP48 as a H2A-specific DUB responsible for "erasing" the ubiquitin mark placed on H2A by BRCA1-BARD1 (Uckelmann *et al*, 2018). Loss of USP48 results in increased repositioning of 53BP1 relative to the central BRCA1 spot and extended resection lengths. Conversely, over-expression of USP48 results in reduced positioning of 53BP1 away from sites of damage and reduced resection lengths. These observations suggest that USP48 fine-tunes resection lengths to preserve genomic integrity.

We hypothesised that applying ExM to investigate the organisation of 53BP1 and BRCA1 accumulations in USP48-depleted cells would reveal nanoscale changes in their relative positioning, similarly to SMARCAD1-depletion. Post-expansion images of USP48-depleted cells in S-phase showed larger 53BP1 structures compared to control cells, some of which exhibited a larger space between BRCA1 and 53BP1 spots or an oligomeric structure of 53BP1 encapsulating BRCA1. Structure classification of USP48-depleted and control cells revealed an increase in class 5 structures (defined as one BRCA1 spot encapsulated by multiple 53BP1 spots). Average structures were generated for control and USP48-depleted cells were generated and revealed alterations to their organisation. As with SMARCAD1-depletion data, control structures were comprised of a central BRCA1 spot encapsulated by 53BP1 with a void between the two proteins. In USP48-depleted structures, this distribution was also observed but on this background the void between 53BP1 and BRCA1 was increased. This change in distribution was recapitulated in radial profiles generated for the average class 5 structures. PCC and MCC values were quantified for the average structures revealing a small decrease in PCC and M2 values in USP48-depleted cells. This suggests a reduction in overlap between 53BP1 and BRCA1.

Further interrogation of these structures revealed heterogeneity in the placement of 53BP1 spots relative to BRCA1, similarly to SMARCAD1-depletion data. We described structures as having an increased separation distance (defined as a separation distance of ~2-2.8 μm) or a control separation distance of ~1.8-2 μm) between 53BP1 and the central BRCA1. All class 5 structures were classified under these definitions, revealing >80% of class 5 structures had an increased separation distance following USP48 depletion whilst in the controls >70% of class 5 structures had a control separation distance. These data are consistent with further positioning of 53BP1 away from the break site and unchecked hyper-resection occurring in the absence of USP48 mediated by SMARCAD1 chromatin remodelling.

Thus far, we have confirmed that USP48-depletion results in increased positioning of 53BP1 relative to BRCA1 in class 5 structures. Uckelmann *et al* observed that this was associated with increased DNA resection lengths. USP48-depleted cells had an increased use of HR and SSA, promoted by RAD51 and RAD52, respectively. The authors observed increased numbers of RAD51 with increased intensity compared to controls. These observations suggested that more copies of RAD51 are recruited to sites of damage on USP48-depletion background. We therefore hypothesised that by applying ExM we could visualise changes in RAD51 structures associated with increased resection lengths following USP48 depletion.

RAD51 and 53BP1 accumulations were investigated in USP48-depleted cells compared to controls. Structure classification was performed in a similar way to 53BP1 and BRCA1 data, and revealed an increase in class 4 structures (defined as multiple RAD51 spots associated with multiple 53BP1 spots) in USP48-depleted cells. Further investigation of these structures revealed continuous, elongated accumulations of RAD51 which were more prevalent in USP48-depleted cells than control cells. These structures are suggestive of increased resection lengths being coated by RAD51 on USP48-depleted background compared to controls.

These observations collectively suggest that following USP48 depletion 53BP1 is positioned further from the core BRCA1. This is mediated by BRCA1-BARD1 E3 ubiquitin ligase function and SMARCAD1-mediated chromatin remodelling. The increased positioning of 53BP1 away from the centre of repair sites results in increased resection lengths and recruitment of RAD51, which we visualise here as an increased number of nucleofilament-like structures in USP48 depleted cells compared to controls. These conclusions are summarised in Figure 5.53.

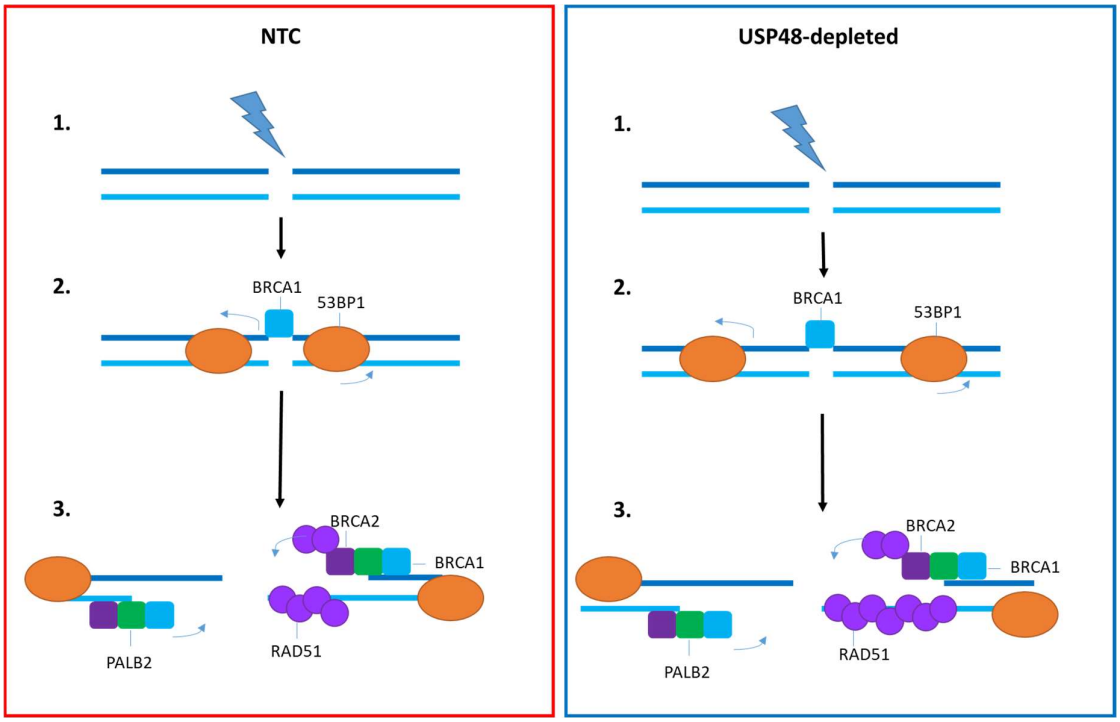

Figure 5.53. Effect of USP48 depletion on foci sub-compartmentalisation. 1) DSB occurs. 2) BRCA1 removes the blockade to resection posed by 53BP1. In control cells, this is mediated by BRCA1-BARD1 E3 ubiquitin ligase function and chromatin remodelling mediated by SMARCAD1. USP48 restrains the position of 53BP1 relative to BRCA1, and therefore resection length on this background. In USP48-depleted cells, USP48 does not fine-tune the position of 53BP1 resulting in 53BP1 being placed further from the break site, and increased resection lengths. 3) RAD51 nucleofilament formation is mediated by BRCA1-PALB2-BRCA2. In control cells the resection length is shorter and so is the formed RAD51 nucleofilament. In USP48-depleted cells resection length is increased and the RAD51 nucleofilament is longer.

To corroborate this model of spatial organisation of RAD51, BRCA1 and 53BP1, we immunostained cells for BRCA1, 53BP1 and RAD51 simultaneously in cells depleted of USP48 compared to control cells. We hypothesised that the increased peak-to-peak distance of 53BP1 and extended resection lengths would allow better delineation of compartments occupied by RAD51, BRCA1 and 53BP1. Qualitative assessment of the spatial organisation of these repair factors revealed substantial heterogeneity in the enrichment of proteins within the same repair focus, and in their relative

spatial organisation within repair foci. To describe this structural heterogeneity, I developed an analytical approach based on known mechanistic information (described in Section 5.3.4).

Spot detection-based analysis of RAD51, 53BP1 and BRCA1 revealed 10 classes of structures. I performed a detailed investigation of structures where RAD51, BRCA1 and 53BP1 were enriched and noted the presence of three key organisations. Class 7 structures were defined as BRCA1, 53BP1 and RAD51 spots closely associated within 1 μm, class 8 structures were defined as RAD51 spot(s) associated with BRCA1 encapsulated by 53BP1, and class 9 structures were defined as multiple RAD51 spots associated with BRCA1 encapsulated by 53BP1. These structures may be indicative of RAD51 recruitment and subsequent loading of RAD51 onto ssDNA to form the nucleofilament (illustrated in Figure 5.54). Class 7 may represent interaction of RAD51 with the BRCA1-PALB2-BRCA2 complex. Class 8 and 9 may indicate loading of RAD51 onto ssDNA.

Classification of repair structures revealed an increase in class 4 structures (defined as multiple RAD51 associated with multiple 53BP1) and class 9 structures (defined as multiple RAD51 spots associated with BRCA1 spot(s) encapsulated by 53BP1 spots) in USP48 depleted cells compared to controls. These observations again suggest that increased resection lengths are detected as RAD51 nucleofilaments following USP48-depletion.Class 4 and class 9 structures were further interrogated with particular interest in the prevalence of continuous accumulations of RAD51 which may be consistent with nucleofilament formation. This analysis revealed higher numbers of continuous accumulations of RAD51 compared to discontinuous accumulations following USP48 loss.

Intriguingly, the placement of BRCA1 relative to RAD51 accumulations was heterogeneous in terms of numbers of BRCA1 spots and location of BRCA1 spots. In the majority of selected structures, one BRCA1 spot was observed to localise at one end of the nucleofilament. This is consistent with observations of Shahid *et al* where electron microscopy was applied to visualise BRCA2-mediated loading of RAD51; BRCA2 was localised at one end of RAD51 ssDNA nucleofilament (Shahid *et al*, 2014). We theorise this may indicate the loading of RAD51 is from that end of the break.

Interestingly, there was no notable symmetry in the repair structures which could indicate that RAD51 coating occurs on one side of the break and then the other subsequently.

Surprisingly, we observed more continuous RAD51 accumulations in the absence of BRCA1 (class 4 structures) than in the presence of BRCA1 (class 9 structures). This may be explained by the association between RAD51 and the BRCA1-PALB2-BRCA2 complex being transient, and BRCA1-PALB2-BRCA2 dissociates once nucleation has been initiated. This idea is consistent with observations that BRCA2 is observed infrequently following longer incubations with RAD51 (Shahid *et al*, 2014). It is possible that we are not visualising D-loop formation as indicated by the relative infrequency of BRCA1 association with continuous RAD51 accumulations. Based on these observations we propose a model as summarised in Figure 5.54.

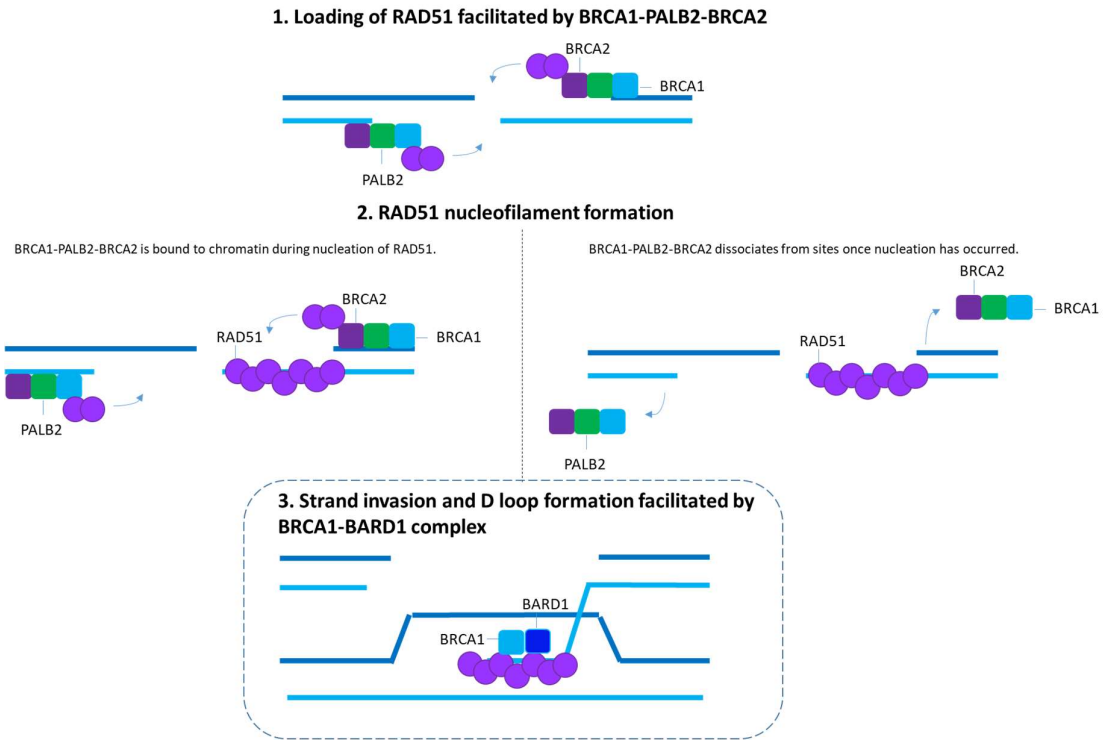

Figure 5.54. Spatial organisation of repair factors indicating steps of HR. 1) BRCA1 mediates removal of 53BP1 further from the centre of the break site allowing for resection by nucleases. BRCA1-PALB2-BRCA2 complex interacts with RAD51. 2) BRCA2 promotes exchange of RPA for RAD51 and subsequently dissociates following filament nucleation. 3) Strand invasion and D loop formation is mediated by RAD51-ssDNA nucleofilament and BRCA1-BARD1 (potentially not visualised here).

In this work, we have shown that SMARCAD1 loss results in little or no positioning of 53BP1 away from the central BRCA1 spot. Densham *et al* showed that this is accompanied by reduced resection lengths due to an inability to remove the 53BP1-mediated block to resection. Conversely, upon USP48 loss, we observed increased positioning of 53BP1 away from the central BRCA1. This increase was shown to be associated with increased resection lengths (Uckelmann *et al*, 2018). We have also shown that RAD51 structures consistent with nucleofilament formation are more prevalent on USP48 depletion background. Both SMARCAD1 and USP48 are known to impact chromatin remodelling proximal to the break, which prompted us to consider if changes in chromatin could be detected on these backgrounds using ExM.

To investigate this, H2A-dendra2-expressing cells were depleted of either SMARCAD1 or USP48 and structures were classified as previous. In these experiments, we particularly focussed on class 5 structures (defined as one BRCA1 spot surrounded by multiple 53BP1 spots) as changes in organisation were visualised in this class. We hypothesised that if chromatin remodelling is occurring via a sliding model, then changes in the intensity maxima of H2A-dendra2 could be visualised relative to BRCA1 and 53BP1 in these foci structures. To investigate this, average class 5 structures were generated for control cells, SMARCAD1- and USP48-depleted cells.

Following SMARCAD1 loss, we visually observed that H2A maxima coincided with BRCA1 and 53BP1 maxima, whereas in the controls H2A maxima exists outside of the core BRCA1 and H2A intensity maxima coincided with that of 53BP1. These distributions indicate that in the absence of SMARCAD1, chromatin remodelling and therefore 53BP1 positioning away from the core BRCA1 is constrained, whilst in the controls 53BP1 is repositioned by SMARCAD1-driven chromatin remodelling, resulting in reduced correlation of 53PB1 and H2A with the core BRCA1. This hypothesis is supported by observations made previously by confocal microscopy (Densham *et al*, 2016) and by FLIM-FRET (Lou *et al*¸2019). In the former case, SMARCAD1 depletion resulted in colocalisation between 53BP1 and BRCA1, whilst in the controls, 53BP1 was positioned outside of the core BRCA1, and in the latter case the authors suggested that chromatin can constrain 53BP1 mobility at sites of damage. Overall, these data suggest that chromatin remodelling during HR initiation may indeed be driven by nucleosomes sliding along DNA.

In the USP48-depleted cells, we observed H2A-dendra2 intensity maxima as a spherical structure which was strongly correlated with BRCA1. This was present in both the control and USP48 depleted cells. We concluded that this pattern may be due to spectral overlap observed in the emission of H2A-dendra2 and Alexa Fluor 568 conjugated to BRCA1. Given this, it was not possible to perform analysis as with SMARCAD1 depleted cells. We concluded that H2A-dendra2 is not an optimal fluorescent protein for this application, and clearer structural data could be obtained by

using a different fluorescent protein with good retention of its fluorescence intensity following a standard ExM preparation. Despite this limitation, these experiments indicate that ExM may provide insight into chromatin compaction/ de-compaction proximal to break sites.

It is also important to note that when analysing the spatial relationship between 53BP1, BRCA1 and H2A following SMARCAD1 depletion, images where spectral emission overlap was observed between the H2A-dendra2 channel and the Alexa Fluor 568-conjugated BRCA1 were removed from subsequent analysis and that overall structure profiles were generated from images where this was minimal or absent. Further, the spot detection analysis includes a background subtraction to prevent detection of background pixels in the spot detection. Given that chromatin at this resolution does not adopt a spot-like structure, it is possible that we are underestimating the chromatin proximal to BRCA1 and 53BP1 in these images by removing intensity derived from spectral emission overlap.

Using the standard ExM protocol, we are visualising features with a resolution of 60-70 nm meaning we are likely detecting chromatin loops and some changes to nucleosomal compaction surrounding sites of damage (Kostiuk *et al*, 2019). To gain further insight, we attempted use of X10 ExM to visualise chromatin architecture with higher resolution. In these experiments, we achieved an expansion factor of 6.3x which equates to an approximate resolution of 40-50 nm (or 250-300 nm / expansion factor), and were able to visualise the nanoscale topology of nuclei with increased detail. However, the expansion factor of the nuclei was lower than the macroscale expansion of the gel suggesting the residual integrity of the nucleus may be constraining its expansion. It may be possible to overcome this limitation by using specific nucleases to allow DNA to expand. There are important considerations when applying this approach (discussed in Section 6.7.2), one key concern being the potential for inducing distortions in the expanded image derived from treating nuclei with nucleases and effectively fragmenting the DNA.

In this chapter, we have demonstrated an ability to detect nanoscale alterations in spatial organisation of 53BP1, BRCA1 and RAD51 following SMARCAD1 and USP48 depletions. We have shown that increased resection lengths may be detected by increased prevalence of a RAD51 nucleofilament-like structures following depletion of USP48. Further we performed multi-colour imaging of RAD51, BRCA1 and 53BP1 following USP48 depletion. These data revealed heterogeneous spatial organisation of repair factors which could be indicative of HR progression. The increased resolution offered by ExM allowed for clear discrimination of compartments occupied by these repair factors. Additionally, ExM allows for rapid, scalable three-dimensional imaging of large numbers of structures which can be quantitatively described using spot detection-based analysis. This approach could allow us to corroborate a spatial map of repair and may provide insight into how mutations of such pivotal regulators can affect this spatial map. Finally, we investigated the possibility of using ExM to characterise changes in chromatin architecture during DSB repair. The preliminary data we show here indicates it may be possible to detect large scale alterations to chromatin architecture using ExM. This approach would complement techniques applied to map chromatin architecture and dynamics.

6. Discussion and Future Perspectives

6.1 Introduction

DSBs are highly toxic DNA lesions which must be repaired accurately to prevent mutations and chromosomal translocations which would otherwise cause severe phenotypes such as immunodeficiencies and malignancies (Matt and Hofman, 2016). DSBs can be repaired by several mechanisms, and the choice of repair pathway is tightly controlled by a number of factors including cell cycle phase, resection at the break site and chromatin remodelling proximal to the break (discussed in Section 1.1.2-1.1.4).

Application of fluorescence microscopy to visualise repair of DSBs has revealed a complex spatiotemporal regulation to damage resolution which appears to be intimately linked to other factors controlling DSB repair (Bekker-Jensen *et al*. 2006, Chapman *et al*. 2012, Kakarougkas *et al*. 2013, Ochs *et al*. 2019, Reindl *et al*. 2017). Use of confocal and SRM techniques such as STED, SIM and STORM have contributed to a spatial map of repair in which a proteins time of arrival and site of residence within a repair focus is indicative of function during repair. However, these techniques offer a compromise between resolution, speed and versatility (described in Section 1.2.4).

A number of studies employing super resolution microscopy have corroborated the concept of spatial organisation being indicative of function of proteins during repair of DSBs. For example, Chapman *et al* employed SIM and showed that BRCA1 initiates HR by excluding 53BP1 away from the core of repair foci, and that this event represents the temporal switch from NHEJ to HR (Chapman *et al*, 2012). CtIP and RPA have similarly been shown to occupy the central region of foci and are encapsulated by 53BP1 (Chapman *et* al, 2012 & Kakarougkas *et al,* 2013). Reindl *et al* applied STED microscopy and revealed this organisation is retained between RAD51 and 53BP1; RAD51 occupied the minima of 53BP1 oligomeric structures (Reindl *et al,* 2015). These observations support the hypothesis of Bekker-Jensen *et al* that repair factors are organised into distinct subcompartments which are critical to function. It is thought that BRCA1, CtIP, RPA and RAD51

present in the core of repair foci represent the resected kilo-base sections of DNA, and this is much smaller than the mega-base spanning chromatin bound proteins such as 53BP1. The retention of 53BP1 in the later stages of HR is perplexing since its loss restores HR in BRCA1-deficient cells. Ochs *et al* showed that 53BP1 loss or exhausting its ability to bind chromatin at sites of damage results in hyper-resection and increased repair via SSA. The authors suggest that 53BP1 plays a role in fostering homology of HR and that its role is not limited to protecting DNA ends for NHEJ (Ochs *et al*, 2016). Since 53BP1 accumulations occupy a reduced volume in foci, it appears that the removal of 53BP1 blockade to resection is more of a redistribution rather than complete removal. The idea of 53BP1 playing a structural role during repair is supported by the observations of Ochs *et al* using SIM and STED microscopy (Ochs *et al*, 2019). In this work, they characterised a structural module comprised of 53BP1 and RIF1. The authors provide evidence that this structural module freezes chromatin proximal to DSBs to prevent unwanted resection of DNA ends and may potentially form a cave-like structure for concentration of repair factors.

In this work, we applied new super resolution technique, expansion microscopy (ExM) in order to overcome some of the limitations associated with other SRM techniques. ExM methodology allows for rapid acquisition of thousands of nanoscale features using a widefield microscope (Wassie *et al*, 2017). This approach is particularly attractive since there is no requirement for sophisticated hardware or software. The ability to image such a large number of features deters users from selecting model foci structures, instead allowing detailed characterisation of the heterogeneous populations of foci structures. By coupling ExM with other molecular techniques, we may visualise previously uncharacterised interactions, dependencies and inter-relationships within repair pathways. Such work will serve to corroborate mechanisms of repair in vivo and may direct therapeutic interventions (Whelan *et al*, 2018).

6.2 Investigating retention of nuclear architecture following Expansion Microscopy (ExM) preparation

The extensive preparation required for ExM means it is critical to quantify the isotropy of expansion (i.e. the uniformity of samples throughout samples) as anisotropy can result in distortions in the final image. Furthermore, it is important to quantify the expansion factor with nanoscale precision for accurate measurement of features in expanded specimens (Pesce *et al*, 2019). Recent evidence suggests that different specimens or sub-cellular compartments expand differentially due to differences in ionic environments between and throughout specimens (Zhao *et* al, 2017 & Pernal *et al,* 2020). The presence of differential expansion renders absolute nanoscale measurements of features challenging. The nucleus is a particular concern as the presence of undigested genomic DNA in the expansion gel has the potential to produce irregularities leading to distortions in the sample which may impact the retention of the relative spatial organisation of DNA- and chromatin-bound complexes (Geertsema & Ewers, 2016). Despite numerous studies employing ExM to investigate nuclear structures, there is no current consensus on how the nucleus should be treated or how the expansion process could impact the nuclear architecture (Tillberg *et al*, 2016, Chozinski *et al*, 2016 & Freifeld *et al*, 2017).

We confirmed that four-fold expansion of the nucleus was achievable in the presence of the nucleic acid anchor, LabelX. An expansion factor of 3.7-4x in each dimension was observed by measuring the areas and volumes of nuclei pre- and post-expansion. This expansion factor is comparable to the macroscale expansion of the gel, suggesting that the physical features of intact genomic DNA does not impact expansion of the nucleus. To confirm nanoscale isotropic expansion of the nucleus we performed a correlative imaging experiment in which we acquired pre-expansion SIM images of nuclei, and post-expansion widefield images of the same nuclei. We confirmed the morphology of the nuclei was retained and nanoscale features were comparable between the pre- and post-

expansion images, suggesting that the nucleus expands isotropically with minimal distortions to the nuclear architecture.

As DNA metabolic processes are occurring in the context of chromatin, and chromatin remodelling is known to play a crucial role in DNA damage resolution, we investigated the architecture of chromatin post-expansion (Misteli & Soutoglou, 2009 & Polo, 2014). We hypothesised the digestion step required for ExM preparation would result in the loss of endogenous histones, so opted to represent chromatin using H2A tagged with either dendra2 or mCherry fluorescent proteins (Tillberg *et al*, 2016). We confirmed a strong correlation between DNA and H2A through quantification of PCC in pre- and post-expansion images of nuclei. The retention of the positive correlation between H2A and DNA in post-expansion images further suggests we are not inducing gross deformations in the nuclear architecture during ExM preparation. Additionally, the use of fluorescently labelled histones has the potential to provide insight into mechanisms of chromatin remodelling which have thus far remained elusive due to the inherent difficulty in visualising chromatin at the level of individual nucleosomes (discussed in Section 6.7.2).

6.3 Nanoscale organisation of repair foci can be visualised following ExM preparation

To investigate the applicability of ExM to investigation of nanoscale features in the nucleus, we opted to investigate the relative spatial organisation of known pivotal regulators, 53BP1 and BRCA1, in EdU-positive cells following irradiation and ExM preparation. The spatial organisation of these proteins has previously been described by other SRM techniques (Chapman *et al*, 2012, Reindl *et al,* 2017 & Schwarz *et al,* 2019).

Strikingly, we observed 53BP1 accumulations as a series of discontinuous spots throughout S-phase, reminiscent of the 53BP1 nano-bodies observed by Ochs *et al* (Ochs *et al*, 2019). In early S-phase classified nuclei 53BP1 appeared as dense accumulations of spots with little or no association with BRCA1, whilst in mid and late S-phase classified nuclei, there was an increase in accumulations

enriched with both BRCA1 and 53BP1 spots. Furthermore, 53BP1 accumulations appeared to occupy a smaller volume in mid and late S-phase nuclei compared to early S-phase nuclei, consistent with observations of Chapman *et al* that 53BP1 occupies a smaller volume in S-phase cells than in G1 cells (Chapman *et al*, 2012).

It is possible that the heterogeneity in BRCA1 and 53BP1 accumulations between early, mid and late S-phase classified nuclei are derived from the different types of damage induced by irradiation (described in Section 1.4). The 53BP1 accumulations with little BRCA1 enrichment observed in early S-phase classified nuclei may represent frank DSBs formed which could be repaired rapidly by NHEJ. Irradiation can also induce complex DSBs and single strand DNA lesions which can exist as clustered damage. The efficiency of repair of these clustered lesions is reduced meaning there is an increased chance of a replication fork encountering these clusters resulting in replication stress and collapse of the replication fork to form DSBs which are distinct from frank DSBs. It is possible some of the accumulations visualised in mid-late S-phase nuclei represent clustered damage and that heterogeneity in BRCA1 and 53BP1 accumulation is therefore cell cycle-dependent. Interpretation of structural heterogeneity in protein accumulations is further complicated by the fact that the cell cycle phase in which damage occurs may also impact accumulations (described in Section 4.6).

Spot detection-based classification of these accumulation revealed five classes of structure. We speculated that class 1 structures (defined as 1 BRCA1 spot within a 2 μm radius) related to endogenous replication stress. BRCA1 association with EdU was assessed in non-irradiated and irradiated cells. Intriguingly, we observed an increase association of BRCA1 accumulations with EdU in irradiated cells when compared with non-irradiated cells which may indicate increased replication stress induced by irradiation. Following investigation of 53BP1 and BRCA1 accumulations and their EdU association, we observed that the majority of accumulations were EdU positive in irradiated cells, and equal proportions of class 1 and class 2 structures which were EdU positive and negative in non-irradiated cells. It appears that a pool of these structures relate

to endogenous replication stress, which may be increased by the presence of single strand lesions following irradiation.

Class 4 structures (defined by the presence of multiple BRCA1 and 53BP1 spots) were investigated and four subclasses were identified. These accumulations may relate to clustered damage arising from irradiation. Alternatively, these structures may or may not relate to a shift in BRCA1 complex composition since BRCA1 forms several functionally distinct complexes which support different functions during HR (Her *et al*, 2016). For example, structures in which BRCA1 spots are detected outside of the 53BP1 spots may represent BRCA1-A complex (RAP80/ Abraxas/ MERIT40), consistent with the observation that both BRCA1 and RAP80 structures occurs outside of 53BP1 nanobodies (Ochs *et al*, 2019). We speculate that accumulations in which BRCA1 is encapsulated by 53BP1 spots may represent a shift in composition to form BRCA1-C complex and therefore may indicate resection initiation (Hu *et* al, 2011). However, it is unclear from this data which BRCA1 complex is responsible for which localisation pattern and further experiments are required to further interrogate this (described in Section 6.7.1)

Class 5 structures, characterised by a discontinuous 53BP1 spots encapsulating the core BRCA1 spot, were reminiscent of structures observed by other SRM techniques (Chapman *et al*, 2012 & Ochs *et al*, 2019) and appear to indicate resection initiation. This idea is further corroborated by observations in structure organisation following depletion of chromatin regulators, SMARCAD1 and USP48 (discussed in Section 6.4). From the average class 5 structures generated we estimate the spacing between BRCA1 and 53BP1 as 60-80 nm, which is now appreciable due resolution of ExM and the ability to assess localisation across hundreds of examples of structures. Following BRCA1 depletion, we observed 53BP1 as dense accumulations throughout S-phase whilst in the control cells 53BP1 accumulations occupied a smaller volume in late S-phase. These observations indicate ExM preparation can detect nanoscale changes in repair protein accumulations consistent with observations via other SRM techniques.

6.4 The impact of chromatin remodelling on foci sub-compartmentalisation can be detected using ExM

Resection is a critical determinant in repair pathway choice and is controlled by antagonism between 53BP1 and BRCA1. 53BP1 and its downstream effectors (e.g. RIF1, Shieldin-CST-polα complex) shield DNA ends from resection and promote repair via NHEJ (Noordermeer *et al*, 2018 & Mirman *et al*, 2018). BRCA1 promotes HR by removing this blockade to resection through a mechanism that remains unclear. Recent evidence suggests that chromatin remodelling events regulated by SMARCAD1 and USP48 play a role in fine-tuning resection lengths and directing faithful repair of DSBs, with SMARCAD1 promoting positioning of 53BP1 away from the break site to allow resection and USP48 constraining the positioning of 53BP1 to prevent hyper-resection (Densham *et al*, 2016 & Uckelmann *et al*, 2018).

We investigated whether ExM could detect changes in nanoscale spatial organisation of BRCA1 and 53BP1 following depletion of SMARCAD1 and USP48 under the hypothesis that 53BP1 positioning relative to BRCA1 would be contracted and extended under these conditions, respectively. We observed that class 5 structures (defined as one BRCA1 spot encapsulated by multiple 53BP1 spots) were decreased following SMARCAD1 loss, and increased following USP48 loss. Average profiles of class 5 structures were generated each condition relative to controls. In SMARCAD1 depleted cells, the void observed between 53BP1 and BRCA1 spots in the controls was absent, whereas in the case of USP48 depleted cells the void was greatly increased. In the case of SMARCAD1, 53BP1 blockade to resection appears to be retained as shown by its close spatial proximity to BRCA1 as compared to controls. By contrast, USP48 depletion appears to result in increased 53BP1 or chromatin mobility as indicated by the larger separation distance between 53BP1 and BRCA1. This is consistent with previous observations via confocal microscopy (Densham *et al*¸2016 & Uckelmann *et al*, 2018). By applying ExM, we are able to robustly detect nanoscale alterations to spatial organisation of repair proteins based on a large number of features imaged in each condition. The

use of spot detection-based analysis together with average structure profile generation allowed us to quantitatively describe the impact of SMARCAD1 and USP48 depletion on 53BP1 positioning relative to BRCA1.

It has been suggested that arrangement of 53BP1 nano-domains is indicative of chromatin structure proximal to DSBs (Ochs *et al*, 2019). This idea is further corroborated by observations using phasor histone FLIM-FRET in which the authors demonstrate that repair focus formation and chromatin architecture are linked (Lou *et al*, 2019). Chromatin architecture appears to constrain 53BP1 mobility at sites of damage, and that chromatin remodels by sliding of nucleosomes to allow access for the repair machinery. It should be noted this model does not exclude eviction or recycling of histones.

We theorised that chromatin architecture would be retained as a compacted focus in SMARCAD1 depleted cells and that the 53BP1 accumulations would exist inside tightly compacted chromatin. Conversely, following USP48 loss, we hypothesised that chromatin would be de-compacted further from the centre of the break site than in controls, and 53BP1 accumulations would be constrained by the chromatin architecture. To determine if ExM could provide insight into chromatin compaction proximal to sites of damage, we investigated H2A-dendra2 intensity relative to BRCA1 and 53BP1 in class 5 structures (defined as one BRCA1 spot encapsulated by multiple 53BP1 spots).

Intriguingly, in control cells the H2A maxima were located outside of the central BRCA1 and H2A intensity coincided with that of 53BP1. By contrast, in the SMARCAD1 depleted cells, H2A intensity coincided with both BRCA1 and 53BP1 maxima. We hypothesised that in the absence of SMARCAD1, chromatin remodelling and therefore 53BP1 mobility is constrained, resulting in a closer spatial proximity or correlation between 53BP1, H2A and BRCA1, whereas in control cells, chromatin remodelling and 53BP1 mobility are not constrained resulting in reduced correlation with the core BRCA1. These data support the idea of chromatin remodelling occurring by

nucleosomal sliding, and that ExM may provide insight into changes to chromatin architecture at the scale of nucleosomal packing.

6.5 Increasing ExM resolution to investigate chromatin architecture

Visualisation of chromatin architecture at the level of individual nucleosomes is challenging owed to their small size (10 nm) (Kostiuk *et al*, 2019). ExM may provide insight into chromatin loops and changes in nucleosomal packing, but is insufficient to detect changes on individual nucleosomes (described in Section 1.3.3 & 5.4.3). To improve the resolution of ExM we attempted X10 ExM, and observed a 6.3x expansion of nuclei compared to standard ExM expansion of 4x. SPIM acquisitions of X10 ExM prepared nuclei revealed increased nanoscale information. However, we were unable to achieve higher expansion factors in the nuclei which we hypothesise is due to the physical and chemical properties of the intact genomic architecture which may impose a limit on the expansion of the nucleus. This could be overcome by homogenisation of the nucleus using nucleases. Alternatively, resolution could be improved by use of ExM combined with other SRM techniques (Halpern *et al*, 2017 & Gao *et al*, 2018) (discussed in Section 6.7.2).

6.6 Investigating RAD51 nucleofilament formation following USP48 depletion

USP48 loss is associated with increased positioning of 53BP1 relative to the central BRCA1 spot. Uckelmann *et al* observed an increase in resection lengths and accumulations of RAD51 following USP48 depletion. We therefore investigated the structure of RAD51 accumulations following USP48 depletion. As anticipated we observed an increase in class 4 structures (defined as multiple RAD51 spots associated with multiple 53BP1 spots) following USP48 depletion. Further interrogation of these structures revealed the majority incorporated continuous, elongated RAD51 structures, consistent with increased resection lengths being coated by RAD51.

An advantage of ExM methodology is ease of multi-colour imaging, a feature we exploited to investigate the relative spatial organisation of RAD51, 53BP1 and BRCA1 in irradiated cells following USP48 loss. Through these experiments, we provide some insight into the initial stages of RAD51

nucleofilament formation. Through spot detection-based analysis, we defined 10 structure classes enriched with 53BP1, RAD51 and/ or BRCA1, of which three contained all three proteins. We suggest the spatial organisation of repair factors within these structure classes may be related to RAD51 recruitment, filament nucleation and elongation at sites of damage. Class 7 structures (defined as RAD51, BRCA1 and 53BP1 spots closely associated) may represent the initial recruitment of RAD51. Class 8 structures (defined as RAD51 spot(s) associated with BRCA1 and encapsulated by 53BP1) could be the nucleation of RAD51 filament facilitated by BRCA2 (complexed with BRCA1 and PALB2). Class 9 structures (defined as multiple RAD51 spots associated with BRCA1 spot(s) encapsulated by 53BP1 spots) may be the initial elongation of the RAD51 nucleofilament, as suggested by their relatively short length when compared to reported resection lengths (Uckelmann *et al*, 2018).

Classification of RAD51, 53BP1 and/ or BRCA1 enriched accumulations revealed an increase in class 4 structures (defined as multiple RAD51 associated with multiple 53BP1) and class 9 structures (defined as multiple RAD51 spots associated with BRCA1 spot(s) encapsulated by 53BP1 spots) in USP48 depleted cells compared to controls. Further interrogation of these classes of structures revealed a prevalence of continuous RAD51 accumulations compared to discontinuous accumulations following USP48 loss.

Surprisingly, we observed more continuous RAD51 accumulations in the absence of BRCA1 (class 4) than in the presence of BRCA1 (class 9). This indicates that the interaction between RAD51 and BRCA1-PALB2-BRCA2 complex being transient; once filament nucleation is initiated BRCA1-PALB2-BRCA2 dissociates and promotes other nucleation events at other sites. This idea is supported by observations of Shahid *et al* that BRCA2 accumulations were infrequent at longer incubations with RAD51.

Intriguingly, in class 9 structures, BRCA1 placement is heterogeneous with BRCA1 present at the end or the middle of the RAD51 structures. It may be that the nucleation and elongation of the

RAD51 nucleofilament is occurring from these points through the action of BRCA2 (which is complexed to BRCA1 through PALB2). This is consistent with observations that RPA poses a barrier to filament formation as it binds ssDNA with a higher affinity than RAD51 (Ma *et al*, 2017). RPA can restrict RAD51 nucleation events, but has no effect on elongation. This inhibitory effect is overcome by recombination mediator, BRCA2. The authors showed that in the presence of RPA, several nucleation events and bi-directional elongation of the filament occur using a DNA curtain assay. The presence of multiple nucleation sites may explain why in some cases we visualise discontinuous accumulations of RAD51 encapsulated by 53BP1 and associated with BRCA1. It was speculated the presence of the RPA barrier to nucleation of RAD51 is to prevent its association with other ssDNA intermediates e.g. okazaki fragments. Accordingly, BRCA2 also ensures nucleation occurs at the correct positions on ssDNA.

Shahid *et al* similarly report multiple nucleation events facilitated by BRCA2, but propose the elongation of the RAD51 nucleofilament occurs 3' to 5' on the ssDNA with little evidence of elongation in the opposite direction (Shahid *et al,* 2014). It is also possible that RAD51 does not form a continuous filament, instead forming multiple nucleofilaments comprised of tens of monomers, covering small patches of DNA. This may allow flexibility required for the subsequent strand invasion step (Heijden *et al*, 2007).

6.7 Future Questions

Numerous studies employing super resolution microscopy have demonstrated there is a critical spatiotemporal regulation in DSB repair. In this thesis, I have shown that ExM can be applied to analyse the spatial organisation of numerous repair factors with nanoscale precision. There are numerous unanswered questions about the organisation of repair factors during HR.

6.7.1 Investigating how BRCA1 complex composition alters during HR

BRCA1 forms several functionally distinct complexes including BRCA1-A, BRCA1-B, BRCA1-C and the BRCA1-BRCA2-PALB2-RAD51 complex (Her *et al*, 2016, Savage and Harkin, 2015). These complexes

play diverse roles during DNA damage resolution in a context-dependent manner. BRCA1 contains a RING domain at its N terminus which is responsible for its E3 ubiquitin ligase activity and interaction with binding partner BARD1. Additionally, BRCA1 also contains two BRCT domains at its C terminus which are responsible for interactions with phospho-peptides. Amongst these peptides are Abraxas, BACH1 and CtIP which associate with the BRCT domains in a phosphorylation-dependent manner. Each of these complexes play unique roles in DNA repair, yet their exact roles remain uncharacterised. Numerous studies have begun to elucidate the involvement of BRCA1 complexes in faithful repair, yet their recruitment and association patterns at sites of damage is unclear. Since BRCA1 has been observed in both ssDNA and chromatin-bound regions of repair foci (Bekker-Jensen *et al,* 2006), this may suggest different locations are indicative of different functions. To better understand the contributions of different BRCA1 complexes I would:

A. Perform a time course experiment and stain cells for 53BP1, BRCA1 and one of Abraxas, CtIP and PALB2/ BRCA2. Samples would be prepared by standard ExM protocol and images acquired post-expansion.
B. The spatiotemporal organisation of BRCA1 complexes would initially be assessed qualitatively, then spot detection-based analysis would be applied to map changes in BRCA1 complex composition throughout DSB repair.

To better interrogate the interplay between different BRCA1 complexes during DSB repair and how the composition of these affects localisation I would additionally:

A. Investigate the localisation of BRCA1-A complex in the presence of a ssDNA marker (e.g. RPA). It has been speculated that this complex binds rapidly to chromatin following damage and inhibits resection (Hu *et al*, 2011), yet there also suggestion that this complex associates later to prevent hyper-resection (Savage & Harkin, 2015).
B. Investigate the localisation of BRCA1-C complex where CtIP has been mutated. For example, S327A (Reczek *et al*, 2013) to abolish the interaction with BRCA1, T847

(Polato *et al*, 2014) which affects end resection in the presence of a ssDNA marker to determine the effect on resection as a function of recovery time.

6.7.2 Investigating chromatin architecture at DSBs using ExM

Chromatin is organised into higher-order structures with various levels of compaction, and this structure is the landscape of numerous DNA metabolic processes. Accordingly, there has been substantial interest in the structure and behaviour of chromatin during processes such as DNA repair and transcription (Pelicci, Diaspro and Lanzano, 2019). Advances in fluorescence microscopy mean it is now possible to visualise the nanoscale organisation of chromatin using optical approaches including STED, SIM and STORM.

In principle, it is possible to increase the resolving power of ExM using two approaches: 1) increasing expansion factor by applying X10 ExM, and 2) by combining ExM with SIM. To develop these approaches I would firstly generate new stable cell lines expressing H2A labelled with a fluorescent protein which has good fluorescence intensity following expansion preparation (e.g. mRuby2) (Tillberg *et al*, 2016). To optimise X10 ExM for visualising chromatin architecture surrounding DSBs I would:

A. Confirm that the structure of the nucleus is constraining its expansion in the X10 ExM preparation by quantifying the expansion of the nucleus as compared to the whole cell. This could be done using an ExM compatible membrane dye, such as those applied in Label retention ExM (Shi *et al*, 2020). The cell membrane could be segmented and the whole cell volume could be measured compared to the nuclear volume. If the nuclear structure is constraining its expansion, we may visualise differential expansion between the nucleus and the rest of the cell.
B. Select nucleases to maximally preserve the architecture of the nucleus whilst allowing X10 expansion factor. To test which nuclease is optimal, I would perform a correlative imaging experiment and quantify distortions induced by the sample preparation.

C. Combine imaging of chromatin with visualisation of repair proteins such as 53BP1 and BRCA1.
D. Perform quantitative spot detection-based analysis and generate foci profiles to determine the spatial organisation of chromatin relative to repair factors on different backgrounds (e.g. SMARCAD1 or USP48 depletion).

It is possible the additional treatment of specimens with nucleases could induce distortions in the nuclear architecture. For this reason, I would also optimise use of SIM with ExM. SIM is advantaged in its simplicity to implement; no complex set up is required (Halpern *et al*, 2017 & Heintzmann and Huser, 2017). It may be required to alter the set up for expansion samples to account for changes in imaging depth derived from axial expansion of the gel, and a silicon lens would be used as its immersion medium is more closely matched to the refractive index of the ExM gels to limit optical aberrations in the final images. To do this I would:

A. Confirm that ExM specimens can be sufficiently immobilised to prevent sample movement during image acquisition. As SIM relies on computational reconstruction, any movement within the specimen would cause reconstruction artefacts. Specimens would likely be immobilised by coating of coverslips with poly-lysine for this approach (Halpern *et al*, 2017).
B. Perform correlative imaging of nuclei pre- and post-expansion using SIM to quantify distortions, and to determine expansion factor for accurate quantitative measurements of features.
C. Combine visualisation of repair foci and chromatin architecture on SMARCAD1- and USP48-depletion backgrounds as in Section 5.4. Spot detection-based analysis would be performed and average foci structures generated to quantitatively describe the relative spatial organisation of chromatin and repair factors during DSB repair.

6.7.3 Investigating RAD51 nucleofilament formation

HR is a multi-step process which culminates in the formation of a helical RAD51 nucleofilament around ssDNA; an event which is required for homology search and strand invasion steps of HR (Sullivan and Bernstein, 2018). During HR, nucleases facilitate resection to produce 3' ssDNA overhangs which are rapidly coated by RPA to protect the resected DNA ends. RPA is subsequently displaced by the formation of the RAD51 presynaptic filament. This is a tightly regulated process to prevent excessive recombination and genomic instability. It appears that RPA poses a barrier to the nucleation of the RAD51 nucleofilament (Ma *et al*, 2017). This inhibitory barrier is overcome by BRCA2 which directs nucleation of RAD51 at specific sites on the resected ssDNA.

The data presented in Chapter 5 of this thesis supports this model; RAD51 nucleofilament-like structures were observed to be associated with BRCA1 and the placement of BRCA1 spots was heterogeneous. Since BRCA2 is recruited via BRCA1, this may indicate BRCA2 is driving nucleation of the RAD51 filament at these sites. Additionally, it has been suggested the RAD51 nucleofilament may not form continuously, leaving bare DNA gaps, to allow for flexibility in the ssDNA to support strand invasion steps (Heijden *et al*, 2007). These bare DNA gaps are thought to act like hinges to allow high flexibility in the RAD51-ssDNA structure. If a continuous filament were to form, its rigidity may prevent sufficient functional interactions during homology search and strand invasion. To better dissect this mechanism, I would investigate the displacement of RPA for RAD51 nucleofilament formation mediated by BRCA2. To do this I would:

A. Perform a time course experiment and fix cells at defined time points following damage induction by irradiation. Cells would be immunostained for RAD51, RPA and BRCA2/ BRCA1. Cells would be prepared by standard ExM protocol and then imaged post-expansion using a widefield microscope.

B. We would firstly qualitatively assess the enrichment of proteins in repair foci in S-phase cells. This, and known mechanistic information, would direct classification of structures. Structures would be analysed using spot detection-based analysis.
C. The relative spatial organisation of RPA, RAD51 and BRCA1/2 would be further analysed within identified classes to provide insight into the mechanism for RPA displacement and RAD51 nucleation and elongation.
D. This experiment would also be performed on USP48 depleted cells and compared to control cells.

This experiment could provide insight into the nucleation of the RAD51 nucleofilament by BRCA2, elongation of the nucleofilament and subsequent strand invasion steps. RAD51 nucleofilament elongation, stability and disassembly is a tightly regulated process, requiring numerous RAD51 mediators (Sullivan and Bernstein, 2018). Amongst these mediators are the RAD51 paralogs (RAD51B, RAD51C, RAD51D, XRCC2, XRCC3 and SWSAP1) which structurally resemble RAD51 and mediate its activity during HR. Mutations in these paralogs have been found in some breast and ovarian cancers. As yet, the function of RAD51 paralogs is not well understood. Visualising the association of these paralogs with the RAD51 nucleofilament, and their relative spatial organisation may provide insight into their function at the RAD51 nucleofilament. To do this I would:

A. Perform a time course experiment. Cells would be immunostained for RAD51 and selected RAD51 paralogs.
B. Enrichment of RAD51 and its paralogs would be qualitatively assessed in S-phase cells. Structure classification would be directed by these observations. Structures would be analysed using spot detection-based analysis.

It will be critical to determine how RAD51 paralogs and other known mediators contribute to filament assembly, homology search and strand invasion (Kaniecki *et al*, 2018). It will also be important to determine how this process occurs within the context of chromatin and how

chromatin remodelling occurs during this stage of HR. Many of the studies performed thus far make use of static models e.g. curtain assays to determine the behaviour of key proteins during RAD51 nucleofilament formation which do not account for the structural changes occurring in vivo.

6.8 Conclusions and Future perspectives

Super resolution imaging is a strong approach in determining the spatiotemporal dimension of DNA repair. The aim is to develop an integrated approach, in which spatiotemporal organisation of repair is characterised through super resolution microscopy and this is complemented by understanding of the mechanisms and consequences of outcomes through continued biochemical and genetic analyses.

In this thesis, I have showcased the application of new fluorescence microscopy technique, expansion microscopy (ExM). This approach uses an innovative chemical preparation to enable acquisition of images with a resolution of 70 nm laterally and 200 nm axially. There is no need for complex software or hardware unlike other super resolution techniques, and imaging can be performed on a standard diffraction-limited microscope (e.g. epifluorescence, confocal) meaning wider application of this technique is possible. As specimens are optically cleared as an inherent property of the preparation, imaging depths and volumes accessible are orders of magnitude higher than other super resolution techniques.

These features of ExM methodology make it feasible to acquire images of hundreds or even thousands of repair structures rapidly as I have completed throughout this work. ExM has the potential to contribute significantly to characterising the spatiotemporal dimension of the DNA damage response. Deconvolution of acquired images revealed complex organisation of repair foci with nanoscale precision. Features within these images were analysed using a semi-automated spot detection-based approach. Using this analytical approach, we analysed a significant number of repair structures and were able to generate model foci structures to quantitatively describe their nanoscale organisation.

Theoretically, if large data sets containing numerous proteins occupying foci sub-compartments were generated, these could be used to train a computational algorithm to classify the spatial organisation of proteins based on stringent parameters defined by the user. This process could be fully automated, meaning images of thousands of features could be acquired and analysed rapidly. This could form a database in which spatiotemporal distributions of repair factors could be mapped on different backgrounds (e.g. BRCA1 mutation). By corroborating a spatial map of repair, this would be a rich source of information which could direct therapeutic interventions in the future.

Appendix

A1 Correlative imaging of nuclei

To confirm the nanoscale topology of nuclei is retained post-expansion, I performed a correlative imaging experiment in which images of nuclei stained with EdU were imaged pre-expansion using SIM, and then post-expansion images were acquired on a widefield microscope and deconvolved. Features within these images were compared and there was qualitatively good retention of these features (Section 3.2.5). The nuclear areas and inter-nuclear distances were measured in the pre-expansion SIM and post-expansion widefield images (Appendix Figure A1).

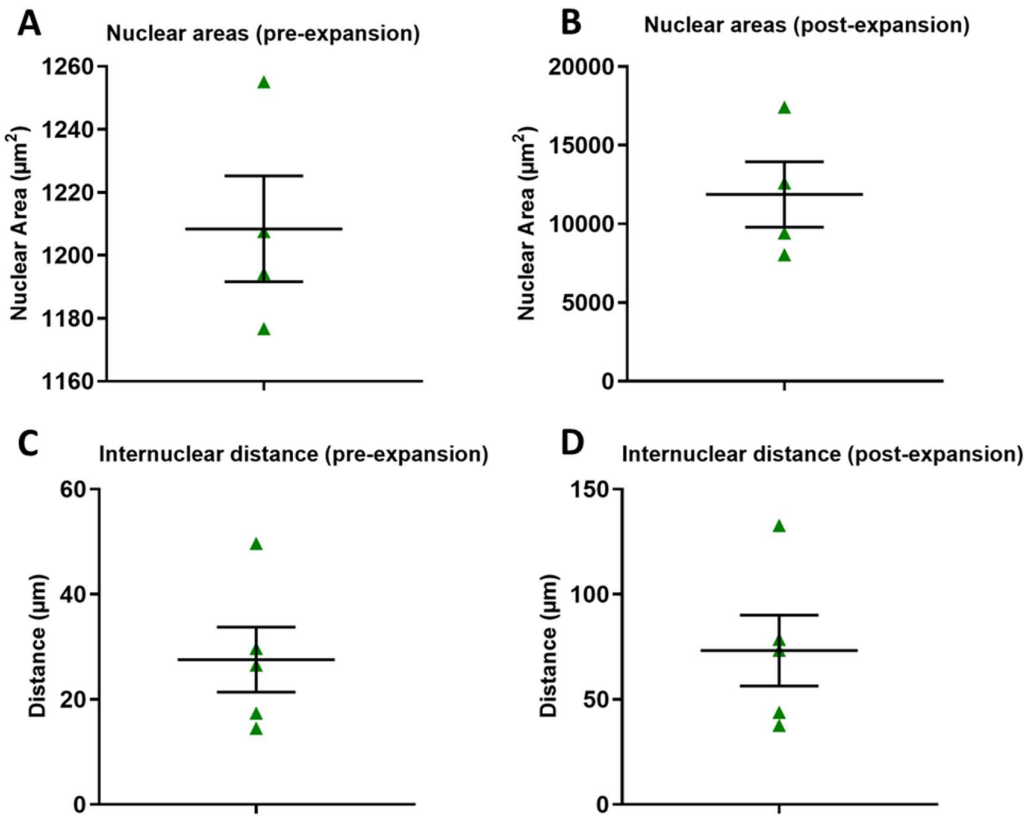

Figure A1. Measuring nuclear areas and inter-nuclear distances in correlative images. Nuclear areas were measured pre- and post-expansion (Panel A & B). Inter-nuclear distances were measured by drawing lines in equivalent locations in the pre- and post-expansion images (Panel C & D).

A2 Discriminating between early, mid and late S-phase using PCNA and EdU

53BP1 and BRCA1 foci distributions are known to alter as a function of cell cycle (Chapman *et al*, 2012). We confirmed we could accurately discriminate between early, mid and late S-phase nuclei using EdU and PCNA. Both EdU and PCNA form distinct patterns indicative of cell cycle phase. These patterns were seen reproducibly across stained nuclei. Cells were treated with EdU for 5 minutes or 1 hour prior to fixation and immunostaining for PCNA.

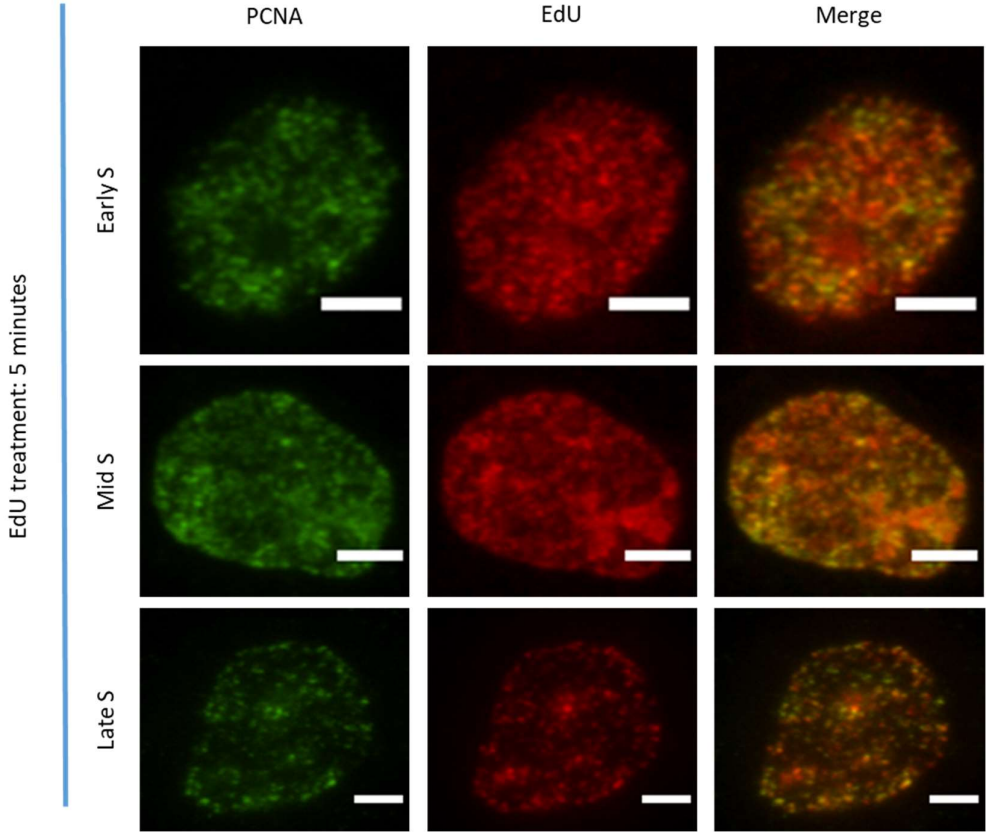

Figure A2.**Confirming EdU and PCNA distribution in U2OS cells.** U2OS cells were treated with EdU for 5 minutes prior to washing with CSK buffer, permeabilisation with Triton-X and fixation with methanol. Click-it reaction was performed for detection of EdU and cells were immunostained for PCNA. Images were acquired on a widefield microscope. Scale 5 µm.

Distinct incorporation patterns of EdU and PCNA were identified in cells which had been pulsed with EdU for 5 minutes (Appendix Figure A2). We opted to use 1 hour treatment for subsequent experiments with EdU as increased incorporation of EdU made discrimination between early, mid

and late S-phase more accurate. Examples of nuclei with characteristic PCNA and EdU patterns for early, mid and late S phase were selected (Appendix Figure A3-A5).

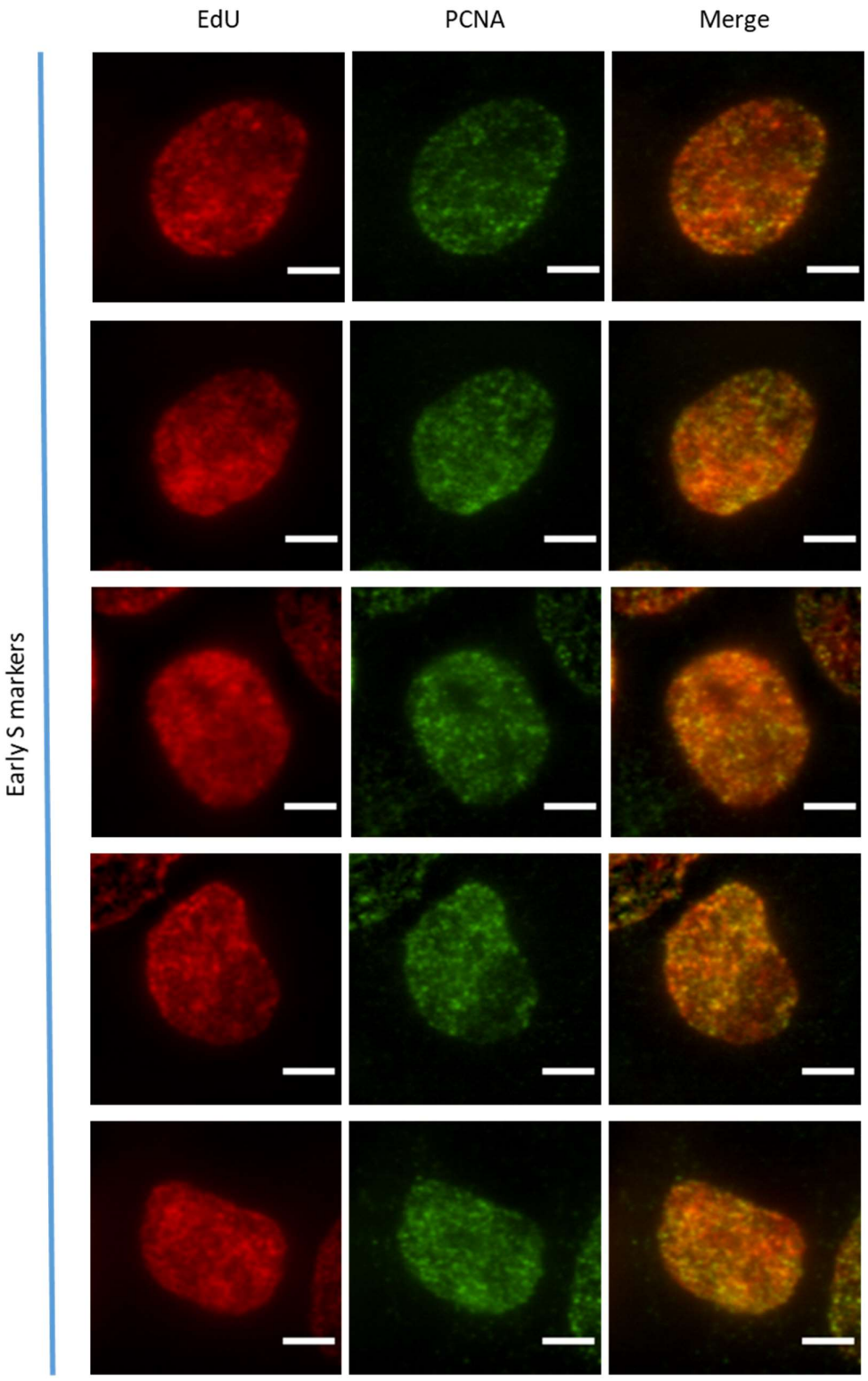
EdU
PCNA
Merge
Early S markers

Figure A3. **Confirming cell cycle phase using PCNA and EdU as markers.** U2OS cells were treated with EdU for 1 hour prior to washing with CSK buffer, permeabilisation with Triton-X and fixation with methanol. Click-it reaction was performed for EdU detection and cells were immunostained for PCNA. Images were acquired on a widefield microscope. Examples of cells with patterns consistent with early S-phase were selected. Scale 5 µm.

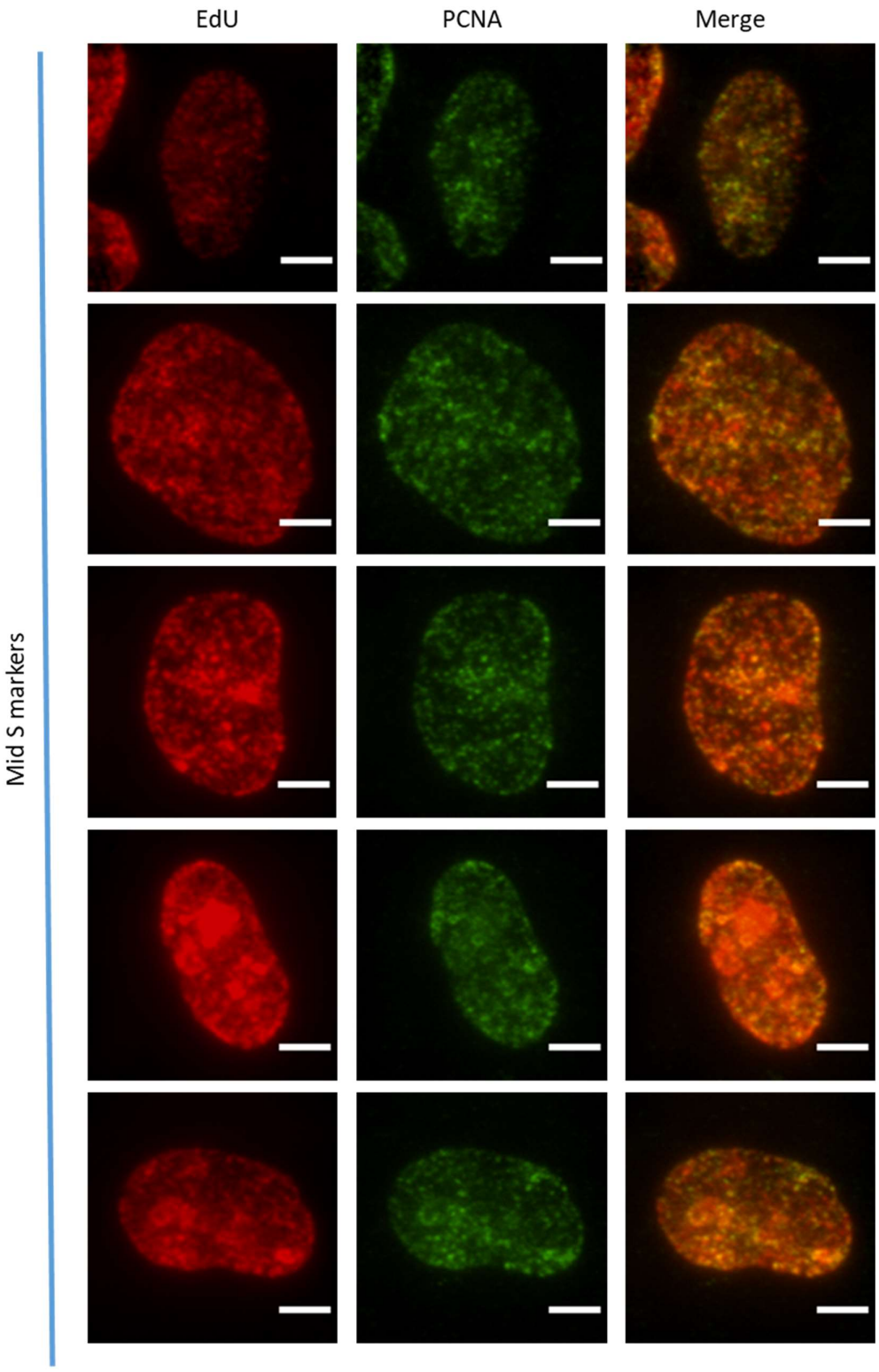
EdU
PCNA
Merge
Mid S markers

Figure A4. Confirming cell cycle phase using PCNA and EdU as markers. U2OS cells were treated with EdU for 1 hour prior to washing with CSK buffer, permeabilisation with Triton-X and fixation with methanol. Click-it reaction was performed for EdU detection and cells were immunostained for PCNA. Images were acquired on a widefield microscope. Examples of cells with patterns consistent with mid S-phase were selected. Scale 5 µm.

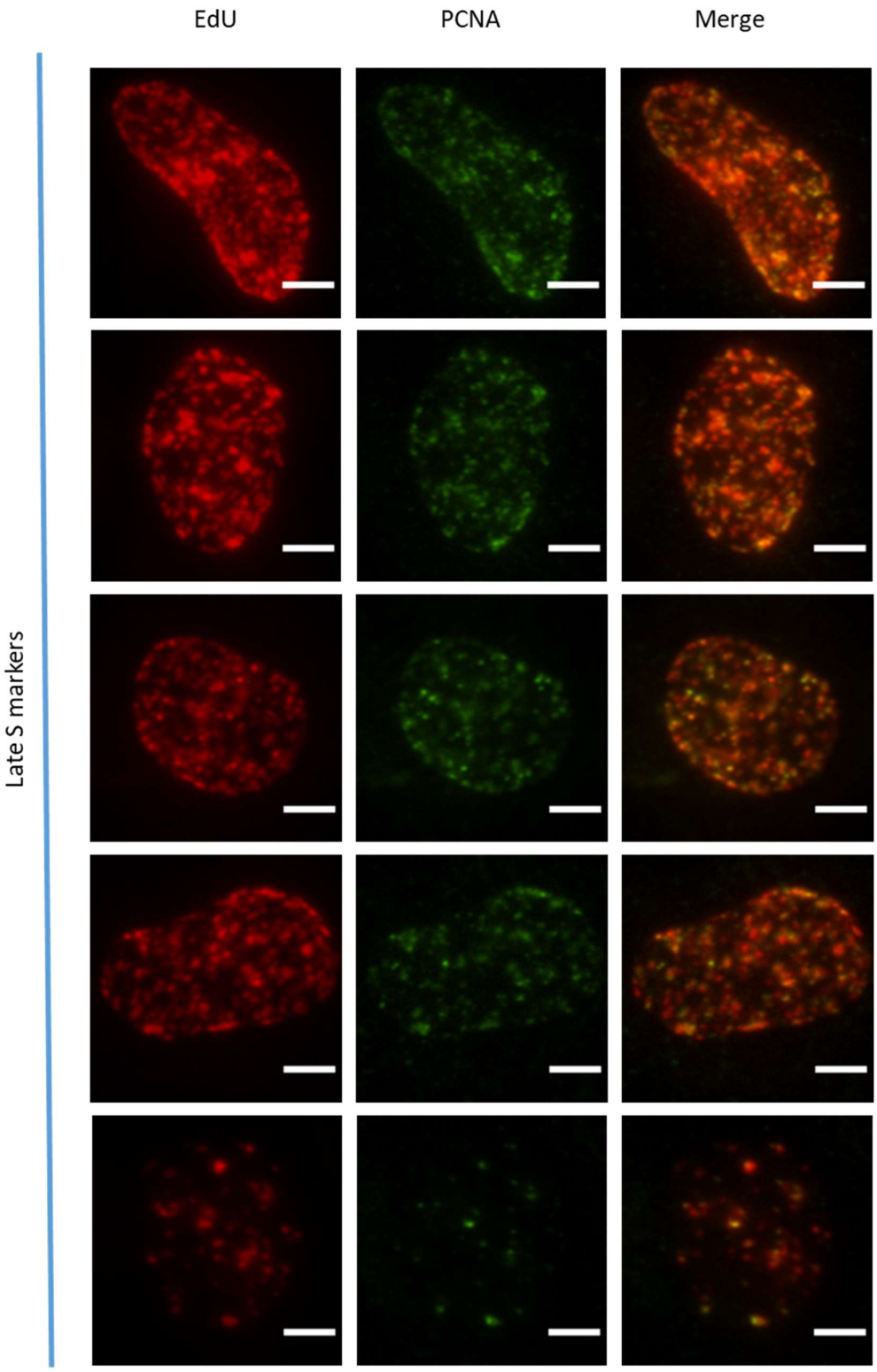
EdU
PCNA
Merge
Late S markers

Figure A5. Confirming cell cycle phase using PCNA and EdU as markers. U2OS cells were treated with EdU for 1 hour prior to washing with CSK buffer, permeabilisation with Triton-X and fixation with methanol. Click-it reaction was performed for EdU detection and cells were immunostained for PCNA. Images were acquired on a widefield microscope. Examples of cells with patterns consistent with late S-phase were selected. Scale 5 µm.

To quantify the correlation between PCNA and EdU staining, PCC values were measured for early, mid and late S phase classified nuclei (Appendix Figure A6). PCC values indicated a positive linear correlation between EdU and PCNA in cells which were treated with EdU for 5 minutes and for 1 hour.

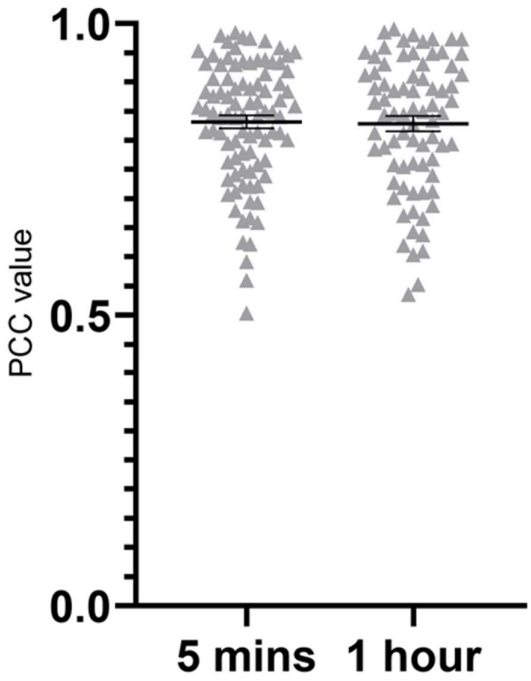

Figure A6. Quantifying PCC between EdU and PCNA in S-phase cells. U2OS cells were treated with EdU for either 5 minutes or 1 hour prior to washing with CSK buffer, permeabilisation with Triton-X and fixation with methanol. Click-it reaction was performed for EdU detection and cells were immunostained for PCNA. PCC values were measured as described in Section 2.7.8. Means ± s.e.m.

A3 Investigating 53BP1 structures following BRCA1-depletion

BRCA1 has been shown to drive positioning of 53BP1 further from the break site during HR initiation. To confirm the mutual exclusivity of BRCA1 and 53BP1 in class 5 structures (defined as one BRCA1 spot encapsulated by multiple 53BP1 spots) is due to BRCA1, we depleted BRCA1 using siRNA and compared 53BP1 structures in these cells to those in control cells. Structures were qualitatively assessed in BRCA1-depleted cells compared to controls (Appendix Figure A7).

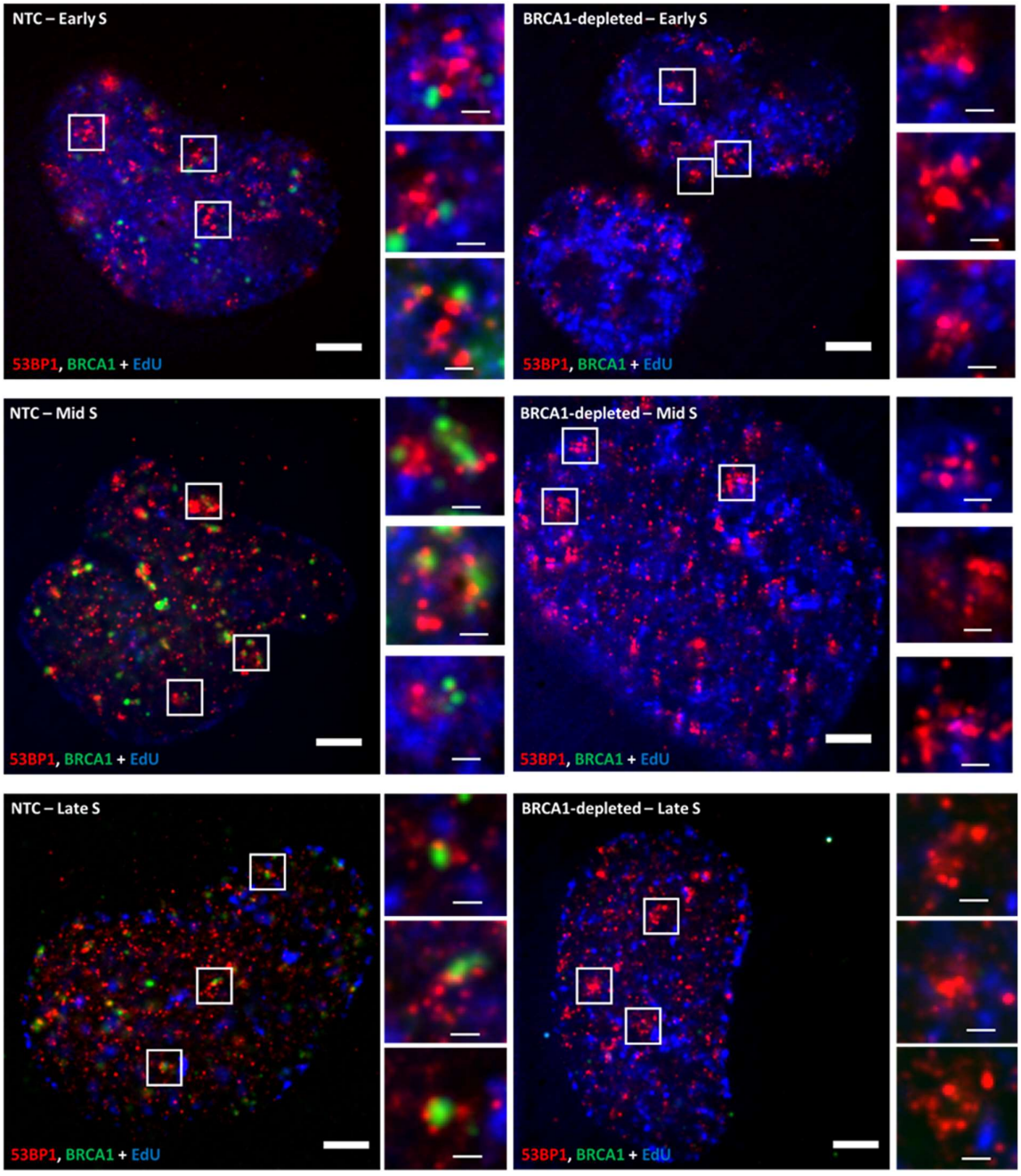

Figure A7. Visualising 53BP1 distribution in BRCA1-depleted compared to control cells. Cells were treated with siBRCA1 or control siRNA for 72 hours. They were treated with EdU prior to damage induction by irradiation (2 Gy). Cells were allowed 1 hour to recover, pre-extracted and fixed. Cells were stained for EdU and immunostained for 53BP1 and BRCA1. ExM preparation was completed and post-expansion Z stacks were acquired on a widefield microscope. Example images of nuclei classified as early, mid and late S-phase are shown for NTC and BRCA1-depleted cells. Scale bars 10 µm and 2 µm.

A4 53BP1 and RIF1 are closely associated

We aimed to investigate if RIF1 was occupying the spaces between 53BP1 spots in class 5 structures (defined as multiple 53BP1 spots encapsulating a core BRCA1 spot). To do this, cells were treated with EdU prior to irradiation and fixation. Cells were immunostained for 53BP1 and RIF1 and then images were acquired pre- and post-expansion. To measure colocalisation, we calculated Pearson's correlation coefficient (PCC) between RIF1 and 53BP1 pre- and post-expansion (Figure A8).

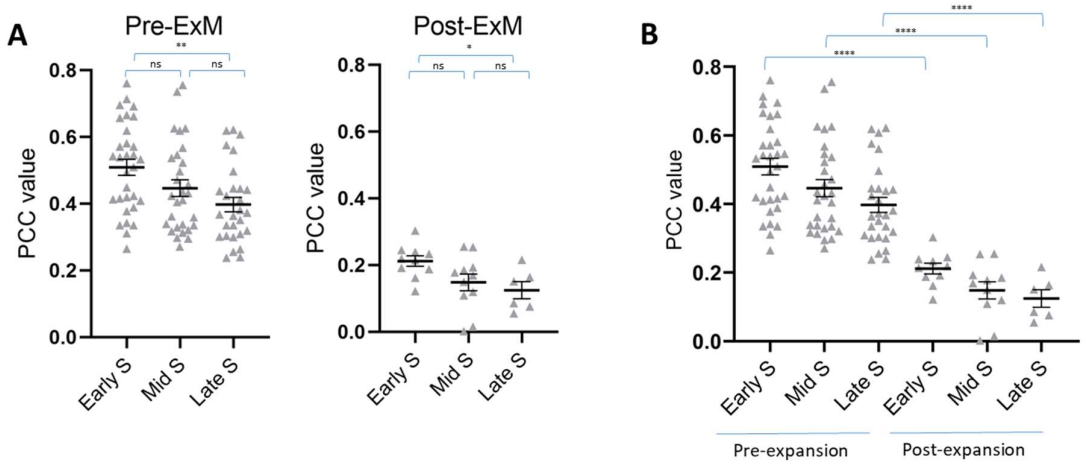

Figure A8. Measuring correlation between 53BP1 and RIF1. Cells were treated with EdU prior to irradiation (2 Gy). Cells were fixed and immunostained for 53BP1 and RIF1. PCC analysis was carried out on pre- and post-expansion images of nuclei classified as early, mid and late S-phase as described in Section 2.7.8 (Panel A). Combined PCC values for pre- and post-expansion images are shown (Panel B). Measurements were taken from 30 nuclei per cell cycle phase pre-expansion and >6 nuclei post-expansion. N=1; error = s.e.m. Throughout figure, **** P<0.001; **P <0.01;*P < 0.05 NS, not significant by two-sided Student's t test.

A5 Characterising 53BP1 and BRCA1 foci distributions as a function of recovery time

In mid and late S-phase classified nuclei, we observed heterogeneity in the spatial distribution of 53BP1 and BRCA1. This heterogeneity was described using a spot detection-based analysis and structures were defined as one of five classes. To understand the source of this heterogeneity we investigated the distribution of these classes as a function of recovery time following damage

induction by irradiation. To do this, cells were pulsed with EdU for 10 minutes and washed prior to damage induction by irradiation (2 Gy). Cells were then fixed at defined time points following damage. Cells were stained for EdU and immunostained for BRCA1 and 53BP1. Pre-expansion images were acquired to determine staining efficacy across all time points. Examples of early, mid and late S-phase nuclei at each time point are shown (Appendix Figure A9-A11).

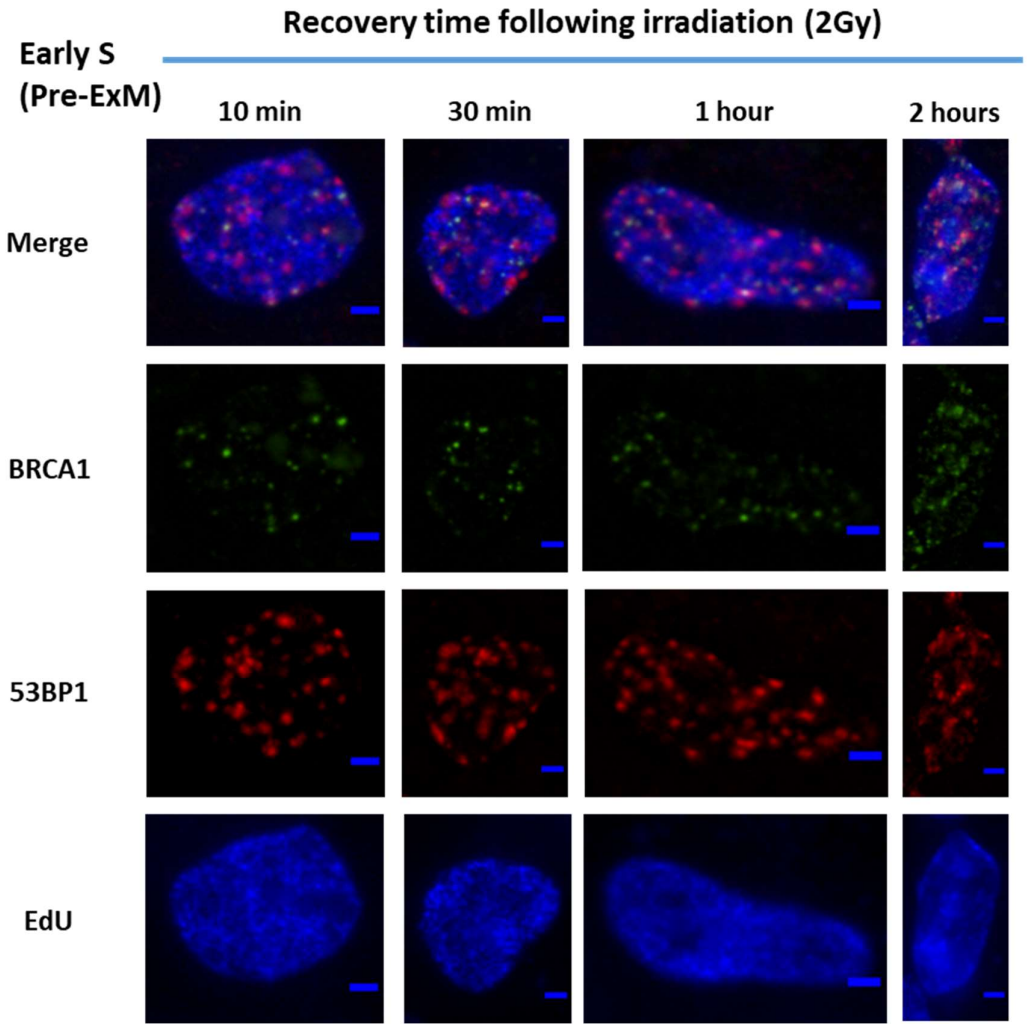

Figure A9. Visualising DSB repair progression. U2OS cells were pulsed with EdU for 10 minutes and washed prior to irradiation (2 Gy). Cells were allowed to recover for the times shown prior to CSK pre-extraction and fixation. Cells were stained for EdU and immunostained for BRCA1 and 53BP1. Pre-ExM images were acquired. Scale bars 2.5 µm.

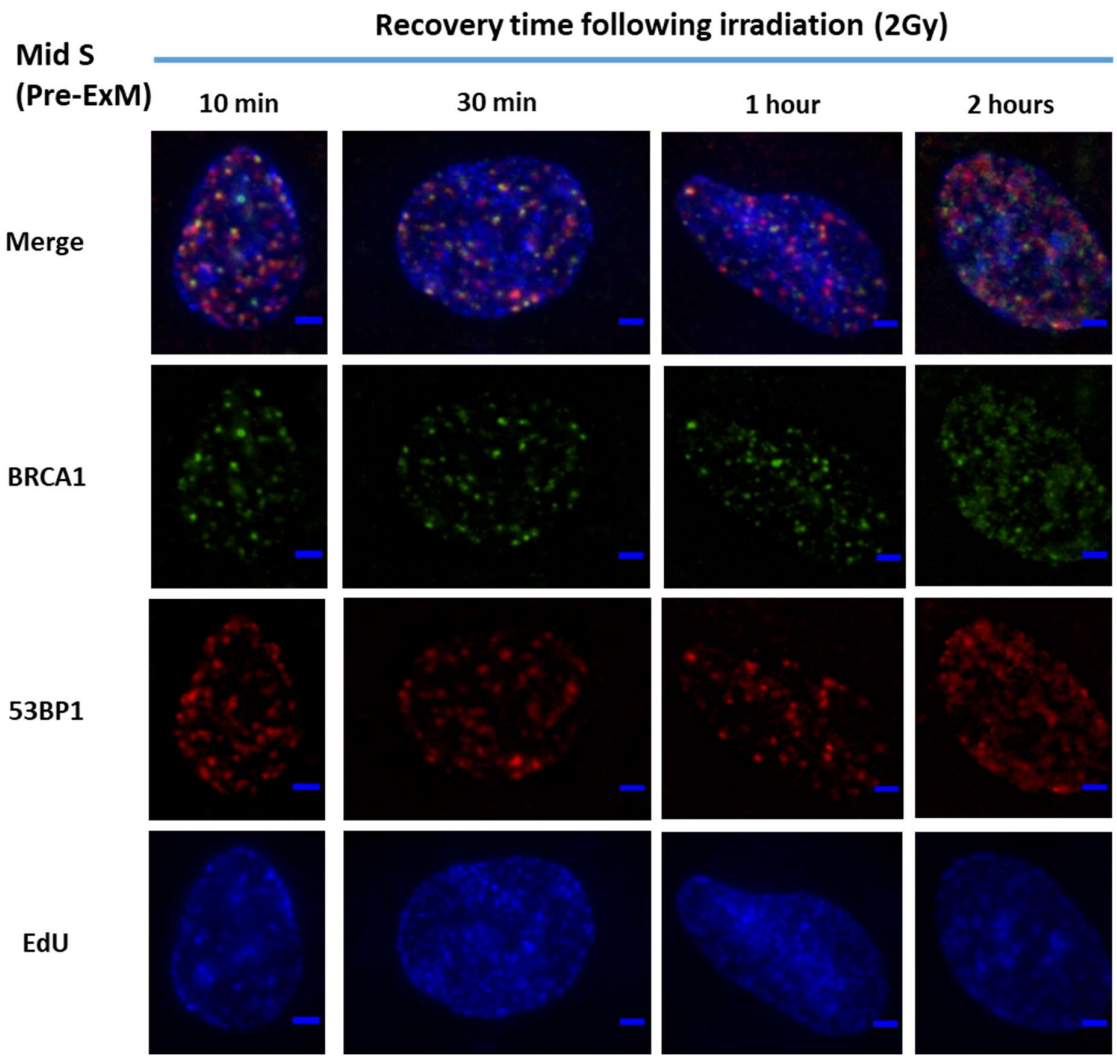

Figure A10. Visualising DSB repair progression. U2OS cells were pulsed with EdU for 10 minutes and washed prior to irradiation (2 Gy). Cells were allowed to recover for the times shown prior to CSK pre-extraction and fixation. Cells were stained for EdU and immunostained for BRCA1 and 53BP1. Pre-ExM images were acquired. Scale bars 2.5 µm.

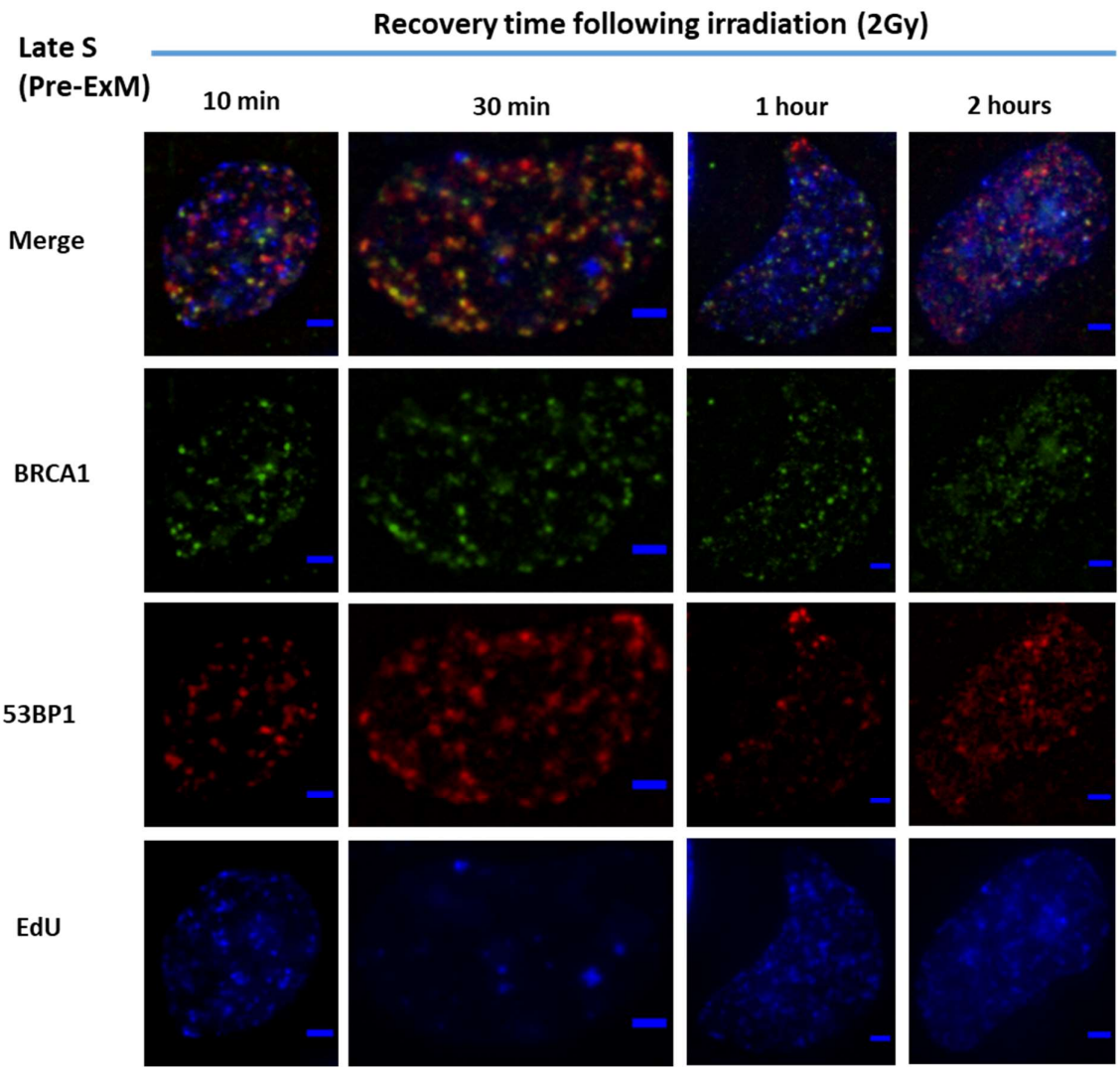

Figure A11. Visualising DSB repair progression. U2OS cells were pulsed with EdU for 10 minutes and washed prior to irradiation (2 Gy). Cells were allowed to recover for the times shown prior to CSK pre-extraction and fixation. Cells were stained for EdU and immunostained for BRCA1 and 53BP1. Pre-ExM images were acquired. Scale bars 2.5 µm.

Post-expansion images of nuclei classified as early, mid and late S-phase were acquired following ExM preparation. Early S-phase nuclei selected for each recovery time are shown in Appendix Figure A12.

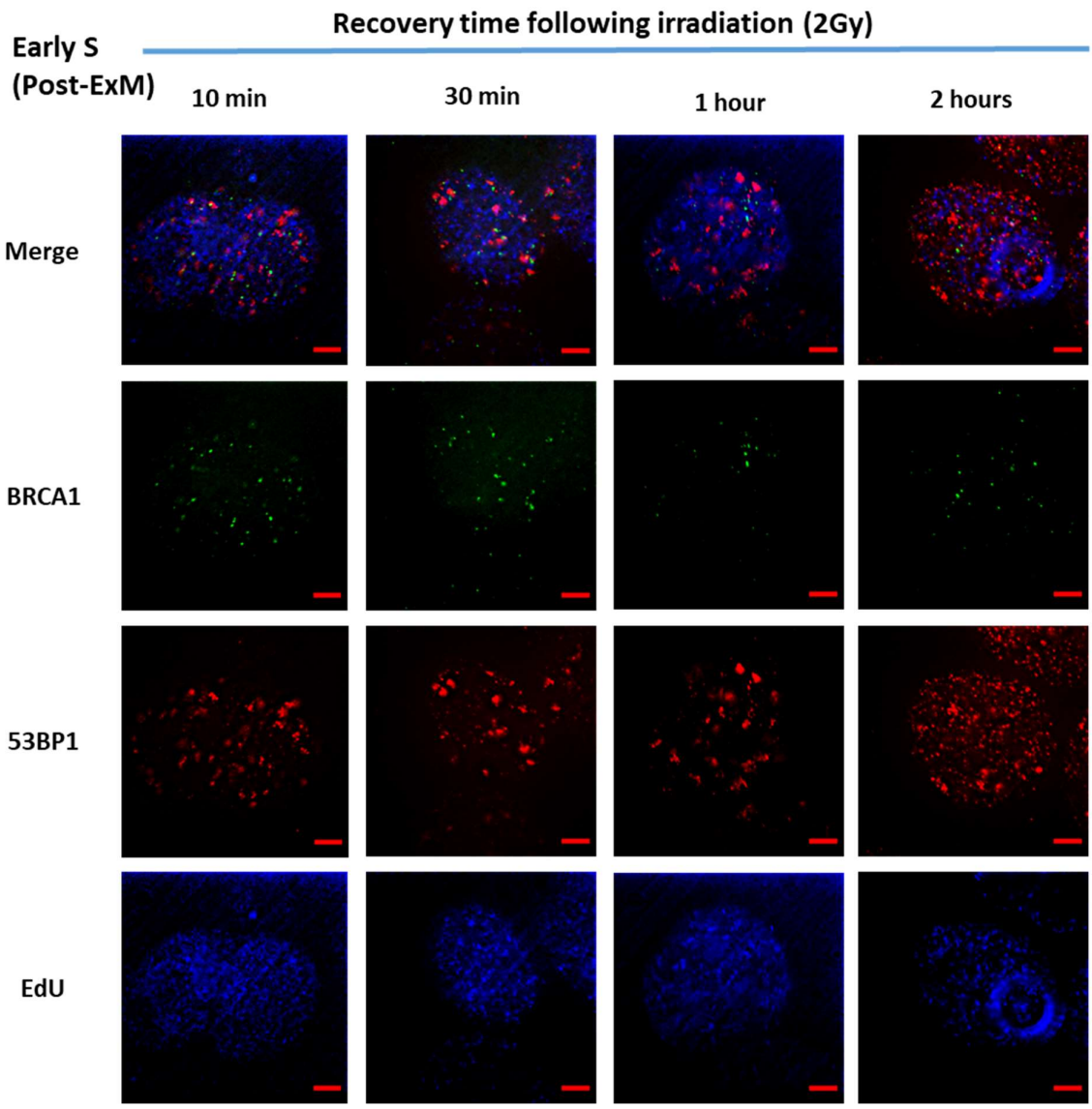

Figure A12. Visualising DSB repair progression. U2OS cells were pulsed with EdU for 10 minutes and washed prior to irradiation (2 Gy). Cells were allowed to recover for the times shown prior to CSK pre-extraction and fixation. Cells were stained for EdU and immunostained for BRCA1 and 53BP1. ExM protocol was performed and post-ExM Z stacks were acquired on a widefield microscope. Scale bars 10 µm.

A6 Describing positioning of 53BP1 relative to BRCA1 following SMARCAD1-depletion

Following depletion of SMARCAD1, we observed a decrease in class 5 structures (defined as one BRCA1 spot associated with multiple 53BP1 spots). We investigated the overall distribution of these

structures in SMARCAD1-depleted cells compared to controls by generating average class 5 structures using a Matlab script (Section 2.7.6). In control cells, BRCA1 was encapsulated by 53BP1 with a visible void between the proteins. This void was absent in cells depleted of SMARCAD1. We also noted heterogeneity in the position of 53BP1 relative to the central BRCA1 which lead us to define structures as having a reduced or control separation distance between 53BP1 and the core BRCA1 spot (defined as a void between 53BP1 and BRCA1 of <0.5 µm and 1.8-2 µm, respectively). We investigated the placement of 53BP1 spots relative to BRCA1 on all class 5 structures in the control and SMARCAD1-depleted cells to determine the prevalence of control and reduced separation distance. We observed that the majority of class 5 structures had a reduced separation distance in SMARCAD1-depleted cells, whilst in the control cells the majority of class 5 structures had a control separation distance. Average structures and line profiles were generated each condition. Additionally all structures were visualised in 3D (shown in Appendix Figures A13-A16).

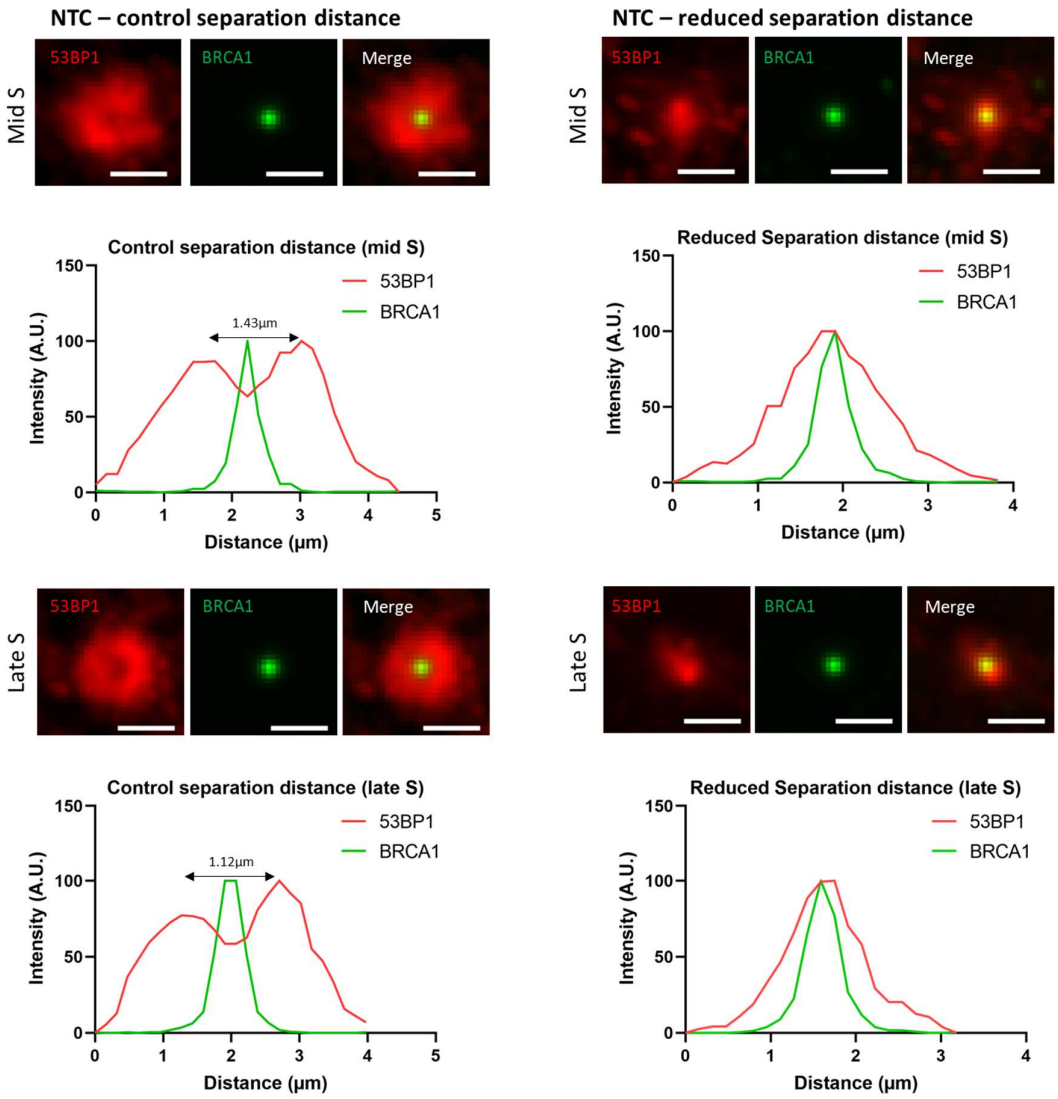

Figure A13. Sub-classifying class 5 structures in control cells for comparison to SMARCAD1-depleted cells. All class 5 structures in control cells classified as mid and late S-phase were further sub-classified as having a control or reduced separation distance between 53BP1 and BRCA1. The structures in each class were then averaged together using the matlab script (described in Section 2.7.6 & 5.2) and their max projections are shown here. Line profiles were also generated for each and are shown below the max projections. N = 3, control separation distance (mid S) = 315 structures, control separation distance (late S) = 417 structures, reduced separation distance (mid S) = 45 structures and reduced separation distance (late S) = 52 structures. Scale bars 2 µm.

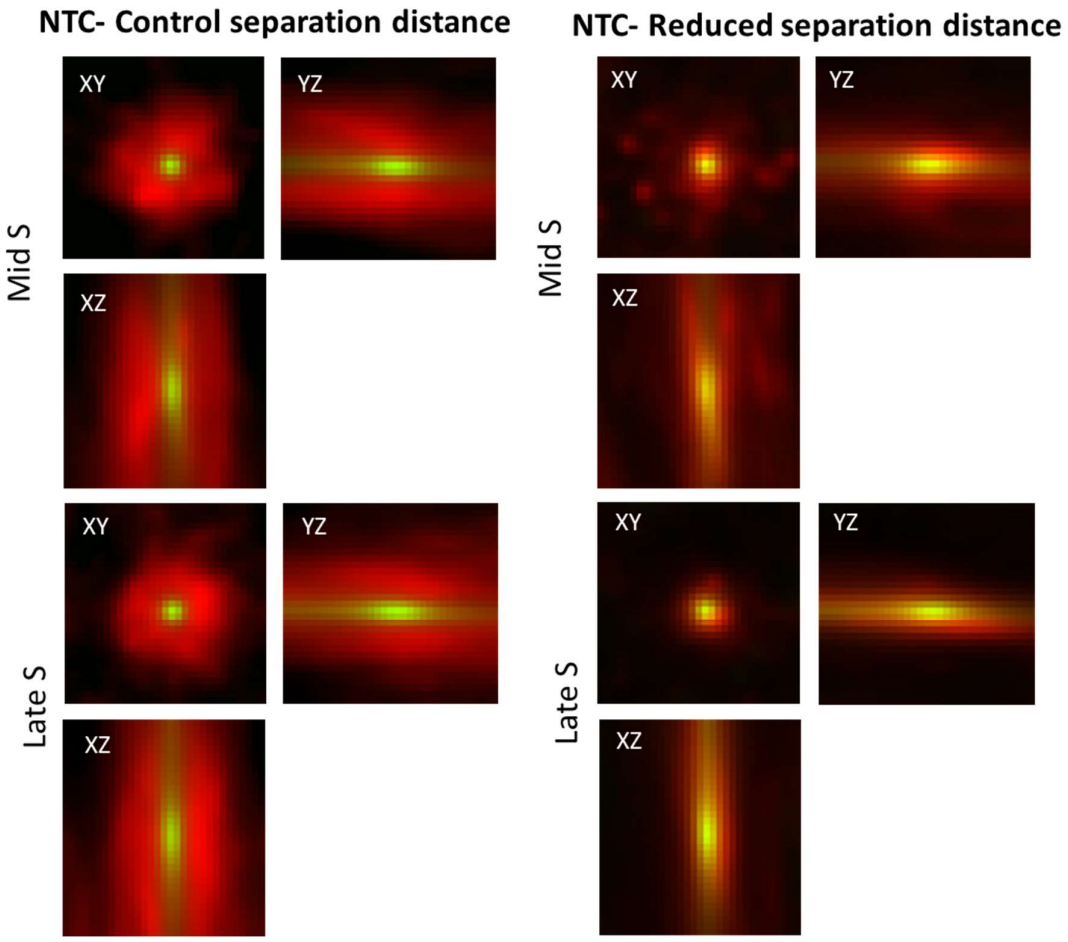

Figure A14. **Sub-classifying class 5 structures in control cells for comparison to SMARCAD1-depleted cells.** Orthogonal views of averaged class 5 structures generated in figure A13 are shown. N = 3, control separation distance (mid S) = 315 structures, control separation distance (late S) = 417 structures, reduced separation distance (mid S) = 45 structures and reduced separation distance (late S) = 52 structures.

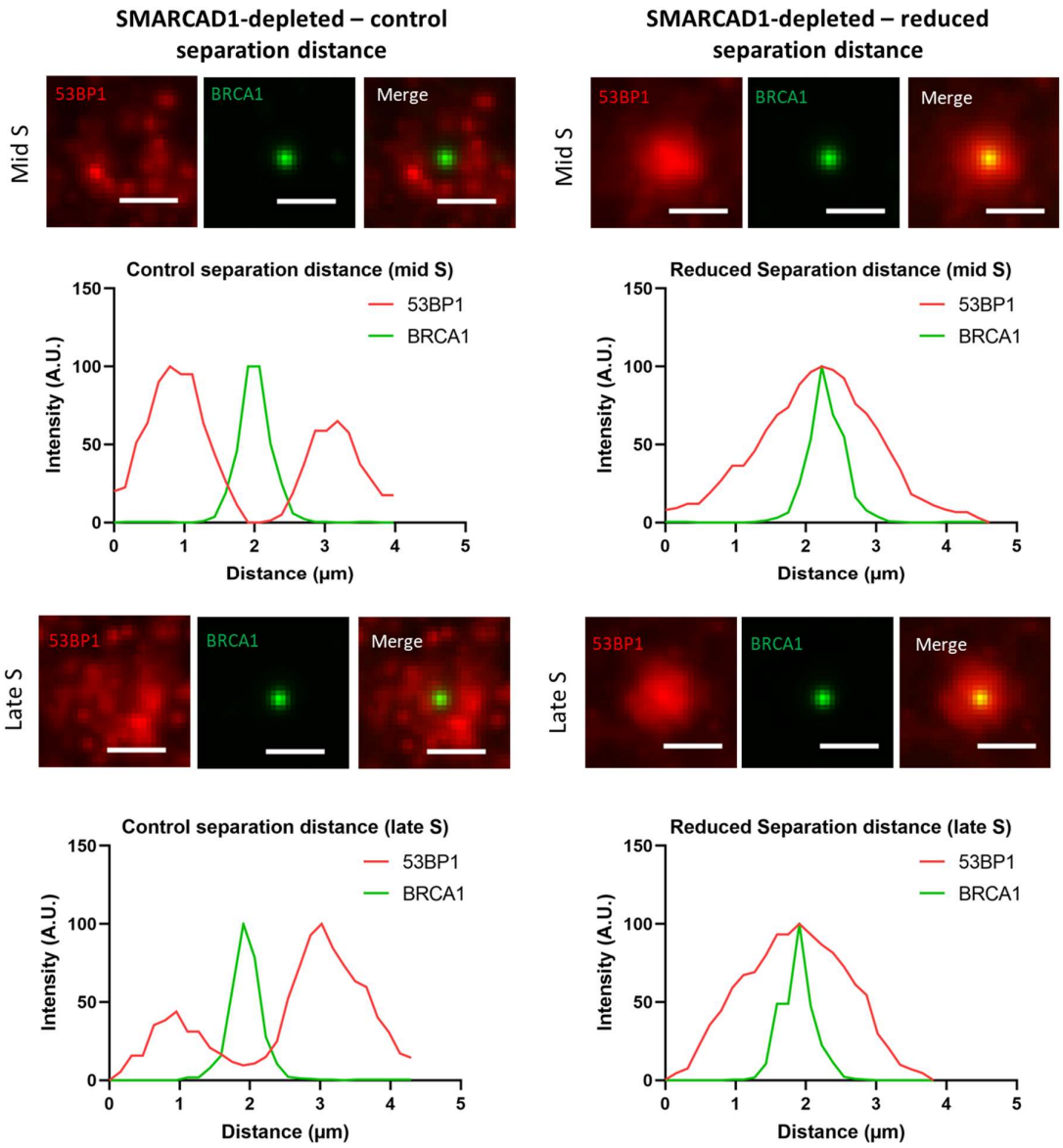

Figure A15. Sub-classifying class 5 structures in SMARCAD1-depleted cells for comparison to control cells. All class 5 structures in control cells classified as mid and late S-phase were further sub-classified as having a control or reduced separation distance between 53BP1 and BRCA1. The structures in each class were then averaged together using the matlab script (described in Section 2.7.6 & 5.2) and their max projections are shown here. Line profiles were also generated for each and are shown below the max projections. N = 3, control separation distance (mid S) = 43 structures, control separation distance (late S) = 50 structures, reduced separation distance (mid S) = 255 structures and reduced separation distance (late S) = 261 structures. Scale bars 2 µm.

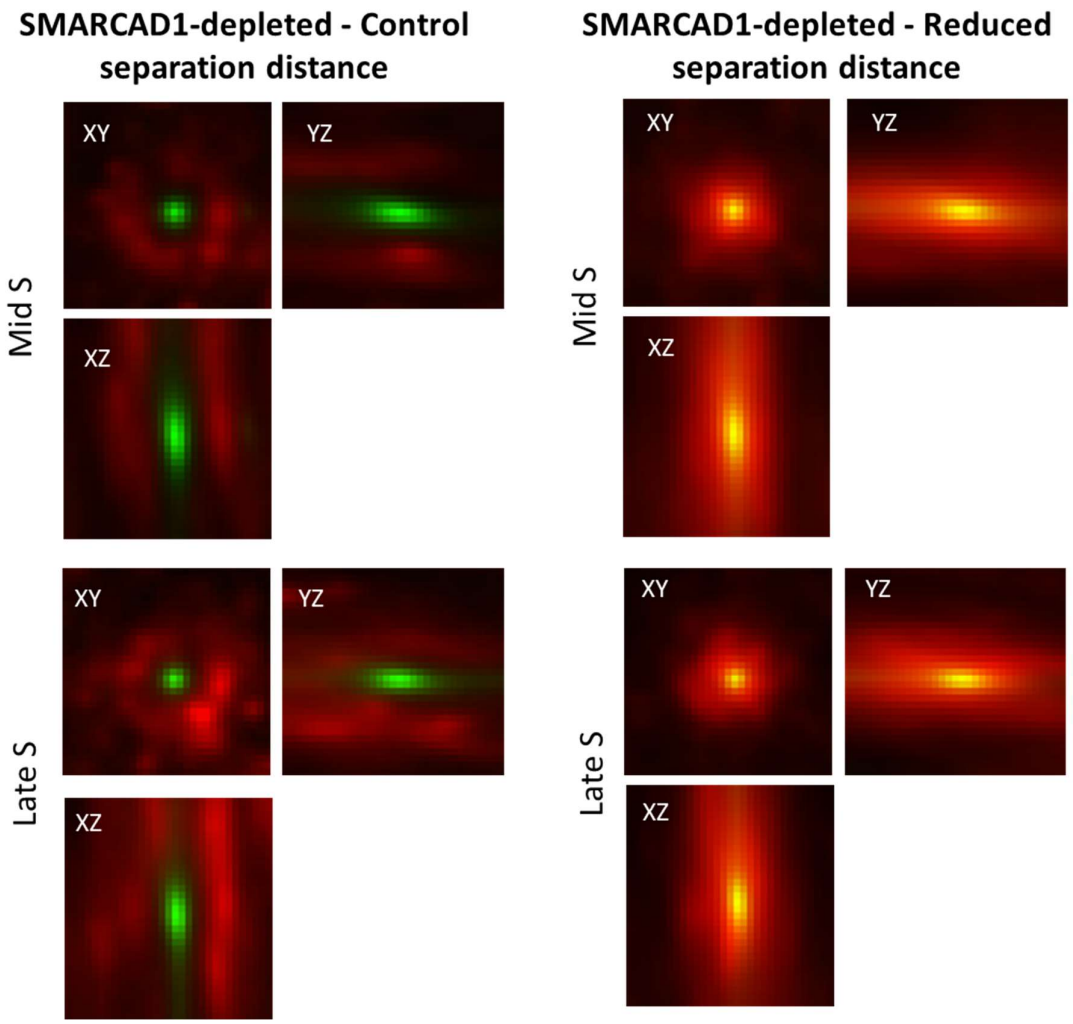

Figure A16. Sub-classifying class 5 structures in SMARCAD1-depleted cells for comparison to control cells. Orthogonal views of averaged class 5 structures generated in figure A15 are shown. N = 3, control separation distance (mid S) = 43 structures, control separation distance (late S) = 50 structures, reduced separation distance (mid S) = 255 structures and reduced separation distance (late S) = 261 structures.

A7 Describing positioning of 53BP1 relative to BRCA1 following USP48-depletion

Following USP48-depletion, we observed an increase in class 5 structures (defined as one BRCA1 spot associated with multiple 53BP1 spots). We investigated the overall distribution of these structures in USP48-depleted cells compared to controls by generating average class 5 structures using a Matlab script (Section 2.7.6). As with SMARCAD1 depletion data, BRCA1 was encapsulated by 53BP1 with a visible void between the proteins in the control cells. This void was increased in cells depleted of USP48 based on an increased peak-to-peak distance in 53BP1 intensity maxima. We also noted heterogeneity in the position of 53BP1 relative to the central BRCA1 which lead us to define structures as having an increased or control separation distance between 53BP1 and the central BRCA1 spot (defined as a void between 53BP1 and BRCA1 of 1.8-2 µm and 2-2.8 µm, respectively). We investigated the placement of 53BP1 spots relative to BRCA1 on all class 5 structures in the control and USP48-depleted cells to determine the prevalence of control and increased separation distance. The increased separation distance was prevalent in the USP48 depleted cells, and the control separation distance was prevalent in the control cells. Average structures and line profiles were generated for each condition. Additionally all structures were visualised in 3D (shown in Appendix Figures A17-A20).

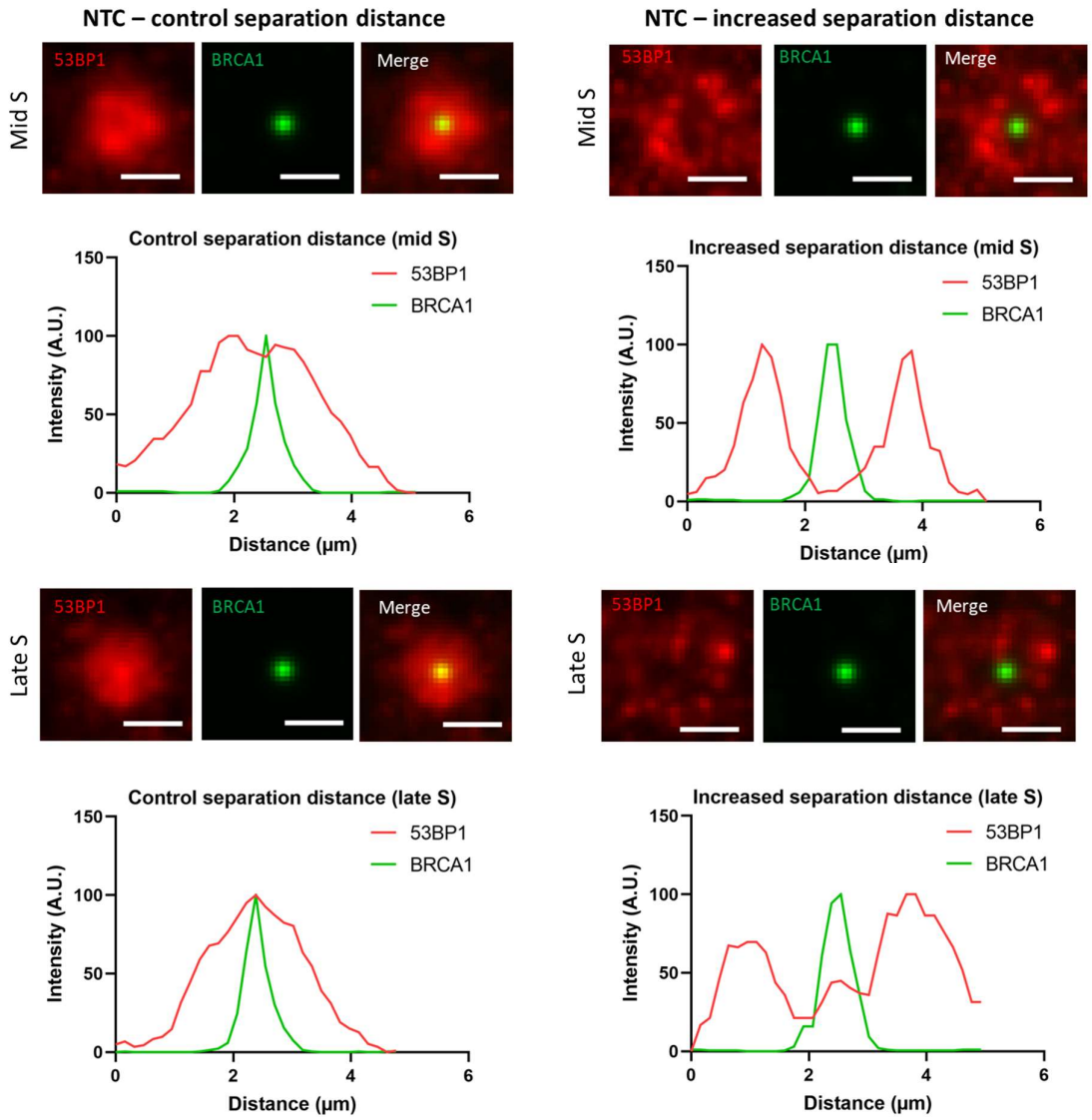

Figure A17. Sub-classifying class 5 structures in control cells for comparison to USP48-depleted cells. All class 5 structures in control cells classified as mid and late S-phase were further sub-classified as having a control or increased separation distance between 53BP1 and BRCA1. . The structures in each class were then averaged together using the matlab script (described in Section 2.7.6 & 5.2) and their max projections are shown here. Line profiles were also generated for each and are shown below the max projections. N = 3, control separation distance (mid S) = 326 structures, control separation distance (late S) = 288 structures, increased separation distance (mid S) = 88 structures and increased separation distance (late S) = 96 structures. Scale bars 2 µm.

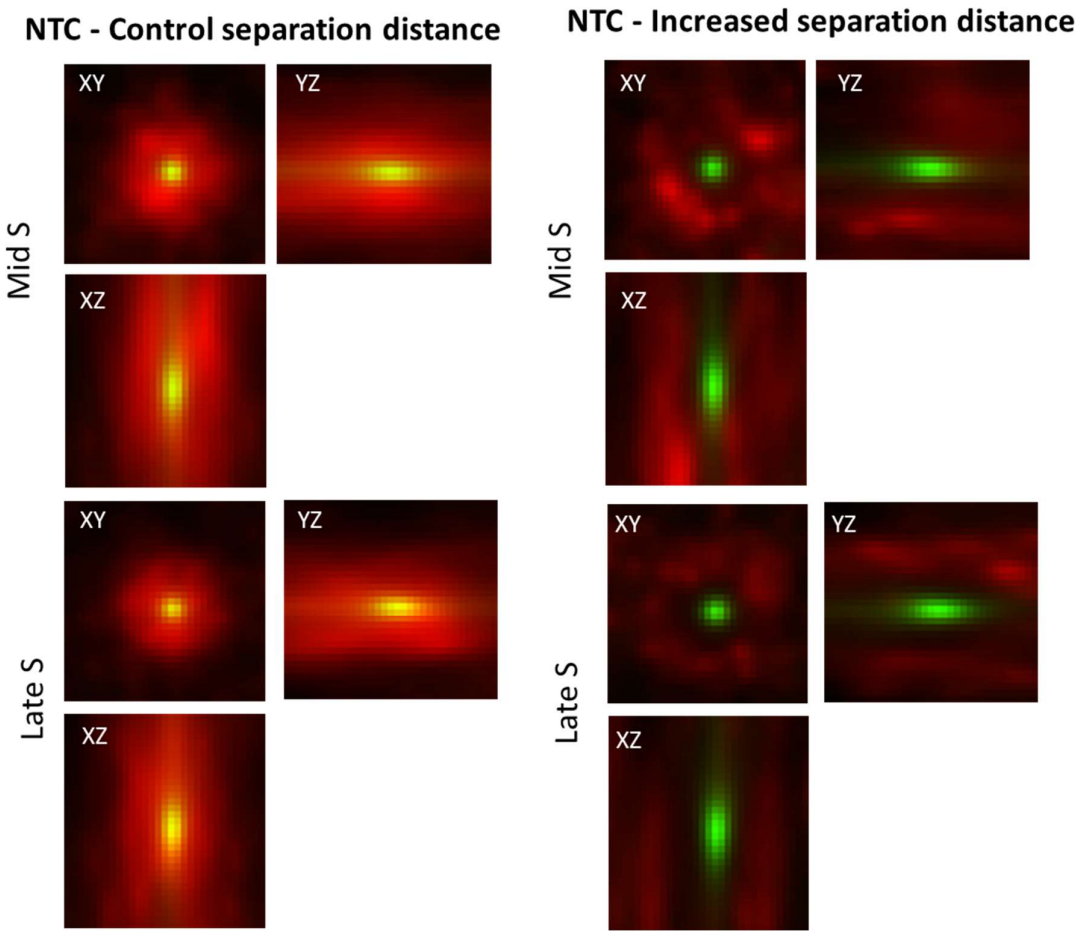

Figure A18. Sub-classifying class 5 structures in control cells for comparison to USP48-depleted cells. Orthogonal views of averaged class 5 structures generated in figure A17 are shown. N = 3, control separation distance (mid S) = 326 structures, control separation distance (late S) = 288 structures, increased separation distance (mid S) = 88 structures and increased separation distance (late S) = 96 structures.

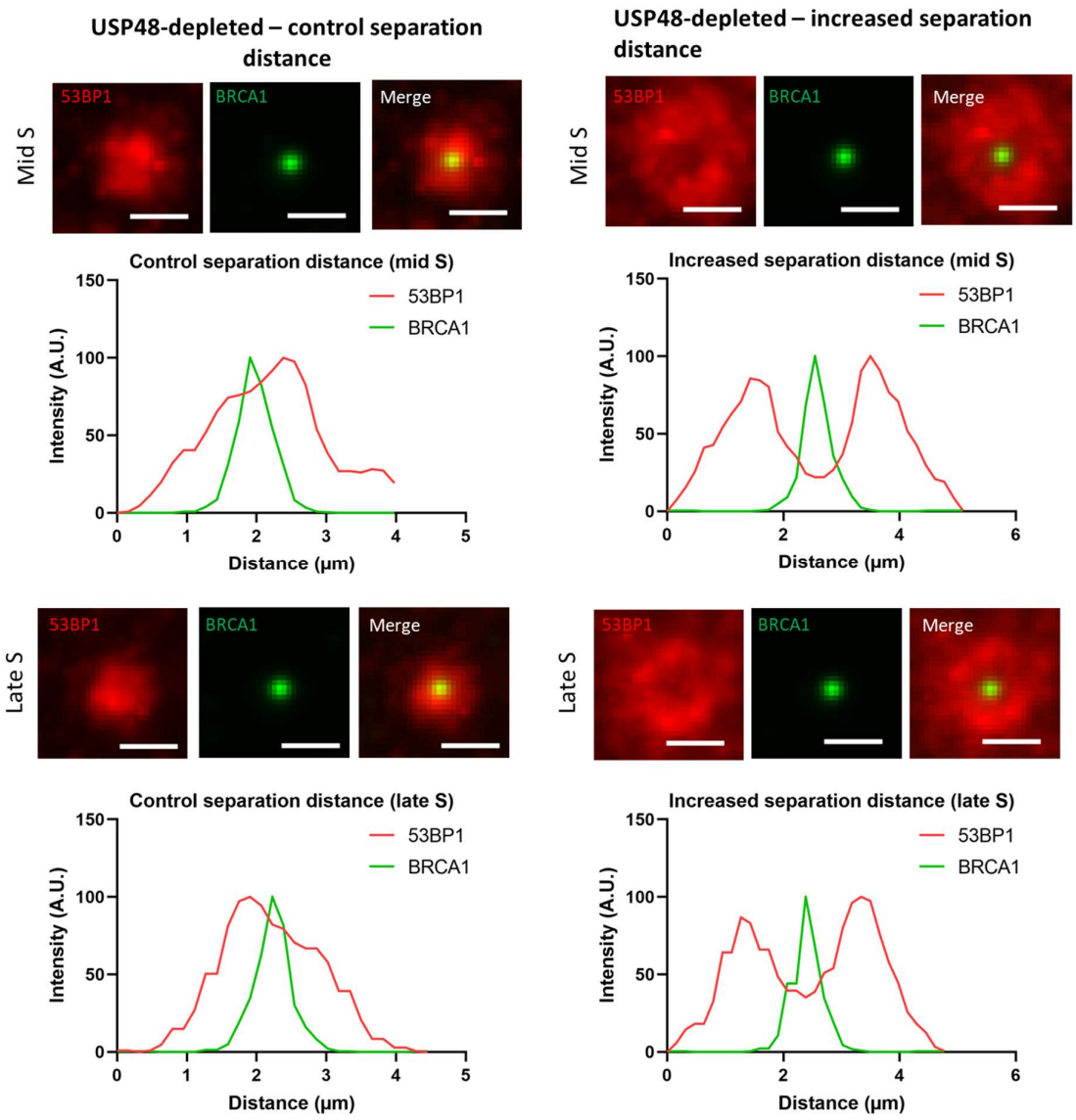

Figure A19. Sub-classifying class 5 structures in USP48-depleted cells for comparison to control cells. All class 5 structures in control cells classified as mid and late S phase were further sub-classified as having a control or increased separation distance between BRCA1 and 53BP1. The structures in each class were then averaged together using the matlab script (described in Section 2.7.6 & 5.2) and their max projections are shown here. Line profiles were also generated for each and are shown below the max projections. N = 3, control separation distance (mid S) = 64 structures, control separation distance (late S) = 96 structures, increased separation distance (mid S) = 340 structures and increased separation distance (late S) = 513 structures. Scale bars 2 µm.

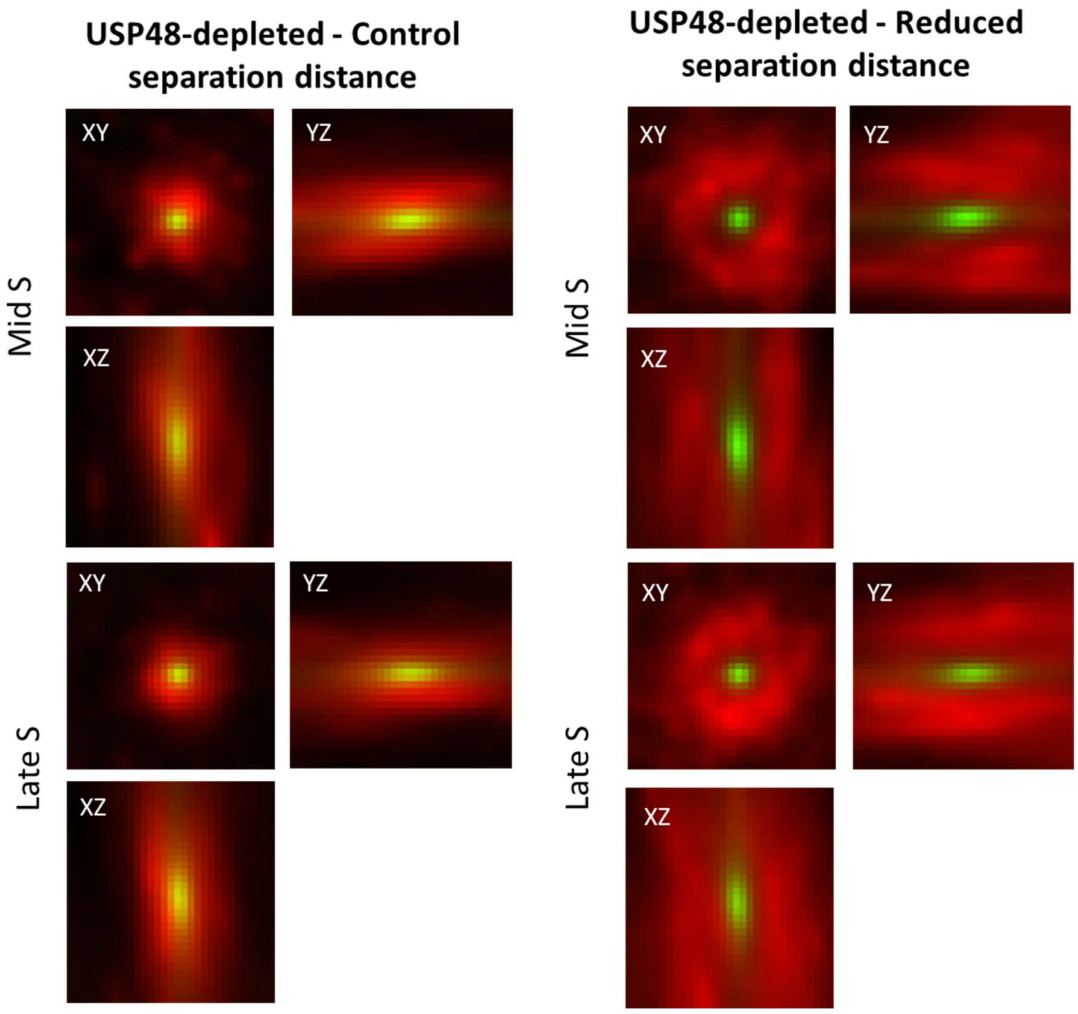

Figure A20. Sub-classifying class 5 structures in control cells for comparison to USP48-depleted cells. Orthogonal views of averaged class 5 structures generated in figure A19 are shown. N = 3, control separation distance (mid S) = 64 structures, control separation distance (late S) = 96 structures, increased separation distance (mid S) = 340 structures and increased separation distance (late S) = 513 structures.

A8 Investigating RAD51 foci structures following USP48-depletion

RAD51 and 53BP1 structures were investigated following USP48-depletion. In the post-expansion Z series, RAD51 structures consistent with a nucleofilament were observed in both the control and USP48-depleted cells. These structures were qualitatively assessed across a range of mid and late S-phase nuclei in control and USP48 depleted cells (Appendix Figure A21-A22).

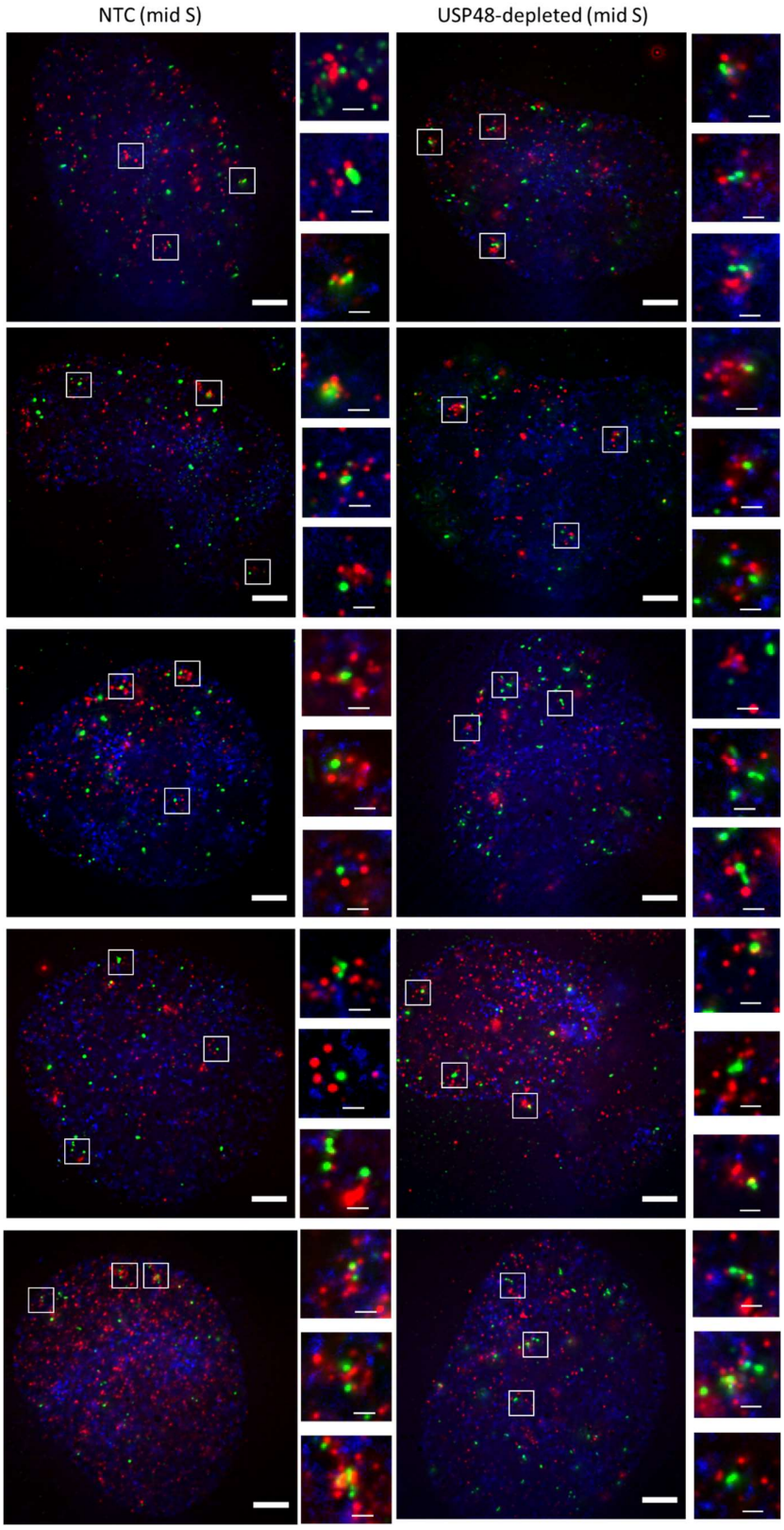
NTC (mid S)
USP48-depleted (mid S)

Figure A21. Investigating RAD51 enrichment in USP48-depleted cells. U2OS cells were treated with either control or USP48 siRNA for 72 hours. Cells were then treated with EdU and irradiated (2 Gy). Cells were allowed to recover for 1 hour prior to CSK pre-extraction and fixation with 4% PFA. Click-it reaction was completed to visualise the EdU (blue) and cells were immunostained for 53BP1 (red) and RAD51 (green). ExM protocol was completed and post-ExM images acquired. Example images of nuclei classified as mid S-phase were selected from USP48-depleted and control cells. Foci structures were selected in each set and shown as zoomed in images. Scale bars 10 μm and 2 μm.

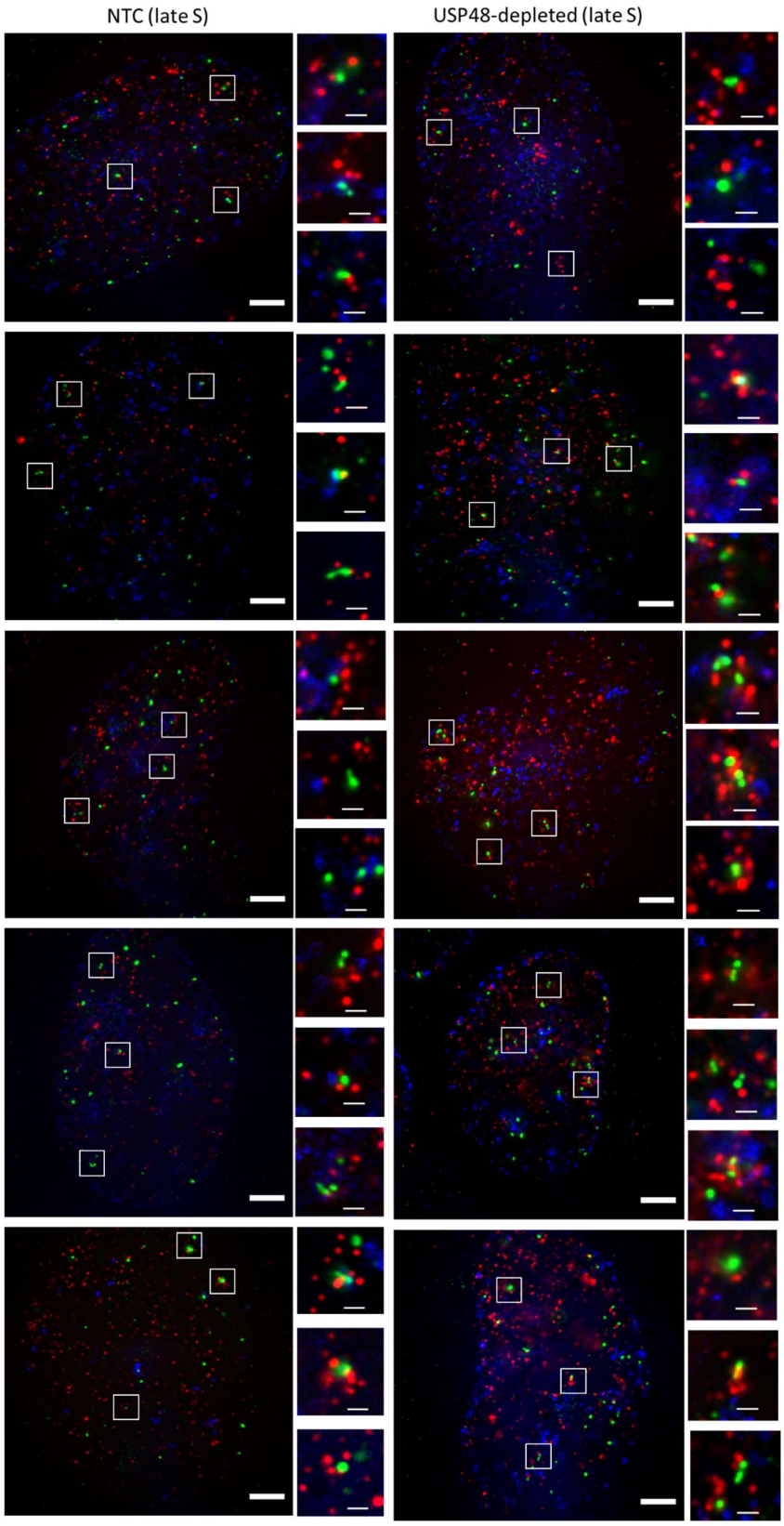
NTC (late S)
USP48-depleted (late S)

Figure A22. Investigating RAD51 enrichment in USP48-depleted cells. U2OS cells were treated with either control or USP48 siRNA for 72 hours. Cells were then treated with EdU and irradiated (2 Gy). Cells were allowed to recover for 1 hour prior to CSK pre-extraction and fixation with 4% PFA. Click-it reaction was completed to visualise the EdU (blue) and cells were immunostained for 53BP1 (red) and RAD51 (green). ExM protocol was completed and post-ExM images acquired. Example images of nuclei classified as late S-phase were selected from USP48-depleted and control cells. Foci structures were selected in each set and shown as zoomed in images. Scale bars 10 μm and 2 μm.

A9 Characterising the nanoscale spatial organisation of 53BP1, BRCA1 and RAD51 after USP48 depletion

The spatial organisation of 53BP1, BRCA1 and RAD51 was investigated in cells depleted of USP48 compared to controls. Significant heterogeneity in enrichment of proteins within the same repair focus, and in their relative spatial organisation within repair foci was observed (Appendix Figure A23 & A24).

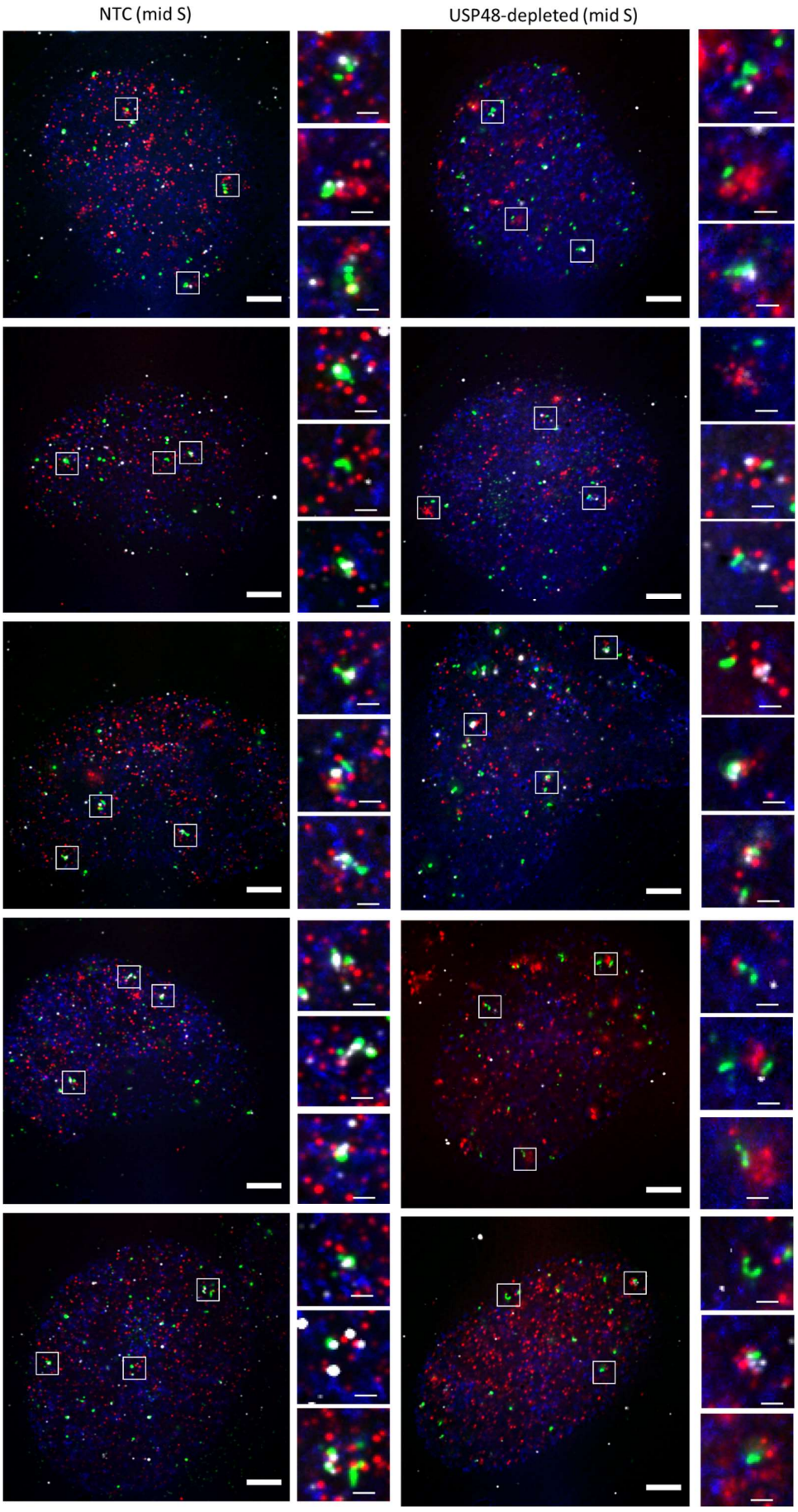
NTC (mid S)
USP48-depleted (mid S)

Figure A23. **Investigating RAD51, BRCA1 and 53BP1 enrichment in USP48-depleted cells.** U2OS cells were treated with either control or USP48 siRNA for 72 hours. Cells were then treated with EdU and irradiated (2 Gy). Cells were allowed to recover for 1 hour prior to CSK pre-extraction and fixation with 4% PFA. Click-it reaction was completed to visualise the EdU (blue) and cells were immunostained for 53BP1 (red), BRCA1 (white) and RAD51 (green). ExM protocol was completed and post-ExM images acquired. Example images of nuclei classified as mid S-phase were selected from USP48-depleted and control cells. Foci structures were selected in each set and shown as zoomed in images. Scale bars 10 µm and 2 µm.

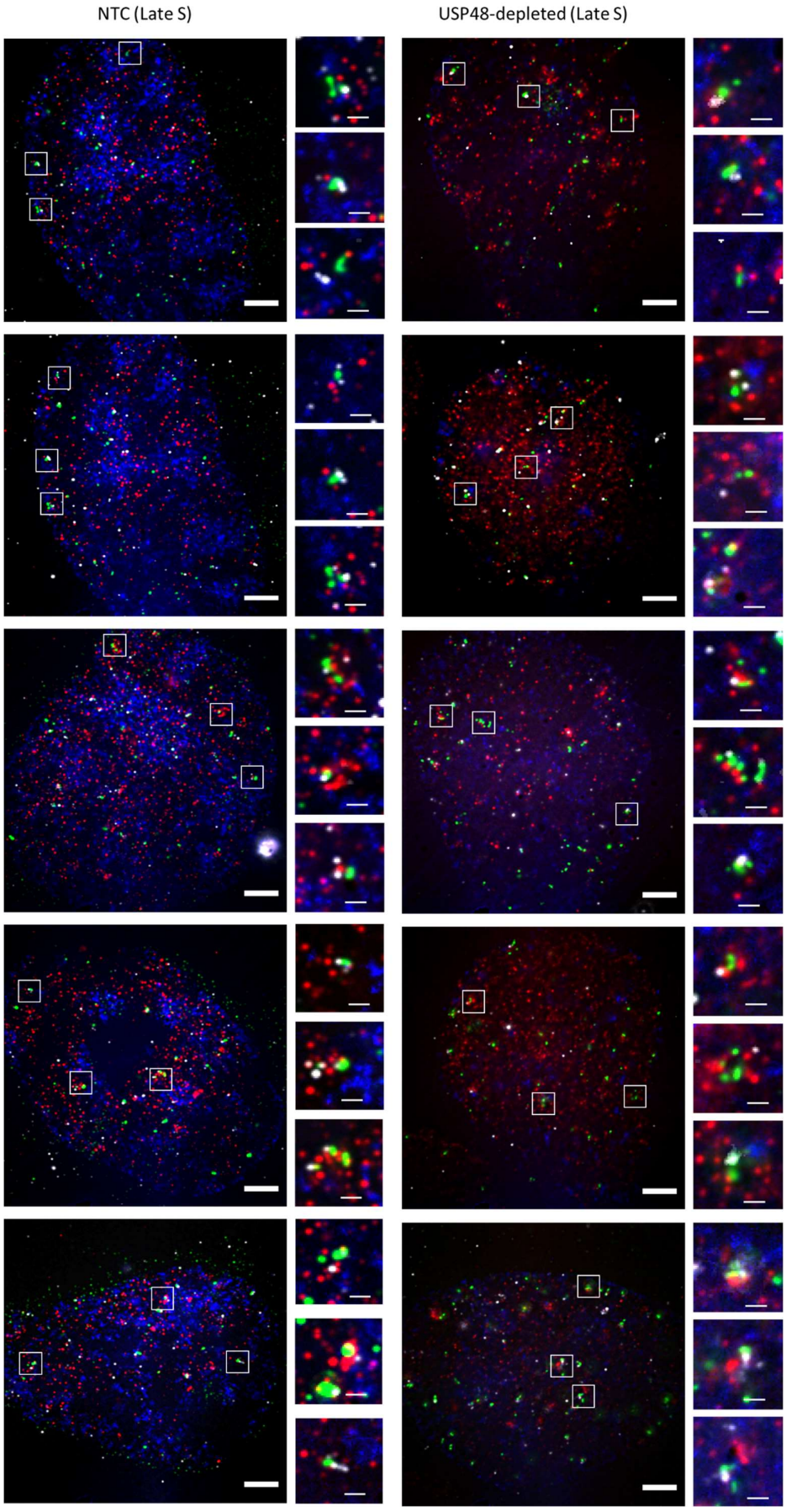
NTC (Late S)
USP48-depleted (Late S)

Figure A24. **Investigating RAD51, BRCA1 and 53BP1 enrichment in USP48-depleted cells.** U2OS cells were treated with either control or USP48 siRNA for 72 hours. Cells were then treated with EdU and irradiated (2 Gy). Cells were allowed to recover for 1 hour prior to CSK pre-extraction and fixation with 4% PFA. Click-it reaction was completed to visualise the EdU (blue) and cells were immunostained for 53BP1 (red), BRCA1 (white) and RAD51 (green). ExM protocol was completed and post-ExM images acquired. Example images of nuclei classified as late S-phase were selected from USP48-depleted and control cells. Foci structures were selected in each set and shown as zoomed in images. Scale bars 10 µm and 2 µm.

To quantitatively describe the observed heterogeneity, accumulations were classified into one of ten classes using spot detection-based analysis. These classifications are shown as a fraction of the total number of structures per nucleus (Appendix Figure A25).

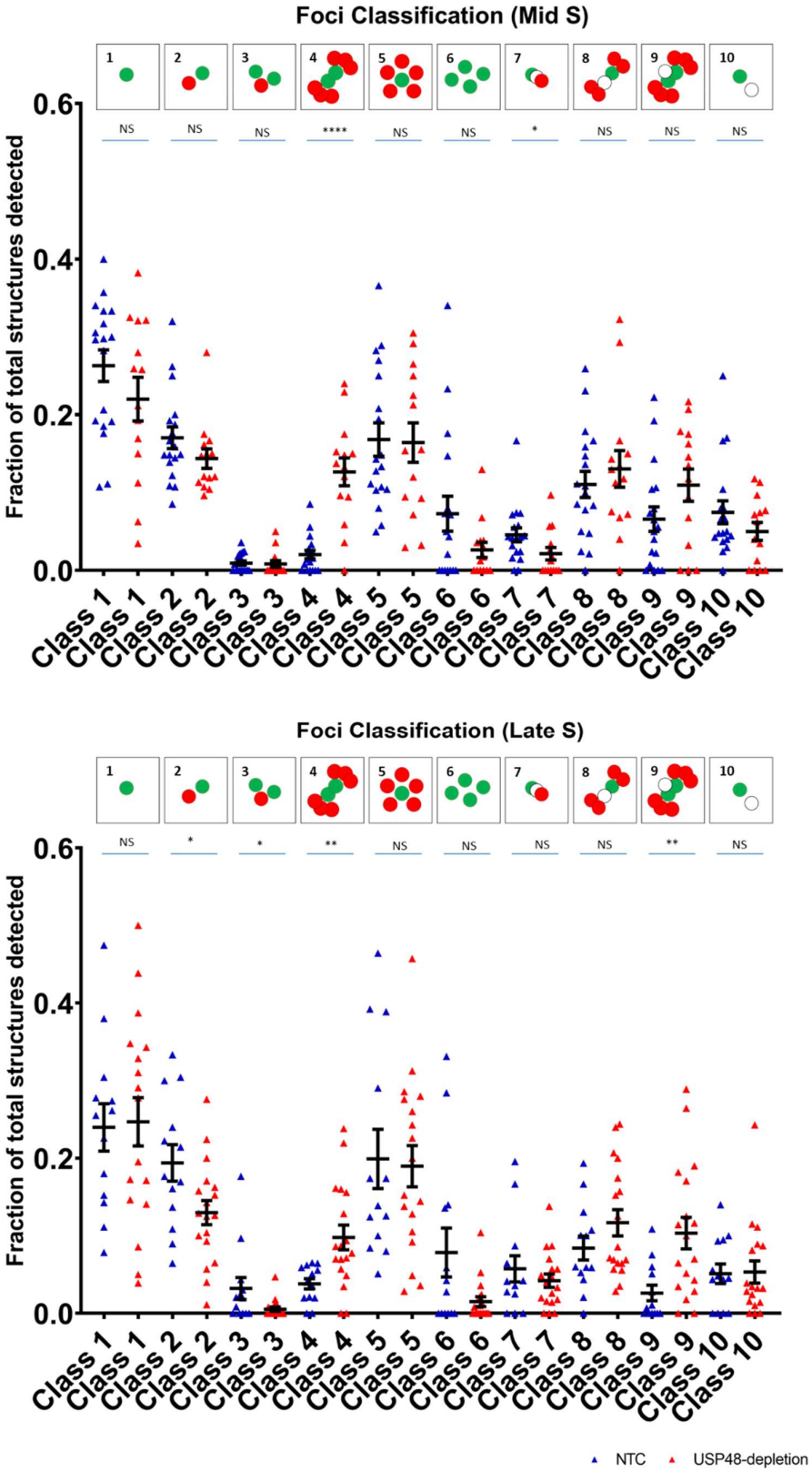
Foci Classification (Mid S)
Fraction of total structures detected
0.6
0.4
0.2
0.0
1
2
3
4
5
6
7
8
9
10
NS
NS
NS
****
NS
NS
*
NS
NS
NS
Class 1
Class 1
Class 2
Class 2
Class 3
Class 3
Class 4
Class 4
Class 5
Class 5
Class 6
Class 6
Class 7
Class 7
Class 8
Class 8
Class 9
Class 9
Class 10
Class 10
Foci Classification (Late S)
Fraction of total structures detected
0.6
0.4
0.2
0.0
1
2
3
4
5
6
7
8
9
10
NS
*
*
**
NS
NS
NS
NS
**
NS
Class 1
Class 1
Class 2
Class 2
Class 3
Class 3
Class 4
Class 4
Class 5
Class 5
Class 6
Class 6
Class 7
Class 7
Class 8
Class 8
Class 9
Class 9
Class 10
Class 10
NTC
USP48-depletion

Figure A25. Classifying BRCA1, 53BP1 and RAD51 distributions on USP48-depleted cells. Spot detection-based analysis was performed on Z stack data acquired in control and USP48 depleted cells. Structures were scored for nuclei in mid and late S-phase according to the identified classes shown schematically above where BRCA1 = white, RAD51 = green and 53BP1 = red. RAD51 was treated as the centre in these datasets. Classifications are shown as numbers of structures detected per nucleus for mid and late S-phase classified nuclei. N=2, >14 nuclei per phase. Throughout Figure, **** P<0.001; ***P < 0.005; **P <0.01;*P < 0.05 NS, not significant by two-sided Student's t test.

A10 Visualising repair foci in the context of chromatin

To determine if chromatin compaction and/or de-compaction could be detected using ExM, SMARCAD1 and USP48 depletions were performed on cells expressing H2A-dendra2. Some of the images had poor signal-to-noise ratio and were omitted from the spot detection-based analysis on this background (Appendix Figure A26).

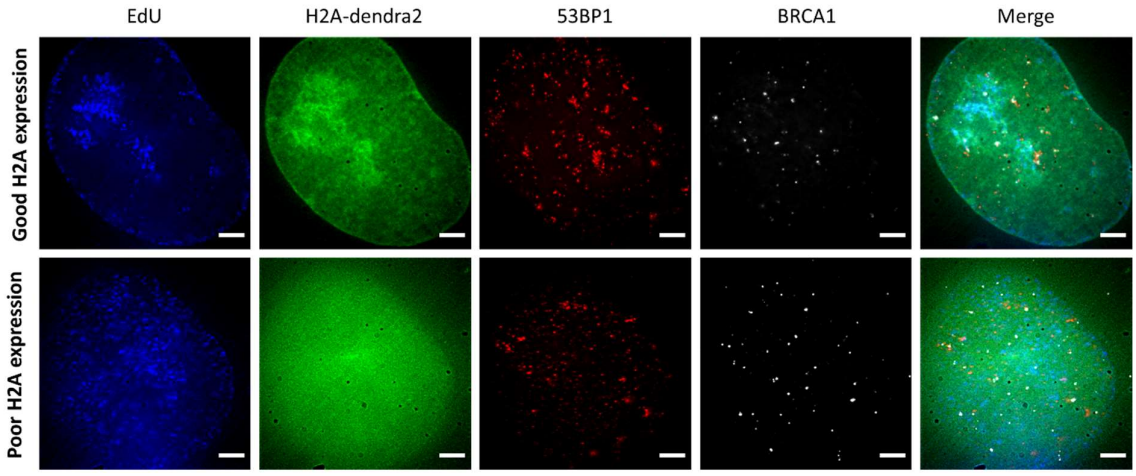

Figure A26. Poor intensity from H2A-dendra2 observed when investigating effects of SMARCAD1- and USP48-depletion on chromatin proximal to sites of damage. Examples of good and poor signal derived from H2A-dendra2 are shown. These examples were selected from images of cells following SMARCAD1-depletion as described in Section 5.4.1. Images with poor signal intensity in H2A-dendra2 channel were excluded from spot detection based analysis. Scale bar 10 µm.

A11 Increasing resolution of ExM

To improve resolution, we attempted X10 ExM to visualise nanoscale changes in chromatin architecture. SPIM images were acquired on nuclei which were 6.3x expanded (Appendix Figure A27).

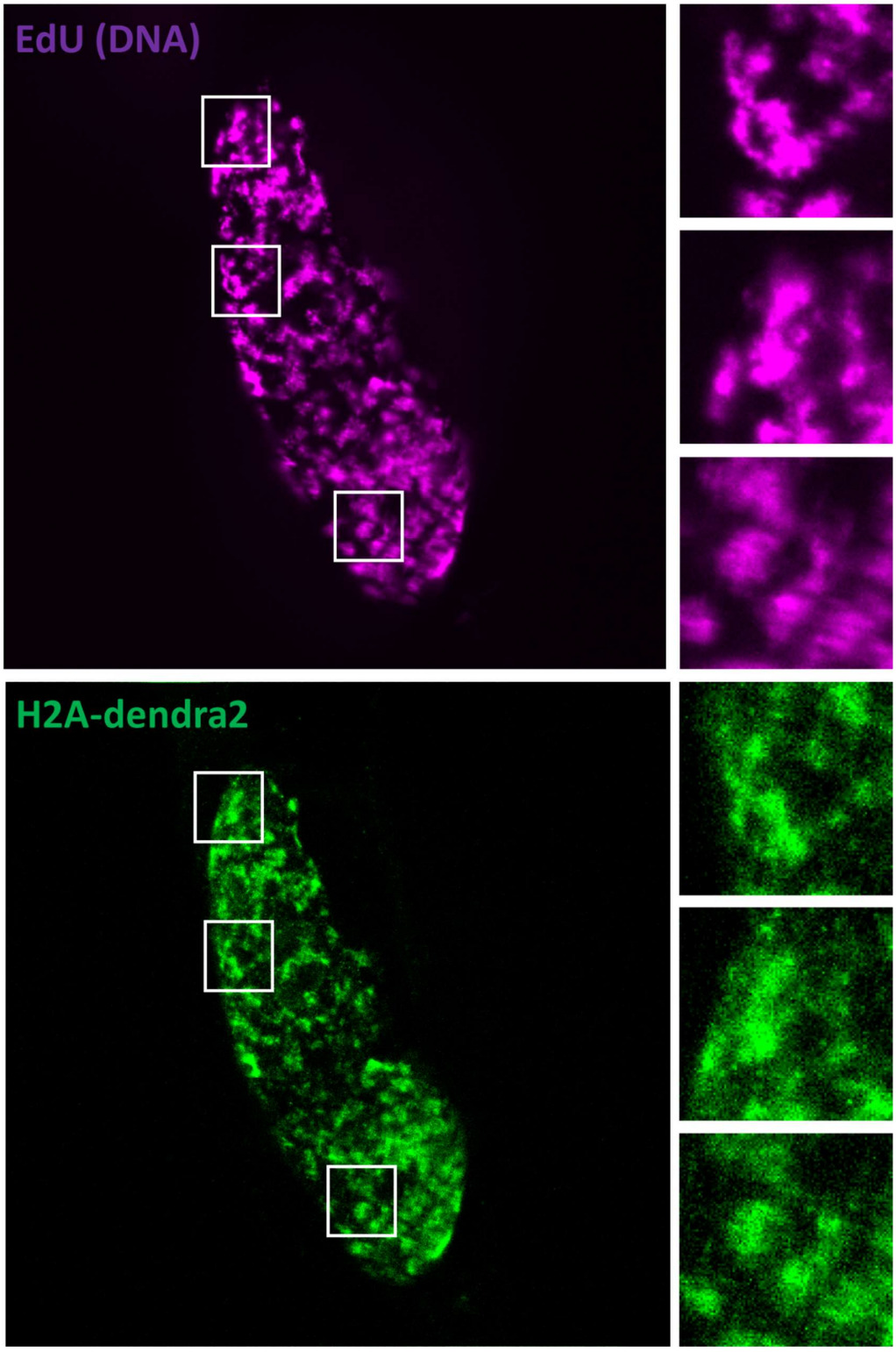

Figure A27. X10 ExM reveals nanoscale topology of chromatin and DNA. A slice from a SPIM acquisition is shown. DNA is shown in magenta and H2A-dendra2 is shown in green.

7. References

Alon, S., Huynh, G. H., & Boyden, E. S. (2019). Expansion microscopy: enabling single cell analysis in intact biological systems. *FEBS Journal*, *286*(8), 1482–1494.

Applied Scientific Instrumentation (no date). Dual inverted selective plane illumination microscope (iSPIM and diSPIM). Available at: http://www.asiimaging.com/products/light-sheet-microscopy/dual-inverted-selective-plane-illumination-microscope/. (Accessed 06/09/20).

Balinovic, A., Albrecht, D., & Endesfelder, U. (2019). Spectrally red-shifted fluorescent fiducial markers for optimal drift correction in localization microscopy. *Journal of Physics D: Applied Physics*, *51*(20).

Bates, M., Huang, B., Zhuang, X. (2008) Super-resolution microscopy by nanoscale localisation of photo-switchable fluorescent probes, 12: 505-514.

Bekker-Jensen, S., Lukas, C., Kitagawa, R., Melander, F., Kastan, M. B., Bartek, J., & Lukas, J. (2006). Spatial organization of the mammalian genome surveillance machinery in response to DNA strand breaks. *Journal of Cell Biology*, *173*(2), 195–206.

Beppu T., & Ishida, Y. (1994). Detection of S phase cells with an antibody to proliferating cell nuclear antigen (PCNA). *Journal of Histotechnology.* 17(4): 325-328.

Berg, S., Kutra, D., Kroeger, T., Straehle, C. N., Kausler, B. X., Haubold, C., Schiegg, M., Ales, J., Beier, T., Rudy, M., Eren K., Cervantes, J. I., Xu, B., Beuttenmueller, F., Wolny, A., Zhang, C., Koethe, U., Hamprecht, F. A., Kreshuk,, A. (2019). ilastik: interactive machine learning for (bio)image analysis. *Nature Methods 16*, 1226–1232.

Betzig, E. (2015). Single Molecules, Cells, and Super-Resolution Optics (Nobel Lecture). *Angewandte Chemie International Edition*, *54*(28), 8034–8053.

Bleuyard, J. Y., Buisson, R., Masson, J. Y., & Esashi, F. (2012). ChAM, a novel motif that mediates PALB2 intrinsic chromatin binding and facilitates DNA repair. *EMBO Reports*, *13*(2), 135–141. https://doi.org/10.1038/embor.2011.243

Bohgaki, T., Bohgaki, M., & Hakem, R. (2010). DNA double-strand break signalling and human disorders. Genome Integrity 1:15.

Borde, V., & de Massy, B. (2013). Programmed induction of DNA double strand breaks during meiosis: Setting up communication between DNA and the chromosome structure. *Current Opinion in Genetics and Development*, *23*(2), 147–155.

Cejka, P. (2017). Complex assistance for DNA invasion. *Nature*. 550: 342–343

Chang, J., Chen, F., Yoon, Y., Jung E. E., Babcock H., Kang J. S., Asano, S., Suk, H., Pak, N., Tillberg, P. W., Wassie, A. T., Cai, D., Boyden, E. S. (2017). Iterative Expansion Microscopy. *Nature Methods*, *14*(6), 593-604.

Chapman, J. R., Barral, P., Vannier, J.-B., Rie Borel, V., Steger, M., Tomas-Loba, A., Sartori A. A., Adams I.R., Batista F.D., & Boulton, S. J. (2013). RIF1 Is Essential for 53BP1-Dependent Nonhomologous End Joining and Suppression of DNA Double-Strand Break Resection. *Molecular cell 49*, 858-871.

Chapman, J. R., Sossick, A. J., Boulton, S. J., & Jackson, S. P. (2012). BRCA1-associated exclusion of 53BP1 from DNA damage sites underlies temporal control of DNA repair. *Journal of Cell Science*, *125*, 3529–3534.

Chapman, J. R., Taylor, M. R. G., & Boulton, S. J. (2012). Playing the End Game: DNA Double-Strand Break Repair Pathway Choice. *Molecular Cell, 47*, 497–510.

Chen F., Wassie A. T., Cote A. J., Sinha A., Shahar A., Shoh A., Daugharthy E. R., Chang J., Marblestone A., Church G. M., Raj A., Boyden E.S. (2016). Nanoscale imaging of RNA with expansion microscopy. *Nature Methods*, *13*(8), 679–84.

Chen, F., Tillberg, P. W., & Boyden, E. S. (2015). Expansion microscopy. *Science*, *347*(6221).

Chen, F., Wassie, A. T., Cote, A. J., Sinha, A., Alon, S., Asano, S., Daugharthy E. R., Chang J., Marblestone A., Church G. M., Raj A., Boyden, E. S. (2016). Nanoscale imaging of RNA with expansion microscopy. *Nature Methods*, *13*(8), 679–84.

Cho I., Seo J. Y., & Chang J. (2018). Expansion microscopy. *Journal of Microscopy*, *271*(2), 123–128.

Chozinski T. (2018) Expansion Microscopy for the Interrogation of Nanoscale Features in Complex Biological Systems. Thesis. University of Washington. Available at: https://digital.lib.washington.edu/researchworks/handle/1773/42234. Accessed 27/09/18.

Chozinski T. J., Halpern, A. R., Okawa, H., Tremel, G. J., Wong, R. O. L., Vaughan, J. C. (2016) Expansion microscopy with conventional antibodies and fluorescent proteins. Nature methods 13: 485-488.

Cipriano, B. H. Banik S. J., Sharma R., Rumore D., Hwang W., Briber R. M. & Raghavan S. R. (2014) Superabsorbent hydrogels that are robust and highly stretchable. *Macromolecules*, *47*, 4445–4452.

Clouaire, T., & Legube, G. (2019). A Snapshot on the Cis Chromatin Response to DNA Double-Strand Breaks. *Trends in Genetics*, *35*(5), 330–345.

Conchello, J. A., & Lichtman, J. W. (2005). Optical sectioning microscopy. *Nature Methods*, *2*(12), 920–931.

Daley, J. M., & Sung, P. (2014). 53BP1, BRCA1, and the Choice between Recombination and End Joining at DNA Double-Strand Breaks.

Densham, R. M., & Morris, J. R. (2019). Moving Mountains—The BRCA1 Promotion of DNA Resection. *Frontiers in Molecular Biosciences*, *6*(79).

Densham, R. M., Garvin, A. J., Stone, H. R., Strachan, J., Baldock, R. A., Daza-Martin, M., Fletcher, A., Blair-Reid, S., Beesley, J., Johal, B., Pearl, L. H., Neely, R., Keep, N. H., Watts, F. Z., Morris, J. R. (2016). Human BRCA1–BARD1 ubiquitin ligase activity counteracts chromatin barriers to DNA resection. *Nature Structural and Molecular biology, 23*(7), 6–4.

Dev, H., Chiang, T. W. W., Lescale, C., de Krijger, I., Martin, A. G., Pilger, D., Coates, J., Sczaniecka-Clift, M., Wei, W., Ostermaier, M., Herzog, M., Lam, J., Shea, A., Demir, M., Wu, Q., Yang, F., Fu, B., Lai, Z., Balmus, G., Belotserkovskaya, R., Serra, V., O'connor, M. J., Bruna, A., Beli, P., Pellegrini, L., Caldas, C., Deriano, L., Jacobs, J. J. L., Galanty, Y., Jackson, S. P. (2018). Shieldin complex promotes DNA end-joining and counters homologous recombination in BRCA1-null cells. *Nature Cell Biology*, *20*(8), 954–965.

Dietz C., Berthold M.R. (2016) KNIME for Open-Source Bioimage Analysis: A Tutorial. In: De Vos W., Munck S., Timmermans JP. (eds) Focus on Bio-Image Informatics. Advances in Anatomy, Embryology and Cell Biology, vol 219. Springer, Cham.

Dimitrova, D. S., & Berezney, R. (2002). The spatio-temporal organisation of DNA replication sites is identical in primary, immortalised and transformed mammalian cells. *Journal of Cell Science*, *108*(3), 1205–1215.

Dunn, K. W., Kamocka, M. M., & McDonald, J. H. (2011). A practical guide to evaluating colocalization in biological microscopy. *American Journal of Physiology-Cell Physiology*, *300*(4), C723–C742.

Escribano-Díaz, C., Orthwein, A., Fradet-Turcotte, A., Xing, M., Young, J. T. F., Tkáč, J., Cook, M. A., Rosebrock, A. P., Munro, M., Canny, M. D., Xu, D., Durocher, D. (2013). A Cell Cycle-Dependent Regulatory Circuit Composed of 53BP1-RIF1 and BRCA1-CtIP Controls DNA Repair Pathway Choice. *Molecular Cell*, *49*(5), 872–883.

Faulkner EL, Thomas SG, Neely RK. (2020). An introduction to the methodology of expansion microscopy. *The International Journal of Biochemistry & Cell Biology.* 124:105764.

Feng, W., Jasin, M., & Gerstner, L. V. (2017). Homologous recombination and replication fork protection: BRCA2 and more! HHS Public Access. *Cold Spring Harb Symp Quant Biol*, *82*, 329–338.

Fernandez-Vidal, A., Vignard, J., & Mirey, G. (2017). Around and beyond 53BP1 nuclear bodies. *International Journal of Molecular Sciences*, *18*(12), 1–20.

Fischer, R. S., Wu, Y., Kanchanawong, P., Shroff, H., & Waterman, C. M. (2011). Microscopy in 3D: A biologist's toolbox. *Trends in Cell Biology*. *21(12):* 682-691.

Freifeld, L., Odstrcil, I., Förster, D., Ramirez, A., Gagnon, J. A., Randlett, O., Costa, E. K., Asano, S., Celiker, O. T., Gao, R., Martin-Alarcon, D. A., Reginato, P., Dick, C., Chen, L., Schoppik D., Engert, F., Baier, H., Boyden, E. S. (2017). Expansion microscopy of zebrafish for neuroscience and developmental biology studies. *Proceedings of the National Academy of Sciences of the United States of America*, *114*(50), E10799–E10808.

Galbraith, C.G., Galbraith, J.A. (2011) Super-resolution microscopy at a glance, Journal of Cell Science, 124: 1607-1611 3.

Gambarotto, D., Zwettler, F. U., Le Guennec, M., Schmidt-Cernohorska, M., Fortun, D., Borgers, S., Heine, J., Schloetel J., Reuss, M., Unser, M., Boyden, E. S., Sauer, M., Hamel V., Guichard, P. (2019). Imaging cellular ultrastructures using expansion microscopy (U-ExM). Nature Methods, 16(1), 71–74.

Gao, M., Maraspini, R., Beutel, O., Zehtabian, A., Eickholt, B., Honigmann, A., & Ewers, H. (2018). Expansion Stimulated Emission Depletion Microscopy (ExSTED). *ACS Nano*, *12*(5), 4178–4185.

Gao, R., Asano, S. M., & Boyden, E. S. (2017). Q&A: Expansion microscopy. *BMC Biology*, *15*(1), 50.

Garini, Y., Vermolen, B. J., & Young, I. T. (2005). From micro to nano: Recent advances in high-resolution microscopy. *Current Opinion in Biotechnology*, *16*, 3–12.

Geertsema, H., & Ewers, H. (2016). Expansion microscopy passes its first test. *Nature Methods*, *13*(6), 481–482.

Ghezraoui, H., Oliveira, C., Becker, J. R., Bilham, K., Moralli, D., Anzilotti, C., Fischer, R., Deobagkar-Lele, M., Sanchiz-Calvo, M., Fueyo-Marcos, E., Bonham, S., Kessler, B. M., Rottenberg, S., Cornall, R. J., Green, C. M., Chapman, J. R. (2018). 53BP1 cooperation with the REV7–shieldin complex underpins DNA structure-specific NHEJ. *Nature*.

Ghodke, I., & Soutoglou, E. (2019). 53BP1–RIF1: sculpting the DNA repair focus in 3D. *Nature Structural and Molecular Biology*, *26*(December), 1087–1088.

Gonfloni, S. (2013). Targeting DNA damage response: Threshold, chromatin landscape and beyond. *Pharmacology and Therapeutics*, *138*(1), 46–52.

Gupta, R., Somyajit, K., Narita, T., Maskey, E., Stanlie, A., Kremer, M., Typas D., Lammers, M., Mailand, N., Bussenzweig, A., Lukas, J., Choudhary, C. (2018). DNA Repair Network Analysis Reveals Shieldin as a Key Regulator of NHEJ and PARP Inhibitor Sensitivity. *Cell*, *173*(4), 972–988.e23.

Gurskaya N.G., Verkhusha V.V., Shcheglov A.S., Staroverov, D. b., Chepurnykh, T. V., Fradkov, A. F., Lukyanov, S., Lukyanov, K. A. (2006). Engineering of a monomeric green-to-red photoactivatable fluorescent protein induced by blue light. *Nature Biotechnology 24(4)*:461-465.

Gustafsson, M. G. L. (2000). Surpassing the lateral resolution limit by a factor of two using structured illumination microscopy. Journal of Microscopy, 198(2), 82–87.

Gustafsson, M.G., Shao, L., Carlton, P. M., Wang, C. J., Golubovskaya, I. N., Cande, W. Z., Agard, D. A., & Sedat. J. W. (2008). Three-dimensional resolution doubling in wide-field fluorescence microscopy by structured illumination. *Biophysical Journal. 94(12):*4957–4970.

Halpern, A. R., Alas, G. C. M., Chozinski, T. J., Paredez, A. R., & Vaughan, J. C. (2017). Hybrid Structured Illumination Expansion Microscopy Reveals Microbial Cytoskeleton Organization. *ACS Nano*, *11*(12), 12677–12686.

Heijden, T. Van Der, Seidel, R., Modesti, M., Kanaar, R., Wyman, C., & Dekker, C. (2007). Real-time assembly and disassembly of human RAD51 filaments on individual DNA molecules, 35(17), 5646–5657.

Heintzmann, R., & Huser, T. (2017). Super-Resolution Structured Illumination Microscopy. *Chemical Reviews 117:* 13890-13908.

Heintzmann, R., Sarafis, V., Munroe, P., Nailon, J., Hanley, Q. S., & Jovin, T. M. (2003). Resolution enhancement by subtraction of confocal signals taken at different pinhole sizes. *Micron*, *34*(6–7), 293–300.

Her, J., & Bunting, S. F. (2018). How cells ensure correct repair of DNA double-strand breaks. *Journal of Biological Chemistry 293(27)*: 10502-10511.

Her, J., Soo Lee, N., Kim, Y., & Kim, H. (2016). Factors forming the BRCA1-A complex orchestrate BRCA1 recruitment to the sites of DNA damage. Acta Biochimica et Biophysica Sinica, 48(7), 658–664.

Hess, S. T., Girirajan, T. P. K., & Mason, M. D. (2006). Ultra-high resolution imaging by fluorescence photoactivation localization microscopy. *Biophysical Journal*, *91*(11), 4258–4272.

Hu, Y., Scully, R., Sobhian, B., Xie, A., Shestakova, E., & Livingston, D. M. (2011). RAP80-directed tuning of BRCA1 homologous recombination function at ionizing radiation-induced nuclear foci. Genes and Development, 25(7), 685–700.

Huang, B. (2010). Super-resolution optical microscopy: multiple choices. *Current Opinion in Chemical Biology*, *14*(1), 10–14.

Huang, B., Bates, M., & Zhuang, X. (2009). Super-Resolution Fluorescence Microscopy. *Annual Review of Biochemistry* 78: 993-1016.

Huber M., Gerace L. (2007). The size-wise nucleus: nuclear volume control in eukaryotes. *The Journal of cell biology. 179(4):* 583-584.

Huertas, P. (2010). DNA resection in eukaryotes: Deciding how to fix the break. *Nature Structural and Molecular Biology*, *17*(1), 11–16.

Huisken, J., & Stainier, D. Y. R. (2009). Selective plane illumination microscopy techniques in developmental biology. *Development*, *136*(12), 1963–1975.

Huisken, J., Swoger, J., Del Bene, F., Wittbrodt, J., & Stelzer, E. H. K. (2004). Optical sectioning deep inside live embryos by selective plane illumination microscopy. *Science (New York, N.Y.)*, *305*(5686), 1007–9.

Isono, M., Niimi, A., Oike, T., Hagiwara, Y., Sato, H., Sekine, R., Yoshida, Y., Isobe, S., Obuse, C., Nishi, R., Petricci, E., Nakada, S., Nakano, T., Shibata, A. (2017). BRCA1 Directs the Repair Pathway to Homologous Recombination by Promoting 53BP1 Dephosphorylation. *Cell Reports*, *18*(2), 520–532.

Jackson, S. P., & Bartek, J. (2009). The DNA-damage response in human biology and disease. *Nature*, *461*. 1071-1078.

Jae-Byum Chang, Fei Chen, Young-Gyu Yoon, Erica E Jung, Hazen Babcock , Jeong Seuk Kang, S. A., & Ho-Jun Suk, Nikita Pak, Paul W Tillberg, Asmamaw T Wassie, D. C. & E. S. B. (2017). Iterative Expansion Microscopy. *Nature Methods, 14(6).* 593-599.

Jazayeri, A., J. Falck, C. Lukas, J. Bartek, G.C. Smith, J. Lukas, and S.P. Jackson. 2006. ATM- and cell cycle-dependent regulation of ATR in response to DNA double-strand breaks. *Nature Cell Biology 8*:37–45.

Kakarougkas, A., Ismail, A., Katsuki, Y., Freire, R., Shibata, A., and Jeggo, P. A. (2013). Co-operation of BRCA1 and POH1 relieves the barriers posed by 53BP1 and RAP80 to resection. *Nucleic Acids Research 22:* 10298-10311.

Kaniecki K., De Tullio L., & Green E.C. (2018). A change of view: homologous recombination at single-molecule resolution. Nature Reviews Genetics. 19(4): 191-207.

Kilic, S., Lezaja, A., Gatti, M., Bianco, E., Michelena, J., Imhof, R., et al. (2019). Phase separation of 53BP1 determines liquid-like behavior of DNA repair compartments. EMBO J 38:e101379.

Kostiuk, G., & Bucevicius, J., Gerasimaite, R., Lukinavicius, G. (2019). Application of STED imaging for chromatin studies. Journal of Physics D: Applied Physics 52: 504003.

Ku, T., Swaney, J., Park, J.-Y., Albanese, A., Murray, E., Cho, J. H., Park, Y., Mangena, V., Chen, J., Chung, K. (2016). Multiplexed and scalable super-resolution imaging of three-dimensional protein localization in size-adjustable tissues. *Nature Biotechnology*, *34*(9).

Leonhardt, H., Rahn, H.-P., Weinzierl, P., Sporbert, A., Cremer, T., Zink, D., & Cardoso, M. C. (2000). Dynamics of DNA Replication Factories in Living Cells. *The Journal of Cell Biology*, *149*(2), 271–279.

Lomax, M. E., Folkes, L. K., O'Neill, P. (2013). Biological consequences of radiation-induced DNA damage: relevance to radiotherapy. *Clinical Oncology.* 25(10): 578-585.

Lou, J., Scipioni, L., Wright, B. K., Bartolec, T. K., Zhang, J., Pragathi Masamsetti, V., Gaus, K., Gratton, E. Cesare A. J., Hinde, E. (2019). Phasor histone FLIM-FRET microscopy quantifies spatiotemporal rearrangement of chromatin architecture during the DNA damage response. *Proceedings of the National Academy of Sciences of the United States of America*, *116*(15), 7323–7332.

Lukas, C., Savic, V., Bekker-Jensen, S., Doil, C., Neumann, B., Pedersen, R. S., Grofte, M., Chan, K. L., Hickson, I. D., Bartek, J., Lukas, J. (2011). 53BP1 nuclear bodies form around DNA lesions generated by mitotic transmission of chromosomes under replication stress. Nature Cell Biology, 13(3), 243–253. https://doi.org/10.1038/ncb2201

Ma, C. J., Gibb, B., Kwon, Y., Sung, P., & Greene, E. C. (2017). Protein dynamics of human RPA and RAD51 on ssDNA during assembly and disassembly of the RAD51 filament. *Nucleic Acids Research*, *45*(2), 749–761.

Mao, Z., Bozzella, M., Seluanov, A., & Gorbunova, V. (2008). DNA repair by nonhomologous end joining and homologous recombination during cell cycle in human cells. *Cell Cycle*, *7*(18), 2902–2906.

Martínez, G. F., Gazal, N. G., Quassollo, G., Szalai, A. M., Cid-Pellitero, E. Del, Durcan, T. M., Fon E. A., Bisbal M., Stefani F. D., & Unsain, N. (2020). Quantitative expansion microscopy for the characterization of the spectrin periodic skeleton of axons using fluorescence microscopy. *Scientific Reports*, *10*(1), 1–11.

Matt, S., & Hofmann, T. G. (2016). The DNA damage-induced cell death response: a roadmap to kill cancer cells. *Cellular and Molecular Life Sciences*, *73*. https://doi.org/10.1007/s00018-016-2130-4

Miki, Y., Swensen, J., Shattuck-Eidens, D., Futreal, P. A., Harshman, K., Tavtigian, S.,Liu, Q., Cochran, C., Bennett, M., Ding, W. Bell, R., Rosenthal, J., Hussey, C., Tran, T., McClure, M., Frye, C., Hattier, T., Gholami, Z., Shaffer, D., Stone, S., Bayer, S., Wray, C., Bogden, R., Dayananth, P., Ward, J., Tonin, P., Narod, S., Bristow, P. K., Norris, F. H., Helvering, L., Morrison, P., Rosteck, P., Lai, M., Barrett J. C., Lewis C., Neuhausen, S., Goldgar, D., Wiseman, R., Kamb, A., Skolnick, M. H. (1994). A strong candidate for the breast and ovarian cancer susceptibility gene BRCA1. *Science*, *266*(5182), 66–71.

Min, K., Cho, I., Choi, M., & Chang, J.-B. (2020). Multiplexed expansion microscopy of the brain through fluorophore screening. *Methods 174*: 3-10.

Mirman, Z., Lottersberger, F., Takai, H., Kibe, T., Gong, Y., Takai, K., Bianchi, A., Zimmermann, M., Durocher, D., Titia De Lange, &. (2018). 53BP1–RIF1–shieldin counteracts DSB resection through CST- and Polα-dependent fill-in. *Nature*.

Misteli, T., & Soutoglou, E. (2009). The emerging role of nuclear architecture in DNA repair and genome maintenance. *Nature Reviews Molecular Cell Biology*, *10*(4), 243–254.

Misteli, T., Soutoglou, E. (2009). The emerging role of nuclear architecture in DNA repair and genome maintenance. *Nature Reviews*, 10 (4): 243-254.

Nagy, Z., & Soutoglou, E. (2009). DNA repair: easy to visualize, difficult to elucidate. *Special Issue – Imaging Cell Biology*. 19(11): 617-629.

Natale, F., Rapp, A., Yu, W., Maiser, A., Harz, H., Scholl, A., Grulich, S., Anton, T., Horl, D., Chen, W., Durante, M., Taucher-Scholz, G., Leonhardt, H.,Cardoso, M. C. (2017). Identification of the elementary structural units of the DNA damage response. *Nature Communications, 8*: 15760.

Nepomuceno, T. C., De Gregoriis, G., de Oliveira, F. M. B., Suarez-Kurtz, G., Monteiro, A. N., & Carvalho, M. A. (2017). The role of PALB2 in the DNA damage response and cancer predisposition. *International Journal of Molecular Sciences*, *18*(9), 1–20.

Nickoloff, J. A., Boss, M. K., Allen, C. P., La Rue S. M. (2017) Translational research in radiation-induced DNA damage signalling and repair. *Translational Cancer research*. 6: (S875-S891).

Noordermeer, S. M., Adam, S., Setiaputra, D., Barazas, M., Pettitt, S. J., Ling, A. K., Olivieri, M., Alvarez-Quilon, A., Moatti, N., Zimmermann, M., Annunziato, S., Krastev, D. B., Song, F., Brandsma, I., Frankum, J., Brough, R., Sherker, A., Landry, S., Gingras, A., Martin, A., van Attikum, H., Jonkers, J., Lord, C. J., Rottenberg, S., Durocher, D. (2018). The shieldin complex mediates 53BP1-dependent DNA repair. *Nature 560*: 116-121.

O'Driscoll, M. (2012). Diseases associated with defective responses to DNA damage. Cold Spring Harbor Perspectives in Biology, 4(12), 1–25.

Ochs, F., Karemore, G., Miron, E., Brown, J., Sedlackova, H., Rask, M. B., Lampe, M., Buckle, V. Schermelleh, L., Lukas, J., Lukas, C. (2019). Stabilization of chromatin topology safeguards genome integrity. *Nature*, *574*(7779), 571–574.

Ochs, F., Somyajit, K., Altmeyer, M., Rask, M.-B., Lukas, J., & Lukas, C. (2016). 53BP1 fosters fidelity of homology-directed DNA repair. *Nature Publishing Group*, *23*.

Panier, S., & Boulton, S. J. (2013). Double-strand break repair: 53BP1 comes into focus. *Nature reviews Molecular cell biology*, *15*: 7-18

Pelicci, S., Diaspro, A., & Lanzanò, L. (2019). Chromatin nanoscale compaction in live cells visualized by acceptor-to-donor ratio corrected Förster resonance energy transfer between DNA dyes. Journal of Biophotonics, 12(12), 1–13.

Pernal, S. P., Liyanaarachchi, A., Gatti, D. L., Formosa, B., Pulvender, R., Kuhn, E. R., Ramos, R., Naik, A. R., George, K., Arslanturk, S., Taatjes, D. J., & Jena, B. P. (2020). Nanoscale imaging using differential expansion microscopy. *Histochemistry and Cell Biology*, doi: 10.1007/s00418-020-01869-7. |(Epub ahead of print)

Pesce, L., Cozzolino, M., Lanzanò, L., Diaspro, A., & Bianchini, P. (2019). Measuring expansion from macro- to nanoscale using NPC as intrinsic reporter. *Journal of Biophotonics*, *12*(8).

Polato, F., Callen, E., Wong, N., Faryabi, R., Bunting, S., Chen, H.T., Kozak, M., Kruhlak, M.J., Reczek, C.R., Lee, W.H. et al. (2014) CtIP-mediated resection is essential for viability and can operate independently of BRCA1. *Journal of Experimental Medicine*. 211, 1027–1036.

Polo, S. E. (2014). Reshaping Chromatin after DNA Damage: The Choreography of Histone Proteins. *Journal of Molecular Biology*, *427*, 626–636.

Polo, S. E., & Almouzni, G. (2015). Chromatin dynamics after DNA damage: The legacy of the access-repair-restore model. *DNA Repair*.

Prakash, R., Zhang, Y., Feng, W., & Jasin, M. (2015). Homologous recombination and human health: The roles of BRCA1, BRCA2, and associated proteins. *Cold Spring Harbor Perspectives in Biology*, *7*(4), 1–27.

Preibisch, S., Saalfeld, S., Schindelin, J., & Tomancak, P. (2010). Software for bead-based registration of selective plane illumination microscopy data. Nature Methods, 7(6), 418–419.

Prochazkova, J., & Loizou, J. I. (2016). Programmed DNA breaks in lymphoid cells: Repair mechanisms and consequences in human disease. Immunology, 147(1), 11–20.

Reczek, C.R., Szabolcs, M., Stark, J.M., Ludwig, T. & Baer, R. (2013) The interaction between CtIP and BRCA1 is not essential for resection-mediated DNA repair ortumor suppression. *Journal of Cell Biology.* 201, 693–707.32

Reindl, J. Drexler, G. A., Girst, S., Greubel, C., Siebenwirth, C., Drexler, S. E., Dollinger, G., Friedl A. A. (2015) Nanoscopic exclusion between Rad51 and 53BP1 after ion irradiation in human HeLa cells. *Physical Biology 12,* 66005

Reindl, J., Girst, S., Walsh, D. W. M., Greubel, C., Schwarz, B., Siebenwirth, C., Drexler, G. A., Friedl, A. a., Dollinger, G. (2017). Chromatin organization revealed by nanostructure of irradiation induced γH2AX, 53BP1 and Rad51 foci. *Scientific Reports*, *7*, 40616.

Ryabichko S. S., Ibragimov A. N., Lebedeva L. A., Kozlov E. N., Shidlovskii Y. V. Super-Resolution Microscopy in Studying the Structure and Function of the Cell Nucleus. (2017). *ACTA NATURAE*, *9*(4), 42–51.

Salic, A., & Mitchison, T. J. (2008). A chemical method for fast and sensitive detection of DNA synthesis in vivo. *PNAS* 105(7): 2415-2420.

Savage, K. I., & Harkin, D. P. (2015). BRCA1, a "complex" protein involved in the maintenance of genomic stability. FEBS Journal. Blackwell Publishing Ltd.

Schermelleh L., Ferrand, A., Huser, T., Eggeling C., Biehlmaier, O., Drummen G.P.C. (2019) Super resolution microscopy demystified. Nature cell biology. 21: 72-84.

Schermelleh, L.., Heintzmann, R., Leonhardt, H. (2010). A guide to super-resolution fluorescence microscopy. *J. Cell Biol*, *190*(2), 165–175.

Schipler, A., Iliakis, G. (2013). DNA double-strand-break complexity levels and their possible contributions to the probability for error-prone processing and repair pathway choice, *Nucleic Acids Research. 41:* 7589–7605,

Schwarz, B., Friedl, A. A., Girst, S., Dollinger, G., & Reindl, J. (2019). Nanoscopic analysis of 53BP1, BRCA1 and Rad51 reveals new insights in temporal progression of DNA-repair and pathway choice. *Mutation Research/Fundamental and Molecular Mechanisms of Mutagenesis*, *816–818*, 111675.

Scientific Volume Imaging (no date). Deconvolution. Available at: https://svi.nl/Huygens-Deconvolution#Deconvolution. [Accessed on: 27/08/20]

Scientific Volume Imaging (no date). Non-linear iterative restoration methods. Available at: https://svi.nl/NonLinearIterativeMethod. [Accessed on 27/08/20].

Shahid, T., Soroka, J., Kong, E. H., Malivert, L., McIlwraith, M. J., Pape, T., West, S. C., Zhang, X. (2014). Structure and mechanism of action of the BRCA2 breast cancer tumor suppressor. Nature Structural and Molecular Biology, 21(11), 962–968.

Shaw, P. J. (2006). Comparison of widefield/deconvolution and confocal microscopy for three-dimensional imaging. *Handbook of Biological Confocal Microscopy: Third Edition*, (Dic), 453–467.

Shi, X., Li, Q., Dai, Z., Tran, A., Feng, S., Ramirez, A. D., Lin, Z., Wang, X., Chow, T. T., Seiple, I. B., Huang, B (2019). Label-retention expansion microscopy. *BioRxiv*, 687954.

Shin, Y., Chang, Y. C., Lee, D. S. W., Berry, J., Sanders, D. W., Ronceray, P., Wingreen, N. S., Haataja, M., Brangwynne, C. P. (2018). Liquid Nuclear Condensates Mechanically Sense and Restructure the Genome. Cell, 175(6), 1481–1491.e13.

Sibarita, J. (2005). Deconvolution Microscopy. *Advances in biochemical engineering/ biotechnology. 95*: 201-243.

Smeenk, G., & van Attikum, H. (2013). The Chromatin Response to DNA Breaks: Leaving a Mark on Genome Integrity. *Annual Review of Biochemistry*, *82*(1), 55–80.

Soria, G., Polo, S. E., & Ve Almouzni, G. (2012). Molecular Cell Review Prime, Repair, Restore: The Active Role of Chromatin in the DNA Damage Response. *Molecular Cell*, *46*, 722–734.

Sullivan, M. R., & Bernstein, K. A. (2018). RAD-ical new insights into RAD51 regulation. Genes, 9(12).

Swoger, J., Pampaloni, F., & Stelzer, E. H. K. (2014). Light-sheet-based fluorescence microscopy for three-dimensional imaging of biological samples. *Cold Spring Harbor Protocols*, *2014*(1), 1–8.

Symington, L. S., & Gautier, J. (2011). Double-Strand Break End Resection and Repair Pathway Choice. *Annual Review of genetics 45*: 247-71.

Tanaka, T. Fillmore, D., Sun, S., Nishio, I., Swislow, G., Shah, A. (1980). Phase transitions in ionic gels. *Physical Review Letters. 45,* 1636–1639.

ThermoFisher (2012). Flp-In T-REx Core Kit. Available at: https://www.thermofisher.com/order/catalog/product/K650001?SID=srch-srp-K650001#/K650001?SID=srch-srp-K650001. (Accessed: 07/04/2021)

Tillberg P.W., Chen F., Piatkevich K.D., Zhao Y., Yu C. English B.P., Gao L., Martorell A., Suk H., Yoshida F., DeGennaro E.M., Roossein D.H., Gong G., Senevirtene U., Tannenbaum S.R., Desimone R., Cai D., Boyden E.S.

(2016). Protein-retention expansion microscopy of cells and tissues labeled using standard fluorescent proteins and antibodies. *Nature Biotechnology* , *34*(9). 987-992.

Tillberg, P. W., & Chen, F. (2019). Expansion Microscopy: Scalable and Convenient Super-Resolution Microscopy. *Annual Review of Cell and Developmental Biology*, *35*(1): 683-701.

Tinevez, J. Y., Perry, N., Schindelin, J., Hoopes, G. M., Reynolds, G. D., Laplantine, E., Bednarek S. Y., Shorte, S. I., Eliceiri, K. W. (2017). TrackMate: An open and extensible platform for single-particle tracking. *Methods*, *115*, 80–90.

Truckenbrodt, S., Maidorn, M., Crzan, D., Wildhagen, H., Kabatas, S., & Rizzoli, S. O. (2018). X10 expansion microscopy enables 25-nm resolution on conventional microscopes. *EMBO Reports*, *19*(9), 1–12.

Uckelmann, M., Densham, R. M., Baas, R., Winterwerp, H. H. K., Fish, A., Sixma, T. K., & Morris, J. R. (2018). USP48 restrains resection by site-specific cleavage of the BRCA1 ubiquitin mark from H2A. Nature Communications, 9(1), 229. https://doi.org/10.1038/s41467-017-02653-3

Umen, J. G. (2005). The elusive sizer. *Current Opinion in Cell Biology*, *17*, 435–441.

Van De Linde, S., Löschberger, A., Klein, T., Heidbreder, M., Wolter, S., Heilemann, M., & Sauer, M. (2011). Direct stochastic optical reconstruction microscopy with standard fluorescent probes. *Nature Protocols*, *6*(7), 991–1009.

Vicidomini, G., Bianchini, P., & Diaspro, A. (2018). STED super-resolved microscopy. *Nature Methods*, *15*(3), 173–182.

Wallace, W., L.H. Schaefer, and J.R. Swedlow. (2001). A workingperson's guide to deconvolution in light microscopy. Biotechniques. 31:1076–1097.

Wassie, A. T., Zhao, Y., & Boyden, E. S. (2019). Expansion microscopy: principles and uses in biological research. *Nature Methods*, *16*(1), 33–41.

Wen, G., Vanheusden, M., Acke, A., Valli, D., Neely, R. K., Leen, V., & Hofkens, J. (2020). Evaluation of Direct Grafting Strategies via Trivalent Anchoring for Enabling Lipid Membrane and Cytoskeleton Staining in Expansion Microscopy. ACS Nano.

Whelan, D. R., Lee, W. T. C., Yin, Y., Ofri, D. M., Bermudez-Hernandez, K., Keegan, S., Fenyo, D., Rothenberg, E. (2018). Spatiotemporal dynamics of homologous recombination repair at single collapsed replication forks. *Nature Communications*, *9*: 3882.

Wooster, R., Bignell, G., Lancaster, J., Swift, S., Seal, S., Mangion, J., Collins, N., Gregory, S., Gumbs, C., Micklem, G., Barfoot, R., Hamoudl, R., Patel, S., Rice, C., Biggs, P., Hashim, Y., Smith, A., Connor, F., Arason, A., Gudmundsson, J., Flcenec, D., Kelsell, D., Ford, D., Tonin, P., Bishop, D. T., Spurr, N. K., Ponder, B. A. J., Eeles, R., Peto, J., Devliee, P., Cornelisse, C., Lynch, H., Narod, S., Lenoir, G., Eglisson, V., Barkadottir R. B., Easton, D. F., Bentley, D. R., Futreal, P. A., Ashworth, A. Stratton, M. R. (1995). Identification of the breast cancer susceptibility gene BRCA2. *Nature*, *378*(6559), 789–792.

Xu, H., Tong, Z., Ye, Q., Sun, T., Hong, Z., Zhang, L., Bortnick, A., Cho, S., Beuzer, P., Axelrod, J., Hu, Q., Wang, M., Evans, S. M., Murre, C., Lu, L., Sun, S., Corbett K. D., Cang, H. (2019). Molecular organization of mammalian meiotic chromosome axis revealed by expansion STORM microscopy. *Proceedings of the National Academy of Sciences*, *116*(37), 18423–18428.

Zhang, F., Ma, J., Wu, J., Ye, L., Cai, H., Xia, B., & Yu, X. (2009). PALB2 Links BRCA1 and BRCA2 in the DNA-Damage Response. *Current Biology*, *19*(6), 524–529.

Zhao Y, Bucur O, Irshad H, Chen F, Weins A, Stancu AL, Oh E-Y, DiStasio M, Torous V, Glass B et al. (2017) Nanoscale imaging of clinical specimens using pathology-optimized expansion microscopy. *Nature Biotechnology* 35, 757–764.

Zhao, W., Steinfeld, J. B., Liang, F., Chen, X., Maranon, D. G., Jian Ma, C., Kwon, Y., Rao, T., Wang, W., Sheng, C., Song, X., Deng, Y., Jiminez-Sainz, J., Lu, L., Jensen, R. B., Xiong, Y., Kupfer, G. M., Wiese, C., Greene, E. C., Sung, P. (2017). BRCA1-BARD1 promotes RAD51-mediated homologous DNA pairing. *Nature*, *550*(7676), 360–365.

Zimmermann, M., & de Lange, T. (2014). 53BP1: pro choice in DNA repair. *Trends in Cell Biology*, *24*(2), 108–117.